

UWMAK-II, A Conceptual D-T Fueled, Helium Cooled, Tokamak Fusion Power Reactor Design

B. Badger, R.W. Conn, G.L. Kulcinski, M.A. Abdou, R. Aronstein, H.I. Avci, R.W. Boom, E.T. Cheng, J. Davis, J.M. Donhowe, G.A. Emmert, Y. Eyssa, N.M. Ghoniem, S. Ghose, W. Houlberg, J. Kesner, W. Lue, C.W. Maynard, A. Mense, N. Mohan, H.A. Peterson, T.Y. Sung, I.N. Sviatoslavksy, D.K. Sze, W.F. Vogelsang, R. Westerman, L.J. Wittenberg, T.F. Yang, J. Young, and W. Young

October 1975

UWFDM-112

FUSION TECHNOLOGY INSTITUTE

UNIVERSITY OF WISCONSIN

MADISON WISCONSIN

UWMAK-II, A Conceptual D-T Fueled, Helium Cooled, Tokamak Fusion Power Reactor Design

B. Badger, R.W. Conn, G.L. Kulcinski, M.A. Abdou, R. Aronstein, H.I. Avci, R.W. Boom, E.T. Cheng, J. Davis, J.M. Donhowe, G.A. Emmert, Y. Eyssa, N.M. Ghoniem, S. Ghose, W. Houlberg, J. Kesner, W. Lue, C.W. Maynard, A. Mense, N. Mohan, H.A. Peterson, T.Y. Sung, I.N. Sviatoslavksy, D.K. Sze, W.F. Vogelsang, R. Westerman, L.J. Wittenberg, T.F. Yang, J. Young, and W. Young

Fusion Technology Institute
University of Wisconsin
1500 Engineering Drive
Madison, WI 53706

http://fti.neep.wisc.edu

October 1975

UWFDM-112

Preface

This report represents the efforts of many scientists and engineers whose purpose is to better understand the technological aspects of tokamaks as potential fusion power reactors. The method of approach to this broad problem is to carry through a comprehensive conceptual power reactor design such that the problems presented can be understood in their proper context. This report is a presentation of the detailed understanding we have developed of this particular reactor concept. A quantitative assessment of most technological problems is presented and, in some cases, potential solutions are developed. It is our hope that a comprehensive study of this type will help guide the continually growing worldwide research effort in fusion technology and will provide basic input information for many other research groups on topics not directly addressed in the report.

The preparation of the report itself was a difficult and trying task that was ably managed by our secretarial staff. We therefore particularly acknowledge the diligent work of Mrs. Connie Linehan, Mrs. Suzan Steindorf, and Mrs. Sandy Ingham, who did the bulk of the typing and Mrs. Debby Kamperschroer who followed the details of having the report printed.

The research represented by this report was carried out with financial support from the United States Energy Research and Development Administration, Division of Controlled Thermonuclear Research, the former U. S. Atomic Energy Commission, and the Wisconsin Electric Utilities Research Foundation. We clearly would not have been able to complete this study without the support of these government and private agencies and we thank them for their confidence in us.

Robert W. Conn
Professor and Director
Wisconsin Fusion Technology Program

Gerald L. Kulcinski
Professor and Associate Director
Wisconsin Fusion Technology Program

UWMAK-II

A CONCEPTUAL TOKAMAK POWER REACTOR DESIGN

by

The University of Wisconsin Fusion Feasibility Study Group

B. Badger
R. W. Conn
G. L. Kulcinski
M. A. Abdou
R. Aronstein[a]
H. I. Avci
R. W. Boom
T. E. Cheng
J. Davis[b]
J. M. Donhowe
G. A. Emmert
Y. Eyssa
N. M. Ghoniem
S. Ghose[a]
W. Houlberg
J. Kesner
W. Lue
C. W. Maynard
A. Mense
N. Mohan
H. A. Peterson
M. M. H. Ragheb
T. Y. Sung
I. Sviatoslavsky
D. K. Sze
W. F. Vogelsang
R. Westerman[c]
L. J. Wittenberg[d]
T. F. Yang
J. Young[c]
W. D. Young

UWFDM-112

Fusion Technology Program
Nuclear Engineering Department
The University of Wisconsin
Madison, Wisconsin 53706
U.S.A.

October 1975

(a) Bechtel Corporation
(b) McDonnell-Douglas Astronautics Company-East
(c) Battelle Northwest Laboratories
(d) Monsanto Chemical Corp., Mound Laboratories

TABLE OF CONTENTS

	Page
Preface	1
Summary	2
I. Overview	I-1
A. Introduction	I-A-1
B. Description of Main Nuclear Island Design	I-B-1
1. Basic Operating Cycle, Plasma & Divertor Conditions, and the Vacuum Systems	I-B-1
2. Magnets for UWMAK-II	I-B-13
3. Blanket and Shield Design	I-B-24
a. Module Design	I-B-24
b. Neutronics	I-B-27
c. Thermal Hydraulics	I-B-32
d. Mechanical Design and Blanket Disassembly	I-B-33
4. Tritium Considerations	I-B-39
5. Radiation Damage	I-B-45
6. Radioactivity and Afterheat	I-B-58
C. Power Cycle for UWMAK-II	I-C-1
D. Plant Design for UWMAK-II	I-D-1
E. Resource Requirements for UWMAK-II Type Reactors	I-E-1
F. Economic Study	I-F-1
II. Plasma and Divertor	II-1
A. Plasma & Divertor Considerations for Tokamaks	II-A-1
1. Principles of Tokamak Operation	II-A-2
2. Transport in Tokamaks and Scaling Laws	II-A-8
a. Classical Theory	II-A-8
b. Neoclassical Theory	II-A-10
c. Anomalous Transport	II-A-17
3. Impurities in Tokamak Reactors	II-A-26
4. The Carbon Curtain Concept	II-A-31
5. Impurity Diffusion in Tokamaks; Impact on Divertor Considerations.	II-A-36
B. Plasma and Divertor Analysis for UWMAK-II	II-B-1
1. Fuel Cycle and Dimensions	II-B-1
2. Startup	II-B-6
3. Neutral Beam Heating and Plasma Burn	II-B-16
1. Calculational Model	II-B-16
2. Heating to Plasma Burn Conditions	II-B-23
3. Plasma Burn Conditions	II-B-31
4. Divertor Operation and Magnetic Field Design for UWMAK-II	II-B-37
a. General Considerations	II-B-37
b. Magnetic Field Design	II-B-39
c. Estimates of the Divertor Performance in UWMAK-II	II-B-42
d. Preliminary MHD Equilibrium and Stability Studies	II-B-49
5. Analysis of Losses Due to Toroidal Field Ripple and Determination of the Number of TF Coils on UWMAK-II.	II-B-57
6. Vacuum Pumping and Particle Collection Systems for UWMAK-II.	II-B-68
a. Cryo-vacuum Pumps	II-B-68
1. Cryo-vacuum Pump Specifications	II-B-70
2. Cryo-vacuum Pump Regeneration	II-B-72
3. Cryo-vacuum Pump System Design	II-B-72

	Page
b. Liquid Lithium Trapping Surfaces	II-B-74
c. Evacuation of the Magnet Enclosure	II-B-77

	Page
III. Magnet System	III-1
A. Toroidal Field Magnets	III-A-1
1. Specifications	III-A-3
2. Construction Techniques	III-A-3
3. General Restraints and Design Factors	III-A-3
a. Vertical and Radial Support Structure	III-A-8
b. Radiation Damage to the Copper Stabilizer	III-A-10
c. Dewars	III-A-10
4. Lateral Support and Structural Safety	III-A-14
a. Design Requirements Based on the Failure of One Toroidal Field Magnet	III-A-14
b. Design Requirements based on the failure of two adjacent toroidal field magnets	III-A-17
c. Shell Design	III-A-17
d. Dewar Design	III-A-19
e. Dewar Strut Design	III-A-20
f. Design Requirements	III-A-23
g. Design requirements for the external pressure on the toroidal shell structure due to the vacuum	III-A-23
h. Design to allow for penetration of the toroidal shells	III-A-23
B. Divertor and Transformer Coils	III-B-1
1. Specifications	III-B-1
a. Description and Specifications	III-B-1
b. Comparison with UWMAK-I	III-B-1
2. Design Factors	III-B-4
a. Composite Conductor Design	III-B-4
b. Stress Analysis and Reinforcement	III-B-10
c. Coil Winding	III-B-10
d. Dewars and Supports for the Divertor Coils	III-B-11
3. AC Losses in Divertor and Transformer Coils	III-B-11
a. Eddy Current Loss	III-B-11
b. Coupling Loss	III-B-13
c. Hysteresis Loss	III-B-14
C. Magnetic Field Structure	III-C-1
1. Toroidal Field Structures	III-C-1
2. Poloidal Field Structure	III-C-1
3. Stray Fields	III-C-18
4. Interaction of the "D" Coils with the Poloidal Field	III-C-18
D. Refrigeration	III-D-1
1. Heat Losses	III-D-1
2. Refrigerators	III-E-1
E. Power Supplies	III-E-1
1. Toroidal Field Magnets	III-E-1
2. Divertor and Transformer Coils	III-E-1
a. Basic System	III-E-4
b. Circuit Arrangement	III-E-4
F. Cost Estimate	III-F-1
1. Toroidal Field Magnets	III-F-1
2. Divertor and Transformer Coils	III-F-1
3. Refrigeration System	III-F-2
4. Power Supplies	III-F-2

	Page
a. Toroidal Field Magnets	III-F-2
b. Poloidal Field Magnets	III-F-3
5. Entire Magnet System	III-F-3
IV. Blanket and Shield	IV-1
A. Introduction and General Design Philosophy	IV-A-1
B. General Materials Considerations for Blanket and Shield Design.	IV-B-1
1. Coolants	IV-B-1
2. Structure	IV-B-2
3. Neutron Multipliers	IV-B-2
4. Breeder Materials	IV-B-5
a. Lithium	IV-B-5
b. Intermetallic Compounds	IV-B-5
c. Non-Metallic Compounds	IV-B-7
C. Neutronics and Photonics	IV-C-1
1. General Survey Studies of Low Li Inventory Blankets	IV-C-1
2. UWMAK-II Blanket and Shield Design Studies	IV-C-8
D. Heat Transfer Analysis	IV-D-1
1. General Discussions	IV-D-1
2. Blanket Design Considerations	IV-D-2
3. General Design Guidelines and System Description	IV-D-5
4. Pressure Drop and Heat Transfer Calculations	IV-D-8
E. Mechanical Design Considerations	IV-E-1
1. Blanket Stresses	IV-E-5
2. Overall Support of the Blanket	IV-E-7
3. Shield Design	IV-E-10
4. Front Wall Replacement	IV-E-11
F. Final Neutronics Analysis by Monte Carlo of the UWMAK-II Design	IV-F-1
A. Macrocell Model	IV-F-1
B. Sensitivity Studies	IV-F-6
C. Comparison with Previous Calculations	IV-F-13
D. Conclusions and Recommendations	IV-F-13
G. Tritium Removal	IV-G-1
1. Release Rate	IV-G-1
2. Tritium Inventory Considerations	IV-G-2
a. Diffusion of Tritium	IV-G-3
b. Solubility of Tritium	IV-G-5
c. Tritium Inventory at Higher Density for the Breeding Material.	IV-G-6
d. Tritium Extraction System for Breeding Cycle	IV-G-9
3. Tritium Extraction from Helium Coolant	IV-G-14
a. Tritium Escape into Steam System	IV-G-14
b. Tritium Permeation Through the Sodium Intermediate Heat Transfer System	IV-G-19
4. Divertor Tritium Recovery System	IV-G-22
H. Radiation Damage	IV-H-1
1. Introduction	IV-H-1
2. The Scope of Radiation Damage Problems in UWMAK-II	IV-H-1
3. Bulk Radiation Damage to Carbon Curtain	IV-H-3
4. Radiation Damage to 316 Stainless Steel Structural Material	IV-H-10
a. Displacement and Gas Production Rates in UWMAK-II	IV-H-10
b. Transmutation Rates in UWMAK-II 316 Stainless Steel	IV-H-15

	Page
c. Sputtering Effects on UWMAK-II Carbon Curtain and 316 Stainless Steel First Wall	IV-H-18
d. Void Induced Swelling in 316 Structure of UWMAK-II	IV-H-21
e. Effect of UWMAK-II Environment on the Mechanical Properties of 316 SS	IV-H-30
5. Radiation Effects to $LiAlO_2$	IV-H-45
6. Radiation Damage to Beryllium Neutron Multiplier in UWMAK-II	IV-H-50
7. Radiation Damage to UWMAK-II Graphite Reflector	IV-H-53
8. Radiation Effects to UWMAK-II Shielding	IV-H-53
9. Radiation Damage to UWMAK-II Superconducting Magnet	IV-H-55
I. Radioactivity, Afterheat and Safety Considerations	IV-I-1
1. Introduction	IV-I-1
2. Radioactivity Calculations	IV-I-1
3. Biological Hazard Potential	IV-I-5
4. Afterheat Calculations	IV-I-16
5. Emergency Cooling of the First Wall	IV-I-23
J. Fabrication Procedures and Cost Estimates for UWMAK-II Blanket	IV-J-1
V. Energy Conversion System	V-1
A. Introduction	V-A-1
B. Selection of the Energy Storage System	V-B-1
a. Heat of Vaporization	V-B-6
b. Solids	V-B-7
c. Liquids	V-B-11
d. Stagnant Sodium System	V-B-12
e. Circulating Sodium System	V-B-12
f. Heat of Fusion	V-B-14
C. Blanket Energy Transport and Conversion	V-B-15
1. Primary Helium System	V-C-1
2. Intermediate Sodium System	V-C-1
3. Steam Cycle	V-C-5
4. Cooling Water System	V-C-5
D. Divertor Energy Transport and Conversion	V-C-5
1. Primary Lithium System	V-D-1
2. Intermediate Sodium System	V-D-1
3. Steam Cycle	V-D-1
4. Cooling Water System	V-D-3
E. Shield Energy Rejection	V-D-3
1. Primary Helium System	V-D-3
2. Cooling Water System	V-D-3
F. Auxiliary Power	V-D-3
G. Plant Performance	V-D-5
VI. Plant Design	VI-1
A. Introduction	VI-A-1
B. Plant Arrangement	VI-B-1
1. General	VI-B-1
2. Containment Building	VI-B-2
a. Function	VI-B-2
b. Equipment Location	VI-B-2
c. Equipment Handling	VI-B-5
d. Penetrations	VI-B-9

	Page
3. Reactor Service Building (Hot Cell)	VI-B-9
4. Reactor Auxiliary Building	VI-B-9
5. Heat Exchanger Building	VI-B-11
6. Turbine Building	VI-B-12
7. Control Building	VI-B-12
8. Other Buildings & Facilities	VI-B-13
a. Reprocessing & Fabrication Buildings	VI-B-13
b. Radwaste Building	VI-B-13
c. Blanket Module Transfer Tunnel	VI-B-13
d. Inductive Energy Storage Building	VI-B-13
e. Helium Storage Building	VI-B-13
f. Administration Building	VI-C-1
g. Warehouse & Shop Building	VI-C-1
h. Diesel-Generator Building	VI-C-1
C. Civil/Structural	VI-C-1
1. General	VI-C-1
2. Plant Structure	VI-C-2
a. Reactor Containment Building	VI-C-2
b. The Reactor Service (Hot Cell Building)	VI-C-3
c. Heat Exchanger Building	VI-C-3
D. Conclusions	VI-D-1
VII. Resources and Economics	VII-1
A. Materials Resource Assessment for UWMAK-II	VII-A-1
1. Materials Requirements of UWMAK-II	VII-A-1
a. Nuclear Island Requirements	VII-A-3
b. Balance of Plant Requirements	VII-A-4
2. Availability of Metals	VII-A-10
a. General Statement	VII-A-10
b. Metals for 316 SS	VII-A-10
c. Aluminum	VII-A-13
d. Boron	VII-A-13
e. Silicon	VII-A-14
f. Lead	VII-A-14
g. Niobium	VII-A-14
h. Copper	VII-A-14
i. Lithium	VII-A-15
j. Yttrium	VII-A-15
k. Zirconium	VII-A-15
l. Sodium	VII-A-15
m. Beryllium	VII-A-15
B. Economics	VII-B-1
1. The UWMAK-II Operating Cycle	VII-B-2
2. Fusion Reactor Plant Factor	VII-B-6
a. The Biennial Wall Replacements	VII-B-6
b. Unscheduled Outage Time	VII-B-7
c. The Length of the Burn Period	VII-B-7
d. The Length of the Rejuvenation Period	VII-B-9
e. The General Plant Factor Correlation	VII-B-9
f. Summary	VII-B-10
3. Capital Costs	VII-B-10
4. The Electricity Production Cost	VII-B-36
a. The Operations and Maintenance Cost	VII-B-36

	Page
b. Fuel Costs	VII-B-41
c. The Annual Return on Capital	VII-B-41
d. The Total Electricity Cost	VII-B-43
5. Summary and Critical Analysis	VII-B-44
a. Low Inner Wall Neutron Flux	VII-B-44
b. Low Thermal Efficiency	VII-B-44
c. Use of Beryllium Neutron Multiplier and Lithium Aluminate as a Stationary Breeding Material	VII-B-44
d. Short Inner Wall Life	VII-B-45
e. Intermittent Reactor Operation	VII-B-45
f. High Shield and Magnet Costs	VII-B-45
g. High Neutral Beam Injector Costs	VII-B-45
h. Use of Stainless Steel	VII-B-46
VIII. Conclusions	VIII-1
Appendix A	A-1

Summary

UWMAK-II is a conceptual design study of a circular, low β tokamak fusion reactor. The primary fuels are deuterium and tritium and the breeding material is the solid compound, lithium aluminate ($LiAlO_2$). The structural material of the blanket is 316 stainless steel and the primary coolant is helium. The design has a low aspect ratio, 2.6, and a low value for the toroidal field on axis, 3.57 T. The maximum field at the toroidal field (TF) magnets is 8.3T and all TF magnets are fully cryogenically stable. There are 24 such coils which have the shape of a modified constant tension "D". An air core transformer is used with superconducting windings outside the TF coils. The vertical field magnets, on the other hand, are inside the extended "D" shaped TF coils and have been well overdesigned to provide extra reliability. The energy stored in the poloidal field after the 10 second current rise is only 1.9 MW-hr and a 1 MW-hr inductive energy storage unit together with 500 MWe from the line is sufficient to energize the plasma current. After the current rise phase, 200 MW of neutral beams are used to heat the plasma to ignition in another 20 seconds. The superconductor in all coils is NbTi.

The plasma current in UWMAK-II is 14.9 MA at q(a) equal to 2.3. The poloidal beta is 2.275 and the toroidal beta is 0.064. The plasma parameters during the burn period of 5400 seconds have been determined using relatively pessimistic scaling laws based on trapped particle instabilities. The average electron temperature is 12 keV, the average ion temperature is 13.2 keV, the $n\tau_E$ value is $2.8 \times 10^{14} cm^{-3}$-s, and the fractional burnup is 4.85%. The average ion density is $7.33 \times 10^{13} cm^{-3}$, the energy containment time is 3.64 s and the particle confinement time is 8.28 s. The plasma equilibrium is thermally stable based on trapped ion mode scaling and cold pellet fueling is assumed to maintain the density over the burn period.

A double null poloidal divertor has been designed for impurity control and particle pumping. Analysis indicates plasma in the scrape off zone will have a loss cone distribution and be unstable against the usual microinstabilities associated with magnetic mirror machines. We estimate that the divertor will be greater than 99% efficient at collecting particles diffusing from the plasma.

Since neutron sputtering will generate impurities that can return to the plasma, the concept of using a 2 dimensional woven carbon cloth as a curtain to protect the vacuum chamber wall has been developed and included in UWMAK-II. Detailed analysis shows that much higher levels of carbon (up to several percent) can be tolerated compared with high Z impurities such as Fe, Mo, and W. Further, assuming the divertor is greater than 99% efficient at collecting particles diffusing from the plasma but only 10% efficient at shielding the plasma, the carbon concentration ($\frac{n_c}{n_e}$) is calculated to be 0.22% assuming the impurity confinement time, τ_{imp}, is equal to $\tau_{D,T}$. For multiples of the τ_{imp}/τ_{DT} ratio (M), $\frac{n_c}{n_e} = .0002M$. Thus, M values of 100 to 1000 may be acceptable under these circumstances and still allow long burn times. Based on this analysis, it is also

assumed that the levels of low Z impurities in the plasma are essentially negligible and that there are no sources of high Z impurities.

The blanket system uses 316 stainless steel with helium cooling and lithium aluminate as the breeder. Beryllium is used as the neutron multiplier and estimates of the breeding ratio range from 1.06 based on Monte Carlo calculations to 1.19 based on a one dimensional cylindrical neutronics analysis. The energy per fusion event is 21.56 MeV, the wall loading is 1.16 MW/m^2 and the tritium inventory in the blanket is estimated to be relatively low, 725 g.

The interaction of the solid blanket components with the D-T plasma radiation environment produces radiation damage which requires significant design changes in the UWMAK-II structure. The most significant of these changes is the requirement that certain components be replaced on a frequency ranging from 2 to 10 years. The most critical material is the 316 SS first wall which will lose ductility such that it may not be able to safely accomodate the strains produced by the ~ 4500 start up and shut down cycles per year. It has been determined that the first wall must be replaced every two years and because of dimensional instabilities in the carbon curtain, $LiAlO_2$, and Be multiplier, these materials will be replaced on the same frequency. The rest of the UWMAK-II blanket structure and graphite reflector will be replaced every 10 years. The shield and magnets have been designed to last the entire lifetime (~30 years) of the reactor.

Pertinent radiation damage parameters are maximum displacement rates of ~8.6 dpa/year (at 80% plant factor) in the first wall with ~200 appm He generated in the steel. The displacement rates in the carbon curtain are also ~8.6dpa/year but as much as 2200 appm He is produced per year. The major damage parameters in the $LiAlO_2$ and Be are the high helium production rates of 30,000 and 2400 appm He per year respectively. The graphite reflector suffers a maximum of 1.8 dpa per year and the maximum dpa rates in the metals of the shield and magnet are 0.12 and 8×10^{-7} dpa/year respectively.

The tritium inventory in the entire reactor is 17.7 kg with the majority of that (73%) required for a 1 day reserve in the event of a breakdown in the T_2 processing equipment in the divertor region. The T_2 leakage rate to the environment is ~ 1 curie per day through the steam cycle.

The total radioactivity in UWMAK-II is $\sim 10^6$ $Curies/MW_{th}$ after two years of operation. This activity is mainly due to Mn-54 and Ni-57 (75%) and requires ~10 years to decay by a factor of 10.

This means that repair of module failures or changing of first walls will have to be done remotely, increasing the costs associated with the reactor. The afterheat is slightly over 1% of the thermal power level and when spread out over the large mass in the blanket results in a relatively low afterheat power density (<0.1 W/g).

The main power cycle is based on a He-Na intermediate heat exchanger and a Na-steam heat exchanger. The intermediate sodium loop is used to minimize tritium leakage through the power cycle and to provide a working fluid for thermal energy storage during the plasma burn such that the plant electrical output is constant even though the reactor has a pulsed power cycle.

Detailed materials resource studies have been carried out to analyze the impact of an economy of UWMAK-II type reactors. Beryllium particularly presents a problem with regard to adequate resources and several other materials, such as chromium and nickel, may present problems of procurement. A general economic study has been made of UWMAK-II which indicates a capital cost of ~$950/kWe and an operating and maintenance cost of ~25 mills/kw-hr. The prime determinants of the cost are identified and alternatives are discussed.

A general set of conclusions is presented in the last chapter of the report.

I. Overview

I-A. Introduction

This report describes the conceptual design of a Tokamak fusion power reactor, UWMAK-II. The aim of this study is to perform a self consistent and thorough analysis of a probable future fusion power reactor in order to assess the technological problems posed by such a system and to examine feasible solutions. Such work provides a perspective on the relative difficulties and importance of various technical problems and can act as a guide for further research. In earlier work,[1-3] we presented a conceptual tokamak fusion reactor design, UWMAK-I based on the D-T cycle with liquid lithium acting as the coolant, moderator, and tritium breeding material while contained in a 316 stainless steel structure. That design was conservative in terms of materials choices and operating conditions and it generated several fundamental results. One of the most important is the need to periodically replace the reactor first walls because of radiation damage. Overall, there are many advantages to a system like UWMAK-I and these are documented in reference 1-3. Nevertheless, two of the major areas of concern were the maximum temperature limit of 500°C in the stainless steel due to compatibility problems and the relatively large tritium inventory (8.7 kg) in the liquid lithium coolant. In addition, there were twelve toroidal field coils which produced a large (~20%) field ripple and the removal and disassembly of the first wall for repair or replacement involved moving very heavy modules (3500 metric tons).

UWMAK-II is a conceptual Tokamak fusion reactor designed to deliver 1716 MW_e continuously and to generate 5000 MW(th) during the plasma burn. The structural material is 316 stainless steel and the primary coolant is helium. As in our earlier work, most design choices were guided by the philosophy that decisions should be based, wherever possible, on present-day technological capabilities. The major characteristics of the design are summarized in Table I-1 and two general views of the main reactor are shown in Fig. I-1 and I-2. As can be seen, UWMAK-II is a low aspect ratio, low field design and includes a double null, axisymmetric poloidal field divertor for impurity control. In addition, a carbon curtain, made of two dimensional woven carbon fiber, is mounted on the first vacuum chamber wall to protect the plasma from high Z impurities and to protect the first wall from erosion by charged particle bombardment.

The blanket is designed to minimize the inventory of both tritium and lithium while achieving a breeding ratio greater than one. This has led to a blanket design based on the use of a solid breeding material ($LiAlO_2$) with beryllium as a neutron multiplier. The lithium is enriched to 90% ^6Li and the blanket coolant is helium at a maximum pressure of 750 psia ($5.2 \times 10^6 N/m^2$). A cell of the UWMAK-II blanket design is shown in Fig. I-3. The breeding ratio is between 1.11 and 1.19 based on one-dimensional discrete ordinates transport calculations, depending on the method of homogenization. Detailed Monte Carlo calculations, which take into account the more complicated geometry, give a breeding ratio of 1.06. The total energy per fusion is 21.56 MeV, which is fairly high.

Table I-1.

MAJOR CHARACTERISTICS OF UWMAK-II

Structural Material	316 SS
Coolant	He
Breeding Material	$LiAlO_2$
Neutron Multiplier	Be
Fuel Cycle	(D-T), Li
Number of Toroidal Field Magnets	24
Magnet Superconductor	TiNb
Impurity Control Methods	Divertor + Low Z Liner
Neutron Wall Loading	1.16 MW/m^2
Plasma Dimensions	
Major Radius	13 m
Plasma Radius	5 m
Aspect Ratio	2.6
First Wall Radius	5.5m
Burn Time	5400 sec.
Rejuvenation Time	330 sec.
Duty Factor	0.942
Power Cycle	He-Na-Steam
Estimated Plant Factor	0.80
Power Output During Plasma Burn	5000 MW(th)
Average Electrical Power	1716 MW_e

UWMAK-II Tokamak Fusion Reactor

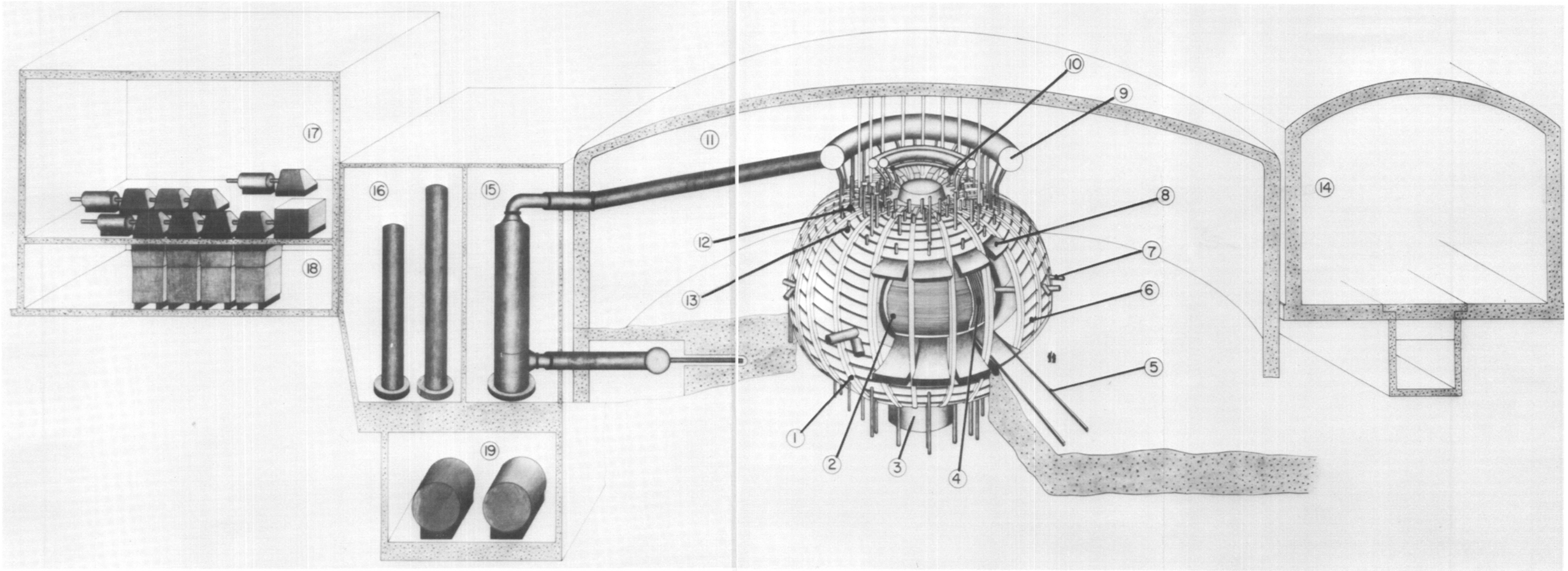

1 TOROIDAL FIELD MAGNETS (24)
2 PLASMA CHAMBER
3 CENTRAL SUPPORT COLUMN
4 BLANKET MODULES
5 BLANKET REMOVAL TRACKS

6 LATERAL SUPPORT STRUCTURE & SECONDARY VACUUM WALL
7 FUELING PORTS (4)
8 SHIELD
9 HELIUM COOLANT HEADERS
10 TRANSFORMER COIL (18)

11 OVERHEAD SUPPORT BEAMS
12 VERTICAL FIELD COIL SUPPORTS
13 HELIUM INLET & OUTLET PIPES
14 SERVICE HOT CELL
15 PRIMARY HEAT EXCHANGER ROOM
16 SECONDARY HEAT EXCHANGER ROOM

17 TURBINE & GENERATOR ROOM
18 CONDENSER ROOM
19 DUMP TANKS

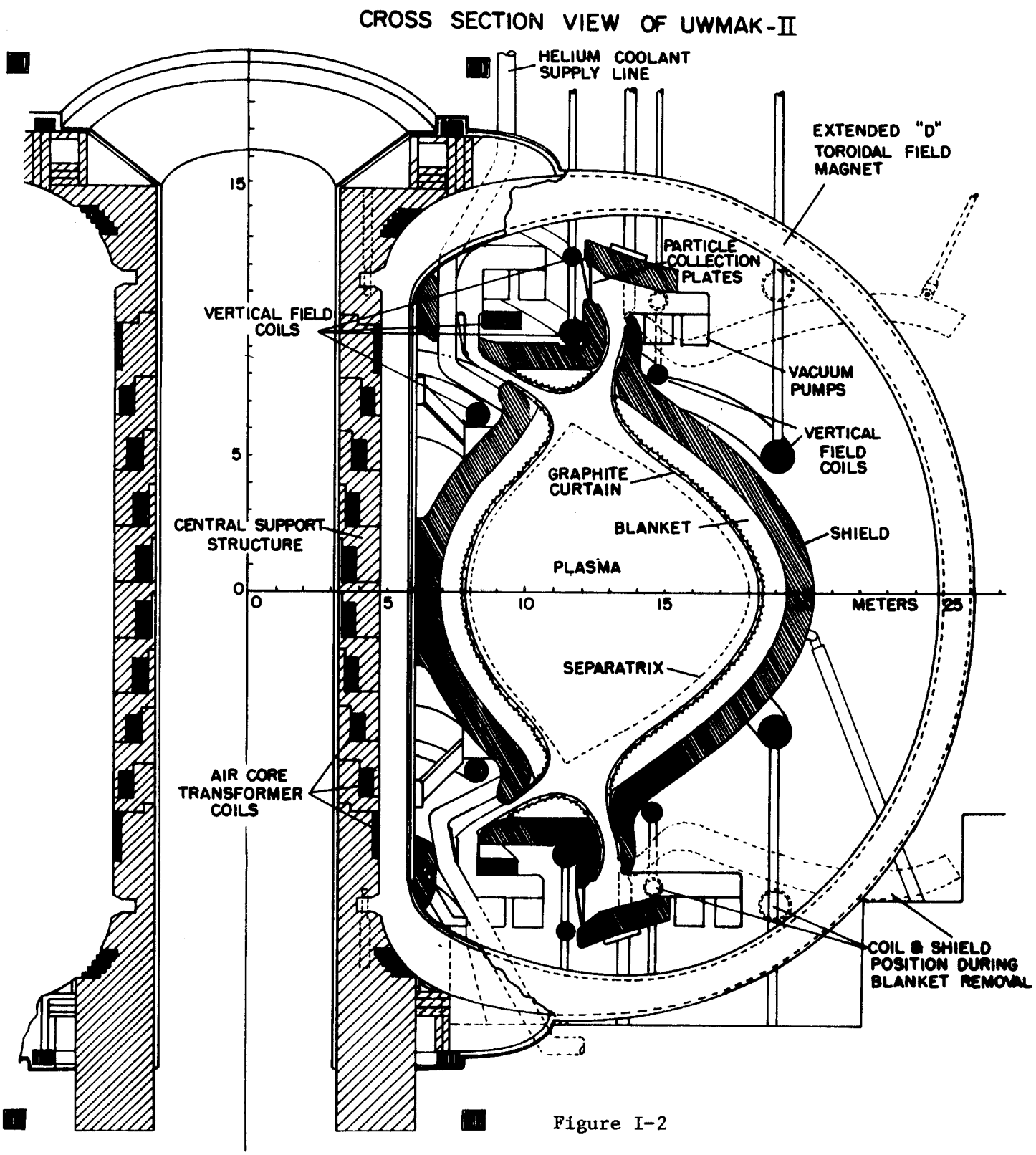
CROSS SECTION VIEW OF UWMAK-II
HELIUM COOLANT SUPPLY LINE
EXTENDED "D" TOROIDAL FIELD MAGNET
PARTICLE COLLECTION PLATES
VERTICAL FIELD COILS
VACUUM PUMPS
VERTICAL FIELD COILS
GRAPHITE CURTAIN
BLANKET
SHIELD
CENTRAL SUPPORT STRUCTURE
PLASMA
SEPARATRIX
AIR CORE TRANSFORMER COILS
COIL & SHIELD POSITION DURING BLANKET REMOVAL
15
5
0
0
5
10
15
METERS
25

Figure I-2

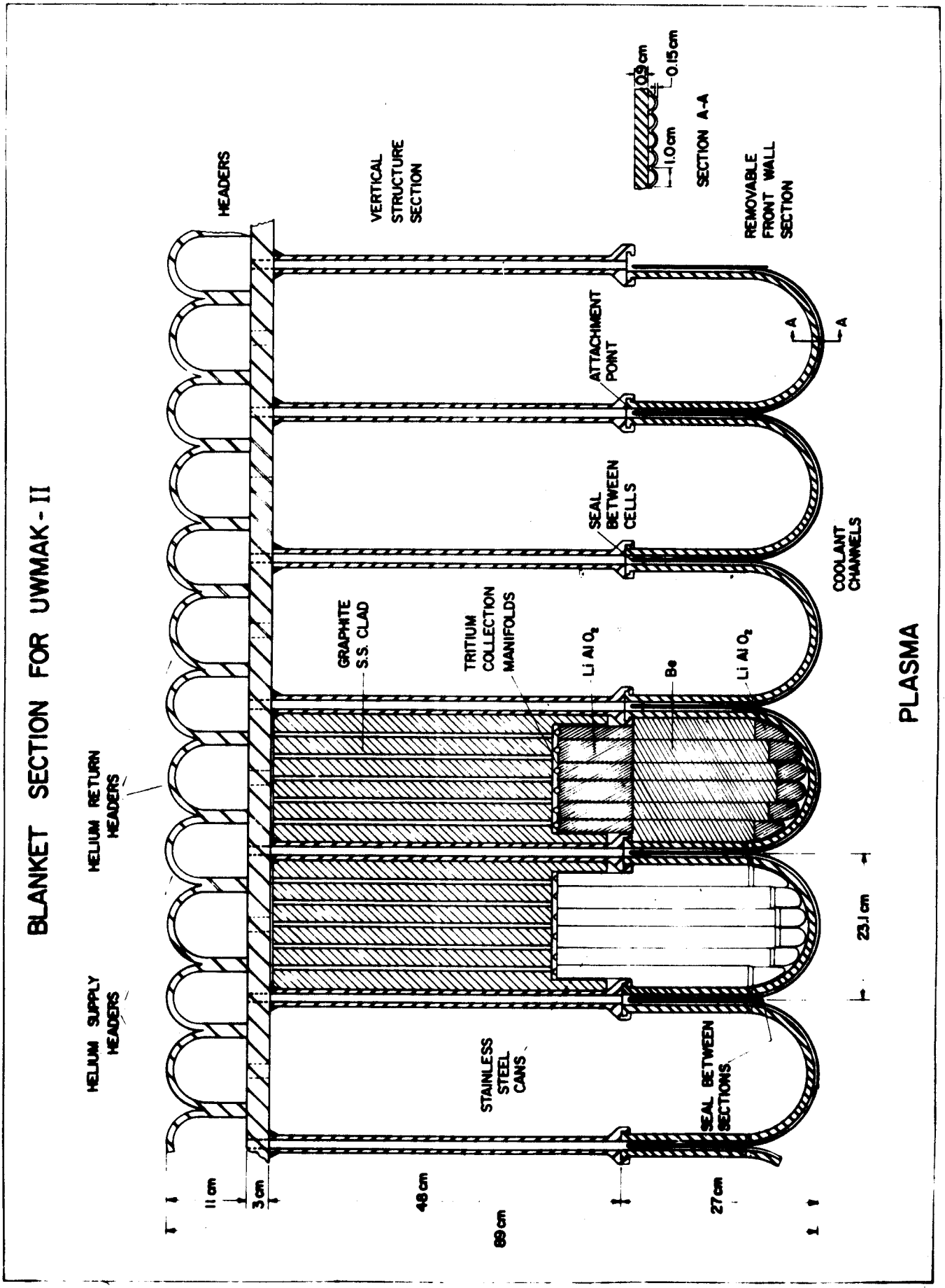
BLANKET SECTION FOR UWMAK-II
HELIUM SUPPLY HEADERS
HELIUM RETURN HEADERS
HEADERS
VERTICAL STRUCTURE SECTION
REMOVABLE FRONT WALL SECTION
SECTION A-A
0.9 cm
0.15 cm
1.0 cm
ATTACHMENT POINT
SEAL BETWEEN CELLS
COOLANT CHANNELS
GRAPHITE S.S. CLAD
TRITIUM COLLECTION MANIFOLDS
Li Al O2
Be
Li Al O2
STAINLESS STEEL CANS
SEAL BETWEEN SECTIONS
PLASMA
11 cm
3 cm
48 cm
27 cm
89 cm
23.1 cm
A
A

Figure I-3

In addition, the use of solid breeding material may allow the tritium inventory in the blanket to be very low, approximately ~130g if 50% dense and ~730g if 90% dense $LiAlO_2$ is used and if sintering of the ceramic can be prevented. The radiation damage problems are similar to those in the UWMAK-I study[1] and the results for UWMAK-II again indicate that periodic replacement of the first 20 cm of the blanket modules approximately every two years will be required.

The toroidal field (TF) magnets are a set of 24 "extended D" superconducting coils of TiNb in Cu with stainless steel structure. The extension of the "D" shape beyond the outside edge of the shield allows the shield to be opened as indicated in Fig. 1 and a blanket module removed between coils without removing the TF coils. The vertical field (VF) coils have been deliberately placed inside the TF coils to minimize the energy stored in the poloidal magnetic field. This value is now 10.4×10^9 joules compared to 53.4×10^9 joules in UWMAK-I, where the VF windings are placed outside the TF coils. The design philosophy for the coils is crucial when they are placed inside the TF set and this is discussed Chapter III. A superconducting air-core transformer is used and the transformer (OH) windings are outside the main TF coils.

In the next three sections of this overview, we describe the main technical aspects of the UWMAK-II study including the results and resolution of many of the technical problems such a system will pose.

I-B. Description of Main Nuclear Island Design

I-B-1. Basic Operating Cycle, Plasma and Divertor Conditions, and the Vacuum Systems

UWMAK-II uses deuterium and tritium as the basic nuclear fuels and lithium for breeding tritium. The basic operating cycle for the reactor is based on the assumption that the combination of a divertor and a low Z liner will provide sufficient impurity control to allow long plasma burns. Nevertheless, the burn time is finite (5400 sec) and the outline of the basic cycle is given in Fig. I-4. During the initial 10 seconds, the plasma current rises linearly with time to its final value of 14.9 MA. This means that the average plasma current density is 19 A/cm^2 and that the plasma radius increases from some small value ($\lesssim$ 50 cm) to 5 m as $\sqrt{t}$ over this time period. During this initial 10 seconds, the currents in the vertical field (VF) or divertor coils also increase to their final values. The ohmic heating (OH) windings change current in such a way as to provide the requisite time changing flux to drive the plasma current. The placement of the OH and VF coils in an R-Z plane are shown in Fig. I-5 and the currents in these coils are listed in Table I-2. Over the next 5420 seconds, the currents in the OH windings continue to change, albeit slowly, in order to maintain the plasma current against the resistive drop due to the finite plasma conductivity at the operating conditions. Thus, the values of the current in the OH windings at the end of the plasma burn are also listed in Table I-2.

Following the 10 second current rise phase, there is a 20 second period during which 200 MW of 500 keV neutral deuterium beams are used to heat the plasma to the conditions required during the burn phase. The scenario is shown in Fig. I-6 where the average ion temperature is plotted versus time. Neutral beam injection begins at t=10 sec into a plasma with an average electron density of $4 \times 10^{13} cm^{-3}$. At t=17 sec, the average density is raised to $7.7 \times 10^{13}/cm^3$ without causing the plasma to become

One operating cycle

	Phase 1		Phase 2	Phase 3			
150 Sec. Transformer Coil Reset	10 Sec. Current Rise Time	20 Sec. Heating to Operating Conditions	90 Minute Burn Period	100 Sec. Plasma Current Decrease	50 Sec. Chamber Purge	150 Sec. Transformer Coil Reset	10 Sec. Current Rise Time

TIME

Figure I-4

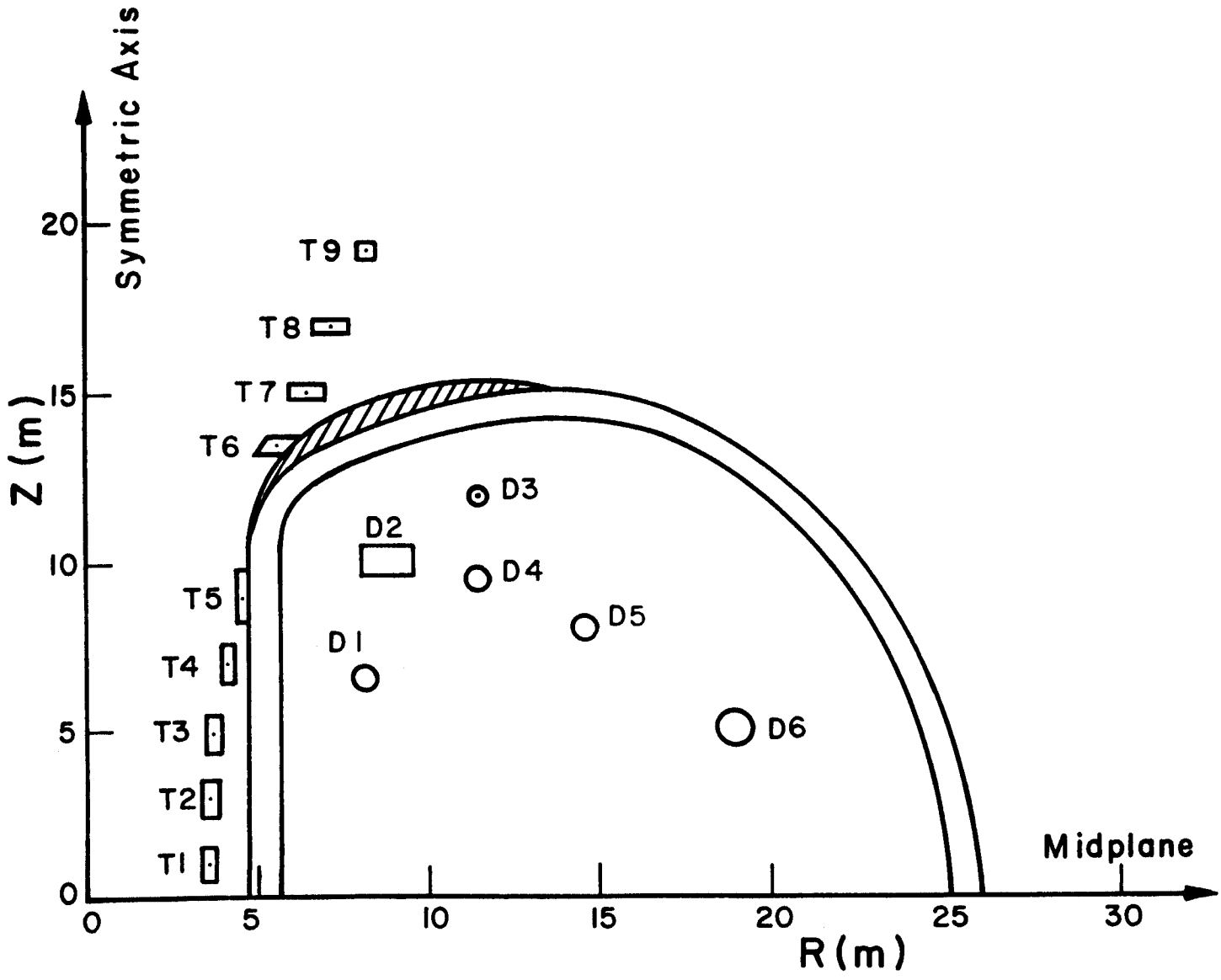
Symmetric Axis
Z (m)
R (m)
Midplane
0
5
10
15
20
25
30
T1
T2
T3
T4
T5
T6
T7
T8
T9
D1
D2
D3
D4
D5
D6

Figure I-5

Table I-2

Divertor Current

	R(m)	Z(m)	$I(10^6 amp)$
D1	8.2	6.5	-3.70
D2	8.8	10.0	+4.89
D3	11.5	12.3	-1.46
D4	11.5	9.5	+3.40
D5	14.6	8.0	-1.57
D6	19.0	5.0	-6.82

Transformer Current

	R(m)	Z(m)	$I_o(10^6 amp)$ initial current	$I_s(10^6 amp)$ (end of start-up)	$I_f(10^6 amp)$ (final current)
T1	3.61	1.00	2.74	1.66	-4.13
T2	3.72	3.00	2.64	1.60	-3.99
T3	3.94	4.99	2.39	1.45	-3.61
T4	4.25	6.96	2.26	1.37	-3.41
T5	4.66	8.92	1.89	1.14	-2.85
T6	5.43	13.50	2.22	1.15	-3.36
T7	6.50	15.05	2.21	1.34	-3.34
T8	7.25	17.00	1.66	1.00	-2.51
T9	8.22	19.3	1.46	0.88	-2.20

Change of Transformer Current

	$-\Delta I_s$	$-\Delta I_B$	$-\Delta I$
T1	1.08	6.87	7.95
T2	1.04	6.63	7.67
T3	0.94	6.00	6.94
T4	0.89	5.67	6.56
T5	0.75	4.74	5.49
T6	1.07	5.58	6.65
T7	0.87	5.55	6.42
T8	0.66	4.17	4.83
T9	0.58	3.66	4.22

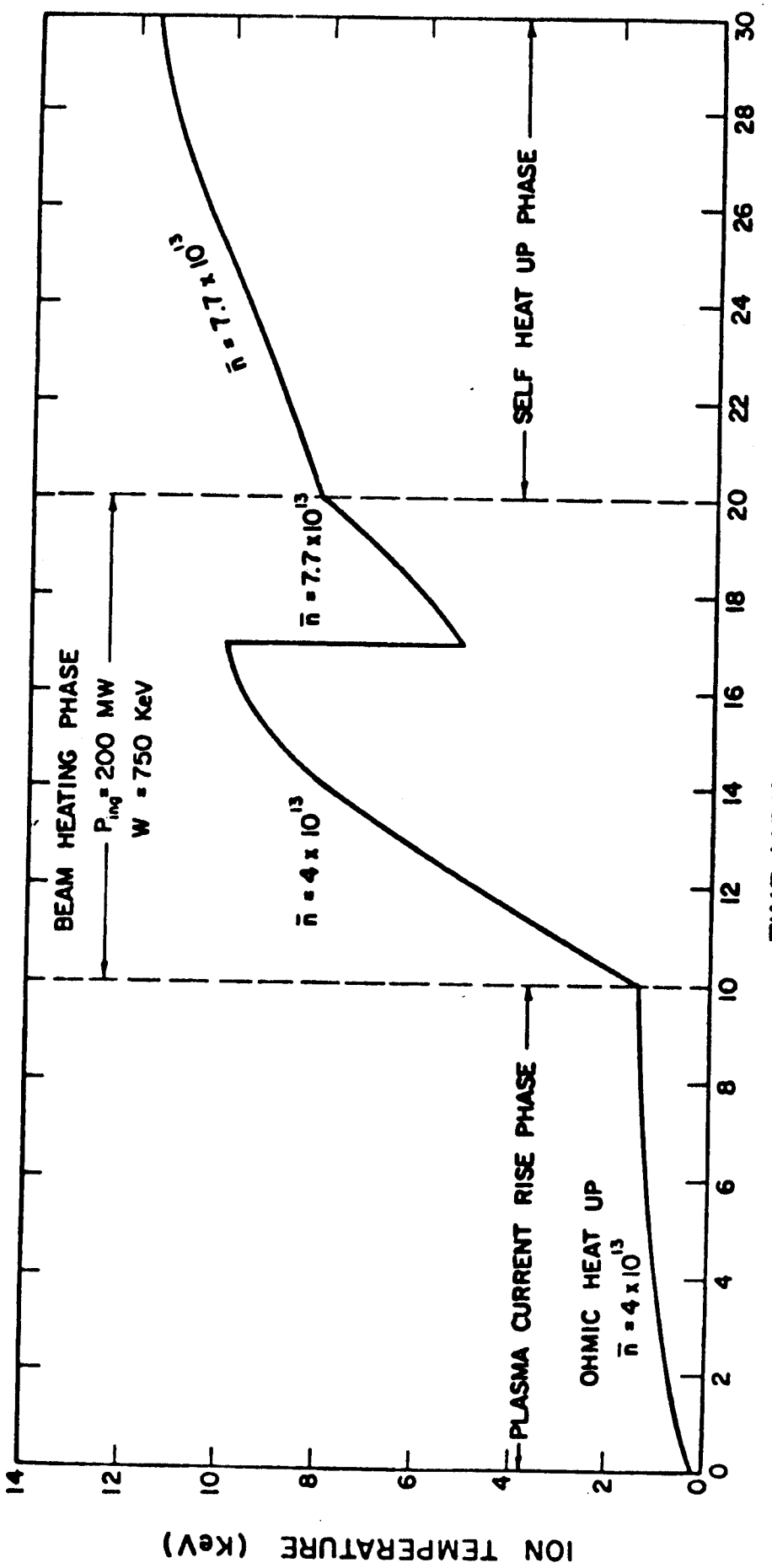

Figure I-6

Ion Temperature as a Function of Time During Reactor Startup.

unignited. The region for the initial low density heating phase is to allow better penetration during this period. It is assumed throughout that fueling with cold D-T, perhaps by the injection of D-T pellets, can maintain the plasma density at any desired value. Following the density increase at t=17 sec, the beams are left on for 3 sec more to put the plasma on a sufficiently fast self heating rate. At t=20 sec, the beams are turned off and the plasma self-heats via alpha heating to the thermally stable operating point.

The plasma characteristics during the burn time are listed in Table I-3. To determine these parameters, it has been assumed that plasma transport in such large plasmas will roughly follow the predictions of microinstability theory related to the trapped electron and trapped ion instabilities.[4] Since these scaling laws are relatively pessimistic (energy containment time, $\tau_E \alpha T^{-9/2}$ for the trapped ion mode), such an assumption roughly constitutes a worst case approach. Interestingly, these scaling laws predict confinement times short enough to allow for removal of the spent fuel (alphas) while being long enough to allow for reasonable fractional burnups (~5%) and thermally stable plasma operation at constant density. This in in constrast to the predictions of neoclassical theory where the confinement time would be too long for a UWMAK size system.(1)

To achieve long burn times, it will be necessary to control the amount of impurities which enter the plasma, particularly high Z impurities. In UWMAK-II, a double-null axisymmetric poloidal field divertor has been designed and analyzed. The divertor coils located at the positions listed in Table I-2 produce the plasma shape shown in Fig. I-7. Circulating particles on field lines within the separatrix remain in the plasma while particles on lines outside the separatrix are diverted to the collector plates above and below the null points.

The effectiveness of the divertor in reducing the charged particle flux to the wall has been estimated using a simple model where the plasma density profile in the scrape-off region is determined by cross-field diffusion (with some coefficient $D_\perp$) and by plasma flow along the diverted field lines to the particle collectors on a time scale $\tau_{||}$. The characteristic scale length, d, for the density profile is $\sqrt{D\,\tau_{||}}$. Larger values of d are better for ionization of entering impurities before they get to the separatrix while small d is better for reducing wall erosion. A pessimistic choice of $D_\perp$ is ~0.1 D_{Bohm}. One may visualize the Bohm-like scaling to come from low frequency turbulence caused by steep density gradients in the scrape-off zone. A minimum value for $\tau_{||}$ is L/v_s where L is the distance along the field lines to the collectors and v_s is the ion sound speed ($v_s = [\mathrm{Max}(T_i, T_e)/m_i]^{1/2}$). In the outer divertor (Fig. I-7), the plasma must pass through a region of higher B on its way to the collector so that magnetic mirroring can be important in determining $\tau_{||}$. The plasma, however, would have a loss-cone distribution and thus be susceptible to all the usual microinstabilities associated with mirror machines. These instabilities will have the effect of filling the loss-cone on a time scale comparable to L/v_s. Thus, we have chosen $\tau_{||} = L/v_s$ in our model. This model gives a characteristic thickness, d, of 2-3 cm which is quite small compared with the 50 cm wide scrape-off zone. As a consequence, the divertor is very effective at preventing charged particles from reaching the wall but ineffective at ionizing impurities before they reach the separatrix. We have therefore taken

Table I-3

Plasma Parameters for UWMAK-II*

I_p = 14.9 MA	τ_p = 8.28 s*
q(a) = 2.3	τ_E = 3.64 s*
β_θ = 2.275	$n_e\tau_E = 3.2 \times 10^{14}$ s - cm^{-3}
B_T(axial) = 3.57 T	Plasma Volume = 6415 m^3
T_i = 13.2 keV	Energy Content of Plasma = 2.95 GJ
T_e = 12.0 keV	
$n_e = 7.71 \times 10^{13}$ cm^{-3}	Tritium Consumption Rate = 0.624 kg/d
$n_{D+T} = 7.33 \times 10^{13}$ cm^{-3}	Fueling Rates
$n_\alpha = 1.87 \times 10^{12}$ cm^{-3}	Tritium 12.85 kg/d
Fractional Burnup = 4.85%	Deuterium 8.57 kg/d

*Based on trapped ion mode scaling, this operating point is thermally stable and assumes the plasma density is controlled and maintained by external, cold fueling.

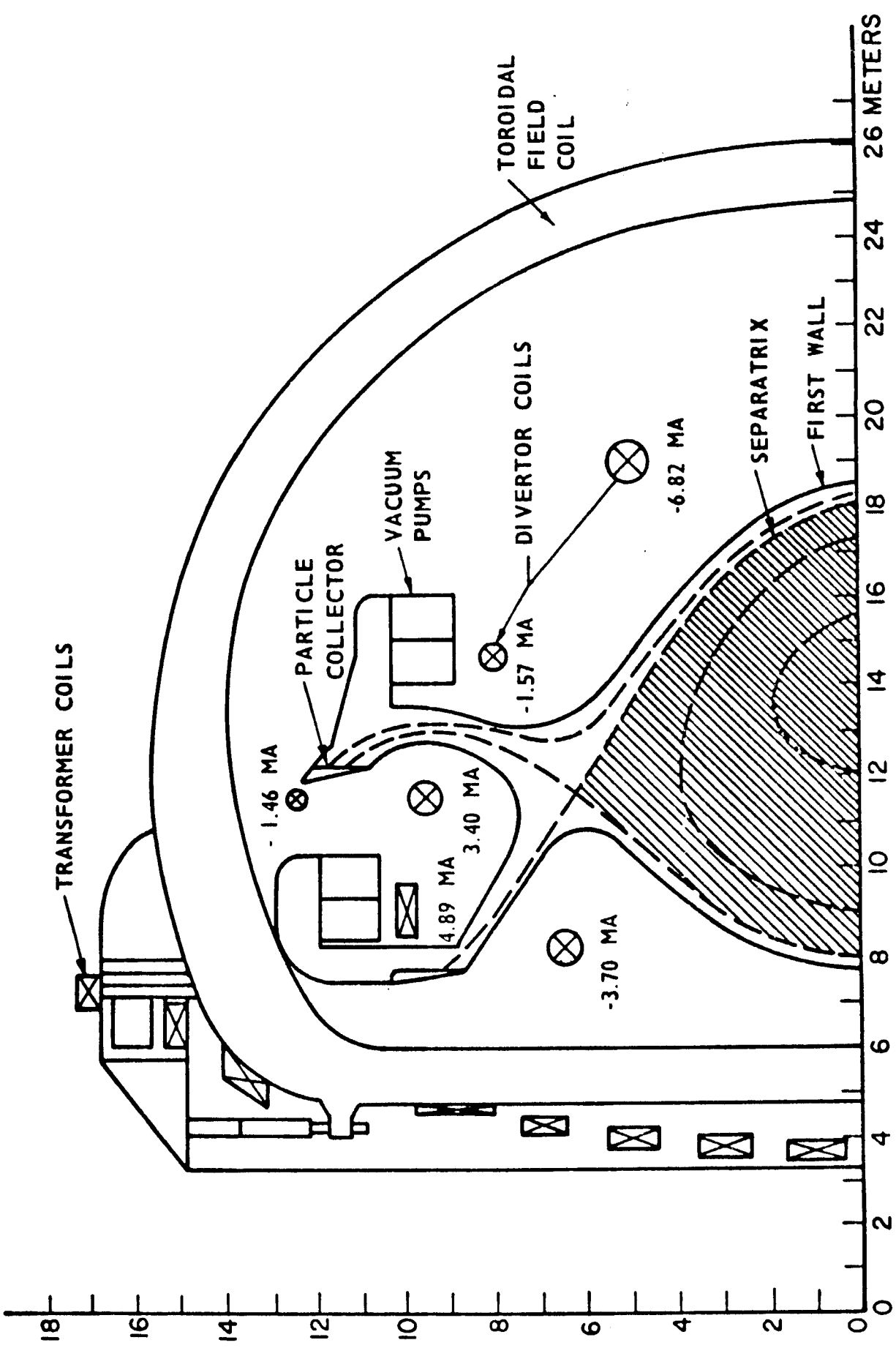
TOROIDAL FIELD COIL
TRANSFORMER COILS
PARTICLE COLLECTOR
VACUUM PUMPS
DIVERTOR COILS
SEPARATRIX
FIRST WALL
-1.46 MA
4.89 MA
3.40 MA
-1.57 MA
-6.82 MA
-3.70 MA
UWMAK - II POLOIDAL DIVERTOR
26 METERS
0
2
4
6
8
10
12
14
16
18
20
22
24

Figure I-7

the divertor efficiency to be $\gtrsim$ 99% for collecting particles diffusing from the plasma. On the other hand, because the plasma density drops so rapidly near the separatrix, the scrape off layer will be ineffective in protecting the plasma from wall atoms sputtered by neutrons. If these sputtered atoms have a low Z, they will have a much less serious impact on plasma operation and for this reason, we have developed the concept of a carbon curtain. The curtain will act as a low Z liner that can minimize the effects of impurities. In particular, it is proposed that a flexible, two dimensionally woven carbon cloth be placed between the plasma and the metallic vacuum wall.

The carbon cloth suggested for protecting the plasma consists of continuous carbon filaments, normally 5-10 microns in diameter, collected into bundles of 700-1000. A scanning electron micrograph is shown in Fig. I-8. These bundles may be twisted together to form threads and the threads twisted together to form yarns of any diameter. The yarns are then woven, by conventional techniques, into cloth which is flexible and porous. Such cloths typically have a surface area of 1-3m^2 per gram of material.

It is proposed that such a cloth be hung between the plasma and the first wall to collect the ions and neutral atoms leaking from the plasma. The curtain will also collect any metallic atoms emanating from the vacuum walls and will only be cooled by radiation. At the present time there is no structural role envisioned for the curtain in the reactor.

The first question that occurs when contemplating the use of a carbon curtain is its compatibility with the vacuum requirements for fusion reactors. This problem can be considered in two ways: First, what is the vapor pressure of the graphite at the operating temperature and second, how much dissolved and adsorbed gas will be evolved at the operating temperature of the curtain? The vapor pressure of carbon as a function of temperature has been measured. If we assume that fusion reactor plasmas require vacuums of 10^{-5} torr or better, then the operating temperatures must be limited to 2000°C or less. The equilibrium temperature of the carbon curtain in a plasma chamber can be calculated given the heat flux and appropriate sink temperatures and emissivities. Assuming a 10 watt/cm^2 heat load, an effective emissivity coefficient of $\tilde{=}$ 0.5, and a first wall temperature of 600°C, it is calculated that the curtain will heat up to 960°C. The vapor pressure of carbon at this temperature is less than 10^{-19} torr.

Graphite is commonly thought to adsorb gases readily because of experience with carbon and charcoal at high pressures and low temperatures. However, most gases adsorb poorly on graphite. The rapid advance in graphite technology has led to new forms of graphite and carbon-carbon composites which have demonstrated extremely good properties in high vacuums.

The level of carbon impurities to be expected has been estimated using a simple model. Assuming the divertor is greater than 99% efficient at collecting particles diffusing from the plasma but only 10% efficient at shielding the plasma, the carbon concentration (n_c/n_e) is calculated to be 0.02% assuming the impurity confinement time, τ_{imp}, is equal to $\tau_{D,T}$ (for M = 1 where M is the ratio of $\tau_{imp}/\tau_{D,T}$). For $\tau_{imp} = M\tau_{D,T}$, one finds $n_c/n_e = .0002\ M$. Thus values of M to

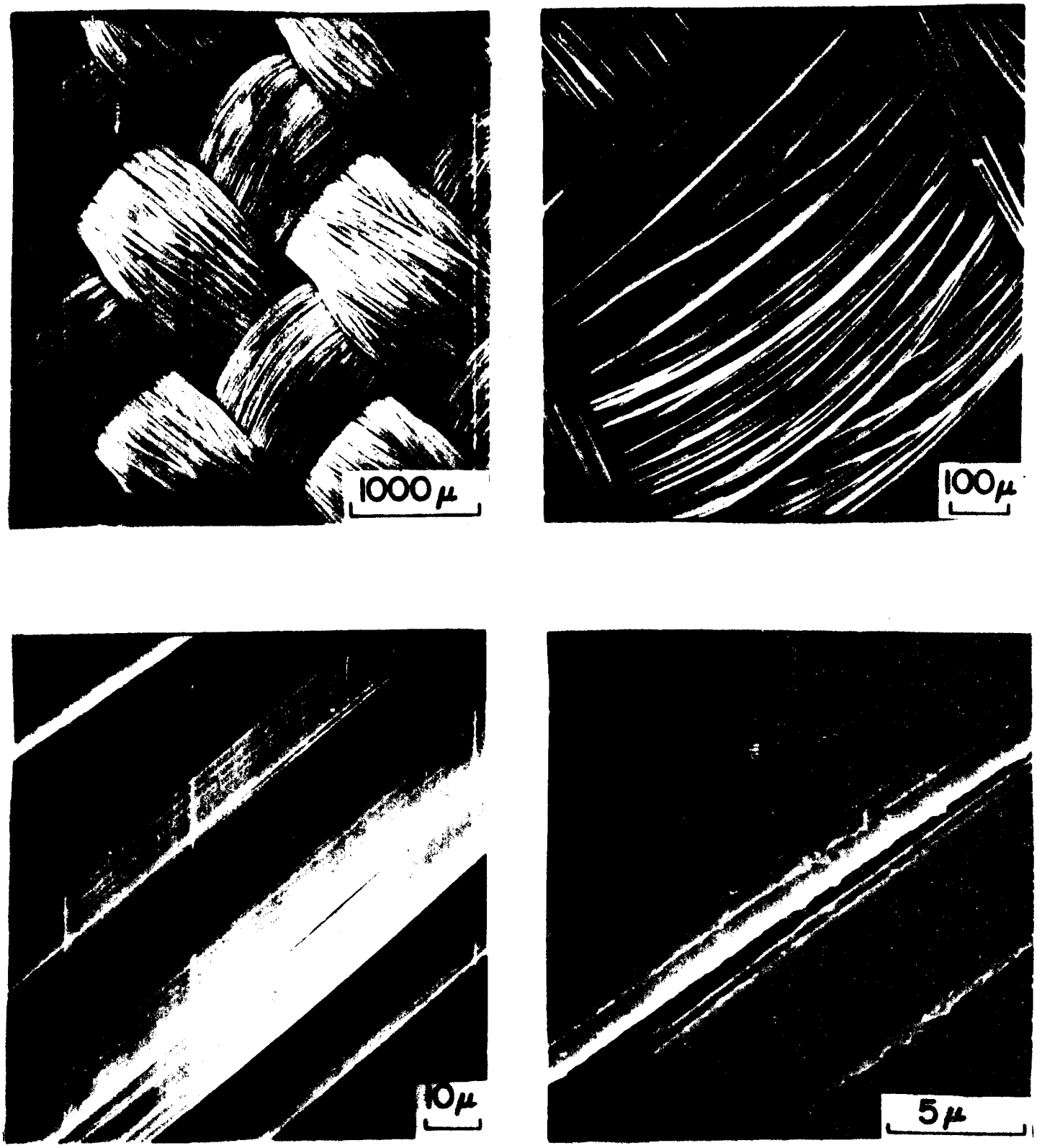

Figure I-8 Photographs of Graphite Fabric at a Number of Magnifications

1000 may be acceptable under these circumstances and allow long burn times. Based on the present calculations, it is found that the levels of low Z impurities in the plasma are essentially negligible and that if there are no sources of high Z impurities UWMAK-II can have a burn time of 5400 sec.

The vacuum system design in UWMAK-II is based entirely on cryopumps and molecular sieves. These pumps offer the advantages of reliability and a minimum amount of normal servicing. They also do not introduce large amounts of highly volatile and potentially toxic chemicals (i.e. Hg) into the reactor building. Each cryopump is 1.3 m in diameter and 1 m in height and the coolant capacity of each pump is: liquid helium, 270 liters; liquid nitrogen, 150 liters. The cryogen usage is ~90 ℓ/day of liquid helium and ~450 ℓ/day of liquid nitrogen if gases at thermal velocities are pumped. Since the particles incident upon the cooled chevron surfaces exceed thermal velocities, the cryogen usage rate will be considerably greater. The net pumping speeds for each pump, at 10^{-4} torr, are:

$$S^{\circ}_{D,T} = 7.5 \times 10^{4} \text{ ℓ/sec}; \quad S^{\circ}_{He} = 5 \times 10^{4} \text{ ℓ/sec};$$

$$S^{\circ}_{air} = 4 \times 10^{4} \text{ ℓ/sec}.$$

The service lifetime for 96 pumps on-line at one time is greater than 24 hours. Normal usage involves daily regeneration of the 96 pumps which have pumped the residual gases of the fusion reaction by heating the molecular sieve and cold (20°K) chevron panel to 30°K. By using nitrogen-injection to avoid contamination, this can be accomplished in seconds. The cycling sequence for regeneration will require several minutes for outgassing and less than an hour for subsequent cooling of the molecular sieve.

The system must be capable of handling a gas throughput of $Q_{D,T} = 6.4 \times 10^{3}$ torr ℓ/sec. Liquid lithium surface trapping in the divertor is expected to trap 90% of the deuterium and tritium but we conservatively assume that none of the helium is trapped. Half (96) of the cryopumps will be on-line during the burn, evacuation, and fueling cycle. Net pumping speed in the equilibrium pressure range of 1×10^{-4} torr to 75 torr is 7.5×10^{6} ℓ/sec for D and T, and 5×10^{6} ℓ/sec for He. The base pressure during burn is 8×10^{-5} torr for D+T and 3×10^{-5} torr for He. The initial evacuation from 75 torr to ~2×10^{-6} torr will require 96 of the pumps, and require only a few seconds. Regeneration of these pumps after the initial pump down will require ~2 hours because they must be heated to 25°C after the original pump down, regeneration at 30°K will require only ~1 hour.

The design for trapping hydrogen isotopes diffusing from the plasma in liquid lithium follows that for UWMAK-I.(1) Experiments indicate a trapping efficiency of 96% for D and T ions to a dose of approximately 2×10^{19} particles per cm^2 of trapping surface. The UWMAK-I design relied on 92% trapping of the incident D^+, T^+ ions, and 50% of the He^{++} ions. These requirements are relaxed in the present design to 90% of D^+, T^+, and no trapping of helium. Although some helium will be trapped, none is required in the UWMAK-II design since 96 cryo-vacuum pumps easily are capable of maintaining partial pressures of deuterium and tritium at ~8×10^{-5} torr and of helium at ~3×10^{-5} torr.

It is advantageous to evacuate the surrounding enclosure, in order to ease the vacuum pumping problems associated with the main vacuum chamber. If the enclosure is maintained at about 75 torr, problems of voltage breakdown and sector seal leakage can be minimized or avoided. A 75 torr pressure is maintained within the structure built around the lateral support struts between TF coils, as shown in Fig. I-1. A more detailed description of this lateral support structure is given later.

I-B-2. Magnets for UWMAK-II

There are 24 superconducting toroidal field magnets in UWMAK-II. The design philosophy for these coils is that full cryogenic stability of the conductors and reliable solid structures are required for fusion power reactors. The design is a modified constant tension "D" shaped toroid producing a magnetic field of 3.67T at a radius of 13m, the plasma center. The important dimensions of these coils are shown in Fig. I-9 and other views of the coils are shown in Figs. I-1 and I-2. Circumferential clearance between the dewars of the toroidal field magnets is provided so that segments of the shield and blanket can be removed separately (see Fig. I-1). This design requires that the outer portion of the "D" coils be extended to a much greater radius than our previous design[1] and would create a very tall and costly magnet if we adhered to the constant tension design. It is therefore necessary to deviate from a constant tension design and use a modified "D" shape that is no higher than required for the internal system components. One must provide extra structure to account for bending in the discs and for support from the central core over the non-constant-tension portion of each toroidal field magnet. An "embedded disc" type winding design is used to hold the conductor rigidly against the support structure. Redundancy in both the number of turns per disc and the total number of discs is also incorporated.

The UWMAK-II TF coil is a constant tension design with no bending stresses in the outer portion from the top of the magnet (point C, Fig. I-9) to the bottom. Inward from the top and bottom sections, the forged discs are increased in depth in order to sustain the bending stresses and the hoop stresses created by the magnetic loading.

The forged discs as shown in Fig. I-9 are too small to accomodate the loads and still maintain stress and deflection levels. Therefore, the central cylindrical core is extended in the regions directly above and below each toroidal field magnet to provide additional support. This cantilever support is sized in conjunction with the increased magnet dimensions in this region in order to keep the maximum stress in the stainless steel discs to less than 4.14×10^8 N/m^2 (60,000 psi) and to match the slope and deflection at the end of the reinforced portion of the magnet to those of the constant tension outer part. The copper will yield at the design maximum stress level in the stainless steel discs, but the maximum strain will not exceed 0.2%; thus, the conductivity will not be degraded appreciably.

The stress analysis was carried out using 17 discs in each of the 24 magnets at the current value required to produce the specified field. However, the conductor design is for cryogenic stability at a current level which is 13.3% higher so that a magnet can operate with only 15 discs (and still be cryogenically stable). The actual number of discs per magnet is 19. Thus, there are two degrees of redundancy built into the "D" magnets: First, the coils are normally operated with 19 discs at reduced current (26.7% less than the stability limiting value) and an electro-mechanical load designed for 17 discs only. If two adjacent discs are disabled by an arc (or some other reason), they can be disconnected by the electrical leads connecting the discs on the outer surface of the outer leg of the magnet at midplane where an access port has been provided. Second, if further problems arise, a second pair of discs or two discs at locations apart from each other

UWMAK-II TOROIDAL FIELD MAGNET DESIGN

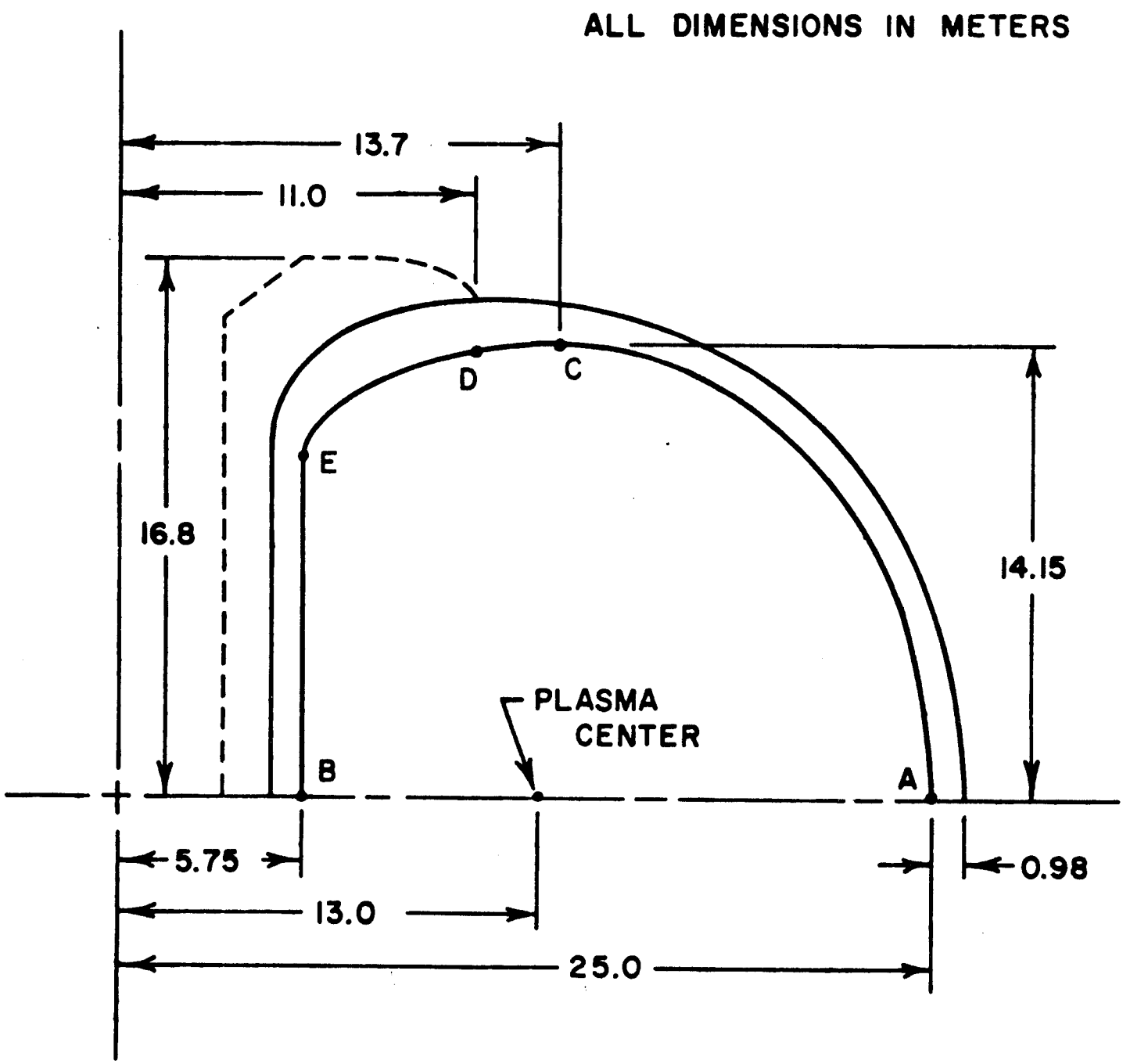

Figure I-9

"D" Shaped Toroidal Field Magnet Design

can be disconnected without exceeding the allowed stress or current densities. All 19 discs will still share the mechanical load even if not all are electrically powered. Table I-4 is a list of the primary specifications of the UWMAK-II TF coils.

The divertor field and transformer coils are also cryogenically stable and use TiNb superconductor. (For coil positions, see Fig. I-5). The maximum current carrying capacity is 20,000 A per conductor and the conductor size and the number of filaments per conductor are calculated individually for each of the 12 divertor and the 18 transformer coils according to their respective ambient magnetic field. A redundancy of 10% extra material and 10% extra turns is included for all the divertor and transformer coils (as a safety measure).

The superconducting filaments are extruded with cupronickel which are then twisted and transposed inside a high purity copper matrix. To reduce ac losses, all the transformer coils (except two) are housed inside the toroidal central structure (see Fig. I-2) and no interleaved reinforcing steel is necessary for the winding of these coils. On the other hand, some of the higher stressed divertor coils will need reinforcing steel interleaved between turns. The general specifications of all the divertor and transformer coils are given in Table I-5.

An important point here relates to the placement of the vertical field or divertor coils in UWMAK-II. These were deliberately located inside the TF coils to reduce the maximum energy stored in the poloidal field and to improve vertical field control. The maximum stored energy in the poloidal field is 2.9 MWh (10.6 GJ) which is a factor of five less than in the UWMAK-I design.[1] The result is that the energy storage unit required for UWMAK-II is rated at 1 MWh even though the current rise time is 10 sec (compared to 100 sec in UWMAK-I.) Built-in design redundancy should allow the coils inside the TF magnets to have an expected lifetime exceeding that of the plant.

During the charging and discharging of the divertor and transformer coils, substantial ac losses are produced in the copper stabilizer as well as in the superconducting filaments (see Fig. I-3). The ac losses in each cycle are induced from the eddy current loss in the normal metal, from multifilament coupling loss, and from hysteresis loss in the superconducting filaments. Losses from these three phenomena have been evaluated and are summarized in Table I-6.

The refrigeration requirements for the total UWMAK-II magnet system are satisfied using ten 3 kW refrigerators with seven in operation at any given time and the other three in reserve. The 300,000 liters of helium in storage could supply the refrigeration for 18 hours of operation in the event of total liquefier failure thus leaving adequate time for repair or replacement of faulty equipment.

The pulsed power requirements for the divertor and transformer coils impose both excessive peak power and peak reactive power demands upon the power system source. This can result in system frequency and voltage fluctuations. These adverse effects can be eliminated or at least kept to a minimum if the pulsed loads are fully or partially supplied through an energy storage unit.

Table I-4

Specifications of the Toroidal Field Magnets

a. Field Specifications	
On-axis field at a radius of 13m, B_o	3.67T
Field at inside turn of far edge (pt. A Fig. I-9)	1.91T
Maximum field at the conductor, Bm (Pt. B Fig. I-9) (@ 5.75 m)	8.30T
Maximum field in the self-supported portion (Pt. D Fig. I-9)	4.48T
Field ripple along the far edge of plasma	0.05%
Total magnetic energy stored	62 MWh
b. Design Stress	
Design stress in 316 stainless steel at 4.2K	4.14×10^8 N/m^2 (60,000 psi)
Design Strain	$\leq$ 0.002
c. Magnet Components	
Number of Magnets	24
Number of discs per magnet	19
Number of conductor turns per disc	58 (29 each side)
Conductor current	9,065A @19 discs 10,131A @17 discs 11,482A @15 discs
Disc cross section (see Figure III-A-2)	5x98cm
Superconductor composite: TiNb in copper matrix thickness of composite strip. (=0.5cm, diameter=0.038cm, filament twisted every 30 cm)	500 filaments
Copper stabilizer cross section	2.87cm wide x 190cm thick on inside turn taper to 1.70x1.13 cm on outer most turn
Insulation between conductor and stainless steel disc	0.10 cm reinforced epoxy.
Average copper to superconductor ratio (volumetric)	8:1
Spacer between discs	0.64cm thick micarta, covering 50% of the area.

Table I-4

Specifications of the Toroidal Field Magnets (Cont.)

	Aluminum alloy bolts to fasten the discs together against slipping, 1" diameter	2630
	Lateral support between the magnet and dewar: reinforced epoxy struts on each side of cross section	5500cm^2
	Each magnet weight	710 Mt.
d.	Total Materials required	
	TiNb alloy superconductor	164 Mt*
	Copper stabilizer	8000 Mt.
	Stainless steel in discs	7230 Mt.
	Stainless steel in dewar	941 Mt (removable portion only)
	Reinforced epoxy in discs	395 Mt.
	Micarta spacers between discs	255 Mt.
	Reinforced epoxy struts in dewars	16 Mt
	Aluminum alloy bolts to assemble discs	95 Mt.
	Cryogenic insulation	850,000 m^2
	Liquid helium inside dewars	160,000 liters

* Mt = Metric tonne = 10^3 kg.

Table I-5

General Specifications of the Divertor and Transformer Coils

(1) Conductor: TiNb + CuNi sleeve + Copper stabilizer, fully cryogenically stabilized;

(2) Conductor current = 20,000 A

(3) Conductor current density = 1700 A/cm^2 to 2,200 A/cm^2

(4) Conductor width to height ratio = 1:10 (0.95 x 9.5 cm to 1.08 x 10.8 cm cross section)

(5) TiNb-CuNi-Cu composite strip: 0.5 cm x 2.5 cm with 50 to 2500-0.038 cm diameter filaments, twisted every 30 cm.

(6) Average copper to superconductor ratio = 70:1

(7) Design stress at 4.2K: 2.76 x $10^8 N/m^2$ (40,000 psi) in 316 stainless steel, 0.83 x $10^8 N/m^2$ (12,000 psi) in copper; strain level $\leq$ 0.002.

(8) Jelly roll winding approach with 4 conductors per pass plus transposition of conductors between pancakes.

(9) 0.05 cm thick Kapton insulation between conductors; 0.64 cm thick micarta spacers between pancakes which cover 50% of the surface.

(10) Design limits temperatures to 5.2K in a 4.2K bath for all normal situations

(11) Total TiNb alloy superconductor required: 36 Mt.

(12) Total copper required (matrix + backing strip): 16,760 Mt.

(13) Maximum $\frac{dB}{dt}$ = 0.57 T/sec.

(14) Maximum Stored Energy = 2.9 MWh (10.4GJ)

(15) Maximum Total Current = 58 MA

Table I-6

AC Losses Per Cycle in the Divertor and Transformer Coils

Coil*	Eddy Current Loss E_e(kWh)	Coupling Loss E_c(kWh)	Hysteresis Loss E_h(kWh)
D_1	0.338	0.0044	0.010
2	0.796	0.0079	0.017
3	0.963	0.0006	0.003
4	0.412	0.0048	0.012
5	0.091	0.0008	0.005
6	2.535	0.0286	0.055
T_1	0.329	0.0042	0.014
2	0.316	0.0039	0.015
3	0.338	0.0045	0.013
4	0.316	0.0045	0.014
5	0.087	0.0019	0.013
6	0.461	0.0067	0.015
7	0.487	0.0070	0.025
8	0.401	0.0059	0.013
9	0.385	0.0053	0.013
Total Losses in 30 Magnets	14.71	0.182	0.237

Total ac losses at 4.2K = 15.1 kWh

* See Figure I-5

The charging-discharging and the accompanying power cycles for the divertor and transformer coils are sketeched in Fig. I-10. The maximum energy stored in the poloidal field is estimated to be 2.9 MWh. During the initial 10 sec current rise time, the divertors are charging while the transformers are discharging. On the other hand, the divertor current turn-off and reset time for the transformers is 100 sec and 150 sec, respectively. Hence, the high power demand occurs only in the initial rise time. Assuming that a maximum power of 500 MW can be bought directly from an electric utility, an additional 500 MW can be obtained from an energy storage unit. The superconductive energy storage dipole magnet designed for Fermi National Laboratory[5] is appropriate for the present purpose. The energy required from the storage unit is estimated as 1/2 x (500 MW) x (3.75/3600 h) = 0.26 MWh. Assuming that only 25% of the energy stored in the storage coil is to be transferred to the divertor coils, a storage unit of about 1 MWh in size is planned. We have adopted the above mentioned FNAL superconductive energy storage unit. However, the interface between the storage and load inductor is based on a thyristorized bridge network design.

The proposed system which can achieve the desired objectives is shown in the block diagram in Fig. I-11. In this basic system, there is a large superconductive inductor energy storage unit which is charged from the three phase, 60 Hz power system through a converter. It is possible to draw upon the energy stored in the storage inductor with the help of a double conversion (dc/ac/dc) subunit. This subunit consists of two ac/dc converters and a shunt capacitor bank which provides the reactive power for the commutation of the two converters. As shown in Fig. I-11, a plurality of loads of arbitrary magnitudes and durations can be supplied from a single storage unit with P_{d1}, P_{d2} etc. nearly equal to P_{d1}', P_{d2}', etc. respectively. The small differences are due to losses in the capacitor bank and in the converters. Power P_{ds} required to keep the storage unit charged is the sum of the average power required by the individual loads plus the losses in the system.

In addition to the power supplied from the storage unit, a limited amount of pulsed power P_{d1}'', P_{d2}'', etc. can be directly obtained from the power system source through the ac/dc converters. Since the power flow through the converters is reversible, it is possible to retrieve the minimum waste the energy stored in the inductive loads during a part of the load cycle. This is the case when the loads are the divertor and transformer coils.

A significant change in the problem of supports between TF magnets was made possible when it was decided to provide a secondary vacuum wall (shown in Fig. I-1) at the location of the toroidal field magnet dewar instead of at the wall of the reactor room. The vacuum wall between coils must carry atmospheric pressure. It can also adequately carry the operating lateral loads between magnets and the overall torsional loading exerted from the top to the bottom of the toroidal field magnets by the vertical fields of the transformer, the divertor magnets, and the plasma current.

A preliminary examination of various modes of failure has been made in an attempt to provide an adequate design against catastrophic failure of toroidal magnet system. Although it is conceivable that several adjacent toroidal field magnets could simultaneously experience a complete loss of current in a matter of a few minutes, the decision was made to design the shell structure between magnets to withstand this condition even if it suffers large deformations. This

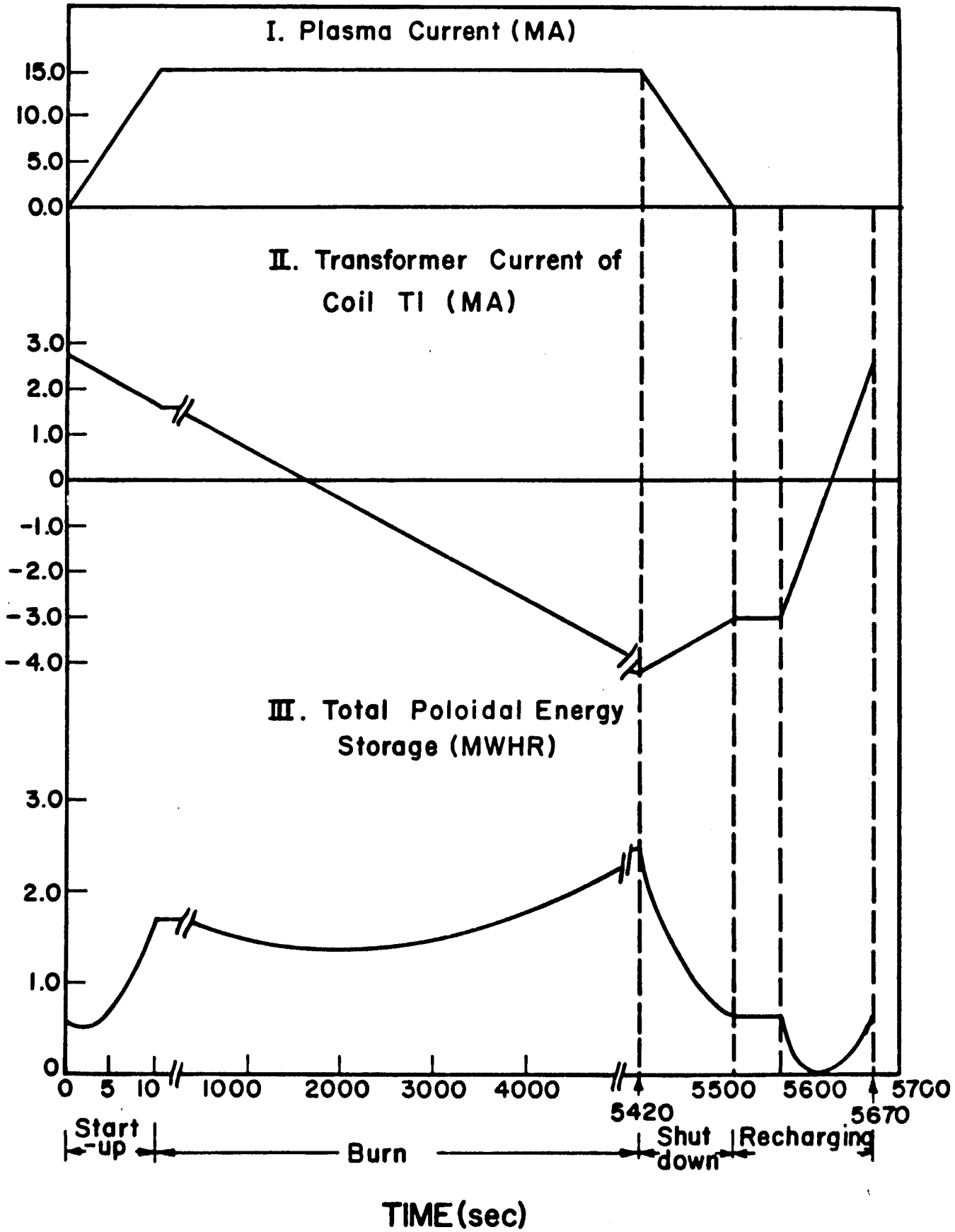

Figure I-10 Power Requirements During Start-up, Burn, Shut-down and Recharging Periods. Note the Difference of Time Scale in Each Period.

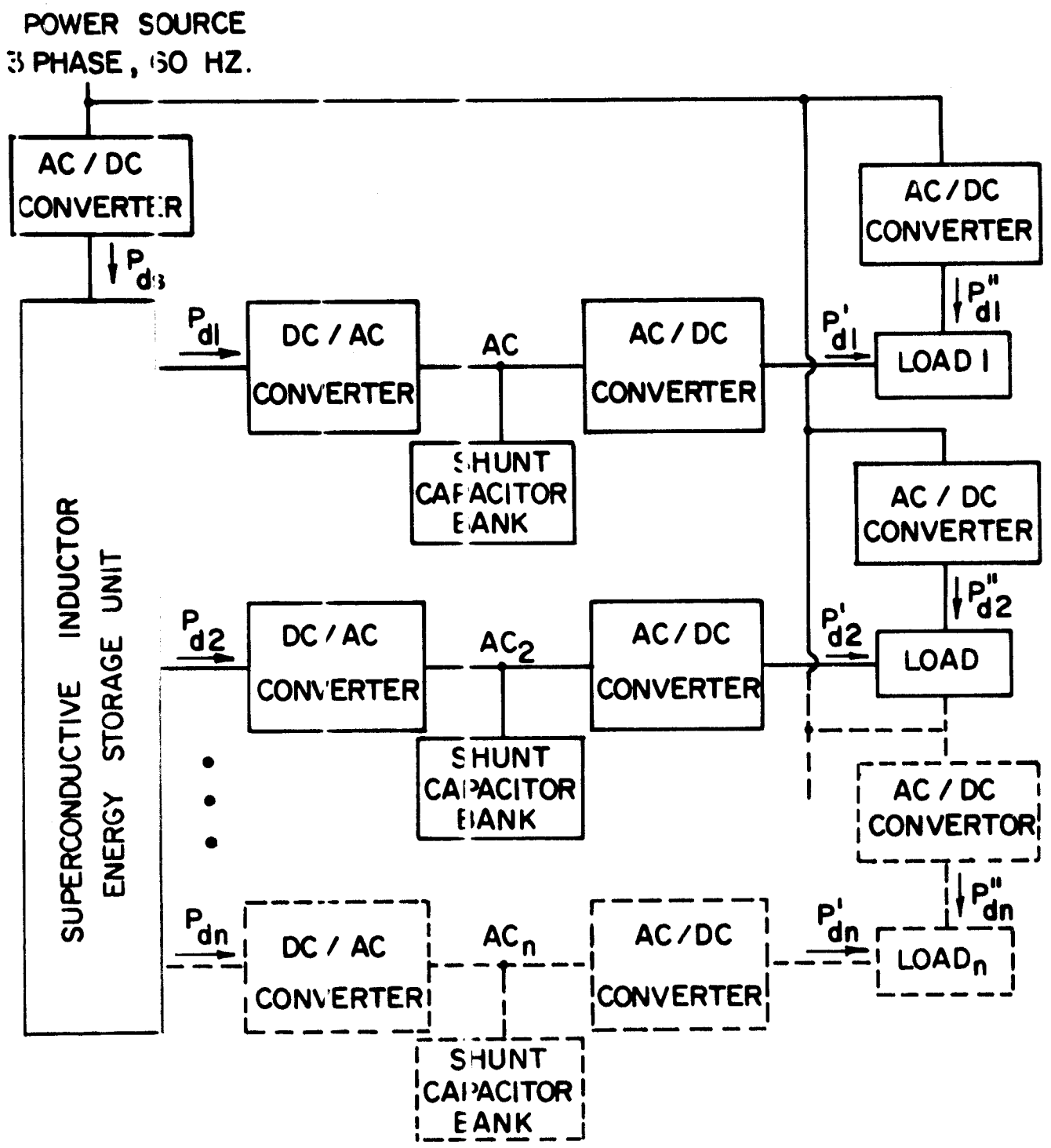
POWER SOURCE
3 PHASE, 60 HZ.
AC / DC CONVERTER
P_{d3}
SUPERCONDUCTIVE INDUCTOR ENERGY STORAGE UNIT
P_{d1}
DC / AC CONVERTER
AC
AC / DC CONVERTER
SHUNT CAPACITOR BANK
AC / DC CONVERTER
P''_{d1}
P'_{d1}
LOAD 1
AC / DC CONVERTER
P''_{d2}
P_{d2}
DC / AC CONVERTER
AC_2
AC / DC CONVERTER
P'_{d2}
LOAD
SHUNT CAPACITOR BANK
AC / DC CONVERTOR
P''_{dn}
P_{dn}
DC / AC CONVERTER
AC_n
AC/DC CONVERTER
P'_{dn}
$LOAD_n$
SHUNT CAPACITOR BANK

Figure I-11

decision was prompted by the assumption that such an occurrence would in all probability be caused by an accident which would render the toroidal field magnets useless and would necessitate their removal. The replacement of the shell walls and the penetrations through the walls in the area involved would also be necessary. The savings in repair costs which might occur if a heavier shell were used would be more than offset by the added cost of the heavier wall.

One of the failure modes analyzed is a case in which the current in a single toroidal field magnet is assumed to drop to some low value in less than three or four minutes. The lateral support structure is designed such that this will not cause excessive deformation or motion of the magnet or dewars. A second failure mode for which design calculations were carried out is one in which two adjacent toroidal field magnets suffer a loss of current simultaneously. In this instance, the design permits relatively large motions of the dewars but keeps the stresses low enough to assure that no permanent deformation takes place in the magnets, dewars, or the secondary vacuum wall.

Finally, a detailed cost analysis has been carried out for the complete magnet system, including supporting structure, refrigerators, power supplies, and energy storage units. The total capital cost is estimated to be $\$300 \times 10^6$ or ~25% of the total direct costs.

I-B-3. Blanket and Shield Design

The basic blanket design philosophy for UWMAK-II was to achieve a relatively low blanket tritium inventory design within the constraint that current technology should be employed wherever possible. The choice of structural material was based primarily on such current technology considerations and skepticism over the near term availability of a large refractory metals industry led to the choice of 316 stainless steel.

The choice of a coolant was influenced by some of the problems we found in designing UWMAK-I.[1-3] In particular, tritium recovery from liquid lithium at very low concentrations made a large reduction in the lithium inventory desirable. In addition, the temperature limitation of approximately 500°C due to the Li-stainless steel corrosion combined with the tritium extraction difficulties led us to consider other coolants besides liquid lithium.

Based upon presently developed technology, the choice of a coolant lies between helium, a liquid metal or a fused salt. Each of these fluids must be circulated at rather high flow rates from the blankets to external equipment for heat and/or tritium removal. The ability to transport tritium is a very important determining factor in the choice of a coolant. Also, the MHD pressure drop associated with pumping conducting fluids across magnetic flux lines must be overcome by judicious design of the fluid flow channels or the development and utilization of non-conducting tubing. Simpler flow designs are possible if helium is utilized, and chemical compatibility problems are reduced by the use of this inert gas. In addition, the neutronics interactions with helium are insignificant, except for the approximately 200 p.p.b of ^{3}He which would be rapidly transmuted in an operating reactor. Consequently, the utilization of helium does not perturb the neutronic behavior of the proposed blankets. Thus, helium is chosen as the coolant for this study.

The idea of low lithium inventory with recovery at reasonably low concentrations also tends to reduce the tritium inventory. This does not fix the choice of breeding material nor does it insure that adequate tritium production can be achieved in such a system. Adequate breeding with a small lithium inventory usually requires the use of a neutron multiplier (Be is used in UWMAK-II) which then must be combined with the use of lithium enriched in ^{6}Li.

Of course, if liquid lithium is not used, another form of Li bearing compound is required and for reasons to be described, lithium aluminate ($LiAlO_2$) has been chosen. Tritium extraction from such compounds appears feasible if excessive particle sintering does not take place.

I-B-3a Module Design

After carrying out many survey calculations, the final design for a blanket module is that shown in Fig. I-3. The blanket in UWMAK-II consists of three major parts, the removable front wall cells containing the breeding material, the vertical structure which connects the front wall cells to the headers, and the helium gas supply and return headers.

The very high pressure of the helium coolant in UWMAK-II makes the design of the front wall of the blanket somewhat complex. A single wall structure capable

of containing the coolant pressure would have such large thermal stresses reasonable design stresses are likely to be exceeded. A solution to the problem was found in the use of a composite front wall. This wall is made of small semicircular tubes 1.0 cm in diameter and 0.15 cm thick attached to a thicker (0.9 cm) backing material. The insert in Fig. I- 3 shows a section of the composite wall. Coolant gas from the supply headers passes through channels in the vertical structure and then traverses the front wall through the semi-circular tubes before emerging into the blanket region. This maintains the front wall as the coolest part of the front wall structure. It also means that the thermal stresses associated with the surface wall loading appear across this material only and are minimized. The pressure stresses are carried by both components of the front wall and are also kept low by appropriately selecting the thickness of the backing material. Major constraints are fabrication, loss of cold work in the areas where welding takes place, material quantity and neutronic considerations.

The removable part of the blanket is made up of semi-cylindrical cells, 23.1 wide, 27.0 cm high and varying in length from 0.6 m to 1.5 m. Since these cells are oriented in the toroidal direction, their length depends on their location in the blanket.

The junction between the removable front wall cells and the vertical structure serves both as the attachement between the two structures as well as a gas distribution manifold. Every other tube is closed off to permit countercurrent flow of gas across the front wall to reduce thermal gradients. At this point, the thin component of the front wall is straightened out so that it can be welded to the adjacent cell as can be seen in Fig. I-3 and I-12. This will constitute the seal between cells. Five cells welded together make up a section as shown in Fig. I- 3 . These sections have skirts attached to them which protrude slightly beyond the flat portion of the cell wall. Welding the skirts of adjacent sections from the plasma side provides the seal between sections.

The vertical structure which connects the front wall to the headers is continuous for each module, has an effective thickness of 1.2 cm and has 1.0cm diameter holes spaced 2.0 cm apart built into it. As can be seen from Fig. I-3, it terminates in a latching concept which allows front wall sections to slide in and become attached to the vertical structure. This point of attachment also acts as a manifold which distributes the flow between adjacent cells. The vertical structure is welded to the bottom plate of the headers on the other end. This bottom header plate has holes in it to allow the cooling gas to enter the vertical structure from the supply header. After the gas traverses the front wall and the blanket region, it exits through more holes in the plate to a return header. In Fig. I- 3 , each header located directly above a vertical structure is a supply header and the intervening ones are return headers.

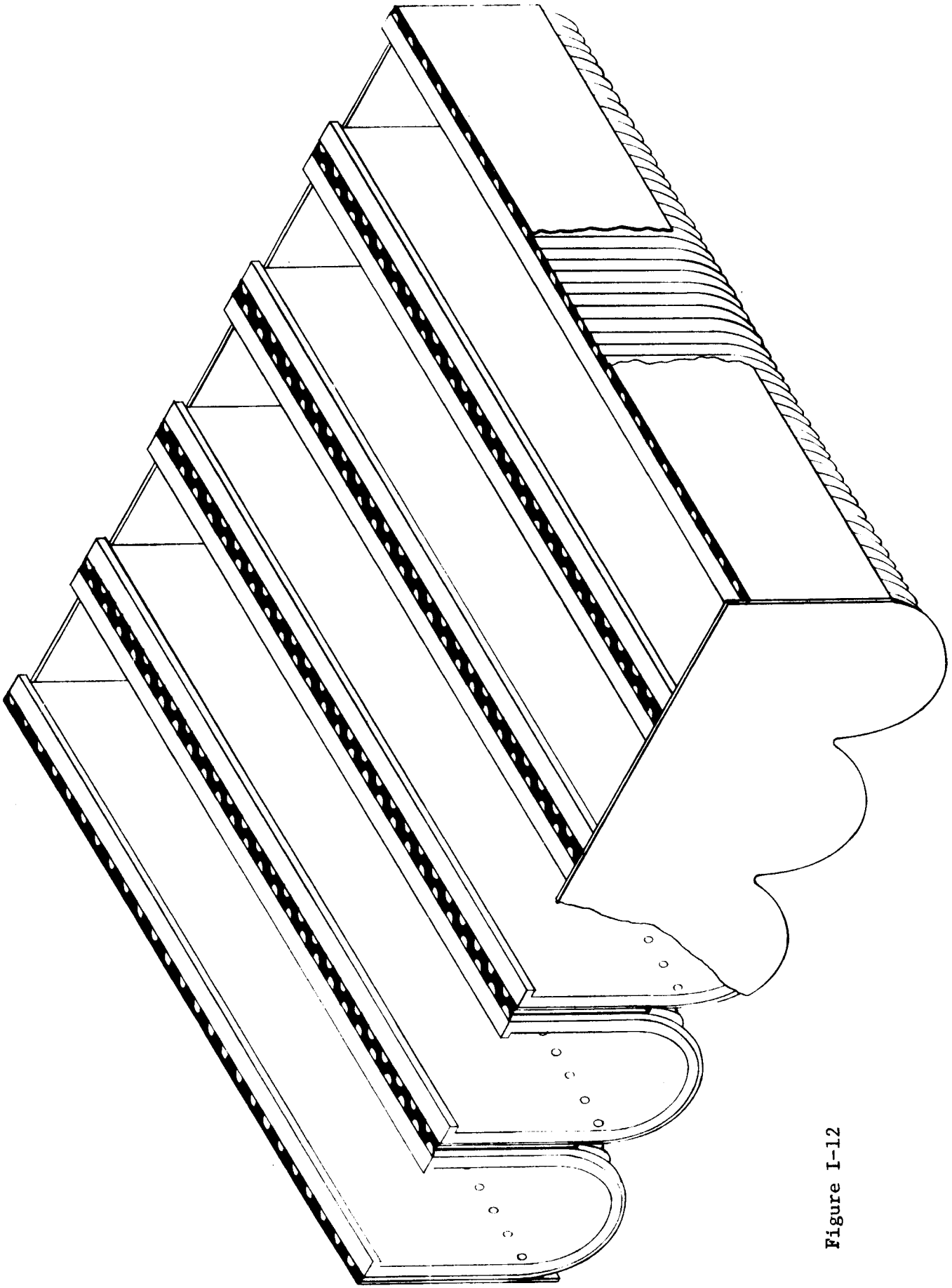

Figure I-12

I-B-3-b. Neutronics

A schematic of the UWMAK-II blanket and shield used in one dimensional neutronics calculations is given in Fig. I-13. While the reactor is toroidal in geometry, the neutron and gamma transport calculations were carried out in cylindrical geometry. The first-wall thickness was determined from considerations which included hoop and thermal stresses, sputtering, blistering, and corrosion problems. The physical thickness of the first wall is 2 cm but 50% of the volume is occupied by the helium coolant. Since helium does not perturb the transport calculations to any measureable degree, a density factor of 0.5 for stainless steel in the 2 cm wall was used.

The stainless steel required for the structural components and coolant tubing was estimated at 10% of the physical volume of the blanket and shield. The blanket is conceived as composed of cells, each 20 cm wide and 90 cm deep, and the stainless steel cell walls are about 7 mm thick. The lithium aluminate and beryllium will be packed in pins with an average stainless steel wall thickness of 0.75 mm. A summary of the neutronics results on tritium breeding, nuclear heating, energy leakage from the magnet shield, and radiation damage in UWMAK-II, is given in Table I-7 which shows that the contribution of ^{7}Li to tritium production is very small and that the tritium breeding ratio of 1.19 comes almost entirely from the $^{6}Li(n,\alpha)t$ reaction (a one dimensional neutronics calculated with twice the amount of structure in the breeding zones gives 1.11 which is closer to the Monte Carlo results). This is in contrast to reactors operating on a high energy spectrum in natural lithium in which about 40% of the tritium breeding comes from the $^{7}Li(n,n'\alpha)t$ reaction.[1] It is important to note that 0.01 tritium atoms per DT neutron are produced in the Be(n,t) reaction. While this amount of tritium is not crucial from a breeding point of view, it is extremely important to extract it as it represents a production rate of approximately 6 grams per day in a 5000 MW(th) reactor and allowing it to accumulate in the beryllium could double the tritium inventory in the blanket in a month or so of operation.

The total energy deposition in the blanket and shield of the UWMAK-II design is shown to be about 18 MeV, which is 1.5 MeV higher than that in the UWMAK-I. This can be explained on the basis of the additional (n,2n) reactions in Be and the increase in the exothermic reactions in the highly enriched lithium in the UWMAK-II. The nuclear radiation load to the magnet in UWMAK-II is only 256 watts, which is quite small.

To more exactly determine the breeding ratio for the UWMAK-II blanket design, detailed three dimensional Monte Carlo calculations have been carried out. A detailed view of a blanket subcell is shown in Fig. I-14 and the Monte Carlo calculations were based on a detailed modeling of this cell. The results are given in Table I-8 and show a breeding ratio of 1.06 ± 0.02. It should be noted that the original reason for demanding a breeding ratio of between 1.15 and 1.2 from one dimensional calculations was to allow for uncertainties due to nuclear data or to the homogenization procedures required by one dimensional calculations. The results of the Monte Carlo analysis show the prudence of that approach.

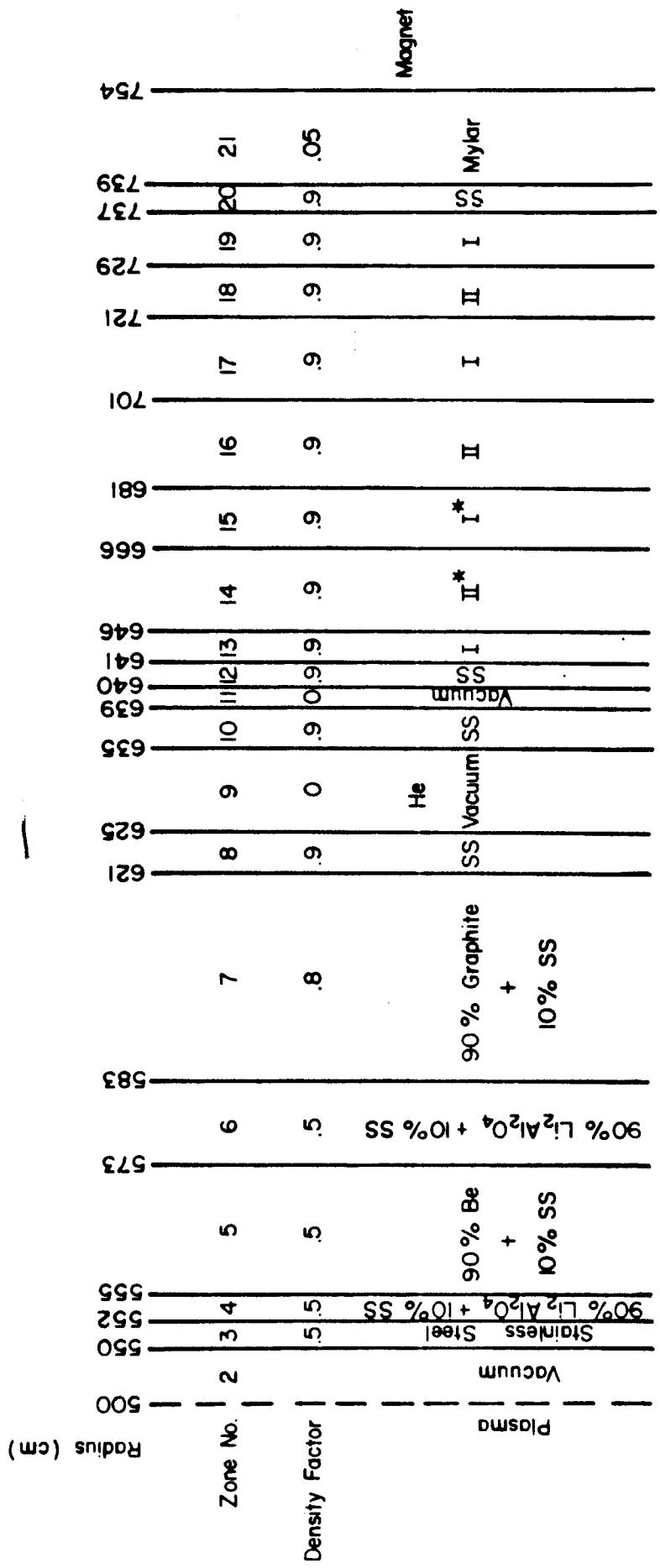

Material I is a mixture of 90% B_4C + 10% SS and Material II is a mixture of 90% Pb + 10% SS

Figure I-13 **A Schematic of UWMAK-II Blanket and Shield**

Table I-7

Summary of Tritium Breeding, Nuclear Heating, Energy Leakage, and Radiation Damage Parameters in the UWMAK-II Design*

(One Dimensional Transport Calculations)

Parameter	UWMAK-II	
^{6}Li (n,α)t	1.1801	
^{7}Li (n,n'α)t	0.0034	
^{9}Be (n,t)	0.0105	
Tritium Breeding Ratio	1.1935	
Neutron Heating	13.1088	MeV/DT neutron
Gamma Heating	4.9563	MeV/DT neutron
Total Heating From Neutrons	18.0651	MeV/DT neutron
Over Heating (incl. alpha particles)	21.5851	MeV/DT neutron
Neutron Energy Leakage to the magnet	0.884×10^{-6}	MeV/DT neutron
Gamma Energy Leakage to the magnet	0.137×10^{-6}	MeV/DT neutron
Total Nuclear Radiation Load to the magnets (watts)	256	

* Based on One Dimensional Transport Calculations.

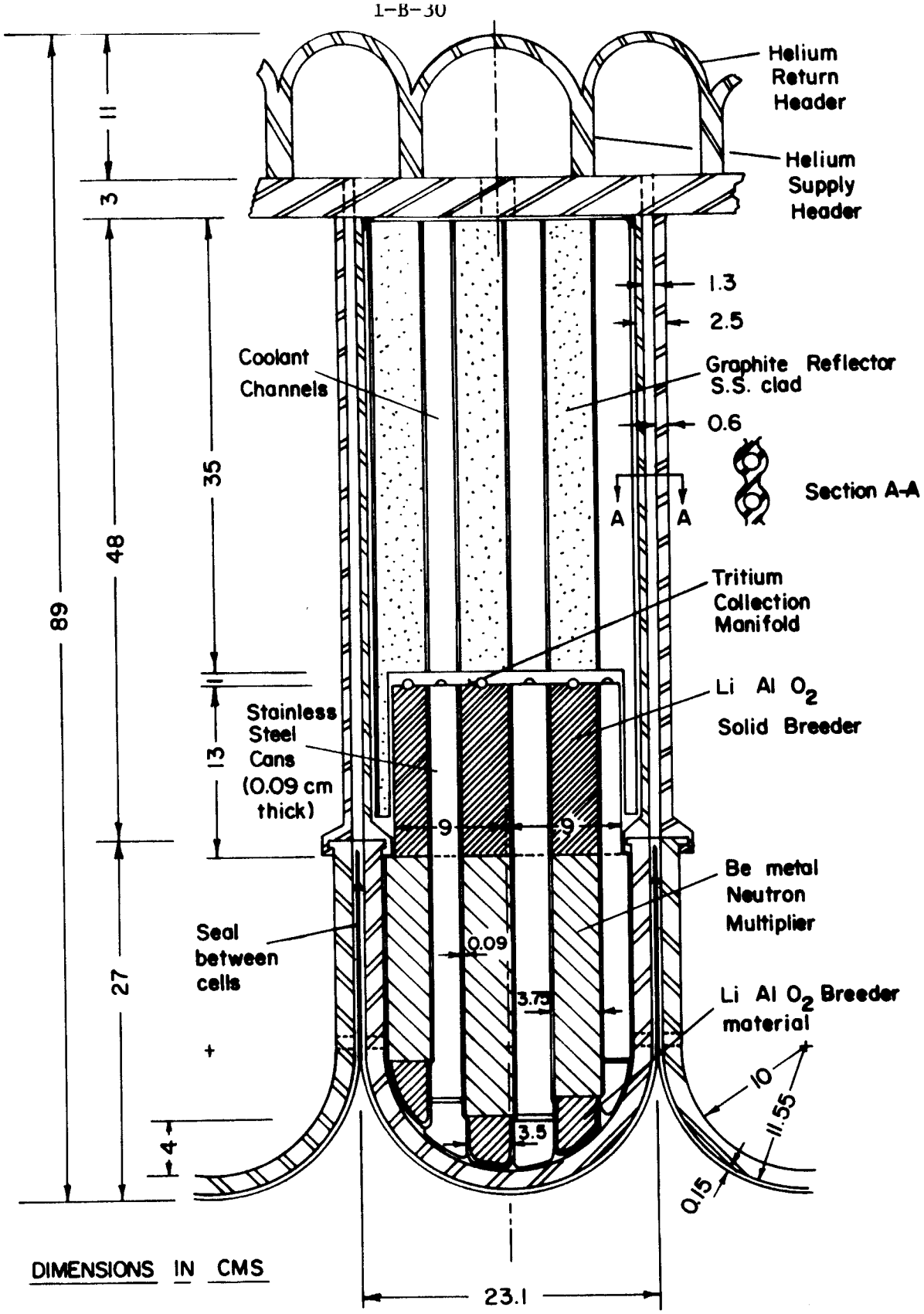

Figure I-14

Vertical Section through solid blanket cells

Table I-8

Breeding Ratio for UWMAK-II

	One Dimensional Discrete Ordinates	Three Dimensional Monte Carlo
$^{6}Li(n,\alpha)T$	1.1801	1.0502 ± 0.021
$^{7}Li(n,n'\alpha)T$	0.0034	0.00408 ± 0.00016
Be(n,T)	0.0105	0.00559 ± 0.00033
TOTAL	1.19	1.06 ± 0.022

I-B-3-c. Thermal Hydraulics

The energy produced by the D-T reaction is distributed mainly in three zones in the reactor, the blanket, the shield, and the divertor. About 85% of the energy is deposited in the blanket, which has to be extracted at as high a temperature as possible to obtain high thermal efficiency. Since pressurized helium is the coolant, the thermal design aspect of helium cooled fusion reactor closely resembles that of a HTGR. It is well known that large coolant circulating power is required for a gas cooled reactor. The design criterion is, therefore, to achieve a system which minimum pumping power while providing adequate heat transfer.

The unique features of the UWMAK-II blanket design are as follows: the first wall temperature is maintained relatively low, ~550°C; the hoop stress and thermal stress in the first wall are uncoupled; and the breeding material is contained in rods to separate tritium from the primary coolant.

The first wall of the blanket is subject to the maximum stress. Therefore, it is advantageous to keep the temperature of the first wall low. The UWMAK-II design directs the coolant toward the first wall before it enters the blanket. This automatically causes the blanket to be made of either U-shaped or hexagonal-shaped module cells. U-shaped cells are used because they are easier to fabricate. A view of a module cell is given in Fig. I-3.

The stainless steel required for the structural components and coolant tubing was estimated at 10% of the physical volume of the blanket and shield. The blanket is conceived as composed of cells, each 20 cm wide and 90 cm deep, and the stainless steel cell walls are about 7 mm thick. The lithium aluminate and beryllium will be packed in pins with an average stainless steel wall thickness of 0.75 mm.

Zones 4 and 6 in Fig. I-13 are the tritium production zones. They are 3 and 10 cm thick, respectively, and the lithium is enriched to 90% in ^{6}Li. Due to the slow tritium diffusion predicted, the lithium aluminate must be fabricated as very small pellets and these must remain small during the high temperature irradiation exposure. Thus a large void fraction (~50%) exists in the lithium aluminate region. Zone 5 in an 18 cm thick region of 90% beryllium plus 10% stainless steel. A density factor of 0.5 is used in this zone in order to accomodate the swelling resulting from excessive helium production in the beryllium.

Zone 7 is 38 cm of 90% graphite plus 10% SS. The graphite serves as moderator for the high energy neutrons streaming out of the neutron multiplication and tritium production zones and reflects some of the neutrons back into these zones.

The headers for the primary helium coolant are idealized in the one-dimensional model by zones 8, 9, and 10. The 8 cm of stainless steel in zones 8 and 10 serve also as a neutron reflector and they extract the greater part of the useful kinetic energy remaining with the neutrons and photons.

Zone 11 is a 1 cm vacuum gap and it serves as a thermal barrier between the high temperature blanket (about 600°C) and the low temperature shield (approximately 200°C). Zones 12 through 20 comprise the magnet shield. The shield composition and dimensions resulted from optimizing the total cost of the shield, magnet, and the helium refrigerators required to cool the superconducting magnet to about 4°K. The shield is 96 cm thick and consists of alternating zones of lead and boron carbide on an equal volume basis with 10% of the total volume occupied by stainless steel for structural purposes. The 1 cm of stainless steel in zone 12 is a structural support for the heavy weight of the shield. Zone 20, which is 2 cm of stainless steel, is a part of the magnet and it represents the dewar for the cryogenic system. Zone 21 is thermal insulation for the magnet and cryogenic systems and about 95% of this zone is vacuum in order to prevent heat transfer by conduction. The mylar superinsulation reduces the thermal radiation losses.

As mentioned earlier, the U-shaped module has a thick wall to contain the high helium pressure and small coolant channels with thin walls which face the plasma. The coolant is fed from the supply headers to the small coolant channels to cool the first wall and then enters the main part of the blanket.

The pressure of the helium coolant is 750 psia and the coolant temperature rise through the blanket is 200°C. The maximum exit temperature is 650°C and the inlet temperature is 450°C. The coolant temperature and the temperature of the structure along the coolant flow path in the blanket is shown on Fig. I-15. The maximum temperature on the first wall is 550°C, which limits the maximum first wall stress to 10,000 psi. The maximum structure temperature in the blanket reaches 686°C in the interior of the blanket. This is not, however, stress bearing structure so that the high temperature is acceptable.

The size of the rods containing the breeder material and beryllium is chosen so that the maximum temperature in the interior of the rod would be comfortably below the melting point of the breeding material. One of the reasons for picking $LiAlO_2$ is its high melting temperature. A calculation of the steady state temperature distribution for a typical rod shows that the maximum temperature in the $LiAlO_2$ zone is only 1100°C. This is well below the melting temperature but may cause problems due to excessive sintering.

The maximum coolant pressure drop has been calculated to be 29 psi and the pumping power required is 282 MW_{th}. A summary of the major thermal hydraulics parameters is given in Table I-9.

I-B-3-d. Mechanical Design and Blanket Disassembly

The blanket and shield configuration in UWMAK-II is not continuous but is made up of many different regions (See Fig. I-2). Before we can describe the support of the blanket, we will define these regions.

The part of the blanket lying between the inner top and inner bottom divertor slots will be referred to as the inner blanket. Similarly, the part lying between the outer top and bottom divertor slots will be called the outer blanket. Those regions falling between the divertor slots will be called central blanket regions.

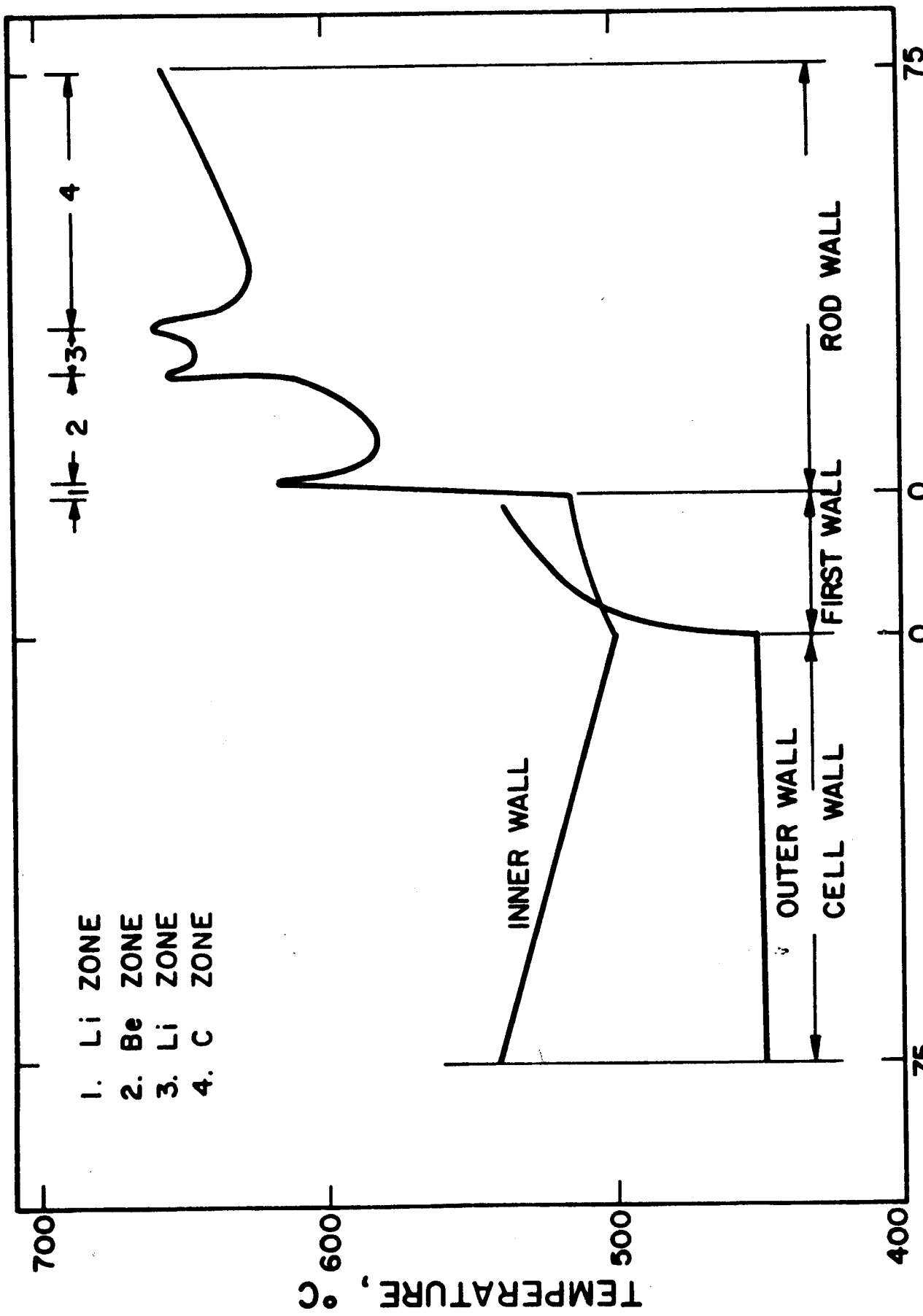

Figure I-15 Structure Temperature in the Blanket

Table I- 9

Summary of UWMAK-II Thermal Hydraulics

Breeding material	$LiAlO_2$
Neutron Multiplier	Be
Reflector	C
Moderator	C
Coolant, primary	He
Coolant, Secondary	None
Coolant inlet temperature	450°C
Coolant exit temperature	650°C
Maximum first wall temperature	550°C
Maximum structure temperature	654°C
Maximum blanket temperature($LiAlO_2$)	1097°C
Maximum first wall pressure	750 psia (5.2×10^6 N/m^2)
Maximum first wall stress	8103 psi (5.6×10^7 N/m^2)
Coolant flow rate	4,303 kg/sec
Maximum coolant pressure drop	29 psi (2×10^5 N/m^2)
Pumping power required	282 MW_{th}

The complete toroid is divided into 24 equal modules and each blanket region is further divided into sections which will be discussed later. Table I-10 gives the mass distribution in the blanket. The inner shield is directly supported on the dewar and provides the base for the support of the inner blanket. Because of the difference in temperature between blanket and shield, a non-rigid attachment will have to be provided between them. In addition, expansion joints between modules are provided. Expansion gaps of 1.94 cm and 4.6 cm between inner and outer blanket modules respectively have to be provided. Fig. I-16 shows a possible scheme for providing expansion joints between modules. The single convolution welded bellows attached to flanges surrounds the toroid in the poloidal direction. In the inner blanket region (Fig. I-16 (a)) the flanges are designed to be attached to the blanket module by means of a weld from the plasma side while on the outer blanket region the weld is external. In some places, the expansion joint is permanently attached to structure which is not normally removed during front wall replacement. Blanket regions are also welded to permanent structures in the toroidal direction. The central blanket is attached to the central shield which in turn is supported on structure extending to massive roof beams on top and to the ground on the bottom.

In the case of the outer blanket, the situation is somewhat different. The outer shield has been designed to open up clam-shell wise making the outer blanket accessible from the outside. (See Figs. I-1 and I-2). The back legs of the extended D toroidal magnets are far enough apart as to allow a module of the outer shield to swing out between them. A small wedge at the outer perifery of the shield between modules will have to be removed beforehand to make this possible.

Each half of an outer shield module weighs 330 MT and an outer shield module weighs 158 MT. The structure needed to support this load, as well as to resist the large bending moments produced when the shield is in the open position, will have to be quite massive. There is room in this region for such structure. Ultimately, the load is transferred to the roof beams by means of supports extending between the magnets.

The outer blanket modules will be attached to reinforced plates which also make up the wall of the outer divertor slots. These plates are an integral part of the structure which supports the outer shield. As mentioned previously, welding outer blanket modules in the poloidal direction to the expansion joint and in the toroidal direction to the outer divertor plate constitutes the vacuum seal in the plasma toroid.

The neutron radiation damage to the front wall necessitates its periodic replacement every two years. In order to make the blanket accessible, the following functions would have to be performed: First, the outer divertor slot vacuum pumps will have to be disconnected and removed. Second, the two outermost vertical field coils, both upper and lower, will have to be retracted. Third, the helium supply and return lines are disconnected and finally, the outer shield halves are swung open. (See Fig. I-1 and I-2). The back side of the outer shield is now exposed. Rails can be placed radially between the magnets (see Fig. I-1) and a special counterbalanced carriage designed to support the outer blanket can be rolled in. While the carriage supports the outer blanket, remotely controlled plasma cutting torches will burn away the seal wall between adjacent modules as well as the top and bottom seals to the support plates. The outer blanket module can now be rolled out on the carriage to a service area for front wall replacement. Once the outer blanket is removed, it makes the remaining inner and central blanket regions accessible. These regions can also be disconnected and removed to the service areas.

Table I-10

UWMAK-II Blanket (Weight in Metric Tonnes)

	Inner	Outer	Central
Removable Front Wall (S.S.)	222.18	460.78	115.43
Vertical Structure and Headers (S.S.)	616.83	1277.60	320.00
Canner for Breeder and Moderator (S.S.)	182.00	392.00	84.00
Be and $LiAlO_2$	225.00	486.00	104.00
Graphite	567.00	1174.00	147.10
Total in Reactor	1813.81	3790.88	770.76
Total per Module	75.57	157.95	32.1
			Or 16.05 each

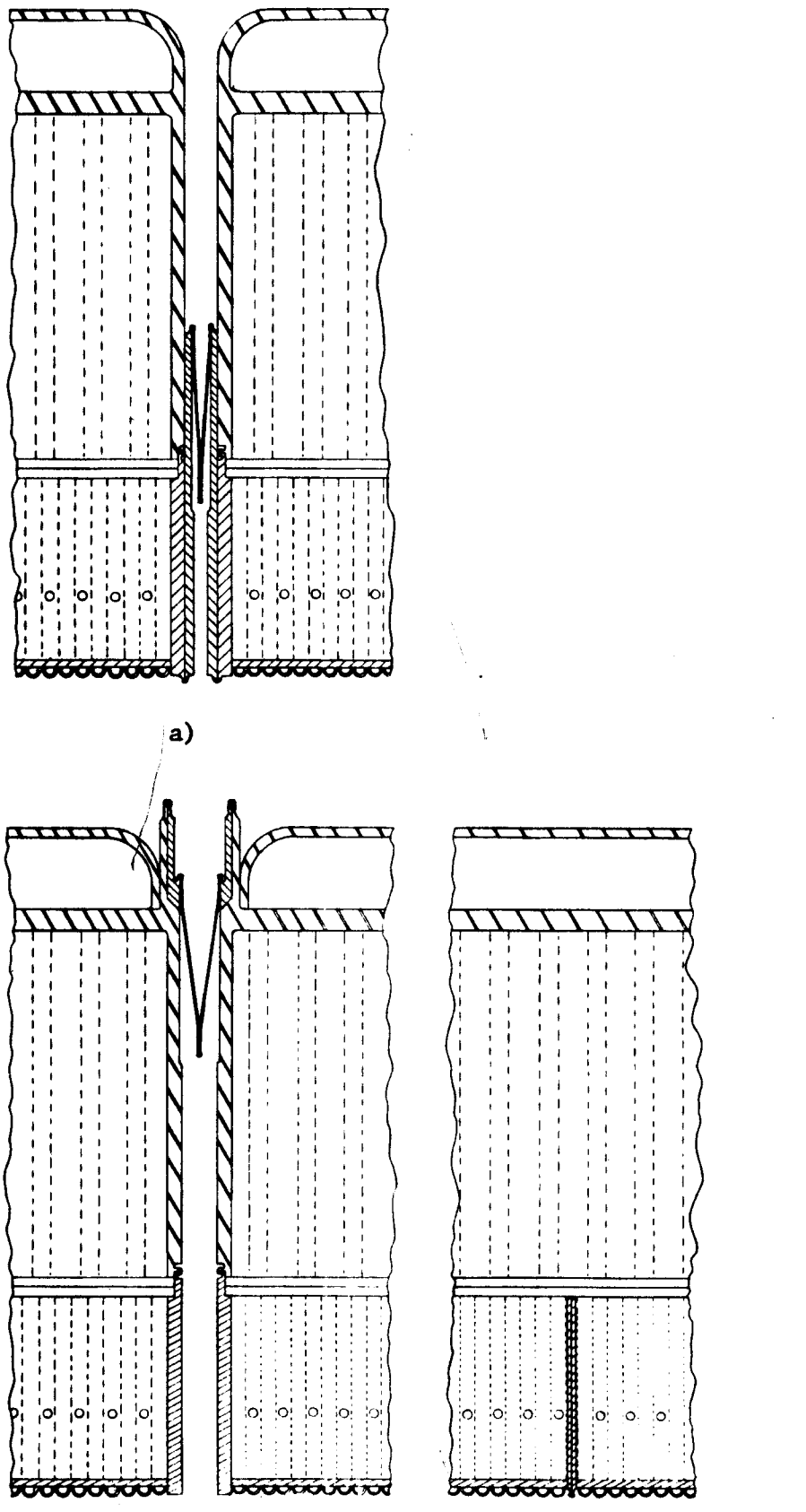

Figure I-16

It is significant to note that in UWMAK-I design,[1] recycling the front wall required the removal of 12 modules weighing 3600 MT each. In UWMAK-II, there are 24 modules weighing 265 MT each and the heaviest piece in each module weighs 175 MT. Clearly, the handling problem has been simplified.

I-B-4 Tritium Considerations

During operation, tritium is present in the blanket, the helium coolant, the tritium extraction beds, the plasma, the divertor, the fuel injectors, and the fuel reprocessing equipment. Many of these systems are composed of a large number of individual pumps, valves, pipes, flanges, etc. Permeation and leakage of tritium from this multitude of components is inevitable. Because tritium is by far the most mobile of all the radioactive constituents in a fusion power plant, it will be necessary to design high integrity systems and back them with tritium scavenger systems which will contain the tritium leakage within the reactor building so that the tritium release to the environment is minimal.

Nearly all of the tritium handling equipment is housed in a reactor hall which will be hermetically sealed from the environment. All gases and liquids which may exit from the reactor hall are scavaged for traces of tritium-bearing material before being discharged to the environment. Because the hermetic seal is at ambient temperature where diffusion is very slow, and the scavenging systems are very efficient, the tritium release from the reactor hall can be kept to a relatively low value, <1 Ci/day.

The tritium escape route which appears to be the most difficult to control is permeation through the heat exchanger which will permit the transfer of tritium from the helium coolant to the steam system. Recovery of very dilute tritiated water from the steam system at a reasonable cost is beyond present technology.

The diffusion of tritium in the non-metallic compounds like $LiAlO_2$ is more difficult to estimate than for intermetallic compounds like LiAl because few measurements have been published on either hydrogen or tritium diffusion in ceramic materials. The relevant data are summarized in Fig. I-17. A conservative diffusion rate for tritium in $LiAlO_2$ or Li_2SiO_4 is proposed, as shown in Fig. I-17. Based upon the predicted diffusion coefficients for tritium in $LiAlO_2$, an approximate tritium inventory due to diffusion can be calculated from Jost's relationship once the temperature has been established. The temperature profile is assumed to be parabolic with a maximum of ~1100°C to an edge temperature of ~700°C in the hottest portion of the rod. In the 'coolest' part of the $LiAlO_2$ zone, the temperature varies from 850°C to 700°C. It has been calculated that the minimum tritium inventory due to diffusion processes ranges from 127 grams if a uniform 20 micron diameter particle size is used (i.e. a density of ~50% of theoretical is maintained) to ~730 grams if a mixture of particle sizes is used to achieve a 90% density factor. The numbers may be actually be somewhat larger than this because of tritium holdup in the cooler parts of the breeding section and if substantial sintering of the particles take place.

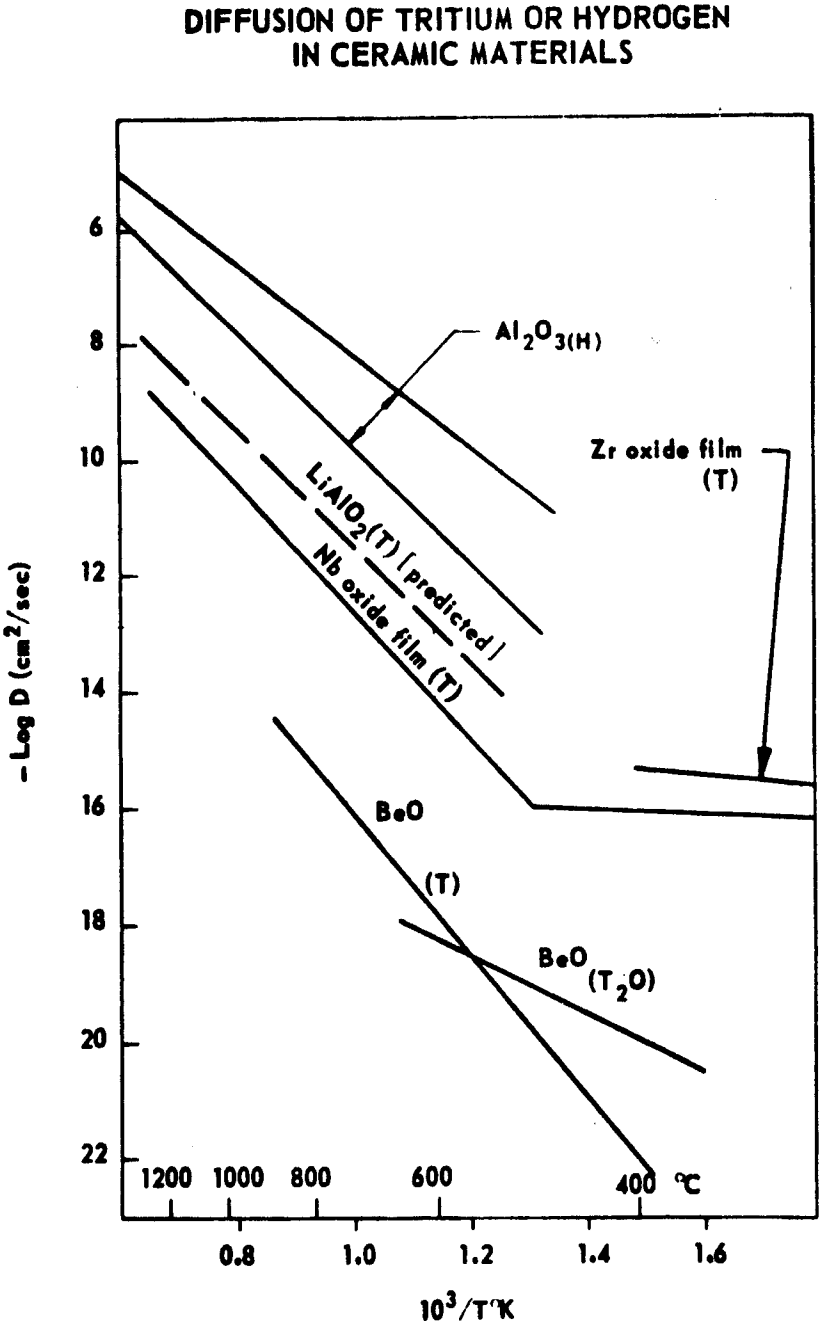
DIFFUSION OF TRITIUM OR HYDROGEN
IN CERAMIC MATERIALS
- Log D (cm²/sec)
6
8
10
12
14
16
18
20
22
Al2O3(H)
Zr oxide film
(T)
LiAlO2(T) [predicted]
Nb oxide film (T)
BeO
(T)
BeO
(T2O)
1200 1000 800 600 400 °C
0.8 1.0 1.2 1.4 1.6
10³/T°K

Figure I-17

The need for small sized particles means a bed of finely crushed powders cannot be cooled directly by the circulation of main helium coolant because the pressure drop would be excessively large. Consequently, the bed is cooled only by the conduction of heat to the surface.

The breeder material and the beryllium are therefore placed inside stainless steel tubes approximately 3.5 cm in diameter with a wall thickness of 0.75 mm and nearly 30 cm long. (see Fig. I-3.) These tubes would be closed at the end facing the plasma and connected at the other end to a small gas plenum attached to a tritium extraction system external to the reactor. Alternatively, the exhaust ends of these tubes could be closed by the use of a porous metal plug. This plug would retain the ceramic powder inside of the tube but permit the tritium to diffuse into the helium coolant where it would be extracted. Such a technique would increase the tritium inventory within the tubes, increase the partial pressure of tritium in the helium coolant and subsequently increase the permeation of tritium through the primary heat exchanger. The design philosophy chosen is to minimize the tritium contamination in the helium coolant and extract the tritium directly from the tubes in a separate recovery system.

Conceptually, the tritium gas can be removed from these tubes by using a flowing helium stream or by continuous pumping with a vacuum system. We have chosen a flowing helium stream and for a helium pressure inside the tubes of 1.4 atm, the tritium pressure can be kept to 10^{-4} torr.

Turning to the problem of tritium escape into the primary helium coolant and then from the reactor, we note that the partial pressure of T_2 inside the breeder tubes is 10^{-4} torr. This would lead to 1.35×10^{4} cm^3 (STP)/day, or 3.6×10^{4} Ci/day of tritium leaking into the main He coolant and hence from the plant, clearly too large a value.

An extraction system which is not easily poisoned can be provided when oxygen is admitted to the helium system. The radiation present within the helium coolant passageways of an operating reactor should be sufficiently reactive so that the following equilibrium is quickly established:

$$T_2 + 1/2\ O_2 = T_2O.$$

The equilibrium constant for this reaction has been estimated to be 6.3×10^{11} torr$^{-1/2}$ at 525°C, approximately the median temperature of the helium in the blanket. If the partial pressure of oxygen is maintained at 10^{-2} torr and the T_2O is continuously removed so that its partial pressure is $\sim 10^{-3}$ torr, then the partial pressure of tritium can be calculated to be 1.6×10^{-14} torr. At this partial pressure, the tritium leakage to the steam system is only 0.8 Ci/day. This permeation rate could be reduced if the oxide coating in a SS-steam generator reduces tritium diffusion, or if a duplex steam generator tube is developed.

A summary of the tritium breeding and recovery system parameters are given in table I-11 and a diagram outlining the main coolant flows and showing the tritium extraction systems is given in Fig. I-18. The calculated tritium release rate is 0.8 Ci/day.

The tritium and deuterium leakage from the plasma is very large, nearly 950 gT/hr. These fuel particles will be recovered by a combination of liquid lithium trapping and vacuum pumping. A yttrium bed is proposed for the removal of the D+T from the liquid, as described in UWMAK-I.[1] Preliminary estimates of the tritium inventory in this system are included in Table I-12.

TABLE I-11

Parameters of Tritium Breeding and Recovery Systems for UWMAK-II

	UWMAK-II
Coolant	Helium (10^6 moles)
T_2 Breeder	$LiAlO_2$ (90% Li-6)
Li in Blanket, kg	4.1×10^4
Coolant Temperature, Max. (°C)	650
Tritium Inventory in Breeder	
Solubility	7.0 g
Diffusion, 10 μm path *	120.0 g
Total	127.0 g
Tritium Pressure in Breeding Zone (torr)	10^{-4}
Tritium pressure for diffusion into steam (torr)	1.6×10^{-14}
Tritium Generation Rate, g/sec	1×10^{-2}
Additive to Coolant	O_2 (10^{-2} torr)
Tritium Species in Coolant for Recovery	T_2O
Extraction Bed	Molecular Sieves
τ (coolant transit time) sec	1
Fraction coolant to bed	0.7%
Intermediate Heat Exc.	none
Tritium Leakage to steam, Ci/day	1
Heat Exchanger, helium - steam	SS
Area, cm^2	8.3×10^8
Thickness, mm	4.0
Temperature, avg. °C	460

*assuming no sintering

COOLANT FLOWS FOR UWMAK-II

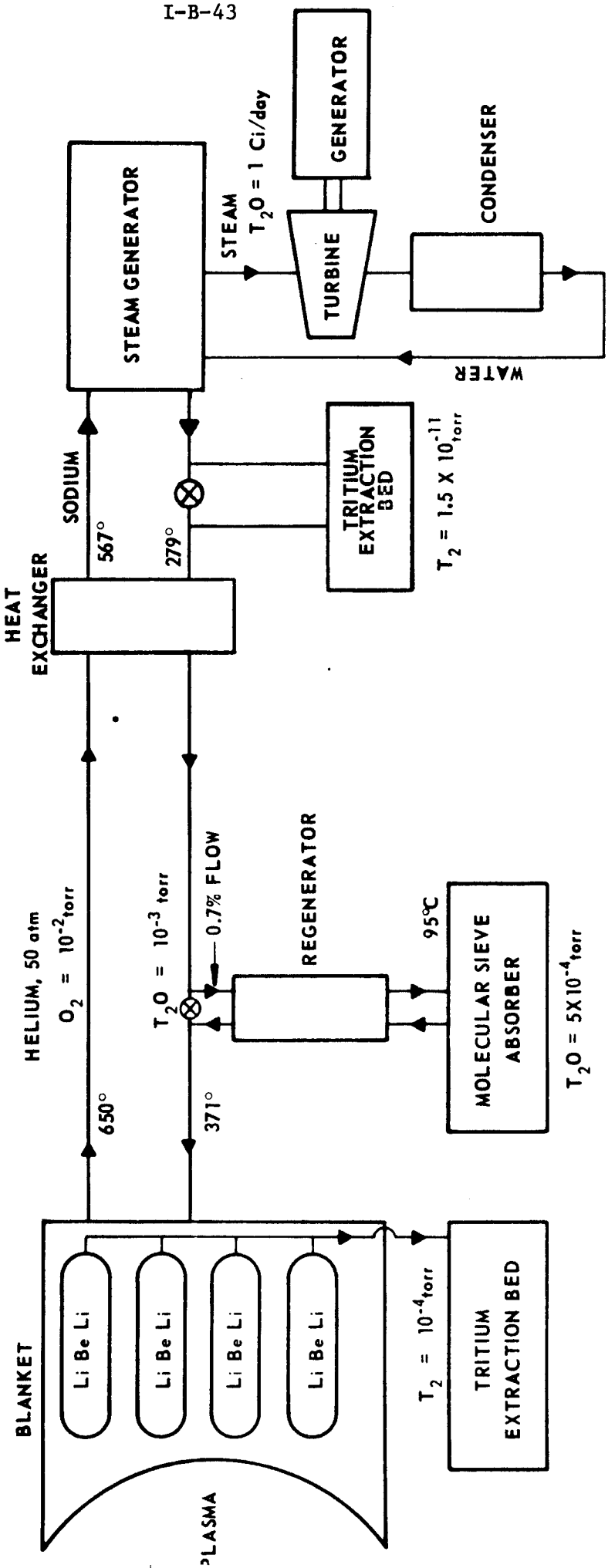

Figure I-18

Table I-12

Equilibrium Tritium Inventories for UWMAK-II

(in grams of T)

Location	
Breeder	
Material	120-725
Coolant External to Breeding Zone	0.2
Recovery Beds (12 hr cycle)	420
Total in breeder system	540-1145
Divertor	
In Lithium	8
Recovery bed (4 hr cycle)	3500
Vacuum system (4 hr cycle)	125
Fuel System	12850
(1 day supply)	———
Total in reactor area	17.1-17.7 kg*

*This number is very dependent on the reserve amount of T_2 in the fueling system. For example, if as much as one week's reserve must be maintained, the total tritium inventory would be ~95 kg.

I-B-5 Radiation Damage

Outside of the plasma physics problems, it still appears that the most severe CTR technological problem that must be solved before commercialization of fusion power is the degradation of the materials performance in the environment of neutrons, charged particles and photons released from the D-T reaction. This conclusion is even more true for UWMAK-II than it was for UWMAK-I. Several new problems have arisen for the neutron multiplier and solid breeder which can have a significant effect on the overall reactor performance. We will attempt to highlight only the most severe radiation damage problems here while the details are given in the bulk of the report.

The radiation damage problems in UWMAK-II can be broken up into seven convenient categories, working from the plasma outward:

1. Curtain (carbon)
2. Structure (316 SS)
3. Breeder ($LiAlO_2$)
4. Neutron Multiplier (Be)
5. Reflector (carbon)
6. Shielding (Pb, B_4C)
7. Magnet Materials (Cu, NbTi, Mylar insulation)

The operating environments for each of these areas is given in Table I-13.

The carbon curtain, which is closest to the plasma experiences the most severe environment in terms of temperature and neutron bombardment. Its temperature will vary from ~1200°C during the burn to ~650°C during the recycle period between burns. The curtain will also accumulate neutron fluences of ~$2.6 \times 10^{21} cm^{-2} yr^{-1}$ (E>13.5 MeV) and ~$1.1 \times 10^{22} cm^{-2} yr^{-1}$ (E>1 MeV) at the upper temperature. The stainless steel structure will operate at a much lower temperature (T<660°C) and will be subject to a wide variation of fluences in the blanket, shield and toroidal field magnets.

The breeder material will also be subject to high fluences of neutrons as well as high internal heating rates (3-14 watts/cm^3). Large temperature gradients will exist across the lithium ceramic rod, operating at 640-1100°C resulting in thermal gradients of ~225°C/cm. Similar neutron fluences will be incident on the Be multiplier but the thermal gradients should be much less (<5°C/cm) because of the much higher thermal conductivity of Be.

The graphite reflector will suffer moderate damage in the temperature range of 600-700°C while accumulating neutron fluences of up to $3.7 \times 10^{21} n/cm^2/yr$ (E>1 MeV). Dimensional instability is the major concern here.

Table I-13

Summary of the Environment for the UWMAK-II Solid Materials

Function	Material	Distance From First Wall-cm	Temperature Range °C	Neutron Fluence $n/cm^2/yr \times 10^{21}$ (a)			Maximum Nuclear Heating $Watts/cm^3$	Other
				> 13.5 MeV	> 1 MeV	Total		
Curtain	C	-2	650-1200	2.4	11	14		1200°C during burn, 650°C during recycle
Structure	316 SS	0-89 (Blanket)	450-660	0.0017-2.4	0.14-11	0.18-14	12	4500 cycles yr^{-1}, 5 $watts/cm^2$
		89-189 (Shield)	50-200	1.3×10^{-8}-1.7×10^{-3}	1.6×10^{-6}-0.14	1.8×10^{-6}-0.18	0.08	High pressure He cooling
		204-302 (Magnet)	-269	$\leq 1.3\times10^{-8}$	$<1.6\times10^{-6}$	$<1.8\times10^{-6}$	2×10^{-4}	Liquid He Temperature
Breeder	$LiAlO_2$	2-4.5	640-1100	1.5-1.8	9.8-10	12-13	9-14	Large thermal gradient across breeder pins
		23-32	690-950	0.22-0.37	3.7-5.4	4.8-7.1	3-10	Large thermal gradient across breeder pins
Neutron Multiplier	Be	5-22	580-615	0.39-1.3	5.4-9.8	7.1-9.8	2-4	
Reflector	C	32-70	655	5.8×10^{-3}-0.22	0.35-3.7	1.0-4.8	0.3	
Shielding	Pb, B_4C, SS	89-189	50-200	1.3×10^{-8}-1.7×10^{-3}	1.8×10^{-6}-0.16	1.8×10^{-6} - 0.18	0.08	High pressure He cooling
Magnet Materials	Cu, NbTi	204-302	-269	$<1.3\times10^{-8}$	$<1.8\times10^{-6}$	$<1.8\times10^{-6}$	2×10^{-4}	Warm up to room temperature every few years

(a) 80% Plant Factor

The damage to the Pb in the temperature range of 50-200°C at fluences of up to 1.6 x 10^{20}n/cm^2/yr is not expected to be severe, especially since the Pb is not structural material. However, one point which was not investigated here and should be looked into in the future is the neutron induced swelling in Pb in this temperature fluence range. The operating environment for the B_4C is essentially the same as for UWMAK-I except that the UWMAK-II shield is thicker and provides more attenuation of neutron damage. The neutron flux leaking to the UWMAK-II magnet is far less than that of UWMAK-I and hence, the damage was found to be much smaller, almost to the point of no concern.

a. Damage in Carbon Curtain

The displacement damage in the carbon curtain has been calculated to be ~8.6 dpa per year assuming an 80% plant factor. This should correspond to ~1.2 x 10^{22}n/cm^2/year in a fission reactor. Estimates of the time required for the graphite to pass through the initial shrinkage phase and enter the breakaway swelling regime vary from roughly 1 to 2 years of operation if the cloth has properties similar to type 9640 graphite (Figure I-19). This means that the curtain should be changed every time the first wall is changed. Since the curtain does not have a structural role and is relatively cheap (~25$/m^2) such a change over should not adversly effect the reactor operation.

It has also been calculated that ~2200 atomic parts per million of helium gas will be generated in the carbon per year of operation. The behavior of carbon at high temperatures (≳1000°C) with such large amounts of helium needs to be investigated but preliminary considerations show that the helium may diffuse out of the carbon.

Finally, erosion by charged particle and neutron sputtering are estimated to be ~1 micron per year if neutron sputtering values of ~10^{-2} are used for E_n < 10 MeV and 10^{-4} for E_n = 10-15 MeV. If the high 'chunk' sputtering values of Kaminsky are used then ~100 microns per year could be lost from the carbon. Such erosion is not particularly important from the standpoint of thickness reductions but could present a problem to the vacuum system. (an erosion rate of 100 microns per year amounts to ~1 tonne of carbon per year). Removal of carbon by blistering at >1000°C is virtually an unknown quantity but using pessimistic numbers from metal blistering reveals that less than 1 micron a year could be lost by this mechanism.

b. 316 Stainless Steel Structure

Perhaps the most critical component in the UWMAK-II blanket is the 316SS structure. It must maintain a vacuum environment under the combined action of thermal and mechanical stresses in the face of a constantly changing microstructure. A summary of the displacement and helium production rates is given in Table I-14

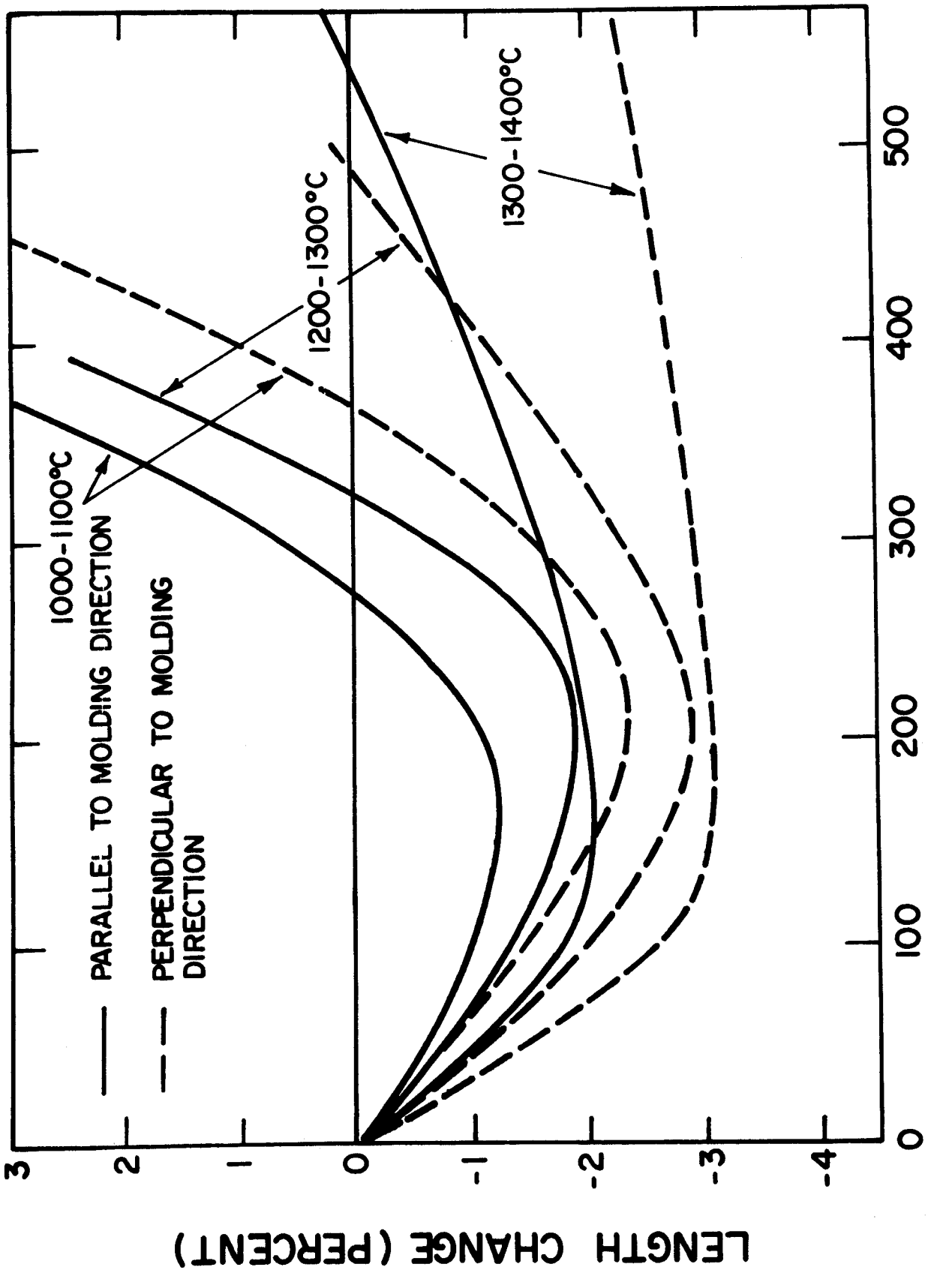

FIGURE I-19 - Length Changes of 9640 Type Graphite [9]

for various positions through the blanket, shield and into the magnet region. The displacement rate varies from a maximum of 8.58 dpa/year (80% plant factor) at the first wall to 0.117 dpa/year at the blanket-shield interface. The helium production rate varies from 187 appm per year at the first wall to 0.33 appm/year at the blanket-shield interface. The temperature of the 316SS varies from 450-658°C over this same distance.

The displacement and gas production rates are rather small in the shield region varying from ~$2x10^{-6}$ to 0.117 dpa/year and $5x10^{-6}$ to 0.33 appm He/year. The temperature is also quite modest (50-200°C) so that little, if any, change in mechanical properties is expected. The dpa rates correspond to fission neutron fluxes of $2x10^{20}$n/cm^2/year or ~$6x10^{21}$n/cm^2 total fluence over the lifetime of the reactor

Sputtering of the 316SS first wall should be considerably reduced over that from UWMAK-I because there is no direct charged particle flux (i.e. the reason for the carbon curtain). In fact, if the 14 MeV neutron sputtering coefficient is in the neighborhood of 10^{-4}, then the wall erosion is mainly due to the back scattered neutrons and amounts to less than 1 micron per year (including sputtering from both sides). If the high neutron sputtering values of Kaminsky are applicable then the erosion rate could approach 100 microns per year or ~200 microns over the anticipated first year wall life. This is ~13% of the thickness of the outer coolant channels and is close to presenting a significant problem.

The amount of swelling induced in the 20% cold worked material is truly negligible up to two years being less than 0.01% (see Table I-15 and Figure I-20). However, after 10 years of exposure swelling of as much as 10-13% could occur in the first wall and by 30 years the first wall swelling could approach 50%.

The actual construction of the UWMAK-II blanket requires many welds where the structure would lose its cold worked structure. This would cause the structure to behave as a solution treated alloy which is much more susceptible to swelling. Calculations show that we might expect swelling values of as high as 5% per year at the first wall, ~10% after 2 years and 50% after five years of irradiation. The existance of high swelling regions, spaced 1 cm apart on the first wall, next to regions of low swelling will certainly generate large stresses. The complete analysis of this problem is hampered by knowing the rate at which irradiation creep might cause the swelling to be relaxed.

It is concluded that the absolute values of swelling in the UWMAK-II structure can be accomodated if the wall is changed every few years, even taking into account the existence of welded zones. However, it is still an open question of whether the stress (or strain) gradients associated with large swelling gradients can be accomodated without premature failure.

Table I-14

Summary of Displacement Rates and Helium Gas Production in 316 SS as a Function of Distance from the First Wall of UWMAK-II (1.16 MW/m^2 . 80% Plant Factor)

Interval	Distance From First Wall-cm	Zone	dpa/yr	appm He/yr[b]	T_{min} °C	T_{max} °C
3	0	First Wall	8.58[a]	187[b]	450	567 [c]
6	1.5	First Wall	7.4	154	450	567 [c]
9	3	I-$LiAlO_2$ (middle)	6.71	133		593 [d]
13	5	Be-$LiAlO_2$ Interface	5.91	109		592 [d]
19	12.7	Be (middle)	3.90	60.8		584 [d]
27	23	II-$LiAlO_2$-Be Interface	2.26	30.9		609 [d]
39	28	II-$LiAlO_2$ (middle)	1.77	22.6		646 [d]
51	33	C-II $LiAlO_2$	1.24	16.7		658 [d]
86	51.5	C (middle)	0.75	4.50		655 [d]
123	71	Header-C	0.266	1.05		650 [d]
141	90	Shield-Blanket	0.117	0.33		650
149	93.3	1st B_4C Zone (middle)	0.0756	0.25	50	200
175	105.5	1st Pb Zone (middle)	0.0256	5.87 E-2	50	200
215	123.	2nd B_4C Zone (middle)	4.21 E-3	0.87 E-2	50	200
258	140.5	2nd Pb Zone (middle)	9.67 E-4	1.18 E-3	50	200
300	160.6	3rd B_4C Zone (middle)	6.66 E-5	1.26 E-4	50	200
334	175	3rd Pb Zone (middle)	1.23 E-5	2.22 E-5	50	200
351	182.6	3rd B_4C Zone (middle)	4.61 E-6	1.0 E-5	50	200
365	188.5	Outside Shield	1.92 E-6	5.1 E-6	50	200
368	204	Inside Magnet	1.81 E-6	2.81 E-6		-269

(a) Note on the scale of displacement cross sections used for UWMAK-I this would be ~16.9 dpa per year at 100% plant factor, however the present numbers reflect the current displacement damage models.

(b) On the basis of 62.6 at. % Fe, 19.5 at. % Cr, 13.4 at. % Ni only, total amount including all impurities approximately 13% higher.

(c) Cell wall

(d) Rod wall temperatures

Table I-15

Summary of Swelling Data for UWMAK-II 316 Stainless Steel Structure

Data Point *	T°C	dpa/yr	$\Delta V/V_o$(%) Solution Annealed 1yr	2yr	10yr	30yr	20% Cold Worked 1yr	2yr	10yr	30yr
1	450	0.18	0.04	0.08	0.42	1.3	<0.01	<0.01	<0.01	<0.01
2	450	0.46	0.10	0.21	1.0	3.1				↓
3	450	1.1	0.25	0.50	2.5	7.5				0.43
4	450	1.6	0.36	0.73	3.6	10.9			↓	1.5
5	450	3.4	0.77	1.5	7.7	23.2			0.50	5.2
6	481	8.6	3.7	7.4	37.2	111			7.1	28.8
7	512	8.6	4.9	9.9	49.5	148			10.4	42.3
8	520	8.6	5.0	10.0	50.2	151			11.2	45.3
9	532	8.6	4.9	9.8	49.1	147			12.3	49.1
10	540	8.6	4.7	9.4	47.0	141			12.9	50.1
11	523	3.4	2.0	4.0	19.9	59.6			0.96	14.7
12	565	1.6	0.89	1.8	8.9	26.8			<0.01	3.1
13	505	1.1	0.61	1.2	6.1	18.4			↓	0.59
14	505	0.46	0.25	0.51	2.5	7.6				<0.01
15	505	0.18	0.10	0.21	1.0	3.1				<0.01
16	515	7.4	4.3	8.6	43	129			8.5	36.7
17	590	3.4	0.81	1.6	8.1	24.4		↓	3.1	17.6
18	660	1.6	0.03	0.05	0.25	0.75		0.02	0.92	3.7
19	624	1.1	0.08	0.15	0.75	2.75		<0.01	0.13	3.3
20	642	0.46	0.02	0.03	0.17	0.52		↓	0.01	0.64
21	658	0.8	<0.01	0.01	0.04	0.12	↓		<0.01	0.06

*See Figure I-20

FIGURE I-20 SCHEMATIC OF UWMAK-II CELL USED TO CALCULATE SWELLING IN 316 STAINLESS STEEL STRUCTURE[a)]

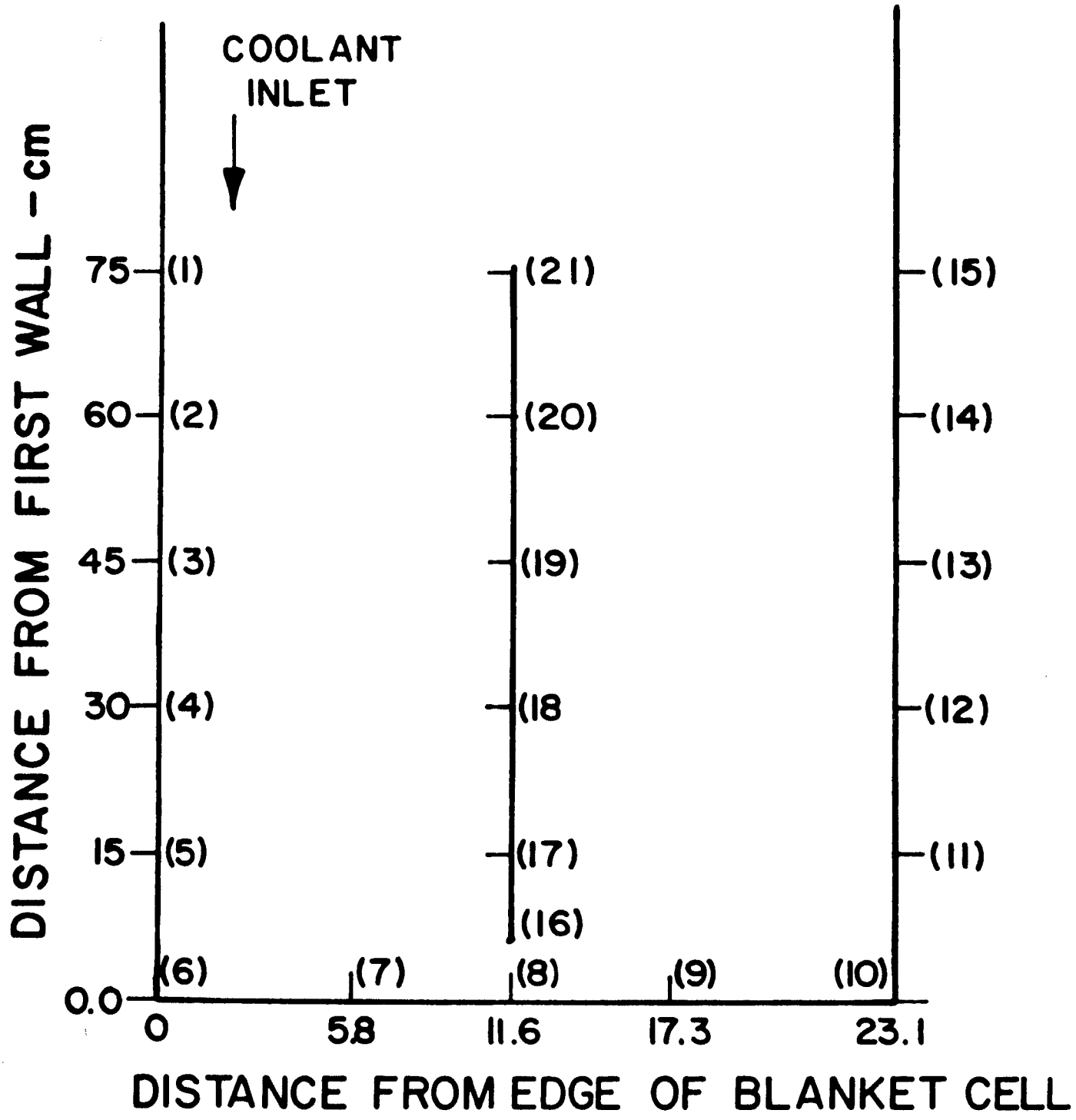

a) Swelling Was only Calculated at the Data points in the Parenthesis and Reported in Table IV-H-1.

The change in mechanical properties of the structure are probably the most severe problems to be faced and also the most difficult to calculate. The major problem is that there are no known specimens of 316 stainless steel (cold worded or otherwise) which have been irradiated to damage levels of 10-20 dpa while accumulating at least 200-400 appm He, at temperatures of 500-650°C while being stressed at ~10 ksi and cycled some 5000-10,000 times. In the absence of such information we are forced to extrapolate fast reactor date (with low helium contents) as thermal reactor data (irradiated in the unstressed state).

One such extrapolation was made on the basis of stress rupture life. It was found that, on the basis of fast reactor data, the stress rupture life for an 8 ksi ($6 \times 10^7 M/m^2$) first wall stress could be ~300 years at 540°C. However this stress rupture life drops dramatically as the allowable stress rises as shown below

σ-ksi	t_r-years
8	284
10	69
12	21
14	7.3
16	3

The question now is how much of a safety factor will be required for fusion reactors. Or stated another way, how much of "stress factor" is reasonable to assign to local thinning, temperature inhomogeneites, higher helium generation, swelling gradients, machining imperfections, etc. It is probably not unreasonable to apply a factor of 50-100% to the calculated stresses in order to assuage high vacuum integrity. Such a factor would place the minimum rupture life between 3 and 21 years, less than the lifetime of the plant.

Another problem may occur in the cans holding the breeder and neutron multiplier. Here the temperature can approach 660°C (1220°F) and damage will accumulate at the rate of 1.77 dpa per year ($3.8 \times 10^{21} n/cm^2$, E >0.1 MEV equivalent). The predicted rupture life of these cans after 10 years of irradiation would be ~1 year at ~16 ksi. Whether or not such stresses could arise from swelling of the Be or $LiAlO_2$ is a question which should be closely examined.

Perhaps an even more restrictive criteria on the steel structure is to retain a measure of ductility in the period between burn when the temperature and/or coolant stresses are changing very rapidly. This situation is somewhat unique in that the critical stresses will occur when the sample is not being irradiated with neutrons. It is difficult to calculate the transient stress-strain behavior during shut down and start up but considering that the temperature could vary by 100-200°C, the thermal stress due to plasma radiation could drop by ~1000 psi ($6.9 \times 10^6 M/m^2$) in a second, or the stress induced by the high pressure gas could vary by a few thousand psi in less than a minute, it is not unreasonable to expect strain approaching a few tenths of a percent may be present in the structure. This may be especially true for the cans holding the $LiAlO_2$ because of the high heating rates in the rod compared to the cans.

We have somewhat arbitrarily chosen a minimum uniform elongation limit of 0.5% for the design of UWMAK-II. This is slightly above the 0.4% UE limit for LMFBR cladding although the operating conditions are quite different for each reactor. After having chosen this limit we then must rely on fast reactor data to indicate when the 316SS might drop below this ductility limit. Such a consideration shows (Figure I-21) that we might drop below this limit after ~2 years of displacement damage.

Perhaps an even more critical question is how high helium content may effect this limit. While, recent experiments at ORNL are not conclusive on this subject, they do indicate that the limit may be reached at low dpa values (2-4) and helium contents of 30-50 appm He. This would correspond to 3-4 months in UWMAK-II. However, it is encouraging that at very high helium contents (~4000-6000 appm He) and dpa value (~50 dpa) the ductility properties are not any worse and perhaps slightly better. More data is required to make a statistically meaningful conclusion from this recent data.

Nevertheless, we see no data that would change our general conclusion that one should change the first wall approximately every two years to avoid fracturing a relatively brittle structure during the shutdown or start up period between burns. It should be noted that this analysis does not include the effects of fatigue or irradiation induced creep both of which may result in shorter wall lifetimes.

c. Solid Tritium Breeder

The basic function of the $LiAlO_2$ also turns out to cause its major problem, that is, the Li(n,T) reaction also produces a helium atom. It has been calculated as much as 30,000 appm of helium gas could be produced in the $LiAlO_2$ per year of operation. Such high helium contents at temperatures of 1000-1100°C (70% of the melting point), in temperature gradients of ~230°C per cm will certainly cause large dimensional changes. There is no known data for these conditions but calculations show that the swelling could amount to 50% or more per year. depending on the bubble size (Figure I-22). Even more significant than the fact that the initial density of the $LiAlO_2$ must be reduced to a level which cuts the breeding ratio dangerously low, may be the stress imposed on the cladding. This is very similar to the case for the swelling of oxide fuel in fission reactors. A rupture of the cladding in UWMAK-II would release a large amount of T_2 into the primary He coolant and could significantly increase the tritium leakage rate to the steam cycle. Therefore, since the first wall should be changed every two years, we will also change the $LiAlO_2$ at the same time.

d. Beryllium

The major problem of Be is the same as for $LiAlO_2$, high helium gas production at high temperatures. The calculated helium production rate is ~2430 appm per year at ~56% of the melting point. Calculated swelling values are on the order of 50% per year. Again this forces a initially low density to accomodate such swelling without inducing unacceptable stresses in the cladding. This also means the Be will be changed every two years. Such a strategy results in a

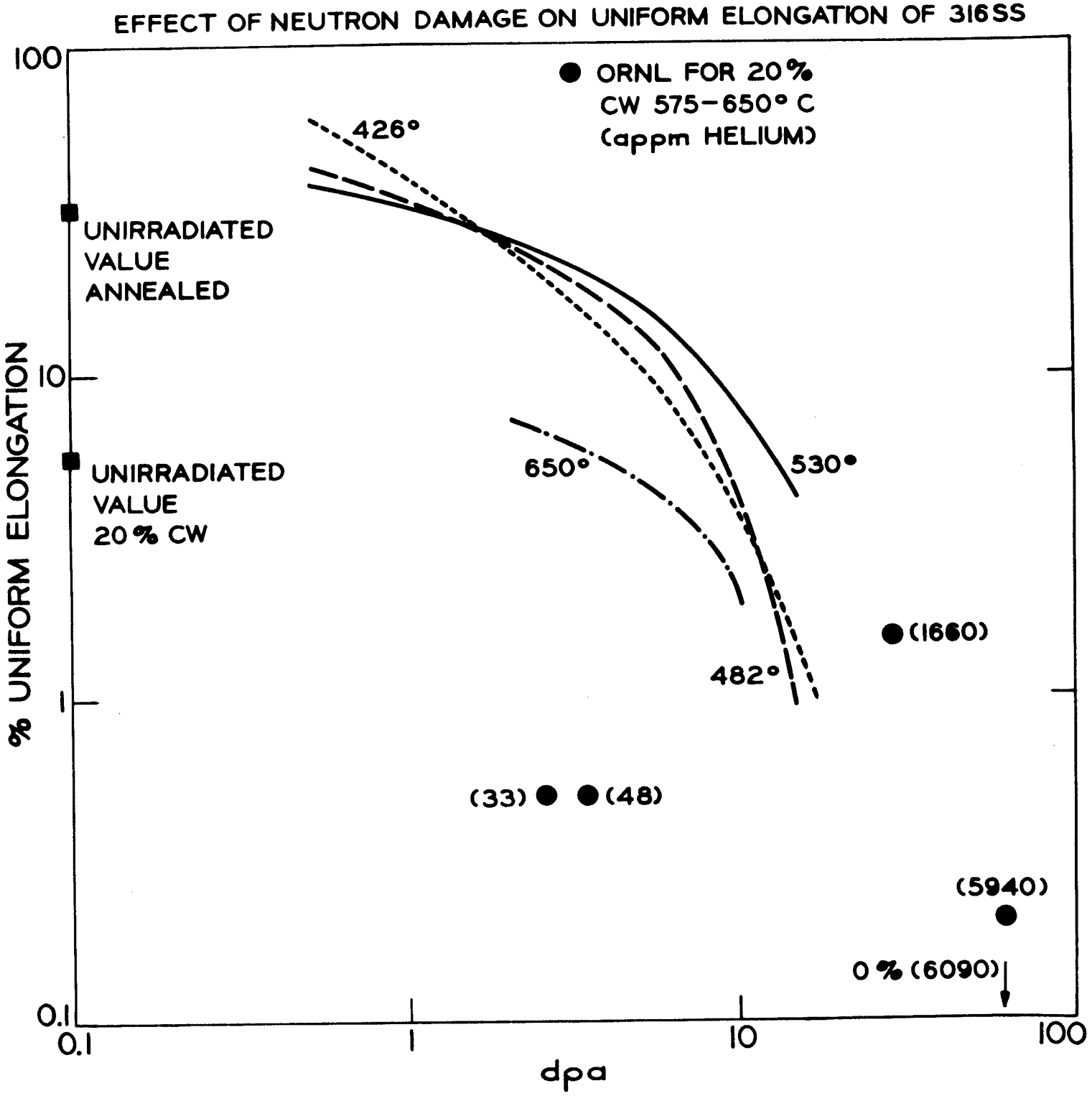
EFFECT OF NEUTRON DAMAGE ON UNIFORM ELONGATION OF 316SS
ORNL FOR 20%
CW 575-650° C
(appm HELIUM)
426°
530°
650°
482°
UNIRRADIATED
VALUE
ANNEALED
UNIRRADIATED
VALUE
20% CW
(1660)
(33)
(48)
(5940)
0% (6090)
% UNIFORM ELONGATION
100
10
1
0.1
0.1
1
10
100
dpa

Figure I-21

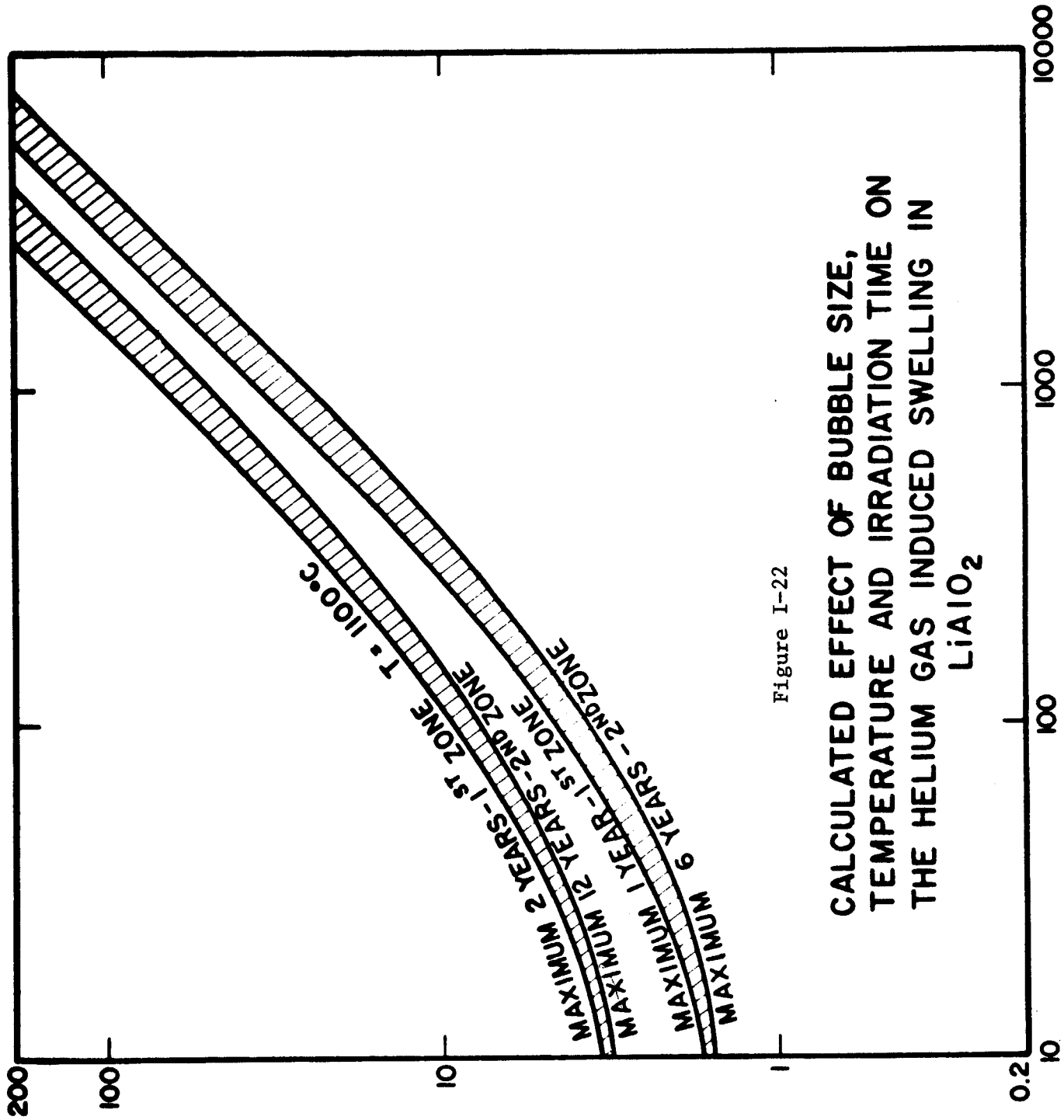
CALCULATED EFFECT OF BUBBLE SIZE, TEMPERATURE AND IRRADIATION TIME ON THE HELIUM GAS INDUCED SWELLING IN $LiAlO_2$
BUBBLE RADIUS - Å
0.2
10
100
1000
10000
1
10
100
200
MAXIMUM 6 YEARS - 2ND ZONE
MAXIMUM 1 YEAR - 1ST ZONE
MAXIMUM 12 YEARS - 2ND ZONE
MAXIMUM 2 YEARS - 1ST ZONE
T = 1100°C

Figure I-22

severe cost penalty due to the high cost and limited availability of Be (see the economics section).

e. Graphite Reflector

The placement of the graphite reflector some 33 cm from the first wall will reduce the damage levels to a maximum of 1.8 dpa per year at ~650°C. Based on fission reactor dimensional changes at ~500°C, it is anticipated that typical nuclear graphite might last ~7 years at an 80% plant factor before it approaches the breakaway swelling regime. Since we will have to replace the 316 SS structure every ~10 years due to ductility loss it is anticipated that the graphite will have to be changed at the same time.

f. Shield Materials

Due to the low flux and temperature of operation in the shield region, it is anticipated that there will be few, if any, radiation damage problems. The production of helium in the B_4C is expected to produce less than a 1% dimensional change. One area that bears further analysis is the irradiation of Pb at 40-60% of its absolute temperature. However 30 year displacement values are much less than 0.01 dpa which is far below the anticipated threshold for void formation.

g. Magnet Materials

The increased shield and blanket thickness of UWMAK-II means that the radiation damage problems in the TF magnets is even less than in UWMAK-I where they were quite nominal.

The energy deposition rates in the mylar insulation is ~6 M rad for 30 years of irradiation far below the level where the tensile strength is significantly reduced by radiation (25% reduction at 120 M rads). A similar conclusion can be drawn for the epoxy electrical insulator.

The damage level of $<10^{-6}$ dpa/year is far below the 10^{-3} dpa required before one observes a 10% drop in critical current. This low damage rate also means that there will be relatively low resistivity increase in the Cu stabilizer and it has been calculated that we could operate ~60 years before the TF coils would have to be warmed up to remove the resistivity increase. Therefore the radiation damage in the TF coils will be well within acceptable levels and no modification need be incorporated into the magnets.

I-B-6 Radioactivity and Afterheat

The 14 MeV neutrons from the fusion reaction induce radioactivity in the structure surrounding the plasma. For UWMAK-II, this radioactivity is shown in Fig. I-23 following shutdown after two years of operation. As we have found earlier,(1) the radioactivity levels reach ~10^6 Ci/MW(th) and begin to decrease rapidly after about 10 years.

The activities of the radionuclides may also be expressed in terms of the "Biological Hazard Potential" (BHP) i.e. the amount of air required per kilowatt of thermal power to dilute the radioactive isotope to its maximum permissible concentration. The use of BHP makes no judgement as to a mode of release or whether it is possible to distribute the material in air. It does, however, present a first attempt to include the biological properties of the radioactive structure.

The BHP calculated for the first wall of UWMAK-II at shut down for two years of operation is shown in Table I-16. The primary contribution to the BHP came from only five isotopes, Mn-54, Ni-57, V-49, Fe-55 and Mn-56 with Mn-54 and Ni-57 alone making 75% of the contribution. The change in BHP with time after shutdown is somewhat similar to that of radioactivity or decay heat and shows a relatively slow initial drop. Approximately two years are required to reduce the BHP by an order of magnitude.

The afterheat for the UWMAK-II blanket is shown in Figure I-24. Because of the larger amounts of steel in UWMAK-II, the afterheat is significantly higher than in UWMAK-I, being over a factor of two greater after shutdown. The first wall is still the major contributor to afterheat and its contribution can be as high as 40% of the total. The afterheat levels in the shield and magnets are quite low. For example, it is only about 75 W at shutdown in the magnets. The radioactivity in the shield and magnets following shutdown after 10y of operation are shown in Fig. I - 25.

FIG. I-23 UWMAK-II
RADIOACTIVITY, 2 YR OPERATION

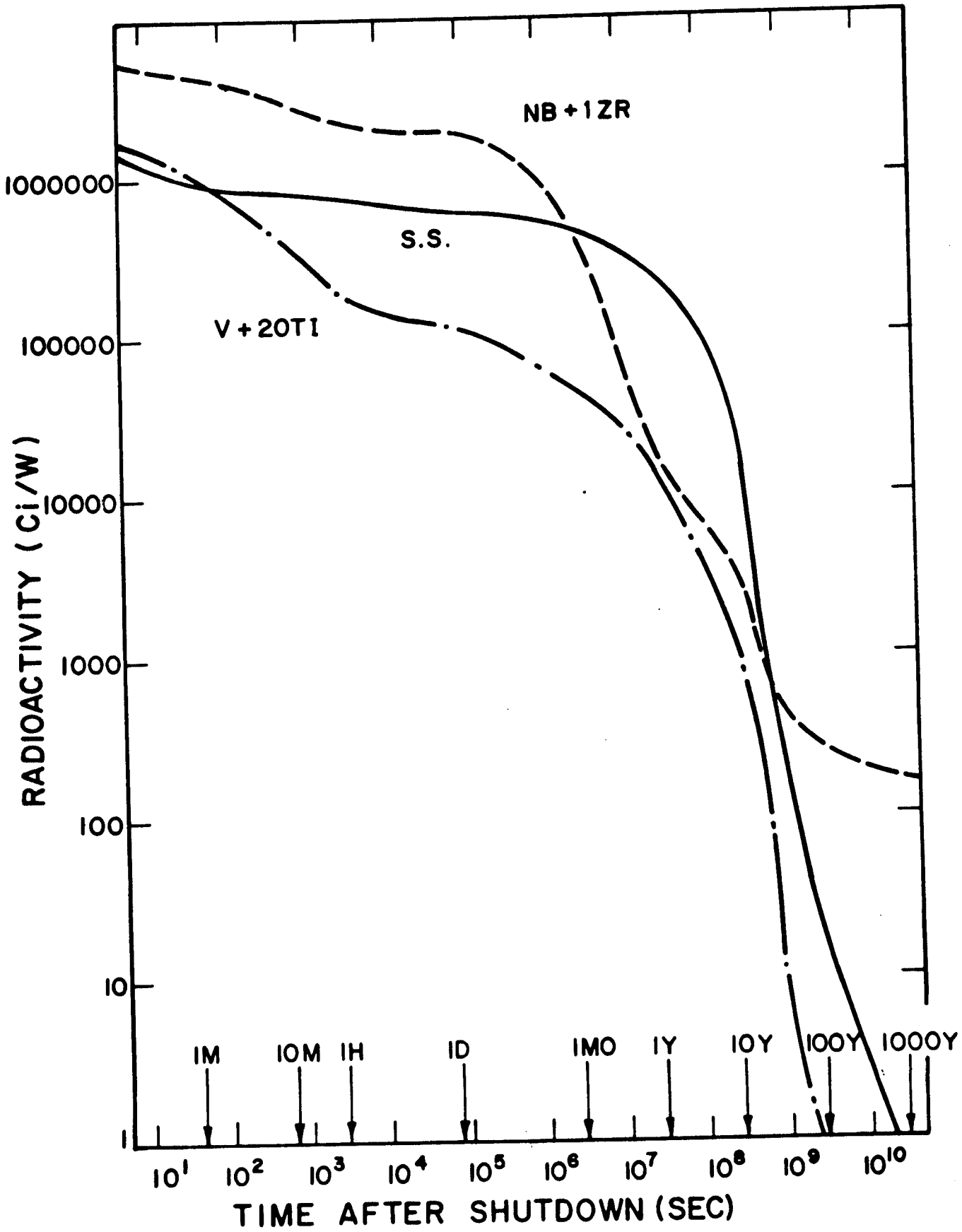

TABLE I-16

Biological Hazard Potential of 316 SS
First Wall at Shutdown for 2 Year Operation

Isotope	Specific Activity dps/cm^3	Activity Ci/kw_{th}	Biological Hazard Potential km^3 of air/kw_{th}
Mg-27	1.09 10(8)	0.03	1.11 10(-3)
Al-28	2.22 10(10)	6.79	0.226
Al-29	3.56 10(8)	0.11	3.46 10(-3)
Al-30	4.19 10(8)	0.13	4.27 10(-3)
V-49	3.08 10(9)	0.94	9.43
V-52	7.08 10(12)	216.5	0.72
Cr-49	1.24 10(9)	0.38	1.27 10(-2)
Cr-51	2.32 10(11)	70.95	0.18
Cr-55	8.46 10(9)	2.59	8.63 10(-2)
Mn-54	1.17 10(11)	35.78	35.8
Mn-56	3.26 10(11)	99.09	3.33
Mn-57	4.75 10(9)	1.45	4.84 10(-2)
Fe-53	2.22 10(9)	0.68	2.27 10(-2)
Fe-55	5.11 10(11)	156.26	5.21
Fe-59	3.36 10(8)	0.10	2.05 10(-2)
Co-57	4.81 10(10)	14.7	0.15
Co-58	1.61 10(11)	49.2	1.65
Co-60m	3.09 10(10)	9.45	0.32
Co-60	1.18 10(10)	3.6	0.36
Co-61	8.60 10(8)	2.63	8.77 10(-3)
Ni-57	1.02 10(10)	3.12	31.1
Ni-63	8.31 10(7)	0.03	1.27 10(-2)
Ni-65	4.00 10(7)	0.01	4.69 10(-4)
TOTAL	2.10 10(12)	675.3	89

FIG. I-24

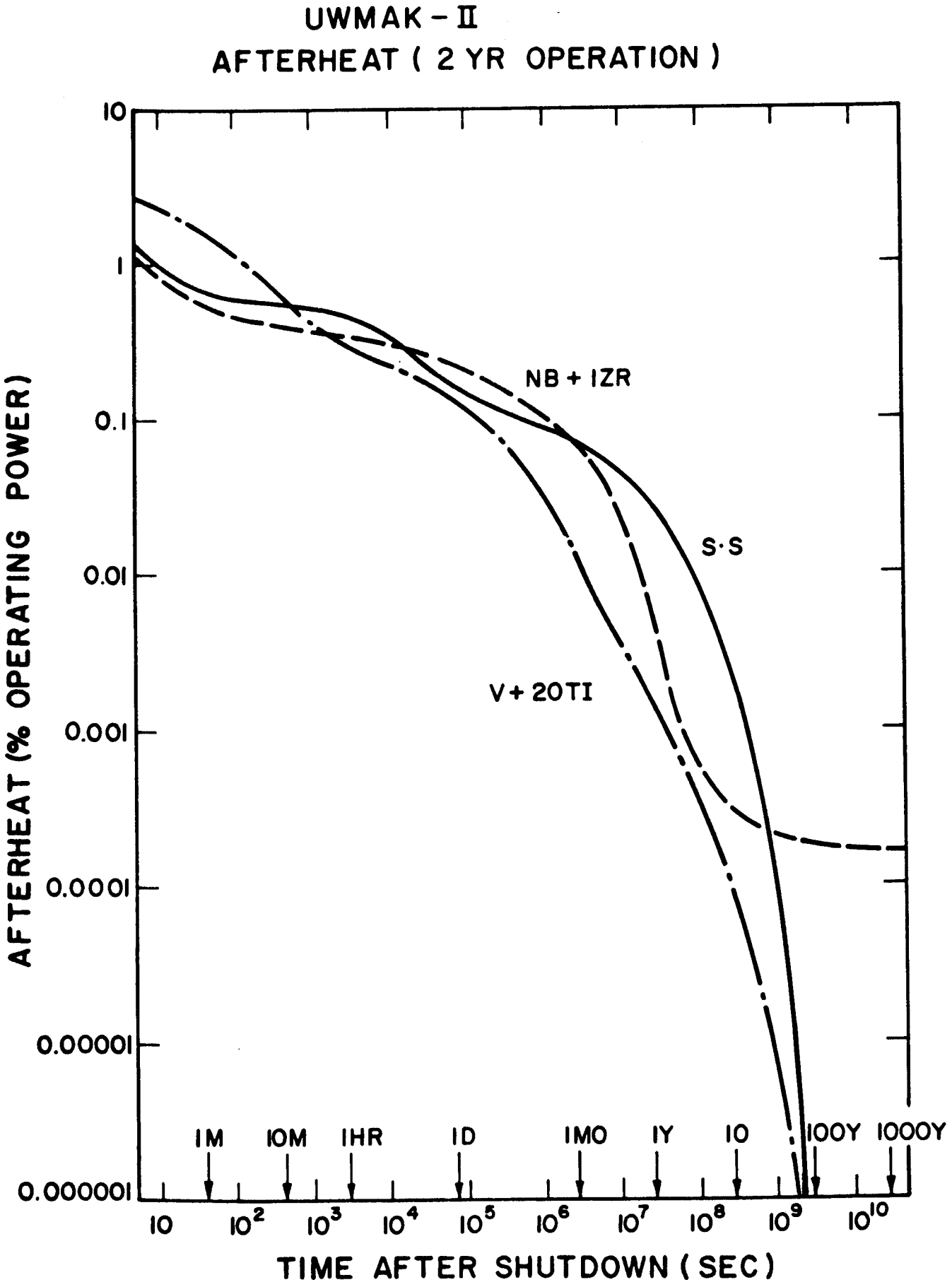
UWMAK - II
AFTERHEAT (2 YR OPERATION)
AFTERHEAT (% OPERATING POWER)
10
1
0.1
0.01
0.001
0.0001
0.00001
0.000001
NB + IZR
S·S
V+ 20TI
IM
10M
IHR
ID
IMO
IY
10
100Y
1000Y
10
10²
10³
10⁴
10⁵
10⁶
10⁷
10⁸
10⁹
10¹⁰
TIME AFTER SHUTDOWN (SEC)

FIG. I-25

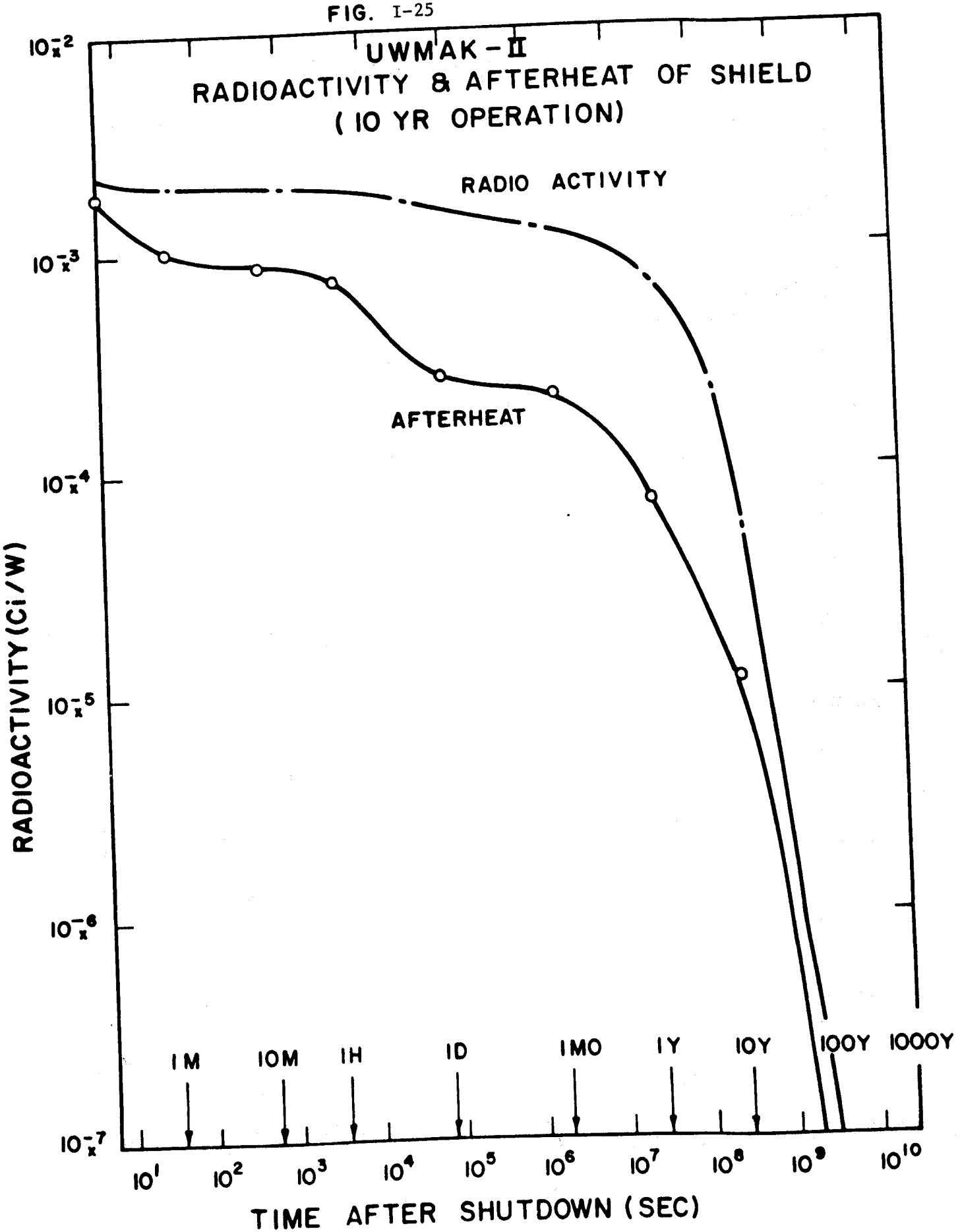
UWMAK-II
RADIOACTIVITY & AFTERHEAT OF SHIELD
(10 YR OPERATION)
RADIO ACTIVITY
AFTERHEAT
RADIOACTIVITY (Ci/W)
10_x^{-2}
10_x^{-3}
10_x^{-4}
10_x^{-5}
10_x^{-6}
10_x^{-7}
1M
10M
1H
1D
1MO
1Y
10Y
100Y
1000Y
10^1
10^2
10^3
10^4
10^5
10^6
10^7
10^8
10^9
10^{10}
TIME AFTER SHUTDOWN (SEC)

I-C. Power Cycle for UWMAK-II

The energy conversion system or power cycle removes the thermal energy generated in the blanket, divertor, and shield from the reactor, converts the thermal energy generated to electrical energy and rejects waste heat to the atmosphere. The system must satisfy these functions subject to technical, economic, safety and environmental constraints. The system designed for UWMAK-II is based on technology under development for gas-cooled and liquid metal-cooled fission reactors wherever it is a reasonable application. New technology areas that are not currently under intensive development were only briefly evaluated. The pulsed nature of the reactor operation imposes unique design problems on the energy conversion system. In the UWMAK-II, energy is generated in the reactor for 90 minutes (burntime); the reactor is then shut down for 5 1/2 minutes (downtime) for recharge. To be a viable electricity-producing machine for electric utilities, energy must be produced at a nearly uniform rate. Several methods for levelizing power are investigated and a scheme using an intermediate sodium loop was selected.

The main parameters of the energy conversion system are listed in Table I-17 and an overall schematic is given in Fig. I-26. The power system consists of four independent cooling loops using a steam turbine-driven helium circulator in each loop. There is an intermediate sodium loop providing energy levelizing. A steam generator is used in each loop with superheater outlet steam conditions of 252 atm. (3690 psia), 510°C (950°F). The circulator turbines are supplied with this steam, which is subsequently routed to the main turbine inlet at 163 atm. (2400 psia) and 510°C (950°F).

The divertor cooling system uses one primary lithium cooling loop with one motor-driven circulating pump in the loop. An intermediate heat exchanger transfers energy from the lithium divertor coolant to the intermediate sodium loop which provides energy levelizing. Steam is generated in the steam generator at 15 atm (220 psia) and 225°C (433°F).

The shield is cooled with helium. One loop with a motor-driven circulator and a helium-to-water heat exchanger is used. Because the energy from the shield is small (49 MW_t) and at low-temperature, conversion to electrical energy was not investigated in this study. Thermal energy from the blanket and divertor is converted to electrical energy by two separate turbine-generator sets. The overall plant heat rate is 9140 Btu/kWh. In addition to the cooling and heat transfer function of the blanket and divertor heat removal systems, a large thermal energy storage device is needed to deliver thermal energy to the steam cycle at a uniform rate. The intermediate sodium system serves this purpose by storing hot sodium during the 90 minute energy generating period. During the 5.5 minutes when energy is not being generated by the reactor, this stored hot-sodium supplies energy to the steam cycle. In the divertor system, the sodium cycle serves a dual purpose. In addition to energy storage, the intermediate system helps to minimize tritium permeation into the steam cycle.

Table I-17

Key Parameters of Energy Conversion System

Parameter	Blanket	Divertor	Shield	Total
Thermal Power, MWt (during reactor burntime)	4232	716	52	5000
Thermal Power, MWt (average continuous)	3989*	675	49	4712
Net Electrical Power, MWe (average continuous)	1541	175	--	1716
Gross Plant Efficiency (%)	38.6	25.9	--	36.4
Primary Cooling System				
Coolant	Helium	Lithium	Helium	
Flow rate, Kg/hr (lb/hr) x 10^6	10.5(23.2)	4.94(10.9)	0.24(0.53)	
Hot Leg Temp., °C(°F)	650(12.02)	320(608)	200(392)	
Cold Leg Temp., °C(°F)	371(700)	200(392)	50(122)	
Intermediate Cooling System				
Coolant	Sodium	Sodium		
Flow rate Kg/hr (lb/hr) x 10^6	43.5(85.9)	17.1(37.7)		
Hot Leg Temp., °C(°F)	567(1052)	292(558)		
Cold Leg Temp., °C(°F)	279(535)	172(342)		
Steam System				
Turbine throttle conditions				
Pressure, atm (psia)	163.3(2400)	15(220)		
Temperature, °C(°F)	510(950)	225(438)		
Flow rate, Kg/hr (lb/hr) x 10^6	6.2(13.6)	1.0(2.2)		
Condenser Pressure, mm HgA (inches HgA)	51 (2.0)	51 (2.0)		
Cooling Water System				
Water flow rate, Kg/hr (lb/hr) x 10^6	150(330)	31.4(69.2)	3.45(7.6)	
Hot water temp., °C(°F)	46(115)	46(115)	46(115)	
Cold water temp., °C(°F)	32.8(91)	32.8(91)	32.8(91)	

*Includes non-recoverable losses of 11 MWt in the He circulator.

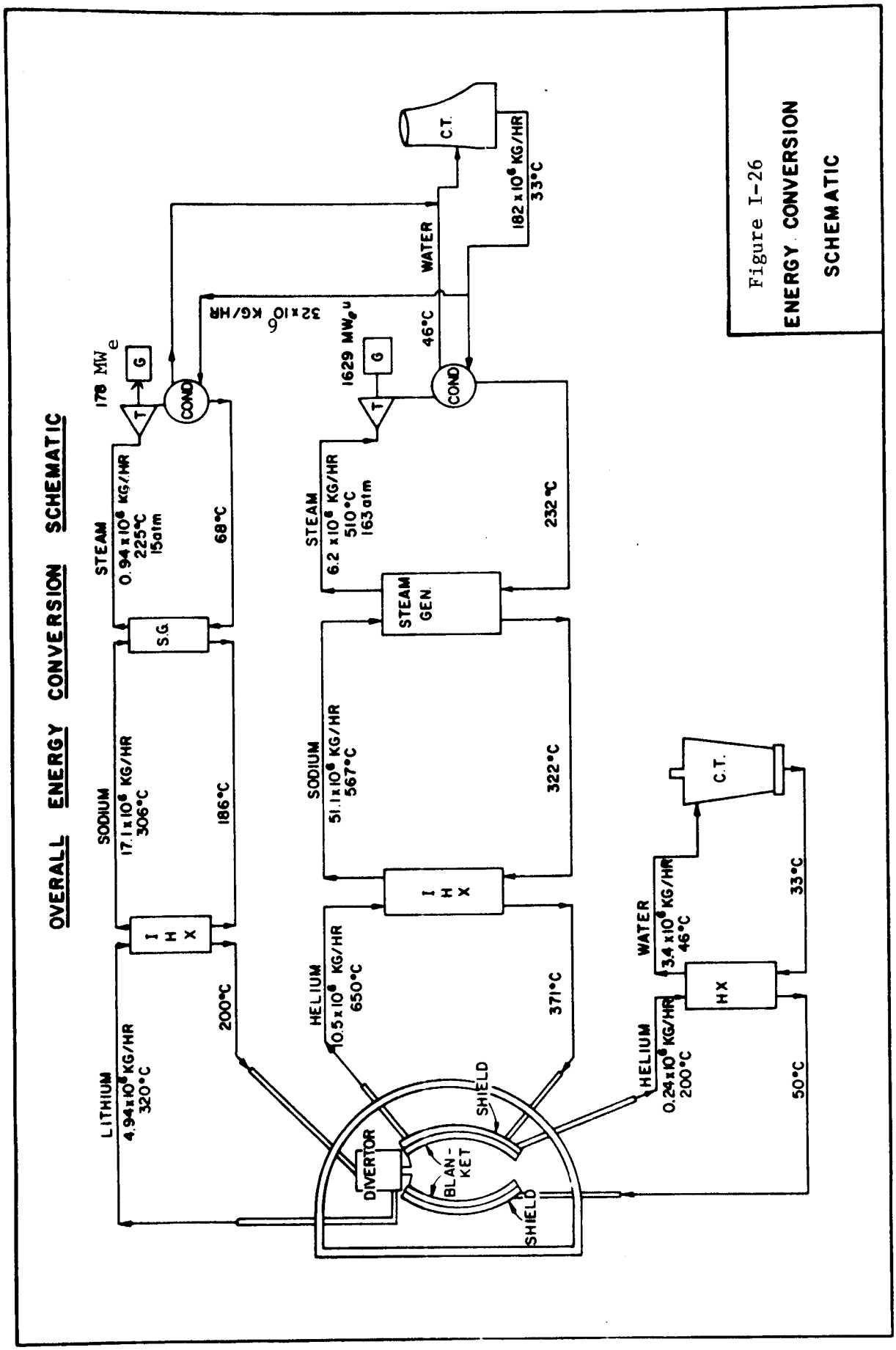
OVERALL ENERGY CONVERSION SCHEMATIC
178 MWe
1629 MWth
LITHIUM
4.94x10^6 KG/HR
320°C
200°C
SODIUM
17.1x10^6 KG/HR
306°C
186°C
I HX
S.G.
STEAM
0.94x10^6 KG/HR
225°C
15atm
68°C
COND
G
T
32x10^6 KG/HR
HELIUM
10.5x10^6 KG/HR
650°C
371°C
SODIUM
51.1x10^6 KG/HR
567°C
322°C
I HX
STEAM GEN.
STEAM
6.2x10^6 KG/HR
510°C
163atm
232°C
46°C
WATER
182x10^6 KG/HR
33°C
C.T.
HELIUM
0.24x10^6 KG/HR
200°C
50°C
HX
WATER
3.4x10^6 KG/HR
46°C
33°C
C.T.
SHIELD
BLAN-KET
SHIELD
DIVERTOR
Figure I-26
ENERGY CONVERSION SCHEMATIC

Fig. I-27 shows the overall energy balance of the blanket and divertor heat removal systems during reactor operation and during reactor downtime. During reactor operation, the blanket generates 4232 MWt. Of this, 243 MWt goes to the energy storage system and 11 MWt (net) goes to non-recoverable losses in the helium circulators leaving 3978 MWt transferred to the steam cycle. During the reactor downtime, 3978 MWt is supplied to the steam generators by the energy storage system. The divertor generates 716 MWt during reactor operation; 41 MWt goes to the energy storage system leaving a net of 675 MWt supplied to the steam generator. During the reactor downtime, 675 MWt is supplied by the energy storage system. The gross plant efficienty is 36.4%.

ENERGY BALANCE SCHEMATIC

DURING REACTOR BURNTIME 90 MINUTES

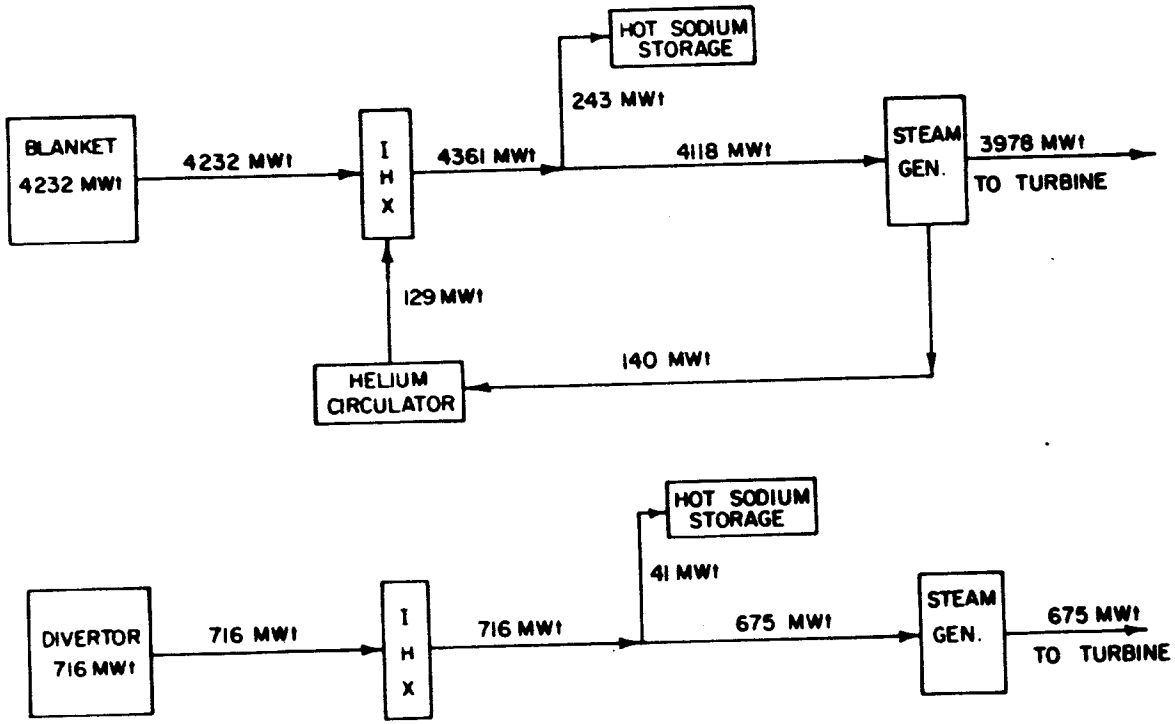

DURING REACTOR DOWNTIME 5.5 MINUTES

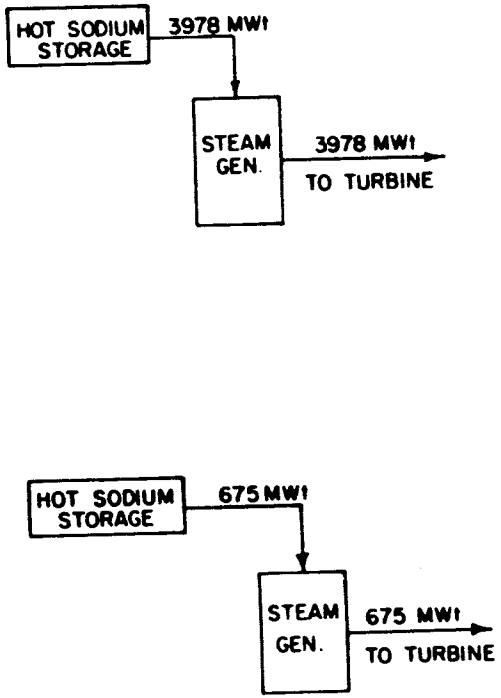

Figure I-27

I-D. Plant Design for UWMAK-II

A conceptual plant design study for the UWMAK-II reactor has been performed to identify the major buildings and structures needed to contain the plant equipment, to define the functional interrelationships among various buildings and structures, to develop a technically feasible, operable, and maintainable plant design, to identify areas in which there are significant technical or cost uncertainties, and to provide a basis for conceptual cost estimates. A general plant arrangement and the internal arrangement of some of the buildings has been patterned wherever possible of a generic concept which has been developed for fission reactor plants. The greatest effort in this study was devoted to those areas unique to the UWMAK-II, such as the Containment Building, the Heat Exchanger Building, and the Reactor Auxiliary Building. Other buildings such as the Control Building and the Turbine Building are similar to those in other nuclear plants, and their arrangements can be adopted readily to this plant.

The general plant arrangement is shown in Fig. I-28 and I-29 and a detailed view of the primary containment and heat exchanger building is shown in Fig. I-30. The major features of the arrangement are as follows The Containment Building is centrally located relative to the other buildings. The Auxiliary Building, Service Building, Radwaste Building, Reprocessing Building, and the Fabrication Building are arranged around the Containment Building. This arrangement seems to have some advantage in handling blanket sections and large volumes of radioactive wastes. The peninsular arrangement of the Turbine Building orients the turbine-generator axis such that any missiles generated by the machine will not strike the Containment Building. Access corridors run the length of the Turbine Building and continue in the Control Building and the Auxiliary Building to provide accessibility to all equipment.

The structures in this plant are significantly larger than those in fission power plants. All the structures are massive because of shielding and other safety requirements. The conceptual design, as described, is considered to be a feasible design consistent with current technology and industry practice. However, some aspects of the design analysis of the structures have to be investigated further before a method for their design can be established. Also, the use of large size piping for transporting high temperature helium gas may be of some concern. Internally insulated piping has been proposed but no stress analysis has been performed to substantiate the piping arrangement. Expansion joints are used to account for the large thermal expansions. Application of internal ceramic insulation and expansion joints is within the state-of-the-art: but the feasibility of their use has to be investigated in this particular service.

Finally reactor maintaince problems especially in regard to blanket removal is an important area to which only preliminary consideration could be

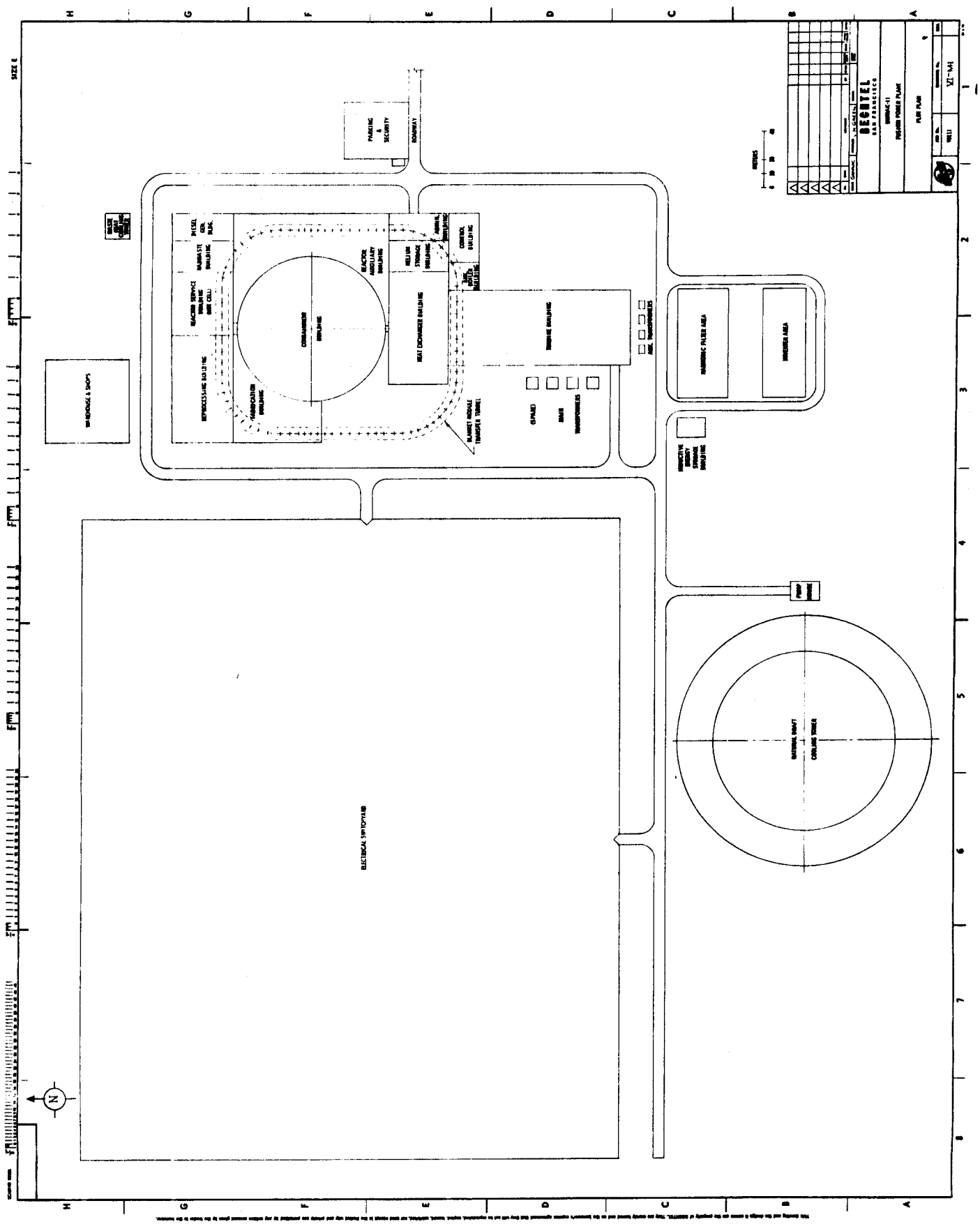
PARKING & SECURITY
ROADWAY
CONTAINMENT BUILDING
REACTOR AUXILIARY BUILDING
HELIUM STORAGE BUILDING
HEAT EXCHANGER BUILDING
TURBINE BUILDING
MAIN TRANSFORMERS
AUX. TRANSFORMERS
HARMONIC FILTER AREA
SWITCHYARD
WAREHOUSE & SHOPS
ELECTRICAL SWITCHYARD
NATURAL DRAFT COOLING TOWER
PUMP HOUSE
BECHTEL
SAN FRANCISCO

Figure I-28

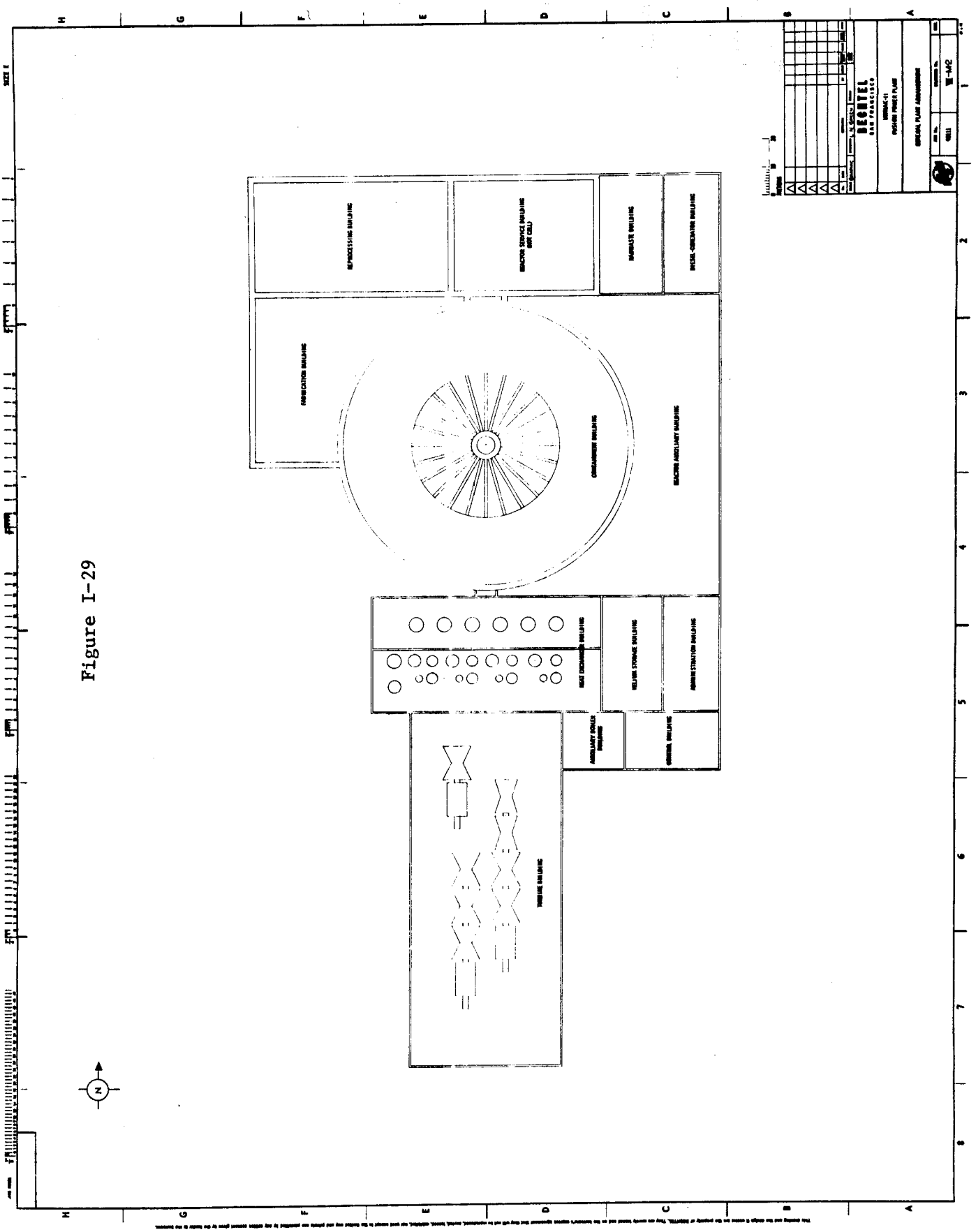
REPROCESSING BUILDING
REACTOR SERVICE BUILDING (HOT CELL)
WASTE BUILDING
DIESEL-GENERATOR BUILDING
FABRICATION BUILDING
CONTAINMENT BUILDING
REACTOR AUXILIARY BUILDING
HEAT EXCHANGER BUILDING
HELIUM STORAGE BUILDING
ADMINISTRATION BUILDING
AUXILIARY BOILER BUILDING
CONTROL BUILDING
TURBINE BUILDING
BECHTEL
SAN FRANCISCO
GENERAL PLANT ARRANGEMENT

Figure I-29

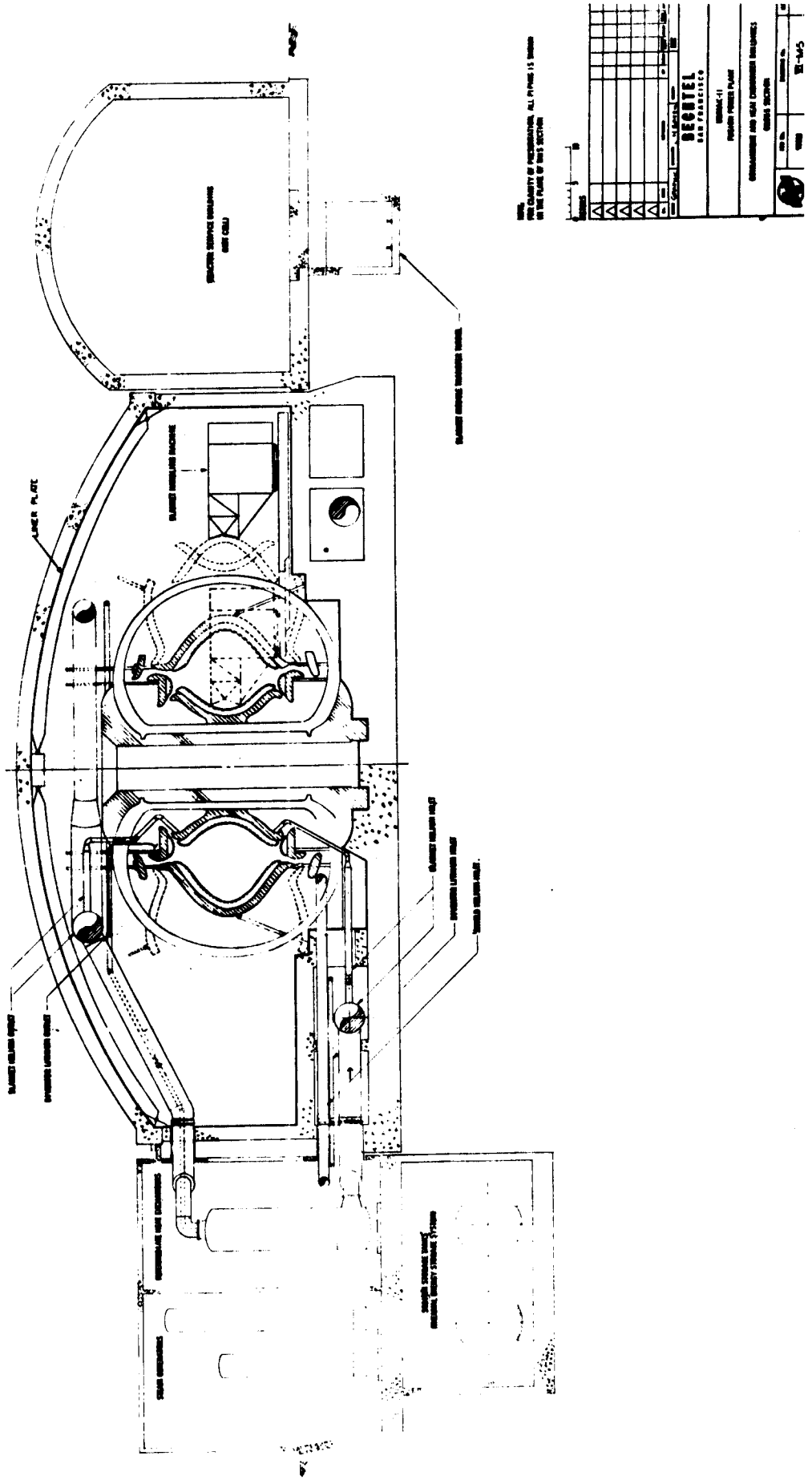

Figure I-30

given in this study. A conceptual blanket handling concept has been proposed but further studies are needed to evaluate the feasibility of the concept and develop procedures and conceptual equipment designs. The problem of radioactive contamination of the plant and equipment must be given serious consideration in this regard.

I-E. Resource Requirements for UWMAK-II Type Reactors

The low power density and large size of low β, circular Tokamaks means it is important to ascertain the resource requirements for such devices. The total material requirements for the UWMAK-II nuclear island and balance of plant have been estimated and are presented in Tables I-18 and I-19. We then compared these requirements with estimates of materials availability both inside and outside the United States, and at present prices, three times present prices, and ten times present prices. A summary is given in Table I-20. The major findings are that the metals for 316 SS present problems or possible problems of availability. In terms of domestic resources, chromium is an especially serious problem. Lithium reserves at present prices are below the requirements for a 10^6 MW_e economy based on UWMAK-II type systems but resources at 3X present prices are large and the chances of discovering additional reserves both in the U.S. and in the world are good.

The major problem with a gas cooled solid breeder system like UWMAK-II is the requirements for an effective neutron multiplier. The best of the non-fissionable materials is beryllium and an analysis of the reserve and resource picture for this material makes it clear that the 10^6 MWe target amount for Be is out of all proportion to the size of known U.S. and world reserves. This appears to mean that while Be can and will be used as a special material in some reactors, a standard system expected to be the dominant type in a 10^6 MWe economy should not rely on the amounts of Be implied by a system like UWMAK-II.

Table I-18

Materials Requirements - UWMAK-II Nuclear Island

(Metric Tonnes)

ELE.	Initial Struc.[a]	1st Wall Sec. Replacement (14 Times)[b]	Canning[c] (14 Times)	Reflec. & Header Replac. (2 Times)	Blanket & Shield Support	Shield Structure	T.F. Magnets and Dewars	T.F. Magnet Bracing[d]	Ver. Field Coils	Ver. Field Coil Support[d]	Vacuum Pumps (d)	Storage	Total (MT)	MTonnes MWe (1710 MWe)	ELE.
Al	184	112	2338	44	-	44	193	1693	2	-	-	-	4766	2.79	Al
B	-	-	-	-	-	4280	-	-	-	-	-	-	4280	2.50	B
C	1307			2376	-	1207							4890	2.86	C
Cr	692	2011	1726	797	52	800	1818	514	48	58	9	-	8525	4.98	Cr
Fe	2385	6929	5940	2746	172	2754	6233	1683	167	191	29		29229	17.1	Fe
Mn	77	223	192	88	5	89	199	51	6	6	1		937	.55	Mn
Mo	77	223	192	88	5	89	179	51	6	6	1		917	0.54	Mo
Ni	538	1564	1344	620	31	622	1378	306	37	35	5		6480	3.78	Ni
Si							1	11					12	0.007	Si
Pb						19800							19800	11.6	Pb
Nb							119		26				145	0.085	Nb
Ti							62	18	13				75	0.054	Ti
Cu	38	112	96	44	3	44	8889	22	1444				10692	6.94	Cu
He	4					1	20		19			25	69	0.04	He
Li	50[e]+300[f]		630										980	0.57	Li
Be	433	552[g]											985	0.58	Be
Total Weight (MT)		11726	12554	6803	268	29730	19091	4353	1768	296	45	25	92782	54.3	

(a) 24 regular modules plus 2 spare blanket modules
(b) First 27 cm only
(c) Canning is the 316 SS needed to contain the breeding and neutron multiplying material as well as the graphite.
(d) 304 SS, includes central support structure
(e) 50 MT is the Li Inventory in the Blanket-This Li is enriched to 90% Li-6 and then requires 12 times this amount in natural Li.
(f) 300 MT is the Li Inventory in the particle collection stream of the divertor
(g) One additional loading plus makeup for burnup and reprocessing losses

Table I-19

UWMAK-II Balance of Plant Materials Requirements

(Metric Tonnes)

Element	Heat Exchanger			Piping												MTonnes / MW_e (1710 MW_e)	Element
	He-Na (a)	Na-Steam (b)	Regenerative (321) (c)	He (316) (d)	Na (304) (f)	Steam (321) (c)	Thermal Flywheel (Na Tanks) (e)	Dump Tanks (Na) (e)	Pumps (Na) (e)	Building Liner (e)	Reinforcing Rods & Structure (g)	Turbine Generator Unit (h)	Energy Storage Unit	Misc.	Total (MT)		
Al	1			19											20	.012	Al
Cr	135	278	8	349	184	30	938	712	540	320		30	81		3605	2.11	Cr
Fe	402	1584	27	1204	607	107	3095	2347	1783	1056	63479	2567	269		78527	45.92	Fe
Mn	7	28	1	39	18	3	94	71	54	32			8		355	.208	Mn
Mo	46	7		39											92	.054	Mo
Ni	310	152	5	271	110	18	563	427	324	192		59	49		2480	1.45	Ni
Na														9816(i)	9816	5.74	Na
Cu				19								295	362		676	.395	Cu
Nb													7.5		7.5	.004	Nb
Ti	19	6	0.2			1							4		7.5	.018	Ti
He	1			5.8									15		21.8	.013	He
Y													2.9(j)		2.9	.0017	Y
Zr													100(k)		100	.058	Zr
Concrete (m^3)											340000 m^3				340000 m^3	199 m^3 / MW_e	

(a) Shell 316 SS Tubes Incoloy 800 (4 regular, 1 spare, 1 divertor)
(b) Croloy 2 1/4 Cr. 1 Mo, and 321 SS (4 regular, 1 spare, 1 divertor)
(c) 321 SS (14 regular + 1 spare)
(d) 316 SS
(e) 304 SS
(f) 321 SS
(g) Low carbon steel
(h) Low alloy steel 21% Ni, 1% Cr and Cu
(i) Secondary loop
(j) Tritium extraction bed for divertor loop
(k) Liquid Na cleanup system

Table I-20

Data Relating to Availability of Metals for UWMAK-II

(All quantities in metric tonnes x 10^6)

Element	Requirements for 10^6 MWe[1]	United States Reserves 1X[2]	United States Reserves 3X[3]	United States Production 1974[4]	Consumption 1974[4]	World: Ex-U.S.A. Reserves 1X[2]	Ex-U.S.A. Production 1974[4]	Element
Al	2.80	~2.00	>1,000.00	~0.40	~4.86		8.3	Al
B	2.50	10.1	Large	~0.18	~0.15	10.1	>0.15	B
Cr	5.51	0.00	1.53	0.00	~.73	~370.0	~2.0	Cr
Fe	63.02	2,000.00	>10,000.00	50.00[5]	80.0[6]	246,000.0	413.0	Fe
Mn	0.75	0.00	>10.00	0.00	~1.60	>2,000.0	~9.0	Mn
Mo	0.59	5.41	> 2.08	0.06	0.04	~13.0	0.21[7]	Mo
Ni	5.24	0.20	~16.00	0.015	0.20	~24.0	0.67	Ni
Si	0.007	Very large	.58	0.66	.58	Very large	1.28	Si
Pb	11.60	59.00	no data	0.68	~0.82	160.00	2.81	Pb
Nb	0.089	0.006	0.070	0.00	.001	7.00	~0.006[7]	Nb
Ti	0.067	34.00	~29.00	0.29	0.20	147.00	~0.077[7]	Ti
Cu	6.65	90.00	>100.00	~1.59	1.79	370.00	5.75	Cu
Li	0.57	0.50	3.90	~0.002	~0.003	>0.80	~0.002	Li
Be	0.58	.03	.005	0.002	0.002	>0.01	0.0002	Be
Na	5.74	Unlimited		?.200[8]	?0.200	Unlimited	no data	Na
Y	0.0017	0.0009	no data	?.00004	0.00009	0.036	0.0002	Y
Zr	0.058	10.00	no data	?.070[9]	.153[9]	>14.0	>0.475[7,9]	Zr

Notes:

[1] Based on 1710 MWe (nominal) per reactor.
[2] Reserves at present metal prices.
[3] Reserves at metal prices 3 times present prices.
[4] Primary metal only. Data, except data for lithium, from U.S. Bur. Mines, Commodity Data Summaries, 1975.
[5] Approximate iron content of domestically produced iron ore.
[6] Approximate iron content of iron ore consumed.
[7] Free World only.
[8] Sodium metal only. About 1 percent of total sodium minerals production.
[9] Zirconium content of Zircon ($ZrSiO_4$) concentrates. No data for U.S. metal production; Free World production (1974) 3750 short tons.

I-F. Economic Study

The primary purpose of the economic study on the UWMAK-II system is to identify major cost items and to determine if fusion systems have the potential to be economically attractive. As such, we do not attach as much significance to individual numbers as we do to whether the costs are close to acceptable levels and whether the potential exists for improvement.

An important item entering such a study is the estimated plant factor. This is determined primarily by estimates of the planned down time and the amount of unscheduled outage. Because of radiation damage, the front part of the blanket section, including the first wall and the rods containing Be and lithium aluminate must be replaced every two years. An estimate of the costs associated with this procedure is summarized in Table I-21. We have used 6 months as the interval between replacement outages. When this is combined with an unscheduled outage time of four weeks per year and the parameters of the periodic burn cycle, the overall plant factor is estimated at 80%.

A summary of the capital costs for UWMAK-II is given in Table I-22, and a summary of the electricity generating costs is given in Table I-23. The cost per kilowatt generated is $944/KWe. The nuclear island (account number 22) accounts for approximately half of this amount. The main interpretation of this result is that low β, circular Tokamaks are capital intensive systems but, given the state of fusion reactor studies, they can be made competitive with further improvements in design. Perhaps the major reason for the high capital costs in UWMAK-II is the low power density and low neutron wall loading. The power density can be increased by increasing the magnetic field or by using a noncircular plasma cross section. The wall loading can be increased by altering the blanket design in ways that have recently been discussed.[6] Thus, one can already envision the improvements required to decrease system size and lower overall cost.

The electricity generating costs are somewhat high (25 mills/kwhr) but this is dominated by interest on capital. Therefore, the reduction in capital investment by the approaches described above will tend to lower the electricity generating costs. Nevertheless these costs are comparable to large fossil and fission plants ordered in 1975.

This concludes the Overview of the UWMAK-II conceptual reactor design. A summary of the major conclusions and recommendations based on this study are given in Chapter VIII of this report.

Table I-21

Wall Replacement Costs for UWMAK-II

Intervals Between Replacement Outages	Number Segments Replaced Per outage*	Annual Outage Time (days)	Annual Costs - millions of dollars			
			Segment Inventory Costs	Outage Costs	Loss of Income	Total
2 yrs.	24	20.5	24	0.58	8.8	33.4
1 yr.	12	23	12	0.66	9.9	22.6
6 mo.	6	28	6	0.8	12.0	18.8
4 mo.	4	33	4	0.94	14.2	19.1
3 mo.	3	38	3	1.09	16.3	20.4

Basis: Outage time = (1.5) (No. segments replaced) + (5) (No. outages)

Inventory cost = ($6,250,000) (No. segments replaced/outage) (0.16)

Outage Costs = (Annual outage time) ($28,500/day)

Loss of income is 10 mills/kwh. or $430,000 per day

*Equals number segments in inventory in order to perform outages. Does not include one additional segment in inventory to cover failures immediately following a replacement outage.

Table I-22

Cost Data

(Prices are Present Day and Based on a 40 Hour Work Week)

Account Number	Account Title	Total
	DIRECT COSTS:	
Nondepreciating Assets:		
20	Land and Land Rights	$1,200,000
Depreciating Assets:		
26	Special Materials	5,820,000
	Physical Plant	
21	Structures and Site Facilities	161,590,000
22	Reactor Plant Equipment	775,179,000
23	Turbine Plant Equipment	160,000,000
24	Electric Plant Equipment	84,218,000
25	Miscellaneous Plant Equipment	19,110,000
	SUB-TOTAL Physical Plant	1,200,100,000
	INDIRECT COSTS (All Depreciating Assets):	
91	Construction Facilities, Equipment and Services	24,300,000
92	Engineering Services	48,500,000
93	Other Costs	90,800,000
	SUB-TOTAL	1,363,700,000
94	Interest During Construction	250,923,000
	TOTAL PLANT CAPITAL INVESTMENT	$1,614,620,000
	COST PER KILOWATT GENERATED	$944/kWe

Table I-23

UWMAK-II Electricity Costs

Cost Item	Annual Cost	Unit Cost (mills/kwh)
Operations and Maintenance	$54,577,000	4.55
Fuel	123,000	0.01
Return on Capital	242,193,000	20.18
		24.74

or ~25 mills/kwh

References for Chapter I

1. B. Badger, M. A. Abdou, R. W. Boom, R. G. Brown, T. E. Cheng, R. W. Conn, J. M. Donhowe, L. A. El-Guebaly, G. A. Emmert, G. R. Hopkins, W. A. Houlberg, A. B. Johnson, J. H. Kamperschroer, D. Klein, G. L. Kulcinski, R. G. Lott, D. G. McAlees, C. W. Maynard, A. T. Mense, G. R. Neil, E. Normand, P. A. Sanger, W. E. Stewart, T. Sung, I. Sviatoslavsky, D. K. Sze, W. F. Vogelsang, L. J. Wittenberg, T. F. Yang, W. D. Young, "UWMAK-I, A Wisconsin Toroidal Fusion Reactor Design", Nuclear Engineering Department Report UWFDM-68, Vol. I (Nov, 1973) and Vol. II (May, 1975) (The University of Wisconsin, Madison).

2. G. L. Kulcinski, R. W. Conn, "Conceptual Design of a 5000 MW_t D-T Tokamak Fusion Reactor", in Fusion Reactor Design Problems (IAEA, Vienna, 1974; Special Nuclear Fusion Supplement) p. 51.

3. R. W. Conn, G. L. Kulcinski, "Technological Implications for Tokamak Fusion Reactors of the UWMAK-I Conceptual Design", Proc. First National Topical Meeting on the Technology of Controlled Nuclear Fusion (CONF-740402-P1, U.S. A.E.C., 1974) 56-71.

4. S. O. Dean et al., "Status and Objectives of Tokamak Systems for Fusion Research", U. S. Atomic Energy Commission Report, WASH-1295 (1974).

5. "Cryogenic Energy Storage System Design Report", Fermi National Laboratory Report FN-264; 8000.00, published as a collaboration with the Energy Storage Project, University of Wisconsin (Oct., 1974).

6. R. W. Conn, G. L. Kulcinski, H. Avci, M. El-Maghrabi, Nucl. Tech. 26 (1975) 125.

II. Plasma and Divertor

II-A. Plasma and Divertor Considerations for Tokamaks and Tokamak Reactors

Introduction

The plasma analysis for UWMAK-II is aimed at estimating the operating characteristics of a large power producing Tokamak reactor plasma. This requires application of our best present day understanding of Tokamak plasma operation and the extrapolation, using theoretical estimates, of the transport behavior of such machines. In addition, the control of impurities which can allow reasonable burn times is equally important and this question is addressed in detail. In particular, we discuss the role of a low Z liner (a carbon curtain) for use in both present day experiments and in a UWMAK-II type reactor.

Since establishing our present understanding of Tokamak plasma behavior and of impurity problems is central to our work, the plasma and divertor section is divided into two parts, A and B. Section II-A is divided into five subsections. In Section II-A-1, we discuss the principles of tokamak operation. In Section II-A-2, we review plasma transport and the estimate of diffusion coefficients, scaling laws. Included is a discussion of anomolous diffusion. In Section II-A-3, we review the general problem of impurities in Tokamaks and consider in detail the effects of low Z and high Z impurities. The idea of a carbon curtain made of two dimensionally woven carbon cloth is presented in Section II-A-4. This idea, developed at Wisconsin, is analyzed with particular emphasis on a description of the carbon curtain and a discussion of its expected properties in a CTR device. Finally, we discuss in Section II-A-5 some new work on the diffusion of impurities in Tokamaks. Whether high Z or low Z, the impurity diffusion is central to our understanding of plasma behavior and of divertor operation. This completes the discussion of specific topics and our work in these important areas.

Section B of Chapter II is made up of 6 sections. Some of the ideas in Sections II-A are applied specifically to the UWMAK-II conceptual reactor design but, in addition, we present specific analysis and design solutions for the problems of plasma startup, heating, burning, impurity control and divertors, particle collection of plasma diffusing into the divertor, and the vacuum systems for UWMAK-II. In Section II-B-1, we describe the reasoning behind the choice of the size and dimensions of UWMAK-II and the fuel cycle used. In Section II-B-2, plasma startup and the current rise phase is described. In particular, we present the OH and vertical field (VF) coil placements, their current carrying capacity, energy storage requirements and so on. This is followed by Section II-B-3 where we describe the analysis and conclusions of neutral beam heating and plasma burn calculations for UWMAK-II. Divertor design and operation is described in Section II-B-4, including coil placement analysis, estimates of plasma diffusion in the scrape off layer, and an estimate of the divertor efficiency. (These are some of the first estimates of divertor efficiency based on relatively detailed analysis.) We also present a discussion of some initial results on the MHD equilibrium and stability of the UWMAK-II plasma shape. In Section II-B-5, we present an analysis of the loss of fast alphas caused by particle trapping in ripples in the toroidal field and consider design options to minimize this effect. Finally, in Section II-B-6, the vacuum system for a UWMAK-II size reactor is described together with the particle collection system designed to collect the particles transported out by the divertor.

II-A-1. Principles of Tokamak Operation

A Tokamak[1-3] is a diffuse toroidal z-pinch in which the nested set of flux surfaces is generated by the current that is induced to flow in the plasma itself. It is characteristically a low-β device, where β is the ratio of the average plasma pressure to the magnetic field pressure,

$$\beta = \frac{\langle p \rangle}{B^2/2\mu_o} \quad . \tag{1-1}$$

The plasma in a Tokamak is confined by the poloidal magnetic field, B_θ, generated by a current carried in the plasma itself, and by the toroidal field, B_ϕ. The basis for the equilibrium analysis of such a system is

$$\vec{j} \times \vec{B} - \nabla p = 0 \tag{1-2}$$

where $\vec{j}$ is the plasma current density. The basic coordinates of this geometry is shown in Figure II-A-1 along with the fundamental dimension of a torus. An externally applied electric field drives the toroidal component of the plasma current, $\vec{j}$, which in turn generates the poloidal field.

A main characteristic of a Tokamak is the use of a strong toroidal magnetic field to suppress MHD instabilities.[4,5] In particular, a strong B_ϕ will suppress the helical kink instability if the MHD stability factor,

$$q(r) = \frac{r}{R} \frac{B_\phi}{B_\theta(r)} \tag{1-3}$$

is greater than one throughout the plasma and vacuum region. Further, the plasma current which produced B_θ provides the rotational transform required to suppress the flute instabilities[6] and to counteract the grad B_ϕ drifts. For a current density which decreases in r ($j_\phi(r)$ decreases from the plasma center to the edge), the criterion to suppress local flute perturbations is the Kruskal-Shafronov limit,

$$q(r) > 1. \quad o \leq r \leq a \tag{1-4}$$

In addition to this limitation on the stability factor, q, there is an additional limitation on the plasma β, namely that [2,7]

$$\beta_\theta < A \tag{1-5}$$

where β_θ is the ratio of the average plasma pressure to the pressure of the poloidal magnetic field and A is the torus aspect ratio. At $\beta_\theta \sim A$, the last closed, nested flux surface has shrunk down to the plasma surface itself. Further increase of β_θ causes a splitting of the magnetic surfaces inside the

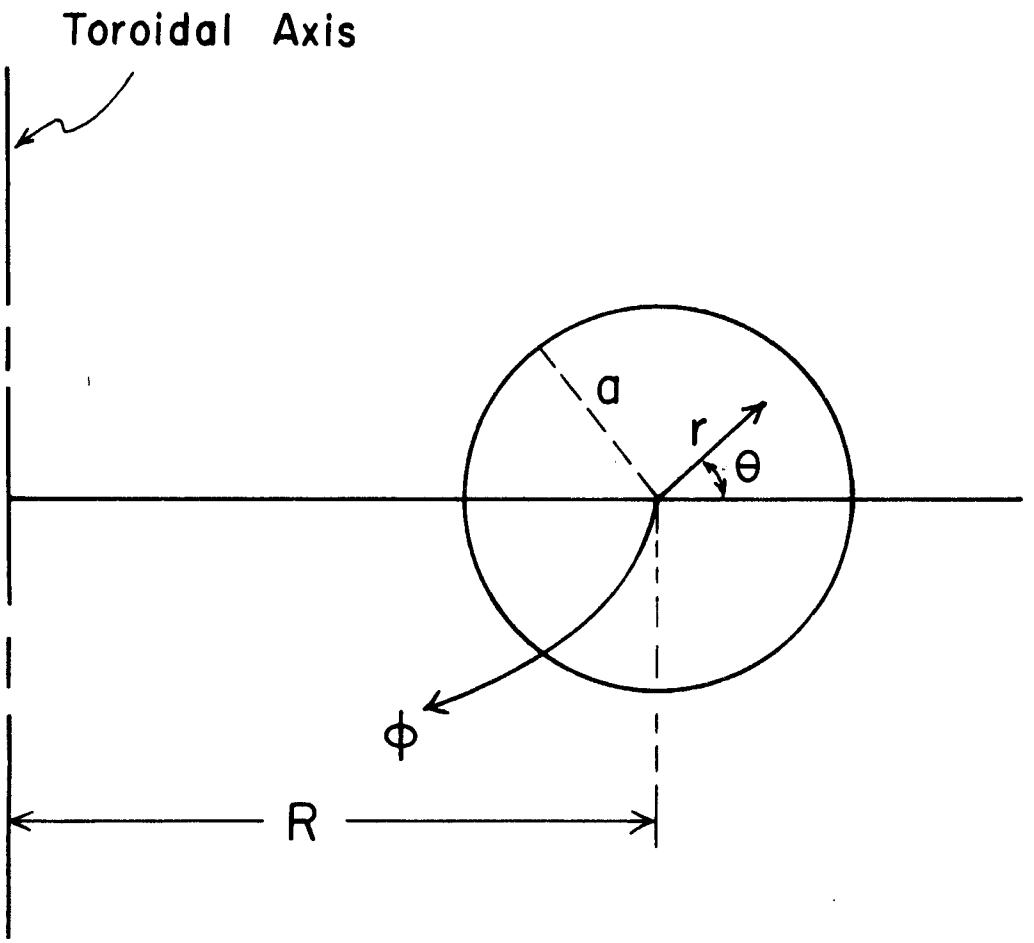

MAJOR RADIUS, R
MINOR RADIUS, a
ASPECT RATIO, A = R/a

TOROIDAL COORDINATE SYSTEM

FIGURE II-A-1

plasma boundary with a resultant deleterious effect on plasma confinement. The two criteria stated by equations (1-4) and (1-5) are fundamental to Tokamak operation and will be met in all the plasma analysis to be reported.

In a Tokamak, therefore, the plasma current plays the dual role of generating the pinch field to trap the plasma and the rotational transform required for stability. To drive this current, the plasma itself is treated as a single turn secondary of a transformer. Energizing the primary side produces a toroidal electric field, E_ϕ, which causes the gas breakdown and plasma formation and drives the toroidal plasma current. The transformer may have an iron or an air core and can have either normal or superconducting windings. An air-core transformer with superconducting windings allows for the smallest aspect ratio and this type of transformer is used in UWMAK-II. Its design is discussed in Section II-B-1.

The plasma has a finite resistivity that varies with electron temperature as $T_e^{-3/2}$. Therefore, plasma heating will be associated with the plasma current, although this Joule heating is insufficient to ignite a fusion reactor plasma. Additional heating in Tokamak devices has been obtained by compression of the plasma in the major radius (the ATC experiment)[9] and by the injection into the plasma of high energy neutral particle beams.[10] Because it requires an externally produced E_ϕ, the Tokamak is inherently a pulsed device. However, at high temperatures and low collision frequency (in the banana regime of neoclassical theory), trapped particle effects have led to the prediction that there will exist a diffusion driven current (a current proportional to a density gradient) which can provide the required rotational transform and trapping magnetic field, even without an externally produced electric field.[11,12] This is the so-called "bootstrap current" and is predicted to exist with $E_\phi = 0$ when $\beta_\theta^\circ \simeq \sqrt{A}$. β_θ° is the ratio of the peak plasma pressure to poloidal magnetic field pressure at the plasma boundary. Under these circumstances, plasma operation could be truly steady state unless other factors, such as impurity buildup, limit the burn time. However, this diffusion driven current has not been observed in experiments, such as Proto-Cleo, where it was calculated to be large enough to observe. We have therefore not assumed the existence of this effect and designed to provide the required core flux to maintain the plasma current for the desired burn time.

The basic ideas regarding equilibrium of the plasma in a Tokamak can also be understood by examining Figure II-A-2. If the plasma were a straight cylinder, the poloidal magnetic pressure would be equal around the plasma boundary. However, because of the toroidal curvature, the poloidal field is stronger on the inside of the plasma loop than on the outside. Without additional fields, the loop would tend to expand in major radius. Therefore, it is necessary for plasma equilibrium to have an additional, vertical field produced by external windings, which subtracts from the poloidal field on the inside of the loop and adds to it on the outside, thus producing an equilibrium configuration. Of course, in many present day experiments, eddy currents driven in a conducting shell surrounding the plasma generate the vertical field required to maintain the discharge in equilibrium[1] but in reactors, it seems clear that an externally produced vertical field will be required. Indeed, this vertical field, added to the poloidal field generated by the plasma current, produces a resultant magnetic field topology that leads naturally to a poloidal field divertor. A separatrix can be produced in this way which becomes a natural plasma boundary. Two such configurations are shown in Figure II-A-3. Magnetic surfaces inside the separatrix remained closed in the plasma volume. However, particles on field lines outside the separatrix are carried away from the plasma surface

TOKAMAK PLASMA CONFINEMENT

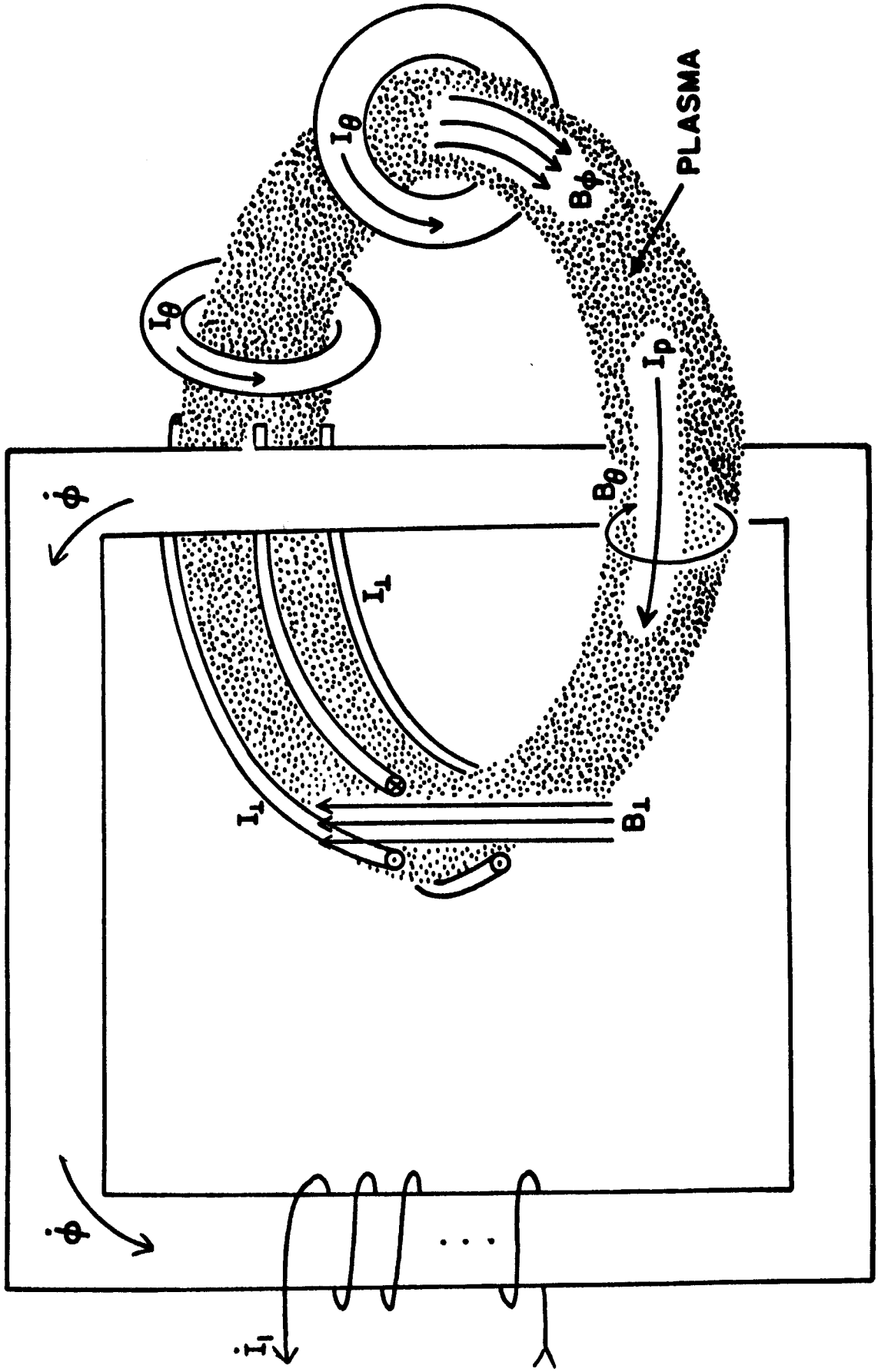

FIGURE II-A-2

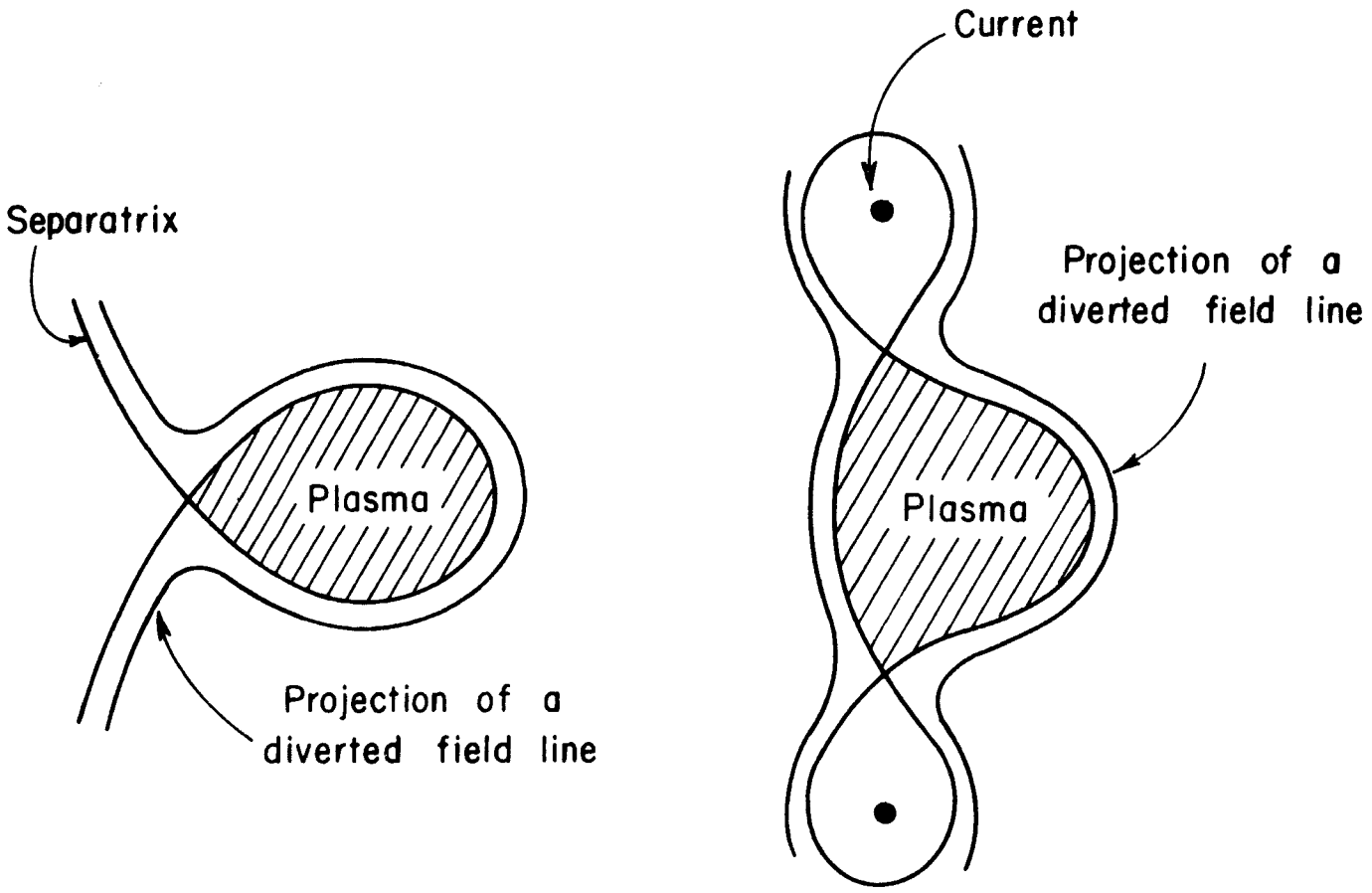

SINGLE NEUTRAL POINT

(Currents not shown)

DOUBLE NEUTRAL POINT

FIGURE II-A-3

and can be collected. The details of the vertical field design and magnetic field topology are discussed in Chapter II-B-4.

If the vertical field, $B_\perp$, is absolutely uniform, then the plasma loop has no restoring force in case of vertical displacements. To stabilize the loop against such displacements, the vertical field must have some curvature characterized by a decay index

$$n = -\frac{R}{B_\perp}\frac{\partial B_\perp}{\partial R} \tag{1-6}$$

For stability against vertical displacements, one requires $n > 0$, and for stability against horizontal displacements, n must be less than .42. The vertical field produced by the divertor coils, as discussed in Chapter II-B-4, is characterized by a decay index in the interval [0,.42].

As discussed, the poloidal field generated by the plasma current provides a rotational transform. When this poloidal field is superimposed on the strong toroidal field, B_ϕ, the resultant field lines are helical, as shown in Figure II-A-4. The rotation generated by the poloidal field compensates for the outward drift of particles caused by the gradient in the toroidal field. The toroidal field is stronger on the inside of the torus, varying as 1/R from the inside to the outside of the loop.

This gradient in B_ϕ can also produce a class of particles which cannot reach the inside of the plasma loop. Since effects associated with these trapped particles are most important in the reactor regime of plasma parameters (high temperature, low collision frequency), we will turn now to a review of transport theories for tokamaks and discuss the scaling laws used to analyze plasma performance in UWMAK-II.

References for Section II-A-1

1. L. A. Artsimovich, Nucl. Fusion 12 (1972) 215.
2. V. S. Mukhavatov and V. D. Shafranov, Nucl. Fusion 11 (1971) 67.
3. B. B. Kadomtsev and O. P. Pogutse, Nucl. Fusion 11 (1971) 605.
4. V. D. Shafranov, Atomm. Energ. 5 (1956) 38.
5. V. D. Shafranov, Zh. tekh. Fiz. 40 (1970) 741.
6. C. Mercier, Nucl. Fusion Suppl. 2 (1962) 801.
7. V. D. Shafranov, Zh. Eksp. Feor. Fiz 37 (1959) 1088.
8. J. M. Greene, J. L. Johnson, and K. E. Weimer, Phys. Fluids 13 (1970) 2593.
9. K. Bol et al., Phys. Rev. Letts.
10. L.D. Stewart et al., "Tokamak Neutral Beam Heating Technology," in Proc. First Topical Meeting on the Technology of Cont. Nuclear Fusion (CONF-740402-P1, USAEC 1974) Vol. 1, p. 365.
11. A. A. Galeev and R. Z. Sagdeev, Zh. Eksp. Theo. 53 (1967) 348.
12. R. J. Bickerton, J. W. Connor, and J. B. Taylor, Nature 229 (1972) 110.

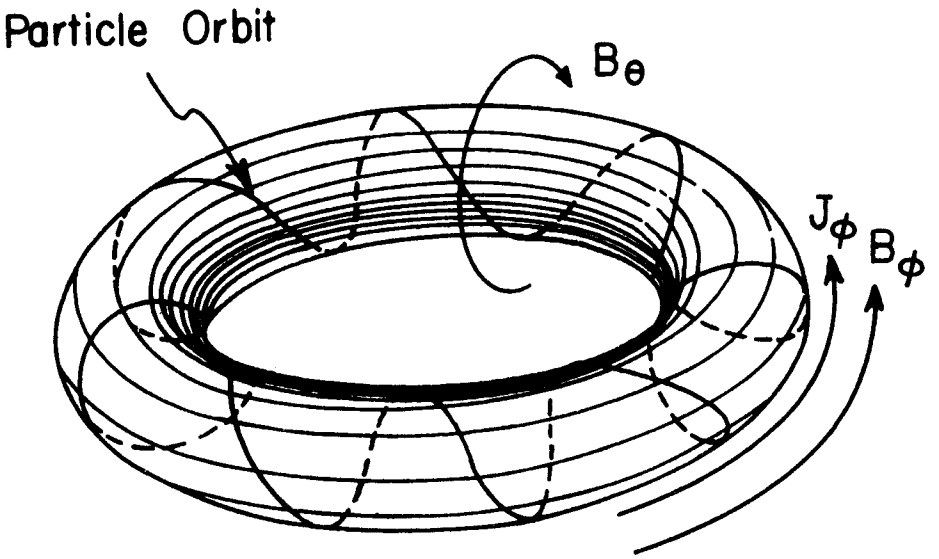

FIGURE II-A-4

II-A-2. Transport in Tokamaks and Scaling Laws

a. Classical Theory

Before considering transport in toroidal systems, let us review briefly the main results of classical theory. Assuming a random walk of particles with a characteristic step size, ρ, and collision frequency, ν, the classical particle diffusion coefficient can be expressed as:[1,4]

$$D \sim \nu\rho^2 \tag{2-1}$$

For classical free diffusion in a homogeneous magnetic field, the step size is given by the electron gyroradius, ρ_e, and the collision frequency is the Coulomb collision frequency for small angle scattering, ν_{ei}.[2,3]

$$D_{cl} \sim \nu_{ei}\,\rho_e^2 \tag{2-2}$$

$$\rho_e = m_e v_\perp / eB$$

$$\nu_{ei} = \frac{4(2\pi)^{1/2}\, q_e^2\, q_i^2\, n_i \ln\Lambda}{3(4\pi\varepsilon_o)^2 m_e^{1/2} (kT_e)^{3/2}}$$

For a plasma with two or more ion species, classical theory predicts the species with the higher charge will diffuse toward the region of higher plasma density. The equilibrium condition for a plasma consisting of two ion species of equal temperatures and no temperature gradients is given by:[2]

$$\frac{\nabla \ln n_1}{q_1} = \frac{\nabla \ln n_2}{q_2}$$

or

$$n_2 \propto n_1$$

Classical theory predicts ion heat conductivity greater than electron heat conductivity normal to the magnetic field, $K_\perp^i / K_\perp^e \sim (m_i/m_e)^{1/2}$, which is due to the larger gyroradius of the ions. Along the magnetic field the electron heat conductivity is greater than the ion heat conductivity, $K_\parallel^e / K_\parallel^i \sim (m_i/m_e)^{1/2}$, because of the higher thermal velocity of the electrons. Braginskii[2] gives the following values for classical heat conductivity:

$$K_\perp^i = \frac{n_i\, kT_i}{m_i \omega_i^2 \tau_{ii}}$$

$$K_\perp^e = C_1 \frac{n_e\, kT_e}{m_e \omega^2 \tau_{ei}} \tag{2-3}$$

$$K_\parallel^i = 3.9 \frac{n_i kT_i \tau_{ii}}{m_i}$$

$$K_{\parallel}^{e} = C_2 \frac{n_e \, kT_e \, \tau_{ei}}{m_e}$$

$$\tau_{ii} = \frac{1}{\nu_{ii}} = \frac{3(4\pi\varepsilon_o)^2 \, m_i^{1/2} (kT_i)^{3/2}}{4\pi^{1/2} \, \ln\Lambda \, q_i^4 \, n_i} \text{ , ion collision time}$$

$$\tau_{ei} = \frac{1}{\nu_{ei}} = \frac{3(4\pi\varepsilon_o)^2 \, m_e^{1/2} (kT_e)^{3/2}}{4(2\pi)^{1/2} \, \ln\Lambda \, q_e^2 q_i^2 n_i} \text{ , electron collision time}$$

$$\omega_i = \frac{q_i B}{m_i} \text{ , ion cyclotron frequency}$$

$$\omega_e = \frac{q_e B}{m_e} \text{ , electron cyclotron frequency}$$

Values of C_1 and C_2 depend on the ion charge, $q_i = Ze$, and are given in Table II-A-1.

The electrical conductivity is greater parallel to the magnetic field than across the magnetic field. The value along the magnetic field is usually referred to as the "Spitzer conductivity."(2,5)

$$\sigma_{\perp} = \frac{e^2 n_e \tau_{ei}}{m_e} = \sigma_1 (kT_e)^{3/2} \quad (\text{ohm-m})^{-1}$$

$$\sigma_{\parallel} = \sigma_{sp} = c_3 \sigma_{\perp} = C_3 \sigma_1 (kT_e)^{3/2} \quad (\text{ohm-m})^{-1} \qquad (2\text{-}4)$$

$$\sigma_1 = \frac{3}{4} \frac{(4\pi\varepsilon_o)^2}{\sqrt{2\pi m_e}} \frac{1}{Ze^2 \ln\Lambda} = \frac{3.1 \times 10^8}{Z \ln\Lambda} \text{ keV}^{-3/2}$$

kT_e is in keV

C_3 depends on the ion charge and is also given in Table II-A-1 for various values of Z.

Table II-A-1

Z	C_1	C_2	C_3
1	4.66	3.16	1.96
2	4.0	4.9	2.27
3	3.7	6.1	2.5
4	3.6	6.9	2.63
"∞"	3.2	12.5	3.33

b. Neoclassical Theory

For a toroidal plasma, the transport coefficients must be modified because of magnetic field gradients and the existence of "bananas." The inclusion of these effects leads to neoclassical transport theory. In an axisymmetric system, these modifications give rise to neoclassical transport theory.

As discussed previously, the magnetic field in a Tokamak consists of a main toroidal component, B_ϕ, and a poloidal component, $B_\theta << B_\phi$, produced by a toroidal current in the plasma (Fig. II-A-4). The toroidal current is produced by an externally applied electric field. The resultant magnetic field lines are helical.

The rotational transform, i, of a Tokamak is defined as the angle through which a field line passes the short way around the torus (θ-direction) on passing once through the long way around the torus (ϕ-direction). The safety factor, q, is defined as

$$q(r) = \frac{2\pi}{i} = \frac{r}{R} \frac{B_\phi}{B_\theta(r)} \qquad (2\text{-}5)$$

where r is the minor radius and R the major radius of the torus (Fig. II-A-1). MHD stability requires $q > 1$ in the plasma and $q \neq m/n$ (where m and n are small integers) in the vacuum gap between the plasma and the plasma chamber and in regions of low electrical conductivity.(3) $q = m/n$ represents a helical field line which closes on itself after passing around the torus m times in the toroidal direction and n times in the poloidal direction (Fig. II-A-4). From eqn. (2-5), it can be seen that $q>1$ is equivalent to imposing an upper limit on the poloidal field for a given toroidal field, i.e.,

$$B_\theta(r) = \frac{r}{q(r)R} B_\phi < \frac{r}{R} B_\phi$$

Since r/R is small, the condition $B_\theta << B_\phi$ arises out of stability considerations. The toroidal current producing the poloidal field is also restricted by the

condition q>1. For a uniform current density, J,

$$B_\theta(r) = \frac{\mu_o J r}{2}$$

$$J > \frac{2\mu_o B_\phi}{R}$$

This is the "Kruskal-Shafranov limit" on the plasma current.

Another parameter related to the stability factor, q, is the magnetic shear, θ. The shear is the rate of change of the direction of magnetic field lines on successive magnetic surfaces:

$$\theta \equiv \frac{r^2}{Rq^2} \frac{dq}{dr}$$

A system with shear provides greater stability since the magnetic field lines cannot be interchanged without distorting them. A system with a uniform current density has q(r) ~ constant and provides no shear. A nonuniform current density thus helps provide stability.

An additional requirement for stability is that β_θ, the ratio of the average plasma pressure to the poloidal magnetic field pressure, should be less than A=R/a, where a is the plasma minor radius:

$$\beta_\theta = \frac{\langle p \rangle}{B_\theta^2/2\mu_o} = \frac{(n_i kT_i + n_e kT_e)}{B_\theta^2/2\mu_o} \leq A \qquad (2\text{-}6)$$

The ratio of the average plasma pressure to the total magnetic field pressure, β, is used to characterize many types of plasma devices. In a Tokamak, the total magnetic field pressure is primarily due to the toroidal field. Using eqns. (2-5,6), the upper limit on β is given by:

$$\beta = \frac{\beta_\theta}{q^2A^2} \leq \frac{1}{q^2A}$$

For present day machines q ≃ 3-4, A ≃ 5 and β ≃ .02, thus characterizing Tokamaks as "low beta" devices.

A charged particle moves along a field line, conserving both energy and magnetic flux contained in its gyro orbit:

$$E = \frac{1}{2} mv^2 = \frac{1}{2} m (v_{\parallel}^2 + v_{\perp}^2) = \text{const.}$$

$$\mu = \frac{mv_{\perp}^2}{2B} = \text{const.}$$

$$v_{\parallel} = \left(\frac{2}{m}(E-\mu B)\right)^{1/2}$$

where $v_{\parallel}$ is the velocity of the particle parallel to the field line and $v_{\perp}$ is the velocity component normal to the field line. $B \sim B_{\phi}$ since the toroidal field is much stronger than the poloidal field. The toroidal field is inversely proportional to the distance from the center of the torus (Fig. II-A-5), so the particle sees a varying magnetic field along the field line.

For a given field line, the maximum magnetic field is at the inside of the torus and can be denoted B_{max}. If a particle has $E > \mu B_{max}$ it will continue to follow the field line around the torus, since the parallel velocity will always be finite--this is called a "circulating" or "untrapped" particle. If $E < \mu B_{max}$, the parallel velocity will vanish at some point and the particle will be reflected back to an area of lower magnetic field--this is called a "trapped" particle. The condition for trapped particles gives

$$\left.\frac{v_{\parallel}}{v_{\perp}}\right|_{\theta=0} < \left(\frac{B_{max}}{B_{min}} - 1\right)^{1/2}$$

or

$$\left.\frac{v_{\parallel}}{v_{\perp}}\right|_{\theta=0} < \left(\frac{2r}{R}\right)^{1/2} \quad \text{for } r \ll R.$$

The fraction of particles trapped is equal to the fraction of velocity space occupied by trapped particles. At r=0, $f_T=0$ and r=a, $f_T \sim (2/A)^{1/2}$ so that on the average $f_T \simeq (1/A)^{1/2}$, where A=R/a is the aspect ratio of the torus.

As the particle moves along a field line, it experiences a force in the vertical direction due to the gradient in the magnetic field. For electrons this drift velocity is given approximately by:[3]

$$v_D^e \simeq \frac{m_e \left(v_{th}^e\right)^2}{eBR}$$

Where $v_{th}^e = \sqrt{\frac{2kT_e}{m_e}}$ is the thermal velocity of the electron. This drift gives the trapped particle orbits their banana shape (Fig. II-A-6). The time a trapped particle takes to travel between mirror points is the bounce time, τ_b. The bounce frequency is then defined as $\omega_b \equiv 1/\tau_b$. For a distance L between mirror points, the bounce frequency is given by:

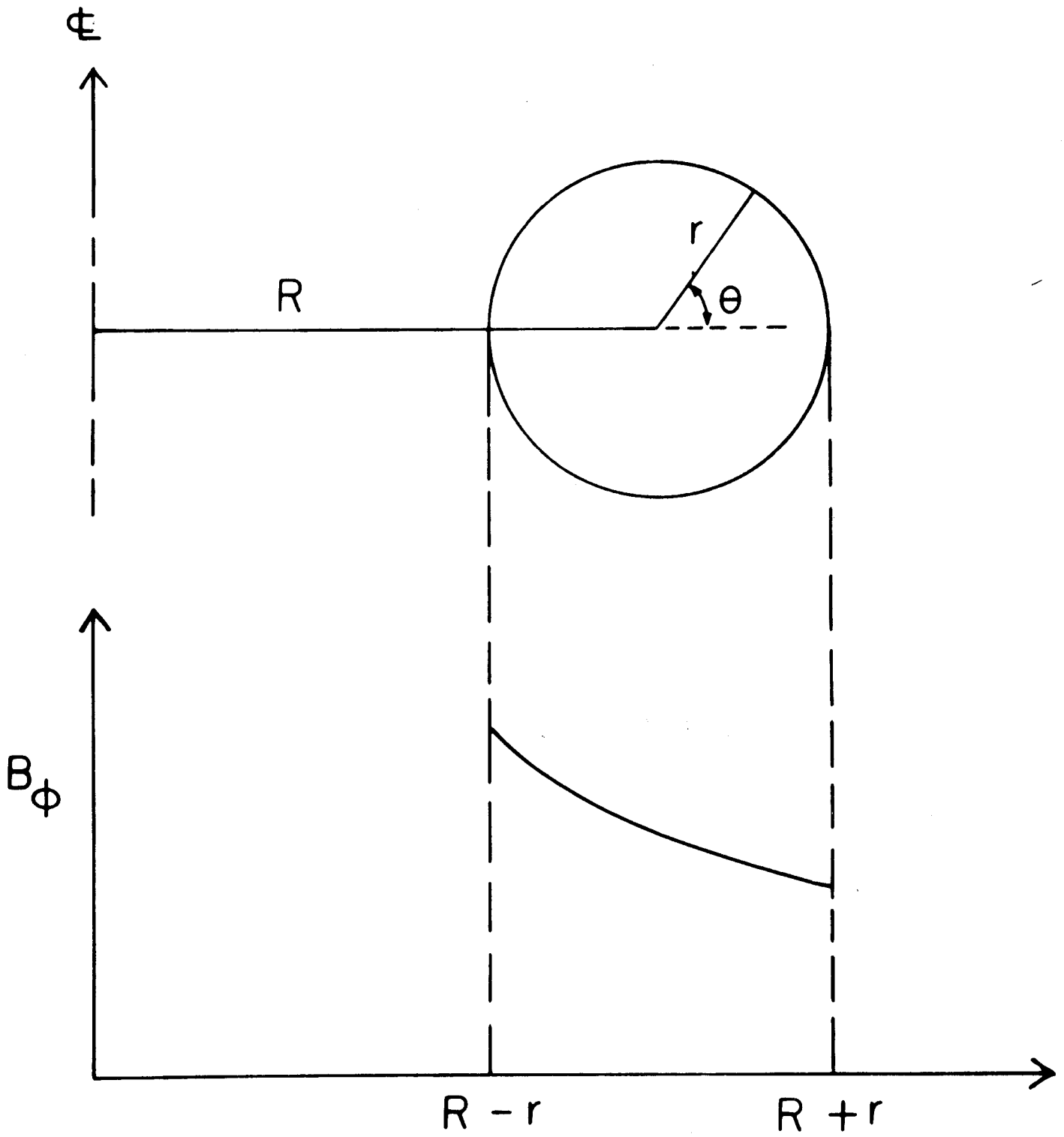

FIGURE II-A-5

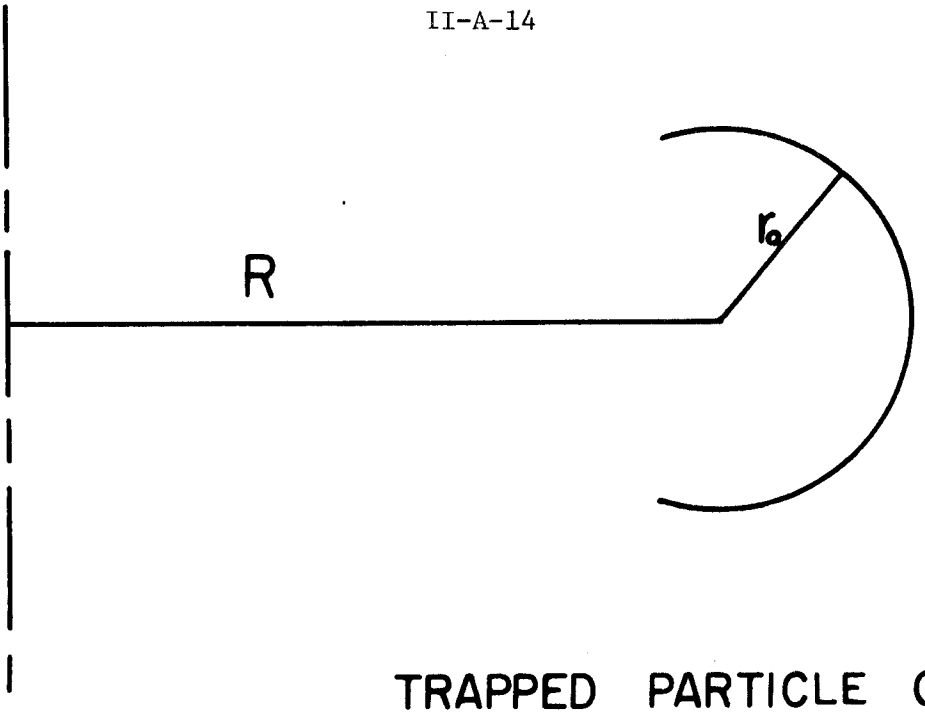

TRAPPED PARTICLE ORBIT
(NO GRAD(B) DRIFT)

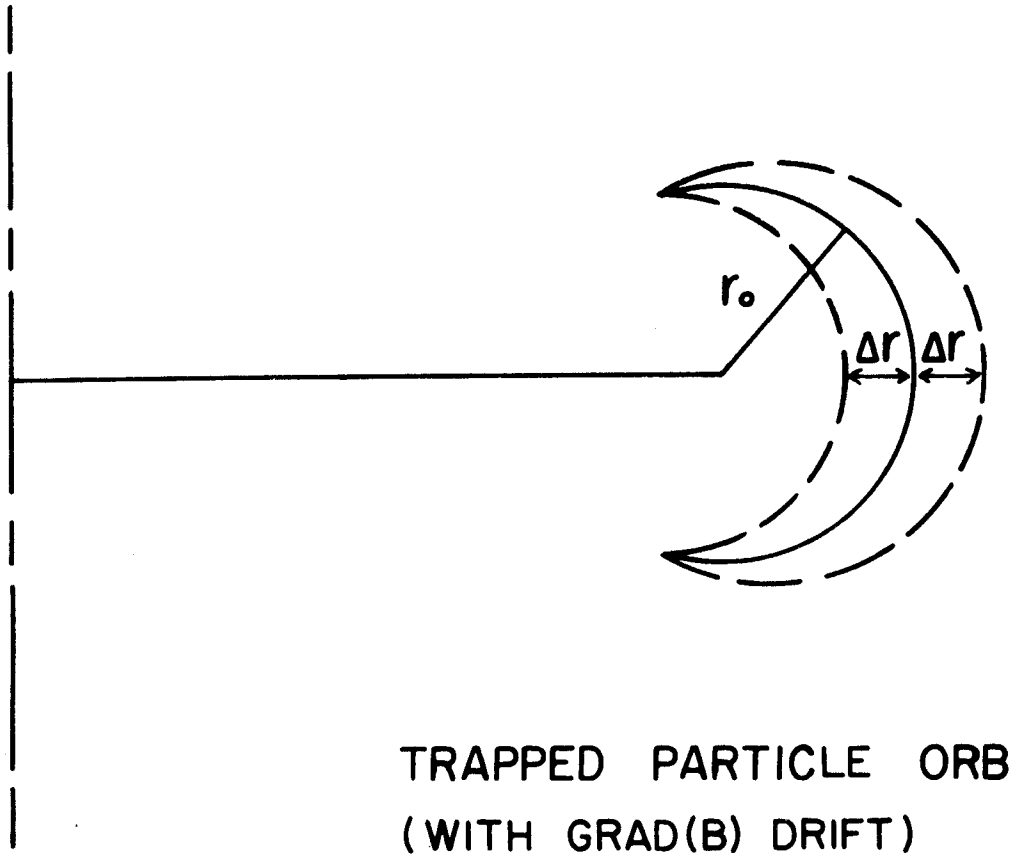

TRAPPED PARTICLE ORBIT
(WITH GRAD(B) DRIFT)

FIGURE II-A-6

$$\omega_b \simeq \frac{v_{\parallel}}{L} \simeq \frac{v_{\perp}\sqrt{1/A}}{qR}$$

$$\omega_b \simeq \frac{v_{th}}{qRA^{1/2}}$$

The width of the banana, Δr_b, is approximately equal to the drift velocity divided by the bounce frequency. For electrons:

$$\Delta r_{be} \simeq \frac{v_D^e}{\omega_{be}} \simeq \rho_e q\, A^{1/2}$$

In neoclassical theory, there are three transport regimes depending on the relative sizes of the collision frequency and the bounce frequency. For $\nu_{ei} >> \omega_{be}$ the plasma is collisional; this is called Pfirsch-Schluter regime. For $\nu_{ei} << \omega_{be}$ the particles can make many transits around the torus or complete many banana orbits before being scattered; this is called the "banana" regime. Intermediate values of ν_{ei} lead to the "plateau" regime.

Pfirsch and Schluter, in an unpublished report, showed that toroidicity adds another term to the classical diffusion expression for a collisional plasma, $\nu_{ei} >> \omega_{be}$. This term is q^2 larger than the classical term:

$$D_{P\text{-}S} \simeq q^2 \nu_{ei} \rho_e^2 \qquad (2\text{-}7)$$

An heuristic derivation of eqn. (2-7) can be made by noting that $D \simeq (\Delta x)^2/t$, where Δx is the displacement of a particle from a magnetic surface in a characteristic time t. The displacement from the magnetic surface is due to the drift velocity, thus $\Delta x \simeq v_D t$. The distance a particle travels along a field line while experiencing an outward drift is Rq. Denoting the diffusion coefficient along the field line as $D_{\parallel}$, t is expressed as:

$$\frac{1}{t} \simeq \frac{D_{\parallel}}{(Rq)^2}$$

$$D_{\parallel} \simeq \frac{v_{th}^2}{\nu_{ei}}$$

$$\frac{1}{t} \simeq \frac{v_{th}^2}{(Rq)^2 \nu_{ei}}$$

The resulting diffusion coefficient is that given by eqn. (2-7):

$$D_{P-S} \simeq (v_D^e)^2 \, t \simeq (v_D^e)^2 \frac{(Rq)^2 \nu_{ei}}{v_{th}^{e\,2}} \simeq q^2 \nu_{ei} \rho_e^2$$

Others have found similar results with more rigorous treatments.[6-7] Hazeltine and Hinton[7] allowed for both density and temperature gradients and found the ion and electron heat conductivities similarly increased by a factor of q^2. Kadomtsev and Pogutse[8] report the enhancement of heat conductivity as $1.6q^2$.

The banana regime has been most extensively studied[6,8-22] because large scale fusion experiments are expected to operate at the high temperatures and thus low collision frequencies of this regime. The enhanced diffusion comes from the increased step size, Δr_b, a particle can take when scattering from a trapped to a circulating orbit. The effective collision frequency for scattering from a trapped to a circulating orbit is also increased since the required scattering angle, $\Delta\theta$, is much less than 90°. ν_{ei} represents the collision frequency for 90° scattering through successive small angle scattering events. Therefore, the effective collision frequency can be expressed as:

$$\nu_{eff} = \frac{\nu_{ei}}{(\Delta\theta)^2}$$

$\Delta\theta$ can be approximated by the fraction of velocity space occupied by trapped particles, i.e., $\Delta\theta \sim v_{\parallel}/v_{\perp} \sim 1/f_T$[8,9] so that

$$\nu_{eff} \sim \nu_{ei} f_T^2 \sim A\nu_{ei}$$

Analagous to the classical expression, the additional diffusion due to bananas is given by:

$$D_{BAN} \simeq f_T (\Delta r_b)^2 \nu_{eff} \sim A^{3/2} q^2 \rho_e^2 \nu_{ei} \qquad (2\text{-}8)$$

where $f_T \simeq 1/A^{1/2}$ is the fraction of particles trapped. This effect was first reported by Galeev and Sagdeev.[9] The heat conductivity is similarly enhanced. More recent analyses have led to expressions for particle and thermal heat fluxes with both temperature and density gradients in the plasma[11-14]. Corrections for finite aspect ratio[12], for multiple ion species[13], and for collision frequencies extending into the plateau region[14] have been made. As in classical theory, neoclassical theory predicts diffusion of higher Z ions toward the center of the plasma.[13]

Several other effects of trapped and circulating particles have been predicted for the banana regime. Collisional mixing of trapped and circulating electrons gives an additional electric current which can be comparable to the toroidal current induced in the plasma. This "bootstrap" effect was shown by Bickerton, Connor and Taylor[15] and then independently by Kadomtsev and

Shafranov.[16] It leads to the possibility of the plasma producing most of its own poloidal field and requires only a small additional induced toroidal current. Unfortunately, the poloidal beta limit for the plasma is reduced to $\beta_\theta \lesssim A^{1/2}$ because of the Kruskal-Shafranov limit on the "bootstrap" current.[16-17]

The externally induced toroidal electric field causes the trapped particles to drift inward at a velocity of order E/B_θ. The inward flux can be quite large since the drift velocity is determined by the smaller poloidal field. This "Ware pinch" effect, first noted by A. A. Ware in 1970[18-19], can balance the outward particle diffusion when $\beta_\theta \sim 1$.[16,18-20] Similar pinching has since been found to occur in the plateau and Pfirsch-Schluter regimes of neoclassical transport theory but on a smaller scale.[20]

The electrical conductivity along the magnetic field is reduced in the banana regime which then requires induced electric fields to produce the toroidal current. Corrections were first found for very large aspect ratios[21] and have since been modified for lower aspect ratios.[12,22] Hazeltine, Hinton and Rosenbluth[12] have used a variational principle to obtain:

$$\sigma_{\parallel} = \sigma_{sp} \left[1 - 1.95(r/R)^{1/2} + .95(r/R)\right] \qquad (2\text{-}9)$$

In the plateau regime, the untrapped particles can be considered collisionless and the trapped particles collisional, i.e., the trapped particles are scattered before they bounce. The collision frequency is given by ν_{eff} and the step size by the banana width, Δr_b. Using ω_b/ν_{eff} as the probability that a trapped particle will complete its orbit before scattering, the diffusion coefficient in the plateau regime becomes:[6,9]

$$D_{PLAT} \simeq f_T \frac{\omega_{be}}{\nu_{eff}} (\Delta r_b)^2 \simeq \omega_{be} q^2 \rho_e{}^2 A^{1/2} \simeq v_{th}^e \frac{\rho_e q^2}{R} \qquad (2\text{-}10)$$

Recently, Hinton and Rosenbluth[14] have used a variational technique to find transport coefficients valid through both the banana and plateau regimes--giving a smooth transition from one regime to the other.

The neoclassical particle diffusion coefficients in the three regimes are plotted vs. collision frequency in Fig. II-A-7. For reference, the classical value and qualitative results of Hinton and Rosenbluth[14] are also shown.

c. Anomalous Transport

Transport coefficients are measurements of the rates of relaxation of various plasma properties toward equilibrium values. The classical and neoclassical transport coefficients were found assuming collisional relaxation in a non-homogeneous plasma, but microinstabilities can also cause plasma transport. The resulting "anomalous transport", though turbulent in nature, exhibits a certain amount of order imposed by the magnetic field.

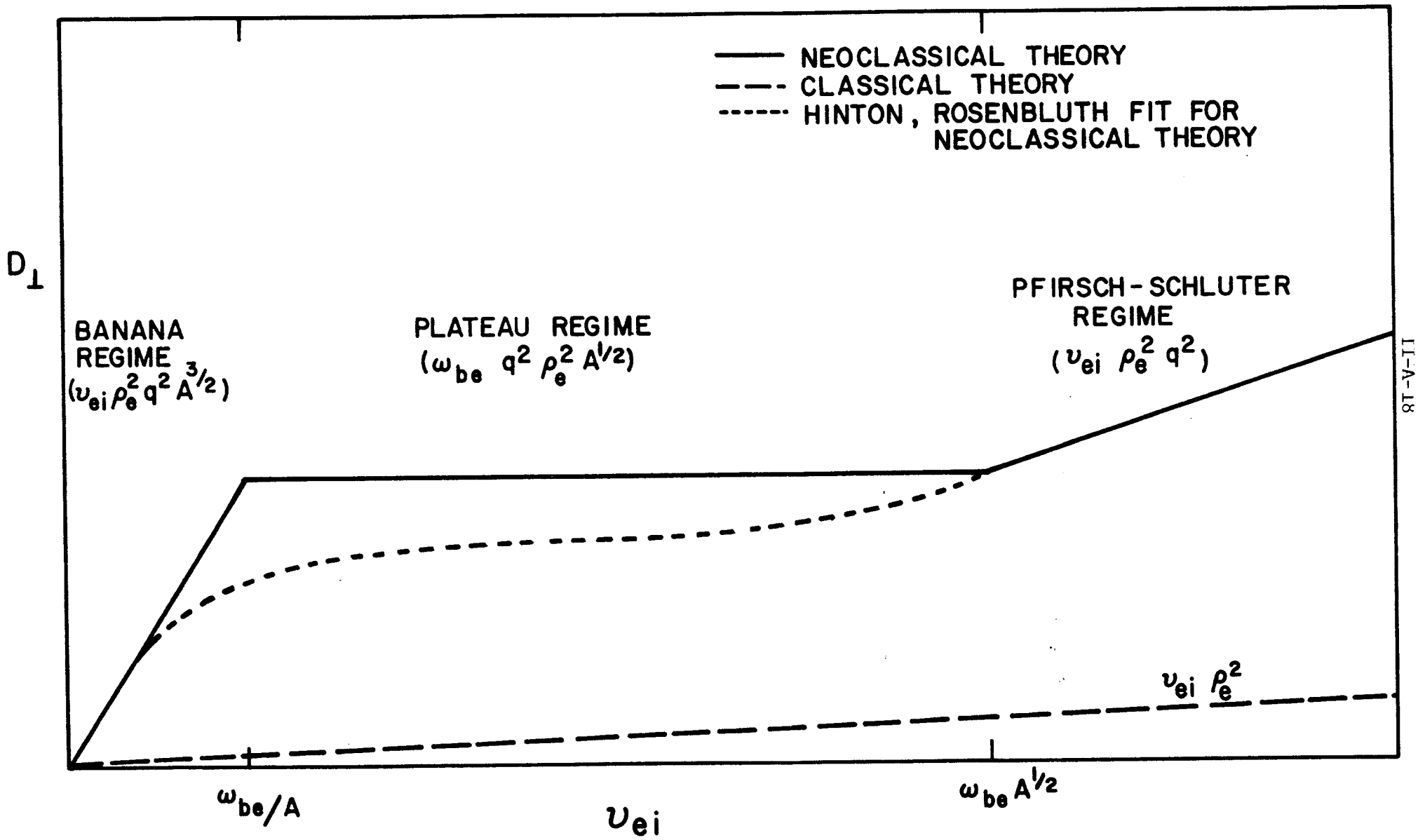
NEOCLASSICAL THEORY
CLASSICAL THEORY
HINTON, ROSENBLUTH FIT FOR NEOCLASSICAL THEORY
$D_\perp$
BANANA REGIME
$(\upsilon_{ei} \rho_e^2 q^2 A^{3/2})$
PLATEAU REGIME
$(\omega_{be}\ q^2 \rho_e^2 A^{1/2})$
PFIRSCH-SCHLUTER REGIME
$(\upsilon_{ei}\ \rho_e^2 q^2)$
$\upsilon_{ei}\ \rho_e^2$
ω_{be}/A
υ_{ei}
$\omega_{be} A^{1/2}$
II-A-18

FIGURE II-A-7

There are several sources of free energy available to drive microinstabilities in a Tokamak. The two main sources are gradients in temperature and density and distortions of the particle distribution functions in velocity space, e.g., differences between trapped and circulating particles. The microinstabilities discussed here are all related to drift waves which are driven by gradients in the plasma.

A fairly complete linear formulation has been developed to study the onset of various microinstabilities characteristic of an inhomogeneous plasma (References 8 and 23 provide a good review). The initial growth rate, γ, for small perturbations can be found from the linear theory but nonlinear effects soon dominate. It is not known how to stabilize all the known micro-instabilities, and perhaps it will not be necessary to do so. In the nonlinear regime their growth is limited. A good nonlinear analysis is needed to determine the saturation levels of the growth rates and the resulting transport coefficients. Much effort is currently being devoted to this area to determine if the transport coefficients will seriously affect large scale experiments.

Because of the radial density gradient in the plasma, there is a diamagnetic drift velocity, V_d, of particles in the poloidal direction:

$$V_d \simeq \frac{kT}{eB} \frac{1}{n} \frac{dn}{dr}$$

A fluctuating poloidal electric field, $\tilde{E}_\theta$, produced by local perturbations in the ion and electron densities, causes radial oscillations of the particles. A drift wave is created with wave numbers k_θ and frequency $\omega_* = k_\theta V_d$. The $\tilde{E}_\theta \times \vec{B}$ drifts of both ions and electrons are the same unless some mechanism, such as collisions, causes them to be out of phase. Once out of phase, the particles exchange energy and momentum with the wave causing it to either grow or be damped. In each regime of collisionality, the growth rate of the wave, γ, can be determined from linear theory. Strong turbulence theory then provides a rough relationship between the linear growth rate and the saturation level for the wave:

$$D \simeq \gamma / k_\perp^2$$

where $k_\perp$ is the perpendicular wave number for the drift wave.

Bohm diffusion is the name given to the observed anomalous diffusion which was dominant in early stellarator experiments. The diffusion coefficient, found empirically, is given by:

$$D_{Bohm} = \frac{1}{16} \frac{kT}{eB} \qquad (2\text{-}11)$$

On a theoretical basis, Bohm diffusion is now thought to be the result of drift dissipative modes which appear in low shear systems[3,23] such as the C-Stellarator. This can explain why Tokamaks, and also stellarators with greater shear, do not observe Bohm diffusion. Although the parametric dependence of D_{Bohm} has been obtained theoretically from the drift-dissipative instability, the coefficient has not.[3,24]

Pseudoclassical transport (PC) is another anomalous transport mechanism which was first found from empirical scaling of experimental results.[25] Although originally used to describe electron thermal conductivity for Tokamaks, attempts have been made since to develop a pseudoclassical theory for both particle and heat transport. From drift dissipative modes, Pogutse[26] found that the radial excursion of electrons, for a fluctuation of potential $e\phi$, is given approximately by:

$$\Delta x \sim v_{th}^{e} \sqrt{\frac{e\phi}{kT}} \quad \frac{m_e}{eB} \quad \left(\frac{k_\theta}{k_{||}}\right) \sim \sqrt{\frac{e\phi}{kT}} \quad \rho_e \quad \left(\frac{k_\theta}{k}\right) \tag{2-12}$$

where $k_\theta \sim 1/q\ R_o$ for a toroidal machine and k is the wave number along the magnetic field. The heat transport coefficient, $\chi_e \equiv K_\perp^e / n_e$, is then:

$$\chi_e^{PC} \simeq f_T \nu_{eff} (\Delta x)^2 \simeq \sqrt{\frac{e\phi}{kT}} \quad \left(\nu_{ei} \frac{kT}{e\phi}\right) \left(\sqrt{\frac{e\phi}{kT}}\ \rho_e \ \left(\frac{k_\theta}{k}\right)\right)^2$$

$$\simeq \sqrt{\frac{e\phi}{kT}} \quad (k_\theta r)^2 \ \nu_{ei} \ q^2 \ \frac{R_o^2}{r^2} \ \rho_e^2$$

$$\chi_e^{PC} \sim C_o \ \nu_{ei} \ \rho_{e\theta}^2 \tag{2-13}$$

$$C_o \sim 4\text{-}10$$

$\rho_{e\theta} = \dfrac{q\ R_o \rho_e}{r}$ is the electron gyroradius in the poloidal magnetic field and the value of C_o was chosen for the expression $\sqrt{e\phi/kT}\ (k_\theta r)^2 \sim \sqrt{\Delta n/n}\ (k_\theta r)^2$ to match the empirical expression given by Artsimovich.[25] Yoshikawa and Christofilos[27] have used a similar analysis to obtain an expression for particle diffusion, again choosing the coefficient to match the empirical results:

$$D_{PC} \simeq C_1 \ \nu_{ei} \ \rho_{e\theta}^2$$

$$C_1 \simeq C_o/3 \tag{2-14}$$

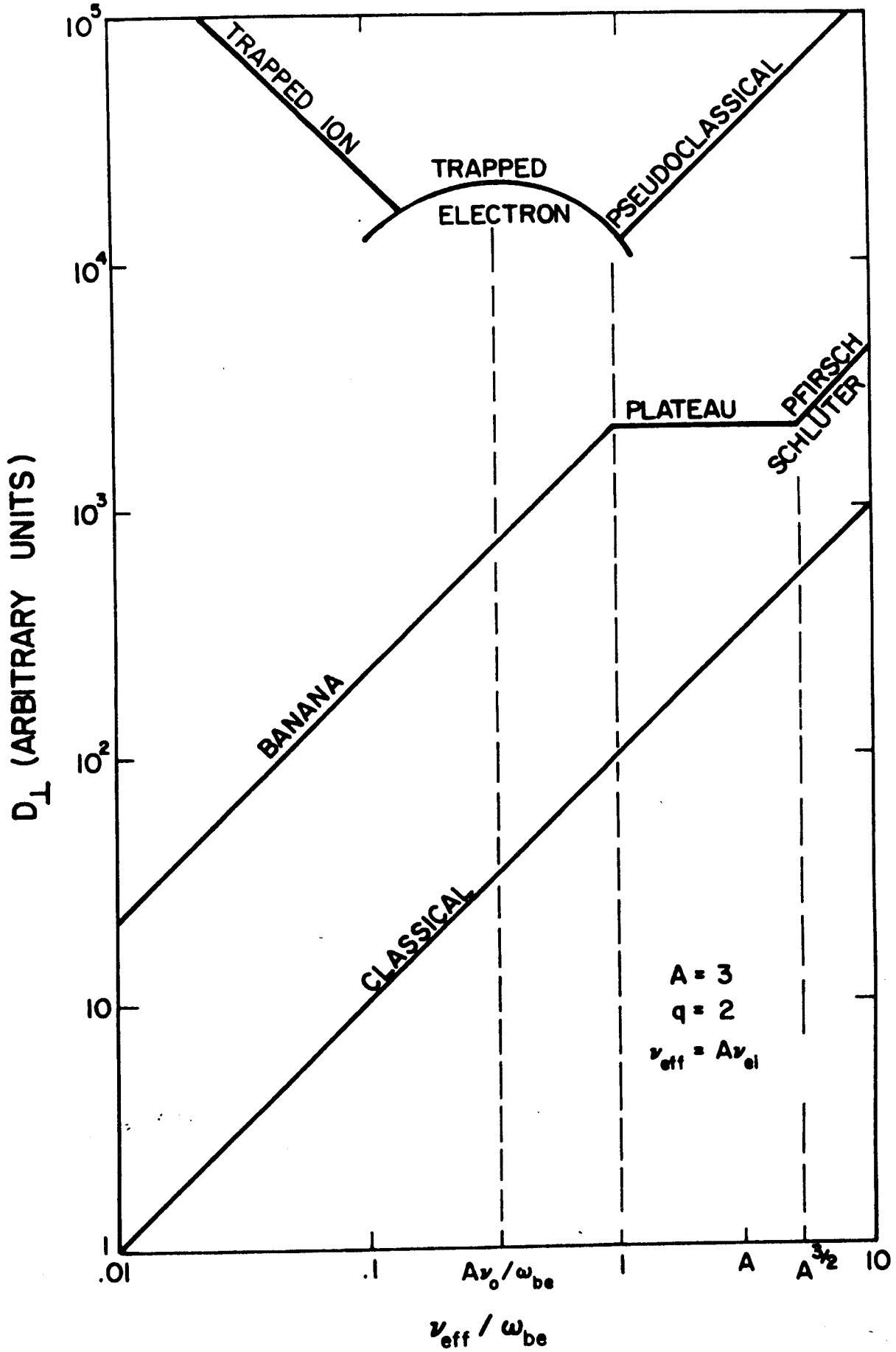
TRAPPED ION
TRAPPED
ELECTRON
PSEUDOCLASSICAL
PLATEAU
PFIRSCH
SCHLUTER
BANANA
CLASSICAL
A = 3
q = 2
$\nu_{eff} = A\nu_{ei}$
$D_\perp$ (ARBITRARY UNITS)
10^5
10^4
10^3
10^2
10
1
.01
.1
$A\nu_o/\omega_{be}$
1
A
$A^{3/2}$
10
ν_{eff}/ω_{be}

FIGURE II-A-8

The derivations are not rigorous, so the regime of validity and extrapolability of the results are subject to question. Figure II-A-8 shows the pseudoclassical diffusion coefficient in a regime based primarily on experimental observation.

The dissipative trapped electron mode (TEM) should appear in a regime where the electrons are "collisionless," $\nu_{eff} \lesssim \omega_{be}$ ($\nu_{ei} \lesssim \omega_{be}/A$). An electron temperature gradient is the primary driving force for the mode. If magnetic drift is taken into account, the growth rate of the mode does not vanish as the electron temperature gradient goes to zero, but decreases by approximately 1/A.

As the collision frequency is decreased from ω_{be}/A, the main contribution to heat and particle transfer is made by oscillations with longer wavelengths. χ_e and D then increase as ν_{ei} decreases. Below the frequency ν_o, the oscillation amplitude of the wave is limited by electrostatic trapping of electrons in the wave which gives a stabilizing effect. D and χ_e are then proportional to the collision frequency. Since a temperature gradient is the main driving force for the instability, the heat transport coefficient is larger than the pasticle diffusion coefficient, $D \sim \chi_e/A$. Over the entire range of the dissipative trapped electron instability, the transport coefficients have been expressed by Kadomtsev and Pogutse [8,28] as:

$$\chi_e^{TEM} \simeq A \frac{m_i}{m_e} \left(\frac{r}{T_e} \frac{d}{dr} (kT_e)\right)^2 \frac{\rho_{e\theta}^2 \nu_{ei}}{1 + \nu_{ei}^2/\nu_o^2} \qquad (2\text{-}15)$$

$$\nu_o = \frac{\theta A^{1/4}}{R} \sqrt{\frac{kTe}{m_i}} \sqrt{\left| \frac{d \ln n}{d \ln kT_e} \right|}$$

$$\theta = \frac{r^2}{Rq^2} \frac{dq}{dr} \sim \frac{B_\theta}{B} \sim \frac{1}{qA} \text{ (Shear)}$$

$$D_{TEM} \sim \frac{\chi_e^{TEM}}{A} \qquad (2\text{-}16)$$

A similar expression has been obtained by Galeev.[29] Figure II-A-B shows the collisionality regime and relative order of magnitude for the diffusion coefficient given by eqn. (2-16).

The dissipative trapped ion mode (TIM) appears when the effective ion collision frequency is much less than the ion bounce frequency, i.e., the ions are basically collisionless. Electron collisions increase the growth rate of the mode while ion collisions, Landau damping,[30] and shear[31] tend to stabilize the mode. A density gradient is necessary to drive the mode but a temperature gradient is not. However, a temperature gradient does increase the growth rate.[30] The transport coefficients are given, for no temperature gradient, by[8]

$$D_{TIM} \simeq \chi_e^{TIM} \simeq \chi_i^{TIM} \simeq \frac{1}{A^{5/2}} \frac{r^2}{\nu_{ei}(1 + T_e/T_i)^2} \left(\frac{kTe}{eBr} \frac{1}{n} \frac{dn}{dr}\right)^2$$

$$\simeq \frac{1}{A^{5/2}} \frac{\rho_e^2 v_{th}^e}{\nu_{ei}} \frac{1}{(1 + T_e/T_i)^2} \left(\frac{1}{n} \frac{dn}{dr}\right)^2 \qquad (2\text{-}17)$$

A plot of D_{TIM} vs ν_{ei} is shown in Figure II-A-8 for the approximate collisionality regime.

The trapped particle interchange mode (TPI) appears in the very collisionless regime--lower than the collision frequency anticipated for a Tokamak fusion reactor. This instability is similar to the MHD flute instability in a mirror machine since it is driven by a pressure gradient and the unfavorable drift of trapped particles.[8] The diffusion coefficient is Bohm-like. For a radial localization width of $\Delta r < (\frac{1}{n} dn/dr)^{-1}$, the diffusion coefficient for this mode is given approximately by:[32]

$$D_{TPI} \sim \frac{1}{A^{3/4}} \frac{kTe}{eB} \frac{(\Delta r)^2}{r} \left| \frac{1}{n} \frac{dn}{dr} \right|$$

The above discussion has been an overview of the various transport mechanisms that can affect plasma behavior in Tokamaks. Neoclassical theory is quite well developed and understood, but does not at present explain the "anomalous" electron heat transport in Tokamaks and "anomalous" transport mechanisms are expected to dominate. The nonlinear theory needed to obtain the transport coefficients due to microinstabilities is still in its early stages of development. Thus, the results here have been order of magntiude estimates and will continue to be refined.

Recent studies leading to the design of next generation machines[32,33] have made the pessimistic assumption that the transport scaling laws will follow the predictions of microinstability theory and will therefore have shorter energy containment times than predicted by neoclassical theory. In our previous study,[34] we assumed the scaling would follow the functional form of classical or neoclassical theory but would lead to anomolously shorter containment times. This is necessary for the removal of the spent fuel. For the UWMAK-II study we have assumed the scaling laws will follow microinstability predictions and that during operation, the plasma will be in the trapped ion mode regime. As stated, this is a pessimistic assumption and, as well, the scaling laws are perhaps no better than order of magnitude estimates. On the other hand, this amounts to roughly a "worst case" approach and our results should be viewed in that light. Indeed, one of the conclusions of the UWMAK-II study is that TIM scaling can lead to acceptable $n\tau$ values for reactors and at the same time allow thermally stable plasma operation in the optimum temperature range [10, 15 keV]. This will be discussed further in section II-B-3.

References for Section II-A-2

1. C. L. Longmire and M. N. Rosenbluth, Phys. Rev. 103, 507(1956).

2. S. I. Braginskii, Reviews of Plasma Physics, M. A. Leontovich, Ed., Vol. I, p. 205.

3. S. O. Dean et al., "Status and Objectives of Tokamak Systems for Fusion Research," WASH-1295, USAEC.

4. J. E. Scharer, Univ. of Wis. Fusion Design Memo - UWFDM-76, (1973).

5. L. Spitzer, Physics of Fully Ionized Gases, Interscience, New York (1964) p. 138.

6. P. H. Rutherford, Phys. Fluids 13, 482 (1970).

7. R. D. Hazeltine and F. L. Hinton, Phys. Fluids 16, 1883 (1973).

8. B. B. Kadomtsev and O. P. Pogutse, Nuclear Fusion 11, 67 (1971).

9. A. A. Galeev and R. Z. Sagdeev, Sov. Phys. JETP 26, 233 (1968).

10. R. Z. Sagdeev and A. Galeev, Comments on Plasma Physics and Controlled Fusion 1, 23 (1972).

11. M. N. Rosenbluth, R. D. Hazeltine and F. L. Hinton, Phys. Fluids 15, 115 (1972).

12. R. D. Hazeltine, F. L. Hinton and M. N. Rosenbluth, Phys. Fluids 16, 1645 (1973).

13. J. W. Connor, Plasma Physics 15, 765 (1973).

14. F. L. Hinton and M. N. Rosenbluth, Phys. Fluids 16, 836 (1973).

15. R. J. Bickerton, J. W. Connor and J. B. Taylor, Nature 229, 110 (1971).

16. B. B. Kadomtsev and V. D. Shafranov, Proc. 4th International Conference on Plasma Phys. and Controlled Nuclear Fusion Research, Madison, Wis., USA (1971), CN-28/F-10.

17. A. A. Galeev and R. A. Sagdeev, Proc. 4th International Conf. on Plasma Phys. and Controlled Nuclear Fusion Research, Madison, Wis., USA (1971), CN-28/C-11.

18. A. A. Ware, Phys. Rev. Letters 25, 15 (1970).

19. A. A. Ware, Phys. Rev. Letters 25, 916 (1970).

20. P. H. Rutherford, L. M. Kovrizhnikh, M. N. Rosenbluth, and F. L. Hinton, Phys. Rev. Letters 25, 1090 (1970).

21. F. L. Hinton and C. Oberman, Nuclear Fusion 9, 319 (1969).

22. B. Coppi and D. J. Sigmar, Phys. Fluids 16, 1174 (1973).

23. B. B. Kadomtsev and O. P. Pogutse, Reviews of Plasma Physics, M. A. Leontovich, Ed., Vol. V. p. 249.

24. A. A. Galeev, R. Z. Sagdeev, H. P. Furth and M. N. Rosenbluth, Phys. Rev. Letters 22, 511 (1969).

25. L. A. Artsimovich, JETP Letters 13, 70 (1971).

26. O. P. Pogutse, Nuclear Fusion 12, 39 (1972).

27. S. Yoshikawa and N. C. Christofilos, Proc. 4th International Conf. on Plasma Physics and Controlled Nuclear Fusion Research, Madison, Wis., USA (1971), CN-28/F-1.

28. B. B. Kadomtsev and O. P. Pogutse, Sov. Phys. Dokl. 14, 470 (1969).

29. A. A. Galeev, Third International Symposium on Toroidal Plasma Confinement, Garching/Munich, (1973), paper E 1-I.

30. M. N. Rosenbluth, D. W. Ross and D. P. Kostomarov, Nuclear Fusion 12, 3 (1972).

31. N. T. Gladd and D. W. Ross, Phys. Fluids 16, 1706 (1973).

32. "TCT, Two Component Torus, Joint Conceptual Design Study" Princeton Plasma Physics Lab. and Westinghouse Electric Corp. (July, 1974). Vols. 1,2, and 3.

33. P. N. Haubenreich, M. Roberts, eds., "ORMAK F/BX, A Tokamak Fusion Test Reactor, "ORNL-TM-4634, Oak Ridge National Laboratory (June 1974).

34. B. Badger et al., "A Wisconsin Tokamak Reactor Design, UWMAK-I," UWFDM-68, Nucl. Eng. Dept., Univ. of Wis. (Nov. 1973).

II-A-3. Impurities in Tokamak Reactors

Considerable concern has been recently expressed about the erosion of metallic vacuum walls by charged particles leaking from tokamak plasmas[1] and the effect of these impurities on plasma operation.[2] High Z impurities have the most significant effect on plasma performance since they will not be fully stripped of all electrons. This is true of materials such as Mo, Nb, and W and the resulting line and recombination radiation can be orders of magnitude larger than the bremsstrahlung.[3] Even for Fe, which will probably be fully stripped at plasma temperatures above 10keV, recombination radiation is still larger than bremsstrahlung. The result is that the plasma $n\tau$ required to obtain ignition is substantially increased.[4,5] For tokamaks, this means that the plasma current required to achieve ignition will be considerably higher than required for a pure D-T plasma.[5]

The basic problem of impurities in most reactor grade plasmas comes from the fact that escaping ions (deuterion, tritium, and helium) as well as 14.1 MeV neutrons will bombard the first wall facing the plasma. Some of the first wall atoms will be sputtered from the surface and ejected back into the plasma chamber causing wall erosion and plasma contamination.

One major effect of such impurities is to increase radiative energy losses from the plasma. High Z impurities cause increased energy losses via line, recombination, and bremsstrahlung radiation. In a steady state plasma, such losses are approximately given, for a single impurity, by[6]

$$P_{RAD} = P_x \left(1 + \frac{.0397\ \xi Z_{im}^4}{Z_{eff} T_e} + \frac{8.6 \times 10^{-4} \xi Z_{im}^6}{Z_{eff} T_e^2} \right) \qquad (1)$$

where $P_x = 4.8 \times 10^{-31}\ n_e^2\ Z_{eff}\ T_e^{1/2} \quad (w/cm^3)$

and $Z_{eff} = \frac{1}{n_e} (n_i + Z_{im}^2\ n_{im})$.

P_x is the power radiated via bremsstrahlung, the second term in brackets is the ratio of line radiation to bremsstrahlung, and the third term is the ratio of recombination radiation to bremsstrahlung. ξ is the ratio of impurity density (n_{im}) to the electron density (n_e), Z_{im} is the atomic number of impurity, T_e is the electron temperature in keV, and n_i is the hydrogenic (D and T) ion density. When three electrons or more remain, the radiative losses become insensitive to Z and T_e and can be characterized by the formula due to Hinnov[7] namely

$$P_{RAD} \simeq 1.2 \xi n_e^2 \times 10^{-26}\ w/cm^3. \qquad (2)$$

An indication of the improvement in plasma energy balance resulting from low Z versus high Z impurities can be obtained by a simple comparison of radiative losses due to C and Mo impurities. At 10 keV and $n_e = 10^{14} cm^{-3}$, P_{RAD} with 1% Mo (Z=42) is about 2 w/cm^3 and with 1% C (Z=6) is 0.02 w/cm^3. The ratio is 100.

Such high Z radiative losses lead to the need for higher $n\tau$ values. Meade[4] has recently discussed this and noted that a few tenths of a percent of high Z impurities significantly increases the $n\tau$ required to satisfy the Lawson criteria and ignition condition. Such concentrations (~0.5%) have already been observed in the ST tokamak experiments.[7]

We have recently studied[5] the anticipated impact of impurities on large tokamaks using a plasma energy balance that includes alpha heating, radiative losses, and thermal losses due to conduction and convection. This will be discussed in more detail in section II-B-3. To provide a scaling law for the confinement time in large devices, the pessimistic assumption is made that the trapped ion instability[8] controls the diffusion losses in the reactor regime. This was discussed in section II-A-2. From such a model, one can estimate the minimum plasma current required to achieve ignition in a tokamak containing a given percentage of impurity. This is shown in Figure 1 for carbon, molybdenum and iron impurities. Clearly, high Z impurities like Mo or Fe have a more significant effect on the required plasma current and thus on the required machine size. (The associated $n\tau$ values correspond well to those found by Meade[4]). From these results, it would appear that carbon impurity levels of several percent can be tolerated.

Impurities also affect the fuel atom density which can be maintained in a reactor plasma. In a β-limited system, an increase in impurity ions causes a decrease in the density of hydrogenic ions since

$$n_e = n_i + Z_{im} n_{im}$$

For example, 1% Mo impurities means that $n_i/n_e = 0.58$ while 1% carbon means that $n_i/n_e = 0.94$. Since the fusion power is proportional to n_i^2, a reduction in n_i has a large effect on the total power output. The alpha heating rate of the plasma is also dependent on n_i and will decrease if impurities enter the plasma. This effect, together with increased radiative losses, can cause a self sustaining plasma to become unignited as the impurity density is increased.

To estimate the level of impurities in tokamak reactors, assume the reactor has fuel, helium (both thermalized and unthermalized), and impurity ion confinement times of τ_{DT}, τ_{He}, and τ_{im} respectively. Let the various sputtering coefficients of the first solid wall (either carbon or metal) facing the plasma be S_{DT}, S_{He}, S_{im}, and S_n. The latter coeffieicnt is for neutron sputtering. Assume the tokamak has a divertor and let η be the fraction of ions diffusing from the plasma which strike the first wall. Let δ be the fraction of the particles sputtered from the first wall which reach the plasma. A simple mass balance across the interface between the plasma and scrape off layer yields the following expression for the equilibrium concentration of impurities in the plasma:

$$n_{im} = \frac{\eta\delta \left(\frac{n_{DT}}{\tau_{DT}} S_{DT} + \frac{n_{He}}{\tau_{He}} S_{He} \right) \tau_{im}}{(1 - \eta\delta\ S_{im})}$$

$$+ \frac{\delta A_w}{V_p} \frac{S_n\ \phi_n\ \tau_{im}}{(1 - \eta\delta S_{im})} \quad . \qquad (3)$$

ϕ_n is the neutron flux at the wall, V_p is the plasma volume, and A_w is the first wall area. It should be noted that for $\eta\delta S_{im}>1$ there is no equilibrium values of impurities, A similar formula has been derived by Düchs et al.(9) who also discuss its limitations.

Expected impurity concentrations were calculated from the formula for n_{im} using these sputtering coefficients in Table II-A-2, and particle fluxes from UWMAK-II as derived in section II-B-3. The results are summarized in Table II-A-3 for three cases corresponding to no divertor, a moderately good divertor (η=.1, δ=.9), and an excellent one-way divertor (η=0, δ=.9). We have expressed the impurity confinement time as a multiple of the D-T confinement time by

$$\tau_{im} = M\ \tau_{DT}$$

and presented the results as multiples of M.

These results suggest that it may be possible to operate a tokamak without a divertor if M is about 1. This may be the case if turbulent diffusion tends to carry all species from the plasma at the same rate. If the high sputtering values prevail, a divertor is essential. With a moderately good divertor (η=.1, δ=.9), M values of about 5 may be tolerable even with the high sputtering data. With the low or most likely data sets, one could tolerate M multiples of 50 to 100. Finally, if the divertor is very efficient at collecting particles diffusing from the plasma ($\eta\sim0$) but does not shield effectively ($\delta\sim0.9$), M values of the order 10^2 to 10^3 could be tolerated with the low and most likely data sets. If a divertor were also effective at shielding ($\delta<.1$), then M multiples greater than 10^2 could be tolerated even with the highest sputtering values that may occur.

We would conclude from these simple calculations that it may be feasible to operate with a carbon curtain and no divertor if M~1 and that a moderately good divertor can most likely allow operation at acceptable levels of carbon impurity even if the impurity containment time is 10 to 10^3 times the ion confinement time.

TABLE II-A-2

Assumed Sputtering Coefficients for Carbon

	Energy	High	Low	Most Likely
S_D [a]	20 keV	.015	.001	.01
S_T (extrapolated)	20 keV	.0225	.0015	.015
S_{He} (extrapolated)	20 keV	.2	.12	.15
S_{c-c} [b]	20 keV	.8	.4	.6
S_n [c]	0.1-14 meV	.2	.0001	.0015

(a) Based on results in Reference (10)
(b) Based on results in Reference (11)
(c) Pessimistic values from Kaminsky (12) and low values for atomistic sputtering.

TABLE II-A-3

Equilibrium Carbon Concentrations for
Various Carbon Ion Confinement Times, Divertor
Efficiencies and Sputtering Coefficients

	High Sputtering Data	Most Likely Sputtering Data	Low Sputtering Data
No Divertor	M x 9.3%*	M x 3.6%	M x 1.1%
$\eta = 0.1$ $\delta = 0.9$	M x 1%	M x 0.16%	M x 0.06%
$\eta = 0$ $\delta = 0.9$	M x 0.8%	M x 0.02%	M x 0.001%

* Percent of Electron Density and $\tau_{im} = M\,\tau_{D\,T}$

References for Section II-A-3

1. Proceedings on a Conference on "First Wall Surface Problems for D-T Tokamak Reactors," published as a special issue of J. Nucl. Mat., (1974). See also, V. A. Vershkov and S. V. Mirnov, Nuclear Fusion 14, 383 (1974).

2. S. O. Dean et al., Status and Objectives of Tokamak Systems for Fusion Research, WASH-1295-(1974).

3. R. F. Post, J. Nucl. Energy, Part C - Plasma Physics, 3, (1961) 273.

4. D. Meade , Nucl. Fus. 14, (1974) 289.

5. R. W. Conn, W. A. Houlberg, J. Kesner, "Parametric Studies of Driven Tokamaks," UWFDM-106, University of Wisconsin, June 1974.

6. G. Hopkins, "Impurity Radiation Loss Mechanism from Fusion Reactor Plasma," GGA-12374, Gulf Gen. At. Co., October 1972.

7. E. Hinnov, S. L. Dimock, L. C. Johnson and E. B. Meservey, Third Int'l Conf. on Tor. Plasma Confinement, Munich (1973).

8. B. B. Kadomtsev and O. P. Pogutse, Nucl. Fus. 11, (1971) 67.

9. D. Duchs, G. Haas, D. Pfirsch, and H. Vernickel, "On the Impurity Problem in Quasi Steady State Toroidal Plasma Experiments and Fusion Reactors," J. Nucl. Mat. (to be published).

10. R. Behrisch, (personal communication).

11. O. Almen and G. Bruce, Nucl, Inst. and Methods 11, (1961) 279.

12. M. Kaminsky and S. K. Das, "Particle Release from Niobium Under 14-MeV Neutron Impact" p. 37 in Fifth Symposium on Engineering Problems of Fusion Research, Princeton University, Nov. 1973, IEEE Pub. No. 73CH0843-3-NPS.

II-A-4. The Carbon Curtain Concept

It is clear that low Z impurities (e.g. C, O, Si, etc) have a much less serious impact on plasma performance and larger concentrations of such elements can be tolerated. The object of this section is to describe a method by which the benefits of low Z fusion reactor first walls can be achieved while continuing to take advantage of the high strength and ductility of a metallic vacuum wall. This metallic vacuum wall will also be protected from charged particle and neutral atom sputtering thus lowering first wall erosion rates.

The proposed solution is to place a flexible, 2-dimensionally woven carbon cloth between the plasma and the metallic vacuum wall.[1] This cloth will act as a curtain and intercept practically all ions and neutral atoms leaking from the plasma. It will similarly collect all metallic ions emanating from the vacuum wall and prevent their introduction into the plasma.

The carbon cloth suggested for protecting the plasma consists of continuous carbon filaments, normally 5-10 microns in diameter, collected into bundles of 700-1000. A scanning electron micrograph is shown in Figure II-A-9. These bundles may be twisted together to form threads and the threads twisted together to form yarns of any diameter. The yarns are then woven, by conventional techniques, into cloth which is flexible and porous. Such cloth typically has a surface area of $1 m^2$ per gram of material.

It is proposed that such a cloth be hung between the plasma and first wall to collect the ions and neutral atoms leaking from the plasma. The curtain will also collect any metallic atoms emanating from the vacuum walls. The curtain will be cooled by radiation only and has no structural role in a reactor.

The first question that occurs when contemplating the use of a carbon curtain is its compatibility with the vacuum requirements for fusion reactors. This problem can be considered from two positions; first, what is the vapor pressure of the graphite at operating temperature and second, how much dissolved and adsorbed gas will be evolved at the operating temperature of the curtain.

The vapor pressure of carbon has been measured and reported in reference 2. If we assume that fusion reactor plasmas require vacuums of 10^{-5} torr or better, then we find that we are limited to operating temperatures of ~2000°C or less. The equilibrium temperature of the carbon curtain in a plasma chamber can be calculated given the heat flux and appropriate sink temperatures and emissivities. Assuming a 10 watt/cm^2 heat load, an effective emissivity coefficient of $\tilde{=}0.5$, and a first wall temperature of 600°C, we find that the curtain will heat up to 960°C. The vapor pressure of carbon at this temperature is less than 10^{-19} torr.[2]

Graphite is commonly thought to adsorb gases readily because of experience with carbon and charcoal at high pressures and low temperatures. However,

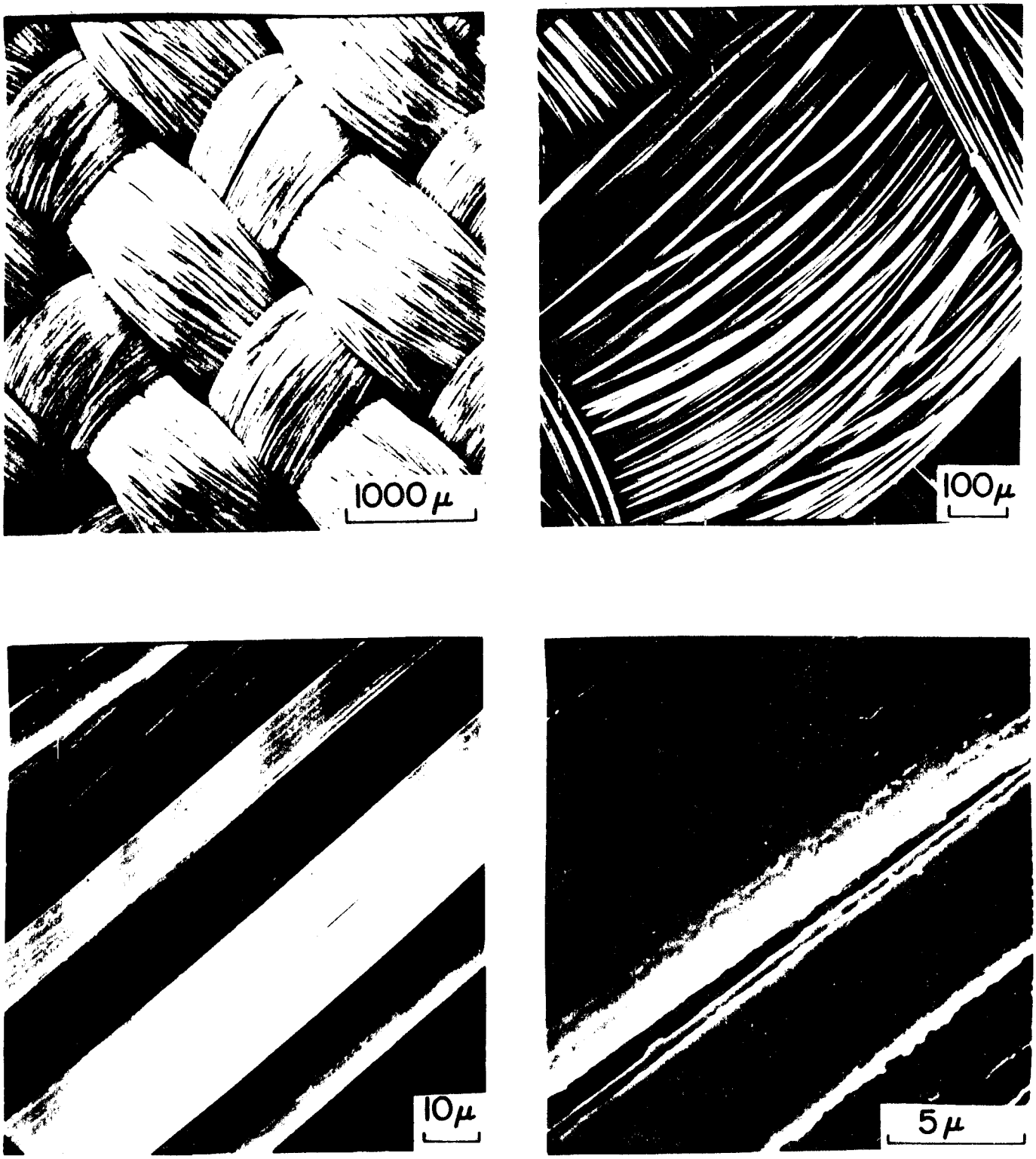

Figure II-A-9. Photographs of Graphite Fabric at a Number of Magnifications

most gases adsorb on graphite.[3] The rapid advance in graphite technology has led to new forms of graphite and carbon-carbon composites which have demonstrated extremely good properties in high vacuums. Beitel[3] has shown that at low pressures, graphite is not as efficient a gas adsorber as was commonly thought. For example, the sticking probability for molecular hydrogen on graphite is $<3 \times 10^{-6}$. The sticking probability of atomic hydrogen (the most likely form of hydrogen isotope in a fusion reactor) has been reported as 0.015[4] and 0.038[5] at room temperature and $p<10^{-5}$torr. Hart et al.[6] found that the maximum oxygen coverage on graphite at 300°K and 10^{-9} torr to be 0.02 monolayers. The sticking probability of CO on graphite is 5×10^{-5} and decreases rapidly as surface coverage approaches 0.01 monolayer.[7] If we assume that in an extreme case, 0.3 of a monolayer of gas were to adsorb on graphite, then a curtain necessary to cover some 3000 m^2 of fusion reactor first wall would contain ~500,000 torr-liters of gas. However, most fusion reactors will have vacuum pumping systems capable of several thousand torr-liters per second so that even this pessimistic assumption about gas adsorption will not present too great a problem to large reactor systems. In other words, this amount of gas could be pumped from the reactor and the pressure returned to $\sim 10^{-5}$ torr in less than one hour. Such a large pumping load would only be encountered after the chamber has been opened to air. (Presumably less than once a year.)

Beitel[7] has also studied the amount of gas evolution in graphite after baking at 300°C for 24 hours. He finds that the evolution varies from 5.7×10^{-3} torr-liters/gram for pyrolytic carbon to 6.3×10^{-2} torr-liters/gram for fine grain, extruded graphite. Again if we assume that worst case, we find that a maximum of 350,000 torr-liters would be evolved in a typical UWMAK-II type carbon curtain.

It is expected that prior baking at higher temperatures or in situ heating before plasma operation can significantly reduce the level of gas evolution compared to the cases considered above. The remaining gas can easily be handled by typical reactor vacuum systems.

Another area for concern is the effect of neutron bombardment on carbon cloth at ~1000°C. Using a typical neutron spectra from UWMAK-II, we find that ~2500 atomic parts per million of helium is produced per year per MW/m^2 neutron wall loading. It is also calculated that the displacement damage amounts to 4.4 dpa/yr/MW/m^2. This is roughly equivalent to the damage produced per year by $7.5 \times 10^{21} n/cm^2$ in a fission spectrum. Analysis of isotropic, near isotropic and anisotropic graphite irradiated from $1\text{-}2 \times 10^{22} n/cm^2$ (fission) shows that there may be some shrinkage (a few percent) or even a few percent expansion per year of exposure to 1 MW/m^2 neutron wall loading.[8] However, one cannot extend this information linearly with time as it is possible that "run away" swelling may occur in less than 5 years of 1 MW/m^2 wall loadings.*

---

* Direct comparison of current irradiation data on graphite to cloth material is difficult because radiation damage in carbon is so dependent on structure.[8]

The induced radioactivity due to C^{14}, and resulting afterheat of such a curtain is also found to be negligible. For example, the radioactivity after one year of exposure amounts to 2×10^4 dps/g and the afterheat resultant from this decay is only 1.5×10^{-10} watts/g.

Some of the carbon will be removed by sputtering due to charged particle and neutron bombardment. Using numbers given in Table I, we calculated that the erosion rate will be approximately 11 microns/year of operation in a reactor like UWMAK-II. Some of this carbon will be transported into the plasma and eventually to vacuum pumps or divertor collector systems, while some of the carbon will deposit on colder sections of the plasma chamber. Since the carbon curtains would probably be greater than 2000 microns thick, there is no particular problem envisioned with respect to curtain thinning.

The compatibility of carbon and a hydrogenic environment also appears to be reasonable.[9] [10] It is known that at pressures of $<10^{-2}$ torr there is essentially no "methane" formation with molecular hydrogen above 400°C. Since the curtain will operate at ~1000°C and drop to the reactor ambient temperature (>500°C) during plasma recycling, there is little problem anticipated here.

From these considerations, it appears that the placement of a carbon curtain between the plasma and first wall of typical fusion reactors can have the following advantages:

- It will intercept all plasma ions and neutrals from plasma, thus preventing blistering and charged particle sputtering of the metal walls.
- It will prevent all neutron sputtered atoms from re-entering the plasma.
- The curtain will effectively exchange low Z impurities for high Z impurities, thus reducing the power radiated from the plasma and the current required in tokamaks for ignition.
- There will be a reduction in hot spots due to inhomogeneous particle fluxes (both in normal operation and in a failure mode).
- The use of a carbon curtain may allow removal of divertor on tokamaks.

This concept could also be useful in near term plasma experiments where impurity levels will be critical.

Potential problems with using carbon in high neutron fluxes include large radiation induced growth and helium generation. Both of these problems could eventually require replacement of the curtain after a few years of operation. However, such a procedure is easily performed at relatively little cost. A more thorough discussion of use of a carbon curtain to protect the first wall, as well as further considerations related to materials properties, outgassing, and radiation damage are discussed in section IV.

References for Section II-A-4

1. G. L. Kulcinski, R. W. Conn, G. Lang, "Reduction of Plasma Contamination Effects and First Wall Erosion in Fusion Devices," accepted for publication in Nuclear Fusion.

2. Union Carbide, Industrial Graphite Engineering Handbook, (1970).

3. G. A. Beitel, J. Vac, Sci. and Technol., 8, (1971) 647.

4. R. K. Gould, Ph.D. Thesis, University of Wisconsin, Madison, Wisconsin, 1969.

5. G. A. Beitel, J. Vac. Sci. Technol. 6, (1969) 224.

6. P. J. Hart, F. J. Vastola, P. L. Walker, Jr., Carbon 5, (1967) 363.

7. G. A. Beitel, Tech. Rep. NASA CR-111829 (1971).

8. G. B. Engle, W. P. Eatherly, High Temperatures and High Pressures, 4, (1972) 119. Also W. J. Gray, E. M. Woodruff, to be published.

9. Nuclear Graphite, R. E. Nightingale, ed., Academic Press, New York, 1962.

II-A-5. Impurity Diffusion in Tokamaks; Impact on Divertor Considerations

It has been known from as early as 1956[1] that, according to classical diffusion in a multi-component plasma, high Z ions diffuse "up" the density gradient of lower Z ions as well as "down" their own density gradient. The particle flux of species i due to Coulomb collisions with species j in a uniform magnetic field B can be written an

$$\vec{\Gamma}_{ij} = b_{ij}\,[Z_i n_i \vec{\nabla} n_j - Z_j\, n_j \vec{\nabla} n_i], \tag{1}$$

where $$b_{ij} = \frac{4}{3}\left[\frac{2\pi m_i m_j}{m_i+m_j}\right]^{1/2} \frac{1}{T^{1/2}} \frac{e^2}{(4\pi\varepsilon_o)^2} \frac{\ell n\Lambda}{B^2} Z_j$$

We have assumed for simplicity that $T_i = T_j$. This is reasonable in a reactor since rethermalization is rapid compared with other processes.

Because of the atomic mass number terms in b_{ij}, impurity ions ($Z_i>1$) diffuse primarily by colliding with hydrogenic ions ($Z_j=1$); the first term in (1) causes an inward flow which steepens the impurity density profile $n_i(\vec{x})$. An equilibrium with $\vec{\Gamma}_{ij} = 0$ is reached when

$$Z_i n_i \vec{\nabla} n_j = Z_j n_j \vec{\nabla} n_i$$

or, equivalently,

$$n_i(\vec{x}) = (\text{constant})[n_j(\vec{x})]^{Z_i/Z_j} \tag{2}$$

For large Z_i/Z_j, this is a strongly peaked profile. The inclusion of impurity-electron collisions modifies eq.(2) only by changing the coefficient of $n_j(\vec{x})$ to $(Z_i/Z_j)-\varepsilon$, where $1>>\varepsilon>0$ for reasonable impurity levels. Neoclassical diffusion[2,3] leads to basically the same result. The primary neoclassical effect is to increase b_{ij} because of finite "banana" width effects. A temperature gradient will have a significant effect only if it is strong compared with the density gradient. Unequal temperatures changes the coefficient in (2) to $(Z_i/Z_j) + (T_i - T_j)/T_j$, which, for cooler impurities, has a slight flattening effect on the profile.[4] Experimental indications of this peaking of the impurity profile has been inferred from some measurements on Soviet experiments,[5] but this conclusion has been disputed elsewhere.

The above considerations give a qualitative indication of the behavior when a pulse is introduced into the plasma. To predict the actual impurity level we consider the time-dependent diffusion equation for the impurities. For simplicity we consider a one-dimensional slab. The plasma is low-β so that the magnetic field in uniform. Let the subscript I denote the impurities of charge Z_e and i denote the normal ions (Z=1).

$$\frac{\partial n_I}{\partial t} + b_{Ii} \frac{\partial}{\partial x} \left[Z\, n_I \frac{\partial n_i}{\partial x} - n_i \frac{\partial n_I}{\partial x} \right] = S_I(x,t),$$

where S_I is the impurity source function. We can rewrite this equation as

$$\frac{\partial n_I}{\partial t} - b_{Ii}\, n_i^{Z} \left[\frac{\partial}{\partial x} \left(\frac{1}{n_i^{Z-1}} \frac{\partial n_I}{\partial x} \right) - \frac{Z}{n_i^{Z}} \frac{\partial^2 n_i}{\partial x^2}\, n_I \right] = S_I(x,t) \qquad (3)$$

Taking n_i to be time-dependent, we can solve eq.(3) by an expansion in eigenfunctions ψ_α of the operator L;

$$L\psi_\alpha \equiv \frac{d}{dx} \left[\frac{1}{n_i^{Z-1}} \frac{d\psi_\alpha}{dx} \right] - \frac{Z}{n_i^{Z}} \frac{d^2 n_i}{dx^2} \psi_\alpha = - \frac{\lambda_\alpha}{n_i^{Z}} \psi_\alpha \qquad (4)$$

We have defined λ_α to be the corresponding eignvalue and n_i^{-Z} to be the weight function. We let

$$n_I = \sum_\alpha a_\alpha(t)\, \psi_\alpha(x)$$

$$S_I = \sum_\alpha b_\alpha(t)\, \psi_\alpha(x)$$

$$b_\alpha = \frac{\int S_I\, \psi_\alpha / n_i^{Z}\, dx}{\int \psi_\alpha^{2} / n_i^{Z}\, dx}$$

and get $$\frac{da_\alpha}{dt} + b_{Ii}\, \lambda_\alpha\, a_\alpha = b_\alpha(t)$$

The solution for a_α is

$$a_\alpha = a_\alpha(o)\, e^{-\lambda_\alpha b_{Ii} t} + \int_o^t b_\alpha(t') e^{b_{Ii} \lambda_\alpha (t'-t)}\, dt'$$

For a steady-state source turned on at t = 0,

$$a_\alpha = \frac{b_\alpha}{b_{Ii}\, \lambda_\alpha} \left[1 - e^{-b_{Ii} \lambda_\alpha t} \right] \qquad \text{if } \lambda_\alpha \neq 0 \qquad (5)$$

$$a_\alpha = b_\alpha t\,, \quad \text{if } \lambda_\alpha = 0 \qquad (6)$$

Negative values of λ_α are forbidden because they would violate causality. We see that if L has a zero eigenvalue a continual buildup of impurities is predicted. Now L does have a zero eignvalue (denote it by $\alpha = 0$) for which the eigenfunction is $\psi_o = n_i^Z$ if this satisfies the boundary conditions at the edges of the slab. Of course, effects neglected in this analysis (e.g. impurity - electron collisions and exclusion of ions because of pressure limitations) cause the impurity density to saturate, but only at intolerably high levels. Now the asymptotic solution ($t \to \infty$) is given by the $\alpha = 0$ term.

$$n_I \to b_o t\, \psi_o(x)$$

But $\psi_o = n_i^Z$, so that

$$b_o = \frac{\int S(x,t)\, dx}{\int n_i^Z\, dx}$$

and

$$n_I \to t \frac{n_i^Z(x)}{\int n_i^Z dx} \int S(x,t)dx \qquad (7)$$

This solution has the interesting property that

$$\int n_I\, dx = t \int S(x,t)dx \qquad (8)$$

which means that if ΔN impurity ions are introduced in time Δt, the total impurity level rises by ΔN ions; none of them escape from the plasma.

In order to have a reasonably pure quasi-steady-state reactor it is necessary to shift the lowest eigenvalue, λ_o, off zero or to make S_I small enough so that n_I is not too large at the end of the burn. One can shift λ_o by changing the operator L (e.g. add turbulent diffusion) or by changing the boundary conditions (addition of a divertor). S_I can be made small by using low sputtering coefficient walls and/or using a divertor. The tolerable level of n_I can be increased by having only low Z ions as possible impurities; the carbon liner falls into this category.

The Soviet tokamak experiments[5] report a substantial drop in the impurity level and a flattening of the profile during MHD oscillations of the plasma column. Studies of the evolution of Ba^{++} impurities in the FM-1 spherator indicate that the barium also exhibits turbulent diffusion as well as classical diffusion.[6] These results suggest that it is not inappropriate to add a turbulent diffusion term to (1). The simplest approach is to add a Fick's law term, $- D_T \vec{\nabla} n_i$, where D_T is a turbulent diffusion

coefficient. The functional dependence of D_T will depend on the unstable modes responsible for the turbulence. For simplicity we take D_T to be a constant. Then

$$\Gamma_I = b_{Ii} \left[Z\, n_I \frac{\partial n_i}{\partial x} - n_i \frac{\partial n_I}{\partial x} \right] - D_T \frac{\partial n_I}{\partial x} \tag{9}$$

in our slab model. We rewrite this as

$$\Gamma_I = - (b_{Ii}\, n_i + D_T) \frac{\partial n_I}{\partial x} + Z\, n_I\, b_{Ii} \frac{\partial n_i}{\partial x}$$

Let

$$f(x) = b_{Ii}\, n_i(x) + D_T. \tag{10}$$

Then

$$\Gamma_I = - f(x) \frac{\partial n_I}{\partial x} + Z \frac{\partial f}{\partial x} n_I = - f(x)^{Z+1} \frac{\partial}{\partial x} \left[\frac{n_I}{f^Z(x)} \right] \tag{11}$$

We look for steady-state solutions to the impurity diffusion equation with a steady-state source.

$$\frac{\partial \Gamma_I}{\partial x} = S_I(x)$$

We impose boundary conditions $n_I(a) = n_i(a) = 0$ and symmetry $n_I(-x) = n_I(x)$, $n_i(-x) = n_i(x)$, where a is the half-width of the slab. By symmetry $\Gamma_I(o) = 0$ so that

$$\Gamma_I(x) = \int_o^x S_I(x')\, dx'$$

We substitute from (11) for Γ_I and integrate once more to get

$$n_I(x) = f(x)^Z \int_x^a \frac{dx'}{[f(x')]^{Z+1}} \int_o^{x'} S_I(x'')\, dx'' \tag{12}$$

We have used $n_I(a) = 0$ and $f(a) \neq 0$ to get this result. Since there are no undetermined constants in (12), the addition of a turbulent diffusion term leads to a steady-state solution for n_I which is linearly dependent on the source term. To estimate $n_I(o)$ we make the reasonable assumption that the impurity atoms are ionized within a distance λ from each edge and $\lambda \ll a$. Then $f(x) \approx f(a)$ for $(a-\lambda) < x < a$ and

$$n_I(o) \cong \frac{f(o)^Z}{f(a)^{Z+1}} \int_o^a dx' \int_o^{x'} S_I(x'')\, dx''$$

We can obtain $S_I(x)$ by calculating the ionization rate of a beam, I_n, of neutral atoms incident on the plasma surface.

$$\frac{dI_n}{dx} = - n_i \sigma n \ , \qquad \sigma = \frac{\langle \sigma_i v_i + \sigma_e v_e \rangle}{v_n}$$

but

$$n_i \cong n_i'(a)\,(a-x) \text{ for } x \to a, \text{ so that}$$

$$I_n = I_n^o \, e^{-\mu(a-x)^2}$$

$$\mu = \frac{n_i' \sigma}{2}$$

Now $S(x) = - \frac{dI}{dx} = 2\mu(a-x) I_n^o e^{-\mu(a-x)^2}$

Thus we get

$$n_I(o) = \frac{f(o)^Z}{f(a)^{Z+1}} \frac{I_n^o}{2} \sqrt{\frac{\pi}{\mu}} \ , \qquad (13)$$

where I_n^o is the flux of neutral atoms incident on each plasma face. We now evaluate $f(x)$ in two limits, one in which turbulent diffusion dominates over the entire plasma and the other in which turbulent diffusion is important only near the edge. In the first case

$$f(a) \cong f(o) \cong D_T \ ,$$

$$n_I(o) \cong \frac{1}{D_T} \frac{I_n^o}{2} \sqrt{\frac{\pi}{\mu}} \ , \qquad (14)$$

and from (12)

$$n_I(x) = n_i(o) \text{ for } 0 \leq x \leq a-\lambda \ ;$$

i.e. the profile is flat over most of the plasma. In the second limit (weak turbulent diffusion)

$$f(o) \cong b_{Ii} \, n_i(o),$$

$$f(a) = D_T \ ,$$

$$n_I(o) \cong \left[\frac{b_{Ii} \, n_i(o)}{D_T} \right]^Z \frac{1}{D_T} \frac{I_n^o}{2} \sqrt{\frac{\pi}{\mu}} \ , \qquad (15)$$

and the profile is basically like $n_i^Z(x)$. The impurity level in (15) is much higher than in (14).

The effect of a divertor is to introduce an absorption term for ions in the scrape-off zone. This can be treated as a boundary condition on the magnetically confined plasma or as a two-zone diffusion problem. We use the latter approach. The half-width of the slab is again a, but the region $a' < x \leq a$ is a scrape-off zone with an absorption term, $-\beta_I n_I(x)$, which models the effect of particles flowing along the field lines to the divertor collectors. The boundary conditions are still

$$\left.\frac{n_I}{dx}\right|_{x=0} = 0 \text{ and } n_I(a) = 0.$$

We define

$$\beta_I(x) = \begin{cases} 0 & 0 \leq x \leq a' \\ \beta_I & a' < x \leq a \end{cases}$$

The diffusion equation for the impurities is

$$\frac{\partial n_I}{\partial t} - b_{Ii}\, n_i^Z \left[L\, n_I - \frac{\beta_I(x) n_I}{b_{Ii} n_i^Z} \right] = S_I(x,t)$$

where L is defined in eq. (4). The eigenvalues (defined with weight function n_i^{-Z}) of the operator $L - \beta\, b_{Ii}^{-1}\, n_i^{-Z}$ can be written as a Rayleigh quotient:

$$\lambda = \frac{\int_o^a \left[\frac{1}{n_i^{Z-1}} \left(\frac{\partial \psi}{\partial x}\right)^2 + \frac{Z}{n_i^Z} n_i'' \psi^2 + \frac{\beta_I(x)\, \psi^2}{b_{Ii}\, n_i^Z} \right] dx}{\int_o^a \frac{\psi^2}{n_i^Z}\, dx}$$

To estimate the lowest eigenvalue, λ_o, we use the eigenfunction $\psi = n_i^Z$ of the operator L as a trial function. The first two terms in the numerator cancel to yield the result

$$\lambda_o \cong \frac{\beta_I}{b_{Ii}} \frac{\int_{a'}^a n_i^Z\, dx}{\int_o^a n_i^Z\, dx} \qquad (16)$$

The steady-state impurity concentration is $\propto (b_{Ii}\lambda_o)^{-1}$ and consequently decreases with increasing plasma density in the scrape-off zone. The reason for this is clear. The impurity ions want to establish an n_i^Z profile; the

more that this extends into the scrape-off zone, the higher the probability of an impurity ion being absorbed by the divertor collectors. This depletes the population in the scrape-off zone. The impurities in the main confinement region diffuse out into the scrape-off zone in an attempt to maintain the n_i^2 profile there. In steady-state this outward diffusion balances the impurity source. Increasing Z means smaller λ_o (or larger $n_I(o)$) because the impurities concentrate more in the center and only a small tail of the impurity profile protrudes into the scrape-off zone.

To be more precise about the expected impurity level we need a model for the scrape-off zone which enables us to calculate $n_i(x)$, β_I, and S_I. We assume the ion transport is dominated by turbulent processes with some average diffusion coefficient D. In the scrape-off zone the ions flow along the field lines with their thermal velocity v_{Ti} to the particle collectors. This gives an absorption coefficient $\beta_I \sim v_{Ti}/L$ for the ions, where L is the length along the field lines to the collectors. The ion density in the scrape-off zone satisfies the equation

$$D \frac{d^2 n_i}{dx^2} = \beta_i n_i \quad , \tag{17}$$

while, in the main plasma region, it satisfies

$$D \frac{d^2 n_i}{dx^2} = S$$

where S is a source (which is taken to be constant) due to refueling. The boundary conditions imposed are $n'(o) = 0$, $n(\infty) = 0$ (the wall is effectively at infinity) and continuity of the density and the particle flux at the separatrix ($x = a'$). The solution is

$$n_i = n_s e^{-\alpha(x-a')} \qquad x>a'$$

$$n_i = n_o \left(1 - \left(\frac{\alpha n_s}{n_o}\right) \frac{x^2}{2a'}\right) \quad , \qquad x<a'$$

with $\alpha = \sqrt{\beta_i/D}$, and

$$\frac{n_s}{n_o} = \frac{2\, n_o}{\alpha\, a' + 2} \quad . \tag{18}$$

It is interesting to relate these results to the divertor effectiveness. Define

$$\varepsilon = \frac{\Gamma(a)}{\Gamma(a')} \quad ,$$

where Γ is the particle flux, and let a-a' = d, the thickness of the scrape - off zone. Then

$$\varepsilon = e^{-\alpha d}$$

or

$$\alpha d = \ln \frac{1}{\varepsilon} \tag{19}$$

Thus

$$\alpha a' = \left(\frac{a'}{d}\right) \ln \frac{1}{\varepsilon} >> 1 \qquad \text{and}$$

$$\frac{n_s}{n_o} \cong \left(\frac{d}{a'}\right) \frac{2}{\ln\left(\frac{1}{\varepsilon}\right)} \tag{20}$$

For the geometric parameters of UWMAK-II this gives $n_s/n_o \sim .05$ if we assume ε=.01.

To calculate the value of λ_o in (16), we approximate n(x) by a Gaussian profile, $n(x) \sim n_o e^{-2\left(\frac{x}{a'}\right)^2}$ for x<a', to get

$$\lambda_o \cong \frac{\beta_I}{b_{Ii}} \left(\frac{n_s}{n_o}\right)^Z \frac{2}{\alpha a'} \frac{1}{\sqrt{Z}}$$

ignoring factors of order unity. We can rewrite this as

$$\lambda_o \cong \frac{\beta_I}{b_{Ii}} \left(\frac{d}{a'}\right)^{Z+1} \frac{1}{\sqrt{Z}} \left[\frac{2}{\ln\left(\frac{1}{\varepsilon}\right)}\right]^{Z+1} \tag{21}$$

In this expression β_I is the absorption coefficient for the impurity ions; $\beta_I = v_{TI}/L$. The impurity confinement time τ is given by

$$\tau = \frac{1}{b_{Ii}\lambda_o} \quad . \tag{22}$$

If we assumed a machine like UWMAK-II has a 90% efficient divertor and fully stripped carbon impurity, the confinement time is $\sim 10^3 - 10^4$ seconds which is impractically long. Lower Z ions (partially stripped carbon or alpha particles) can have a reasonable confinement time (order of a few seconds) because of the $\left(\frac{d}{a'}\right)^{Z+1}$ term in λ_o. In fact, however, the divertor may be much more efficient at collecting particles diffusing from the plasma (ε < .1) but not effective at shielding the plasma from particles sputtered at the walls, particularly by neutrons. The reasons for this will be discussed in detail where we consider the divertor operation in UWMAK-II and employ the results of this section. This will be done in Section II-B-4.

References for Section II-A-5

1. C. L. Longmire and M. N. Rosenbluth, Phys., Rev. 103, 507 (1956).

2. J. W. Connor, Plasma Physics, 15, 765 (1973).

3. F. L. Hinton and T. B. Moore, University of Texas Fusion Research Center FRCR No. 75 (1974).

4. J. B. Taylor, Phys. Fluids 4, 1142 (1961).

5. V. A. Vershkov and S. V. Mirnov, Nuclear Fusion 14, 383 (1974).

6. J. A. Schmidt, N. R. Sauthoff, and R. J. Hawryluk, Phys. Rev. Lett. 33, 1272 (1974).

II-B-1. Fuel Cycle and Dimensions of UWMAK-II

There are several fusion fuel cycles and any number of possible fusion chain reactions which may ultimately prove to be practical. However, for a near-term reactor, there are three primary fuel cycles which could be used and the question here is the choice among these. As will be clear, for a near-term, low-β reactor such as UWMAK-II, the deuterium-tritium (D-T) cycle is clearly the most feasible. The basic fuel cycles are:

1) Deuterium-Tritium (D-T) cycle:

$$ {}_1^2D + {}_1^3T \rightarrow {}_2^4He\ (3.52\ MeV) + {}_0^1n\ (14.06\ MeV) $$

2) Deuterium-Deuterium (D-D) cycle:

$$ {}_1^2D + {}_1^2D \xrightarrow{50\%} {}_1^3T(1.01\ MeV) + {}_1^1H(3.03\ MeV) $$

$$ {}_1^2D + {}_1^2D \xrightarrow{50\%} {}_2^3He(.82\ MeV) + {}_0^1n(2.45\ MeV) $$

3) Deuterium-Helium - 3(D-^{3}He) cycle:

$$ {}_1^2D + {}_2^3He \rightarrow {}_2^4He(3.67\ MeV) + {}_1^1H(14.67\ MeV), $$

Of course, within each of these cycles, reactions from other cycles take place. For example, the tritium produced in D-D reactions can be burned in situ resulting in D-T neutrons. Other reactions, such as $^6Li(p,{}^3He)^4He$, $^6Li(d,T)^5Li$, $^7Li(p,\gamma)^8Be$, etc., could be the basis for long-term CTR fuel cycles. However, the Coulomb barrier is so large in all these reactions that plasma temperatures in excess of 1 MeV are required before a net power output can be expected. Thus, we limit the discussion here to the D-T, D-D, and D-^{3}He cycles most likely to be used in the near term future.

The choice between these cycles becomes clear for a low-β reactor when one examines the fusion cross sections for the various reactions. The cross section for the $^3_1T(d,n)He^4$ reaction has a larger maximum value peaking at lower energies than any of the other reactions. More important from a reactor standpoint, is the fusion reaction rate, $\langle\sigma v\rangle$, where $\langle\ \rangle$ indicates an average over a Maxwellian distribution of target nuclei. The variation of $\langle\sigma v\rangle$ with plasma ion temperature is shown in Figure II-B-1. The reaction rate for the $^3_1T(d,n)^4He$ reaction has a higher maximum occuring at lower temperatures than the other reaction types. The importance of this is that one can ignite a D-T plasma at lower temperatures (10-15 KeV for T_i). Further, Tokamaks have β-limited plasmas so that the expression for the power in such a system is proportional to $\beta^2B^4\langle\sigma v\rangle/T^2$: For a given magnetic field strength and fixed β, we need only $\langle\sigma v\rangle/T^2$, which is plotted in Figure II-B-2 for the three cycles under discussion. Again, the D-T cycle parameter has a larger maximum value

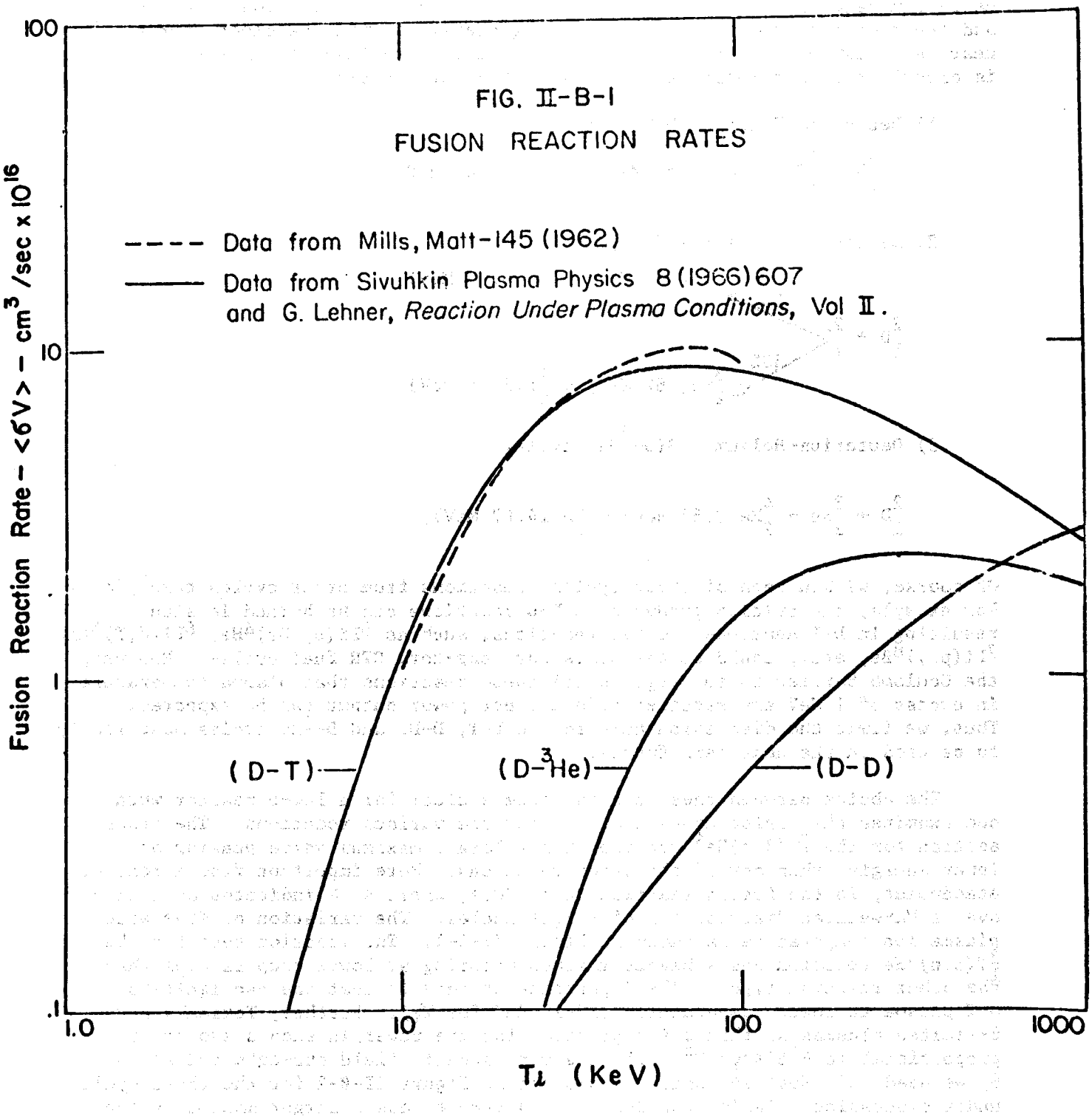

FIG. II-B-1

FUSION REACTION RATES

FIG. II-B-2
FUSION REACTION PARAMETER

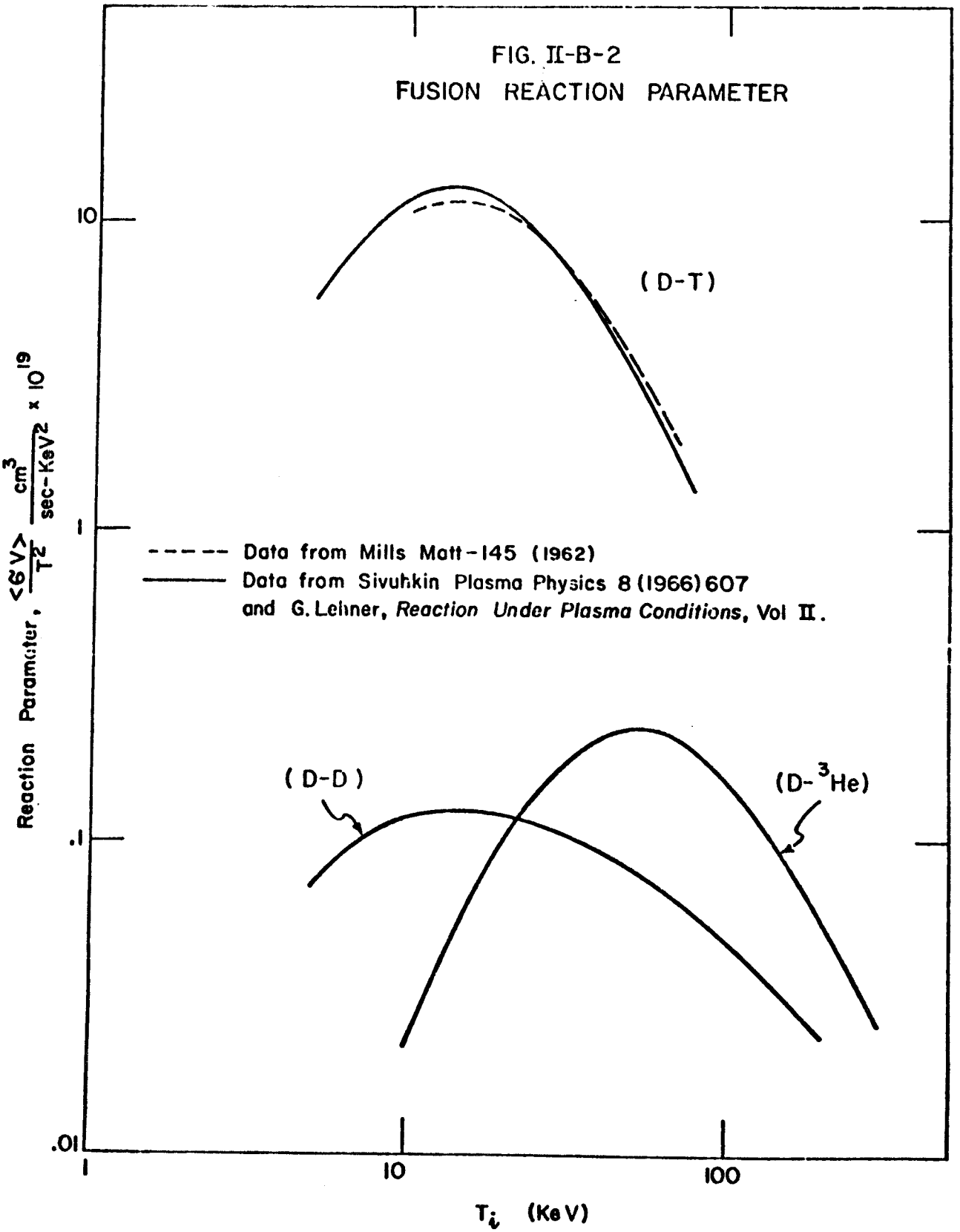

and it occurs in the temperature range 10-15 KeV. Thus, a D-T plasma makes better use, in a β-limited system, of a given magnetic field strength. As noted, this low optimum temperature range (10-15 KeV) translates into lower ignition and operating temperatures. For these reasons, UWMAK-II is assumed to operate on the D-T cycle using a 50-50 mixture of $^{2}_{1}D$ and $^{3}_{1}T$ in the plasma.

The main dimensions of UWMAK-II are the same as in our previous conceptual design.(1) However, it should be pointed out that these dimensions, namely:

MAJOR RADIUS	13m
PLASMA RADIUS	5m
ASPECT RATIO	2.6

have been determined from an optimization study(2) in which the cost per unit power is minimized subject to a constraint that the magnetic field in the throat of the machine arising from the transformer windings should not exceed the maximum allowable field on the superconducting OH windings. The machine costs were assumed to vary with the costs of the toroidal field coils and the minimum in the cost per unit power is found to occur for aspect ratios between 2.2 and 2.6. It is interesting to note that in a more detailed cost estimate of large experimental Tokamaks by Sheffield and Gibson,(3) one also finds that the optimum aspect ratio occurs between 2.3 and 2.6, depending upon assumptions. Thus, it appears that both near term experiments with plasma currents of several MA and tokamak reactors with $I_p \sim 15$ MA will have approximately the same aspect ratio, namely, about 2.5. Such low aspect ratio systems automatically imply relatively low toroidal magnetic fields on axis.

The origin of the basic result is clear(2) and we repeat here for completeness only the essence of the calculation. (Interestingly, the design of the Joint European Torus (JET), as described by Rebut(4), was based on essentially the same considerations.) First, we note that

$$qA = \frac{B_T}{B_\theta} = \frac{aB_T}{2I_p}$$

so that

$$\left(\frac{2qI_p}{a}\right) = \left(\frac{B_T}{A}\right)$$

Thus, we can maintain a particular value of plasma current at a given q by combining large B_T and large A or vice versa. Clearly, one will trade toroidal field by going to low aspect ratio. Secondly, one can see that $A \sim 2$ is optimum by the following simple analysis. The maximum toroidal field is related to the plasma current via

$$B_T^{max}\ (kG) = \frac{2qA^2 I_p\ (MA)}{(R-a-\tau_B)}$$

where τ_B is the distance from the plasma edge to the inside of the toroidal field winding. ($2(a + \tau_B)$ is therefore the magnet bore.) Assume we have superconducting primary windings and the maximum field in the throat is also B_T^{max}. The transformer equation for an inductive load is then

$$\pi d^2\ B_T^{max} = L\ I_p$$

where L is the inductance of the plasma loop and d is the radius of the central throat. L is given by

$$L = 1.257 \times 10^{-6}\ R(m)\ [\ln 8A - 1.75]\ (henry).$$

Substituting for B_T^{max} and using $d = R-a-\tau_b-\tau_c$, where τ_c is the toroidal field coil thickness, we find

$$2\pi\ qA\left(A-1-\frac{\tau_B}{a}-\frac{\tau_c}{a}\right)^2 = 1.257\left(A-1-\frac{\tau_b}{a}\right)\left(\ln\frac{8A}{a}-1.75\right)$$

For reasonable values of $\frac{\tau_B}{a}$ (like 0.4) and $\frac{\tau_c}{a}$ (like 0.2), and q between 2.5 and 3, one can solve for A and find values between 1.7 and 2. This purely illustrative calculation confirms that low aspect ratio, low toroidal field systems are the most cost effective, in agreement with more detailed analysis.[2,3]

References for Section II-B-1

1. B. Badger et al., UWMAK-I, A Wisconsin Toroidal Fusion Reactor Design", UWFDM-68, Nuclear Engineering Department, University of Wisconsin (Nov., 1973).

2. Ibid., chapter II, section B.

3. J. Sheffield, A. Gibson, "Cost Scaling in Tokamaks", to be published in Nuclear Fusion.

4. P. H. Rebut, "First Description of the Joint European Torus", Proc. 8th Symp. on Fusion Tech., EUR 5182e (June, 1974). p. 273.

II-B-2. Startup

At the start of each burn cycle, the plasma current required for Tokamak operation is generated by having the plasma act as a single turn secondary of a transformer. Energizing the primary side produces an electric field that causes gas breakdown and plasma formation in the torus (the plasma could be pre-ionized by other means) and drives the plasma current. Once the desired operation condition is attained, the diffusion-driven current (bootstrap current) is sufficient, according to neoclassical theory[1,2] and no electric field is required. Operation could then be truly steady-state unless other factors, such as impurity buildup, limit the burn time. However, as discussed in section II-A-2, there is no experimental evidence as yet that the bootstrap current exists. Therefore, in UWMAK-II, we generate the necessary electric field to maintain the plasma current by a slowly rising primary current in the transformer. Thus, the Tokamak reactor is a pulsed device but the burn time per pulse can conceivably be quite long. The reactor can be considered steady-state during the burn and for UWMAK-II the burn time is taken as 5400 sec or 90 minutes.

In this section, we discuss the design and operation of the transformer. The primary is assumed to be superconducting and the coupling to the plasma is via an air-core. The transformer currents are assumed to vary from some positive value to some negative value giving a total change in the transformer current of ΔI_T. This procedure gives the smallest core size. The exact limits for the transformer currents are determined by minimizing the required poloidal magnetic field energy. This then minimizes the maximum required power. The determination of these values is discussed shortly. Alternatives to the above approach include using a normal conducting primary programmed to vary from some maximum current to 0 with an air-core or using a superconducting primary programmed the same way with an iron core. Both these possibilities were studied and were found to require larger core sizes than the design chosen.[3] The smallest possible core size is required to allow the smallest possible aspect ratio.

During the burn, the plasma current $I_\phi(t)$ is constant at the design value, I_ϕ. For simplicity, we assume that $I_\phi(t)$ rises linearly in time during the startup. The time, T_1, has been chosen as 10 seconds to keep the maximum power requirements during startup to about 1000 MW_e and to keep the heat load in the superconductor coils due to eddy current loss within acceptable limits. (Eddy current losses are discussed in Chapter III, Section C.)

The plasma resistance is shown in Table I for various values of the electron temperature. The inductance can be calculated approximately from

$$L = \mu_o R_o \left(\ln 8 \frac{R_o}{a} - 1.75\right)$$

where R_o and a are major and minor radii respectively. For UWMAK-II, we have

$$L = 2.41 \times 10^{-5} h$$

The voltage transient equation of the plasma during the startup and shutdown phase can be written as

$$L \frac{dI_p}{dt} + R_p I_p = V_{external},$$

where R_p is the resistance and equals $\frac{2\pi R_o}{\pi a^2} \eta$. The plasma is inductive if

$$R_p I_p < L \frac{dI_p}{dt} .$$

For a 10 second startup and assuming a linear current rise, we have

$$R_p < 2 \times 10^{-6} \text{ ohm},$$

so that

$$\eta = \frac{\pi a^2}{2\pi R_o} R_p = 2 \times 10^{-4} \text{ ohm-cm}$$

which corresponds to $T_e \tilde{=} 128$ ev for Spitzer resistivity with the neoclassical correction. Therefore, for $T_e < 128$ ev, the plasma acts like a resistive load where as for $T_e > 128$ ev, the plasma is an inductive load. To a first approximation, we will neglect the resistive mode and assume that over the entire startup phase, the plasma acts as an inductive load.

The blanket of UWMAK-II contains much less conducting material than in UWMAK-I so that the "soak" of the poloidal field of the plasma current into the blanket is much more rapid. Consequently, the plasma inductance changes little during the current rise phase and there is much less tendency for the plasma current to overshoot. After the plasma current has been fully established, the core flux is increased slowly to make up for the resistive voltage drop in the plasma.

The value of the plasma resistivity has been anomalously high relative to the Spitzer value. Neoclassical theory predicts a reduction in conductivity in the banana regime due to trapped electron effects. The predicted variation is(4)

$$\sigma(r) = \sigma_{sp}(1 - 1.95 (\frac{r}{R})^{1/2} + .95 (\frac{r}{R}))$$

where σ_{sp} is the Spitzer conductivity.(3) Assuming a flat temperature profile, we can average $\sigma(r)$ over the minor radius and obtain, for UWMAK-II parameters, $\langle\sigma\rangle = (\sigma_{sp}/3.65)$. In addition, the conductivity can be reduced due to impurities

Table II-B-1

Electron Temperature (KeV)	Resistivity* (ohm-cm)	Resistivity**
.01	2×10^{-3}	7.3×10^{-3}
.1	8×10^{-5}	2.9×10^{-4}
1.0	3×10^{-6}	1.1×10^{-5}
10	1×10^{-7}	3.65×10^{-7}
15	6.66×10^{-8}	2.43×10^{-8}

* Based on Spitzer resistivity

** Based on neoclassical resistivity assuming a flat temperature profile. The conductivity is assumed to vary as

$$\sigma = \sigma_{sp} \left[\left(1 - 1.95 \left(\frac{r}{R}\right)^{1/2} + .95 \left(\frac{r}{R}\right)\right)\right]$$

where σ_{sp} is the Spitzer conductivity. The values in the table are obtained by averaging over the minor cross section.

by the effective Z of the plasma. For Z_{eff} defined as

$$Z_{eff} = \frac{1}{n_e} \sum_j n_j Z_j^2 ,$$

we have

$$\langle \sigma \rangle = \frac{\sigma_{sp}}{3.65\ Z_{eff}}$$

or, for the resistivity, η,

$$\eta = \eta_{sp}(3.65)Z_{eff}.$$

For a 90 minute burn time, the volt-second requirement is 41.7 Z_{eff} for the Spitzer resistivity case. Therefore, using the neoclassical resistivity implies 152.3 Z_{eff} volt-seconds are required.

In UWMAK-II, the use of a carbon curtain as discussed in Section II-A-4 means that there should be essentially no high Z impurities in the plasma. Low Z impurities, like Z=6 for carbon, give rise to low Z_{eff} even for relatively high concentrations. For reasons described in Section II-B-5 on the divertor operation, we have taken $Z_{eff} \simeq 1$ during the burn phase. Thus, the volt-seconds required is taken as 152.

The transformer coil locations and currents have been determined in the following manner. First, a field line generated only by the plasma current and passing through R = 3.60 meters was calculated. This R was chosen consistent with the size of the D-windings, the anticipated size of the transformer coils, and the space required for supporting structure in the center. A surface current $\Delta I = H\Delta S$ was calculated along the field line. The currents within each 2 meter interval along this field line were then lumped together and placed at the center of each interval. Such a procedure gives the center and radius of each coil. The coil T_6 listed in Table II-B-2, however, covers a larger interval and has been raised one meter to leave enough space for the reinforcement structure shown by the shaded area on the "D" shown in Fig. II-B-3. The transformer coils and currents determined in this manner will give minimum magnetic field contribution at the plasma. This field is less than 50 gauss for the UWMAK-II system.

The transformer currents determined above only fix the ratio between the transformer coil currents, not the magnitude of the currents. The rate of change of current is important and depends on the rate of magnetic flux change required to induce current in the plasma loop. All the divertor currents are programmed to rise with the plasma current. In addition, the same ratio of currents is these coils is maintained in order to keep the plasma cross-section and equilibrium condition at all times. The divertor coils give a net current of -5.26 MA and they contribute about 30% of the flux needed to energize the

Table II-B-2

Divertor Current

	R(m)	Z(m)	$I(10^6 amp)$
D1	8.2	6.5	-3.70
D2	8.8	10.0	+4.89
D3	11.5	12.3	-1.46
D4	11.5	9.5	+3.40
D5	14.6	8.0	-1.57
D6	19.0	5.0	-6.82

Transformer Current

	R(m)	Z(m)	$I_o(10^6 amp)$ initial current	$I_s(10^6 amp)$ (end of start-up)	$I_f(10^6 amp)$ (final current)
T1	3.61	1.00	2.74	1.66	-4.13
T2	3.72	3.00	2.64	1.60	-3.99
T3	3.94	4.99	2.39	1.45	-3.61
T4	4.25	6.96	2.26	1.37	-3.41
T5	4.66	8.92	1.89	1.14	-2.85
T6	5.43	13.50	2.22	1.15	-3.36
T7	6.50	15.05	2.21	1.34	-3.34
T8	7.25	17.00	1.66	1.00	-2.51
T9	8.22	19.3	1.46	0.88	-2.20

Change of Transformer Current

	$-\Delta I_s$	$-\Delta I_B$	$-\Delta I$
T1	1.08	6.87	7.95
T2	1.04	6.63	7.67
T3	0.94	6.00	6.94
T4	0.89	5.67	6.56
T5	0.75	4.74	5.49
T6	1.07	5.58	6.65
T7	0.87	5.55	6.42
T8	0.66	4.17	4.83
T9	0.58	3.66	4.22

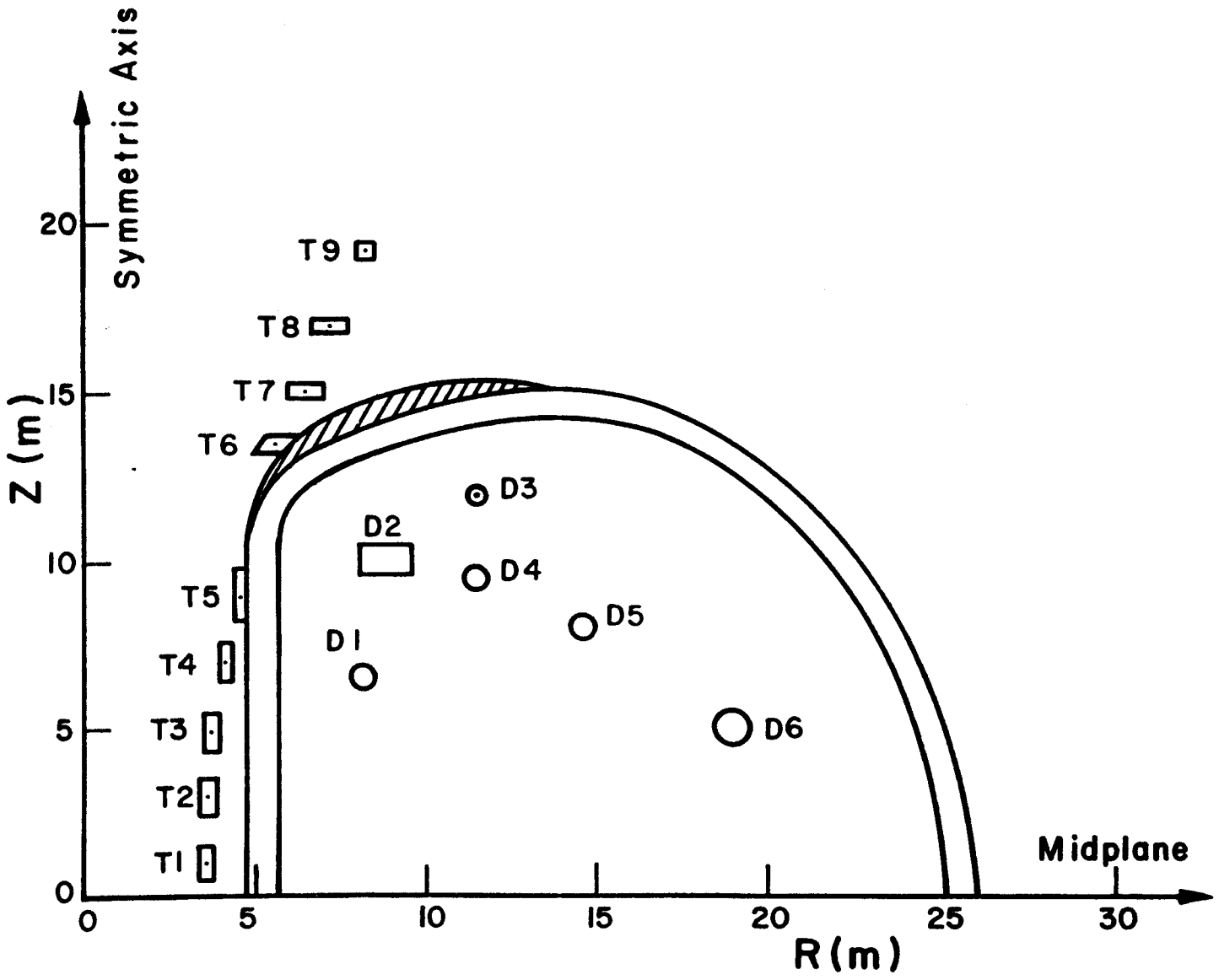
Symmetric Axis
Z (m)
R (m)
Midplane
T1
T2
T3
T4
T5
T6
T7
T8
T9
D1
D2
D3
D4
D5
D6
0
5
10
15
20
25
30

Figure II-B-3

the plasma during the startup or to de-energize the plasma during shutdown. The transformer must therefore provide the remaining 70% of the flux.

During the burn, the divertor coil currents remain constant and flux needed to produce the 152 volt-sec due to plasma resistivity has to be provided by the transformer alone. The current changes during startup, ΔI_S, and during the burn, ΔI_B, have been calculated according to the method described previously.(5) The values of ΔI are listed in Table II-B-2. The total current change from startup to the end of burn is $\Delta I = \Delta I_B + \Delta I_s$.

In principle, one can program the current in the transformer coils to vary from 0 to ΔI. However, we pointed out in our earlier work(5) that the energy stored in the poloidal field and power requirements to drive the OH and VF coils will be lowest if the currents are programmed to vary from $+\Delta I/2$ to $-\Delta I/2$. In addition, the minimum total energy stored does not occur at zero-current, but occurs at -0.9MA in coil T1. Therefore, the current is again off-set by this much, i.e. the current is programmed from ($\Delta I/2$ - .9) to -($\Delta I/2$ +0.9). Another merit of doing this is that the maximum currents in the transformer will be approximately $\Delta I/2$, rather than ΔI, and this will clearly save on the cost of the coils.

The transformer coil currents at the beginning and the end of startup and at the end of plasma burn are also listed in Table II-B-2. The waveforms for the complete operating cycle for plasma current, divertor currents, transformer currents, the total stored energy in the poloidal field, and the power requirements for the coils are shown in Fig. II-B-4a and II-B-4b. These figures require some further explanation.

The complete operating cycle is divided into four phases: the startup phase, 10 sec; the burn phase, 5400 sec (90 min); the shutdown phase 100 sec; and the pump out and recharging phase, 150 sec. (Notice the difference of time scale used for each phase in the figure). Curve I shows the plasma current rising linearly from zero to the full current, 14.9 MA, in 10 sec. A 20 sec time is provided for beam heating and other heating at this point to bring the plasma to the operational temperature during the burn, ~15 keV. The plasma current remains constant for 5400 sec during the burn and then decreases linearly in 100 sec to zero during shut down. We have pointed out previously that the divertor current must be programmed to follow the plasma current so that the waveform for the currents in the divertor coils is the same as that for I_{plasma}.

The current waveforms of each coil of transformer are the same and can be demonstrated by that of T1, shown by Curve II in Fig. II-B-4a. During the startup phase, the current of T1 is initially at +2.75 MA and drops to +1.66 MA in 10 sec. During the burn phase, the divertor current is no longer changing so that the transformer alone provides the required flux. This is done by decreasing the current in coil T1 from +1.66 MA to -4.13 MA. The curve has a very small slope because of the long burn time. The total volt-sec requirement for the burn is 152. During the shutdown phase, the current in T1 rises back to -3.06 MA. The current is then held constant for 50 seconds during the purge

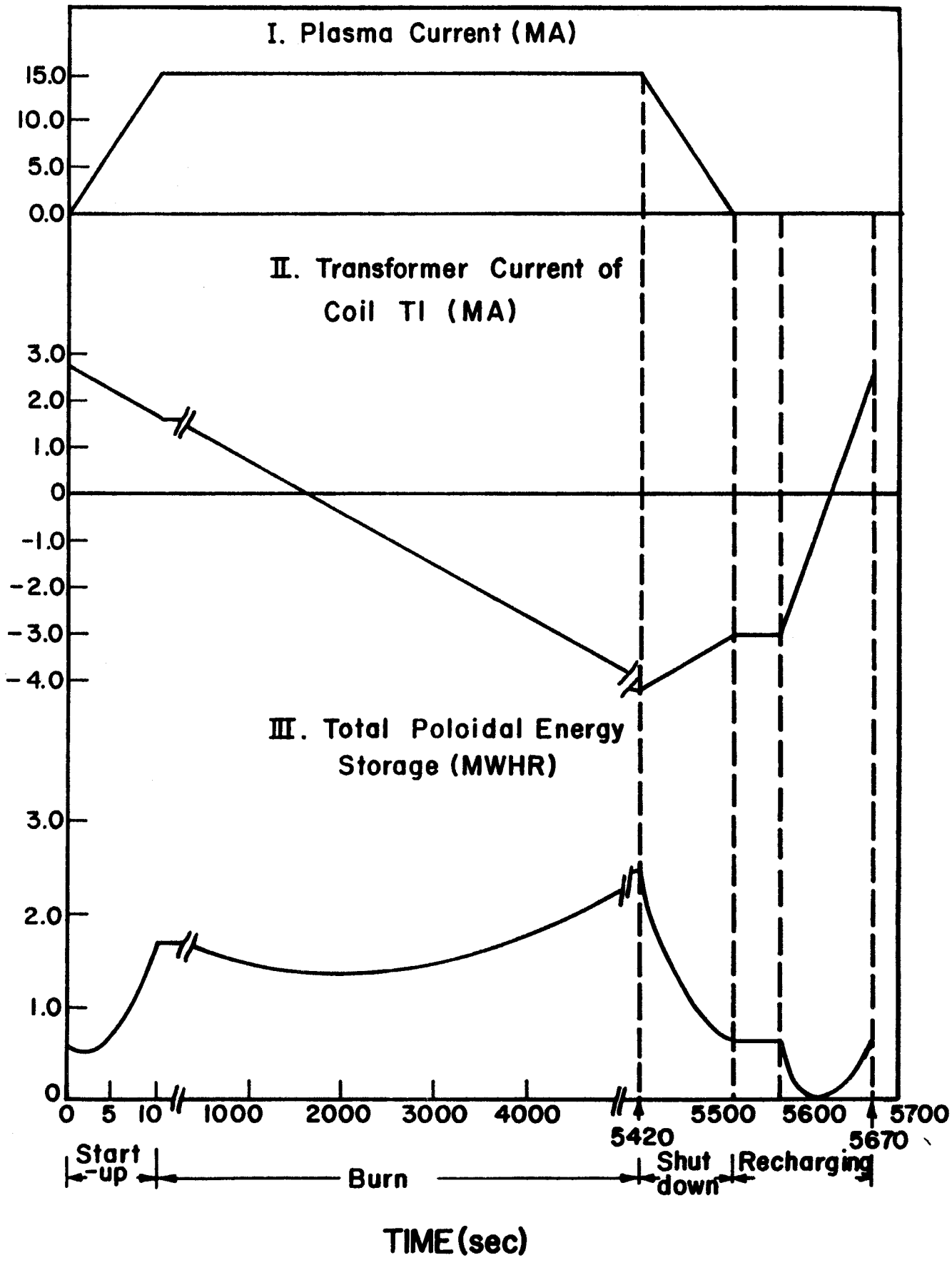

Figure II-B-4a. Power Requirements During Start-up, Burn, Shut-down and Recharging Periods. Note the Difference of Time Scale in Each Period.

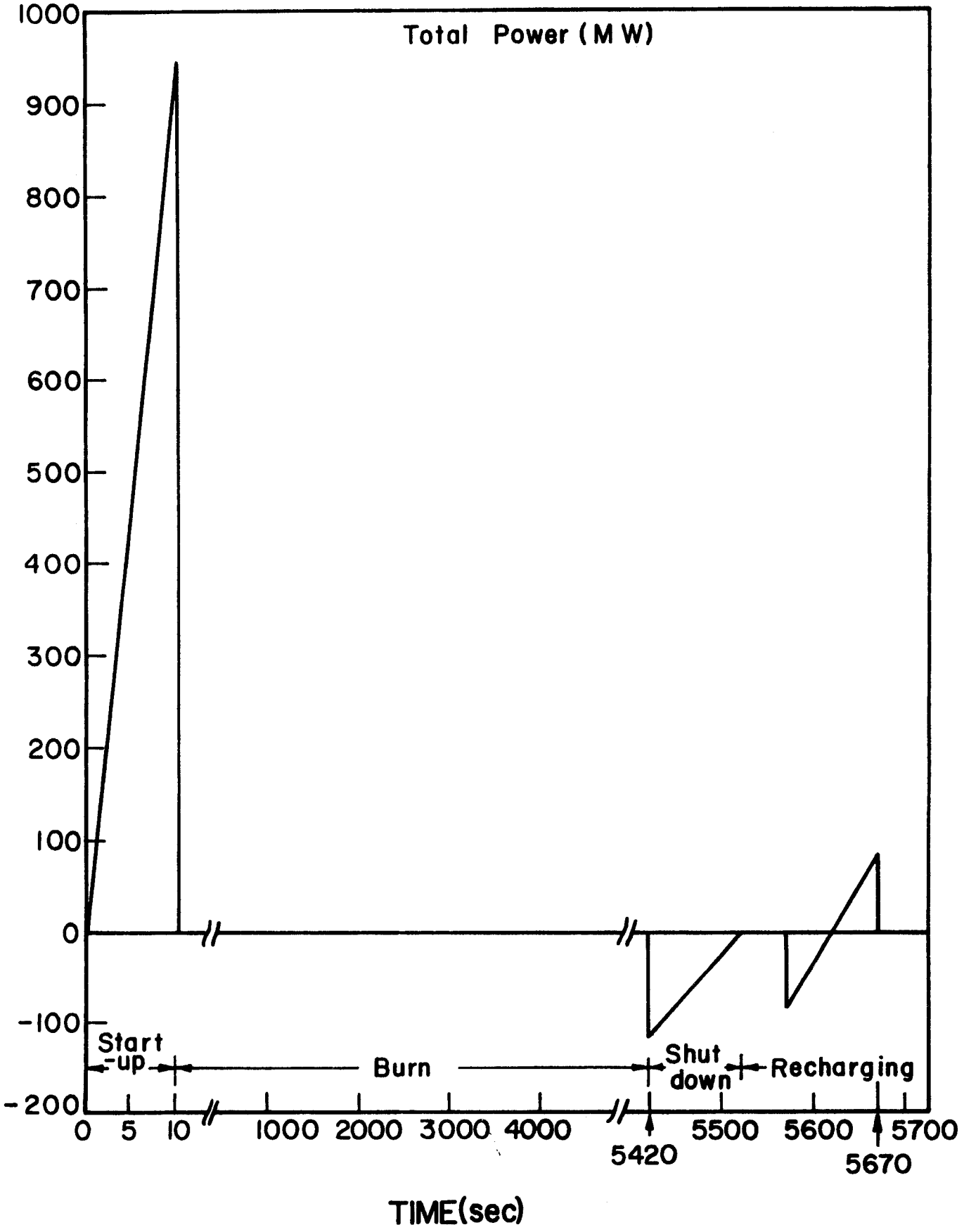

Figure II-B-4b. Plasma Current, Transformer Current and Total Poloidal Energy Storage During Start-up, Burn, Shut-down and Charging Period. Note the Difference in Time Scale in Each Period.

of the chamber so as not to induce gas breakdown and further interaction with the walls. Then, over the next 150 seconds, the coil is recharged to +2.75 MA. This completes a cycle and the system is now ready for fuel gas load and restart.

The total energy storage and power requirements in each phase are shown by Curve II in Figure II-B-4a and the power requirements is shown in Fig. II-B-4b. We notice that the energy decreases in the first few seconds during startup. This means that the system discharges so that the power requirement is negative (output power). The same thing happens during shutdown and the first part of the recharging phases. This energy has to be transferred back to the energy storage system. The energy storage rises to a maximum of 1.9 MW-hr at the end of the 10 sec startup. It takes about 1000 MW_e to accomplish this charging.

During the burn phase, the energy stored in the poloidal field decreases slightly to a minimum at I_{T1} = 0.9 MA. It then increases to a maximum of 2.9 MW-hr at the end of the burn phase. This is the highest value of the stored energy. However, since it is reached over the very long burn time, the power requirements are minimal and can be met by the electrical bridges provided to transfer power during startup. Further, since 100 sec is provided for shutdown, the power output is only 120 MW.

II-B-3. Neutral Beam Heating and Plasma Burn

During the 10 second current rise phase, the plasma is being ohmically heated such that at the end of this period, the electron and ion temperatures will be in the 1-2 keV range. Of course, as has been pointed out previously in many places, such resistive heating becomes ineffective at high temperatures since the plasma resistivity varies as $T_e^{-3/2}$. Therefore, auxiliary heating will be required in Tokamak reactors and in UWMAK-II, we have considered the use of high energy neutral beams. In earlier work,(1) we examined neutral beam heating in large CTR Tokamaks using a space-time plasma simulation program together with a separate calculation of the neutral beam penetration profiles in the plasma. We will not repeat that analysis here but we do want to note that in this earlier work, we assumed that pseudoclassical scaling(2) controlled the electron energy transport while neoclassical scaling(3) controlled ion energy losses. Impurities were treated only via the increase in bremsstrahlung radiation. The reason for assuming pseudoclassical electrons and neoclassical ions is that these scaling laws appear to match present day experimental results, such as in the ORMAK machine.(4) However, as we described in detail in Section II-A-2, anomolous transport due to trapped particle instabilities is predicted to govern plasma behavior in hotter, less collisional, regimes than present day experiments can reach. The differences between the predictions of microinstabilities theory and neoclassical predictions are shown in Fig. II-A-8

For the UWMAK-II study, we assume the scaling laws will follow the predictions of microinstability theory, as summarized in reference 5, since this should correspond to a pessimistic assumption and thereby constitute a "worst case" approach. Indeed, one of our purposes here is to consider the impact of such pessimistic scaling on Tokamak reactor operation. Therefore, we have developed a space averaged calculational model and used it to study heating to ignition and to analyze plasma operation during the burn time. Let us therefore turn to an outline of the calculational model and then proceed to discuss neutral beam heating to ignition and the characteristics of the plasma burn.

1. Calculational Model

The studies reported here required the development of a calculational model which will indicate the expected operating and performance characteristics of large Tokamaks and the scaling of these characteristics with current (or size), neutral beam injection energy and power, target plasma composition, impurities, and transport scaling laws. Since we expected to carry out many calculations, a global plasma model involving the space-average particle densities and temperature has been developed. The basic energy conservation equations are, for ions,

$$\frac{d}{dt}\left(\frac{3}{2} n_i k T_i\right) = W_{inj}^i + W_{BF}^i + W_{PF}^i + W_{ei} - W_E^i \qquad (1a)$$

where W_{inj}^{i} is the fraction of injected power deposited in the ions, W_{BF}^{i} is the fraction of alpha particle energy from beam-plasma fusions deposited in the ions, W_{PF} is the fraction of alpha energy from thermal plasma fusions deposited in the ions, W_{E}^{i} is the energy loss rate due to transport processes, and W_{ei} is the energy exchange rate due to electron-ion rethermalization. The electron energy conservation equation is

$$\frac{d}{dt}\left(\frac{3}{2} n_e k T_e\right) = W_{inj}^{e} + W_{BF}^{e} + W_{PF}^{e} + W_{ohmic} - W_{E}^{e} - W_{ei} - W_{RAD} \quad (1b)$$

Each term in equation (1b) has the same origin as in the ion equation except that W_{RAD} incorporates radiative losses.

The terms, $W_{E}^{i,e}$, represent the energy loss due to both conduction and convection. To evaluate these energy loss rates, it is necessary to assume a scaling law for the particle and energy containment times. As we discussed, to be conservative, we have assumed that when the plasma becomes sufficiently collisionless, turbulence due to trapped particle instabilities governs this transport. This is pessimistic since it leads to high particle and energy loss rates in the collisionless regime. In addition, only theoretical estimates are available for such scaling formulae based on a strong turbulence type of analysis (see Section II-A-2) and these are relatively crude. In general, however, these assumptions may be viewed as a worst-case approach.

When trapped electron and trapped ion mode turbulence is present in a tokamak plasma, a first approximation to the variation of the energy loss rate with electron temperature would be the sawtooth variation as shown in Fig. II-B-5. The dashed curves correspond to expected transition from one regime to another. The three discontinuities in each curve separate four separate regimes where different modes prevail. These have been summarized recently by Dean et al.[5] and were discussed in Section II-A-2. The lowest temperature regime corresponds to pseudoclassical scaling[2] and is followed by two different forms of the trapped electron mode. Finally, as the plasma becomes sufficiently hot, it should enter the trapped ion mode regime in which the energy loss rates scale as $T_e^{9/2}$. This high sensitivity of energy diffusivity to electron temperature will lead to thermally stable operation of the reacting plasma with the temperature in the 10 to 25 keV range, when the density is maintained constant, as seen in Fig. II-B-6. These curves show the electron temperature at ignition and at the thermally stable operating point as a function of the percentage of iron impurity present in the discharge. The dashed curves in Fig. II-B-6 represent the ignition temperatures and the solid curves represent the stable operating temperatures for a reactor.

Returning to a discussion of Fig. II-B-5, the expected transition from one regime to another is shown by the dashed curves. These were obtained by adding the transport coefficients in series, which amounts to adding confinement times in parallel. For example, the transition from the second, or shear stabilized, trapped electron mode to the trapped ion mode regimes is given by

$$D_{\perp} = D_{\perp}^{TEM} + D_{\perp}^{TIM}$$

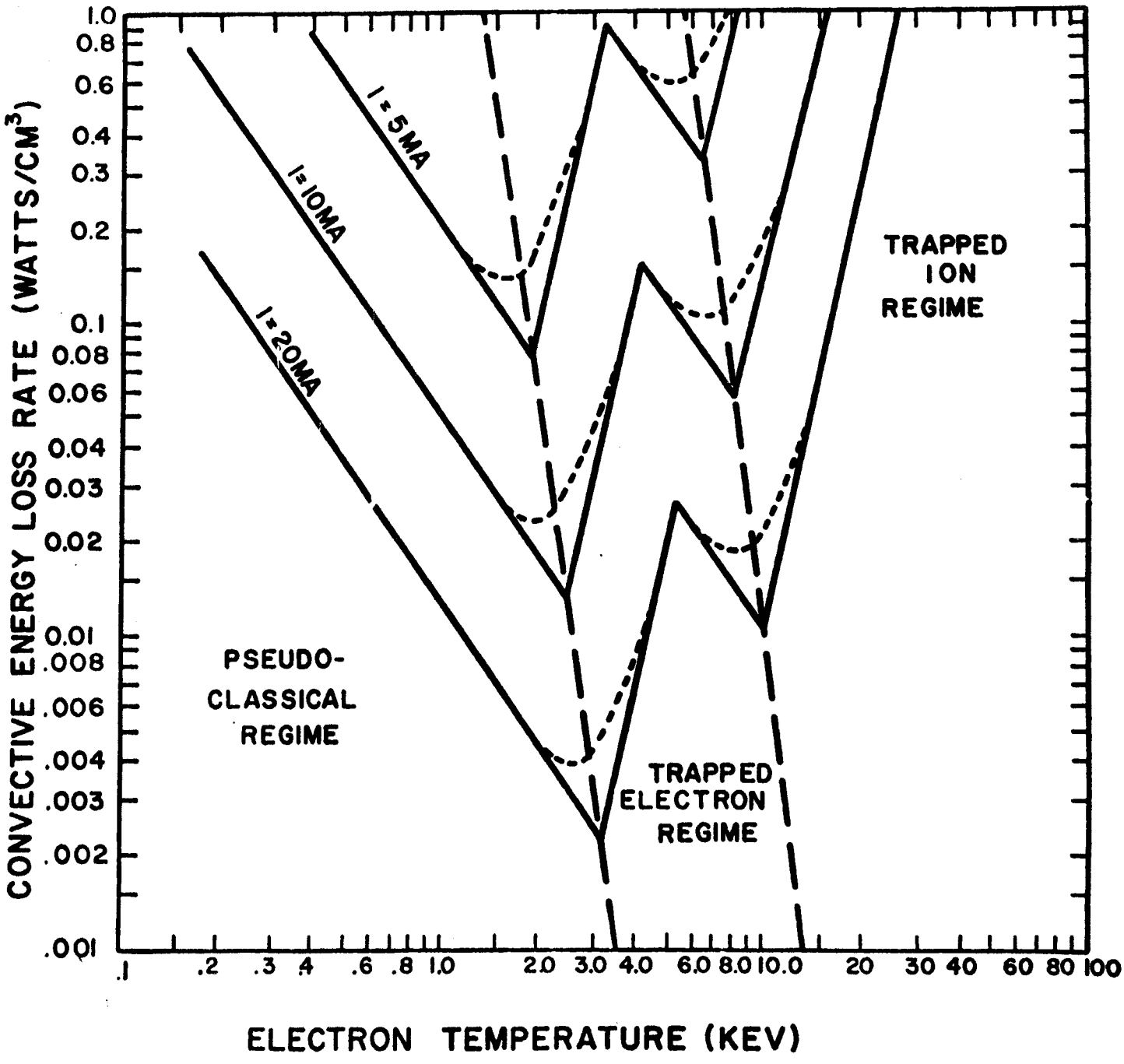
CONVECTIVE ENERGY LOSS RATE (WATTS/CM³)
1.0
0.8
0.6
0.4
0.3
0.2
0.1
0.08
0.06
0.04
0.03
0.02
0.01
.008
.006
.004
.003
.002
.001
I=5MA
I=10MA
I=20MA
PSEUDO-
CLASSICAL
REGIME
TRAPPED
ELECTRON
REGIME
TRAPPED
ION
REGIME
.1
.2
.3
.4
.6
.8
1.0
2.0
3.0
4.0
6.0
8.0
10.0
20
30
40
60
80
100
ELECTRON TEMPERATURE (KEV)

FIGURE II-B-5

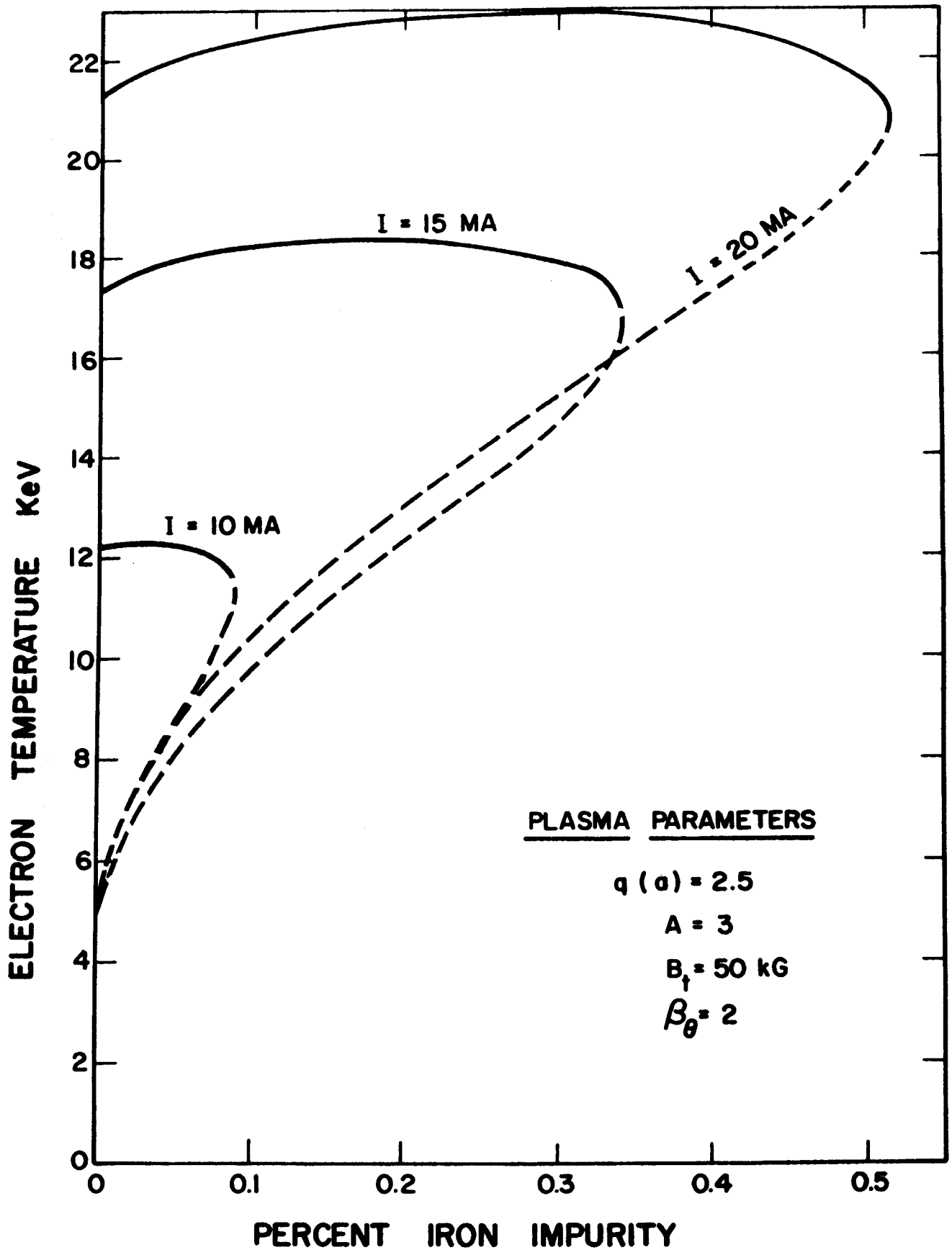
ELECTRON TEMPERATURE KeV
PERCENT IRON IMPURITY
I = 10 MA
I = 15 MA
I = 20 MA
PLASMA PARAMETERS
q (a) = 2.5
A = 3
B_t = 50 kG
β_θ = 2
0
2
4
6
8
10
12
14
16
18
20
22
0
0.1
0.2
0.3
0.4
0.5

FIGURE II-B-6

or

$$\frac{1}{\tau} = \frac{1}{\tau_{TEM}} + \frac{1}{\tau_{TIM}} .$$

To calculate the plasma behavior during the current rise phase, (1a) and (1b) are solved. The plasma conditions during the burn period are then obtained from the steady state limit when the transport is dominated by the trapped ion mode contribution. In this limit, the explicit form of these equations in MKS units with temperature in keV (all terms are in units of watt/m^3) is as follows:

Ion Energy Conservation:

$$1.603 \times 10^{-16} \frac{d}{dt}(n_i T_i) = 6.33 \times 10^{18} \frac{P_{inj} B_T^3 U_{bi}}{q^3 I^3 A^4} + 5.64\times10^{-13} X_\alpha n_i^2 \alpha(1-\alpha)\langle\sigma v\rangle U_{\alpha i}$$

$$+ \frac{2.20 \times 10^{22} X_\alpha P_{inj} B_T^3 F_{BP} U_{\alpha i}}{E_o q^3 I^3 A^4} - \frac{7.32 \times 10^{31} T_e^{7/2} T_i^3 B_T^2 (n_i/n_e)}{A^{13/2} I^4 q^4 Z_{eff} (T_i + T_e)^2}$$

$$- \frac{4.37 \times 10 \quad n_e n_i (T_i - T_e)}{A_p T_e^{3/2}} = 0 \qquad (2a)$$

Electron Energy Conservation:

$$1.603 \times 10^{-16} \frac{d}{dt}(n_e T_e) = \frac{6.33 \times 10^{18} P_{inj} B_T^3 (1-U_{bi})}{q^3 I^3 A^4} + 5.64\times10^{-13} X_\alpha n_i^2 \alpha(1-\alpha)\langle\sigma v\rangle (1-U_{\alpha i})$$

$$+ \frac{3.27\times10^{-9} \ell n\Lambda}{T_e^{3/2} f_{TR}} \left(\frac{0.457 Z_{eff}}{1.077+Z_{eff}}\right) + 0.29 Z_{eff} + \frac{2.20\times10^{22} X_\alpha P_{inj} B_T^3 F_{BP} U_{\alpha i}}{E_o q^3 I^3 A^4}$$

$$- \frac{7.32 \times 10^{31} T_e^{7/2} T_i^3 B_T^2}{A^{13/2} I^4 q^4 Z_{eff} (T_i+T_e)^2} + \frac{4.37 \times 10^{-34} n_e n_i (T_i - T_e)}{A_p T_e^{3/2}} - W_{RAD} = 0 \qquad (2b)$$

In both equations, P_{inj} is the beam power injected at energy E_o, F_{BP} is the fraction of beam particles which undergo fusion while slowing down,[6] B_T is the toroidal magnetic field, q is the stability factor, I is the plasma current, A is the aspect ratio, n_i and n_e are the ion and electron densities, T_i and T_e are the ion and electron temperature, and U_{bi} and $U_{\alpha i}$ are the fractions of beam energy and alpha energy, respectively, going to the ions. Ohmic heating is neglected in this high temperature regime. X_α is the fraction of alphas that do not have orbits extending beyond the plasma radius, a (that is, the fraction of alphas retained), α is the tritium fraction of the plasma ions, and $A_p = 3\alpha + 2(1-\alpha)$ is the effective atomic mass of the plasma ions. The parameter X_α has been computed from a recent study.[7] f_{TR} is a correction due to particle trapping given by

$$f_{TR} = 1 - [1.95 \left(\frac{r}{R}\right)^{1/2} - 0.95\left(\frac{r}{R}\right)]/(1 + V_e^*) \tag{3}$$

where V_e^* is a dimensionless parameter given by

$$V_e^* = 6.92 \times 10^{-24} \frac{R^{3/2} B_T n_e \ell n\Lambda}{r^{1/2} T_e^{3/2} B_\theta(r)} \tag{4}$$

The term, W_{RAD}, includes bremsstrahlung, W_B, as

$$W_B = 4.8 \times 10^{-37} n_e^2 Z_{eff} T_e^{1/2} \tag{5}$$

and synchrotron radiation, W_{Sync}, as [8]

$$W_{Sync} = 3.5 \times 10^{-9} (5 + .18(5-A))^3 \frac{\sqrt{n_e} B_T^3}{\sqrt{q\ AI}} T_e^{2.1} \tag{6}$$

Line and recombination radiation have been included in an emperical formula[9,10] in which the exact coefficients have been determined from a study of carbon radiation. This expression for radiation from an impurity with charge Z is given by

$$W = W_B \left(1 + \frac{3.97 \times 10^{-2} \xi_Z Z^4}{Z_{eff} T_e} + \frac{8.6 \times 10^{-4} \xi_Z Z^6}{Z_{eff} T_e^2} \right) \tag{7}$$

We have found the results using equation (7) to be similar to those obtained using the formulae of Post.[11] Note, however, this formula becomes inaccurate at low temperatures. In that case, we have used the formula of Hinnov,[12]

$$W = 1.2 \xi_Z n_e^2 \times 10^{-26} \tag{8}$$

which is approximately correct for impurities with three or more electrons remaining. In calculations, the smaller value from equations (7) and (8) is used to determine radiative energy losses.

As a general comment, such a global plasma energy balance model is relatively simple and much less expensive to use compared with a detailed spatially dependent calculation.[13,14] It has been found, however, that the results from the global model generally agree well with the more detailed calculations.[15] Thus, since many calculations are involved, the global model has been used.

In addition to the energy conservation equations, the charge neutrality condition

$$n_e = n_i + 2n_\alpha + \sum_j n_j Z_j \tag{9}$$

is maintained and a limit on the total poloidal beta, β_θ, has been imposed. The expression for β_θ is

$$\beta_\theta = \frac{4 \times 10^{-22} q^2 A^2}{B_T^2} \left(n_e T_e + n_i T_i \right.$$

$$\left. + \frac{2}{3} (n_{\alpha BP} + n_{\alpha Th}) (\bar{E}_\alpha \tau_{SD}^\alpha + T_i \tau_p^\alpha) + \frac{2}{3} n_h \bar{E}_b \right) \tag{10}$$

where $n_{\alpha BP}$ and $n_{\alpha Th}$ are the alpha particle production rates from beam-plasma and Maxwellian plasma fusions, respectively, $\bar{E}_\alpha$ is the mean energy of the slowing down alpha particles, τ_{SD}^α is the time to slow down from 3.52 MeV, τ_p^α is the alpha containment time (taken equal to the ion confinement time,) n_h is the density of high energy beam injected particles, and $\bar{E}_b$ is the average energy of the slowing down beam particles.

The calculations of $\bar{E}_\alpha$ and $\bar{E}_b$ were obtained by considering the thermalization of an energetic heavy ion in a multi-species plasma. The analysis is based on a Fokker-Planck treatment and extends the earlier work of Butler and Buckingham.[16] Expressions have also been obtained for $U_{\alpha i}$ and U_{bi}, the fractions of alpha and beam energy, respectively, going to the ions. The analysis pertains only to the mean energy slowing down and not to the spread in energy about the mean.

The test particle energy at which the rate of energy loss to all ion species is equal to the rate of energy loss to the electrons is defined as E_{crit} and is given by[17]

$$E_{crit} = 14.8 A_T T_e \left(\frac{1}{n_e \ln \Lambda e} \sum_j \frac{n_j Z_j^2 \ln \Lambda_j}{A_j} \right)^{2/3} \tag{11}$$

$$E_{crit} = \gamma^{2/3} T_e \tag{12}$$

An analytic expression for the fraction of test particle energy going to all ion species (which rapidly thermalize together) is

$$U_{Ti} = \frac{1}{3}\frac{E_{crit}}{E_{To}}\left\{\ln\left[\frac{E_{crit} - E_{crit}^{1/2}E_{To}^{1/2} + E_{To}}{E_{crit} + 2E_{crit}^{1/2}E_{To}^{1/2} + E_T}\right]\right.$$

$$\left. + 2\sqrt{3}\tan^{-1}\left[\frac{2E_{To}^{1/2} - E_{crit}^{1/2}}{\sqrt{3}E_{crit}^{1/2}}\right] + \frac{\sqrt{3}\pi}{3}\right\} . \qquad (13)$$

This expression is valid for $(T_e, T_i) << (E_{crit}, E_{To})$ and is used for both the injected neutral beam and the alpha particles.

This model has been used to analyze the expected operating conditions for large Tokamaks and the potential of machines which are unignited (for example, because of impurities) but can be externally driven and nevertheless amplify the input power enough to allow for viable power reactors.[18] We will not report this study here but turn to a specific discussion of the heating and burn characteristics of UWMAK-II.

2. Heating to Plasma Burn Conditions

For UWMAK-II, we have assumed that neutral beams[19] with energies in the range of 300-700 keV are available and can be used for supplementary plasma heating. Such high energy beams are required to penetrate a UWMAK size plasma[1] and, as we will show, this problem is exacerbated by trapped particle mode scaling. To attain such beams at acceptable efficiences will require the development of high current density negative ion beams. Positive ion sources become inefficient at energies above 100-200 keV because the charge exchange cross section for H, D, or T begins to drop sharply.[20] It appears reasonable to expect negative ion sources to produce neutral beams with an efficiency of about 60% and this might be improved even further, to perhaps 75-80%, if direct conversion[21] of the unneutralized beam is possible. However, direct conversion of such high current density ion beams is difficult and may take much additional development. We will assume therefore that the neutral beam sources are of the LBL (Berkeley)[22] or ORNL types,[19] employ negative ion beams accelerated to the required voltage, and are then passed through a stripping cell to produce a neutral beam with 60% efficiency. In our previous work,[23] we discussed a detailed conceptual design of such a source based on an extrapolation from the ORNL design.[19]

The beam deposition profile in the plasma is determined by the plasma temperature and density and their profiles. In general, one would like to start injecting into a low density plasma to improve penetration and heating and, following ignition, raise the density by external means to the desired operating level.[1] We have, therefore, considered the minimum plasma density for which it is possible to obtain ignition. Unlike the case[1] with pseudoclassical or neoclassical scaling, one cannot continue to lower the density and still be able to achieve ignition. The reason is that the alpha particle heating of the plasma varies as n^2 whereas for the dissipative trapped ion mode, which governs as ignition is approached, $D_\perp$ and χ vary inversely with n. Therefore, as n decreases, the alpha heating decreases while the transport losses increase. For a UWMAK-II size plasma, the minimum average electron density is found to be about $4 \times 10^{13}/cm^3$ which, for a parabolic density profile, means a central electron density of $8 \times 10^{13}/cm^3$.

An average electron density of $4 \times 10^{13}/cm^3$ is relatively high and makes penetration by neutral beams difficult. In Fig. II-B-7, we show beam energy deposition profiles into a UWMAK-II plasma for several values of injected beam energy assuming deuterium beams. The ordinate is the beam power deposited per unit volume divided by the density profile to give energy deposited per plasma particle, in watts/particle. The injection chord is chosen half way between the inner surface and the plasma axis, as shown in Fig. II-B-8, and is chosen to optimize penetration. Nevertheless, it is clear that beams with energies in the 500-750 keV range are required if penetration is essential. This is in contrast to our previous results[1] where a startup density of $1.5 \times 10^{13}/cm^3$ allowed us to propose the use of 300-500 keV beams. The need for higher energy beams is thus an important factor arising from trapped particle mode scaling.

Assuming neutral beams between 500-750 keV, the beam energy deposition profile will be relatively flat. The next question is the power required to achieve ignition in a given period of time. Based on the calculational model outlined earlier in this section, we have calculated the time to reach ignition as a function of neutral beam power injected. The results are given in Fig. II-B-9. For these and other calculations in this section, we assume $Z_{eff} \simeq 1$ based on the use of a carbon curtain (see Section II-A-4) and a divertor (see Section II-B-4). We will expand on this in the next section. Examining Fig. II-B-9, we see clearly that at lower density, less power is required to achieve ignition in a given time.

For UWMAK-II, we would like to reach the plasma operating point within about 20 seconds of the time that the plasma current reaches its full value. From Fig. II-B-9, we see that 60 MW of injected power will allow the plasma to reach ignition in approximately 10 seconds where $n_e = 4 \times 10^{13}/cm^{-3}$. If the beams are turned off just after ignition, however, the plasma heatup rate is quite slow, as seen in Fig. II-B-10. It would take almost 100 seconds to reach a stable operating point.

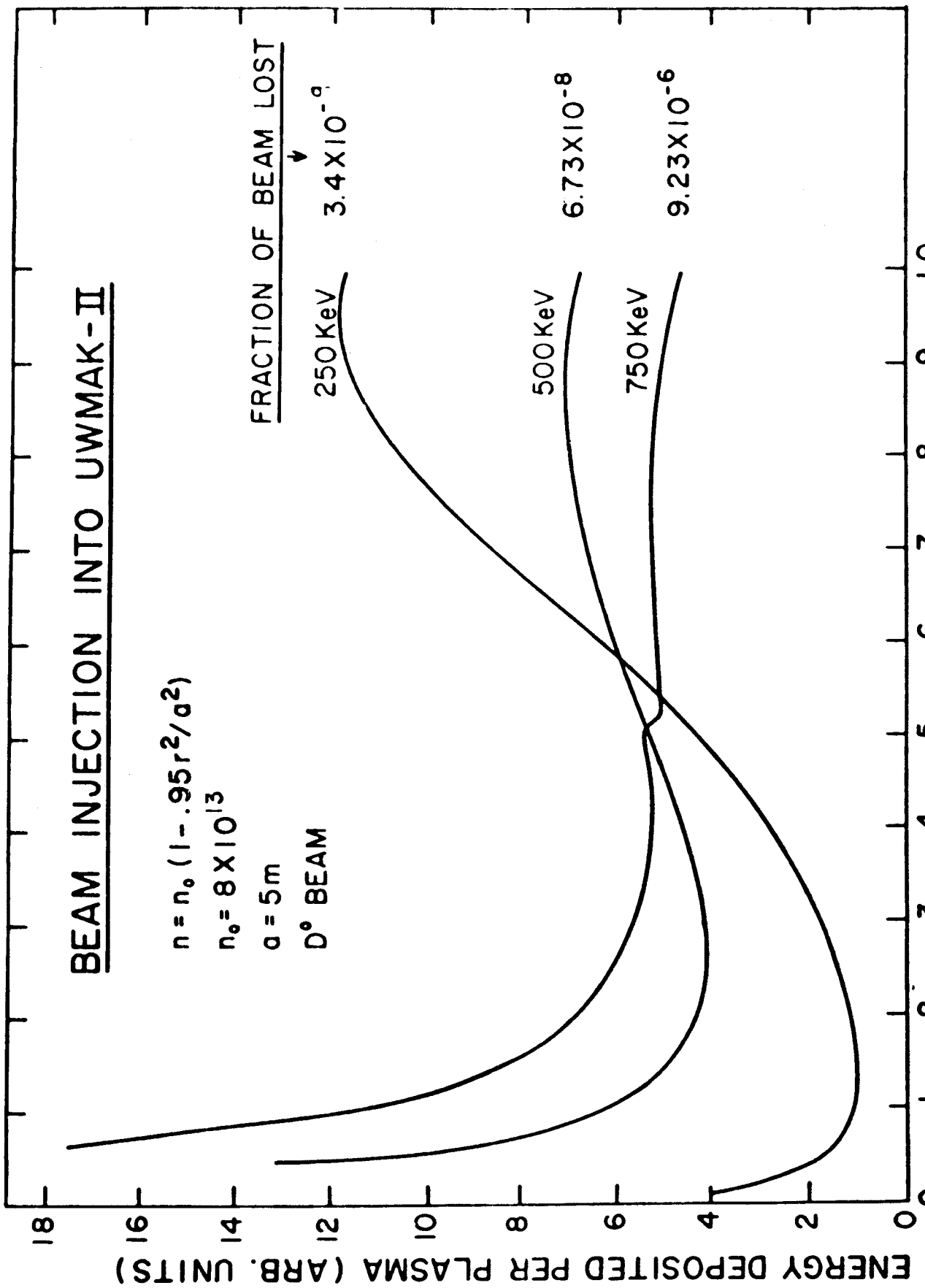
BEAM INJECTION INTO UWMAK-II
$n = n_o(1-.95r^2/a^2)$
$n_o = 8 \times 10^{13}$
a = 5m
D° BEAM
FRACTION OF BEAM LOST
250 KeV
3.4X10⁻⁹
500 KeV
6.73X10⁻⁸
750 KeV
9.23X10⁻⁶
ENERGY DEPOSITED PER PLASMA (ARB. UNITS)
r/a
0
2
4
6
8
10
12
14
16
18
.1
.2
.3
.4
.5
.6
.7
.8
.9
1.0

Fig. II-B-7

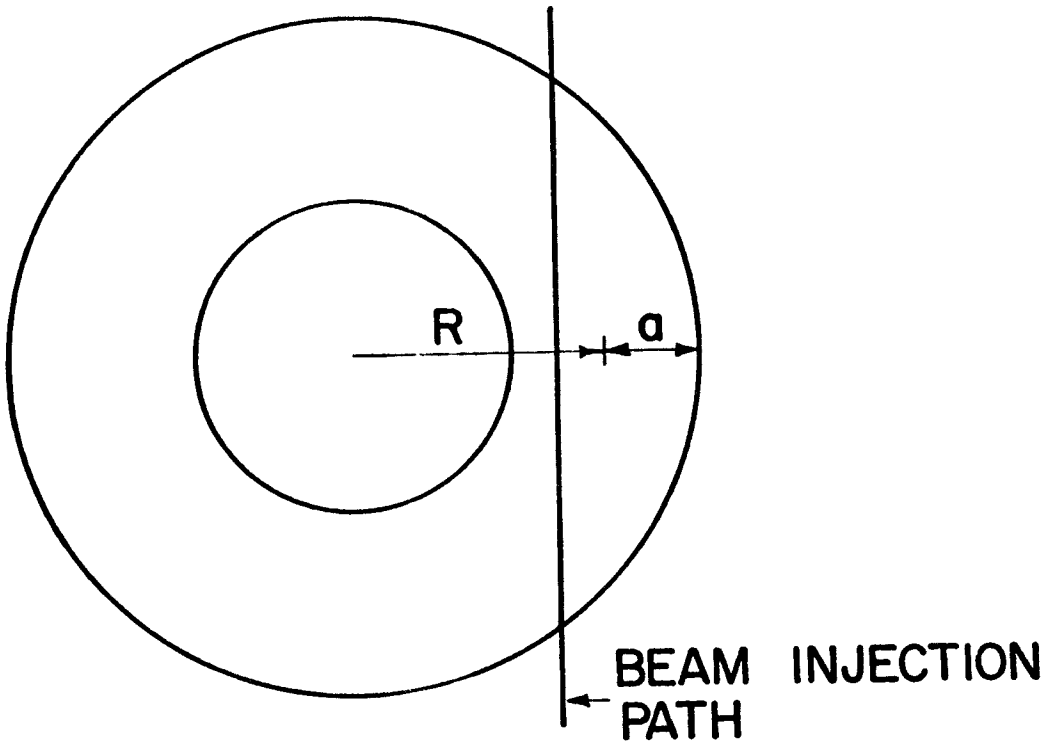

PARAMETERS OF NEUTRAL BEAM INJECTION SYSTEM

TOTAL INJECTION POWER	200 MW
NUMBER OF INJECTORS	16
INJECTOR EFFICIENCY	65%
POWER REQ'D BY INJECTORS	308 MW
BEAM ENERGY (D° AND T°)	750 keV
BEAM CURRENT PER INJECTOR	16.7 A
TIME DURATION OF INJECTION	10 S

Fig. II-B-8

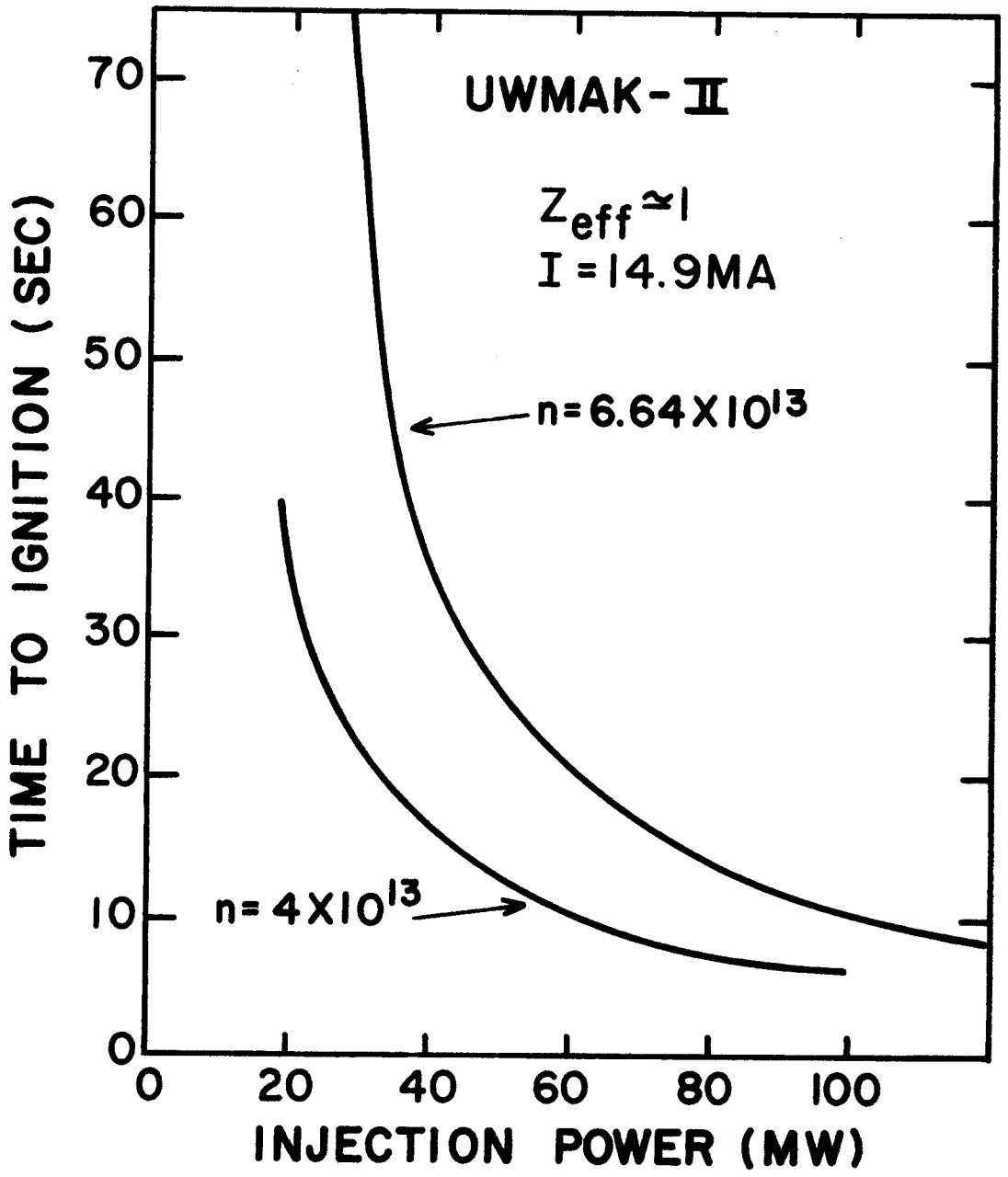
UWMAK-II
$Z_{eff} \simeq 1$
I = 14.9MA
n = 6.64X10^13
n = 4X10^13
TIME TO IGNITION (SEC)
INJECTION POWER (MW)
0
10
20
30
40
50
60
70
0
20
40
60
80
100

Fig. II-B-9

What is required is to inject more power and heat the plasma well past ignition. The density can then be raised to the desired operating value and yet, with perhaps a small amount of additional heating, the plasma will be enough past ignition that a rapid self-heatup phase can be achieved.

The complete scenario for the startup phases of UWMAK-II is shown in Fig. II-B-11. From 0 to 10 seconds, the plasma current is increasing linearly with time from 0 to 14.9 MA. For a constant current density, this means the plasma radius increases as $\sqrt{t}$. The plasma has an average density of $4 \times 10^{13} cm^{-3}$ and reached only ~1.5 keV after the 10 sec ohmic heating phase. The reasons for this low temperature are that Z_{eff} is approximately 1 and that the average current density in the plasma is only about 19 A/cm^2.

At t = 10 sec, 200 MW of 750 keV neutral beams (50%D° and 50%T°) are turned on and the plasma rapidly heats to about 10 keV in 7 seconds. At that point, it is assumed the fueling mechanism instantaneously increases the average plasma density to the operating value of $7.7 \times 10^{13} cm^{-3}$. This lowers the overall plasma temperature to about 5 keV. The beams are left on for another 3 seconds to heat the plasma to about 8 keV. At t = 20 sec, the beams are turned off and the plasma self heats via alpha particle heating to the final operating ion temperature.

It is important to make several comments about this analysis. In the first place, we have assumed throughout that the plasma density can be externally controlled and maintained. In our previous work,[23] we discussed pellet injection[24] as the fueling mechanism although little is known about this approach. We have not carried out a more detailed analysis for this study and so are left to assume some form of pellet fueling can be made to work. Clearly, this is an important problem for Tokamak reactors and more experimental and theoretical work needs to be carried out.

Secondly, the analysis is based on spatially averaged values of temperature and density and some details may change as a result of a full space-time treatment. We are, in fact, pursuing this question and will report the results elsewhere. However, it has generally been found that such global models give reasonable agreement with more detailed calculations.[25]

Finally, the plasma current rise has been assumed to take place linearly with time and that the plasma minor radius begins at about 50 cm and increases to 500 cm in 10 seconds by increasing as $\sqrt{t}$. This keeps the plasma current density constant at ~19 A/cm^2 which is quite a low value compared to the current density in present day experiments, which are the order of 100-200 A/cm^2. The expansion of the plasma cross section may be accomplished using a moving limiter or by compressing the plasma away from a fixed limiter and adding core flux to drive current in the region between the hotter core and the limiter. These ideas require further analysis and are being examined by several groups including our own.

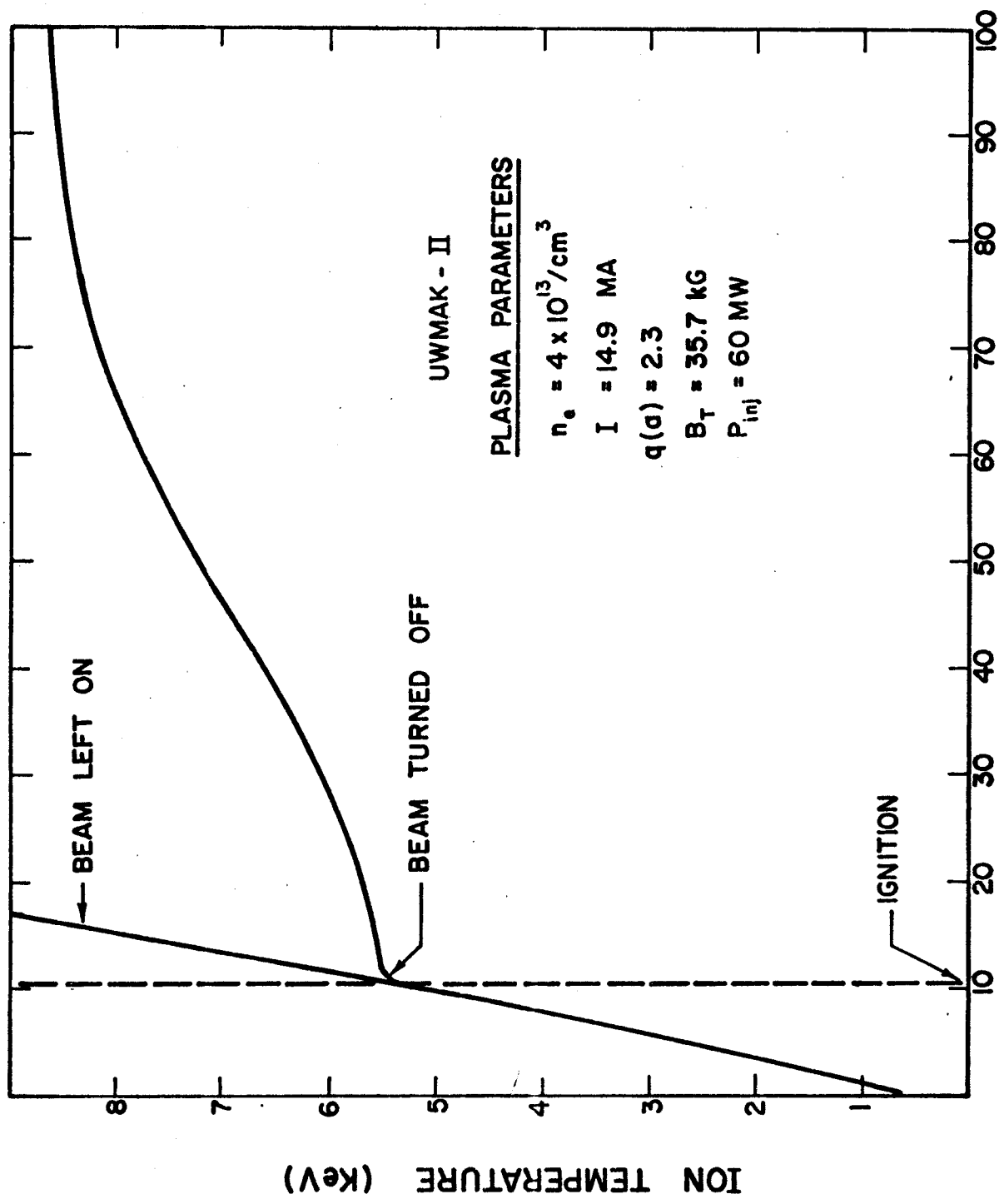

Figure II-B-10

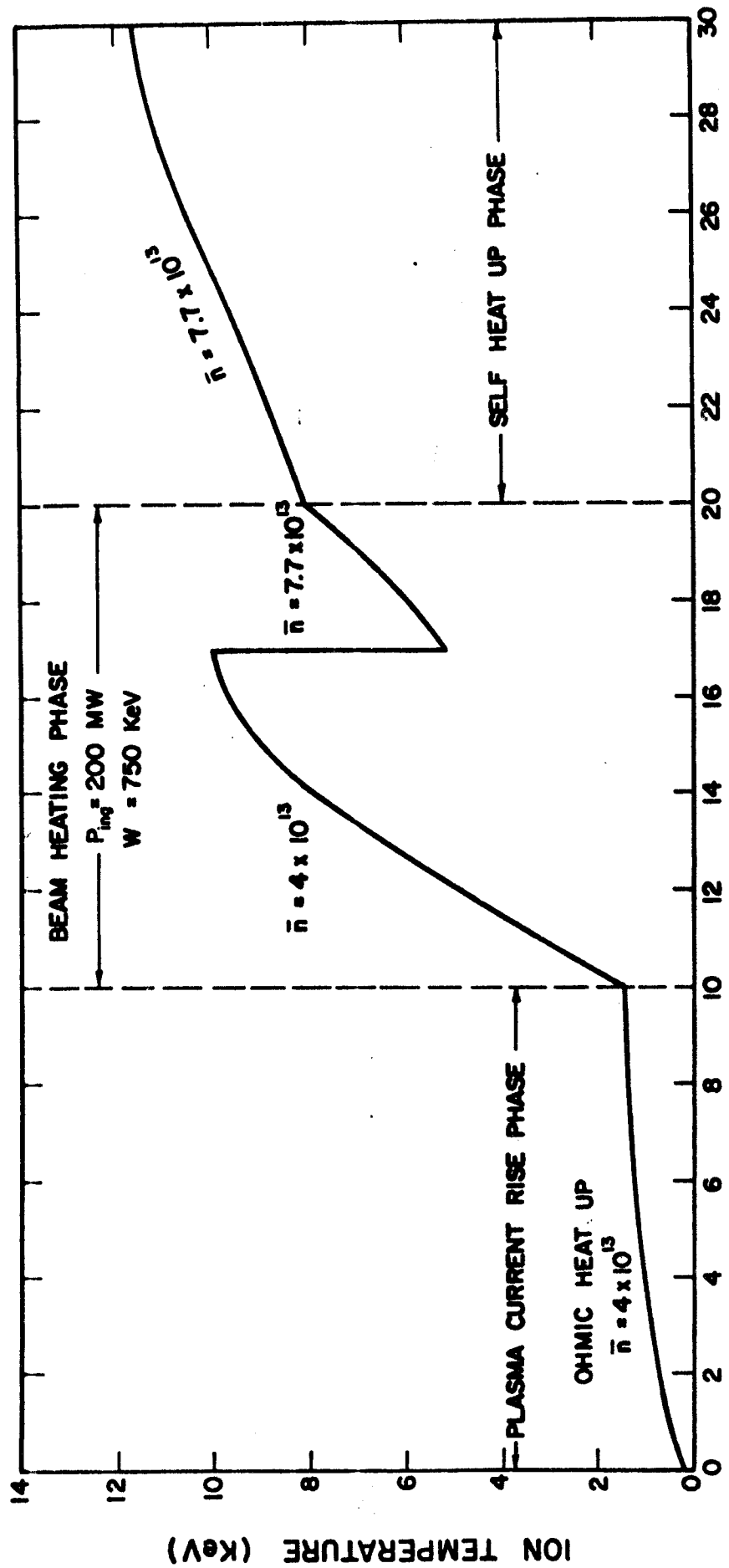

Figure II-B-11

Ion Temperature as a Function of Time During Reactor Startup.

3. Plasma Burn Conditions

Equations (2a) and (2b) were solved to determine the plasma operating conditions during the uninterrupted burn. It is assumed that the density is maintained throughout the burn by cold particle injection, such as with D-T pellets. We have not, however, carried out a detailed study of such a fueling procedure.

The plasma and magnetic field parameters during the burn are listed in Tables II-B-3, II-B-4 and II-B-5. This plasma is thermally stable against perturbations in temperature and the fueling mechanism is assumed to maintain the density constant at the proposed operating value. The energy confinement time (conduction and convection only) is 4.14 while the particle containment time is twice that, or 8.28 s. (The reason is $D_\perp = \chi$ for the trapped particle mode.) The overall energy containment time is 3.64 s. The fractional burnup is 4.85% and the fueling rate for D+T atoms is 5.97×10^{22} per sec. The surface heat load due to bremsstrahlung and synchrotron radiation is 3.67 w/cm^2 and, since the divertor is >99% efficient at collecting particles diffusing from the plasma (see Sec. II-B-4), the heat load due to particles on the wall is essentially zero. The power flowing to the divertor is 713 MW and is this large because the radiation losses are relatively small. However, if impurities keep the plasma edge relatively cool (~1-2 keV), than the temperature drop from an average of ~12 keV to 1-2 keV will have to be dissipated via radiation. In this case, the surface heat load will increase while the power into the divertor could drop by factors of from 2 to 5.

The plasma stability factor of 2.3 at r = a is reasonable for a long term future Tokamak and $\beta_\theta = 2.275$ is less than the aspect ratio. The toroidal field on axis is relatively low (3.57 T) because of the low aspect ratio.

We should comment here on the long burn time we have assumed. As will be discussed in the next section, the effect of the divertor will be to collect particles diffusing from the plasma with an efficiency of greater than 99%. However, particles sputtered from the wall by neutrons will not effectively be screened and will enter the plasma. We discussed in Section II-A-4 the use of a carbon curtain for protecting and for screening the plasma from high Z impurities. We found there that for a UWMAK-II plasma and a divertor operating as described above, impurity confinement times as large as 100 to 1000 times $\tau_p^{D,T}$ can be tolerated with low Z impurities. Based on this analysis, it is assumed low Z impurities are essentially negligible, that there are no sources of high Z impurities, and that it is therefore possible to achieve long burn times. We are presently carrying out detailed space-time plasma calculations to study this conclusion further.

Table II-B-3

Plasma Operating Parameters for UWMAK-II*

Plasma Current, I	14.9 MA
Electron Poloidal Beta, β_θ^e	1.22
Total Poloidal Beta, β_θ	2.275
Total Toroidal Beta, β_ϕ	0.064
Stability Factor, q(a)	2.3
Plasma Radius, a	5 m
Major Radius, R_o	13 m
Axial Toroidal Magnetic Field, B_T°	3.57 T
Plasma Volume	6415 m^3
Energy Content of Plasma	2.95 GJ
Ion Temperature, T_i	13.2 keV
Electron Temperature, T_e	12.0 keV
Electron Density, n_e	$7.71 \times 10^{13}/cm^3$
Ion Density, n_{D+T}	$7.33 \times 10^{13}/cm^3$
Alpha Density, n_α	$1.87 \times 10^{12}/cm^3$
Particle Confinement Time,* τ_p	8.28 s
Energy Confinement Time,* τ_E	3.64 s
$n_e \tau_E$	2.8×10^{14} s-cm^{-3}
Fractional Burnup, f_b	4.85%

*Based on Trapped Particle Mode Estimates of the Diffusion Coefficient and Thermal Conductivity

Table II-B-4

Power Parameters for UWMAK-II

Total Energy Per Fusion	21.56 MeV
Thermal Power During Plasma Burn	5000 MW(th)
Average Power Density in Plasma	0.78 MW/m^3
14 MeV Neutron Wall Loading	1.16 MW/m^2
Surface Heat Loading	0.0367 MW/m^2
Power to Divertor	713 MW

Table II-B-5

Fueling Parameters for UWMAK-II

Tritium Consumption Rate	0.624 kg/d
Deuterium Consumption Rate	0.416 kg/d
Particle Leakage Rate (D + T + α)	5.82×10^{22}/s
Fueling Rates	
Tritium	12.85 kg/d
Deuterium	8.57 kg/d

References for Section II-B-3

1. D. G. McAlees and R. W. Conn, Nuclear Fusion 13, 419 (1974).

2. S. Yoshikawa, Phys. Fluids 13 (1970) 2300. Also, L. A. Artsimovich, Sov. Phys. JETP Lett. 13 (1971) 70.

3. M. N. Rosenbluth, R. D. Hazeltine, F. L. Hinton, Phys. Fluids 15 (1972) 116.

4. L. A. Berry et al., "Plasma Confinement in the ORMAK Device", Paper CN-33/A5-2, Fifth IAEA Conf on Plasma Phys. and Controlled Nucl. Fusion Research (1974). to be published.

5. S. O. Dean et al., "Status and Objectives of Tokamak Systems for Fusion Research", WASH-1295 (U.S.A.E.C., 1974).

6. J. M. Dawson, H. P. Furth and F. H. Tenney, Phys. Rev. Lett. 26, 1156 (1971).

7. D. G. McAlees and H. K. Forsen, Bull. Amer. Phys. Soc. 18, 1305 (1973).

8. T. F. Yang et al., "The Calculation and Parametric Study of Synchrotron Radiation Loss for Tokamak Reactors", (FDM-49, Nucl. Eng. Dept., Univ. of Wis., July 1973).

9. A. P. Vasil'ev, G. G. Dolgov-Savel'ov, and V. I. Kogan, Nucl. Fusion Suppl. Pt. 2, 655 (1962).

10. G. Hopkins, "Impurity Radiation Loss Mechanism from Fusion Reactor Plasmas", (G-A-A12374, Gulf Gen. At. Co., Oct. 1972).

11. R. F. Post, J. Nucl. Energy (Part C, Plasma Physics) 3, 273 (1961).

12. E. Hinnov, Matt 777 (1970); Plasma Physics 14, 755 (1972).

13. D. F. Duchs, H. P. Furth, P. H. Rutherford, in Plasma Physics and Controlled Nuclear Fusion Research (Fourth IAEA Conf., Madison 1971) Vol. II, p. 425.

14. J. T. Hogan, R. A. Dory, Fifth Eur. Conf. on Cont. Fusion and Plasma Physics (Grenoble, 1972) Vol. II, p. 233.

15. J. T. Hogan, D. G. McAlees, private communication.

16. S. T. Butler, M. J. Buckingham, Phys. Rev. 126, 7 (1962).

17 T. Stix, Plasma Physics 14, 367 (1972).

18. R. W. Conn, J. Kesner, "The Potential of Driven Tokamaks as Thermonuclear Reactors", to be published in Nuclear Fusion. See also, UWFDM-106, Nucl. Eng. Dept., Univ. of Wis. (June 1974).

19. G. G. Kelley, Nucl. Fus. 12, 169 (1972). See also, T. Jernigan et al., in Proc. 1st Topical Meeting on Tech. of Cont. Nucl. Fusion (CONF-740402-P1, USAEC, San Diego, 1974) Vol. I, p. 365.

20. A. C. Riviere, Nucl. Fus. 11, 363 (1971).

21. R. W. Moir, Proc. 1st Top. Meet. on Tech. of Cont. Nucl. Fus. (CONF-740402-P1, USAEC) Vol. I, 0. 432

22. K. H. Berkner et al., ibid., p. 392.

23. B. Badger et al., "UWMAK-I, A Wisconsin Tokamak Reactor Design", UWFDM-68, Nucl. Eng. Dept., Univ. of Wis. (Nov. 1973). Chapter II, Sect. D.

24. S. L. Gralnick, Nucl. Fus. 13, 703 (1973).

25. J. Hogan, D. McAlees, ORNL (private communication).

II-B-4. Divertor Operation and Magnetic Field Design for UWMAK-II

a. General Considerations

The UWMAK-II design incorporates a double-null poloidal divertor to "divert" charged particles diffusing out of the plasma away from the first wall. These particles are guided along magnetic field lines to special particle collectors. By this method, one hopes to reduce the erosion of the first wall caused by charged particle bombardment. In turn, this reduces the amount of high Z impurities[1] entering the plasma. As discussed earlier, a small admixture (e.g., .1% Mo or 5% C) can greatly increase the atomic radiation emitted, as discussed in the preceding section, as well as increase the plasma resistivity. This latter effect means more volt-seconds are required from the transformer to maintain the plasma current. Through the resistivity change and radiation cooling, impurities also affect the plasma current profile and the MHD stability properties of the plasma. With a divertor, one hopes to avoid these problems. If the neutral pressure in the zone between the plasma edge and the first wall (the scrape-off zone) is low enough, a secondary benefit of the divertor is to act as a thermal insulator between the plasma and the first wall. This reduces the temperature gradient and thus thermal conduction in the main body of the plasma and results in a higher average power density for a given on-axis plasma pressure, all other factors being equal.

A concept related to a divertor is that of a magnetic limiter which is essentially a divertor without provision for particle collectors. In this concept, one uses the magnetic separatrix to provide a plasma boundary removed from material walls. This separatrix is provided by the interaction of the plasma current with external currents. With proper programming of the external currents, it is conceivable that the discharge can be initiated at a multipole magnetic axis in the center of the chamber. This plasma is small initially and can be allowed to expand in a controlled manner during the current rise in such a way as to avoid skin currents and maintain reasonable values of the MHD stability factor, q. If this proves practical, one can then avoid the impurities produced when the discharge initiates at a metallic limiter. There is no fundamental reason why this can't be done with a poloidal divertor as well. The additional complication is that of keeping the diverted field lines tied to the particle collectors while the plasma and divertor currents are changing. This is more difficult in reactor size plasmas where the blanket and shielding requirements prevent the coils from being close to the collectors.

Toroidal divertors have been used on stellarators[3] and a poloidal divertor[4] is in use on the FM-1 spherator at Princeton. A poloidal divertor has been incorporated in the DIVA[5,6] Tokamak which has just gone into operation at JAERI in Tokai, Japan. A sizeable Tokamak experiment (PDX)[7] designed to study poloidal divertors is under construction at Princeton Plasma Physics Laboratory and a bundle divertor[8] is being incorporated in the DITE Tokamak being constructed at Culham Laboratory. Schematics of various divertor types are shown in Figure II-B-12.

Figure II-B-12

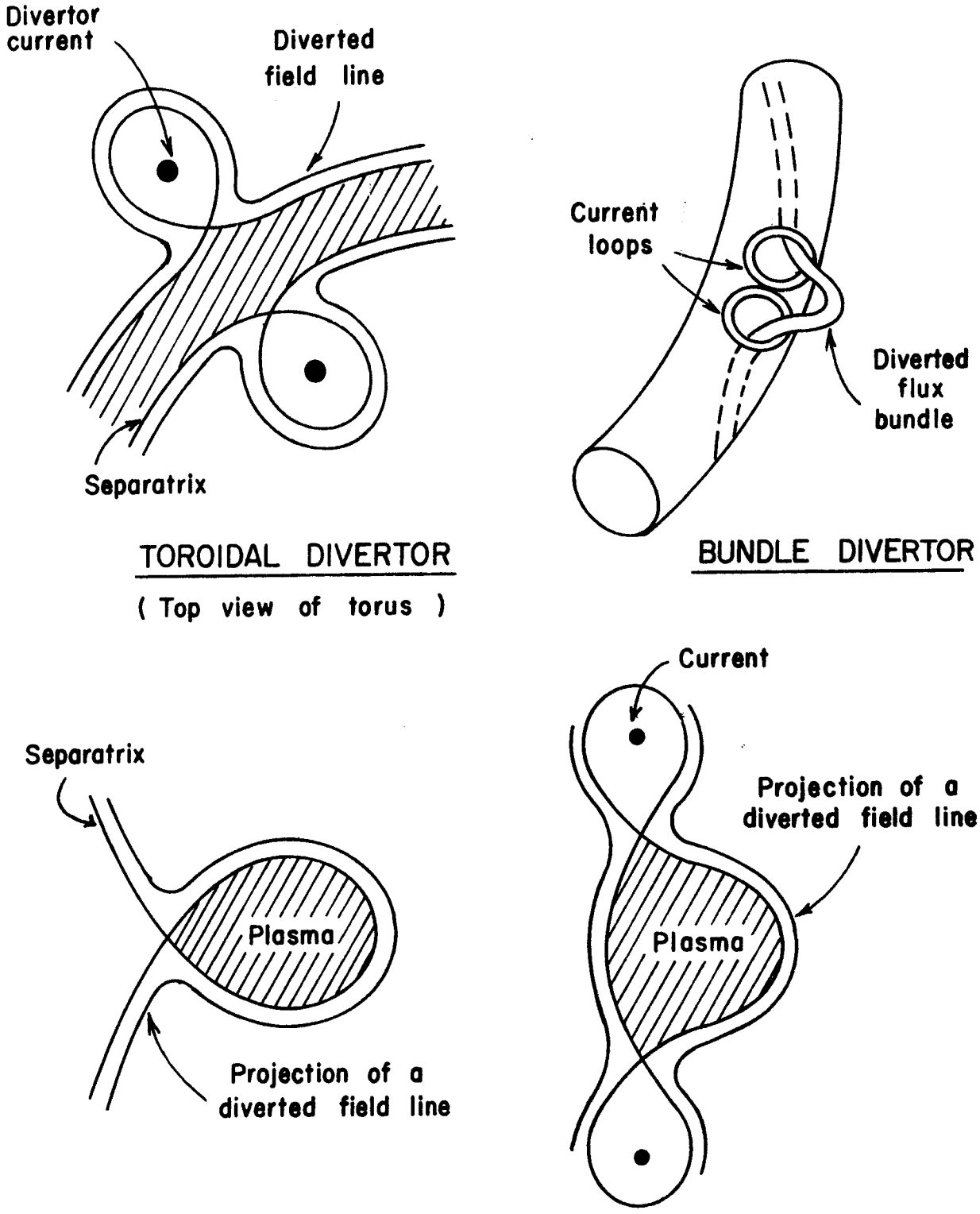

POLOIDAL DIVERTOR

(CROSS-SECTION OF TORUS)

The function of a divertor is clear and the magnetic field design is straightforward but its suitability and effectiveness has not yet been established. This is because the physics involved in the operation of a divertor and its effect on the plasma is inadequately understood and experimental results are still rather limited. We have incorporated a divertor into UWMAK-II in order to study the technological feasibility of divertors in reactor size tokamaks and their interaction with the rest of the system. We are in effect assuming, at least for the time being, that they will prove to be satisfactory from a physics point of view. We are involved in an ongoing theoretical study of the plasma physics of the divertors and some aspects of these studies, namely impurity diffusion, were discussed in Section II-A-5.

The divertor for UWMAK-II is a double-null poloidal divertor similar in principle to that in our UWMAK-I[9] design. However, there are some significant differences, particularly in the location of the divertor coils and the particle collectors. The UWMAK-II divertor (shown in Fig. II-B-13) uses superconducting coils inside the toroidal field magnets to generate the divertor magnetic field. This change was made to reduce the divertor currents and the stored magnetic energy in the poloidal field. In this configuration, the divertor and toroidal field coils are interlocking toruses which cannot be disassembled without destroying the divertor coils. Consequently, they must be designed to have a very high reliability. This is discussed in Chapter III.

The particle collectors have been placed in a more remote location in close proximity to the vacuum pumps. This is done to improve the flow conductance from the collector region to the vacuum pumps and has the effect of reducing the backstreaming of neutral particles (fuel and impurities) to the plasma.

Because of the use of trapped particle, rather than pseudoclassical, scaling to estimate the particle and energy confinement time (see Sec. II-A-2 and II-B-2), the particle and energy flux to the divertor is quite high in UWMAK-II. This high particle flux (or gas throughout) requires high vacuum pumping capacity and necessitates the placement of the pumps inside the toroidal field magnets to obtain the necessary flow conductance. In UWMAK-II, the heat load to the particle collectors is beyond the capability of the simple flowing lithium system used in UWMAK-I. This system has been revised to take a higher heat load but it is not a satisfactory design. Particle collection in divertors on reactor plasmas presents a technological challenge which has not yet been adequately met. Pumping and collectors are discussed in Section II-C.

b. Magnetic Field Design

The magnetic field of the plasma current and the divertor is obtained as a superposition of the magnetic fields from circular filaments. The centers of the filaments all lie on the major axis and the filaments themselves are parallel to the equatorial plane of the plasma. The magnetic field of a filamentary current is known analytically in terms of elliptic integrals. The computer code[10] approximates the elliptic integrals using Hasting's

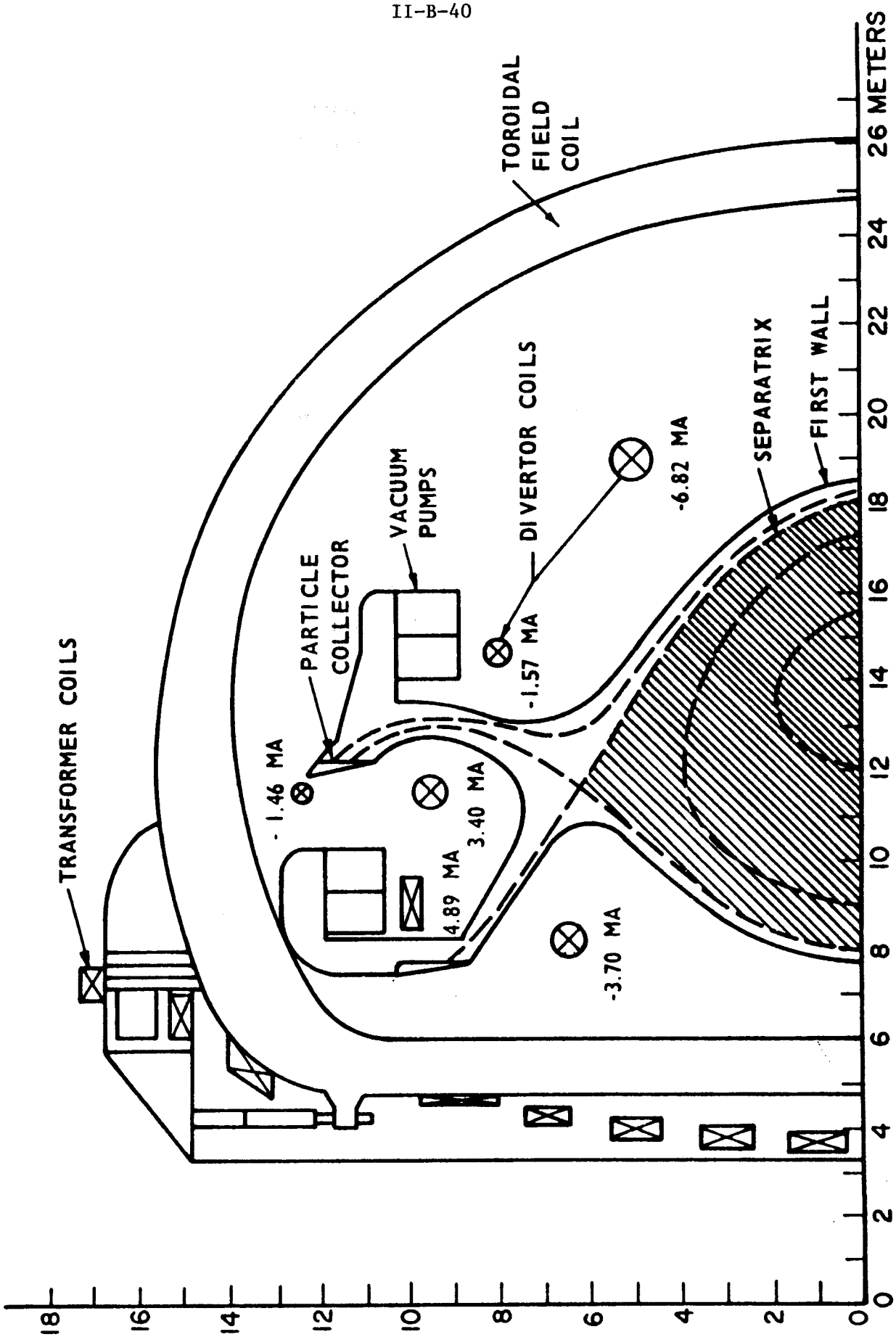

Figure II-B-13

approximation. The use of filamentary loops to represent fields from finite size currents is considered very accurate as long as one is several coil cross sectional radii away from the coil of interest. The plasma current is represented as a filamentary loop placed between the magnetic axis, R_m, and the center, R_ψ, of the last ψ surface of the equivalent circular torus. This is based on the computer calculations by Callen and Dory[11] for Tokamak equilibria with $\beta_\theta \gtrsim 1$. Precisely where in the interval (R_ψ, R_m) the current is placed is arbitrary. The distance $\Delta = R_m - R_\psi$ is given by [12]

$$\Delta = \frac{a^2}{2R}\left[\bar{\beta}_\theta + \frac{l_i}{2} - \frac{1}{2}\right] \tag{1}$$

$$l_i = \frac{1}{\pi a^2 B_\theta^2(a)} \int_0^a B_\theta^2(r)\, 2\pi r dr$$

$$\bar{\beta}_\theta = \frac{2\mu_o}{\pi a^2 B_\theta^2(a)} \int_0^a 2\pi r p(r) dr$$

where R and a are the major and minor radii, respectively, of the equivalent circular torus. Equation (1) is valid only for $\beta_\theta < 1$. There exist similar results[12] for $\beta_\theta \sim A$ which differ from (1) by a factor which depends on the pressure profile, but is of order unity.

The position and magnitude of the external currents are varied to produce a magnetic flux configuration of "reasonable" shape subject to the following constraints:

(1) The volume within the separatrix must be that determined by the plasma physics calculations. (Section II-B-3)

(2) The vertical field at the location of the plasma current filament is the correct value for radial equilibrium of the plasma column[12];

$$B_\perp = \frac{\mu_o I_\phi}{4\pi R}\left(\ln\left(\frac{8R}{a}\right) + \frac{l_i}{2} + \bar{\beta}_\theta - \frac{3}{2}\right). \tag{2}$$

(3) The decay index of the vertical field at the plasma current filament location is in the range required for vertical and radial stability of the plasma, namely[13],

$$0 < -\frac{R}{B_\perp}\frac{\partial B_\perp}{\partial B} < .42 \tag{3}$$

One would like to satisfy the equation (3) over the entire cross section of the plasma. However, it does not seem to be possible to do this and also have a divertor.

It should be noted that equations (1), (2) and (3) are based on the assumptions of low $\bar{\beta}_\theta$, large aspect ratio, and round cross sections. These conditions are not satisfied by the plasma considered here, but nothing else is available in the present state of the theory. Furthermore, since the toroidal current, which is a distributed current, is simulated by a single filament, the resulting magnetic flux configuration is not consistent with the pressure balance equation,

$$\vec{j} \times \vec{B} = \nabla p \qquad (4)$$

In principle, one can design the divertor magnetic field consistent with equation (4), but the calculation is considerably more complicated. It is felt that these more complicated calculations will not change the divertor currents enough to seriously modify the basic characteristics and feasibility of the divertor. The more important and much more difficult question of MHD stability of a Tokamak plasma with a poloidal divertor has not yet been investigated.

The magnetic flux plot for the UWMAK-II divertor and its relationship to neighboring hardware (first wall, collectors, TF coils, etc.) is shown in Fig. II-B-13. The divertor coil currents and locations are given in Table II-B-7 R is the major radius of the coil and Z is its distance above the equatorial plane.

Table II-B-7

UWMAK-II Divertor Currents

R(m)	Z(m)	I(MA)
8.2	±6.5	-3.70
14.6	±8.0	-1.57
8.8	±10.0	+4.89
11.5	±9.5	+3.40
11.5	±12.3	-1.46
19.0	±5.0	-6.82

c. Estimates of the Divertor Performance in UWMAK-II

In earlier work,[9] we proposed a simple transport model for charged particles in the scrape-off zone. We considered neoclassical and Bohm diffusion as two extremes for cross-field diffusion. For flow parallel to the magnetic field, we considered classical mirror confinement in one limit and free-streaming

of the particles with a sheath at the collectors (to have $\Gamma_{//i} = \Gamma_{//e}$) in the other limit. These four combinations gave divertor efficiencies which ranged from miserable to excellent. Since then we have examined more carefully the physics involved to narrow the choice and obtain a better estimate of the divertor efficiency.

Plasma enters the scrape-off zone by cross-field diffusion from the plasma core and leaves primarily by following along the field lines to the collection region. The mean thickness characterizing the plasma density "drop-off" perpendicular to the field lines is determined by a balance between the cross field diffusion with coefficient $D_\perp$ and the parallel flow to the collectors on a time scale $\tau_{//}$.[14] For the model of a poloidal divertor which we consider here this thickness is given approximately by

$$\lambda \sim \sqrt{D_\perp \tau_{//}} \quad .$$

For the purposes of this note $D_\perp$ (in the divertor region) will be taken to be some fraction of the Bohm value

$$D_\perp = \frac{1}{16} \frac{kTe}{eB}$$

This choice reflects a belief, substantiated by some experimental observations,[15] that low frequency turbulence (say drift waves) may be present in the divertor and this causes the Bohm type scaling of $D_\perp$. With this choice for $D_\perp$ one needs to ascertain what $\tau_{//}$ might be. The low frequency turbulence will not effect $\tau_{//}$ because all except the short wavelength (compared to the ion gyro-radius) forms of these waves cannot change the magnetic moment of the particle. Therefore, particle collisions and/or high frequency turbulence ($\omega \geq \Omega_i$ instabilities) will determine parallel transport times.

Since the distance plasma must flow along field lines to reach the divertor collector region is quite long (2m to 10m in possible next generation devices, ~50m in future large scale fusion reactors), a low limit on $\tau_{//}$ is the time it takes the plasma to flow there at the ion speed

$$(\tau_{//})\text{min} \sim L/v_s$$

where L is the mean distance to be traveled to the collector plates and $v_s \simeq (\max (T_e, T_i)/m_i)^{1/2}$. For illustrative purposes, we consider two numerical examples:

1. a next generation tokamak divertor,
and 2. a fusion power reactor.

One notes that for the case 1, $\lambda_{\text{min}} \sim \sqrt{D_\perp (\tau_{//})_{\text{min}}} \sim 1/2$ cm; for case 2, $\lambda_{\text{min}} \sim 2$ cm.

The poloidal configurations considered in this note with reference to Fig. II-B-13, can be seen to be ones in which the plasma once in the (outer) divertor region must move into a higher magnetic field ($B \sim 1/R$) before it can reach the collectors. In these cases, there may be some magnetic confinement as in a mirror machine. The magnetic mirror ratio is less than 2:1 along the field

line so one has a fairly weak mirror. One sees that at least half the plasma in the scrape-off region would not be "trapped" by the mirror; it would flow out in a time $(\tau_{//})_{min}$. The maximum time that the remaining mirror-confined plasma could be trapped would be on the order of the 90° scatter time[16] for ions to be scattered into the loss cone:

$$(\tau_{//})_{max} \sim \tau_{//} \sim \frac{3\times10^{-3} A^{1/2} (T_i/1\ \text{keV})^{3/2}}{[n_e/10^{13}\text{cm}^{-3}]Z^3}\ \text{sec.}$$

As can be seen from $\lambda \sim \sqrt{D_\perp \tau_{//}}$ the density drop-off thickness can vary by as much as a factor of $\sqrt{(\tau_{//})_{max}/(\tau_{//})_{min}} \sim 10$ (case 1) and ~ 100 (case 2), depending upon what is the appropriate parallel flow time.

In addition to the classical processes discussed above, plasma instabilities can decrease the minimum flow time. Specifically, since the mirror-confined plasma has a loss-cone, it is susceptible to all the usual loss-cone driven microinstabilities.[17] The four most important loss-cone driven instabilities[17] for this case are: (1) the Post-Rosenbluth convective loss-cone instability[18]; (2) the absolute loss-cone instabilities[19]; (3) the negative energy loss-cone modes[20]; and (4) the drift-cone modes.[21] Before discussing these modes in detail, one needs to estimate some parameters of this mirror-confined plasma. First, one needs to know the ratio of the ion gyro-radius, ρ_i, to the plasma inhomogeneity scale lengths. For case 1, $\rho_i \sim .13$cm and case 2, $\rho_i \sim .70$ cm. Thus, it appears that the scrape off thickness is from 4 (case 1) to 3 (case 2) ion gyroradii in width. The characteristic inhomogeneity scale length along a magnetic field line is $L_{\nabla B} \sim 3000$ cm. Therefore, $L_{\nabla B}/\rho_i \sim 3800$ for case 1 and 4300 for case 2. This is essentially an infinite, homogeneous plasma for loss-cone instability calculations where

$$\lambda_{//} \sim \rho_i \sqrt{\frac{m_i}{m_e}} \sim (40\text{-}60)\rho_i.$$

The last three of the four loss-cone instabilities listed above are standing wave (or absolute) modes that are typically found to be radially localized within a few gyroradii. The drift-cone mode[21] has been shown to be unstable for radial scale lengths as short as one or two ion gyroradii[22]. The negative energy modes are finite medium forms of the absolute loss-cone and drift-cone modes[17], which are most easily derived in infinite medium theory. In general, for $L >> \lambda_{//}$, as appears to be the case here, these standing instabilities were all unstable for $\omega_{pi} \geq \Omega_i$, (i.e. $n_i > 1.3 \times 10^{10}$ cm^{-3} @ B = 25 kG) where ω_{pi} is the ion plasma frequency and Ω_i is the ion gyro frequency. (These modes generally require $T_{//e} < T_{\perp i}$, which seems reasonable to expect; however n_i may drop below a few 10^{10} cm^{-3} if the above instabilities begin to appear and affect $\tau_{//}$. Thus these modes may stabilize somewhere between the separatrix and the wall.) When this density threshold is exceeded, the mode growth rates range from a few percent (for absolute loss-cone modes) to large fractions (for drift-cone modes) of the ion gyrofrequency. The nonlinear consequences of the modes are apparently to enhance the pitch angle scattering

which causes the loss-cone to be filled in, on a time scale of a few growth times.[23] If one presumes a growth rate of 0.01 Ω_i and requires 10 growth times for significant effects, then the loss-cone fill-in time is $\tau_{inst} \sim 10^3 \Omega_i^{-1} \sim 5$ to 10 μsec. For the divertor scrape off region considered here $\tau_{inst} << (\tau_{//})_{min}$. This indicates that the instability could cause sufficient scattering to keep the loss-cone filled with particles and thus make $\tau_{//}$ only a few times $(\tau_{//})_{min}$, at most.

In addition to the standing wave modes discussed in the preceding paragraph there are the convective loss-cone instabilities, which can give rise to significantly enhanced ("quasi-classical") scattering[24] into the loss cone by virtue of the long range polarization fields of the ions in the convectively unstable plasma. The polarization fields around individual "test" ions extend only a few Debye lengths ($\lambda_D << \rho_i$) perpendicular to the field line, but they extend all the way to the mirror "throat" region along the field lines, i.e., in essence we have a zero of the parallel dielectric coefficient. For the divertor scrape off region where we expect $\omega_{pe} < \Omega_e$ (i.e., $n_i < 6 \times 10^{13} cm^{-3}$ for case 1; $n_i < 9 \times 10^{13} cm^{-3}$ for case 2) and a fairly sharp loss cone, the effective collision frequency for scattering into the loss cone is given approximately by[24]

$$\nu_{eff} \simeq \frac{1}{\tau_{ii}} \left(\frac{T_i}{T_e}\right)^{3/2} \left(\frac{m_e}{m_i}\right)^{1/2} \frac{\exp(2 \operatorname{Im} k\, L)}{\operatorname{Im} k_{//} L \ln\Lambda}$$

where

$$\operatorname{Im} k_{//} \sim \frac{0.1}{\rho_i} \frac{\omega_{pe}}{\Omega_e} cm^{-1} \sim 9.5 \left(\frac{m_e}{m_i}\right)^{1/2} \left(\frac{n/10^{13} cm^{-3}}{T_i / 1\ keV}\right)^{1/2} cm^{-1}.$$

For the parameters used above one finds for case 1 ($\operatorname{Im} k_{//} = .24\ cm^{-1}$, $\omega_{pe} \sim .3\Omega_e$, $L_{\nabla B} \simeq 500$ cm), $\nu_{eff}\tau_{ii} \sim 10^{100}$, and for case 2 ($\operatorname{Im} k_{//} = .01\ cm^{-1}$, $\omega_{pe} \sim .1\Omega_e$, $L_{\nabla B} \simeq 3000$ cm), $\nu_{eff}\tau_{ii} \sim 10^{21}$.

These are absurbly large because L is long and the parallel growth length is on the order of a few hundredths of $L_{\nabla B}$ in both cases. In such a situation, one expects[24] ν_{eff} to be no larger than the ion bounce frequency $\omega_{bi} \sim v_{Ti}/L_{\nabla B}$, since otherwise the instability is filling the loss-cone before the plasma even knows it has one. We thus conclude for the divertor scrape-off region that $\tau_{//} \sim \omega_{bi}^{-1} \sim L/v_{Ti}$ which is equal to $\tau_{//min}$ to within a factor of $\sqrt{\max(T_e, T_i)/T_i}$.

The derivations of the loss-cone driven modes in mirror confined plasmas[17,22,24] have not taken shear into account, since it is unimportant in open-ended systems. However, in tokamaks the magnetic field is sheared in the minor radius direction, with a typical scale length

$$\frac{1}{L_s} \sim \frac{1}{qR_o} \frac{r}{q} \frac{\partial q}{\partial r} \lesssim \frac{1}{10r}$$

and it is worth considering the effects of shear on these modes. The effective parallel wavelength of a mode in a sheared magnetic field is given by[25]

$$k_{\parallel} \simeq k_z + k_y \frac{x}{L_s}$$

where k_y, k_z are the local y,z components of the wave propogation and x is the distance from the surface investigated. For a mode radially localized to a width δx, the effective $k_{\parallel}$ over the region of interest is

$$k_{\parallel} \sim k_z[1 + \frac{k_y \delta x}{k_z L_s}].$$

For the microinstabilities discussed above

$$\delta x \gtrsim \rho_i \sqrt{m_i/m_e} > k_y \rho_i > 1 \text{ and } k_z L_s \sim \frac{L_s}{40\rho_i} .$$

Thus, for a typical shear length of say 1000 cm, the effect of shear on the effective parallel wavelength is quite small. It should be noted that if, in addition to the shear, there was significant fanning of the magnetic field lines as in the minimum-B mirror systems, then these loss-cone driven instabilities might be more significantly affected by the magnetic topology[26]. Shear may also affect $D_{\perp}$.[27]

To summarize the above, we have found that while the scrape-off region in a divertor may appear to contain a mirror-confined plasma, the plasma so confined seems to be unstable to a large variety of microinstabilities driven by the free energy associated with the loss-cone distribution. The net result of the instabilities would apparently be to reduce the expected $\tau_{\parallel\,max} \sim \tau_{ii}$ down to very close to the free flow value of L/v_s. Thus, the best estimate of the parallel flow time is probably $\tau_{\parallel} \sim \tau_{\parallel\,min}$, which implies a relatively thin density "drop off" thickness of only a few centimeters or less.[28]

The effectiveness of the UWMAK-II divertor can now be estimated. The e-folding distance for the decay of the cross-field particle flux and the density is given by

$$\lambda \simeq \sqrt{\frac{D_{\perp} L}{v_s}}$$

where

$$v_s \simeq \sqrt{\frac{T}{m_i}} , \quad L \simeq \frac{\pi}{2} Rq$$

For $D_\perp = 1/50\ D_{Bohm}$ and $T \simeq 10$ keV, we get $\lambda \simeq 2$ cm. Under these conditions, the particle flux at the wall is $\sim 10^{-11}$ of the flux crossing the separatrix. If we had assumed a lower temperature in the scrape-off zone, then the efficiency would be even better. A more pessimistic choice for $D_\perp$ would be $D_\perp = D_{Bohm}$. Using $T \simeq 10$ keV, this gives $\lambda \sim 14$ cm and $\Gamma_{wall} \cong 1/30\ \Gamma_{separatrix}$. We have so far assumed that the length L along the field lines to the collectors is a constant. In fact, however, it is infinite on the separatrix and decreases rapidly to a uniform value about equal to the estimate above. This is shown in Fig. II-B-14. The effect of the variation of L is to reduce the effective scrape-off zone thickness from 50 cm to ~45 cm, which is inconsequential. An unfortunate side effect of λ being small is that the heat load on the collectors is very nonuniform. The difficulties posed by this are given in Sec. II-B-6.

The above analysis also assumes a uniform electron temperature in the scrape-off zone. In actuality, there is a sheath at the collectors which reflects low energy electrons and admits only high energy electrons in order to maintain neutrality in the plasma. This causes the electrons to be cooled since the energy flow to the collectors is then greater than $3/2\ T_e\ \Gamma_{||}$. The reduction of T_e with x causes $D_\perp$ to drop and shortens the e-folding length λ. The effect of this is to reduce even further the particle flux at the wall.

We can now estimate the ability of the divertor to "screen" entering neutral impurity atoms from the plasma core. From eqn 20 of Chapter II-A-5, $n_s/n_o \simeq 1/20$. Consequently, the scrape-off zone plasma has a density of $\sim 5 \times 10^{12} cm^{-3}$ at the separatrix amd decays exponentially in x with scale length $\lambda \sim 2$-3 cm. We can approximate this by a linear density profile with density gradient

$$\frac{dn}{dx} \simeq \frac{n_s}{\lambda} \simeq 2 \times 10^{12} cm^{-4}$$

From the results of Section II-A-5, the fraction f_N of neutrals ionized before reaching the separatrix is

$$f_N = 1 - \frac{I_N}{I_N^o} = 1 - e^{-\mu\lambda^2} \cong \mu\lambda^2$$

where $\mu = \frac{\sigma}{2} \frac{dn}{dx}$. Here σ is an effective total ionization cross section. For 10 eV carbon in a 10 keV plasma, electron-impact ionization dominates and $\sigma \simeq 3 \times 10^{-14} cm^2$. This yields

$$f_N \simeq 10^{-1}$$

about 10% of the neutrals are ionized in the scrape-off zone. Lower electron temperatures reduce f_N slightly.

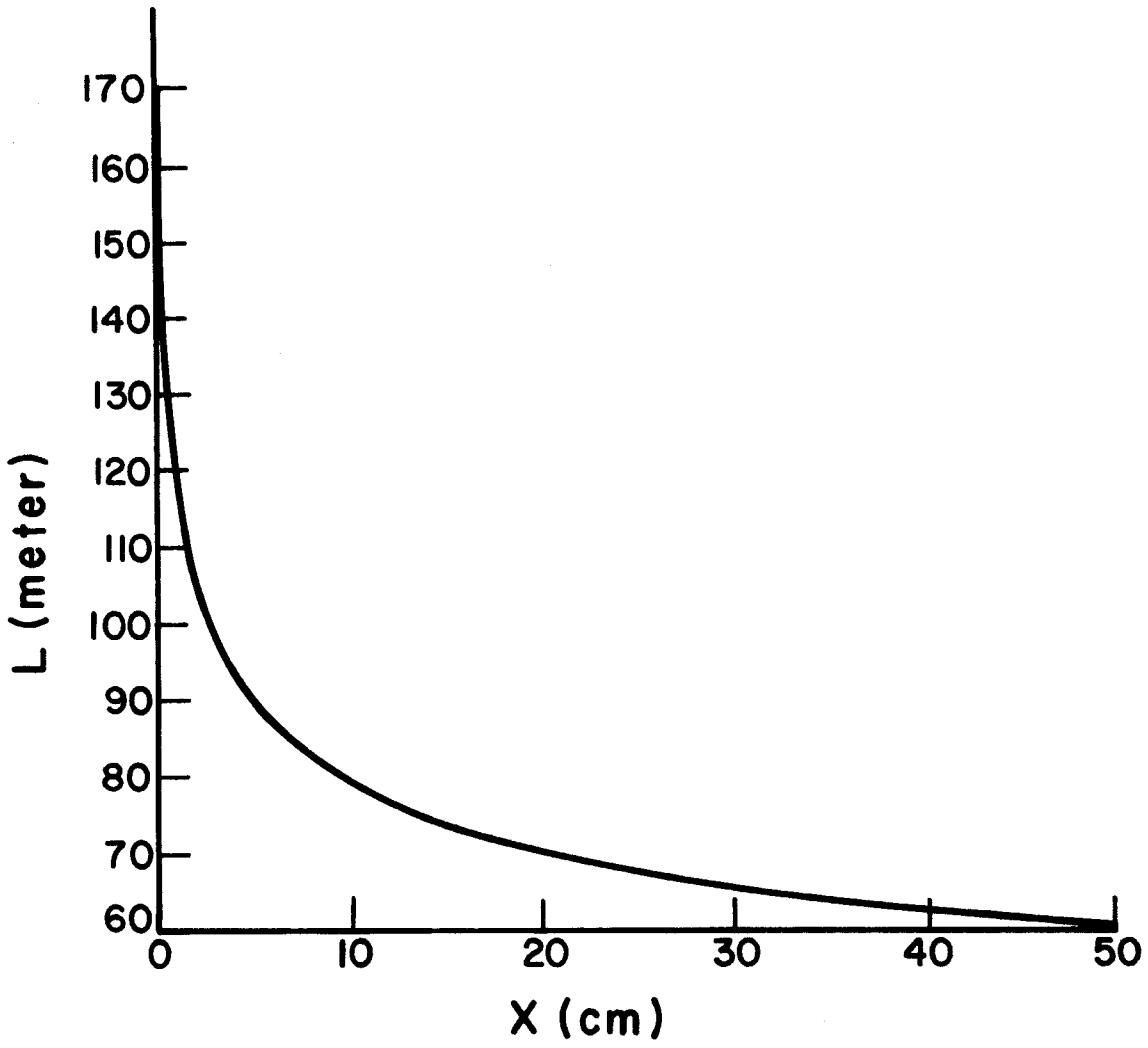

FIGURE II-B-14

We conclude from the above estimates that a lower limit for the fraction of charged particles captured by the particle collectors is 99% (≈1% reach the wall) while only 10%, at best, of the entering neutral impurities are ionized in the scrape-off zone. The divertor is excellent for preventing charged particles from reaching the wall but is useless for "screening" the plasma from neutrals entering from the outside. The one effect neglected in this analysis which might change the capture efficiency is the possibility of charged particles undergoing a charge exchange before reaching the collector. If this happens, a particle has roughly a 50% probability of hitting the wall. Estimating the charge exchange rate requires knowledge of the neutral density in the scrape-off zone. This is essentially unknown because the plasma can "burn out" the neutral density to rather low levels. This effect is under investigation.

d. Preliminary MHD Equilibrium and Stability Studies

As can be noted from Sec.II-B-4b, the initial design of the UWMAK-II plasma cross section was based on rather simple MHD equilibrium results. This was based on the philosophy that, given a desired cross section, one could find the required coil positions and current values to produce it. This is because one is free to position the divertor coils and there are a large number of $[p(\psi), g(\psi)]$ functional forms to choose from. To review briefly,[11,29] in order to be in equilibrium, the plasma must possess surfaces, (magnetic, current, and pressure) labeled $\psi = \psi(r,z)$, such that ψ is a solution to the force balance equation for an axisymmetric plasma,

$$\Delta^*\psi = r\frac{\partial}{\partial r}\left(\frac{1}{r}\frac{\partial\psi}{\partial r}\right) + \frac{\partial^2\psi}{\partial Z^2} = -2\pi r\mu_o J_\phi = -2\pi r\mu_o\left\{2\pi r\frac{dp}{d\psi} + \frac{2\pi}{r\mu_o}\, g\frac{dg}{d\psi}\right\}. \quad (1)$$

Here, $g = rB_\phi$ and we impose the boundary condition that $\nabla\psi = 0$ at the magnetic axis. Obviously, however, all $p(\psi)$ which describe the pressure and $g(\psi)$ which describe the poloidal plasma current must be of such form as to be bounded and reasonably smooth for physically realizable plasmas. No one has to date found any "one best" functional forms for $p(\psi)$ and $g(\psi)$. Two of the most popular choices are however

$$p(\psi) = p_o\left(1 - \left(\frac{\psi_L - \psi}{\psi_L - \psi_{MA}}\right)^N\right) \quad (2A)$$

and

$$g(\psi) = 1 - g_o\left(\frac{\psi_L - \psi}{\psi_L - \psi_{MA}}\right)^Q \quad (2B)$$

where ψ_L = ψ value at limiter or separatrix ($J_{toroidal} = 0$ for $\psi > \psi_L$)

ψ_{MA} = ψ value at magnetic axis

N,Q = real numbers, not necessarily integers usually taken to be in interval [1,2]

Table II-B-8

Divertor Characteristics

Case I	Case II
Next Generation Device	Reactor
Hydrogen	Mass = 2.5 a mu
B_T = 25 kgauss	B_T = 30.8 kgauss
T_e = .3 keV } Divertor	T_e = 7 keV
T_i = .5 keV } Divertor	T_i = 9 keV
L = 1000 cm	L = 6000 cm
q = 3.6	q = 2.3
R_o = 140 cm	R_o = 1300 cm
a = 45 cm	a = 500 cm
$n = 6\times10^{12}\,cm^{-3}$ (@ separatrix)	$n \simeq 10^{11} - 5\times10^{12}\,cm^{-3}$
$D_\perp = \frac{1}{10} D_{Bohm} = 7.5\times10^{3}\ cm^2/sec.$	$D_\perp = \frac{1}{50} D_{Bohm} = 2.8\times10^{4}\,cm^2/sec$
$(\tau_{//})min$ = 45 μsec	$(\tau_{//})min$ = 100 μsec
$(\tau_{//})max$ = 2 msec	$(\tau_{//})max \simeq$ .3 to 13 sec.
$\lambda_{min} \simeq$ .5 cm	$\lambda_{min} \simeq$ 2 cm
$\rho_i \simeq$ .13 cm	$\rho_i \simeq$ .7 cm
$L_{VB} \sim qk_o \sim 500cm \sim 3900\rho_i$	$L_{VB} \sim qR_o \sim 3000cm \sim 4300\rho_i$
$\omega_{pi} > \Omega_i \Rightarrow n_i > 3.3\times10^{10}\,cm^{-3}$	$\omega_{pi} > \Omega_i \Rightarrow n_i > 2.0\times10^{10}\,cm^{-3}$
$\omega_{pe} < \Omega_e \Rightarrow n_e < 6.1\times10^{13}\,cm^{-3}$	$\omega_{pe} < \Omega_e \Rightarrow n_e < 9.2\times10^{13}\,cm^{-3}$
$\Omega_i = 2.4 \times 10^{8}$ rad./sec	$\Omega_i = 1.18 \times 10^{8}$ rad./sec
f = 38.2 MH_z	f = 18.8 MH_z
$\lambda_{De} \simeq 7 \times 10^{-3}$ cm	$\lambda_{De} \simeq$ .2 to .03 cm
Im $k_{//} \simeq .24\ cm^{-1}$	Im $k_{//} \simeq$ .005 to .033 cm^{-1}

p_o = given usually in some form as an input parameter.

g_o = computed parameter which is found from requiring total toroidal current flowing in the plasma to be a given constant value. (Solved for as part of the iteration scheme in finding ψ)

One can proceed to solve (1) to obtain a self consistent equilibrium plasma configuration in any of several ways. A successive over-relaxation method can be used and has been found to handle low β ($\bar{\beta}_p$ <1) cases adequately. The program using this method is a slight modification of one written by Sheffield[30] at Princeton. Recently, however, initial studies have been conducted on UWMAK-II using a more sophisticated version of the Princeton Code which was entirely redone by R. Grimm and S. Jardin[31]. This code uses a modification of Buneman's DCR method[32] to solve (exactly) the left hand side of (1). Taking the resultant $\psi(r,z)$, and using the assumed functional forms of $p(\psi)$ and $g(\psi)$, the program recomputes j_θ and the problem iterates once again to find $\psi(r,z)$. The process is fairly rapidly convergent. (Equilibrium calculation requires ~2.5 min on UNIVAC 1110, stability adds 3 min. to this time.) Extensive tests are only now underway to determine function sensitivity as to the forms of $p(\psi)$ and $g(\psi)$, etc.

Another advantage afforded us using the Princeton Code is that it can provide some stability information. It essentially does a localized interchange (both ideal and resistive) mode stability analysis computing numerically D_I and D_R which are described by Green, Johnson, et al.[33] If these values are less than 0, the plasma is stable to these modes. The program in addition provides $q(\psi)$, the stability factor, so one can judge whether or not the Kruskal-Shafranov criteria is violated within the plasma or between the plasma and the wall. This provides us with at least the minimum information on kink stability. A good general kink mode analysis is not yet available.

To date, several cases have been run on UWMAK-II and one of these is illustrated in Figures II-B-15, 16 and 17 based on some of the graphical output. This particular data set was chosen (see Table I) to demonstrate the effects of the Pfirsch-Schluter current as the plasma pressure is increased. To contain higher pressures the major radius force balance indicates large vertical fields are required. This B_Z acts opposite to B_θ (due to the plasma) on the inside of the torus ($\theta \to \pi$). Thus the pitch of the field lines decreases on the inside of the torus which requires a larger $J_{||}$ to maintain $\vec{\nabla} \cdot \vec{J} = 0$. This is seen clearly by noting the form of the P-S current $(J_{PS})_\phi \propto \frac{1}{B_\theta} \frac{dp}{dr} \cos\theta$.

The plots of ∇p, $J_\phi \times B_\theta$, $J_\theta \times B_\phi$ in Fig. II-B-16 apply on the Z = 0 plane of the plasma and help to physically explain the nature of the force balance. For example, one sees that the poloidal field holds most of the pressure on the outside of the torus, (the toroidal field must hold some pressure for $\bar{\beta}_p > 1$) while the toroidal field has a more substantial role on the inside. Further studies are underway at this time.

Table II-B-9

Maximum Plasma Pressure	$P_o = 9 \times 10^5$ N/m^2
Total Plasma Current	$I_o = 1.49 \times 10^7$ A
Toroidal Field on Axis	$B_o = 3.57$ T

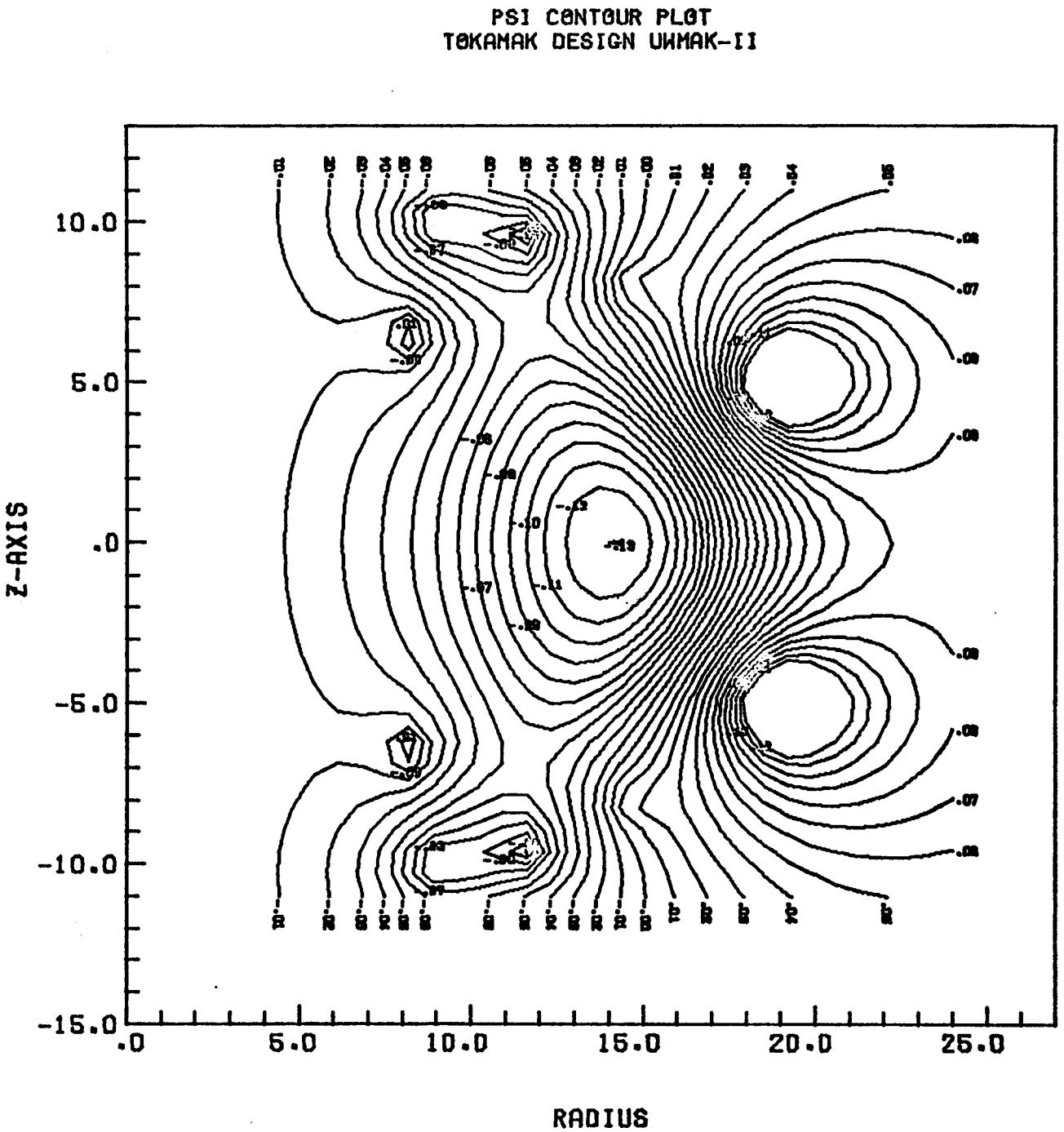

Figure II-B-15

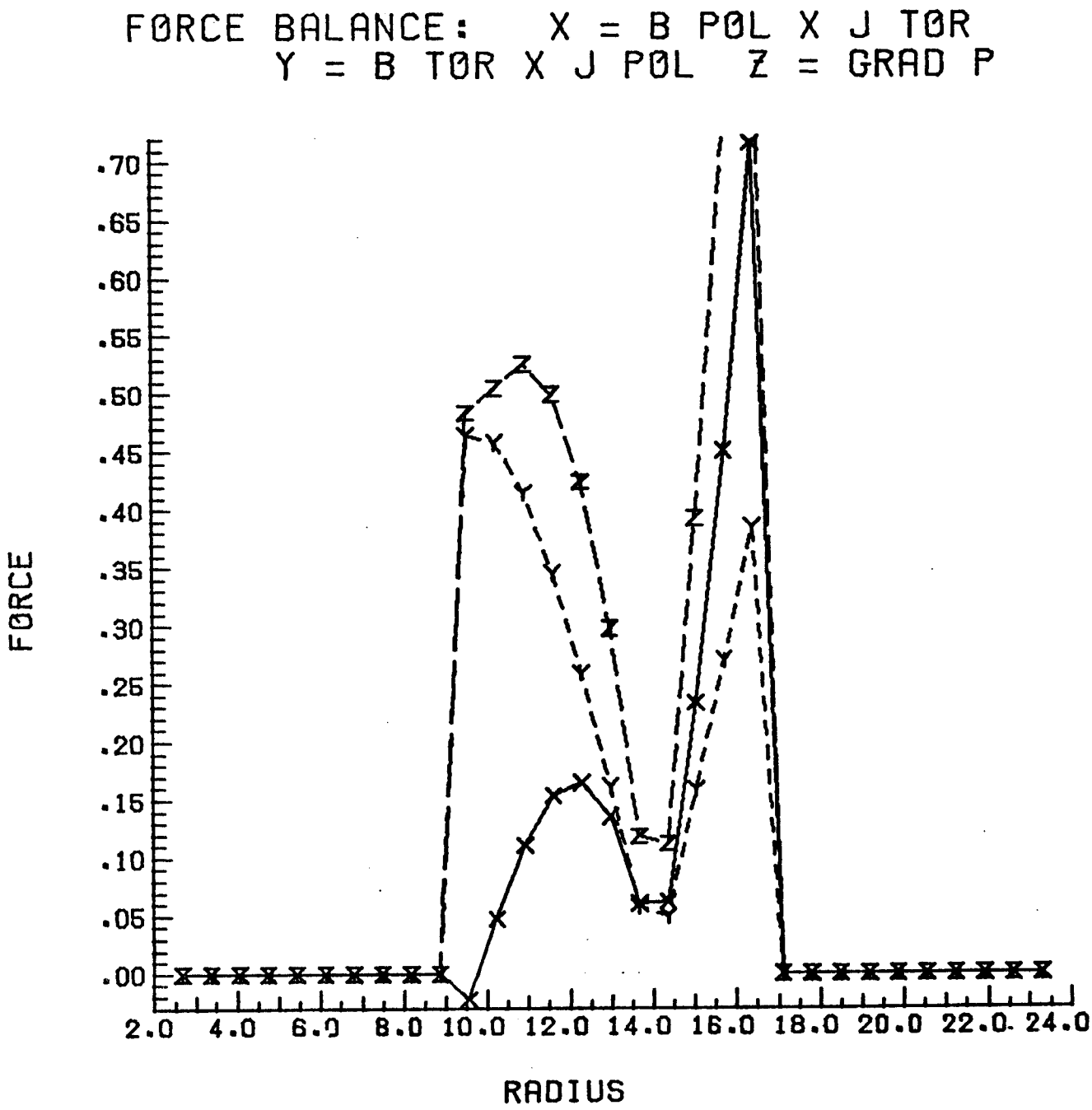

Figure II-B-16

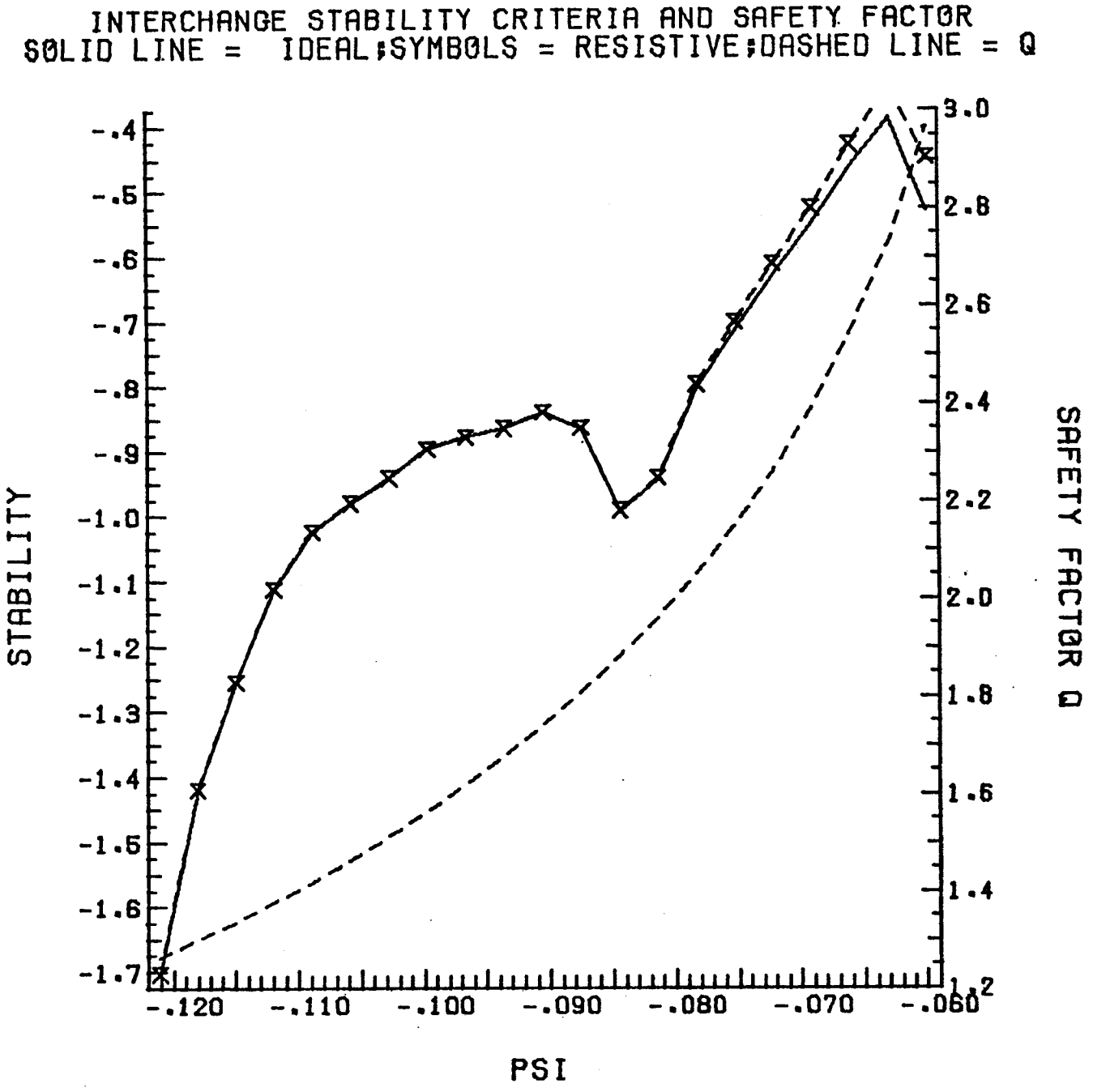

Figure II-B-17

References for Section II-B-4

1. The role of impurities in Tokamak experiments has been reviewed by V. A. Vershkov and S. V. Mirnov, Nuclear Fusion 14, 383 (1974).

2. D. M. Meade, H. P. Furth, P. H. Rutherford, F. G. P. Seidl and D. F. Duchs, 5th IAEA Conf. on Plasma Physics and Controlled Nuclear Fusion Research, Tokyo, 1974. IAEA-CN-33/A15-4.

3. C. R. Burnett et al., Phys. Fluids 1, 438 (1958).

4. K. Ando et al., 5th IAEA Conf. on Plasma Physics and Controlled Nuclear Fusion Research, Tokyo, 1974. IAEA-CN-33/B4-4.

5. A. Kitsunezaki, H. Maeda, Y. Shimomura, M. Yoshikawa, Third International Symposium on Toroidal Plasma Confinement, Garching 1973, paper G-2.

6. M. Yoshikawa et al., 5th IAEA Conf. on Plasma Physics and Controlled Nuclear Fusion Research, Tokyo, 1974. IAEA-CN-33/A1-2

7. PDX, The Poloidal Divertor Experiment, paper #47, Joint Euratom-US Workshop on Large Tokamak Designs, Culham 1974.

8. C. Colven, A. Gibson, P. E. Stott, 5th European Conf. on Controlled Fusion and Plasma Physics, Grenoble, 1972. Vol. I, pg. 6.

9. B. Badger, et al., "Wisconsin Tokamak Reactor Design, UWMAK-I," UWFDM-68, University of Wisconsin, November 1973.

10. The program was furnished to us by Mr. Ufa Christensen of the Princeton Plasma Physics Laboratory.

11. J. D. Callen and R. A. Dory, Phys. Fluids 15, 1523 (1972).

12. V. S. Mukhovatov and V. D. Shafranov, Nuclear Fusion 11, 605, (1972).

13. J. M. Greene, J. L. Johnson and K. E. Weimer, Phys. Fluids 14, 671 (1971).

14. A. T. Mense, G. A. Emmert, Bull. Am. Phys. Soc. 18, 1305 (1973).

15. J. A. Schmidt, private communication about FM-1.

16. S. I. Braginskii, in Reviews of Plasma Physics, Vol. I, p. 215. (consultants Bureau, New York, 1965).

17. For synopses of the modes see: C. W. Horton, Jr., J. D. Callen and M. N. Rosenbluth, Phys. Fluids 14, 2019 (1971), D. E. Baldwin, et al. Plasma Physics and Controlled Fusion Research (IAEA Vienna, 1972), Vol. II, p. 735; J. D. Callen, Ph.D. Thesis, MIT, CST T-68-3 (1968).

18. M. N. Rosenbluth and R. F. Post, Phys. Fluids 8, 547 (1968).

19. J. E. McCune and J. D. Callen, Plasma Physics 12, 305 (1969) and references therin; H. L. Berk, et al. in Plasma Physics and Controlled Fusion Research (IAEA, Vienna) 1968. Vol. II, p. 151; see also ref. 17.

20. H. L. Berk, L. D. Pearlstein, J. D. Callen, C. W. Horton, and M. N. Rosenbluth, Phys. Rev. Let. 22, 876 (1969). See also ref. 17.

21. R. F. Post and M. N. Rosenbluth, Phys. Fluids 9, 730 (1966); A. B. Mikhailovskii, Nuc. Fus. 5, 125 (1965).

22. J. G. Cordey, L. G. Kuo-Petravic, and M. Petravic, Nuc. Fus. 8, 153 (1968); see also ref. 17.

23. See for example: J. A. Byers, M. Grewal, Phys. Fluids 13, 1819 (1970).

24. D. E. Baldwin, J. D. Callen, Phys. Rev. Lett. 28, 1968 (1972).

25. See for example: J. N. Davidson, T. Kammash, Nucl. Fus. 8, 203 (1968).

26. D. E. Baldwin, Phys. Fluids 17, 1346 (1974).

27. Drift waves are sensitively affected by shear, thus the scrape off region may be thinner due to reduction of D .

28. We gratefully acknowledge J. D. Callen (Oak Ridge National Laboratory) As a contributor to the microinstability analysis.

29. A. T. Mense, FDM 71. Nuclear Engineering Dept.; University of Wisconsin, Madison (1973).

30. G. V. Sheffield, Fifth Symposium on Engineering Problems of Fusion Research, Princeton University (1973) p. 350. The Code was kindly provided to us by George Sheffield.

31. Private Communications. Program was developed in part by S. Jardin as Ph.D. dissertation work at Princeton University.

32. See R. W. Hockney, in Methods of Computational Physics, Vol. 9, 1970 p. 155 and references therein.

33. M. S. Chance et al., Matt-1095, IAEAOCN33/A12-4.

II-B-5. Analysis of Losses Due to Toroidal Field Ripple and Determination of the Number of TF Coils on UWMAK-II.

The finite number of coils used to generate the toroidal field of a Tokamak produces a bumpiness or ripple of the magnetic field which in turn causes particles to be trapped between coils in the field ripples and to drift vertically out of the plasma. The bumpiness is illustrated by the magnetic field structure in Fig. II-B-18 of the conceptual design UWMAK-I[1], which has 12 constant-tension "D" shaped toroidal magnetic field coils spaced at 30° intervals. The field line at the outer edge of the plasma column shows that the column is corrugated with a deviation of $\Delta r \approx 0.5$ meter. The amplitude of the ripple is about 20%. Fig. II-B-19 and II-B-20 show the variation of the ripple with the minor radius r and poloidal angle θ. To evaluate the number of toroidal field coils required on UWMAK-II, we have calculated the leakage of α particles trapped in these field ripples. We have also investigated the effect of extending the "D" shaped TF coil on the outside such that there is adequate space between coils for removal of blanket segments without moving the TF coils themselves.

Anderson and Furth[2] have considered the alpha particle loss for a field ripple which has only a radial variation. To include the poloidal angular dependence shown by Figs. II-B-19 and II-B-20 we write

$$B_\phi(r,\theta,\phi) = \frac{B_o}{1 + \frac{r}{R}\cos\theta}\,[1 + \varepsilon(r,\theta)\cos(n\phi)], \qquad (1)$$

where B_ϕ is the true toroidal magnetic field strength, B_o is the mean field on the magnetic axis of major radius R. Here (r,θ,ϕ) are the usual quasi-toroidal coordinates with θ being the poloidal angle. In order to show the variations of ripple with coil number and size, we calculated particle leakage rates when there are 24 TF coils and when the "D" coils have their outer edge extended to larger R. The results are shown by curves II, III and IV in Figs. II-B-19 and II-B-20. A fit to the curves in these figures is

$$\varepsilon(r,\theta) = \varepsilon_a \left(\frac{r}{a}\right)^n \exp\left(-\left(\frac{\alpha\theta}{\pi}\right)^2\right), \qquad (2)$$

where n, ε_a and α are constants determined by a particular design and a is the minor radius of the plasma. For low-β circular Tokamaks, the trajectory of a field line is r=constant, $\phi = \phi_o + q\theta$, where q is the MHD stability factor. The field strength along the field line is

$$B_T(r,\theta,\phi) = \frac{RB_o}{R + r\cos\theta}\,[1 + \varepsilon_a \left(\frac{r}{a}\right)^n \exp\left(-\left(\frac{\alpha\theta}{\pi}\right)^2\right)\cos(Nq\theta + \phi_o)] \qquad (3)$$

neglecting the poloidal field strength. Consider the upper half of the r-θ plane for fixed ϕ_o. Local magnetic wells are produced by the $\cos(Nq\theta + N\phi_o)$ term. These are shown in Fig. II-B-21 for the UWMAK-I design (Number of TF coils = 12, q = 1.75, A = R/a=2.6, ε_a = .20, α = 3.2, n = 3.0). Particles can be trapped in these wells if they have sufficiently large pitch angle relative to the magnetic field. The lower boundary in θ for toroidally trapped particles can be determined from the condition

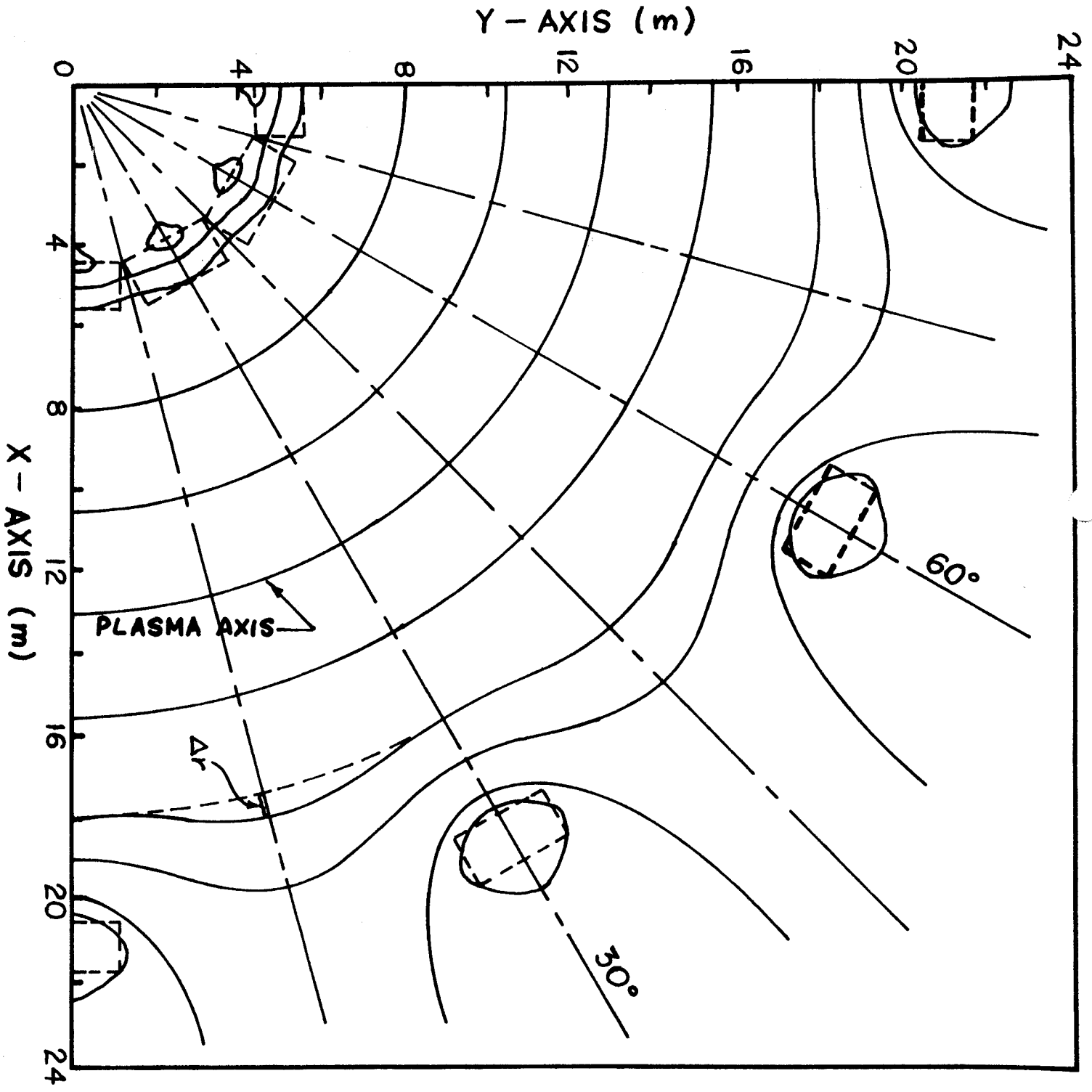

Figure II-B-18

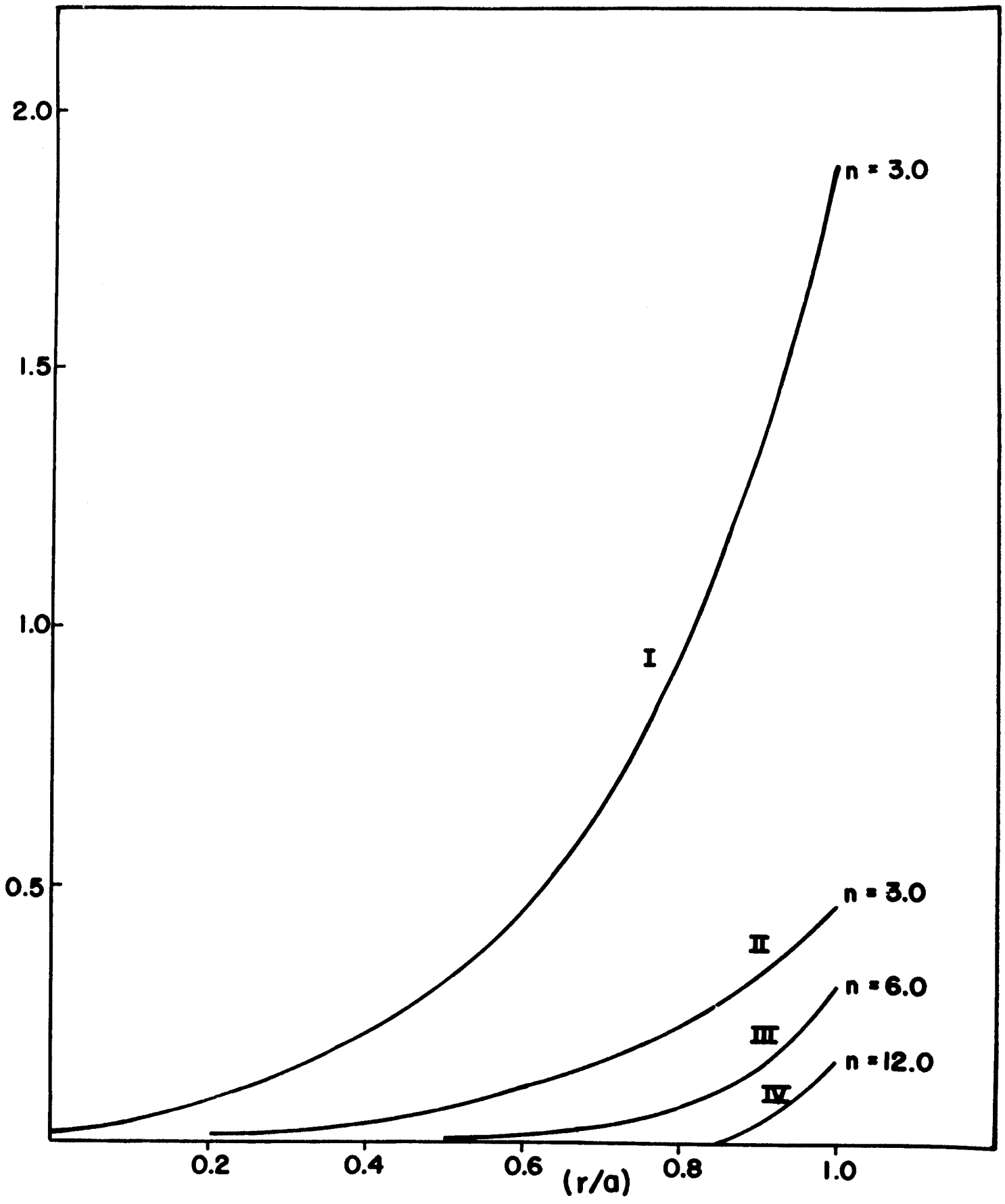

Figure II-B-19

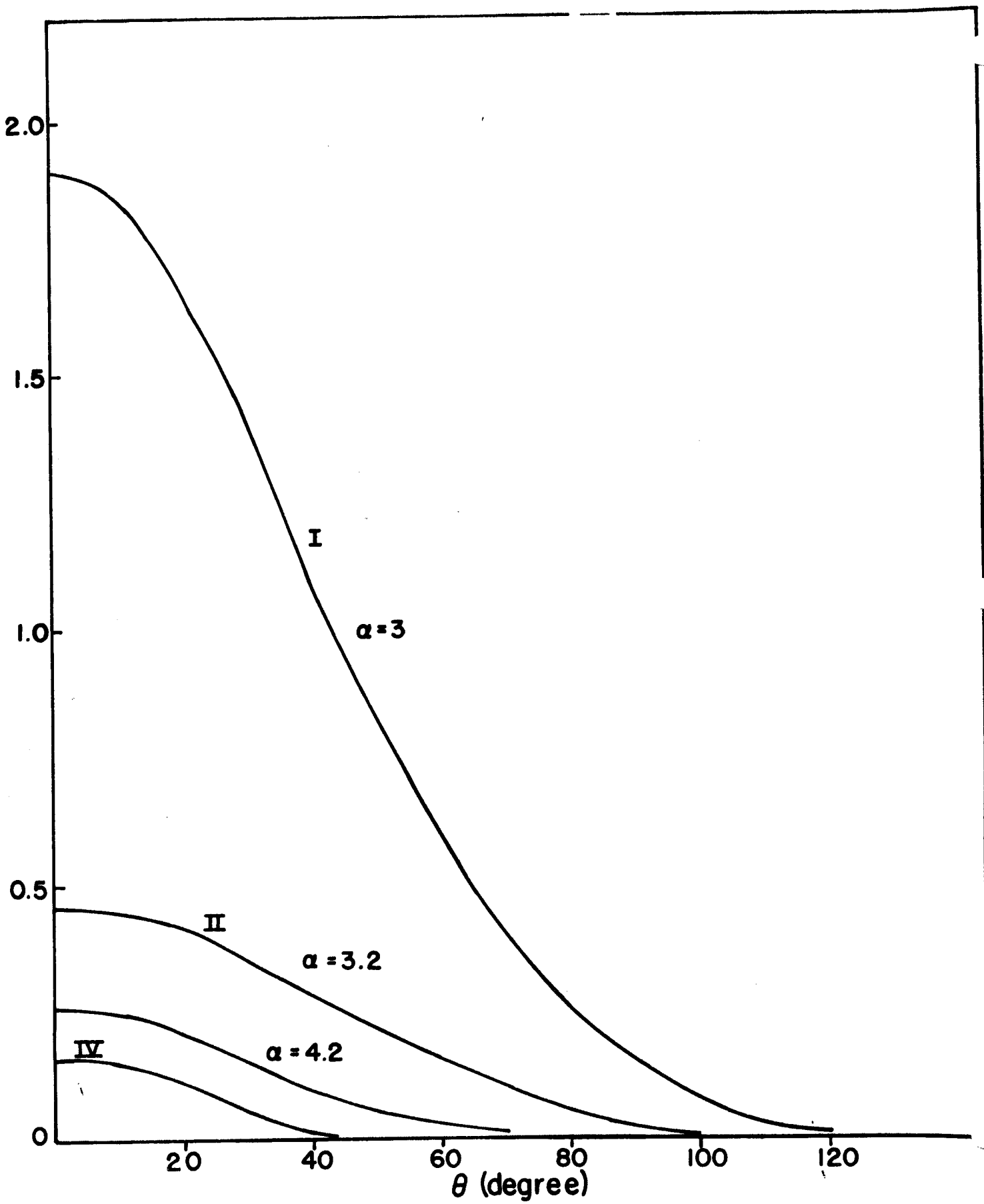

Figure II-B-20

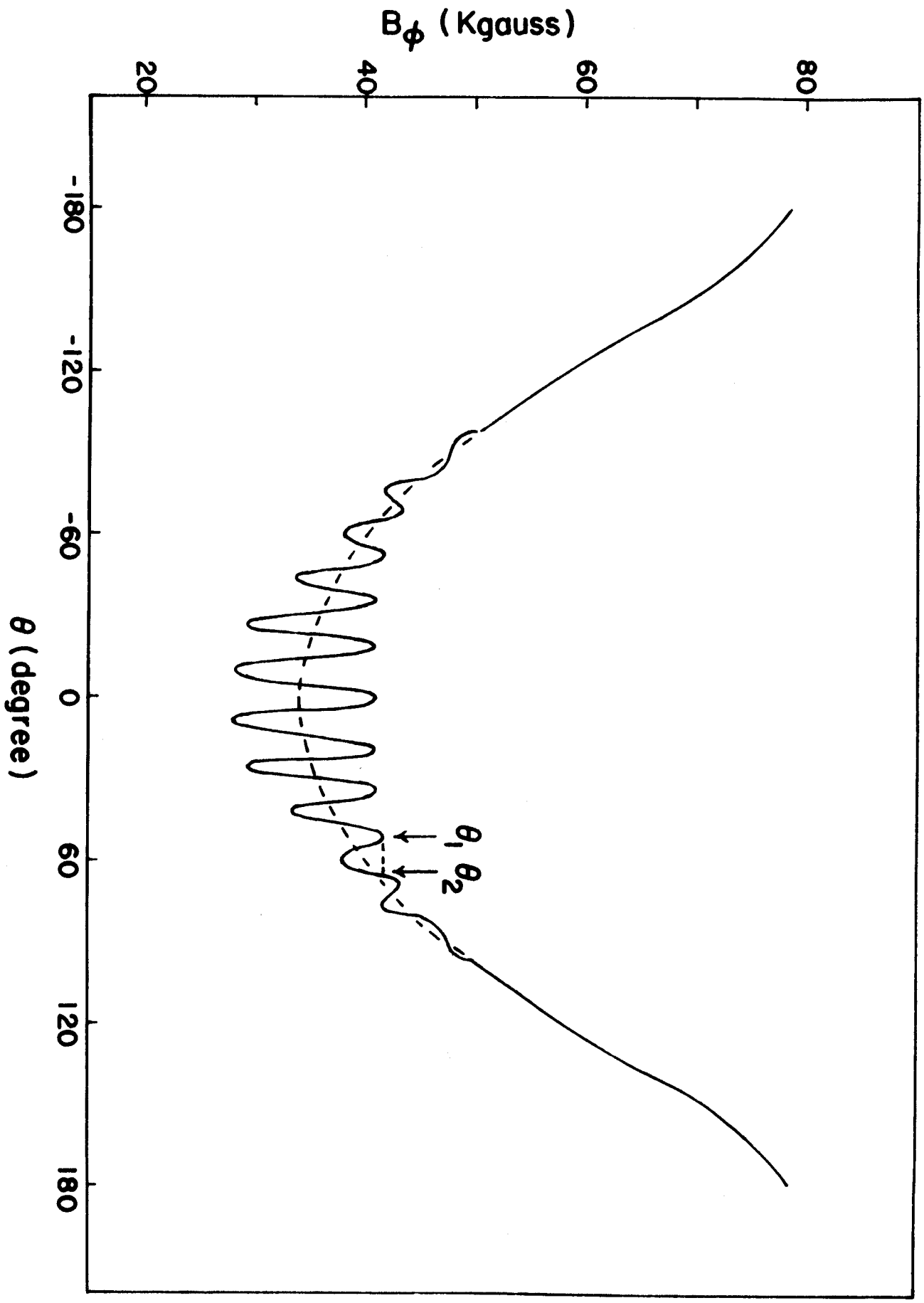

Figure II-B-21

$$\frac{\partial}{\partial\theta}\left(\frac{B_\phi}{B_o}\right)\Bigg| = 0 \qquad (4)$$

using (1) we have

$$\frac{\sin\theta_1}{1+\frac{r}{R}\cos\theta_1} \simeq \frac{aK}{\varepsilon_a r}\left(\frac{r}{a}\right)^n \exp\left(-\left(\frac{\alpha\theta_1}{\pi}\right)^2\right) \sin(Nq\theta_1 + \phi_o) \quad , \qquad (5)$$

where K is defined by[3]

$$K = \frac{\varepsilon_a NqR}{a} \qquad (6)$$

The upper boundary θ_2 is given by $B_\phi(\theta_2) = B_\phi(\theta_1)$. The projection of the trapping regions on the r - θ plane is shown in Fig. II-B-22 for constant ϕ_o. Unlike the case of poloidally uniform ripples, the trapping regions are confined to the first and fourth quadrants of the r - θ plane even though K is large. These locally trapped particles will drift vertically in the gradient of the toroidal field with a velocity

$$v_D = \frac{mv^2}{2eB_o R} \qquad (7)$$

A 3.5 MeV alpha particle can drift to the wall in about 10^{-2} msec, which is much shorter than the time to slow down or to scatter in pitch angle and become untrapped. Consequently, the fraction of alphas formed in the region of phase space corresponding to being locally trapped in the bumpy field will be lost directly from the plasma and will impinge on the first wall in localized zones.

For an isotropic source of energetic particles, the fractions of particles trapped at (r,θ,ϕ) is

$$f(r,\theta,\phi) = \sqrt{1 - \frac{B(r,\theta,\phi)}{B(r,\theta_1)}} \qquad (8)$$

where $B(r,\theta_1)$ is the field at the mirror point on the field line passing through (r,θ,ϕ). From (2),

$$B(\theta_1) \simeq \frac{R\,B_o}{R+r\cos\theta_1}\left[1 + \varepsilon_a\left(\frac{r}{a}\right)^n \exp\left(-\left(\frac{\alpha\theta_1}{\pi}\right)^2\right)\right]. \qquad (9)$$

Since $\cos(Nq\theta_1 + N\phi_o) \simeq 1$, we find

$$\frac{B(r,\theta,\phi)}{B(\theta_1)} = \frac{1 + \varepsilon_a\left(\frac{r}{a}\right)^n \exp\left(-\left(\frac{\alpha\theta}{\pi}\right)^2\right)\cos N\phi}{1 + \varepsilon_a\left(\frac{r}{a}\right)^n \exp\left(-\left(\frac{\alpha\theta}{\pi}\right)^2\right)} \quad , \qquad (10)$$

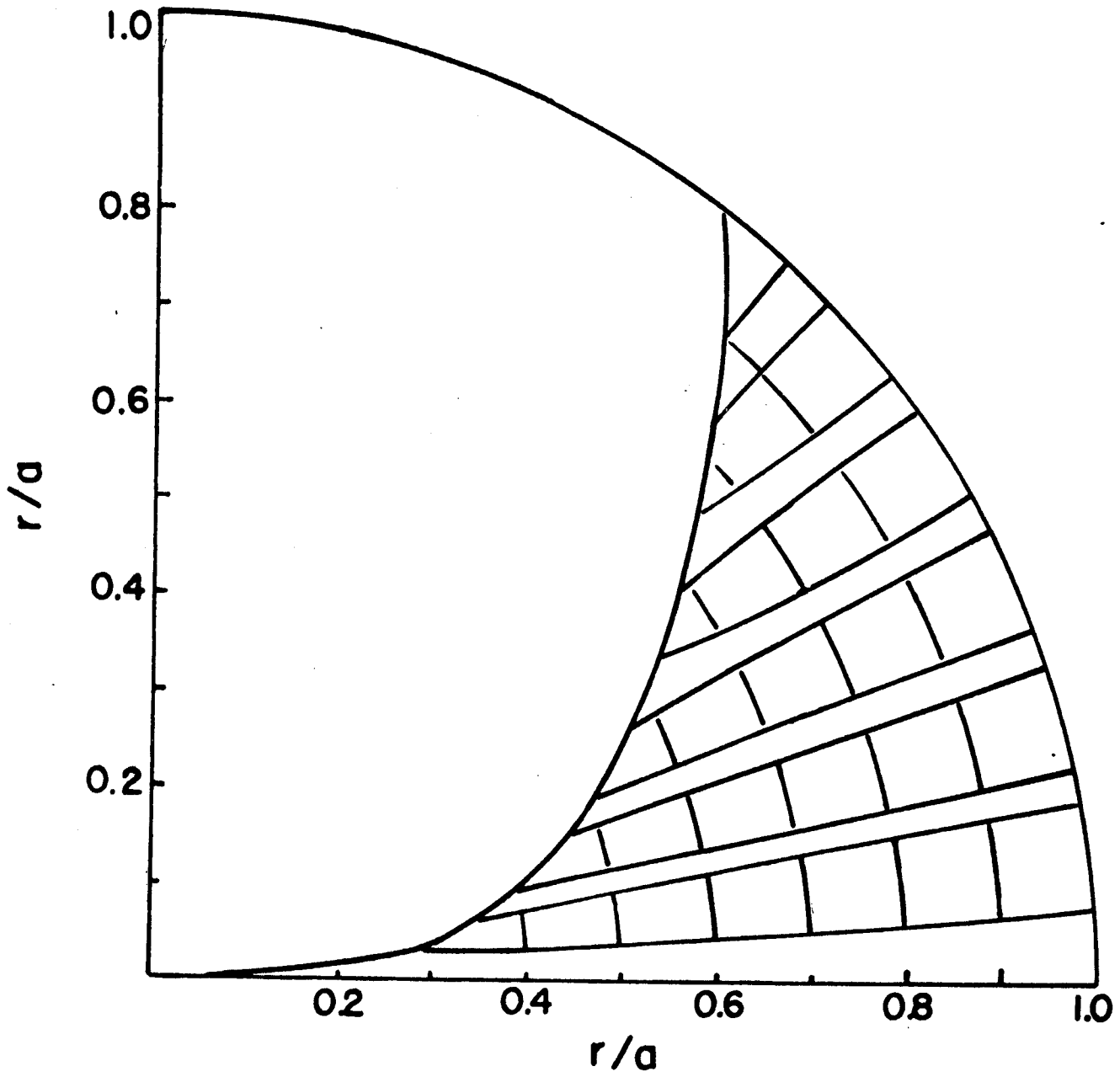

Figure II-B-23

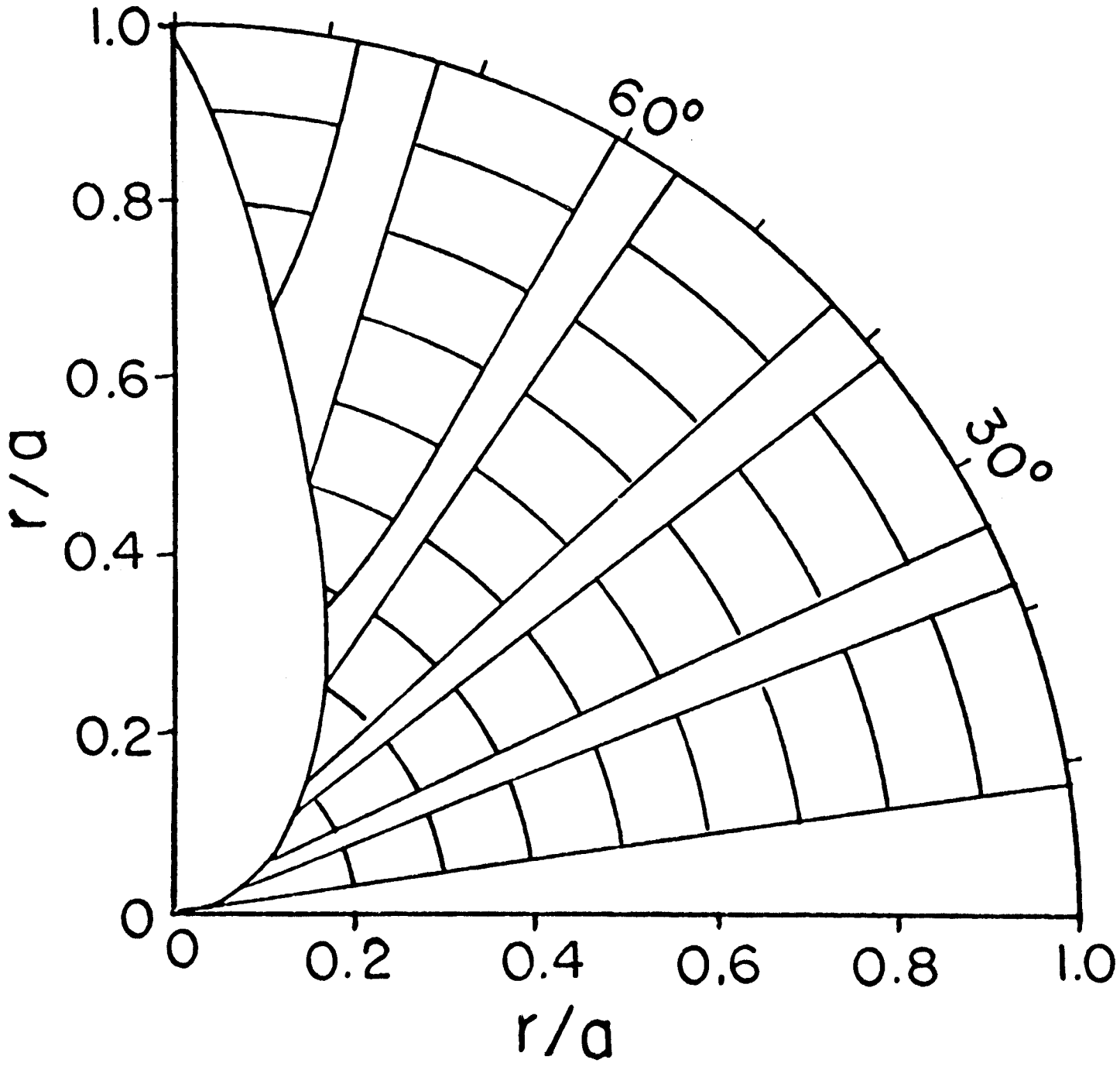

Figure II-B-22

and

$$f(r,\theta,\phi) \simeq \sqrt{\varepsilon_a}\ \left(\frac{r}{a}\right)^{\frac{n}{2}} \exp\left(-\frac{1}{2}\left(\frac{\alpha\theta}{\pi}\right)^2\right) \sqrt{1 - \cos N\phi}\ . \tag{11}$$

The total fraction of particles trapped is

$$f_T = \frac{\int_0^a r\,dr\, S(r) \int_0^{\theta_{max}(r)} d\theta \int_0^{2\pi} d\phi\, f(r,\theta,\phi)}{2\pi^2 \int_0^a r\,dr\, S(r)}\ , \tag{12}$$

where $S(r)$ is a source function independent of θ.

$$f_T = \frac{\sqrt{\varepsilon_a} \int_0^{2\pi} \sqrt{1 - \cos N\phi}\, d\phi \int_0^a dr\, r\, S(r) \left(\frac{r}{a}\right)^{\frac{n}{2}} \int_0^{\theta_{max}(r)} \exp\left(-\frac{1}{2}\left(\frac{\alpha\theta}{\pi}\right)^2\right) d\theta}{2\pi^2 \int_0^a r\,dr\, A(r)} \tag{13}$$

For purposes of estimation, we assume

$$\frac{1}{2\pi} \int_0^{2\pi} \sqrt{1 - \cos N\phi}\ d\phi \simeq 1, \tag{14}$$

and $\frac{\alpha\theta_{max}(r)}{\pi} \gg 1$, and we find

$$f_T = \frac{16\ \sqrt{2\pi}}{(n+4)\ (n+8)\alpha}\ \sqrt{\varepsilon_a} \tag{15}$$

For UWMAK-I conditions,[1] $f_T = 5.6\%$ which means that 5.6% of the 3.5 MeV alpha particles will not be magnetically confined but will strike the wall in localized areas between the coils in the first quadrant of the r - θ plane. This may cause additional wall damage and generation of impurities. We would like to minimize this loss by increasing the number of coils and/or extending the coils at the outside of the torus.

The curves marked III in Figs. II-B-19 and II-B-20 show that the amplitude of the ripple is reduced by a factor of 4 by doubling the number of coils. The amplitude also decreases faster, both radially and poloidally, than when there are only 12 coils. Correspondingly, the trapping regions are also smaller, as shown by Fig. II-B-20. Curves II and IV in Fig. II-B-19 and II-B-20 are ripples for 12 and 24 "extended" D magnets, respectively. The parameters for modeling these ripples and the fraction of trapped alphas are listed in Table II-B-10. We note here that the numerical accuracy in the magnetic field calculation is about 0.01%.

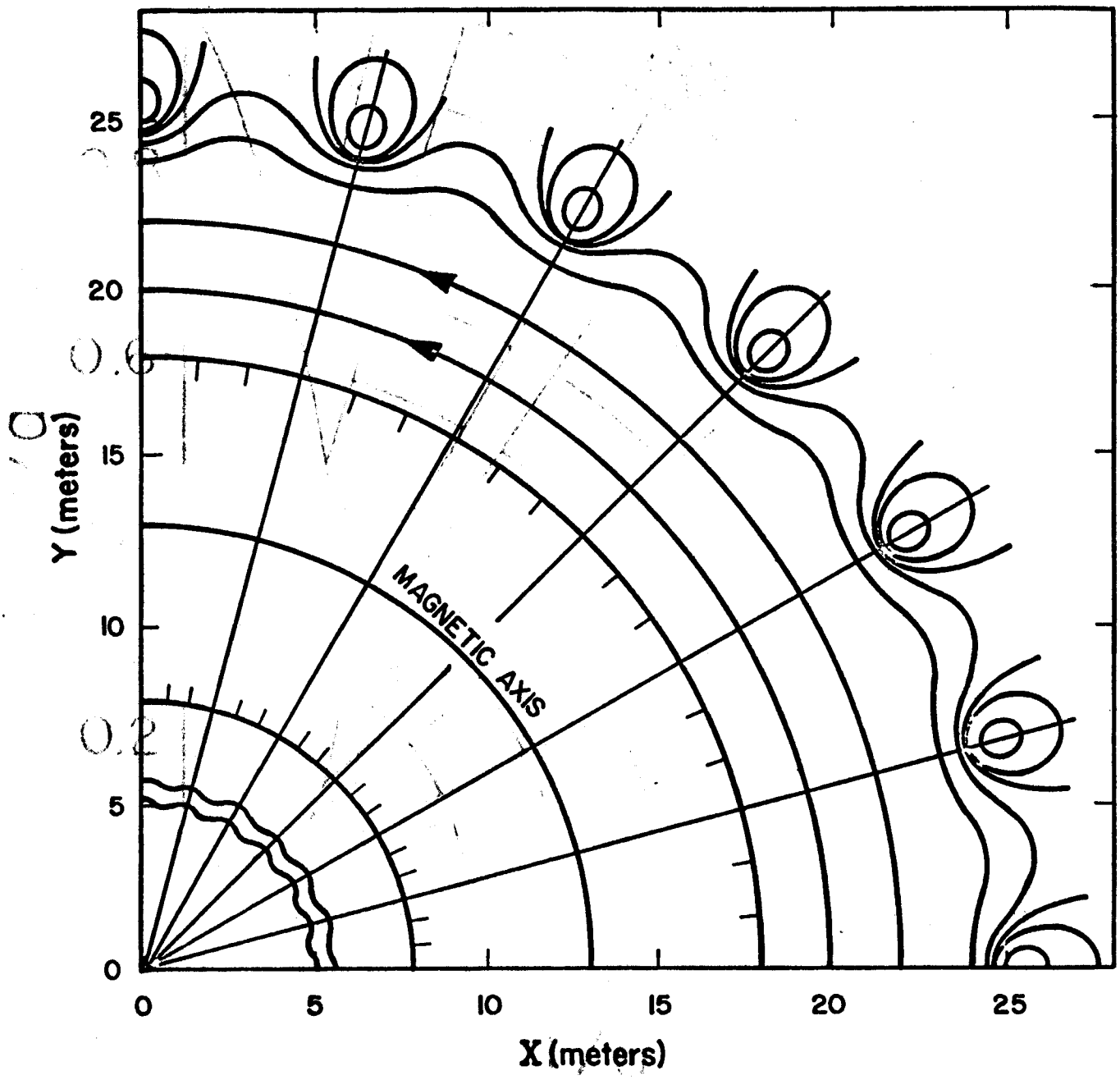

Figure II-B-24

Table II-B-10

Parameters of the Magnetic Field Ripples
for 4 Different Magnetic Field Coil Designs,
and the Total Fractions of the α-Particles
Trapped in Those Ripples

		ε_a	n	α	f_T (%)
UWMAK-I	12 coils	0.25	3	3	5.6
	12 extended coils	0.046	3	3.2	3.4
	24 coils	0.03	6	4.4	1.1
	24 extended coils	0.016	12	5.0	0.3
UWMAK-II	24 extended coils	<0.01	>12	>5	<0.1

Table II-B-10 indicates that for the 24 "extended" D-coils magnet design, as chosen for UWMAK-II, the fast alpha loss rates are very low. An auxiliary reason for extending the TF coil to large R is to allow enough space between coils such that blanket segments can be removed without removing the coils themselves. This is discussed further in Chapter IV.

In conclusion, the UWMAK-II design has 24 "D" shaped toroidal field extended on the outer edge. The field ripple is satisfactorily small, less than 0.01%. The magnetic field structure of UWMAK-II is illustrated by some of the field lines shown in Fig. II-B-24. The corrugation of the plasma column is now <0.01 meter.

References for Section II-B-5

1. B. Badger, et al., "UWMAK-I, A Wisconsin Tokamak Reactor Design," UWFDM-68, Nucl. Eng. Dept., Univ. of Wisconsin, Nov. 1973.

2. O. A. Anderson and H. P. Furth, Nuclear Fusion, 12, 207 (1972).

3. T. F. Yang and G. A. Emmert, Proc. 1st Topical Meeting on the Tech. of Cont. Nucl. Fusion, 2, 400 (1974).

4. J. File, Fifth Symposium on Engineering Problems of Fusion Research, Princeton, N. J., (1973).

II-B-6. Vacuum Pumping and Particle Collection Systems for UWMAK-II

The vacuum pumping systems must serve at least three functions: evacuation of the toroidal plasma chamber to a high vacuum for conditioning and cleaning the vacuum wall; keep the ambient pressure below 1 x 10^{-4} torr during the plasma burn cycle; and evacuate the enclosure surrounding the torus to 75 torr. The systems meeting these requirements are (1) cryo-pumps for evacuation of the toroidal vessel; (2) lithium trapping surfaces in the divertor; and (3) mechanical pumps for evacuation of the building.

The vacuum system in UWMAK-II differs considerably from that in UWMAK-I. In UWMAK-I, the vacuum system consisted of mercury diffusion pumps for use at high pressure which were augmented by cryopumps for increased pumping of deuterium and tritium at low pressures.

Although there is no reason to believe that such a system would not work, we have reassessed the practicality of such a scheme for UWMAK-II and have decided against it. The main reason for this decision is based on the possibility of contaminating the plasma confinement region. A secondary reason is the need for regular servicing of such pumps in a limited access area requiring remote control devices.

Backstreaming in mercury diffusion pumps is a well known problem. It can be prevented by properly designed and cooled baffles. However, because of the high vapor pressure of mercury, liquified gas refrigeration systems are needed to maintain effective operation of the baffle. The temperature range for such operation is very small and serious problems can arise if the limits are exceeded. Backstreaming will occur if the baffles get too warm or mercury freezing if they get too cold. In both cases, the implications are disastrous.

Recent improvements in cryopumps and molecular sieves have encouraged us to attempt a design based entirely on this. Reliability and the minimum amount of servicing needed for cryopumps and molecular sieves are only some of the advantages that they offer. The following section will describe the vacuum pumping system for UWMAK-II.

A. Cryo-vacuum Pumps

Cryo-vacuum pumps of the type manufactured by Excalibur Corp., Waltham, Mass., consist of a molecular sieve bonded to a metal substrate and two sets of chevron-shaped metal surfaces. One of these surfaces is cooled to 80°K, the second to 20°K, and the molecular sieve panel to 5°K. (Figure II-B-25).

Molecular sieves are available from Linde Corp. in powder or pellet form. With apertures of from 10 to 13 Å, the molecular sieves essentially trap gas molecules. If pellets, say type 5-A (Zeolite), 0.3 cm diameter, are bonded to a metal surface and cooled to 77.3°K, the panels are practically sinks. The adsorption of nitrogen, for instance, will continue unabated until 100 cm^3 (STP)/gm adsorbent has been adsorbed (p = 1.3 x 10^{-3} torr).[1] At lower pressures, this high capacity is reached only after the panel has been regenerated four to six times. Saturation effects are observable at high pressure (300 torr) only after 150 cm^3 (STP)/gm is adsorbed.[1]

Pumping efficiency for hydrogen isotopes is even better. Saturation for deuterium and tritium occurs only after 300 cm^3 (STP)/gm adsorbent has been cryo-adsorbed at 77.3°K. These two features permit the design of pumps of higher pumping speed than comparably-sized diffusion pumps, and with long service lifetime before regeneration.

Simple cryopumps also have the advantages of high pumping speed and service lifetime. The capacity for cryo-condensation of deuterium and tritium on polished copper panels cooled to ~5°K is more than 10 cm^3 (STP)/cm^2 of cooling surface. The principal disadvantage is high thermal energy losses, even though radiation losses were minimized with the choice of polished copper surfaces. A major advantage for CTR use, however, is the greatly enhanced pumping speed when nitrogen gas is injected into the system. The ability of relatively immobile deuterium and tritium gases to trap helium on the cryo-surface is enhanced an order of magnitude when a less-mobile gas such as nitrogen is condensed on the surface. The injection method, used at Sandia Labs., Albuquerque, N. Mexico[2], at a partial pressure corresponding to the ambient pressure in the vacuum vessel, increased the effectiveness of the cryo-surface for pumping helium from ~1% that of deuterium to greater than 10% that of deuterium[2]. In developing safe methods for handling tritium, this procedure was used at Sandia where they prescribed the injection of water vapor during emergency or ordinary shut down in order to trap essentially all of the tritium on the cold surface. Nitrogen will perform this function equally well for UWMAK-II, especially since this injection system also can be used for regeneration of the pumps. The advantage of resorting to nitrogen-injection for emergency shut-down is appealing since all cryo-vacuum pumps can be used. In that event, the adsorption - condensation capacity of the system is 1×10^9 torr-liters of deuterium, tritium, and helium in less than 100 seconds.

Hybrid pumps of the Excalibur type, using both cryo-adsorption and cryo-condensation in conjunction with a molecular sieve, are avaliable now. There are no auxiliary pumping fluids, metal vapors, or lubricants exposed to the vacuum. Neither is there a requirement for high voltage, a magnetic field, or moving parts. The hybrid pumps have a higher pumping speed for helium than cryo-condensation alone. Condensable gases or vapors will condense on the 80°K and 20°K chevron surfaces, while hydrogen isotopes as well as helium are adsorbed onto the 5°K molecular sieve surface. Cryo-sorption on this panel is not dependent merely on vapor pressure vs. temperature curves for the gases to be pumped. The pellets hold helium by surface attraction forces even though the 5°K is above its boiling point.

A.1 Cryo-vacuum Pump Specifications

The principal dimensions, 1.3 m diameter and 1 m height, of each pump are given in Figure II-B-25. The coolant capacities are: liquid helium, 270 liters; liquid nitrogen, 150 liters. The cryogen usage is ~90 ℓ. per day of liquid helium and ~450 ℓ. per day of liquid nitrogen if gases at thermal velocities are pumped. Since the particles incident upon the cooled chevron surfaces exceed thermal velocities, the cryogen usage rate will be considerably greater.

The pumping speeds for each pump, at 10^{-4} torr, are:

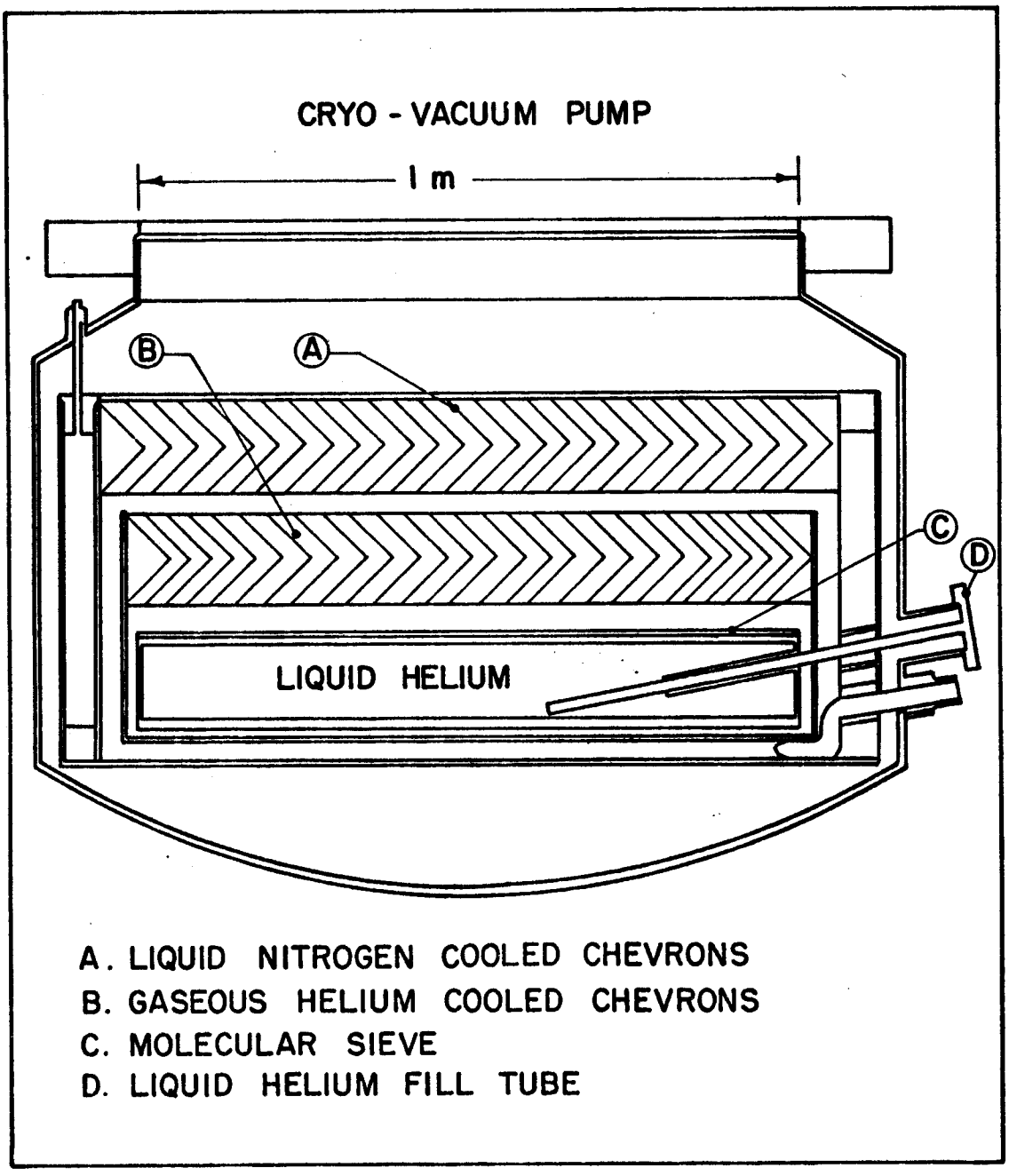

Figure II-B-25

$S^{\circ}_{D,T} = 7.5 \times 10^{4}$ ℓ/sec.; $S^{\circ}_{He} = 5 \times 10^{4}$ ℓ/sec.;

$S^{\circ}_{air} = 4 \times 10^{4}$ ℓ/sec.

These are net pumping speeds since no external valves or traps are necessary. A gate valve will isolate each pump while it is either being regenerated or is placed on stand-by reserve.

A.2 Cryo-vacuum Pump Regeneration

The service lifetime for 96 pumps on-line at one time is greater than 24 hours. To regenerate a pump that has pumped air requires heating to 25°C and outgassing it. Since normal usage involves daily regeneration of the 96 pumps which have pumped the residual gases of the fusion reaction, heating the molecular sieve and cold (20°K) chevron panel to 30°K will be sufficient. By using nitrogen-injection to avoid contamination, this can be accomplished in seconds. The cycling sequence for regeneration will require several minutes for outgassing and less than an hour for subsequent cooling of the molecular sieve.

Repeated regeneration cycles condition the molecular sieve, increasing adsorption capacity at low pressure ($p < 1 \times 10^{-3}$ torr). Repeated inhale-exhaust cycles will improve pump performance (Figure II-B-26), as long as very little water vapor is introduced. Since the molecular sieve has an affinity for water vapor, it will be an effective drying agent. However, if the sieves are used in this manner, they must be regenerated at shorter than normal intervals. Appropriate high vacuum system techniques will increase pump performance and near-equilibrium operation will be reached after about five cycles.

A.3 Cryo-vacuum Pump System Design

The system must be capable of handling a gas through-put of $Q_{D,T} = 6.4 \times 10^{3}$ torr ℓ/sec.; $Q_{He} = 143$ torr ℓ/sec. Liquid lithium surface trapping in the divertor is expected to trap 90% of the deuterium and tritium but we conservatively assume that none of the helium is trapped. Half (96) of the cryo-pumps will be on-line during the burn, evacuation, and fueling cycle. Net pumping speed in the equilibrium pressure range of 1×10^{-4} torr to 75 torr is 7.5×10^{6} ℓ/sec for D and T, and 5×10^{6} ℓ/sec for He. The base pressure during burn is 8×10^{-5} torr for D+T and 3×10^{-5} torr for He. Initial evacuations from 75 torr to $\sim 2 \times 10^{-6}$ torr will require 96 of the pumps, and take only seconds. At this time, when the other bank of pumps is used for conditioning and cleaning the vacuum wall, these pumps must be regenerated by heating to 25°C. After two hours, they will be ready for use and subsequent regeneration at 30°K will require less than an hour.

The degassing of the vacuum wall requires an ultra-high vacuum. The throughput will be less than 4×10^{-3} torr ℓ/sec. Estimated flow conductance of sector seal leaks is ~.02 ℓ/sec., giving a leak rate of 13.7 torr ℓ/sec. Thus, the estimated attainable pressure for cleaning the vacuum wall is

$$P_o = \frac{Q_{degass} + Q_{leak}}{S} = \frac{4 \times 10^{-3} + 13.7}{6 \times 10^{6}} \sim 2 \times 10^{-6} \text{ torr.}$$

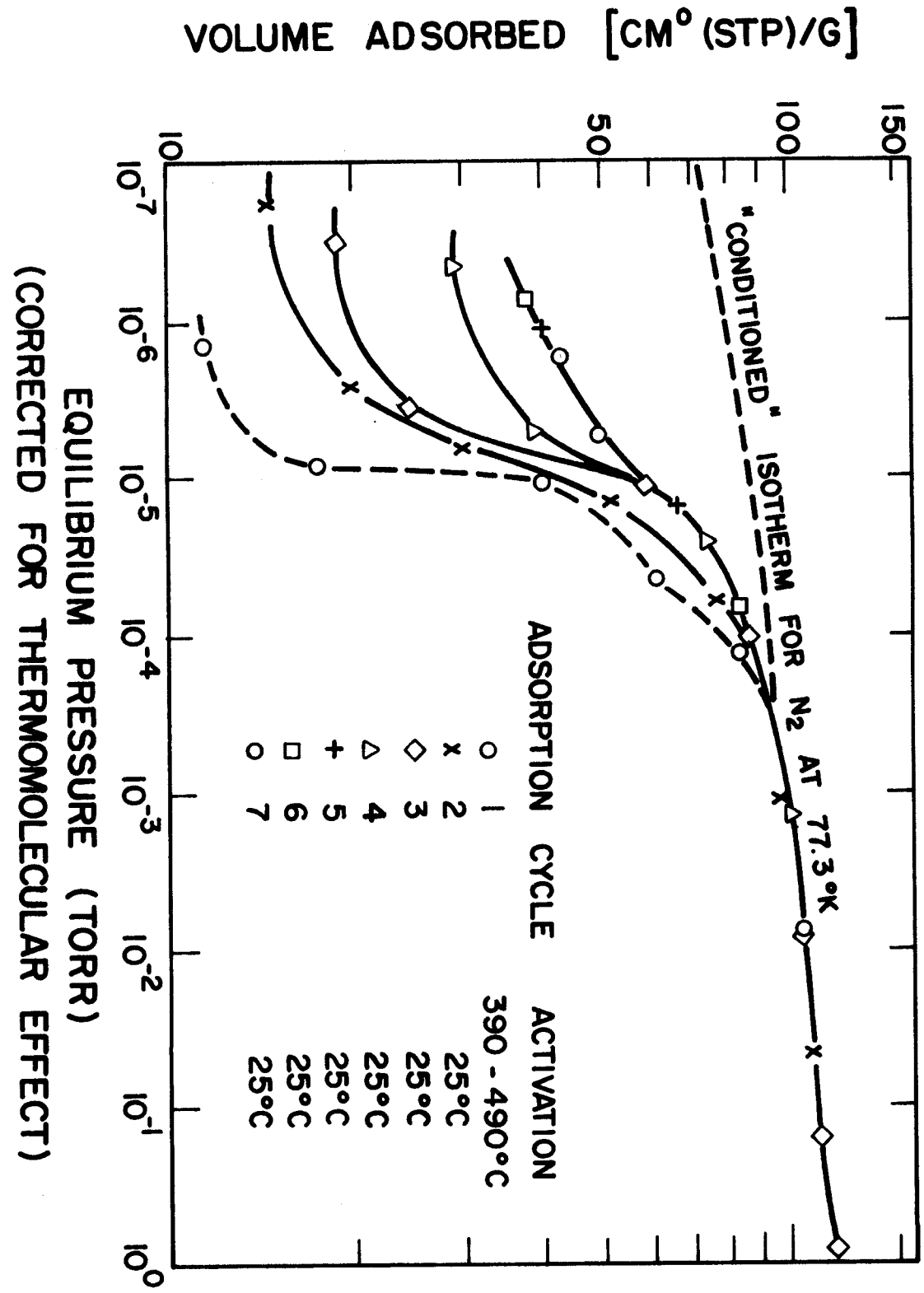

Figure II-B-26

Regeneration of the pumps will require out gassing of the trapped gases and collecting them in canisters for subsequent separation of helium from the hydrogen isotopes. The separation can be simplified if tritium getters can be installed in the holding canisters.

During a burn cycle, each pump will trap 2.3×10^4 torr-liters of gas every hour. On regeneration, this quantity of gas is reemitted and can be exhausted by two Hereous pumps in series (VPR6000A and VPR1600) in less than 200 seconds. The pumping speed of the mechanical pumps is 1600 liters/sec and the vacuum line joining each cryopump with the two Hereous mechanical pumps should be no more restrictive than a 10 meter length tube 20 cm in diameter.

The canisters, or series of getter canisters, into which the mechanical pumps exhaust can be arranged for increased stages of pressurization, and can be removed for tritium removal and separation of helium, purification, and re-fueling of the torus, elsewhere.

The cryo-vacuum pump system is closed during operation of the reactor so the Roots blowers and canisters are valved off from the toroidal vessel at all times. They open to vacuum pumps only during servicing.

B. Liquid Lithium Trapping Surfaces

The divertor collector system has two functions. It has to collect roughly 90% of the D and T particles diffusing from the plasma and it must absorb the kinetic energy associated with the particles. The system proposed is to use a liquid lithium surface located in each divertor slot. Hydrogen isotopes will collide with the lithium surface and form a hydride. Efficient trapping of 96% of the incident ions will continue to doses of 2×10^{19} particles/cm^2.[4] Theoretically, all the atoms striking the lithium surface will condense and be trapped until the pressure is reduced to the vapor pressure of the gas at the temperature of the surface. However, when lithium is used as the trapping material a severe temperature limitation is imposed. The temperature range of the lithium must be from 186°C to 350°C, i.e., from the melting point to the boiling point of lithium at the pressure it faces. This narrow temperature range, in addition to the large amount of energy the particles deposit, creates a critical problem for heat transfer.

The average thermal load on the plates due to the impinging particles is 2.81 MW/m^2. This energy is distributed approximately exponentially along the plate according to the equation

$$Q \simeq 13 \exp\left(-\frac{x}{21.8}\right) \ (\mathrm{MW/m^2}) \qquad (1)$$

In carrying out the heat transfer analysis, one must keep in mind that heat transfer is by conduction only in such a strong magnetic field.

In UWMAK-I design,[3] a lithium film flowing down stainless steel plates was proposed to act as the coolant. It was suggested that lithium will flow down

under gravity and form a film on the stainless steel plate. However, there are experimental results indicating that purified lithium does not wet stainless steel at 315°C but does so at 400°C. Impure lithium will not wet stainless steel below 480°C.(5) Therefore, a lithium film cannot be formed on the stainless steel plate in the temperature range of interest here.

If another structural material can be used on which a lithium film will form, the heat transfer characteristic of a falling lithium film will not be sufficient to absorb the extremely large thermal load on the plates. The volumetric flow rate of lithium on the plate can be calculated from

$$V = Q/[\rho\ C_p\ (T_o - T_i)] \tag{2}$$

where V = volumetric lithium flow rate

Q = thermal load on the plate

ρ = density of lithium

C_p = thermal capacity of lithium

T_o = maximum lithium exit temperature (325°C)

T_i = minimum lithium entrance temperature (200°C).

The average velocity is

$$v = (\rho\ g\ V^2\ \mathrm{Cos}\beta/3\mu)^{1/3} \tag{3}$$

in which v = average lithium velocity

μ = viscosity

$g\ \mathrm{Cos}\beta$ = gravitational force.

This velocity is determined by a force balance between the viscous force and the gravitational force. The thickness of the film is

$$\delta = (3\mu\ V/\rho\ g\ \mathrm{Cos}\beta)^{1/3} \tag{4}$$

which is .15 cm for this case. Such a thick film for a large thermal load means only the layer of lithium near the surface absorbs the heat. The result will be a large surface temperature rise. A thermal analysis performed indicates the temperature on the lithium surface will reach 350°C only 10cm from the top of the plate while most of the lithium remains essentially at the inlet temperature. Therefore, lithium film falling along a plate is clearly not capable of absorbing that large amount of heat.

The velocity of the lithium film is limited by the viscous force. Therefore, a free falling lithium stream is proposed. A lithium flow is introduced at a flow rate determined by eqn. (2). With a proper headstart for the free fall, the lithium can reach high velocity. As such, the lithium film can be thin and the heating of the lithium can be more uniform. This design is shown in Figure II-B-27.

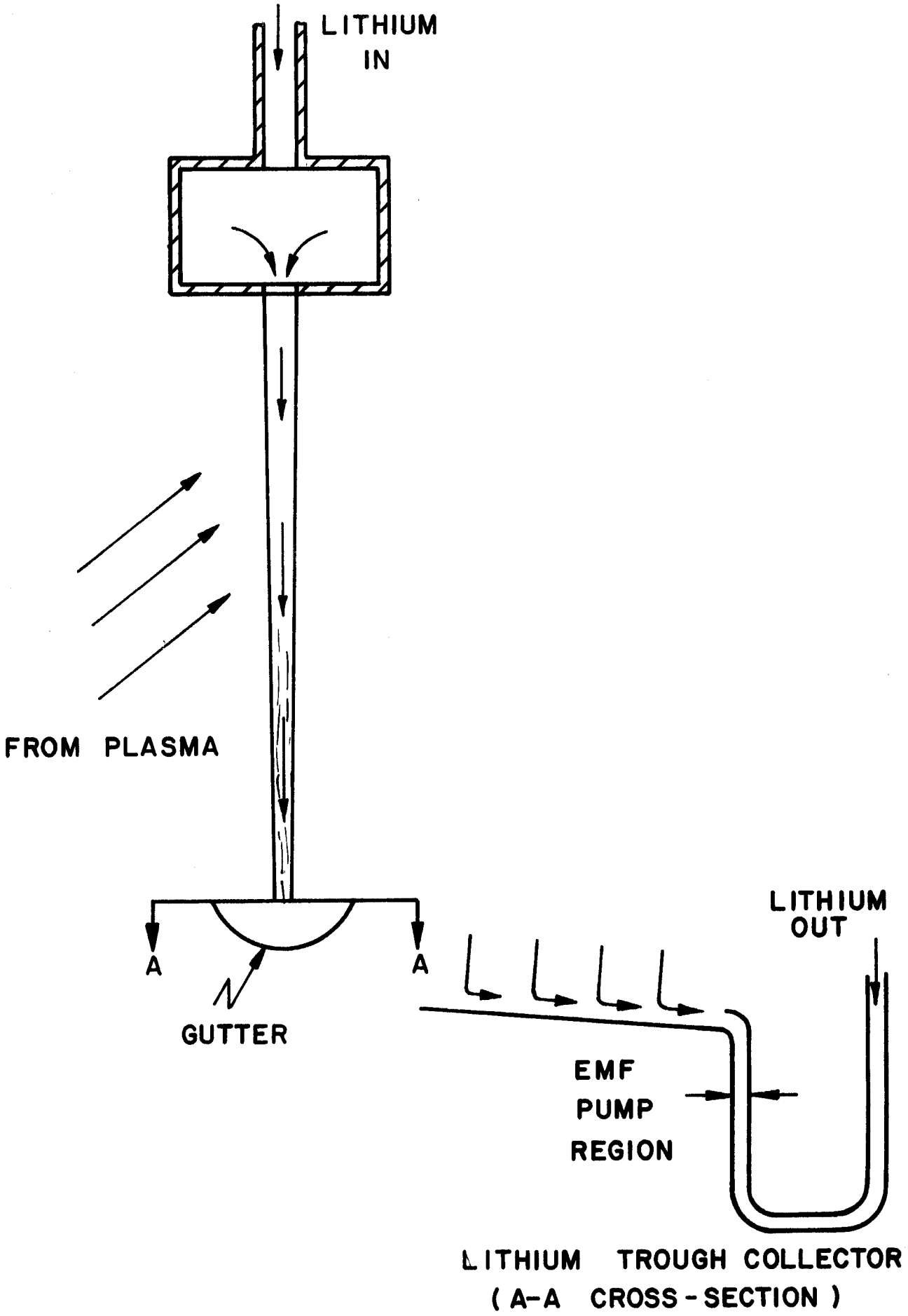

Figure II-B-27

A finite difference computer program has been written to calculate the temperature of the lithium fall. The initial velocity of the lithium is a parameter of the study and will increase until the surface temperature exceeds 350°C. Two heating curves are used. The first is of that given by eqn. (1) while the second assumes the energy distribution is uniform over the plate.

For the case where the thermal load is distributed exponentially, the initial velocity required is 10 m/sec. It takes 5 m for the liquid in free fall to attain this velocity which is not a reasonable solution. The temperature at the lithium surface is shown on Fig. II-B-28. When the thermal load is distributed uniformly over the plates, the initial velocity required is 3.5 m/sec which requires only a 60 cm headstart. The temperature of the lithium surface in this case is shown in Fig. II-B-29. This appears to be a reasonable solution.

The lithium fall may not be stable, i.e., surface tension may break the film into droplets. The effects of the magnetic field is also not clear. However, a theoretical solution of this type of MHD stability problem is not available and is outside the scope of this study. Further work, both theoretically and experimentally, is definitely required if this idea is to be pursued any further.

The particle collection system proposed here is a possible solution but its viability is in doubt. The design of the collectors is made difficult by the large gas throughput and poses a serious dilemma for the designer. The problem can be made less serious by reducing the power load by a factor of about 3. This can be achieved by increasing the plasma confinement time radiating the energy away from the surface. Then the energy of the particles leaking from the plasma can be reduced by roughly a factor of 10 although the particle diffusion rate would remain about the same.

C. Evacuation of the Magnet Enclosure

The advantages of having an evacuated enclosure surrounding the toroidal vacuum chamber can be retained without incurring difficult problems of voltage breakdown and sector seal leakage if the pressure in this enclosure is maintained at about 75 torr.

Kinney oil-sealed mechanical pumps, such as the KD-850 pump, are suitable for evacuating the toroidal magnet enclosure. The pump should have ~10% gas-ballast to prevent contamination of the oil by condensable gases, and it should be heated to ~110°C to prevent condensation of D_2O and T_2O. The discharge pressure is 900 torr, and a compressor can transfer exhausted gases to getter-canisters of the type used for regeneration of the cryo-vacuum pumps. Provision for gas-ballast will not affect the performance of the pump in the pressure range 75-760 torr, so that 20 KD-850 pumps, with a pumping speed of 400 ℓ/sec each, can evacuate the enclosure if the leakage rate is less than 6×10^5 torr ℓ/sec. This implies a flow conductance due to leakage of less than 90 ℓ/sec.

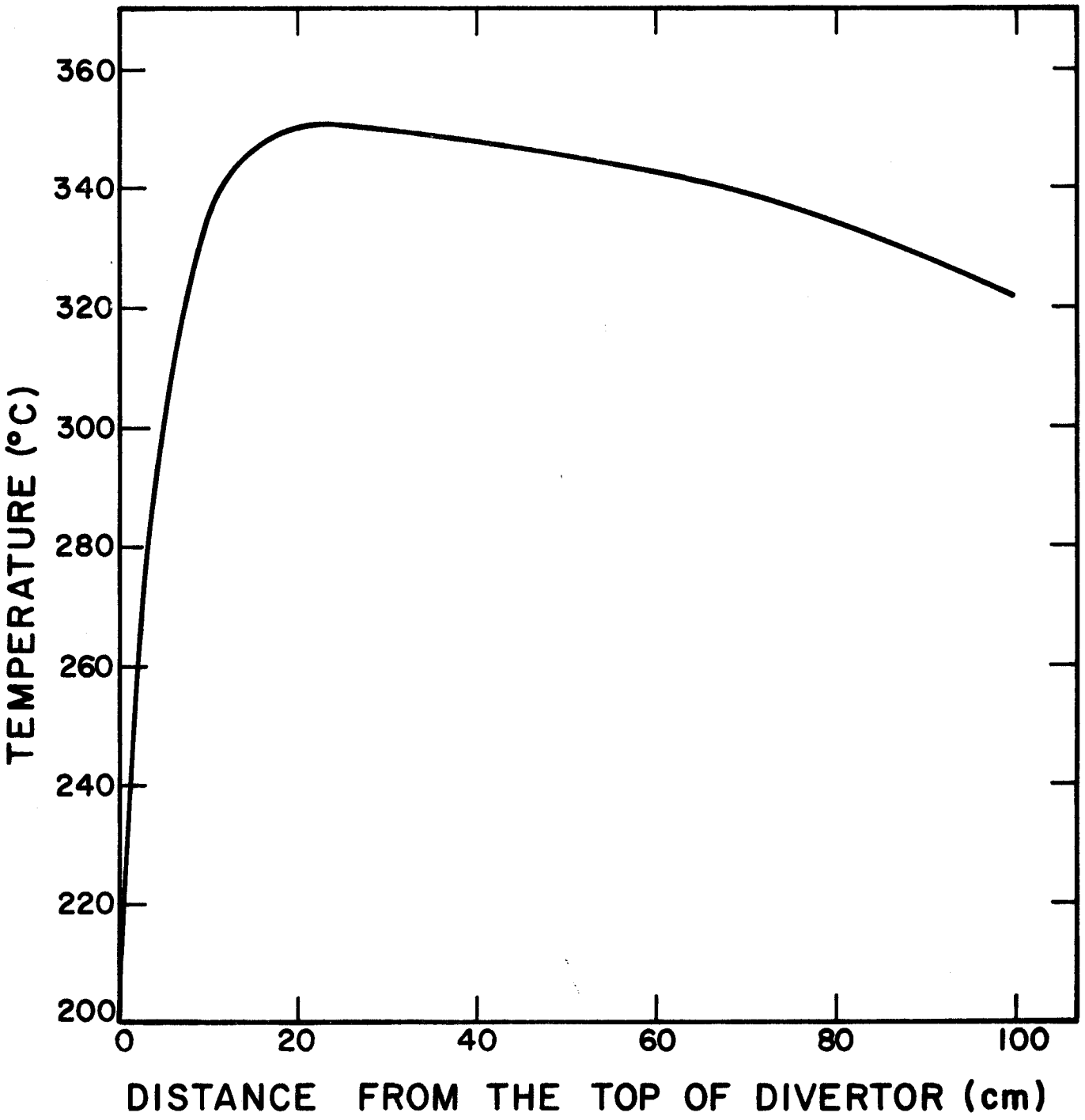

Figure II-B-28

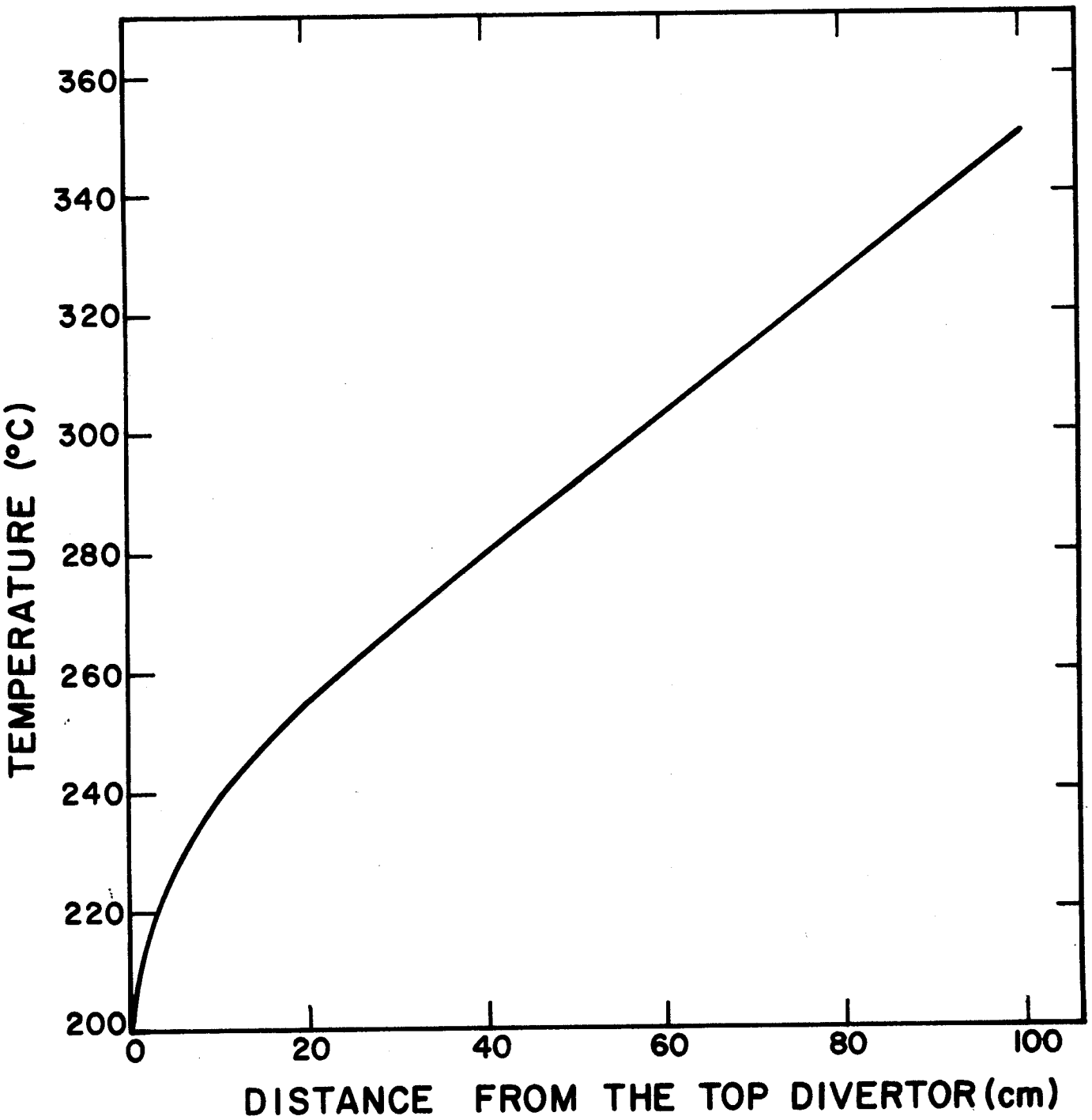

Figure II-B-29

Because of the possibility of hydrogen isotopes condensing and contaminating the oil in the mechanical pumps, the pump oil must be changed on a regular basis. Only one pump need be serviced at a time and the used oil (tritiated-hydrocarbon) would be processed to minimize hazards. Long-term use of the oil would saturate the hydrocarbon but experiments can (and should) demonstrate the service lifetime of the pump oil. This prospect is not pleasing, but it seems preferable to alternative choices for the pumps: (a) steam ejectors; (b) water ring pumps; (c) rotary pumps with mechanical booster; and (d) steam ejectors with interstage condensers.

References for Section II-B-6

1. Stern, S. A. & Pool, F.S.D., JYST 6, 941 (1969).

2. Beavis, L. C., Private Communication.

3. Badger, B. et. al., "UWMAK-I, A Wisconsin Toroidal Fusion Reactor Design" UWFDM-68, Nucl. Eng. Dept., UNW of Wisc, Nov., 1973.

4. McCracken, G., BNES Nuclear Fusion Reactor Conf., Culham, 1969.

5. Achemer, P. Y. "Alkali Metals Evaluation Program Quarterly Report, 1 Oct - 31 Dec, 1966," Aerojet General Corp. Report AGN-8215 (1967).

III. Magnet System

The designs of the toroidal field, transformer, and divertor coils are described in this chapter. All these coils are fully cryogenically stabilized superconducting magnets. The TiNb superconducting filaments are stabilized by a copper backing strip and details of the design factors, construction techniques, supporting structures, heat losses, and power supply requirements are included. The magnetic field profiles of the various coils, the plasma currents, and the combination thereof are also calculated. The toroidal field coils have a modified constant tension "D" shape which most effectively utilizes the structural material. "Embedded disc" type winding techniques are used in order to hold the conductor rigidly against the supporting structure. Redundancy in both the number of turns per disc and the total number of discs are incorporated. The central supporting structure is kept at liquid helium temperature to make the attachment of the 24 toroidal field coils easier. A secondary vacuum shell is built in conjunction with the magnet dewars. This shell structure is designed to sustain the lateral load if one or two adjacent magnets should fail catastrophically. The structure is stronger than is required to withstand the toroidal load due to the pulsed poloidal magnetic fields.

The divertor coils are mounted inside the toroidal field magnets. This reduces the maximum magnetic energy stored in the poloidal field from 16 MWh in UWMAK-I[1] design to only 2.9 MWh here. These coils will be wound with the toroidal field coils in place. 16 of the 18 transformer coils are positioned inside the central structure. They can be wound as the structure is being built from the bottom up. A common conductor shape is used for all the divertor and transformer coils. However, the size and number of superconducting filaments required are determined individually according to the respective ambient magnetic fields.

Estimation of heat losses due to various sources is made. In particular, the ac losses in the divertor and transformer coils due to their own pulsed fields and in the toroidal field coils due to the poloidal pulsed field are calculated in some detail. These ac losses are the largest source of heat losses. On the other hand, because of the great effectiveness of the neutron energy attenuation of the blanket and shield, the nuclear heating load on the magnets is negligibly small.

A superconductive inductor energy storage unit is used to supply the high power requirement of the poloidal field coils. The interface between them is accomplished by dc/ac/dc double conversion bridges. The power flow in these bridges is reversible. Thus, the energy stored in the divertor coils can be returned to the storage unit during the discharge phase. Only losses in the combined system need to be resupplied. The capital cost of the entire magnet system, including the supporting structures, refrigerators, and power supplies, is estimated to be ~~$313~~ 235 x 10^6.

III-A. Toroidal Field Magnets

In this section we describe the design of the main toroidal magnets. The design philosophy is based on the assumed need for full cryogenic stability of the conductors and reliable solid structures. The design is a modified constant tension "D" shaped toroid producing a magnetic field of 3.67T at a radius of 13m, the plasma center.

To provide circumferential clearance between the dewars of the toroidal field magnets so that segments of the shield can be removed separately, it is necessary to extend the outer portion of the "D" coils to a much greater radius than in our previous design.(1) This in turn would create a very tall and costly magnet if the constant tension design were adhered to. It is, therefore, necessary to deviate from a constant tension and use a modified "D" shape that is no higher than required for the internal system components. One must provide extra structure for bending in the discs and for support from the central core over the non-constant-tension portion of each toroidal field magnet.

The design presented is a constant tension design with no bending stresses in the outer portion from the top of the magnet (point C, Fig. III-A-1) to the bottom. Inward from the top and bottom sections, the forged discs are increased in depth in order to sustain the bending stresses and the hoop stresses created by the magnetic loading. In this region, the conductor size and spacing are maintained as elsewhere but is mounted near the inside edge of the disc in order to minimize structural stresses and stored magnetic energy.

The forged discs as shown in Figure III-A-1 are too small to accomodate the loads and still maintain reasonable stress and deflection levels. Therefore, the central cylindrical core is extended in the regions directly above and below each toroidal field magnet to provide additional support. This cantilever support is sized in conjunction with the increased magnet dimensions in this region in order to keep the maximum stress in the stainless steel discs to less than 4.14×10^8 N/m^2 (60,000 psi) and to match the slope and deflection at the end of the reinforced portion of the magnet to those of the constant tension outer part. At the design maximum stress level in the stainless steel discs, the copper will yield, but the maximum strain will not exceed 0.2%; thus, the conductivity will not be degraded appreciably.

The stress analysis was carried out using 17 discs in each of the 24 magnets at a current value required for producing the specified field. However, the conductor design is for cryogenic stability at a current level which is 13.3% higher so that a magnet can operate with only 15 discs (and still be cryogenically stable). The actual number of discs per magnet is 19. Thus, there are two degrees of redundancy built into the "D" magnets:

(1) The coils are normally operated with 19 discs at a reduced current (26.7% less than the stability limiting value) and carrying an electro-mechanical load designed for 17 discs only. If two adjacent discs were disabled by an arc (or some other reason), they can be disconnected by the electrical leads connecting the discs on the outer surface at the top of the magnet where an access port has been provided.

UWMAK-II TOROIDAL FIELD MAGNET DESIGN

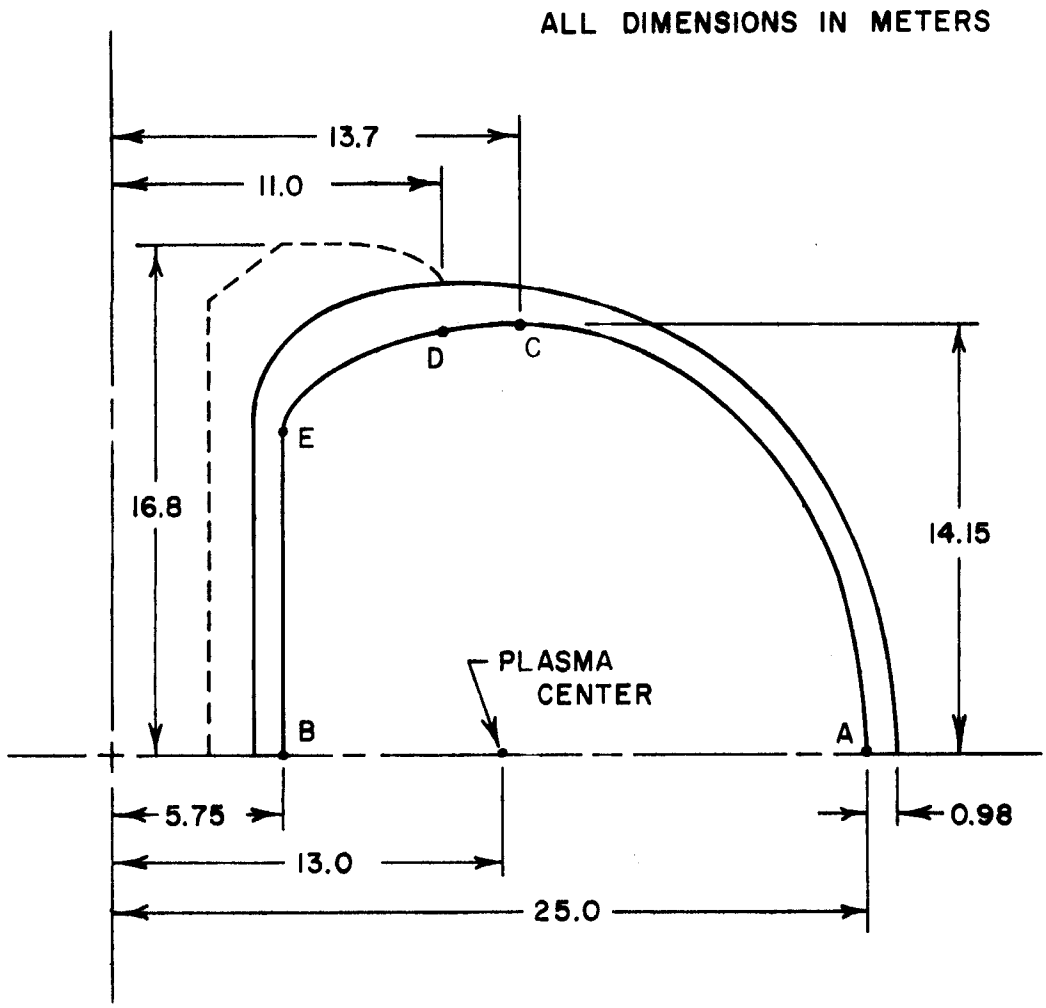

Figure III-A-1

"D" Shaped Toroidal Field Magnet Design

(2) If further problems arise, a second pair of discs or two single discs at locations apart from each other can be disconnected without exceeding the allowed stress or current densities. All 19 discs will still share the mechanical load even if not all are electrically powered.

III-A-1. Specifications

Table III-A-1 lists the specifications of the toroidal field magnets and their comparison with the design for UWMAK-1.(1)

III-A-2. Construction Techniques

The manufacturing and assembly of the conductor and discs as well as the assembly of the magnet and dewar structure are similar to that of UWMAK-I.(1)

The conductor will again consist of an OFHC copper backing strip soldered to the superconductor composite strip which contains twisted TiNb filaments in copper matrix. The cross sections of the conductor are tapered as shown in Figure III-A-2. Further specifications are listed in Table III-A-1.

Each of the 19 discs in each magnet is now an extended "D" shaped washer 5 cm thick and 98 cm wide, weighing 15.8 Mtons. The 29 spiral grooves on both surfaces will be forged, rolled and/or machined into the faces. The 4800 m long conductor, shaped to the cross sections described above, is passed through a hole located at midplane near the inner edge (point A in Fig. III-A-1) and wound into the grooves.

The completed discs are assembled by lowering them over 2630 aluminum bolts. The bolt pattern is such that the center to center spacing is approximately 30 cm, typically. By prestressing the aluminum bolts, the resulting shear resistance enables the assembled magnet to sustain the loads encountered while being assembled into the dewar and raised into a vertical position.

The cross section of an assembled magnet is shown in Figure III-A-3. The inner dewar wall is assembled against micarta spacers to a tight fit around the magnet. A series of reinforced epoxy struts between inner and outer dewar walls provided laterial support to the magnet, particularly in the case of failure of current in an adjacent magnet which would distort the field and produce large laterial, our of plane forces. (See Section III-A-3-c for a more detailed discussion of the lateral support system.)

III-A-3. General Restraints and Design Factors

The design procedure and stress analysis for the "D" shaped toroidal field magnets is discussed in detail in the UWMAK-I report.(1) Except for the few modifications described below, most of the discussion applies equally well here.

Table III-A-1

Specifications of Toroidal Field Magnets

	UWMAK-I	UWMAK-II
a. Field Specifications		
On-axis field at a radius of 13m, B_o	3.83T	3.67T[(a)]
Field at inside turn of far edge (point A)	2.42T @20.5m	1.91T @25.0m
Maximum field at the conductor, B_m (point B) @ 5.75m	8.66T	8.30T
Maximum field in the self-supported portion (point D)	6.3T	4.48T
Field Ripple along the far edge of the plasma	20%	0.05%
Total magnet energy stored	44 MWh	62 MWh
b. Design Stress		
Design stress in 316 stainless steel at 4.2K	$4.14 \times 10^8 N/m^2$ (60,000 psi)	$4.14 \times 10^8 N/m^2$ (60,000 psi)
Design strain	$\leq$ 0.002	$\leq$ 0.002
c. Magnet Components		
Number of magnets	12	24
Number of discs per magnet	34	19
Number of conductor turns per disc	60 (30 each side)	58 (29 each side)
Conductor current	10,212 Amp	9,065A @ 19 discs 10,131A @ 17 discs 11,482A @ 15 discs
Disc cross section (see Figure III-A-2)	5 x 93 cm	5 x 98 cm
Superconductor composite: TiNb in copper matrix, thickness of composite strip = 0.5 cm, filament diameter = 0.038 cm, twisted every 30 cm	600 filaments max.	500 filaments max.
Copper stabilizer cross section	2.99 cm wide x 2.00 cm thick on inside turn, tapers to 1.10 x 1.60 cm on outermost turn	2.87 cm wide x 190 cm thick on inside turn tapers to 1.70 x 1.13 cm on outermost turn

Table III-A-1 (continued)

	UWMAK-I	UWMAK-II
Average copper to superconductor ratio (volumetric)	8:1	9:1
Insulation between conductor and stainless steel disc	0.10 cm reinforced epoxy	
Spacer between discs	0.64 cm thick micarta, covering 50% of the area	
Aluminum alloy bolts to fasten the discs together against slipping, 1" diameter	1670	2630
Lateral support between the magnet and dewar; reinforced epoxy struts on each side of cross section	8500 cm^2	5500 cm^2
Each magnet weight	900 Mt	710 Mt
d. Total materials required		
TiNb alloy superconductor	104 Mt[(b)]	164 Mt
Copper stabilizer	4890 Mt	8000 Mt
Stainless steel in discs	4500 Mt	7230 Mt
Stainless steel in dewars	932 Mt (including core dewar)	941 Mt (removable portion only)
Reinforced epoxy in discs	264 Mt	395 Mt
Micarta spacers between discs	147 Mt	255 Mt
Reinforced epoxy struts in dewars	12 Mt	16 Mt
Aluminum alloy bolts to assemble discs	55 Mt	95 Mt
Cryogenic insulation	516,000 m^2	850,000 m^2
Liquid helium inside dewars	100,000 liters	160,000 liters

(a) T ≡ Tesla = 10^4 Gauss

(b) Mt ≡ Metric ton = 10^3kg.

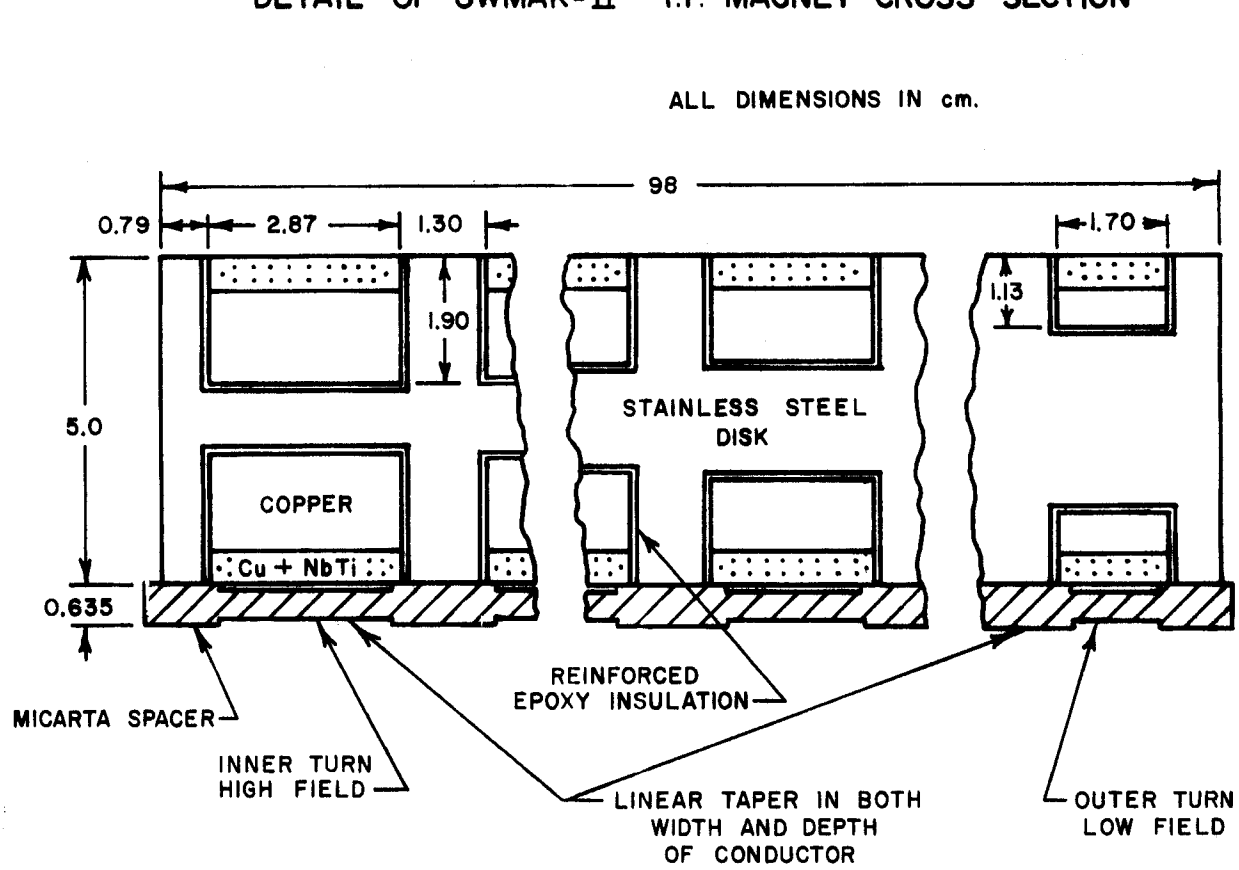

Figure III-A-2

Cross Section of the Conductor and Structural Disc.

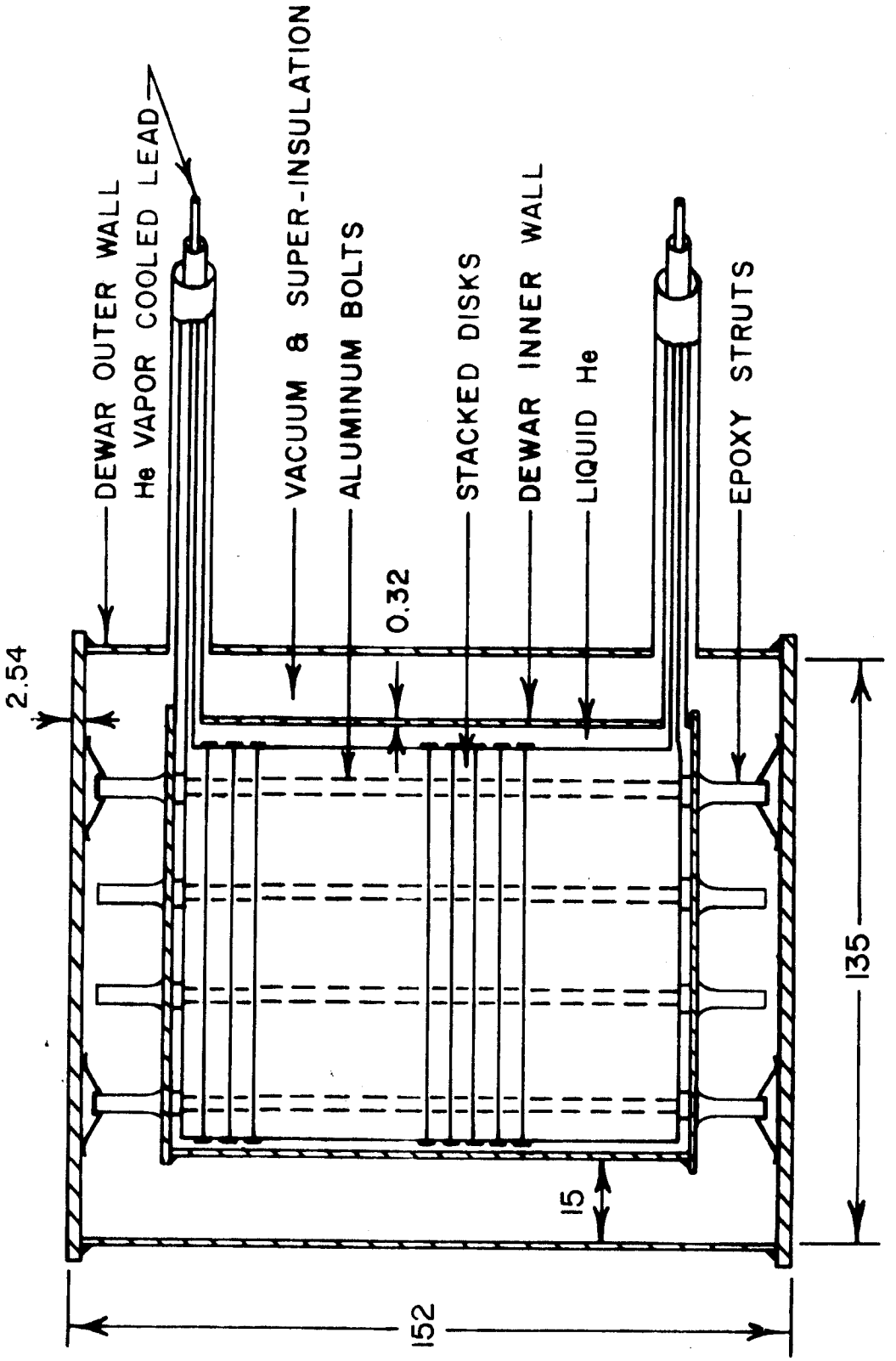

Figure III-A-3. Cross Section of Toroidal Field Magnet.

III-A-3-a. Vertical and Radial Support Structure

The toroidal field magnets designed for UWMAK-I deviated from a constant tension design only in a limited region which was approximately 2 to 2.5 meters in length just above the straight vertical inner portion. The limited unbalanced forces on this portion were carried directly into the cold central structure with no major design problem. The present design, however, requires a much larger portion of the magnet (from point C to point E in Fig. III-A-1) to deviate considerably from a constant tension shape. Furthermore, this section is very nearly horizontal over a sizable portion of its span instead of being nearly vertical as was the case in UWMAK-I.

In order to determine accurately the stress distribution in this nonuniform portion of the magnet, a finite element analysis should be made which would also include the built up central support structure. Instead, an approximate slope and deformation matching technique was carried out to the point where it was clear that the space available was sufficient for the required structure.

The central support structure, which is best shown in Figure III-A-4, is a massive axisymmetric stainless steel cylinder of 3.2 m inner radius and 4.75 m outer radius. It flares out on the top and bottom to a radius of 8 meters. In addition, there are 24 cantilever beams extending over the toroidal field magnets to a radius of 11 meters but not blocking the regions between magnets. This feature is needed for the support of the magnets against the bending moments arising from the non-constant tension portion.

The structural cylinder which also provides winding forms for the transformer coils consists of interlocking rings bolted to each other. The transformer coils will not have steel reinforcing band interweaved with the conductor windings, since the steel in the central structure will provide the support needed to contain the magnetic forces. The central structure, except for a small portion on the bottom, will be contained within the toroidal magnet dewar and will therefore operate at the temperature of liquid helium.

In UWMAK-I, the forces from the toroidal magnets were directed inwards over essentially the full height putting the central support structure into compression. This is not true for the upper and lower portions of the central support structure in the present design. The constant tension portion of the toroidal field magnets extends only part way along the curving section. When the magnet starts deviating from the constant tension configuration, it is made thicker in order to provide additional stiffness against bending as is shown in Fig. III-A-1. The horizontal components of the magnetic field forces acting over the region from C to E in Fig. III-A-1 no longer balance the tension at section C and as a result there is an outward force on the central support structure at E. The total radial force from each magnet is 13 x 10^6kg (28.5 x 10^6lbs) on each support beam which engages the magnets to the central structure.

As mentioned previously, the central structure is at liquid helium temperature and therefore higher values of tensile and shear stresses can be used in designing the supports. We have set upper limits for stainless steel of 414 x 10^6 N/m^2 (60 x 10^3psi) tension and 2.07 x 10^6 N/m^2 (30 x 10^3psi) shear and for high strength alloy employed in the shear pins, a shear stress of 345 x 10^6M/m^2 (50 x 10^3psi).

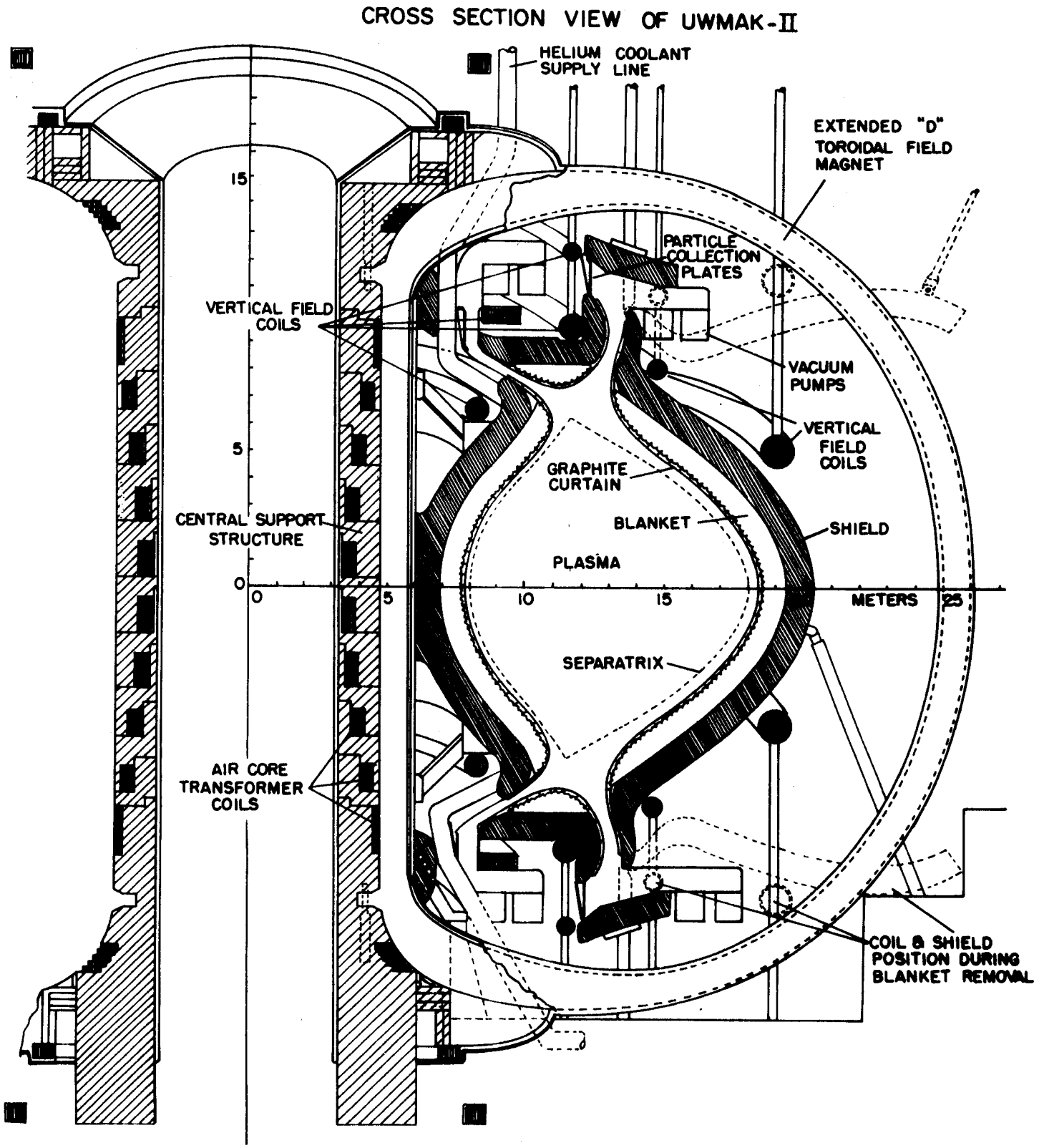

Figure III-A-4

In order to provide the needed pin area in shear, the support beam was segmented as shown in Fig. III-A-5 such that the pins engaged the support beam to the central structure several times. Each pin is subjected to shear in eight places instead of only two. Four pins, 13 cm diameter will have a shear stress of $3.1 \times 10^8 N/m^2$ ($45 \times 10^3 psi$). If the support beam is 112 cm high and 107 cm wide (the width of a magnet) the maximum tensile stress will be $3.9 \times 10^8 N/m^2$ ($56.7 \times 10^3 psi$).

The best way to attach the support beam to the toroidal magnets is to have it forged into the discs which make up the magnet in the first place. As the 19 discs are assembled, the gaps between the discs at the support beam will be filled with weld metal and the final machining performed.

The cylindrical part of the central support structure both at the top and the bottom will be in tension due to the radial forces on the magnets discussed above. The cumulative force from all the magnets distributed over ~130 cm of cylinder height produces an effective internal pressure on the cylinder of $1.24 \times 10^8 N/m$ ($18 \times 10^3 psi$). This produces a tangential stress of $2.9 \times 10^8 N/m^2$ ($42 \times 10^3 psi$) and a radial stress of $1.24 \times 10^8 N/m^2$ ($18 \times 10^3 psi$) in the cylinder wall.

In addition to the radial load, the central support structure will experience an axial force of $20.8 \times 10^6 kg/magnet$ ($45.7 \times 10^6 lbs/magnet$). This force will have to be transferred to the straight leg of the magnet by means of the support beam. The resulting shear stress on the support beam is $1.9 \times 10^8 N/m^2$ ($27.7 \times 10^3 psi$).

III-A-3-b. Radiation Damage to the Copper Stabilizer

The increased attenuation provided by the blanket and shield in the present design removes the need for increasing the conductor cross sections to account for radiation damage to the stabilizer, as was done in UWMAK-I. It should be noted, however, that the redundancy built into the magnet in the form of extra structure, stabilizer, and superconductor would allow for considerable radiation damage if it were not needed for a failure of a disc section. When operating normally with 19 discs connected in series in each magnet as stated before, the current density in the superconductor and in the stabilizer is only 15/19 of the conservative design values. Similarly, the stress level in the discs is only 17/19 of the design value. It should be noted again that all 19 discs are bolted together and will always share the mechanical load even if only 15 are carrying current.

III-A-3-c. Dewars

The design features of the divertor slots in the UWMAK-II blanket has necessitated a new approach in the design of the dewar for the toroidal field magnets. Whereas each individual toroidal field magnet has its own liquid helium container, the insulating vacuum is now common for all the toroidal field magnets. This came about as a result of a decision to surround the straight legs of the toroidal magnets with one continuous outer dewar consisting of a heavily reinforced cylinder subtending the magnets in the toroidal direction. Individual dewars branch off at the top and bottom to cover the curving portion of the magnets as is shown in Figs. III-A-4 and III-A-6. The reasoning behind this decision was the following:

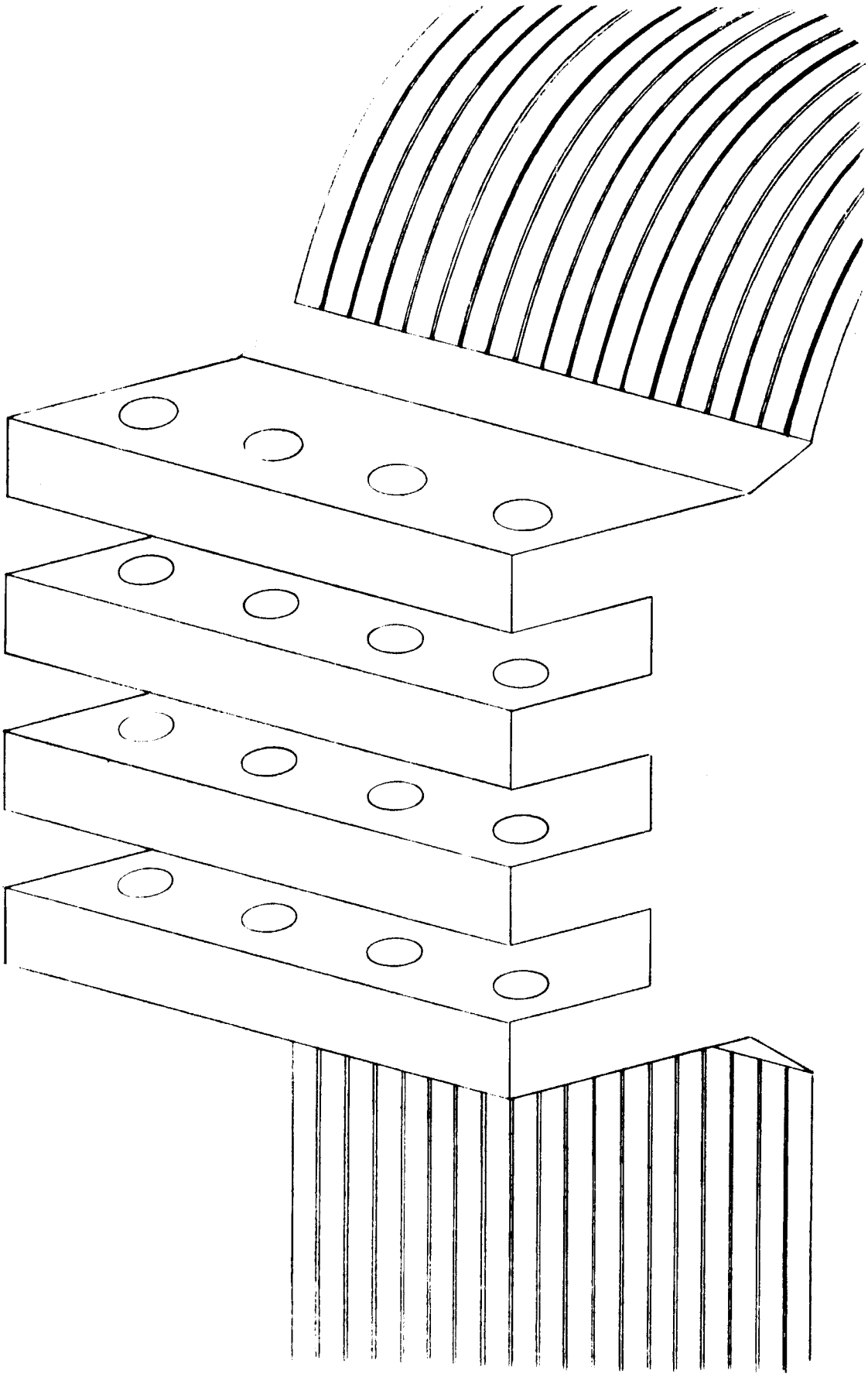

Figure III-A-5

Shear pins - Support Beam Segment

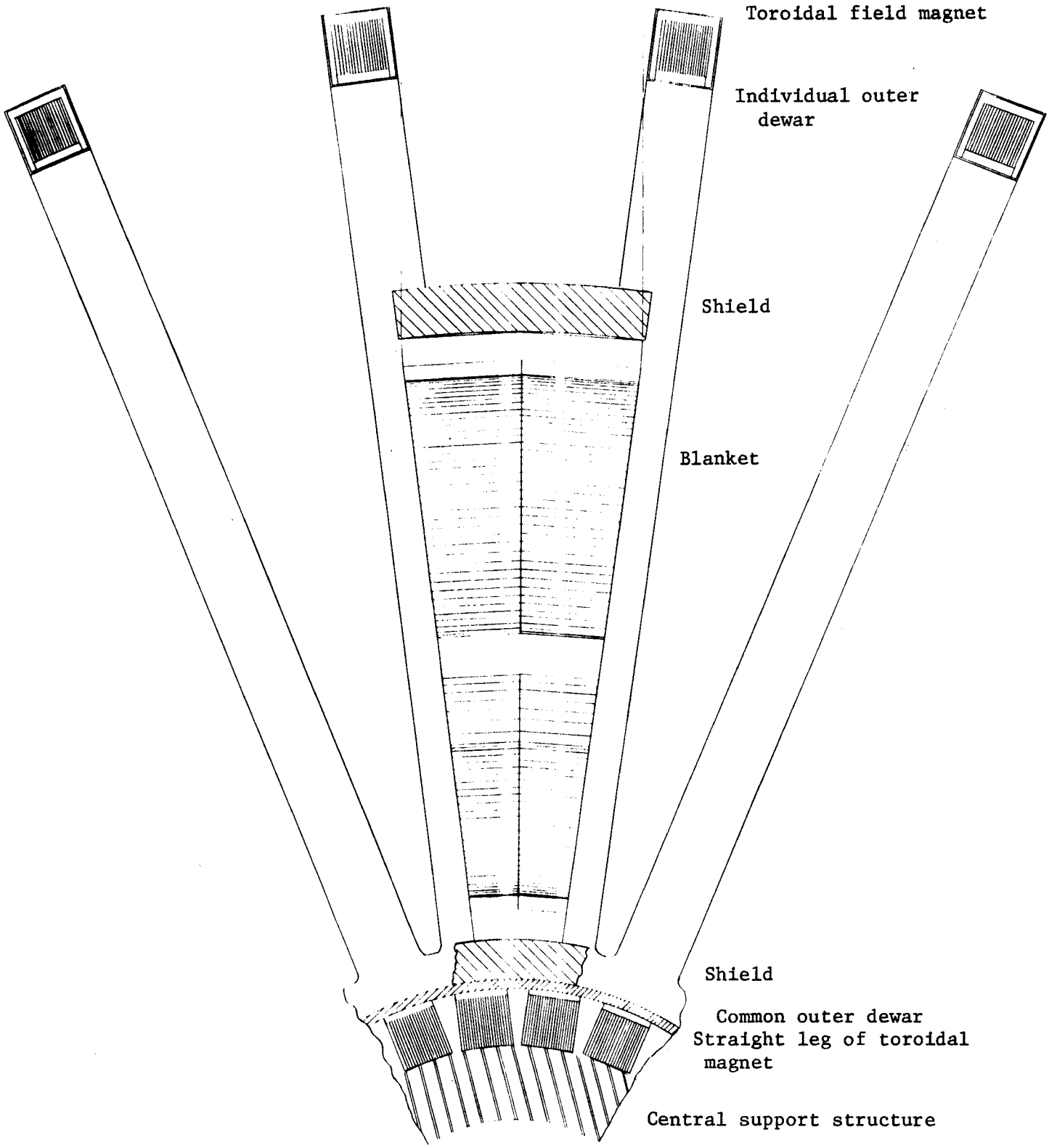

Figure III-A-6

Cross Section Along Mid-Plane of Four Toroidal Magnets Showing the Common Outer Dewar

1. The inner divertor slot left very little room for support structure needed for the inner blanket and shield. A continuous reinforced cylinder could act both as a dewar and as a structural member for supporting the various components.

2. The toroidal field magnets need not be removed for servicing the blanket, obviating the need for individual dewars.

3. The decision to use 24 toroidal magnets coupled with the more conservative magnet design necessitated by the multiple redundancy concept left inadequate space on the inner radius of the toroid for individual dewars.

It has been estimated that a wall thickness of 6 cm would be needed for the cylinder to support the various loads at reasonable stress levels. The total weight of the cylinder will be ~360 MT but the mass it has to support weighs ~10,000 MT. As designed, the horizontal component of the load on the cylinder is 1/6 (10,000) = 1667 MT. If this force is spread over a cylinder height of 1 m, the effective pressure will be 60 psi. This produces a hoop stress of $48 \times 10^8 N/m^2$ (7.0×10^3psi). The vertical component of the load is carried longitudinally by the cylinder at a compressive stress of $0.4 \times 10^8 N/m^2$ (5.8×10^3psi).

The cylinder is supported on the ground on pedestals protruding between the toroidal magnets. There is adequate space between magnets for such supports. A conical shell is used to spread the load from the cylinder to the pedestals as is shown in Fig. III-A-4.

The individual dewars which cover the curving portion of the toroidal magnets are of the conventional type (see Fig. III-A-3) like those used in UWMAK-I. The sidewall thickness is 2.54 cm and the remaining wall covering the inner and outer surfaces of the toroidal magnet are 1.38 cm thick. The weight of an individual dewar is 37.5 MT and will need a brace on the outer surface supporting the dewar on the floor of the reactor. Fifteen centimeters of superinsulation is used between the outer vacuum dewar and the inner liquid helium dewar.

III-A-4. Lateral Support and Structural Safety

A significant change was made possible in the lateral support of the toroidal field magnets when the decision was made to provide a secondary vacuum wall (shown in Fig. III-A-7) at the location of the toroidal magnet dewar instead of the wall of the reactor room. The vacuum wall necessary to carry atmospheric pressure is also adequate to carry the operating lateral loads between magnets as well as the overall torsional loading exerted from the top to bottom of the toroidal field magnets due to the vertical fields of the transformer and divertor magnets, and the plasma current.

In an attempt to provide an adequate design against catastrophic failure of the toroidal magnet system, a preliminary examination of various modes of failure was made. Although it is conceivable that several adjacent toroidal field magnets could simultaneously experience a complete loss of current in a matter of a few minutes, the decision was made not to design the shell structure between magnets to withstand this condition without permitting large deformations. This decision was prompted by the assumption that such an occurence would in all probability be caused by an accident which would render useless the toroidal field magnets involved and would necessitate their removal. In this event, the replacement of the shell walls and the penetrations through the walls in the area involved would also be possible. The savings in repair costs which might occur if a heavier shell were used would be more than offset by the added cost of the heavier wall. A more detailed examination of the problem will be undertaken in the near future.

One failure mode decided upon is a case in which the current in a single toroidal field magnet is assumed to drop to some low value in less than three or four minutes. The lateral support structure is designed such that this will not cause excessive deformation or motions of the magnets or dewars. A second failure mode for which design calculations were carried out is one in which two adjacent toroidal field magnets suffer a loss of current simultaneously. In this instance, the design permits relatively large motions of the dewars but keeps the stresses low enough to assure that no permanent deformation takes place in the magnets, dewars and the vacuum wall.

The following sections will describe in some detail the design process used for the support shell between the toroidal field magnets.

III-A-4-a. Design requirements based on the failure of one toroidal field magnet

If the current in a single toroidal field magnet drops rapidly due to some unforseen mode of failure, the nearby magnets will experience an increase in current, because of their inductive coupling to the failing magnet. Table III-A-2 gives a list of the changes in current, $-\Delta I_k/I_1$, produced in the 24 magnets which comprise the toroidal field system. Magnet number 1 is the magnet which is assumed to be failing. In addition, Table III-A-2 lists the relative magnitudes of the lateral forces, F_k/F_o, acting on each magnet caused by the distortion of the toroidal field as well as the summation of these forces, $\Sigma F_k/F_o$, which creates the shell stresses which are also listed. The last column of data indicates the lateral motion in centimeters of the outer leg of each dewar at the midplane of the magnet. The force F_o is the nominal

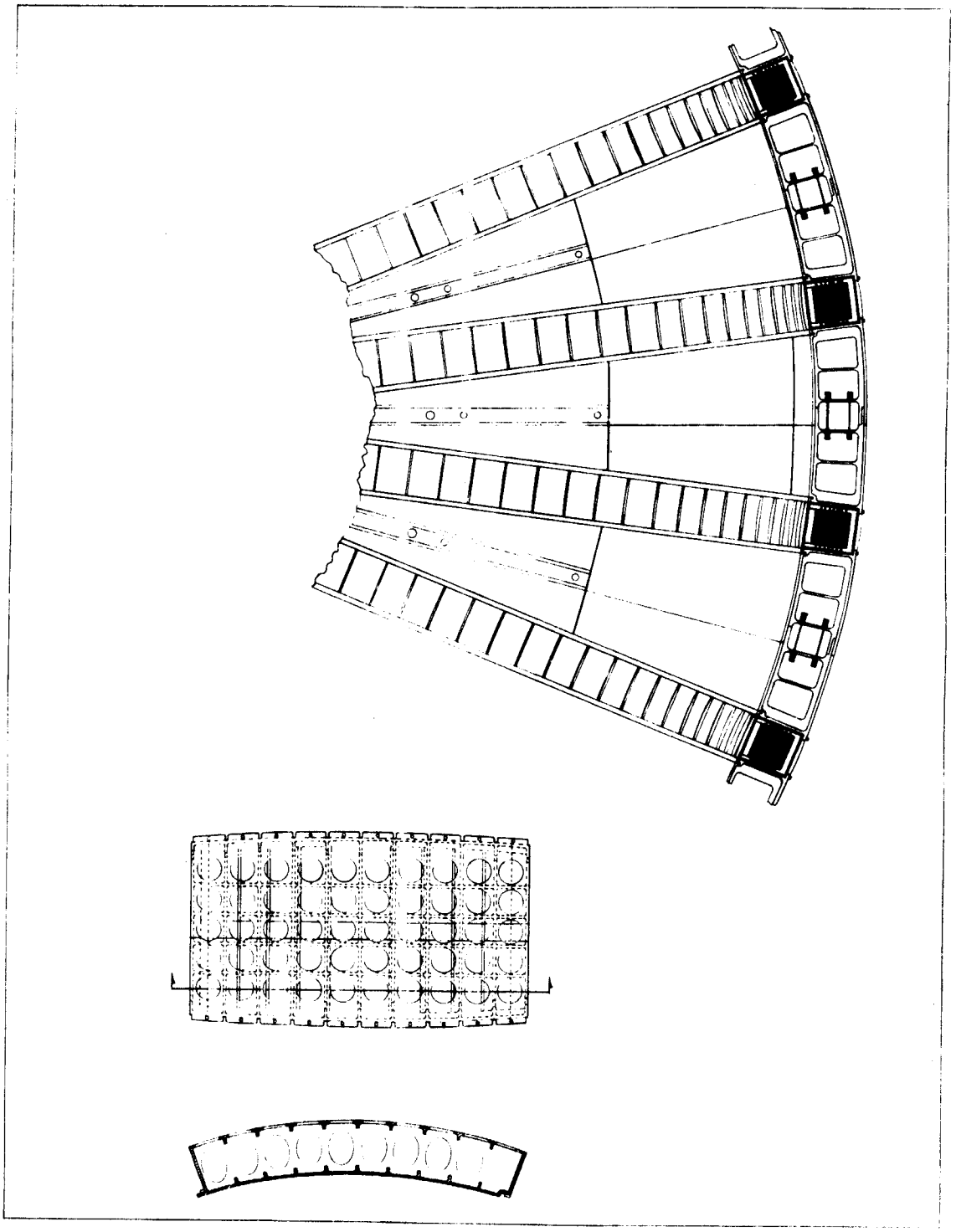

Figure III-A-7

Secondary Vacuum Shell and Lateral Support

Table III-A-2

Induced Currents in the Toroidal Field Magnets and Shell Stresses and Circumferential Motions of the Dewars Due to the Failure of Magnet Number 1

Magnet No. k		$-\frac{\Delta I_k}{\Delta I_1}$	$\frac{F_k}{F_o}$	$\frac{\Sigma F_k}{F_o}$	Lateral Compressive Shell Stress (N/cm^2)	Lateral Dewar Motion (cm)
1		-1	0	0	0	0
2	24	0.2571	1.14	1.14	6920	10.34
3	23	0.0336	0.19	1.33	8670	9.68
4	22	0.0224	0.13	1.46	8860	8.89
5	21	0.0147	0.10	1.56	9460	8.05
6	20	0.0110	0.08	1.64	9950	7.14
7	19	0.0088	0.06	1.70	10310	6.17
8	18	0.0075	0.04	1.74	10560	5.18
9	17	0.0066	0.03	1.77	10740	4.17
10	16	0.0061	0.02	1.79	10860	3.15
11	15	0.0057	0.01	1.80	10920	2.11
12	14	0.0055	0.01	1.81	10980	1.07
13		0.0054	0			0

repulsive force between two parallel conductors, each of which is carrying a current I_o and spaced apart a distance of S meters.

$$F_o = \frac{2(10^{-7})I_o^2}{S} \text{ Newtons/meter}$$

I_o is taken equal to the normal operating current carried by each toroidal field magnet and equals 10.0×10^6 amperes. The current change in the failed magnet, ΔI_1, is taken equal to the negative of I_o.

The force, F_k, is the lateral magnetic loading per unit length on each magnet and the sum of all F_k is the accumulated lateral load which must be carried by the shell structure between the dewars of magnets k and k + 1. There are no tensile forces between the dewars for coils 2 and 24 since the shells are provided with unidirectional slip joints as described in Section III-A-4-c.

III-A-4-b. Design requirements based on the failure of two adjacent toroidal field magnets

It is reasonable to expect the sizeable increases shown in Table III-A-3 for the induced current and lateral forces caused by the simultaneous failure of two adjacent magnets. The magnets which are adjacent to the two disabled ones display an increase in the induced current of less than twice that occurring for a single magnet failure due to the coupling in the second failed magnet. As before, the magnets nearest the failed magnets show the greatest lateral motion.

III-A-4-c. Shell Design

The lateral motions of the dewars could be reduced appreciably if provisions are made for the shells to carry tension in a lateral direction and the attachment between the shells and the dewars is made strong enough to carry this tensile load. We chose not to do this since tensile stresses developed over the much shorter lateral span between magnets 2 and 24, as indicated in Table III-A-2 or between magnets 2 and 23 in Table III-A-3, would be much larger than the compressive stresses indicated. A system capable of carrying the loads in tension would require more structure and would be more costly and difficult to design. To allow for the lateral dewar motions without developing tensile stresses in the shells, a spring-loaded slip joint is provided at the centerline of each shell as shown in Fig.III-A-7. This slip joint is provided with O-ring type seals just as are the joints between the shells and the dewars.

The slip joints will have interlocking lateral lugs to provide the shear resistance necessary to carry the torsional loading created by the poloidal fields. This is discussed in Section III-C-4.

In order to gain access to the shield and blanket area, it would be necessary to remove the shell panels between the outer legs of the toroidal magnet dewars. The shell panels near the top and bottom of the structure have penetrations through them and will not be removed during a normal replacement of the first wall. Each shell panel will be electrically isolated from the dewars and adjacent panels in order to reduce the shielding effect on the changing poloidal fields.

Table III-A-3

Induced Currents in the Toroidal Field Magnets and Shell Stresses and Circumferential Motions of the Dewars Due to the Failure of Two Adjacent Magnets

Magnet No. k		$-\frac{\Delta I_k}{\Delta I_1}$	$\frac{F_k}{F_o}$	$\frac{\Sigma F_k}{F_o}$	Lateral Compressive Shell Stress (N/cm^2)	Lateral Dewar Motion (cm)
1	24	-1.00	0	0	0	3.11
2	23	0.40	2.06	2.06	12500	18.65
3	22	0.09	0.43	2.49	15100	17.45
4	21	0.05	0.28	2.77	16800	15.99
5	20	0.03	0.20	2.97	18000	14.38
6	19	0.02	0.16	3.13	19000	12.65
7	18	0.02	0.12	3.25	19700	10.82
8	17	0.01	0.08	3.33	20200	8.93
9	16	0.01	0.06	3.39	20560	6.99
10	15	0.01	0.04	3.43	20800	5.01
11	14	0.01	0.01	3.44	20870	3.01
12	13	0.01	0.01	3.45	20900	1.01

Since the lateral forces due to the field distortion vary inversely as the distance between magnets and this distance in turn varies almost directly with the radial distance from the central toroidal axis, the wall thickness and the reinforcing rib areas of the shell shown in Fig. III-A-7 vary inversely as the radius. This keeps the compressive stress in the shell structure as nearly constant as possible which in turn holds constant the circumferential unit strain. Under these conditions, the radial plane of each magnet remains essentially plane as it moves laterally. Modifications in this distribution of material are made near the central support structure to compensate for the different circumferential stiffness of the core as compared to the shell. The purpose of the above described procedure is to minimize the lateral bending strains in the magnet.

The ribbed radial edges of the shell panels which are adjacent to the dewars provide the bending resistance needed for the sidewalls of the dewars which are loaded laterally from the many fiber-reinforced epoxy struts shown in Fig. III-A-3. The variation in loading on the sidewall of the dewar which is in turn carried to the ribbed wall of the shell is essentially linear from a maximum on the inner edge of the magnet to a minimum on the outer edge. With this in mind, the material provided for lateral load in the shell is approximately twice as much on the inner shell, which is also the vacuum barrier, as on the perforated outer shell. The perforations in the outer shell are needed for removal of the cores used in casting the shell, for visual inspection of the casting and also permit the use of nearly constant thickness material throughout a given region of the shell. Thus, the outer shell surface, although cast with plate and rib thicknesses similar to those on the inner surface, is only one-half as strong and as stiff.

At midplane where the dewars are spaced apart 6.62 m center to center, the average inner shell thickness is 4 cm, the average outer shell thickness is 2 cm (based on gross area), and the average radial end thickness is 7.5 cm. The flanged ribs necessary on the ends accounts for this greater value. Using these values, the total weight of the aluminum alloy shell is 1405 kg per meter of dewar length at midplane. This same value can be used throughout since the wall thickness increases as the length between dewars decreases. The total weight of shell is, therefore, 1.75×10^6kg.

III-A-4-d. Dewar design

To transmit the circumferential load from shell to shell through the inner and outer dewar walls requires that these walls carry the compressive stresses across a length of 152 cm without suffering any buckling. To accomplish this for the maximum load of 3.45 F_o requires that the inner dewar wall be 2.54 cm thick at midplane of the outer leg of the magnet and be braced with lateral ribs spaced 1 m apart along the length of the dewar. Each rib at midplane is 5 cm in width and tapered in height from 2 cm at the ends to 10 cm at midlength. As the dewar major radius (distance from the central axis of the toroid) decreases the wall thickness and the rib thicknesses must be increased as was discussed for the shell thicknesses.

Similarly the outer dewar wall would be 1.38 cm thick at midplane and be ribbed every 1 m with ribs 3 cm wide and 8 cm deep at midlength. These dimensions would also be increased as the major radius decreases.

The dewar side walls are 2.54 cm thick and need not be increased since the major loading is carried by the braced shell walls.

III-A-4-e. Dewar strut design

The lateral loading on the dewar side walls is transmitted from the toroidal field magnets to the dewars by the fiber-reinforced epoxy struts shown in Figure III-A-8. It is possible to provide struts capable of transmitting the load on magnet 2 (see Table III-A-3), 2.06 F_o, but they cannot be in contact with the outer dewar wall without causing an excessive heat leak into the magnet. Therefore, ten percent of the struts are provided with a nonlinear conical spring cap as shown in Fig. III-A-8. The remainder will be the same strut without the cap and will have a clearance of approximately 1 cm from the outer dewar wall.

The design of the conical spring cap must provide for several functions:

(1) The effective spring constant must provide the proper centering forces when the dewar is assembled (see point A on Fig. III-A-9) and maintain these forces when the magnet is cooled. The spring constant k_o must be large enough to provide for the magneto-elastic stability of the toroidal field magnets under their own radial field forces but at the same time not be so large as to create excessive friction due to the motion of the toroidal field magnets relative to the outer dewars. This spring constant is illustrated at the operating point O in Fig. III-A-8. During cooldown, the maximum relative motion is approximately 8 cm radially at midplane. When the magnets are energized to full current this motion reverses and it moves back approximately 3 cm. The materials used for the conical spring cap must have a low coefficient of friction against the smooth stainless steel dewar wall. A suitable lubricant compatible with a vacuum environment will be used.

(2) The conical spring caps must be designed to provide a much larger spring constant when the toroidal field magnets move laterally under the forces from the poloidal fields (see point P in Fig. III-A-9). Since the poloidal fields will rise and fall every 90 minutes during a burn cycle, any magnet motion will be accompanied by stresses which are cyclic in nature and will be of concern regarding fatigue. Furthermore, the loads from the poloidal fields must not cause the stand-off struts to make contact. Fortunately, there will be no displacements causing friction forces to develop when the lateral loads due to the poloidal fields are imposed.

(3) The conical spring caps must not overload the struts on which they are mounted when a failure condition occurs such as the loss of one or two toroidal field magnets as was previously discussed. Under this condition, the force in the conical spring cap will reach a peak and decrease slightly as all of the stand-off struts move into contact. The proposed shape of the conical spring cap is shown in Fig. III-A-9 along with the desired load deflection curve.

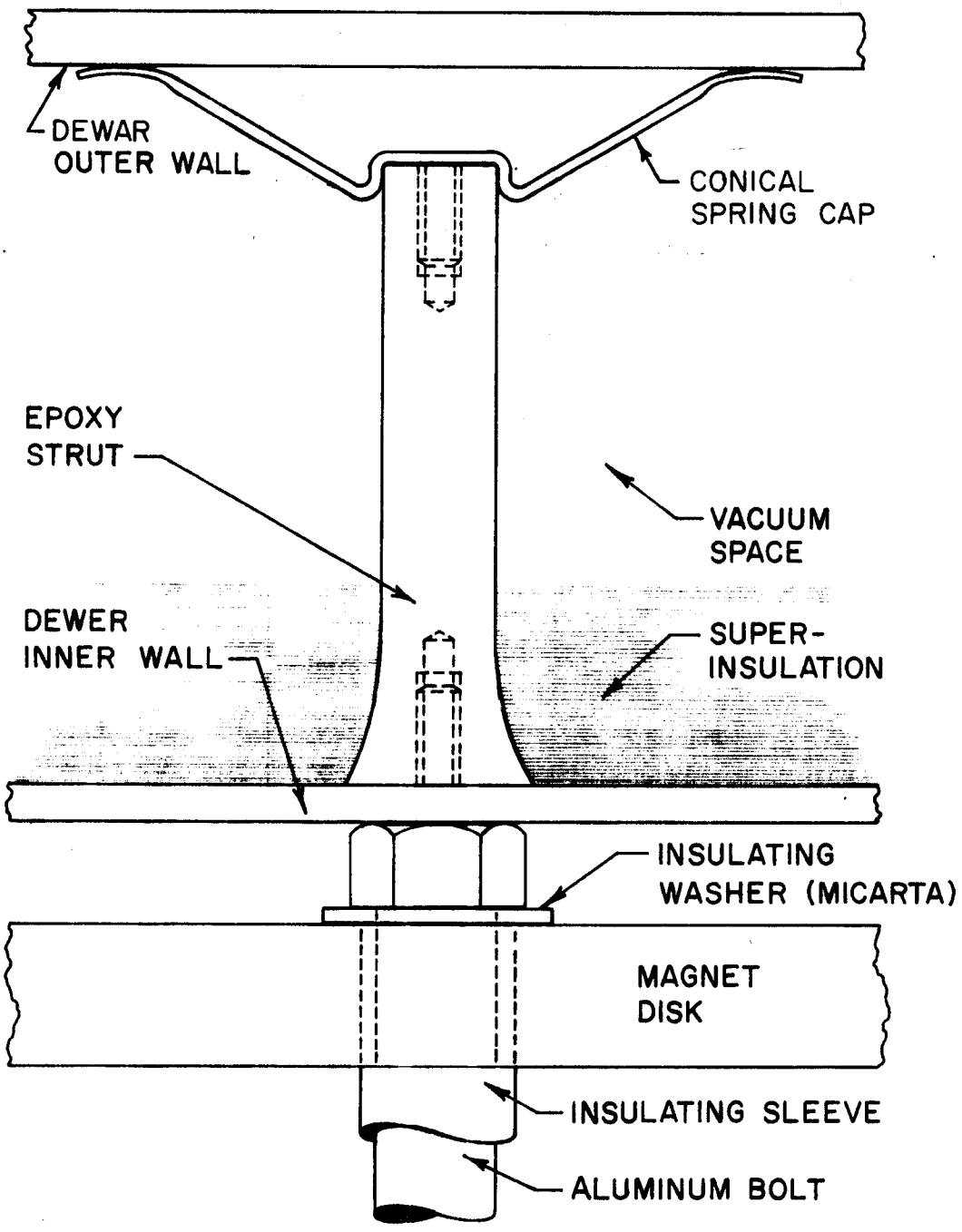

Figure III-A-8

Lateral Load Bearing Epoxy Strut

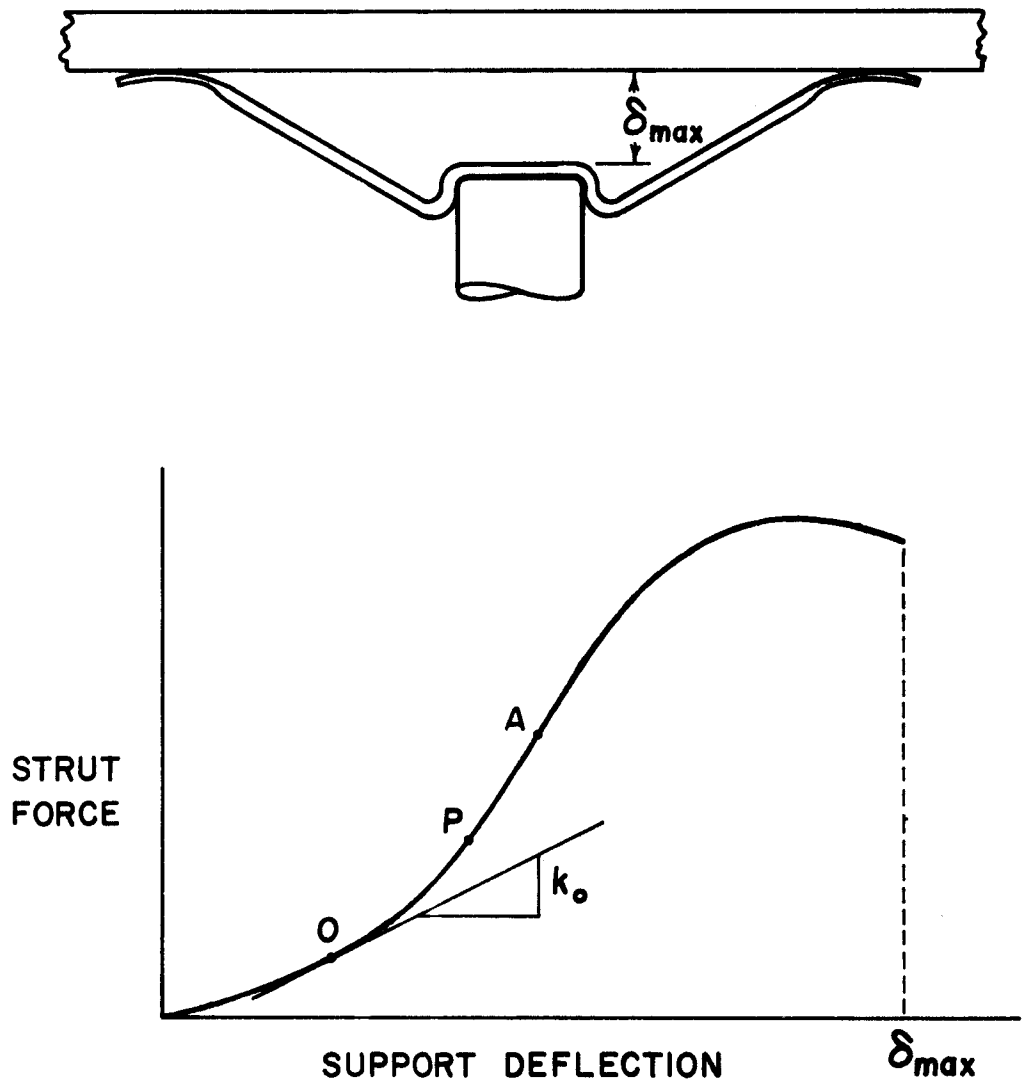

Figure III-A-9

Load Deflection Curve for the Conical Spring Cap.

III-A-4-f. Design requirements for the torsional loading produced by the poloidal fields

The poloidal fields produced by the currents in the divertor coils, transformer coils and the plasma produce lateral forces on the toroidal field magnets. To evaluate these forces, the lateral force on each 1 meter segment of a toroidal field magnet was determined from the current vectors in the toroidal field magnet and the field lines due to the combined divertor, transformer and plasma currents when they are all at their maximum values. Later studies will evaluate the effects of the different combination of currents which occur during a burn cycle. Table III-A-4 lists the lateral forces on the given segment which are numbered from the midplane. The forces are antisymmetric being equal in magnitude but opposite in direction above and below the midplane. The torsional shear stresses in the shell, based on a shell wall thickness and dewar inner and outer wall thicknesses which vary inversely as the major radius (see Sec. III-A-4-c), are also listed in Table III-A-4. They are given for the center of each dewar segment. Since the shell walls were sized and proportional for a failure condition much more drastic than an operating condition, these shear stresses and the accompanying lateral displacements are all very small. The toroidal field magnets, of course, move laterally somewhat more due to the deformation of the coned spring caps on the struts but this is on the order of an additional 1/4 to 1/2 of a centimeter.

The shear stresses in the sliding lugs in the spring loaded shell connections are approximately twice the values given for the shell wall but are still small.

III-A-4-g. Design requirements for the external pressure on the toroidal shell structure due to the vacuum

The shell structure between the dewars of the toroidal field magnets provides the secondary vacuum barrier. Under the external atmoshperic pressure the most critical portion of this shell is at midplane where the wall thicknesses are a minimum and the unbraced spans are the greatest. The 4 cm aluminum wall thickness will carry without buckling three times the atmospheric pressure on a one meter span at a radius of curvature of 1600 cm.

III-A-4-h. Design to allow for penetration of the toroidal shells

Of paramount importance is the need to decouple the motion of the toroidal magnets lateral support shell from the penetrations which are required for the support of components within the toroidal enclosure. In order to do this, the design has to accomodate two functions:

1 - Individual sections of the shell must have the capability of separating in the middle while in tension without imparting forces on the component supports and without breaking the vacuum seals.

2 - Individual sections of the shell must have the capability of being displaced in the toroidal direction without separating while in compression, also subject to the above restrictions.

Table III-A-4

Shear Stresses with Shell Wall and Circumferential Motion of Dewar Walls on the Toroidal Field Magnets due to Maximum Combined Poloidal Fields From Divertors, Transformers and Plasma

Section Number*	Lateral Force on Magnet** N/m	Shear Stress in Shell N/cm^2	Circumferential Motion of Dewar cm
1	-38,150	-1250	-.052
3	-89,170	-1290	-.160
5	216,200	-1240	-.266
7	858,000	- 890	-.350
9	1,310,000	- 270	-.386
11	1,175,000	360	-.369
13	648,000	750	-.312
15	89,200	870	-.241
17	-432,400	720	-.176
19	-503,200	460	-.132
21	-58,500	365	-.101
23	25,200	369	-.070
25	3,580,000	1522	.020
27	5,163,000	880	.025
29	-12,200,000	-190	.020
31	-1,430,000	-390	.010

* Sections are 1 meter in length and are numbered from midplane on the outer leg.

** See Fig. III-C-17 for sign convention.

Upper and lower shell panels, reaching 20m in the radial direction from the center of the reactor will have penetration in them but need not be removable for access to the blanket and shield region. In addition, eight of the twenty four removable panels spanning the central plane of the toroid, will have neutral beam port penetrations.

The penetration will be attached to plates which will be fixed at all times. These plates will fit in both halves of the shell panels and be sealed to them with conventional "O" rings. The fit will be such as to allow the panel halves to separate under tension while the penetration plate will remain stationary. Similarly, under compression, the panel can be displaced toroidally in either direction while the penetration plate remains stationary. Bellows will be used to attach the penetrations to the plated in order to allow for relative motion between them.

It is important to examine the implications of a loss of the secondary vacuum in connection with a seal failure in the vacuum shell. The two most important consequences are:

1 - A rise in the primary vacuum pressure with a time constant of the order of seconds.

2 - A loss of the insulating vacuum which prevents certain sections of the shield from overheating, also having a time constant of the order of seconds.

In both of these cases, monitors of vacuum pressure and temperature will give adequate time for preventative action to take place. Even if preventative action fails, the consequences are not drastic. The rise in the primary vacuum pressure will prevent a burn cycle from continuing and will quench the plasma in an orderly fashion. The thermal capacity of the shield is also high enough as to prevent overheating if the reactor is not immediately shut down.

III-B. Divertor and Transformer Coils

In this section, we will describe the steps used in the design of superconducting divertor and transformer coils. The specific requirements of short rise time and periodic cycling of currents and fields make it necessary to use a different design strategy than that used for the toroidal magnets. This and the lower stress levels experienced by most coils legislate the emphasis on the conductor design and ac loss calculation rather than stress analysis.

II-B-1. Specifications

II-B-1-a. Description and Specifications

As with all our designs, complete cryogenic stability for life-time reliability is our guiding philosophy. The requirements specified above are similar to those for a pulsed energy storage dipole magnet designed by the University of Wisconsin and the Fermi National Laboratory.(2) We will use it as a guideline for out present design. The same maximum current carrying capacity at 20,000 A per conductor is adopted. However, the conductor size and the number of filaments per conductor are calculated individually for each of the 12 divertors and the 18 transformers according to their respective ambient magnetic field.

As a safety measure, a redundancy of 10% extra material and 10% extra turns is included for all the divertor and transformer coils. It may be mentioned here that while the divertors could be designed with less redundancy, since in theory they can be cut out and rewound without disassemblying the central core of UWMAK-II. It is felt that the time and expense of such a procedure warrants the above stated margin in their design.

To reduce ac losses described later in this section, the superconducting filaments are extruded with cupronickel which are then twisted and transposed inside a high purity copper matrix. The UWMAK-I report(1) only suggested these techniques and made no explicit use of them. With the exception of two, the transformer coild are housed inside the toroidal central structure (see Fig. III-A-5) and therefore, no interleaved reinforcing steel is necessary for the winding of these coils. On the other hand, some of the higher stressed divertor coils will need reinforcing steel interleaved between turns. The general specifications of all the divertor and transformer coils are given in Table III-B-1.

III-B-1-b. Comparison with UWMAK-I

Basic changes have also been made as to the placement of the divertors in UWMAK-II which are now placed inside the "D" shaped magnets. This has the effect of reducing the maximum energy stored in the poloidal field by a factor of 5 over UWMAK-I with a substantial decrease in cost. Improved vertical field control is also incorporated. The disadvantage is, however, increased difficulty in winding since the winding machine must operate within the "D" magnets. Table III-B-2 lists a general comparison of the poloidal field coils in UWMAK-I and UWMAK-II.

Table III-B-1

General Specifications of the Divertor and Transformer Coils

(1) Conductor TiNb + CuNi sleeve + copper stabilizer, fully cryogenically stabilized

(2) Conductor current = 20,000 A

(3) Conductor current density = 1,700 A/cm^2 to 2,200 A/cm^2

(4) Conductor width to height ratio = 1:10 (.95 x 9.5 cm to 1.08 x 10.8 cm cross section)

(5) TiNb-CuNi-Cu composite strip: .5 cm x 2.5 cm with 50 to 250, 0.038 cm diameter filaments, twisted every 30 cm

(6) Average copper to superconductor ratio = 60:1

(7) Design stress at 4.2K: 2.76 x $10^8 N/m^2$ (40,000 psi) in 316 stainless steel, 0.83 x $10^8 N/m^2$ (12,000 psi) in copper; strain level $\leq$ 0.002.

(8) Jelly roll winding approach with 4 conductors per pass plus transposition of conductors between pancakes.

(9) .05 cm thick Kapton insulation between conductors; 0.64 cm thick micarta spacers between pancakes which cover 50% of the surface.

(10) Design limits temperatures to 5.2K in a 4.2K bath for all normal situations

(11) Total TiNb alloy superconductor required: 36 Mt

(12) Total copper required (matrix + backing strip): 16,760 Mt

Table III-B-2

Comparison of Poloidal Field Magnets in UWMAK I and UWMAK II

	UWMAK I	UWMAK II
Divertor positions	outside "D" magnet	inside "D" magnet
Transformer positions	6 inside central core; 4 outside	16 inside cent. core 2 outside
Number of divertor coils	8	12
Maximum tension	4.57×10^8 N (1.02×10^8 lbf)	2.44×10^7 N (5.48×10^6 lbf)
Maximum current	24.5 MA[(a)]	6.8 MA
Maximum field	7.59 T	5.72 T
Maximum dB/dT	.076T/sec (100 sec rise time)	0.57 T/sec (10 sec rise time)
Maximum stored energy of the poloidal field	16 MWh[(b)] 57.6×10^9 J	2.9 MWh = 10.4×10^9 J
Maximum total current	128 MA	58 MA
Total eddy current loss		14.71 KWh/charge
Total coupling loss		0.18 KWh/charge
Total hysteresis loss	Not calculated	0.24 KWh/charge
Total conduction loss		850 watts
Total thermal radiation loss		312 watts
Total lead loss		2800 watts

(a) MA ≡ Mega-Ampere = 10^6A

(b) MWh ≡ Mega-Watt-hour = 3.6×10^9J

III-B-2. Design Factors

III-B-2-a. Composite Conductor Design

For the sake of reliability, the cryogenic stability criterion is used. The conductor shape is chosen to be the same as that of NAL 15 ft. bubble chamber magnet.(3) This consists of a rectangular cross section of copper stabilizer with the superconductor composite embedded on one face near the center (shown in Figure III-B-1). Four conductors will be wound in parallel on each turn with kapton insulation and backing steel between them. Each conductor will carry a maximum current of 20,000 A. Cooling channels will be supplied such that about one-half of the face and edge will be in contact with the liquid helium pool. Micarta spacers are used between pancakes covering 50% of the conductor edge.

The external cryogenic stability criterion requires that

$$I_T^2 \frac{\rho_n}{a_n} \leq q \qquad (1)$$

where ρ_n and a_n are the resistivity and area of the copper, P is the cooled perimeter, q is the heat transfer coefficient. In the event that a superconductor goes normal the total current, I_T, is flowing in the copper stabilizer. With the conductor shape described above, this criterion takes the form

$$(2\eta k\ell\, q_e + \xi(\ell - s)q_f + q_f) \geq \frac{I_T^2 \rho_n}{k\ell^2}, \qquad (2)$$

where η = fractions of edge avaiable for cooling = 0.5

ξ = fraction of copper face available for cooling = 0.5

k = ratio of width to height 0.1 (the choice of this value is a compromise between the cooling surfaces obtainable and the number of pancakes required)

ℓ = height of the conductor

s = superconductor composite insert height = 2.5 cm

q_e = edge cooling heat transfer coefficient = 0.4 w/cm^2

q_f = face cooling heat transfer coefficient = 0.15 w/cm^2

In an ambient magnetic field of 5T, the resistivity copper is about $3\times10^{-8}\Omega$-cm. If ℓ=10cm, the above inequality states that the maximum heat generated in the conductor is 1.20 w/cm. Hence, this gives a stability factor of about 0.90. The magnetoresistance of OFHC copper changes with the magnetic field, B (in tesla), as

$$\rho_n = \rho_o (1 + 0.455B), \qquad (3)$$

with $\rho_o = 10^{-8}\Omega$-cm. If I_T, k, η, and ξ are unchanged, the same stability factor can be obtained (approximately) by keeping

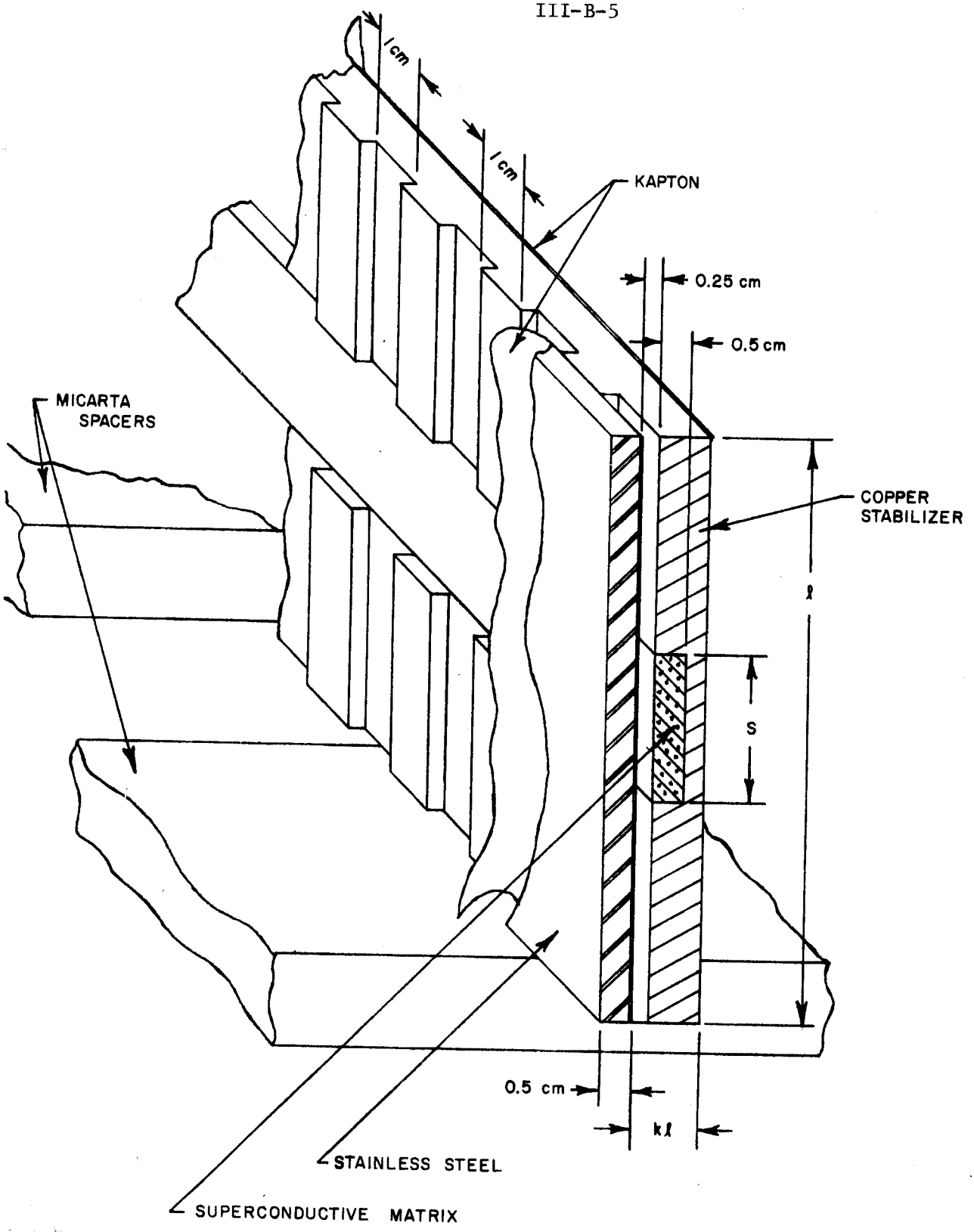

Figure III-B-1

Conductor Cross Section of Poloidal Field Coils

$$\frac{1 + 0.455B}{\ell^3} = \text{constant.} \tag{4}$$

Using this scaling law and taking into account both the toroidal field and the maximum poloidal field, the conductor size for each divertor and transformer is obtained and listed in Tables III-B-3 and III-B-4.

A second "internal" stability criterion determines the amount of superconductor needed. Following any transient temperature raising fluctuation, the current carrying capacity of the superconductor filaments may drop below the design transport current. Part of the current will then flow in the copper with power dissipation in copper as well as in the superconductor. The current sharing characteristics of the composite[3] are shown in Fig. III-B-2. It is shown that the maximum power dissipation in the superconductor occurs when the current is equally shared between the superconductor and the copper stabilizer i.e. equal to one-quarter of the maximum total power dissipation. This heat should be conducted away such that the following inequality is satisfied

$$\frac{1}{4N} \quad W_T \leq 8\pi \, K_s(\bar{T} - T_o), \tag{5}$$

where N = number of superconducting filaments

W_T = maximum total power dissipation = $I_T^2 \frac{\rho_n}{a_n}$

K_s = thermal conductivity of TiNb = 0.5 mW/cm-K

$\bar{T}$ = average temperature of a superconductor filament

T_o = average copper temperature

Using the above typical example and taking T_o = 4.7K and $\bar{T}$ = 5.2K, this inequality requires a minimum number of filaments of 48. However, for the ease of twist and fabrication, a filament size at 0.038 is chosen. To carry a total current of 20,000 A per conductor the number of filaments is given by

$$N = \frac{I_T}{a_s J_c(\bar{T}, B_m)}, \tag{6}$$

where a_s is the filament cross section, J_c is the superconductor critical current density, and B_m is the maximum poloidal field; the parallel toroidal field need not be counted here. This expression given N = 251 for the typical example. In all coils, the N's given by this equation are more than twice that given by eq. (5), so the internal stability is more than satisfied. The values of these N's with 10% redundancy, are also listed in Table III-B-3 and III-B-4. Thus, none of the conductors so designed will ever raise their filament average temperatures above 5.2K under normal conditions. The region that goes normal will not propagate and the superconductivity will recover automatically.

Table III-B-3

Physical Parameters of Divertor Coils

Coil	D_1	D_2	D_3	D_4	D_5	D_6
R(m)	8.2	8.8	11.5	11.5	14.6	19.0
Z(m)	6.5	10.0	12.3	9.5	8.0	5.0
Maximum current (MA)	-3.70	4.87	-1.46	3.40	-1.57	-6.82
Maximum B (T)	2.56	2.73	1.69	2.40	1.75	3.07
Maximum tension (10^6 N)	-6.74*	24.5	1.56	-7.46	10.1	42.8
Conductor height, ℓ(cm)	10.8	10.8	10	10	9.6	9.6
Number of filaments per conductor	70	75	50	65	55	80
Number of turns (4 conductor/turn)	50**	63	20	45	20	84
Number of layers	5	3	4	5	4	7
Magnet minor radius (cm)	32	34 x 136***	22	31	22	44
TiNb (MT)	0.53	0.75	0.21	0.63	0.30	2.40
Copper (MT)	100	140	50	115	60	320
Stainless Steel (MT) for reinforcement	0	12	0	0	10.3	57.5
Micarta spacer (MT)	2.25	4.05	1.88	3.17	2.38	10.2
S.S. in dewar	3.3	14.9	3.4	4.6	3.9	12.3

* Negative value means the coil is under compression.

** The number of turns from the top to bottom are 6,12,14,12,6; other coils can be similarly arranged.

*** Because of the field specification, this should be flat

Table III-B-4

Physical Parameters of Transformer Coils

Coil	T_1	T_2	T_3	T_4	T_5	T_6	T_7	T_8	T_9
R(m)	3.61	3.72	3.94	4.25	4.66	5.43	6.50	7.25	8.22
Z(m)	1.00	3.06	4.99	6.96	8.92	13.50	15.05	17.0	19.3
I_{max}(MA)	-4.13	-3.98	-3.61	-3.41	-2.85	-3.36	-3.34	-2.51	-2.20
B_{max}(tesla)	5.72	5.68	5.40	5.10	4.60	5.14	5.60	4.07	3.93
$T_{max}(10^6 N)$	23.9	22.9	20.2	16.8	8.35	17.4	9.51	6.56	3.57
Conductor height, ℓ(cm)	10.3	10.3	10.3	10	10	10	10.3	9.5	9.5
No. of filaments per conductor	250	240	220	180	120	180	240	110	100
No. of turns (4 conductors/turn)	63	63	56	56	48	60	57	39	36
No. of layers	9	9	7	7	12	5	3	3	4
Magnet size (cm)	100x32	100x32	80x36	78x34	132x20	5(12x52)*	36x100	34x65	45x46
Nb-Ti (MT)	1.05	1.04	0.90	0.79	0.50	1.08	1.64	0.60	0.55
Copper (MT)	52.0	57.5	50.5	51.2	48.2	70.0	84.7	55.8	58.4
Micarta spacer (MT)	1.33	1.37	1.24	1.28	0.69	1.72	2.00	1.44	1.55

*This magnet consists of five single layer coils step stacked against the "D" magnets (see cross section view Fig. III-A-4)

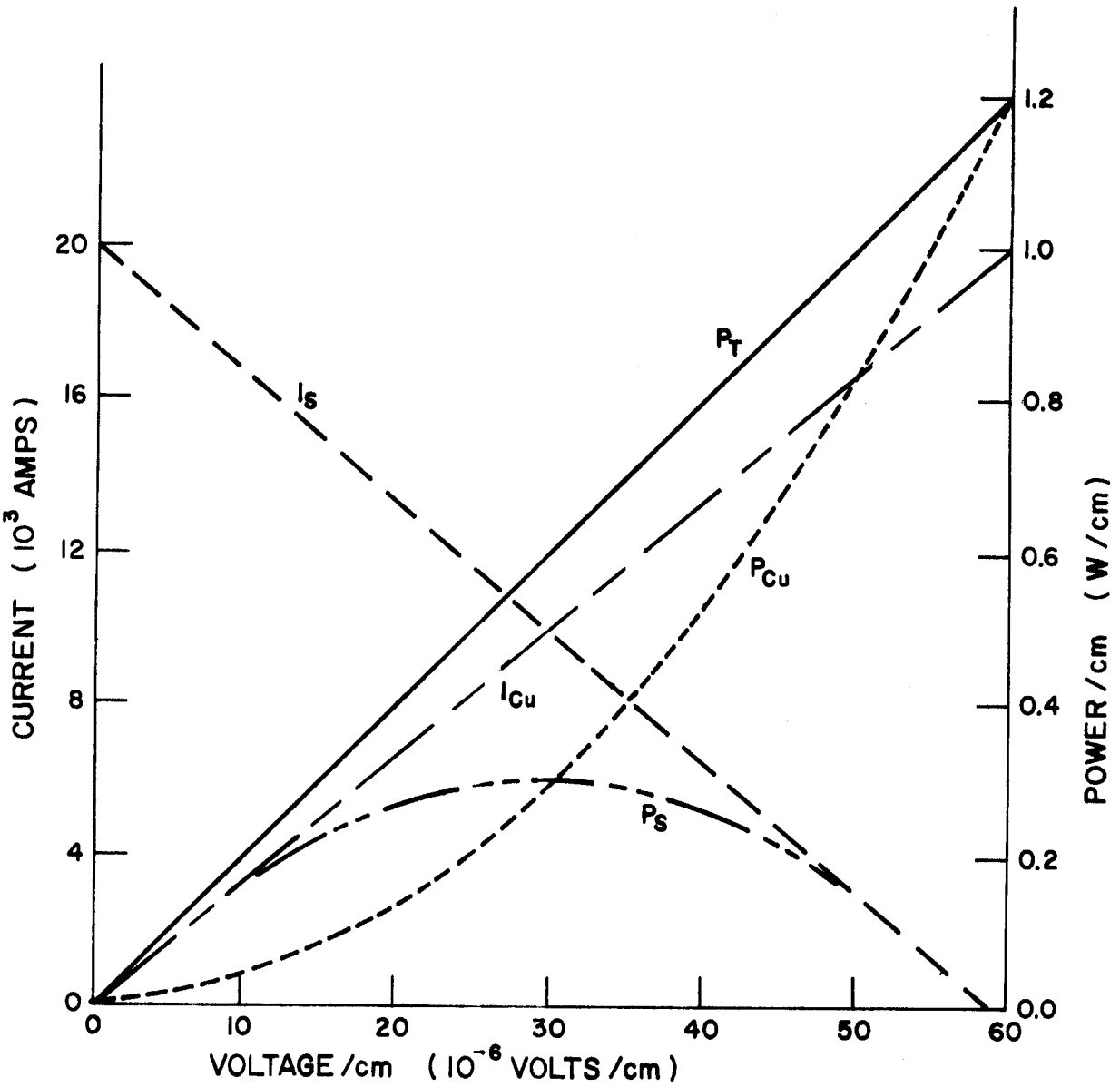

Figure III-B-2

Current Sharing Characteristics of the Superconductor Composite

The ac coupling loss between the filaments calculated later in this section shows that the ac loss for a pure copper matrix is a little too high. The remedy for this is to use some high resistivity cupro-nickel sleeve in the matrix. The superconducting filaments might be extruded first with cupro-nickel sleeves and then twisted and transposed in an OFHC copper matrix. This scheme will reduce the coupling loss by more than two orders of magnitude while leaving the internal stability criteria essentially intact.

III-B-2-b. Stress Analysis and Reinforcement

The maximum total tensile force, T, on the divertor and transformer coils is calculated as

$$T = B_m IR \tag{9}$$

where I is the maximum total current in the coil, and R is the radius of the coil. The values obtained are listed in Table III-B-3 and III-B-4 where negative values represent compression. The transformers are embedded in the central support structure where there is sufficient supporting structure so that no extra reinforcing steel between turns is needed. On the other hand, half of the more highly stressed divertor coils require reinforcing steel strips. The amount of steel needed is estimated by

$$\sigma_{ss} A_{ss} = T - \sigma_{cu} A_{cu} \tag{10}$$

where σ_{ss} = reinforcing stainless steel design stress at 4.2K = $2.76 \times 10^8 N/m^2$ (40,000 psi)

σ_{cu} = copper design stress at 4.2K = $0.83 \times 10^8 N/m^2$ (12,000 psi)

A_{ss} = total cross sectional area of steel needed

A_{cu} = total cross sectional area of copper (the existence of superconductor is neglected)

The reinforcing stainless steel strip thicknesses are 0.54 cm , 0.87 cm, and 0.76 cm per turn for divertor coils D_1, D_2 and D_6 respectively. The amounts of reinforcing steel required are listed in Table III-B-3, also.

III-B-2-c. Coil Winding

As was stated previously, the transformer coils are built inside the torus center-core cold structure. They can be wound with a revolving winding form as the construction of the core proceeds. The winding of the divertor coils poses a more difficult problem. This has to be done after the "D" magnets are erected in place. Part of the dewar and supporting structure are installed first. Then rails will be installed temporarily inside the torus. A carriage carrying the conductors and insulator can now wind the first pancake as it runs along the rail. As a pancake is completed, micarta spacers are laid radially across its face. Additional form sections will have to be added on the edges to provide a base for subsequent pancakes which overhang the preceding ones, before the next pancake can be wound. Since four conductors are wound simultaneously, they will have

different inductances in a pancake. To minimize this difference and the resulting uneven current distribution, the four conductors are transposed before they are wound into the next pancake. Figure III-B-3 shows the transposition. scheme.

III-B-2-d. Dewars and Supports for the Divertor Coils

The dewar structure for the divertor coils will be similar to that used for the "D" magnets. The inner vessel consists of 3 mm stainless steel sheets in tight contact with the magnet through micarta spacer. There will be a 15 cm vacuum space between the inner and outer vessels, where about 1/3 of the volume is filled with superinsulation. The thickness, t, of the outer vessel is dependent upon the size of the magnet through

$$t \approx D^3 \sqrt{\frac{p}{KE}} \qquad (11)$$

where K = a geometric constant = 2.2 for infinite vessel as is the case here (R>>D)

p = loading pressure = 101×10^3 N/m^2 (14.7 psi)

E = stainless steel modulus of elasticity = 2.07×10^{11} N/m^2 (30×10^6psi)

D = dewar diameter = magnet diameter + 30 cm

The thickness ranges from 4mm to 7mm. All the dewar and magnet assembly will be supported by some vertical structure penetrating through the vacuum chamber between the toroidal field magnets. This structure is sized to provide the necessary centering and vertical loads on each magnet (see Fig. III-A-4).

III-B-3. AC Losses in Divertor and Transformer Coils

The operting cycles of the reactor requires charging and discharging of the divertor and transformer coils. During the 10 sec plasma current rise time the divertor coils are charging while the transformer coils are discharging. Substantial ac losses are produced in the copper stabilizer as well as in the superconducting filaments by these rapid current (and thus field) variations. The plasma current turn-off and transformer reset time are from 100 to 150 sec. Hence, the ac losses in these stages will be comparatively smaller as compared to the current rise stage. The ac losses in each cycle are induced from the following mechanisms:

a) eddy current loss in the normal metal

b) multifilament coupling loss

c) hysteresis loss in the superconducting filaments

III-B-3-a. Eddy Current Loss

Because of the large cross section of the stabilizing copper used, the eddy current loss inside it constitutes the largest contribution to the ac losses. The superconducting composite at the front face center of the conductor (see Fig. III-B-1) complicates the eddy current pattern. By treating the composite section as a perfect conductor, it was shown[4] that the eddy current loss per pulse in a coil can be estimated from

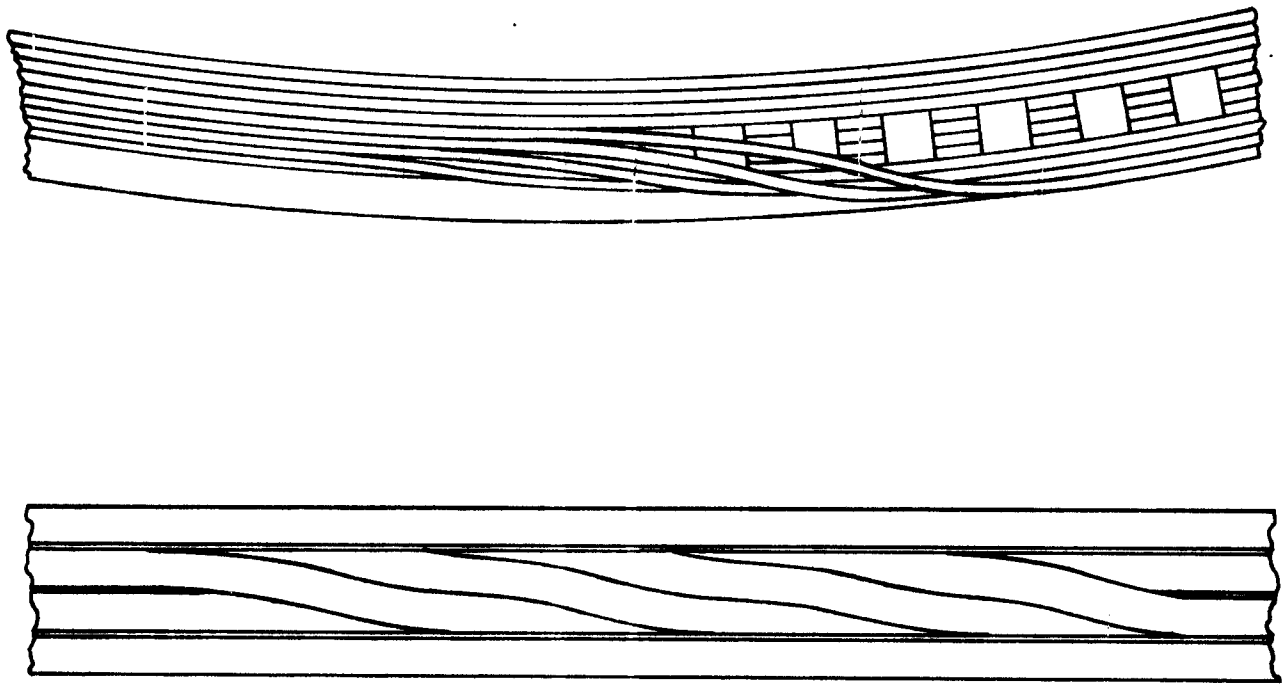

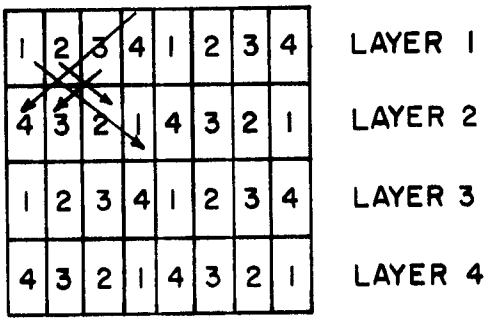

Figure III-B-3

Conductor Transposition Scheme Between Pancakes

$$E_d = \frac{32\ h^3}{\rho_c \pi^3 t}\ nwR\ \langle B_{\perp}^2 \rangle \qquad (12)$$

where h = normal conductor section height = $\frac{1}{2}(\ell - s)$ in Fig. III-B-1.

t = current rise time = 10 sec

$\langle B_{\perp}^2 \rangle$ = the square of the horizontal component of the maximum field over the coil cross section

n = number of conductor turns = four times that listed in Table III-B-3 and III-B-4

ρ_c = copper resistivity $\simeq 2 \times 10^{-10}\ \Omega$-m

w = conductor width = 0.1 ℓ

R = major radius of the magnet

All quantities are in I.S. unit.

It is found that the contribution to $\langle B_{\perp}^2 \rangle$ is negligible as compared to the self field. It is also realized that winding the coil into a circular cross section will decrease $\langle B_{\perp}^2 \rangle$ and thus reduce the eddy current loss.

By solving the diffusion equation in the normal metal together with the continuity equation and the equation of motion in the superconductor, a more accurate result can be obtained.(5) However, this requires a lengthy finite-difference numerical calculation. The eddy current loss in each coil is estimated by using equation (12) and is listed in Table III-B-5.

III-B-3-b. Coupling Loss

When a superconducting composite is subjected to a changing magnetic field, shielding currents are induced in the filaments. Depending on the length of the filaments part or all of these shielding currents will flow across the normal metal matrix.(6) Thus, resistive loss is caused by the coupling between the filaments. This coupling can be reduced by twisting the filaments and thus decreasing the equivalent filament length. However, because of the large conductor and filament size chosen, a twist pitch of less than 30 cm cannot be obtained easily. Under this situation, the coupling loss per cycle for each coil can be estimated by using(7)

$$E_c = \frac{2s^2L^2}{\rho_e t}\ nR\ \langle B_{\perp}^2 \rangle, \qquad (13)$$

where s = composite height

L = one-quarter twist pitch = 0.075 m

ρ_e = effective resistivity between the filaments.

It was found then that using pure copper as the matrix material will produce fairly large coupling losses for some of the coils. To reduce these losses, a more resistive matrix (and thus larger ρ_e) should be used. However, this will affect the thermal stability of the magnet, since the thermal conductivity is correspondingly reduced. To overcome this difficulty, a mixed matrix is proposed. The composite conductor will be manufactured in the following sequence:

(1) Extrude and draw each TiNb filament in a Cu-Ni sheath

(2) Twist and transpose these filaments in high purity copper matrix

The resultant composite cross section shown in Figure III-B-4 has superconducting filaments arranged in an approximate heaxagonal array. The effective resistivity between the filaments increased by a factor, k, over ρ_c

$$k = \frac{\rho_{cn} \ell_n (b/d) + \rho_c \ell (a/b)}{\rho_c \ell n (a/d)}$$

where d = TiNb filament diameter = 0.00038 m

b = filament diameter including Cu-Ni sheath

a = the distance between filaments

ρ_{cn} = resistivity of Cu-Ni = $4.3 \times 10^{-7} \Omega$-m

ρ_c = pure copper resistivity $\simeq 2 \times 10^{-10} \Omega$-m.

Choosing b = 0.050 cm and a = 0.087 cm one has k = 660. In this case, the thin Cu-Ni sheath (0.006 cm thick) poses negligible thermal resistance. The coupling losses estimated by using equation (13) with $\rho_e = k\rho_c$ are listed in the second column of Table III-B-5.

III-B-3-c. Hysteresis Loss

Hysteresis loss in a hard superconductor is a well known phenomenon. It is caused by the flux motion against the pinning forces as the ambient field changes. The loss can be calculated by several different approaches.[8] The loss for a circular filament subjected to a field change such that the maximum field is greater then the full penetration field (this applies to the poloidal field coils), is given by Morgan[9] as

$$P_h = \frac{2}{3\pi} d\, I_c\, B \quad . \qquad \text{(watt/m)} \qquad (15)$$

Multiplying by the charge (or discharge) time, this equation shows that the hysteresis loss depends only on the maximum field change but not on the rate of change. Hence, an equal amount of loss occurs in the discharge state as in the charge stage. The total hysteresis loss per cycle of each coil should then be found from

$$E_h = \frac{8}{3} d\, I_c\, mnR\langle B\rangle \simeq \frac{8}{3} d\, I_m R\langle B\rangle \ , \qquad (16)$$

where I_c = filamentary critical current

m = number of filaments per conductor

$\langle B\rangle$ = average maximum field over the coil

I_m = maximum total current of the coil.

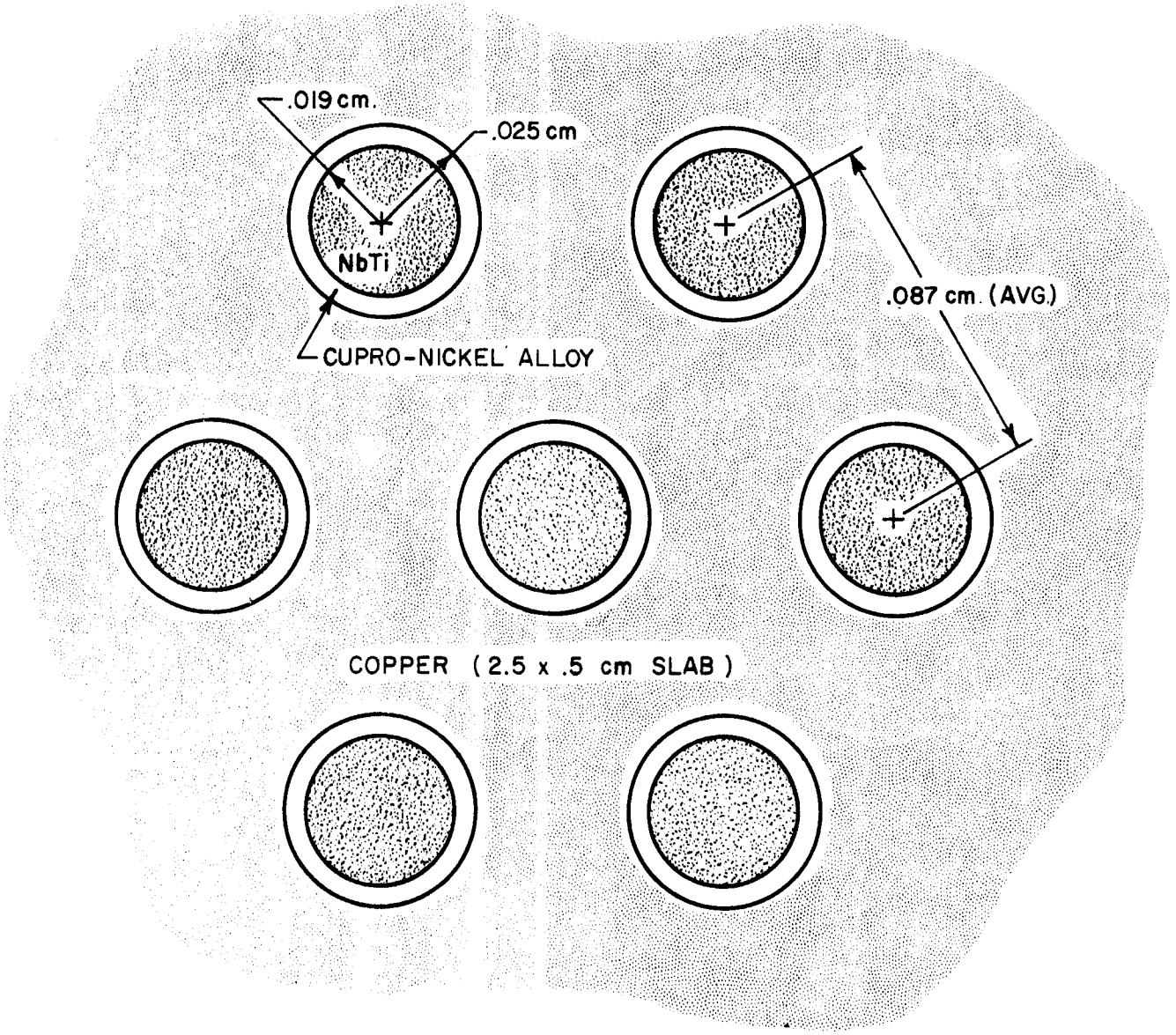

Figure III-B-4

TiNb-CuNi-Cu Composite Cross Section

Table III-B-5

AC Losses Per Cycle in the Divertor and Transformer Coils

	Eddy Current Loss	Coupling Loss	Hysteresis Loss
Coil	E_e(kWh)	E_c(kWh)	E_h(kWh)
D_1	0.338	.0044	0.010
2	0.796	.0079	0.017
3	0.063	.0006	0.003
4	0.412	.0048	0.012
5	0.091	.0008	0.005
6	2.535	.0286	0.055
T_1	0.329	.0042	0.014
2	0.316	.0039	0.015
3	0.338	.0045	0.013
4	0.316	.0045	0.014
5	0.087	.0019	0.013
6	0.461	.0067	0.015
7	0.487	.0070	0.025
8	0.401	.0059	0.013
9	0.385	.0053	0.013
Total Losses in 30 Magnets	14.71	0.182	0.237

Total ac losses at 4.2K = 15.1 kWh

It can be seen now from Table VI that the majority of the ac losses is due to the eddy current loss in the copper stabilizer. A fully stabilized magnet is expensive not only in the capital cost but also in the (ac) operation cost. The total ac losses for the 12 divertors and 18 transformers amounts to 15.1 kWh at 4.2K.

III-C . Magnetic Field Structure

The magnetic fields of UWMAK-II have been calculated and given here in detail. The toroidal and poloidal field intensities were calculated separately. The magnetic forces on the current carried by the toroidal coils has also been calculated.

III-C-1. Toroidal Field Structures

According to the analysis given in Section II-B-5, 24 "D" shaped toroidal field coils with extended outer edges are needed to produce acceptably low toroidal field ripple and alpha particle leakage. The geometry of the upper half of each "D" coil as shown in Fig. III-C-1 is used for the calculations. Also shown is that of UWMAK-II for comparison. This geometry has been determined by the stress analysis discussed in UWMAK-I report. This coil is approximated by 12 arc sections and one straight section. The TF coil cross section has a radial width, ΔR = .98m, and axial width ΔZ = 1.07 m. The 24 coils are spaced equally at 15° intervals.

The magnetic field on the midplane is illustrated by some of the field lines shown in Figure III-C-2. The contour of $|B|$ is shown in Fig. III-C-3. These figures show that the region of toroidal field occupied by the plasma is almost perfectly axisymmetric. The maximum deviation at R = 18 m and ϕ = 7.50 is $\Delta R \approx 0.01$ m and the field ripple is $Ea \leq 0.05\%$. The energetic alpha particle leakage is less than 0.1% for such a field ripple. This has been discussed in Section II-B-5.

The contours of $|B|$ over the cross sections at the outer edge, AA, and inner edge, BB, of the "D" coil are shown in Figures III-C-4 and III-C-5. The contours become those of Figures III-C-6 and III-C-7 if the coil at 345° is removed. This corresponds to an accidental failure of this coil.

III-C-2. Poloidal Field Structure

The poloidal magnetic field is axisymmetric. The design methods used to determine the divertor currents and transformer currents have been discussed in Chapter II, sections C and E. The parameters and currents of these coils were listed in Tables III-C-1 compared with UWMAK-I. The separatrix which defines the plasma cross section was calculated from the divertor currents as listed in the table and by the plasma current loop taken at R = 14.5 m due to the finite β effects. For the purposes of studying the interactions of the currents in the TF coils with poloidal magnetic field and other stray fields, we have calculated the total poloidal fields from divertor, transformer and plasma current together. A detailed plot of the contour of $|B_p|$ in the reactor itself is shown in Figure III-C-8. The course plot of the contour in the region extending 100 meters radially and 100 meters vertically is shown in Figure III-C-9. Detailed contours over the cross sections of the divertor coils are shown in Figures III-C-10 to III-C-15, respectively. (Note: This is for the rectangular cross section of the magnets. As was discussed in Section III-B-3, for the purpose of reducing ac losses the coils have now adopted circular cross sections.)

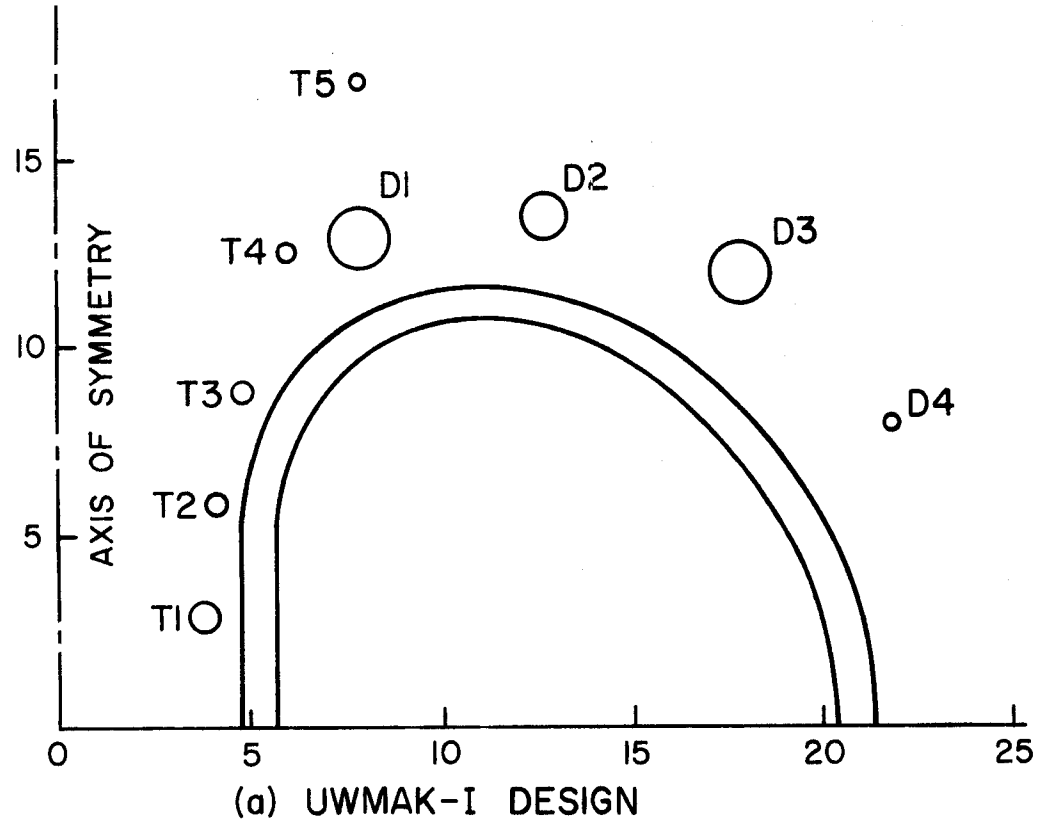

(a) UWMAK-I DESIGN

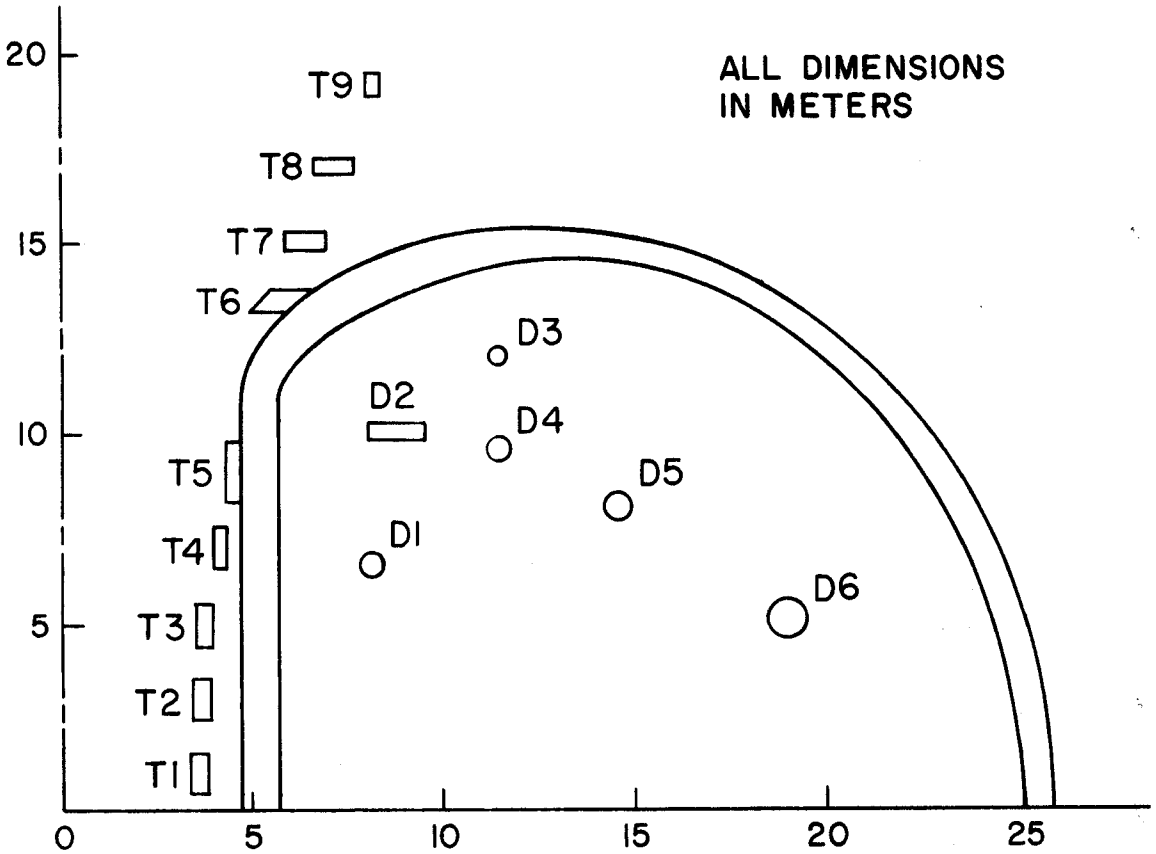

(b) UWMAK-II DESIGN

Figure III-C-1

"D" Coils

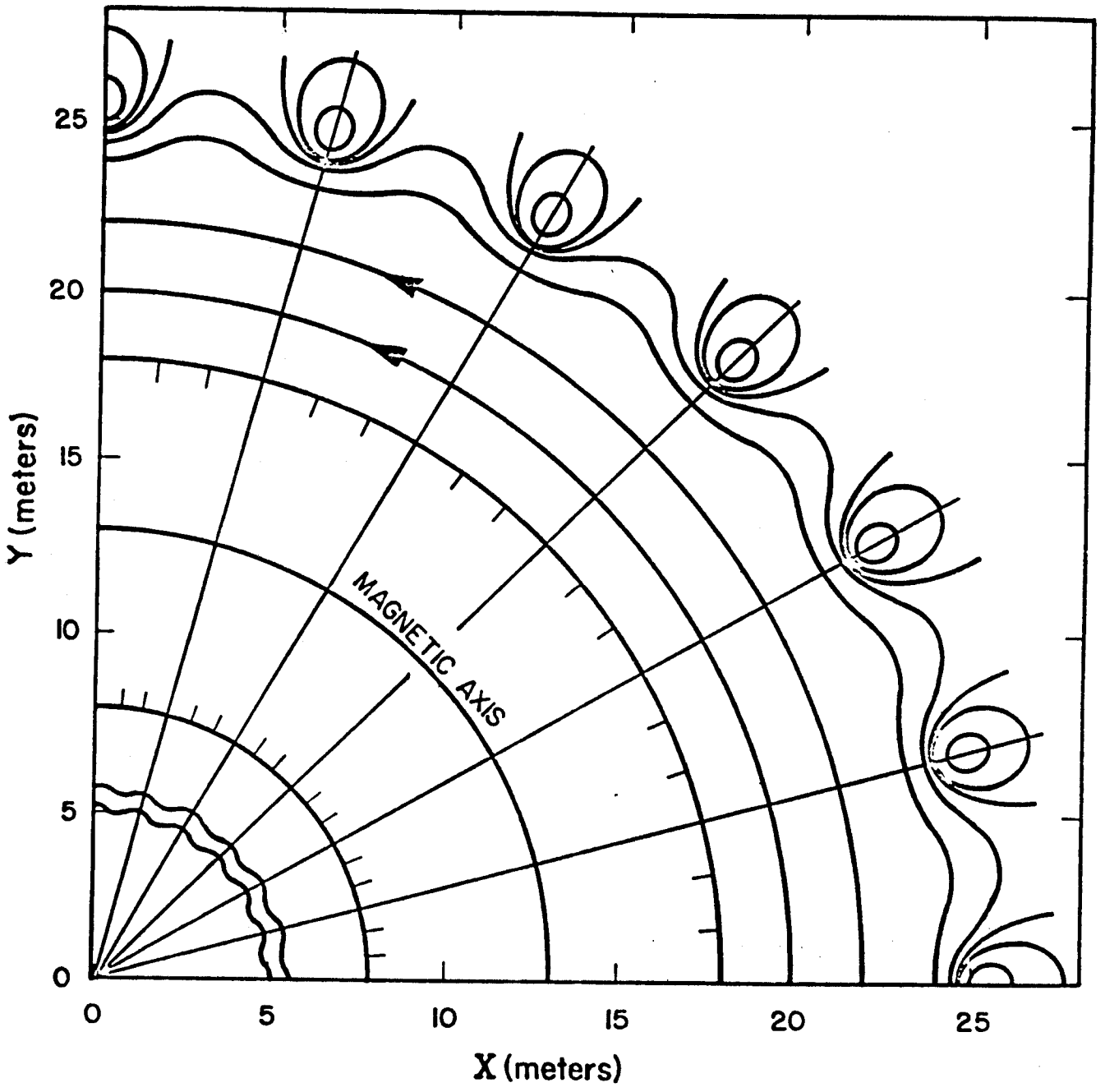

Figure III-C-2

Magnetic Field Lines on Midplane

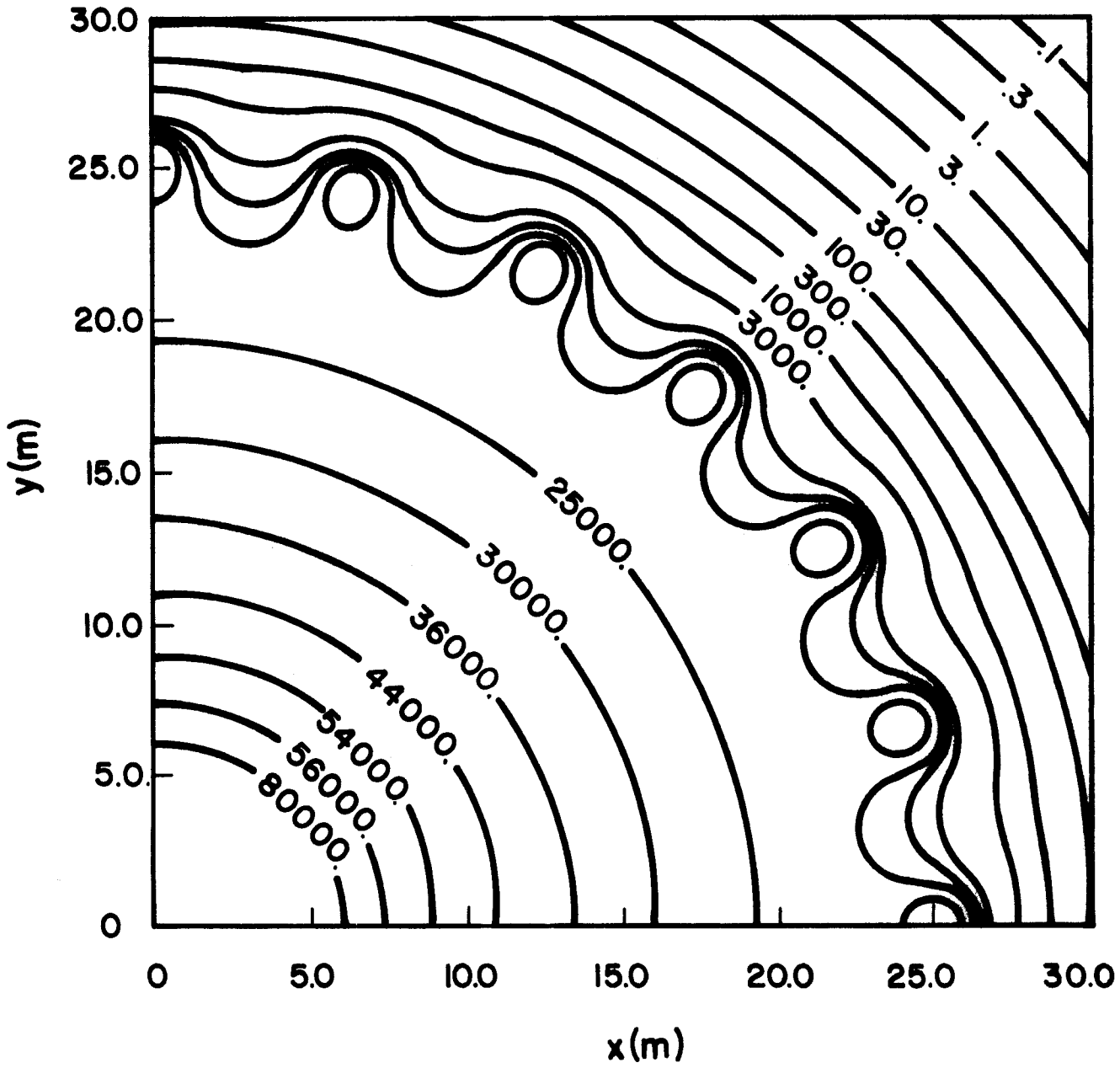

Figure III-C-3. Contour plot of constant toroidal field $|B_T|$ in Kgauss on the midplane inside of the reactor.

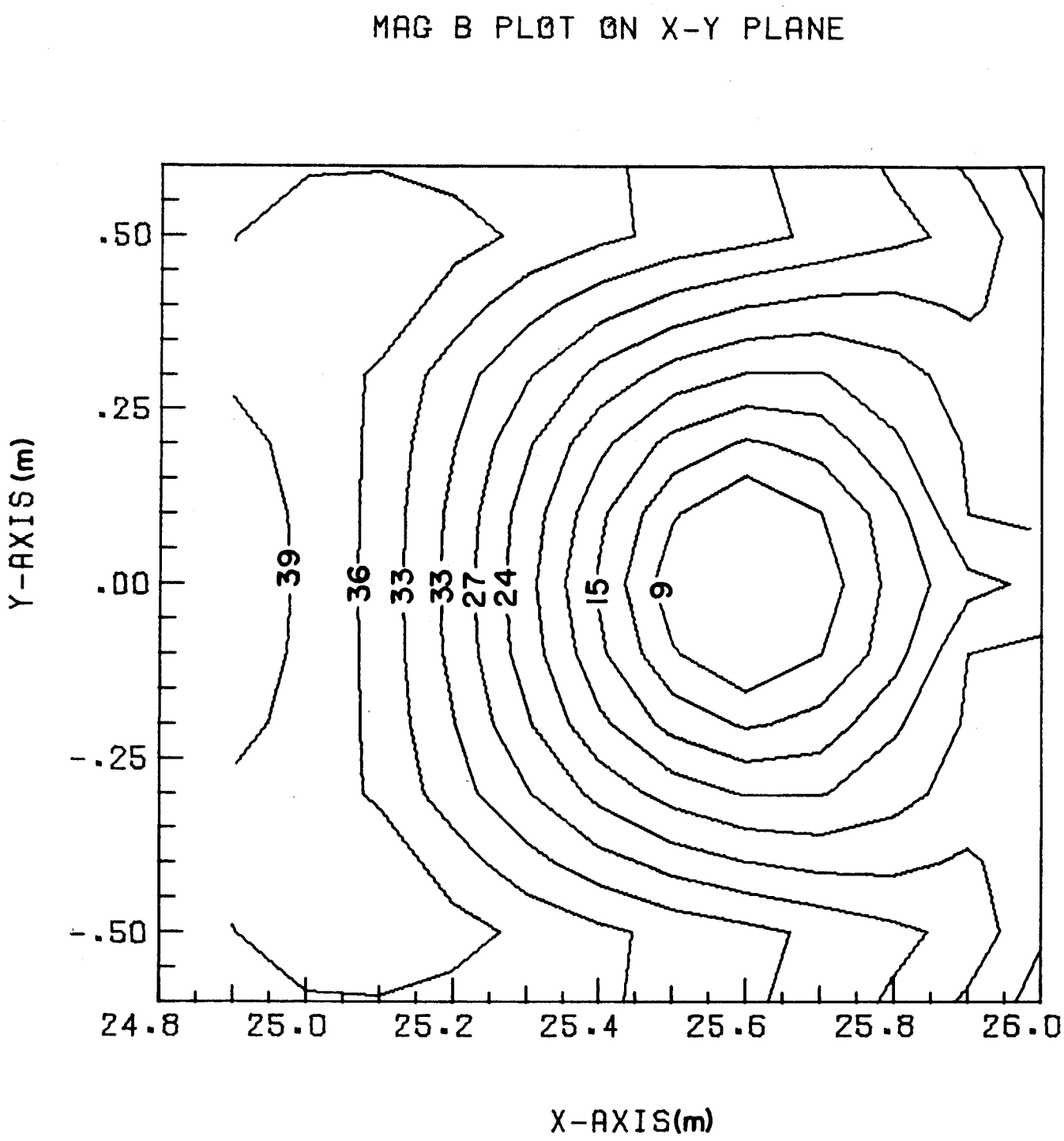

Figure III-C-4. Contour plot of constant toroidal field B_T in k Gauss over the cross-section intersected by x-y plane.

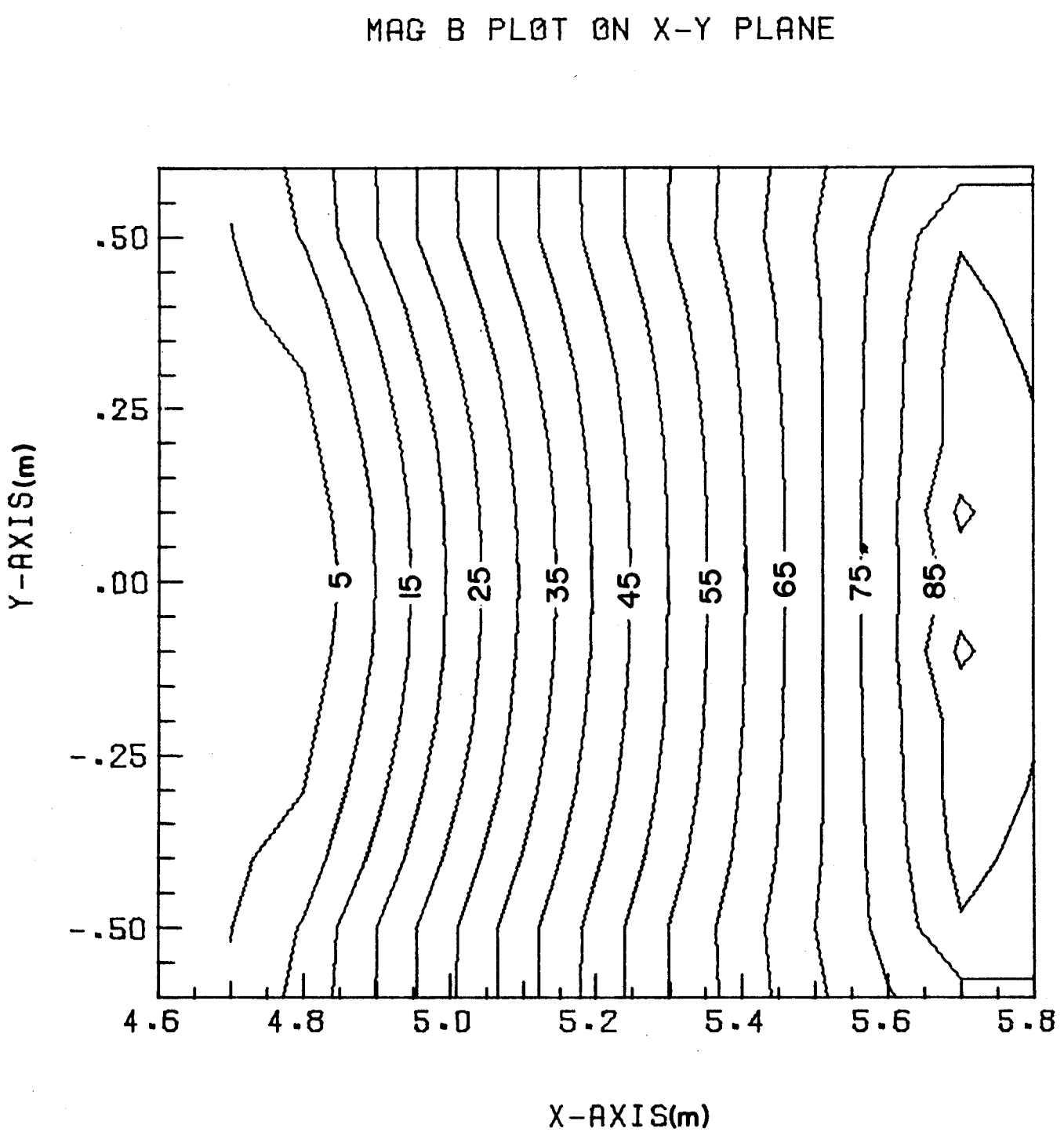

Figure III-C-5. Contour plot of constant toroidal field $|B_T|$ in k gauss over the cross-section intersected by x-y plane.

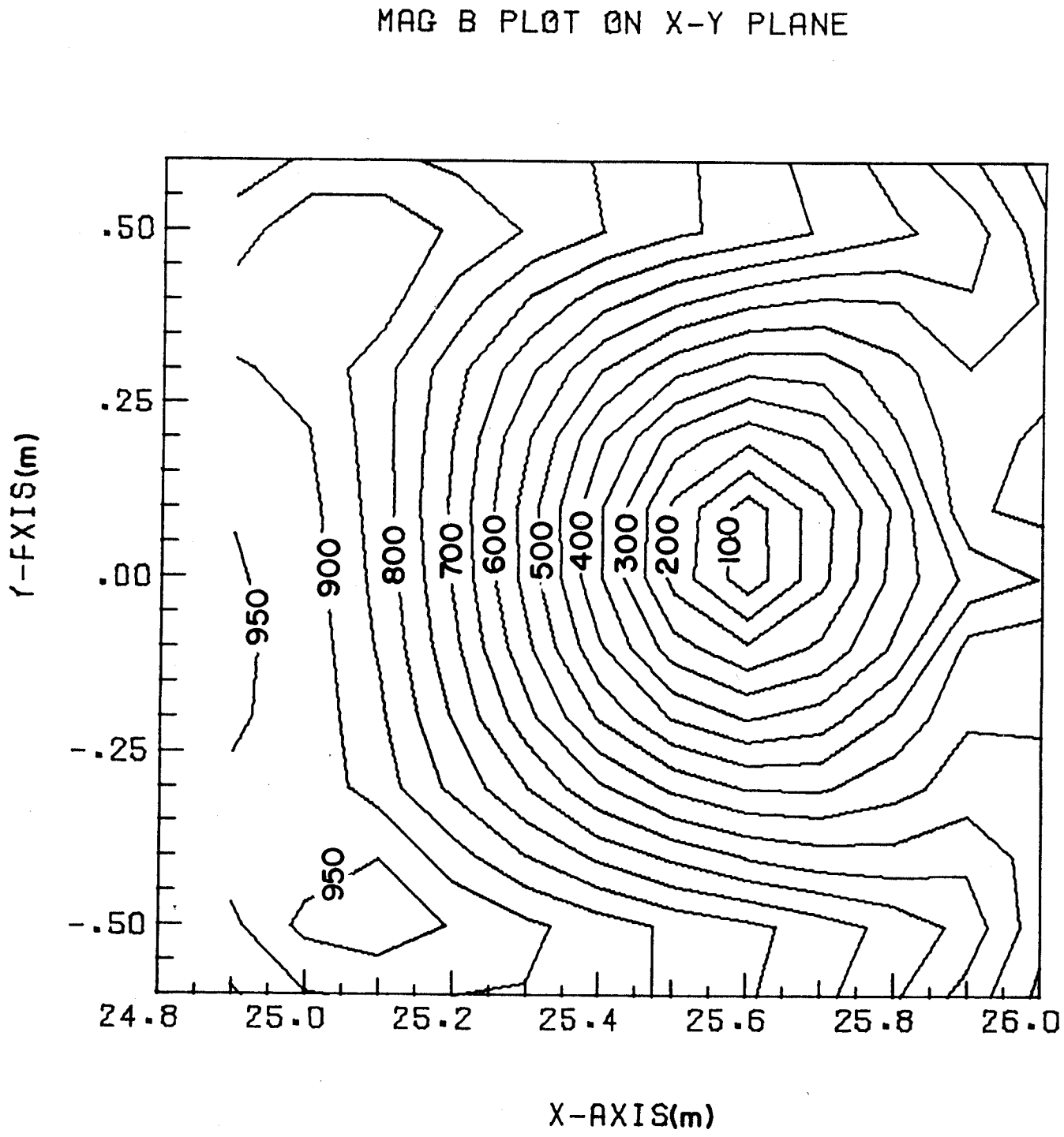

Figure III-C-6. Constant $|B|$ in 10^3 Tesla, contour plot, over the cross-section of the toroidal coil intersected by x-y plane at AA shown by fig. III-C-17.

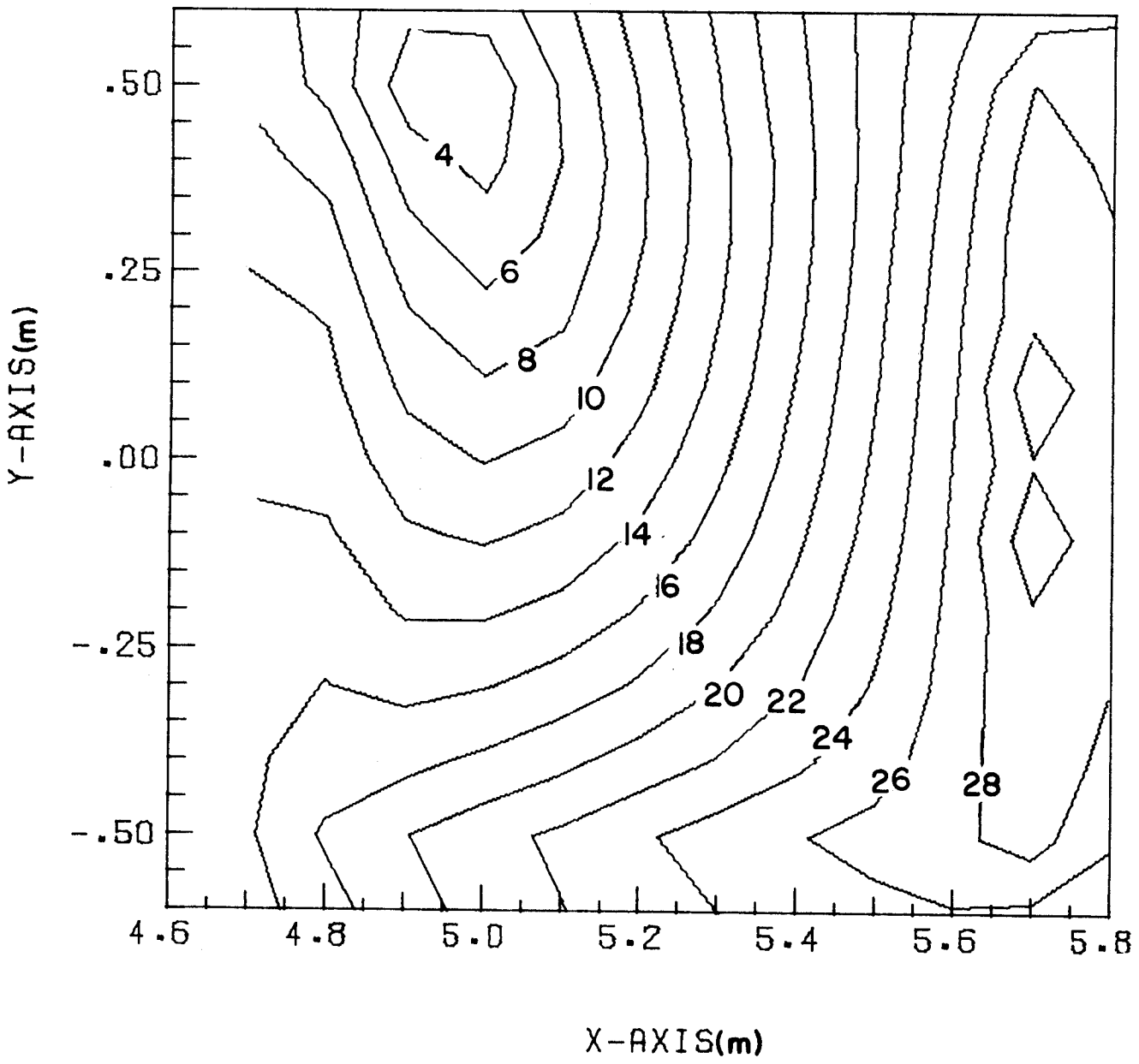

Figure III-C-7. Constant $|B|$ in 10^3 Tesla contour plot over the cross-section of the toroidal coil at 15° intersected by x-y plane at BB shown in figure III-C-17 with the toroidal toroidal coil at 0° missing.

TABLE III-C-1

Divertor Coil Currents

	UWMAK-II			UWMAK-I		
	R(m)	Z(m)	I(10^6amp)	R(m)	Z(m)	I(10^6A)
D1	8.2	6.5	-3.70	8	13	+24.0
D2	8.8	10.0	+4.89	13	13.5	+12.0
D3	11.5	12.3	-1.46	18	12	-24.0
D4	11.5	9.5	+3.40	22	8	-2.4
D5	14.6	8.0	-1.57			
D6	19.0	5.0	-6.82			

Transformer Coil Currents

			(UWMAK-II)		
	R(m)	Z(m)	I_o(10^6amp) initial currents	I_s(10^6amp) (end of start-up)	I_f(10^6amp) (final currents)
T1	3.61	1.00	2.74	1.66	-4.13
T2	3.72	3.06	2.64	1.60	-3.99
T3	3.94	4.99	2.39	1.45	-3.61
T4	4.25	6.96	2.26	1.37	-3.41
T5	4.66	8.92	1.89	1.14	-2.85
T6	5.43	13.50	2.22	1.15	-3.36
T7	6.50	15.05	2.21	1.34	-3.34
T8	7.25	17.00	1.66	1.00	-2.51
T9	8.22	19.3	1.46	0.88	-2.20

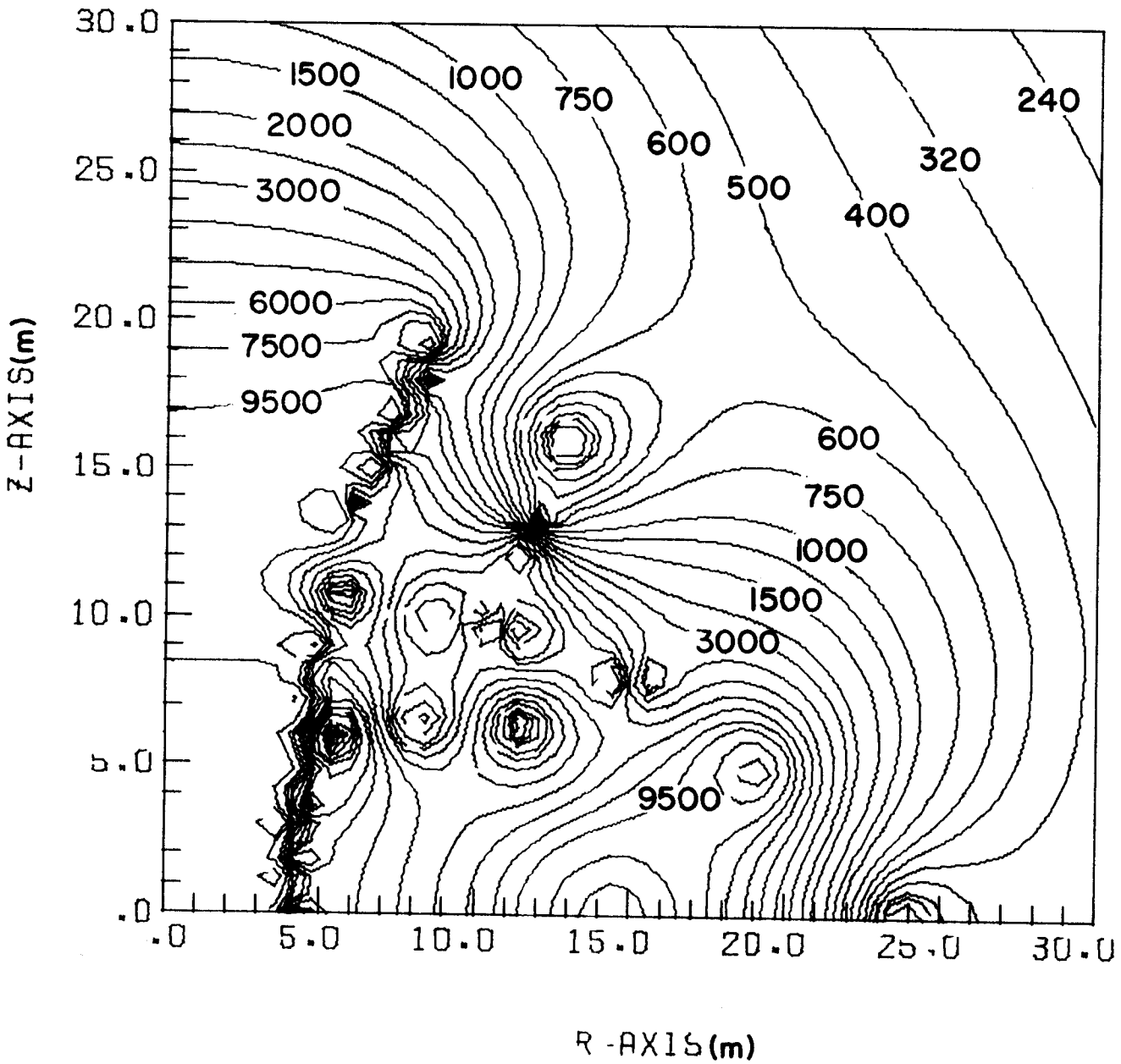

Figure III-C-8. Contour plot of constant poloidal field $|B_p|$ in gauss inside of the reactor.

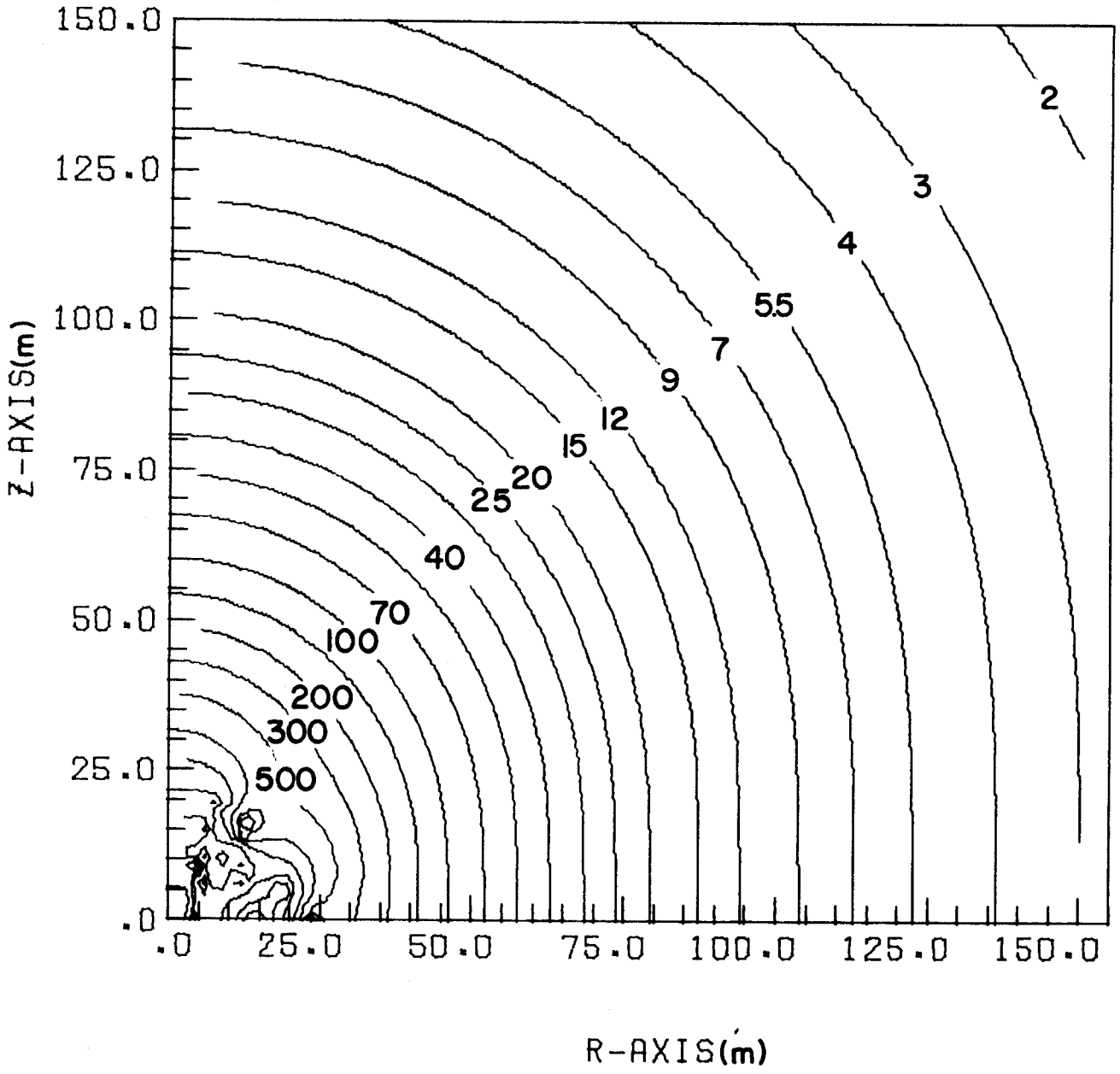

Figure III-C-9. Constant $|B_p|$, in gauss, contour plot of the poloidal field at large distance from center of the reactor.

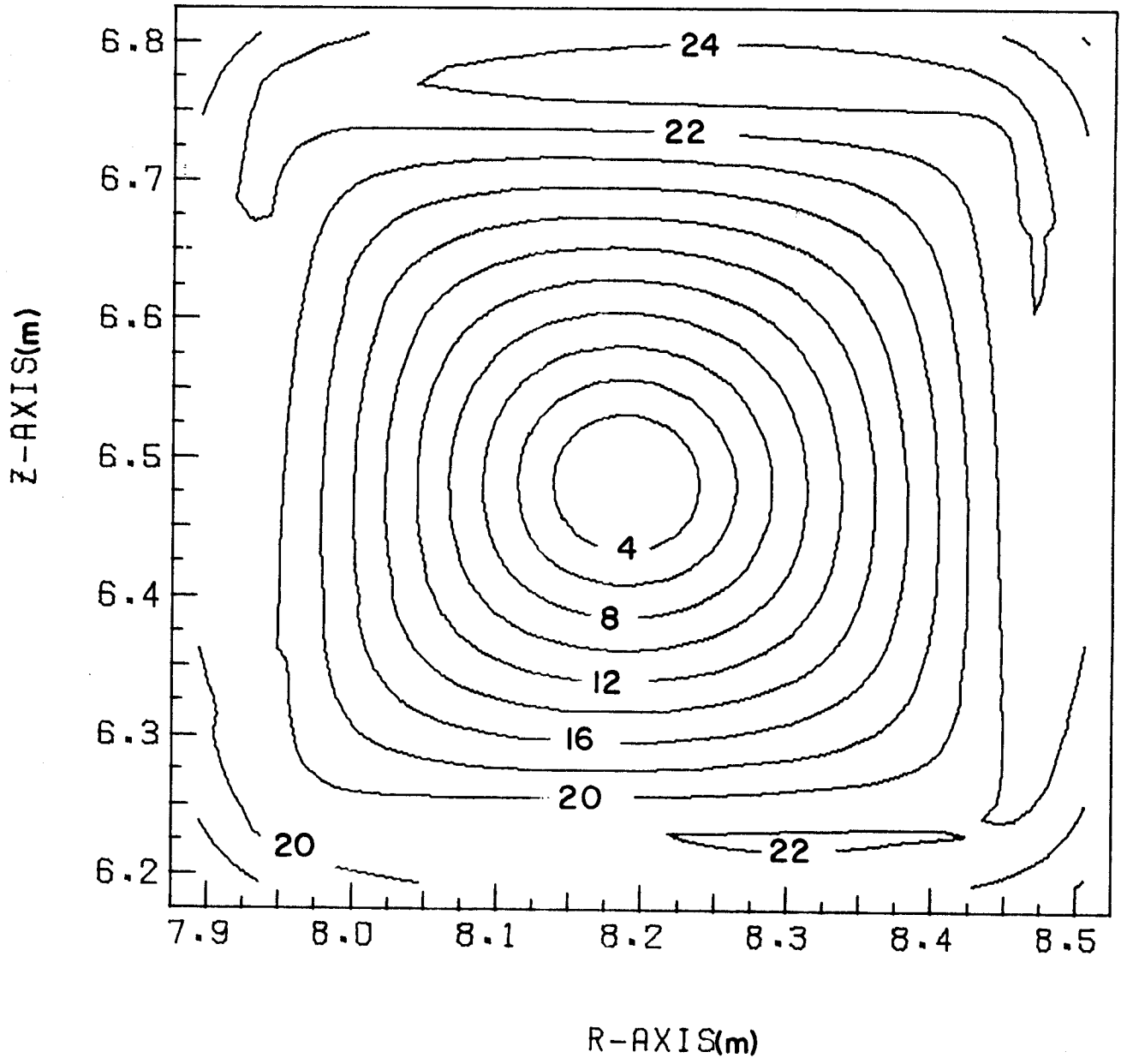

Figure III-C-10. Constant $|B_p|$, in k gauss, contour plot over the cross-section of coil D1.

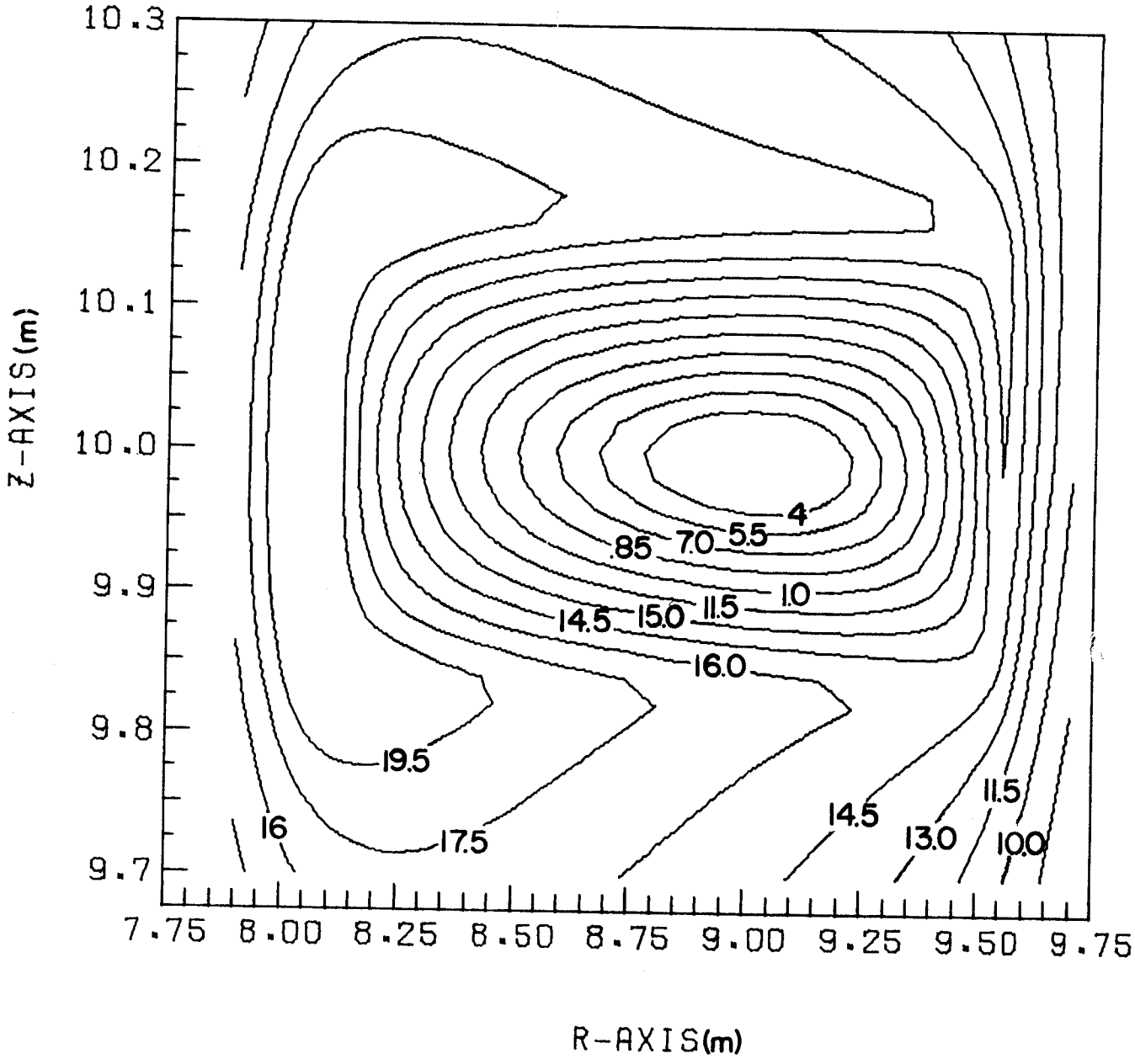

Figure III-C-11. Contour plot of constant poloidal field $|B_p|$ in k gauss over the cross-section of D2. Note the difference in scales used for R and Z.

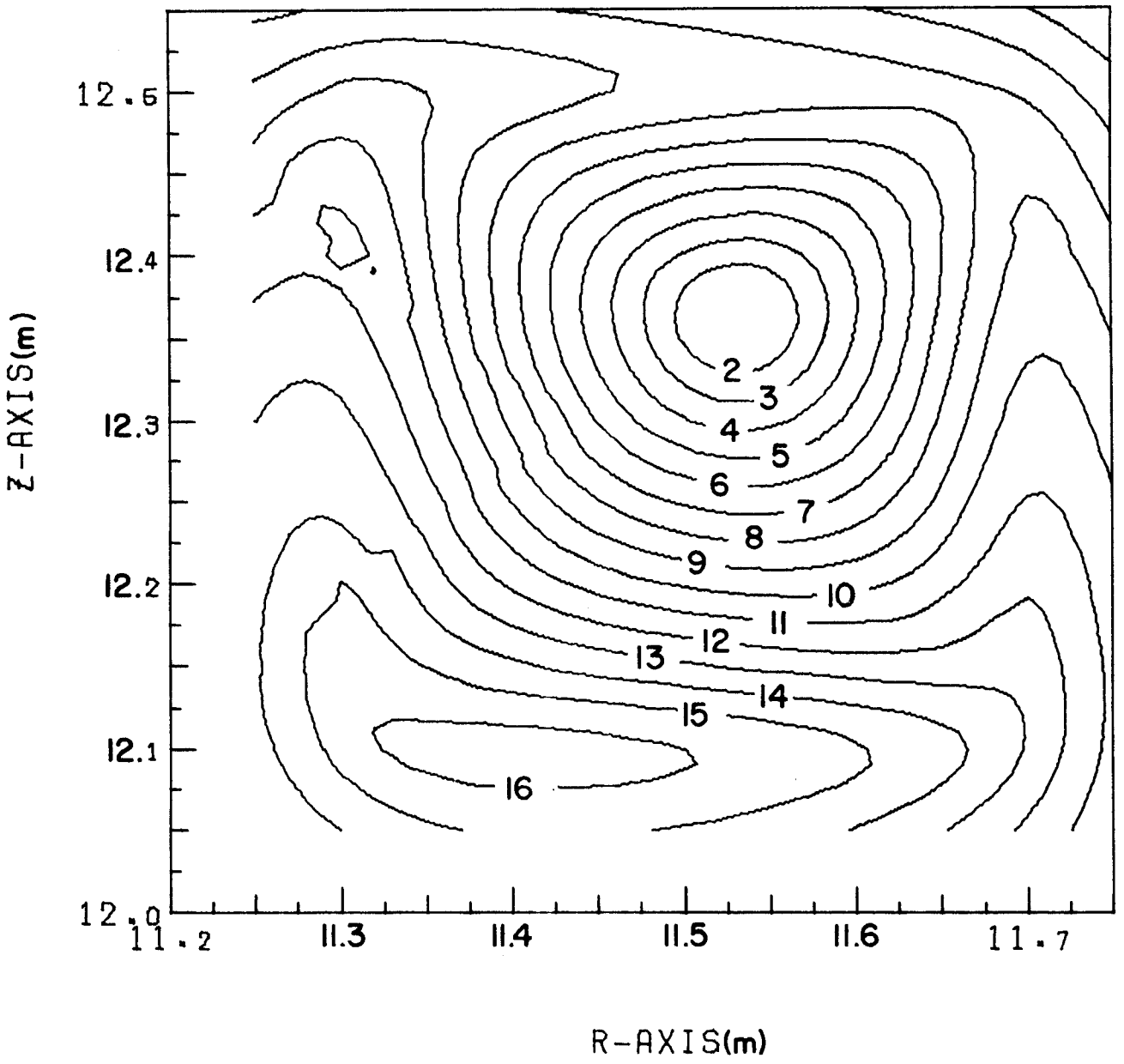

Figure III-C-12. Contour plot of constant poloidal field $|B_p|$ in k gauss over the cross-section of D4.

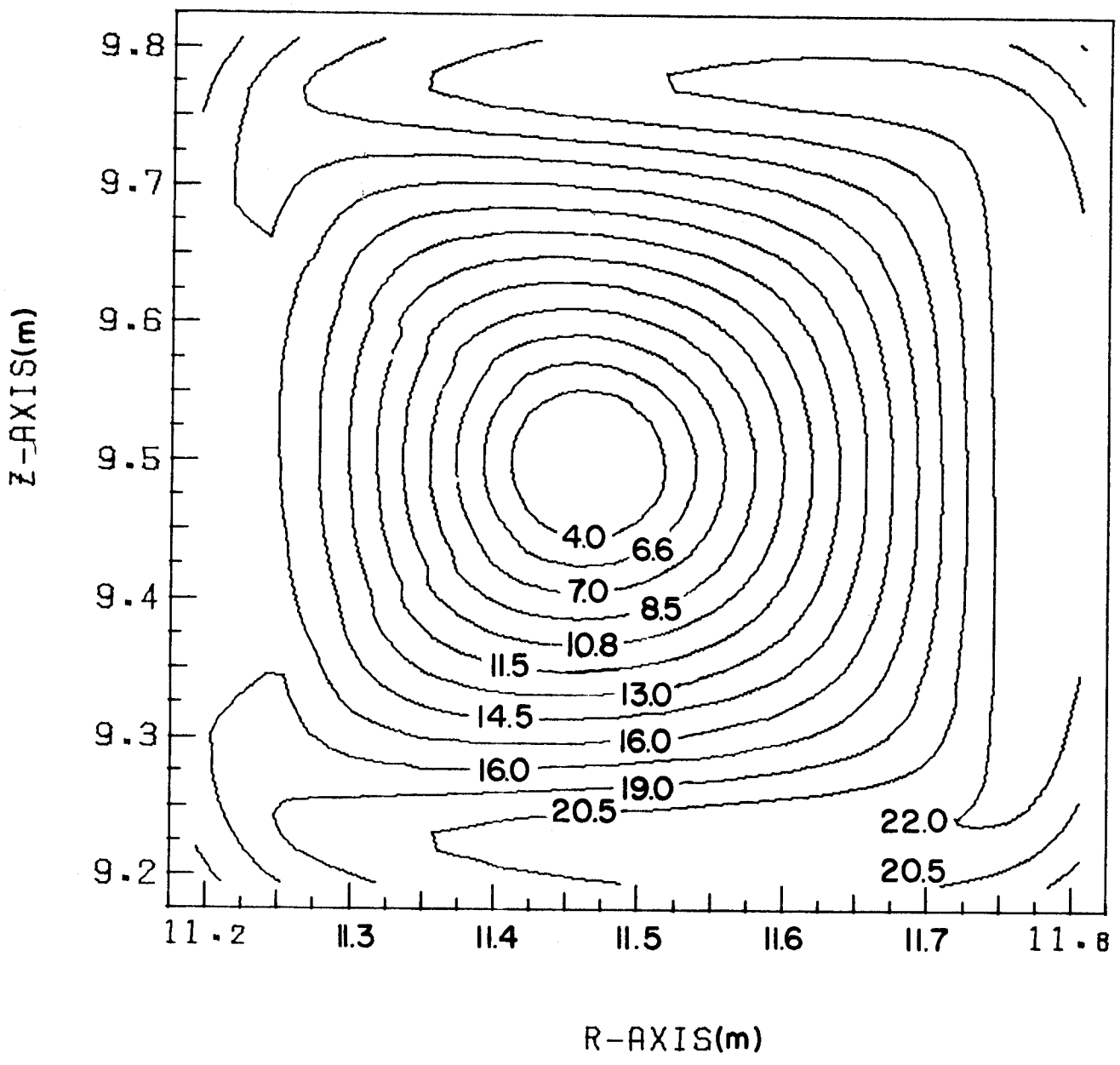

Figure III-C-13. Contour plot of constant poloidal field $|B_p|$ in k gauss over the cross-section of D4.

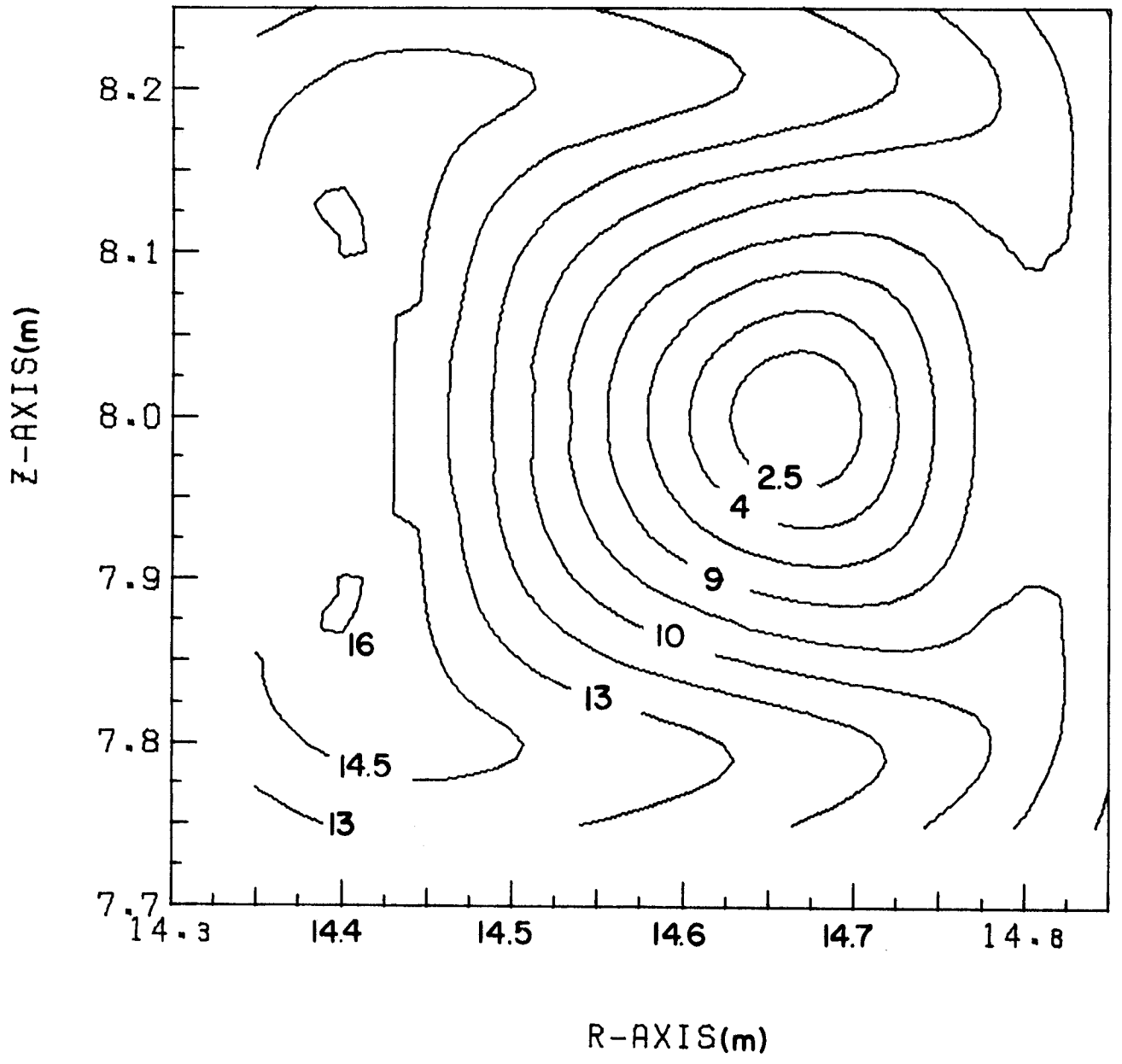

Figure III-C-14. Contour plot of constant poloidal field $|B_p|$ in k gauss over the cross-section of D5.

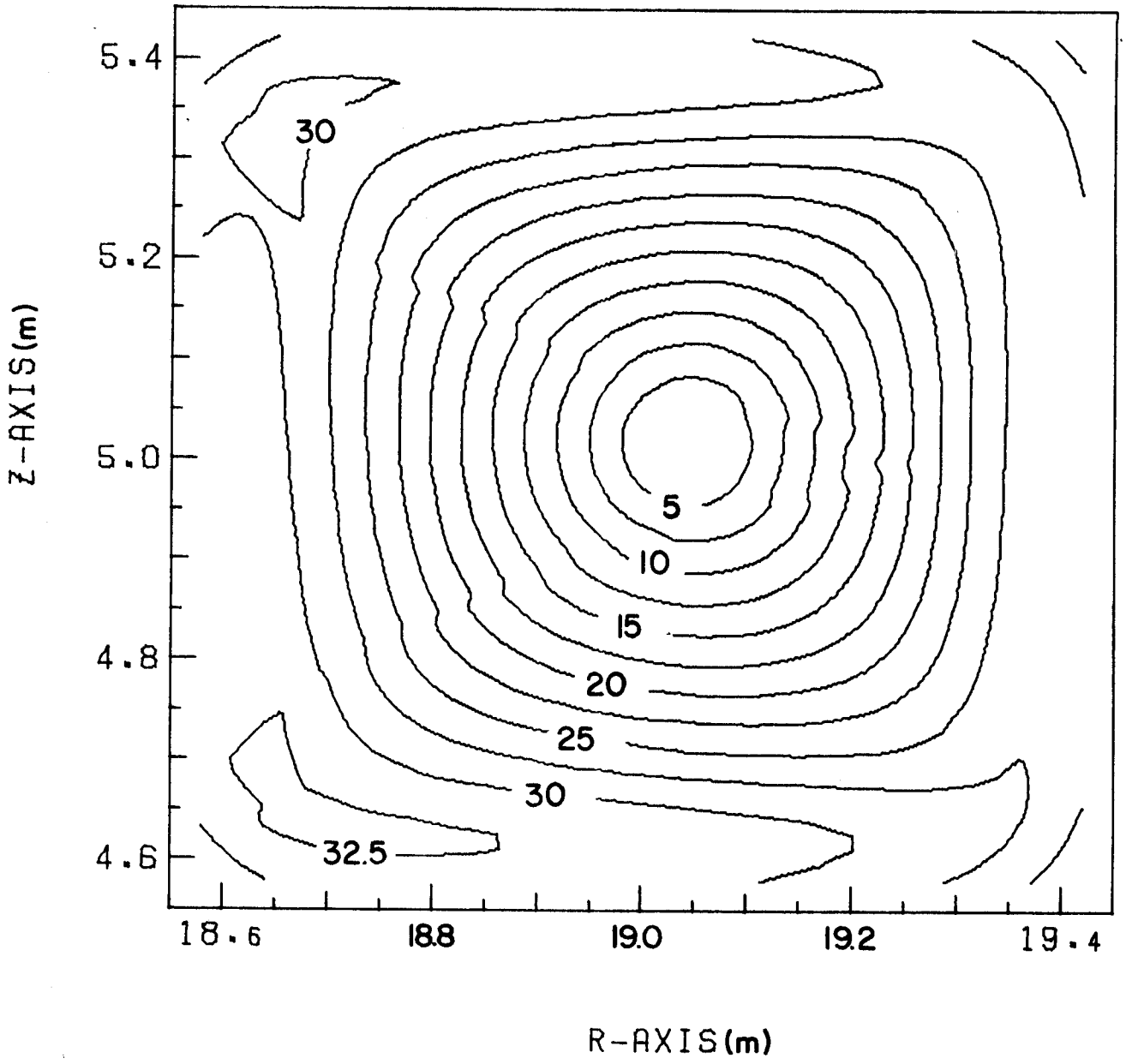

Figure III-C-15. Constant $|B_p|$, in k gauss, contour plot over the cross-section of coil D6.

III-C-3. Stray Fields

Figure III-C-16 compares the toroidal field intensities outside the TF "D" coils for UWMAK-II and our previous design UWMAK-I,[1] plotted as functions of radius along this axis on the mid-plane at 0°. This figure shows that the stray toroidal field intensity for UWMAK-II is less than that of UWMAK-I by two orders of magnitude. Doubling the number of TF coils reduces the stray field drastically. This is one of the reasons, in addition to minimizing the field ripple and therefore the α-particle leakage, for using 24 TF coils in the present design rather than 12 TF coils as in the UWMAK-I design. The toroidal field strength at R = 40 m is less than 1 gauss, whereas the poloidal field strength is about 200 gauss. Therefore, the stray field is dominated by poloidal field. The stray poloidal field at 100 meters radially from the center of the machine is about 10 gauss for UWMAK-II which is only about one tenth of that of UWMAK-I. This reduction in stray field is due to the fact that we have less plasma current (~15 MA) and have placed the divertor coils inside the TF coils. The divertor coils for UWMAK-I were outside the TF coils and the total absolute current was 62.4 MA, whereas the divertor coils for UWMAK-II are inside the TF coils (Fig. III-C-1) and the total absolute current is now 21.84 MA. Thus, the divertor coils of UWMAK-II are closer to the centerline and carry less current than those of UWMAK-I. The stray field is due to the dipole moment of the net current in the combined transformer, divertor and plasma current system. The net current of UWMAK-II is only -35.55 MA in comparison with -56.7 MA of UWMAK-I. Therefore, all these reasons make the poloidal field strength at large distance decrease faster than that in UWMAK-I. At distances greater than 100 meters the poloidal field in the median plane can be estimated from the following equation

$$B_p = \left(\frac{100}{\rho}\right)^3 B_p(\rho = 100),$$

where ρ is the polar radius from the center of the reactor. The stray field drops to less than 1 gauss beyond 300 meters. Although this is about the magnitude of the earth's magnetic field (which ranges from 0.6 to 0.7 gauss in the state of Wisconsin), the geological fluctuation of the earth's field is only in the range 0 to 2000 gammas (1 gamma = 10^{-6}gauss).

III-C-4. Interaction of the "D" Coils with the Poloidal Field

As shown by Fig. III-C-8 the poloidal field is highly non-uniform within the Tokamak. This will produce fluctuating lateral forces, F_ϕ, in the toroidal direction along the circumference of the "D" coil. The force per unit arc length at the inner circumference of the "D" coil has been calculated from

$$F_\phi = \int_{\theta_1}^{\theta_2} \int_{\rho_1}^{\rho_2} B_p \times j_\phi \; \rho d\theta \, d\rho \, \Delta t,$$

where Δt is the axial thickness of the "D" coil, ρ_1 and ρ_2 are the radii of curvature of the inner and outer surfaces, respectively, and θ_1 and θ_2 are the integration limits which give $\int_{\theta_1}^{\theta_2} \rho_1 d\theta = 1$ meter along the inner surface.

Figure 7

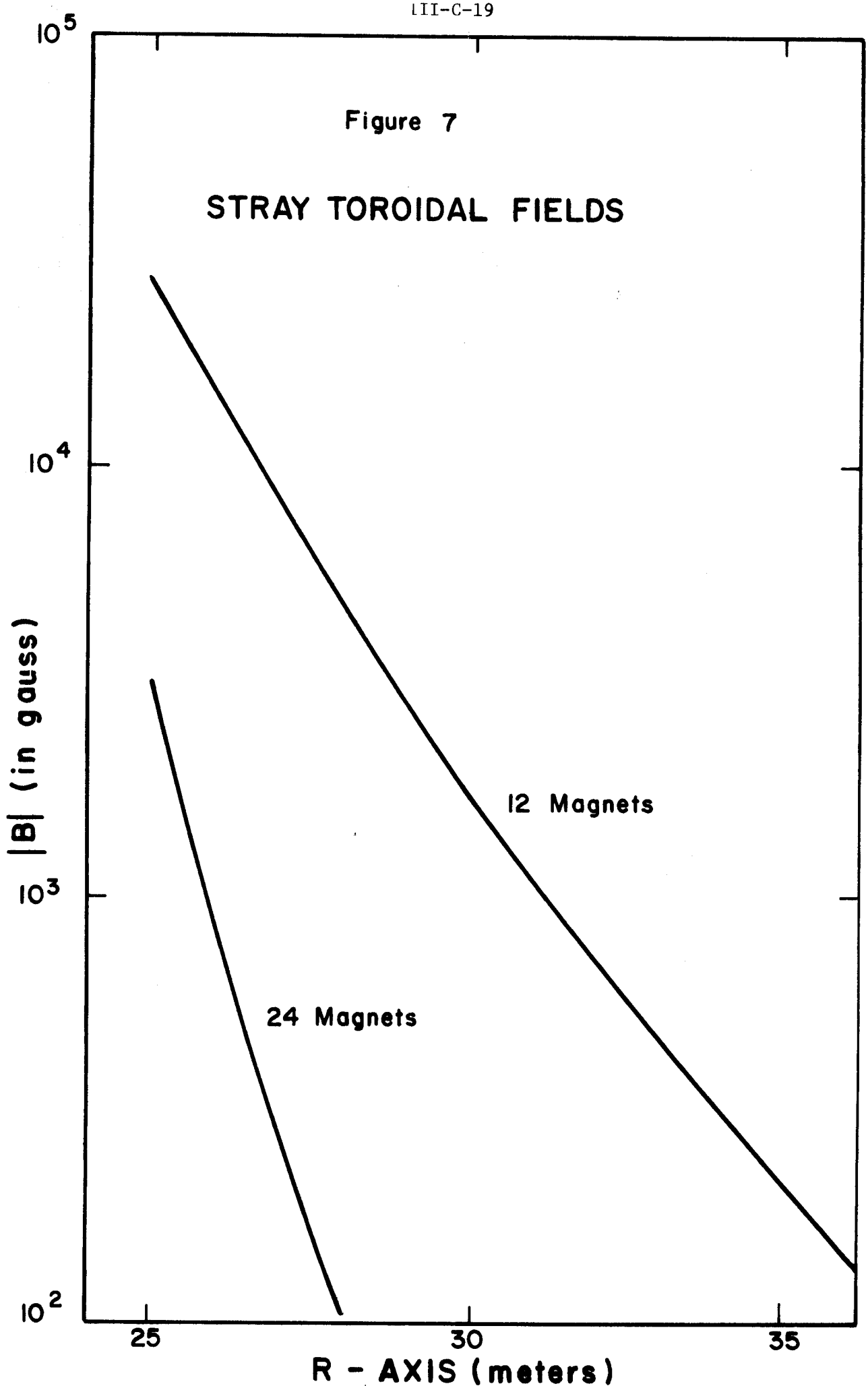

Figure III-C-16

The fluctuation of the lateral force E_ϕ is demonstrated by Figures III-C-16 and III-C-17. Fig. III-C-17 shows the sense of the lateral force E_ϕ along the "D"; the positive sign indicates that the force points out of the plane while the negative sign indicates that the force points into the plane. Fig. III-C-17 shows the variation of the force along the portion ACB as labeled in Fig. III-C-16 The forces due to the fields produced by the divertor and plasma currents and forces resulting from the field of the transformer coils were also calculated separately and are shown in Figures III-C-18 and III-19. Total forces can be obtained by suitable linear superposition of the two separate forces for cases where the divertor and plasma currents and the transformer current do not peak simultaneously at the same values.

III-D. Refrigeration

In this section, the sources of heat loss will be listed and the magnitude estimated. It is found that in addition to the liquid helium in various dewars an additional storage of 300,000 liters is desired. It demands ten 3 kW refrigerators for the cooling of the entire magnet system.

III-D-1. Heat Losses

The sources of heat loss can be itemized as follows:

a. Thermal radiation loss - The outer surface of the TF coils is facing room temperature while the inner surface facing a temperature of 400°K. Using an average radiation loss of 7.5 $\mu W/cm^2$ and a total surface area of 11,000 m^2 for the "D" magnets, one obtains a radiation loss of 824 watts.

The 2,600 m^2 surface of the divertors and transformers is facing a temperature of 400°K. A unit loss of 12 $\mu W/cm^2$ gives a total radiation loss of 312 watts. Thus, the total radiation loss in all the magnets amounts to 1136 watts.

b. Conductive loss - It was estimated earlier that about 5,500 cm^2 cross section of reinforced epoxy on each side of each toroidal magnet is required for the lateral support between the inner and outer dewars. Each of the struts is 15 cm long and about 10% of them contact the dewar wall in normal operation. Assuuming a conductive loss between 300 K and 4.2 K of 1700 mW/cm for the epoxy struts, the total conductive loss in the "D" magnet is $1700 \times 10^{-3} \times (2 \times 5500) \times 0.1 \times 24 \div 15 = 2992$ watts.

Similar supporting struts for the divertors require a total cross sectional contact of about 5000 cm^2 in a 10 cm length, which causes a conductive loss of 850 watts for all divertors.

c. Resistive loss in conductor joints - The conductor joints to the toroidal magnets are made at the outside edges where the field is essentially zero, $\rho_B = 10^{-8}\Omega cm$. At that location, the 1.7 cm wide conductors are overlapped for a 20 cm length and clamped tightly together. Assuming a 0.5 cm path length, the normal path resistance will be $10^{-8} \times \frac{0.5}{20 \times 1.7} = 0.015 \times 10^{-8}\Omega$. In addition,

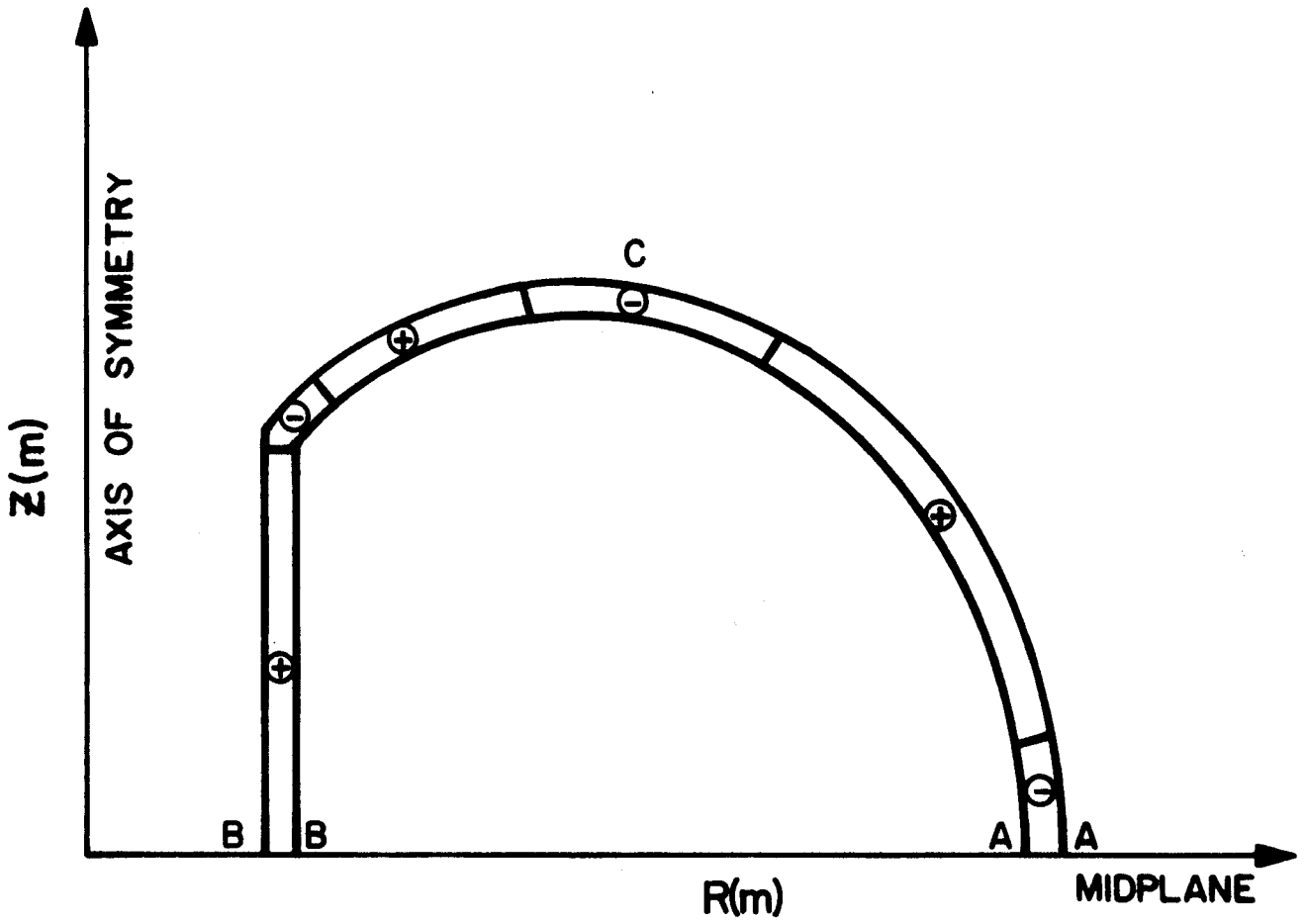

Figure III-C-17. The sense of force produced by poloidal field on the toroidal coil, where (-) indicates force points out of the paper and (+) indicates force points into the paper.

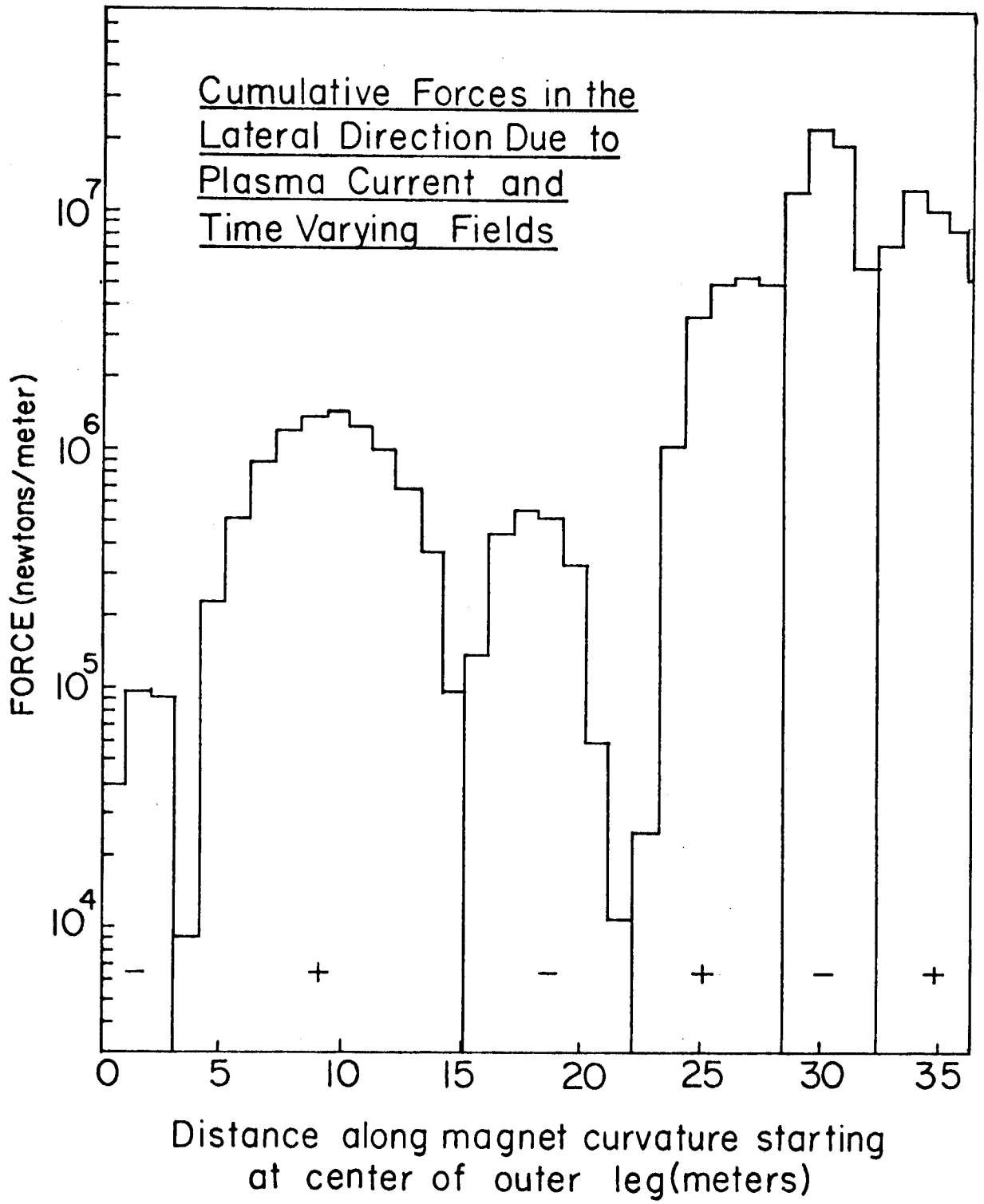

Figure III-C-18

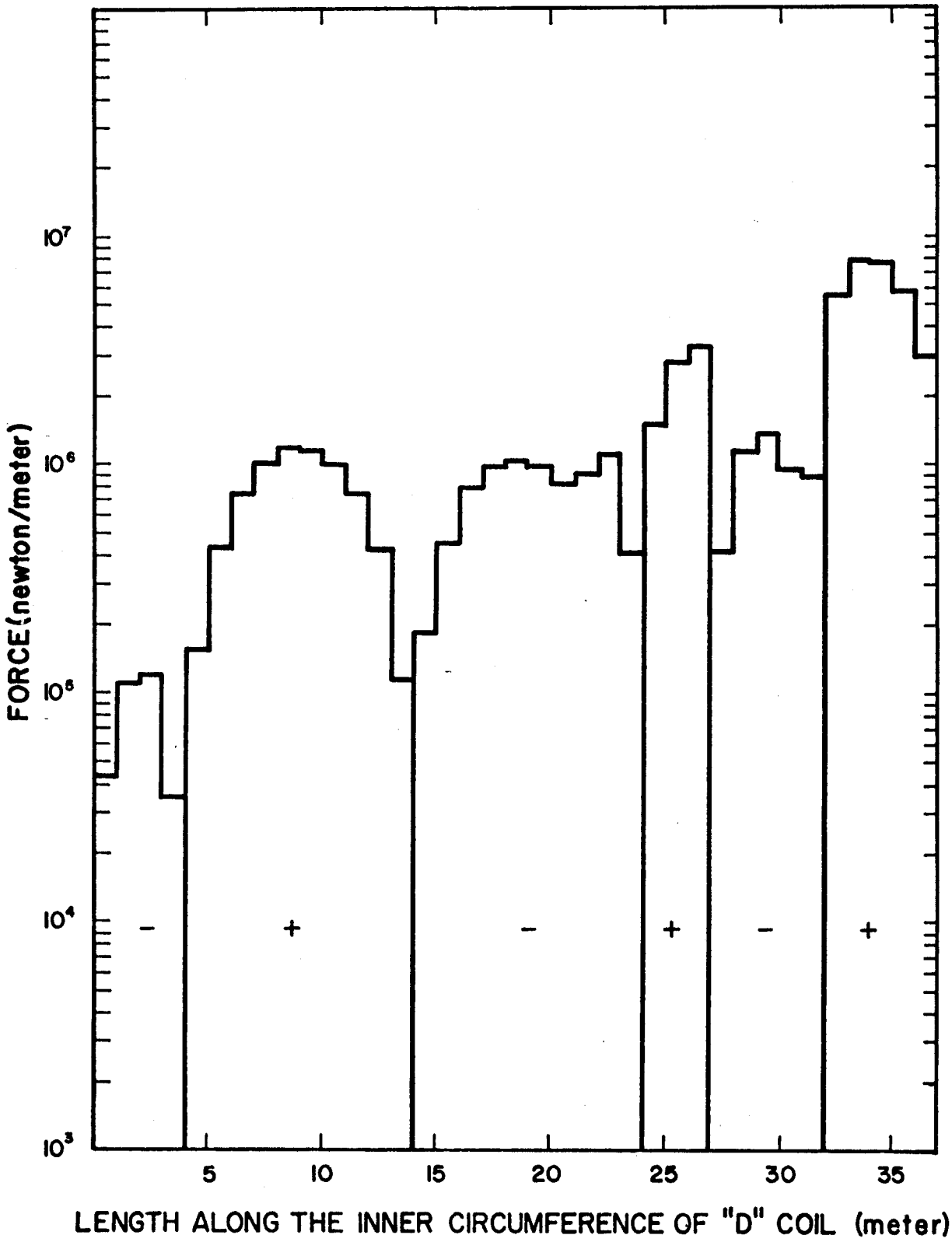

Figure III-C-19

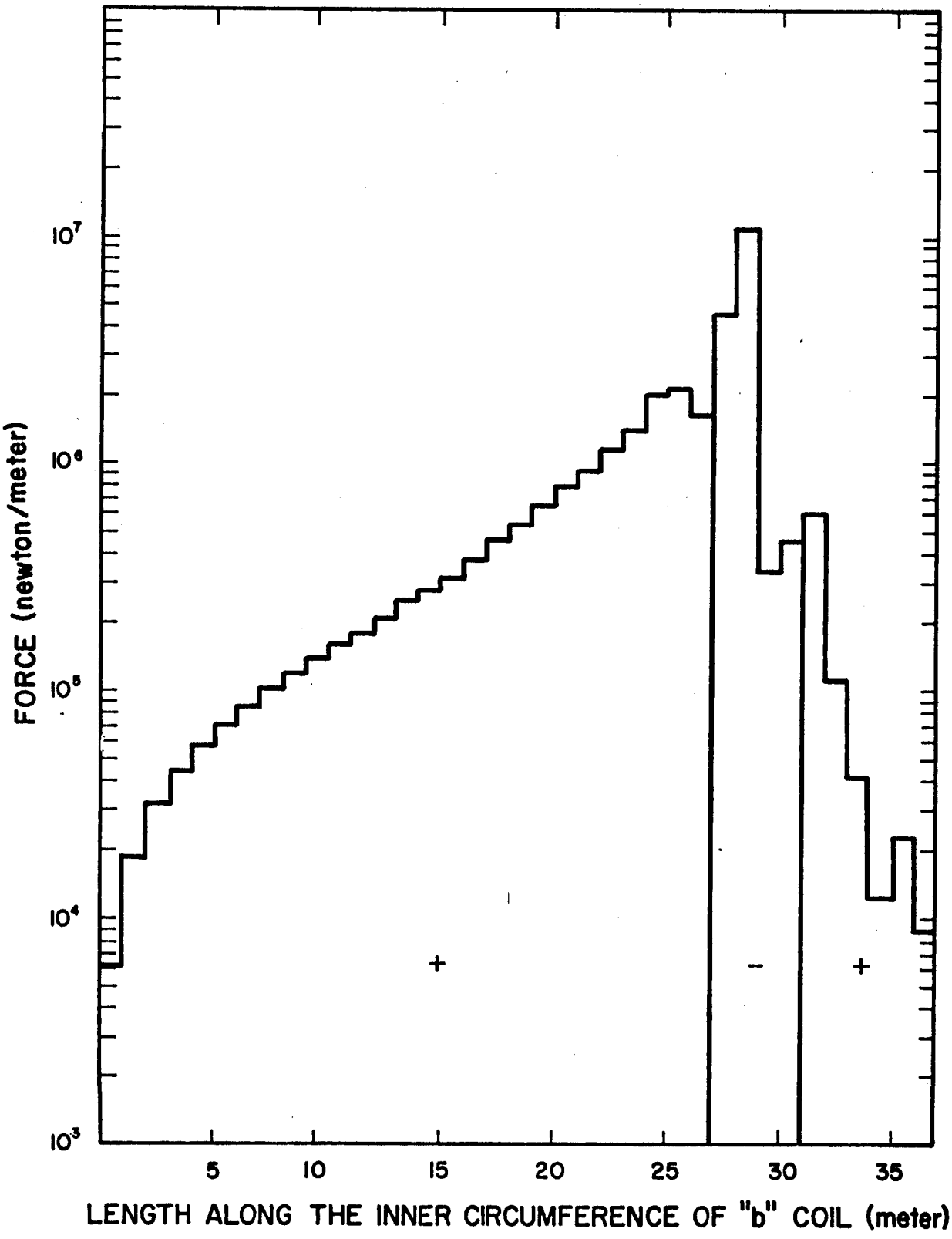

Figure III-C-20

a $10^{-8}\Omega$ contact resistance is expected. Thus, the total joint resistive power loss in the "D" magnet is $(9065)^2 \times (1 + .015) \times 10^{-8} \times 19 \times 24 = 380$ watts, which is present at all times the "D" magnets carry current. The pulsed resistive joint loss in the divertor and transformer coils is negligible.

d. Lead losses - Allowing a loss of 5 mW/A for properly designed vapor cooled current leads, the 24 pairs to the "D" magnets will have lead losses equal to $5 \times 10^{-3} \times 9065 \times 48 = 2175$ watts. While the divertors are carrying the full 18 kA current most of the time, the current flowing in the transformers has an average value of only 3.6 kA. The total lead losses for the 13 divertors and the 18 transformers are found to be 2160 + 648 = 2808 watts.

e. Nuclear heating - The blanket and shield of the present design are quite effective and the energy attenuation is 6×10^{-8}. Assuming half of the leakage is intercepted by the magnets, the total nuclear heating is $1.16 \times 10^6 \times 3300 \times 6 \times 10^{-8} \times 0.5 = 115$ watts, deposited at 4.2 K.

f. AC losses - The total ac losses in the divertors and transformers were calculated in Section III-B-3 to be 15.1 kWh per cycle. Dividing by the length of a burn cycle, 5730 sec., the averaged ac power loss amounts to about 9487 watts.

Similar procedures will be used now to calculate the ac loss in the TF coils due to the pulsing plasma, divertor, and transformer currents. From Fig. III-C-8 we see that at the TF coils conductor the poloidal component of the pulse field has an average value of $\Delta B_{//} = 0.15$ T, and on the straight edge of the "D" there is also a component of the pulse field perpendicular to the conductor of about $\Delta B_{\perp} = 0.4$ T.

The eddy current loss is due primarily to the poloidal pulse field with a power loss per unit length per conductor of

$$P_{e//} = \frac{w\, h^3}{2\pi^2 \rho_c} (\Delta B_{//})^2 \quad \text{(all quantities in I.S. units)}$$

where w = conductor width
h = conductor depth
ρ_c = copper stabilizer resistivity.

This gives an average power loss of 0.0036 W/m at the current rise phase, and a total eddy current loss of 0.023 kWh per cycle.

The filament coupling loss is due only to the perpendicular pulse field which induces current flowing along the superconducting filaments. Power dissipation occurs when this current flows across the composite matrix and is given by

$$P_{c\perp} = \frac{d_e^2 \; L^2}{\pi \; \rho_e} \; (\Delta B_\perp)^2, \; (w/m)$$

where d_e = effective composite diameter = $(4wh/\pi)^{1/2}$

L = quarter twist pitch = 0.075 m

ρ_e = effective matrix resistivity $\simeq 4 \; \rho_c$.

The average power loss of a conductor at the current rise phase is found to be 0.344 W/m, and the total filament coupling loss is 0.667 kWh per cycle. Both poloidal and perpendicular pulse fields give rise to hysteresis loss in the superconducting filaments. The pulse fields are now less than the filament full penetration field which is equal to 0.8 T. The power loss per unit length per conductor is

$$P_h = \frac{(\Delta B)^3}{6\mu_o^2 J_c d\tau} \; \frac{I_T}{J_{cd}}$$

where $\mu_o = 4\pi \times 10^{-7}$

J_c = filament critical current density at the ambient temperature and field

d = filament diameter

τ = field rise or fall time

I_T = total current per conductor

J_{cd} = design filament critical current density

The hysteresis loss due to the poloidal pulse field is found to be 0.0013 W/m per conductor at the current rise phase. The total loss per cycle is 0.015 kWh. The loss due to perpendicular pulse field is 0.027 W/m at the current rise phase, and 0.094 kWh total.

Thus, the total ac loss on the TF coils per cycle is 0.799 kWh. The averaged ac power loss is 50 watts, It is worthwhile noting that the total average ac power loss per unit length of the conductor at the current rise phase is 0.376 W/m, while the average helium surface cooling power is 92 W/m. There will be no thermal problem caused by this ac loss.

g. Transfer lines and storage tank losses - The losses in this category are about the same as in UWMAK-I and were estimated to be about 800 watts.

The total magnet system heat loss is 20.8 kW at 4.2K. The total power at room temperature required to run the refrigerator is about 20.8 kW x 300 = 6.24 MW.

III-D-2. Refrigerators

Ten 3 kW refrigertors are proposed with seven of them in operation and the other three in reserve. The 300,000 liters of helium in storage could supply the refrigeration for 12 hours of operation in the event of total liquefier failure. Thus, there is plenty of time for repair.

III-E. Power Supplies

III-E-1. Toroidal Field Magnets

The total energy stored in the "D" magnets is found by integrating the magnetic energy density, $B^2/2\mu_o$ over the whole torus volume. This gives 62 MWh or 223 GJ. The inductance of the toroidal magnet system is then found by equating the above energy to $1/2\ LI^2$. With I equal to 9,065A, the normal operating current for 19 discs per magnet, $L \simeq 5400$ henries. Assuming a 24h charging time, the voltage rating of the power supply will be 570 volts. Hence, an ac/dc bridge rates at 5,200 kW is required for the power supply of the "D" magnets.

III-E-2. Divertor and Transformer Coils

The charging-discharging and the accompanying power cycles for the divertor and transformer coils are sketched in Figure III-E-1 and III_E-2. The maximum energy stored in the poloidal field is estimated to be 2.9 MWh. During the initial 10 sec current rise time, the divertors are charging while the transformers are discharging. On the other hand, the divertor current turn-off and reset time for the transformers is 100 sec and 150 sec respectively. Hence, only in the initial rise time does high power demand occur. Assuming that a maximum power of 500 MW can be bought directly from an electric utility, an additional 500 MW peak power is required from an energy storage unit. The superconductive energy storage dipole magnet designed for Fermi National Laboratory(2) is appropriate for the present purpose. From Fig. III-E-1, the nergy required from the storage unit is estimated as 1/2 x (500 MW) x (3.75/3600 h) = 0.26 MWh. Assuming that only 25% of the energy stored in the storage coil is to be transferred to the divertor coils, a storage unit of about 1 MWh in size is planned. We will simply adopt the above mentioned FNAL superconductive energy storage unit.(2) However, the interface between the storage and load inductors warrants more detailed description. The present solution to the coupling between the superconducting storage unit, the power source and the divertor coils is by means of a thyristorized bridge network designed by Peterson and Mohan.(9) This new design is thought to be a significant improvement over the other concepts previously proposed.(10) This circuit system serves to minimize both the pulsed power and the corresponding reactive volt-ampere requirements from the three-phase power system.

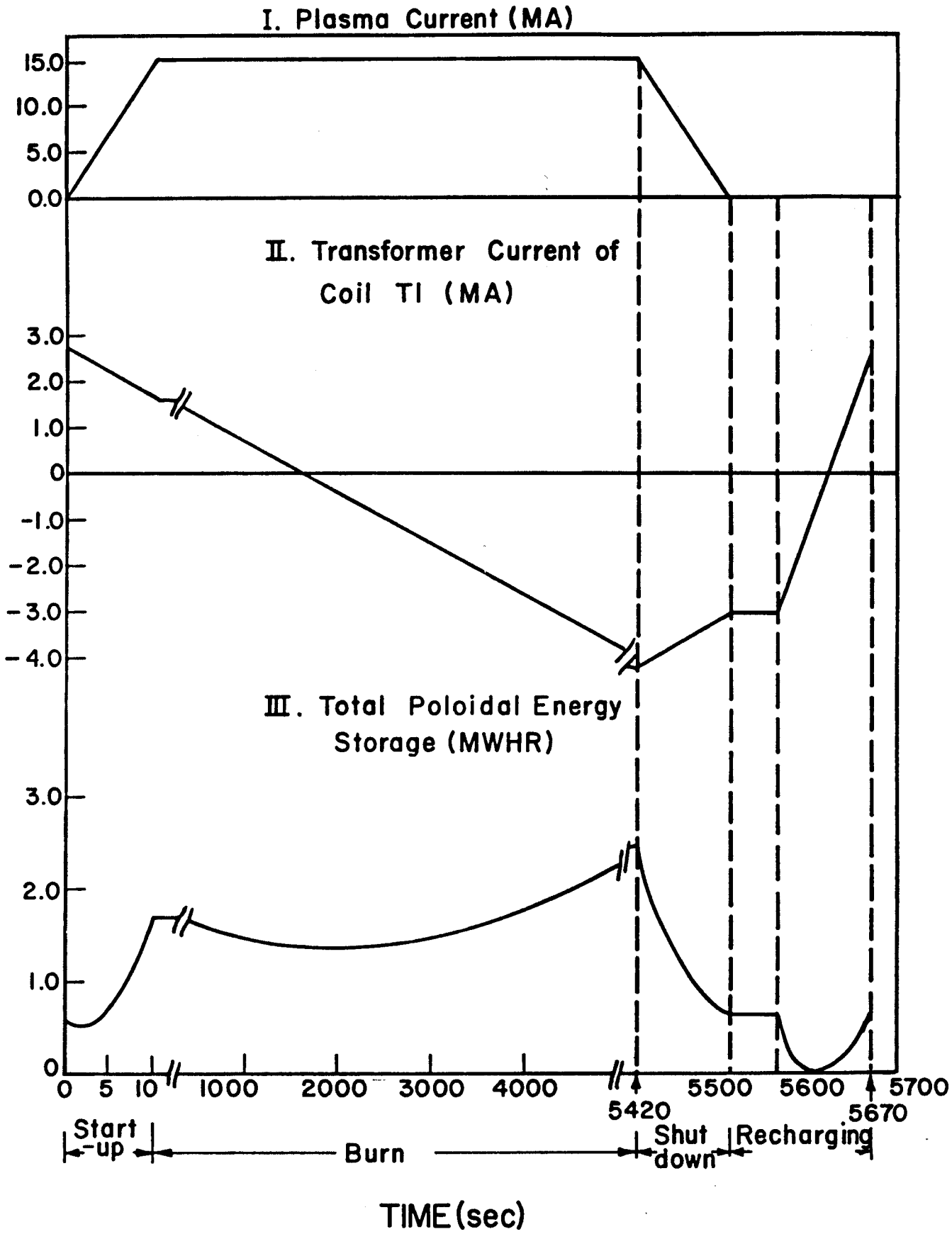

Figure III-E-1. Charging cycles of the poloidal field coils.

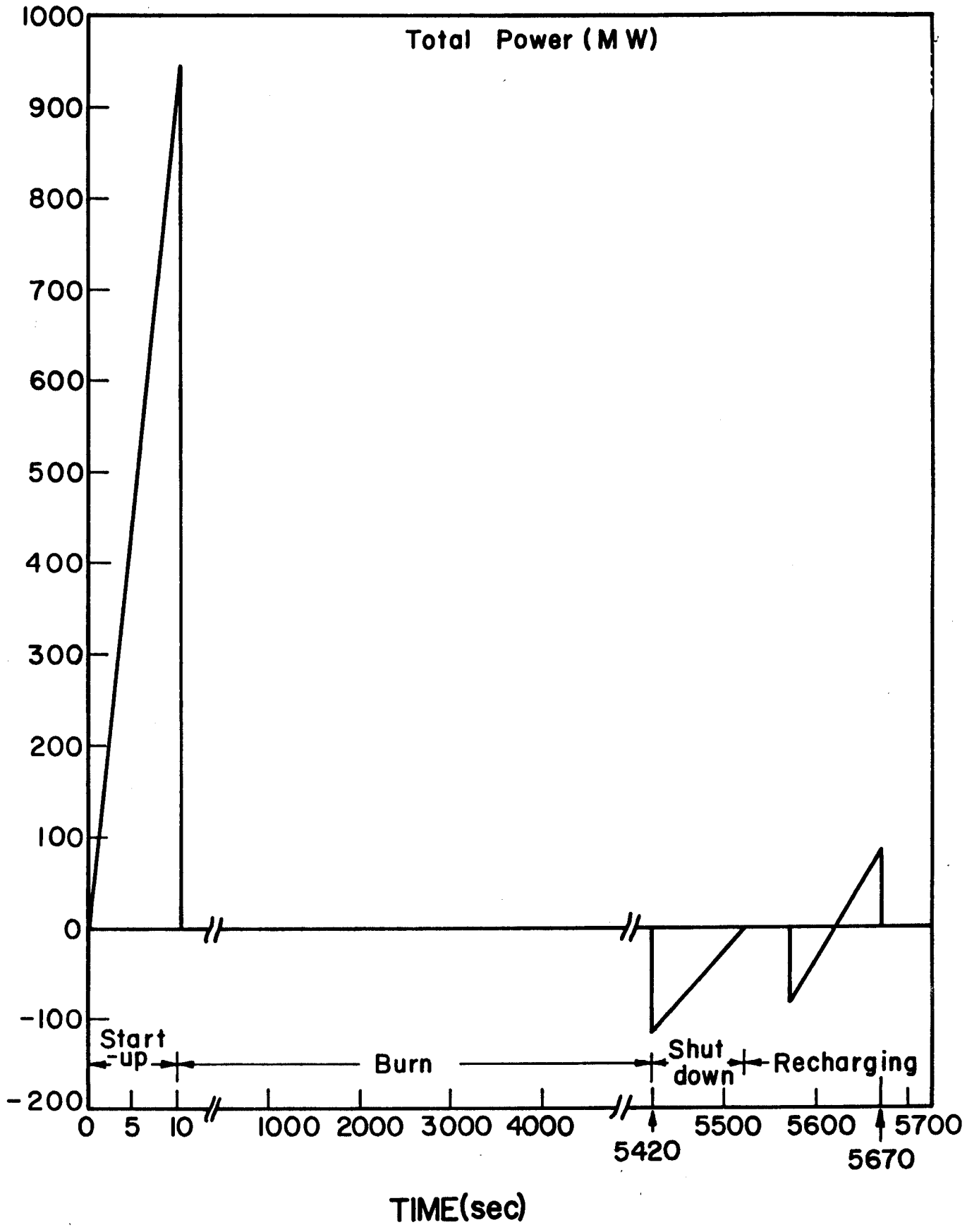

Figure III-E-2. Power demand curve of the poloidal field coils.

III-E-2-a. Basic System

The proposed system is shown in block diagram form in Figure III-E-3. The planned superconductive inductor energy storage unit (1 MWh capacity) is to be charged from the three phase power system by means of the power source converter (PSC). Its stored energy can also be returned to the power source as desired by appropriate control of the PSC phases. More than one pulsed power load of varying nature, magnitude and duration can be connected to the storage unit via dc/ac/dc double conversion subunits. DC power is drawn out of the storage unit, converted to ac, back to dc, and finally flows into the loads. This scheme is necessary to avoid the excessive losses incurred in simply connecting one inductor to another for energy transfer. The capacitor banks shown in Fig. III-E-3 provide the Q's required to achieve successful commutation for both conversions. Since the power flow is reversible in these double conversion bridges, and the divertor loads are inductive, the stored inductive energy can be returned to the storage unit during the discharge cycle. Thus, the only need for connecting to the power source (after initial charge) is to supply the losses in the entire system. Furthermore, allowing only a small fraction (25% maximum) of the energy stored in the storage inductor to be drawn out, the storage inductor current remains essentially constant. Hence, the power source P and Q requirements are essentially constant small quantities with the PSC operating at a fixed delay angle.

III-E-2-b. Circuit Arrangement

A circuit diagram for the arrangement with two inductive loads is shown in Figure III-E-4. The power source convertor provides the interface between the energy storage inductor, L_o, and the three-phase power system. Although the current rating of the PSC should be the same as the inter-inductor convertors, the voltage rating (and therefore the power rating) can be much smaller. This is because, as discussed in the previous paragraph, the PSC only has to supply the losses in the entire system. The limiting sensor, V_{L_o}, is employed to put PSC in bypass or reduced voltage mode when I_{L_o} tends to increase beyond the rating due to lesser pulsed load requirements and the associated losses. Delay angle control of the thyristors permits return of the energy stored in L_o to the power source, and permits a degree of Q control which may be beneficial from a system voltage regulation point of view.

The converters #1 and #1' (as well as #2 and #2') together with the capacitor bank for communication of both convertors form the dc/ac/dc double conversion sub-unit. It may be worthwhile to compare this subunit with the ac/dc/ac conversion of the dc power transmission system. It requires an ac system at both ends to provide for commutation and the corresponding Q as well as P requirements. Our dc/ac/dc conversion subunit uses internal commutation. The common ac terminals are connected to a capacitor bank, which provides commutation and the corresponding Q requirements for both convertors. The commuting frequency, f, can be varied over a wide range by a proper choice of capacitor bank size. For a given phase angle, the load voltage is roughly inversely proportional to f. It should be noted that the dc/ac/dc conversion subunit is not limited to the three-phase system shown in Figure III-E-4. Any (odd) multiphase operation (for smoother dc terminal voltage) can be obtained without any transformers needed to achieve phase shifting for more commutations per cycle.

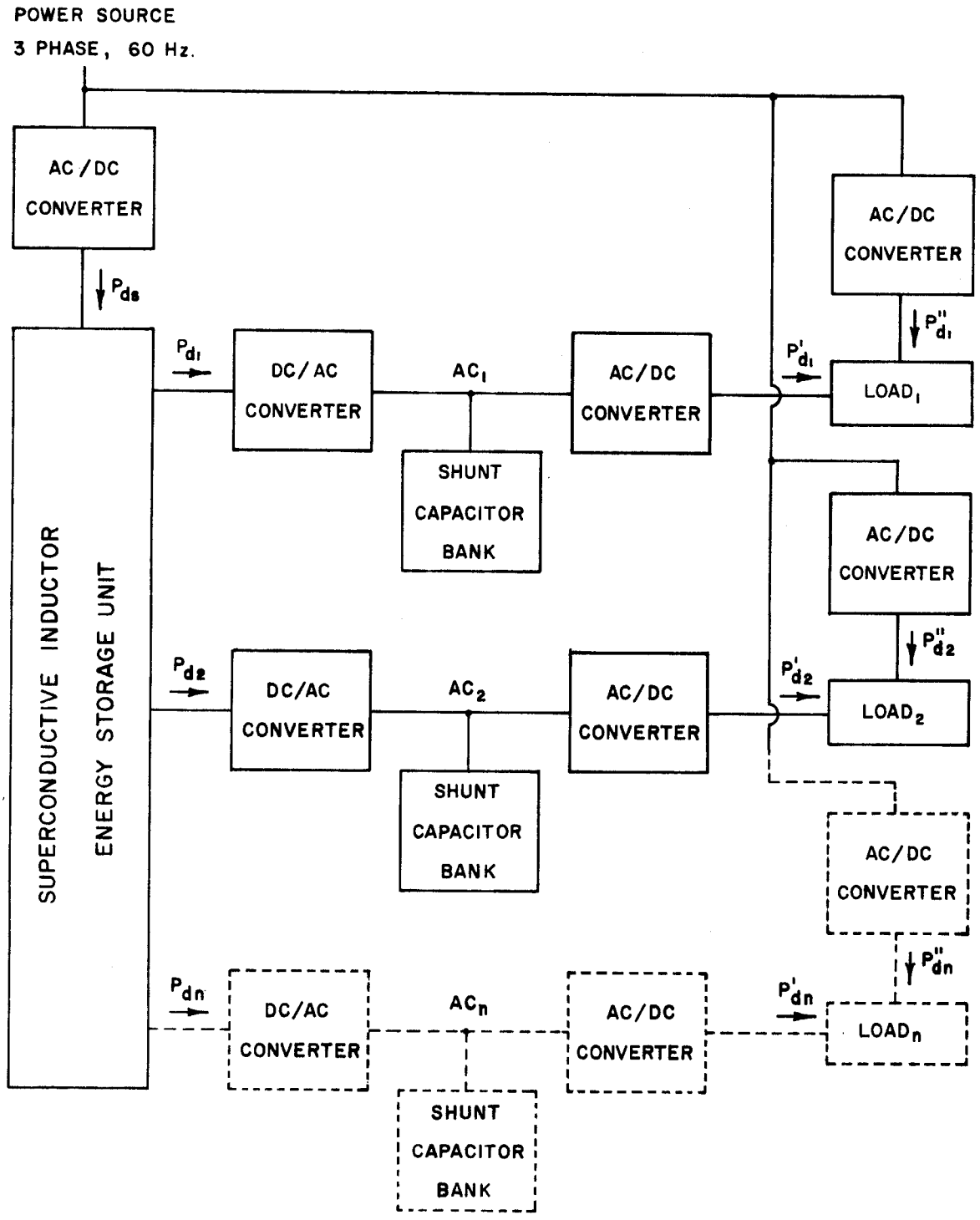

Figure III-E-3. Block diagram of storage inductor - Bridges - Loads system.

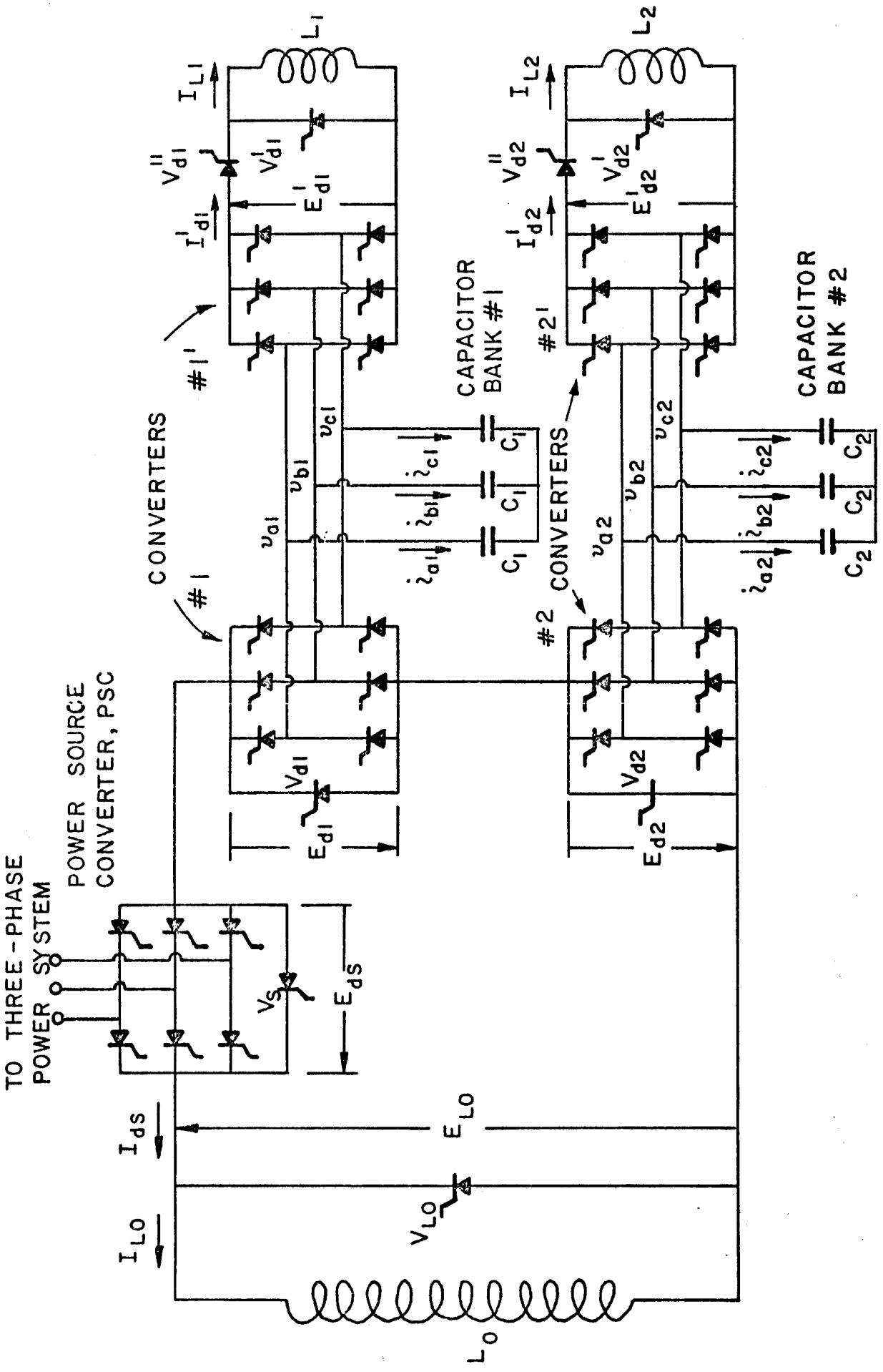

Figure III-E-4. Circuit diagram of an energy storage unit with two inductive loads.

III-F. Cost Estimate

III-F-1. Toroidal Field Magnets

The amount of materials required for the "D" magnets listed in Table III-A-1 shows that UWMAK-II "D" magnets require roughly 60% additional material compared to UWMAK-I. The center support structure requires 2550 MT of stainless steel, and the lateralsupports comprised of 1750 MT of aluminum (these two items were not included in UWMAK-I TF magnets cost estimates.) By using the same materials cost estimates as in UWMAK-I, the total installed cost for the "D" magnets is estimated to be $\$162 \times 10^6$.

III-F-2. Divertor and Transformer Coils

Due to the different arrangement and more detailed study of these coils, a cost comparison with the poloidal coils of UWMAK-I is invalid. Below are the cost estimates for UWMAK-II divertor and transformer coils

a. COST ANALYSIS OF DIVERTOR COILS

Material	Weight MT	Unit Cost $/kg	Total Cost $10^6
TiNb	10	33.00	0.33
Copper matrix	50	2.20	0.11
Fabrication of above (incl. Cu-Ni coating)	(60)	5.50	0.33
Copper Stabilizer	1,520	3.30	5.02
(Total conductor)	(1,580)	(3.34)	(5.79)
Reinforcing S.S.	160	4.40	0.71
Spacer and insulator	50	4.40	0.22
S. S. dewar & support	375	4.40	1.65
Super insulation (0.2 in thick)	$39,200 m^2$	$3.96/m^2$	0.07
Assembly and installation	(2165)	2.20	4.76
Total Divertors	(2165)	(6.10)	(13.20)

b. COST ANALYSIS OF TRANSFORMER COILS

	Weight MT	Unit Cost $1/kg	Total Cost $10^6
Ti Nb	26	33.00	0.86
Copper matrix	104	2.20	0.29
Fabrication of the composite	(130)	5.50	0.72
Copper stabilizer	956	3.30	3.16
(Total conductor)	(1,086)	(4.64)	(5.03)
Spacer and insulator	32	4.40	0.14
Assembly	(1,118)	2.20	2.46
Total Transformers	(1,118)	(6.82)	(7.60)

The total cost for the divertors and transformers is estimated to be 20.8×10^6.

III-F-3. Refrigeration System

Material		Unit Cost	Total Cost
Ten 3kw refrigerator		$583,000/kw	17.5×10^6
Liquid Helium inventory			
"D" magnet =	160,000 liters		
Divertor & Transformer =	150,000 liters		
Storage =	300,000 liters		
Total =	610,000 liters	$3/liter	1.8×10^6

The refrigeration system cost for UWMAK-II magnets is estimated to be 19.3×10^6

III-F-4. Power Supplies

a. Toroidal field magnets. As estimated earlier, an ac/dc bridge rated at 5,200 kW is needed. Assuming $40/kW, the capital cost of this power supply is 0.21×10^6.

b. Poloidal Field Magnets

The ac/dc bridge which provides one-half of the peak power to the poloidal coils directly from the ac line is rated at 500 MW at a cost of about \$20/kW or \$10 x 10^6 total. The lower unit cost of \$20/kW (rather than \$40/kW) for this bridge system is due to its infrequent pulse usage (10 to 150 sec per 95 min). The superconductive storage unit of 1 MWh size is estimated to cost \$15 x 10^6.(2) The dc/ac/dc conversion bridge discussed in Sec. III-E-2 is also rated at 500 MW but costs only \$15/kW or \$7.5 x 10^6 total (the power source converter cost is negligible), due to its great simplicity in parts. Hence, the power supply for the divertors and transformers is estimated to cost \$32.5 x 10^6. The total power supply capital cost amounts to about \$32.7 x 10^6.

III-F-5. Entire Magnet System

The total cost of the magnets, refrigeration system, and power supplies is estimated to be (162 + 20.8 + 19.3 + 32.7) x 10^6 ≃ \$235 x 10^6.

References for Chapter III

1. B. Badget et al., "UWMAK-I, A Wisconsin Toroidal Fusion Reactor Design," UWFDM-68, Nuclear Engr. Dept., Univ. of Wisconsin (Nov. 1973) Vol. I.

2. "Cryogenic Energy Storage System Design Report," Fermi National Laboratory Report FN-264, 8000.00 in collaboration with the University of Wisconsin, Oct. 1974.

3. "Superconducting Magnet for the 15 ft NAL Bubble Chamber" J. Purcell, H. Desportes, and D. Jones, Argonne National Lab. Feb. (1973).

4. M. A. Hilal, UWFDM 110, Univ. of Wisconsin - Madison, Sept. (1974).

5. M. A. Hilal and R. W. Boom, IEEE Transactions on Magnetics, Mag-11, 544 (1975).

6. M. N. Wilson et al., J. Phys. D3, 1517 (1970).

7. G. H. Morgan, J. Appl. Phys. 41, 3673 (1970).

8. S. L. Wipf, Proc. Summer Study on Superconductivity Devices and Accelerators, BNL 50155 (1969).

9. H. A. Peterson, N. Mohan, R. W. Boom and W. C. Young, Int. Conf. Energy Storage, Compression and Switching, Torino, Italy, Nov. 5-7, 1974.

10. R. W. Boom and H. A. Peterson, IEEE Trans. on Magnetics, MAG-8 (1973).

IV. Blanket and Shield

IV-A. Introduction and General Design Philosophy

The basic blanket design philosophy for UWMAK-II was to achieve a low tritium inventory, low lithium inventory design within the constraint that current technology should be employed wherever possible. The choice of structural material was based primarily on such current technology considerations and skeptism over the near term use of refractory metals led to the choice of 316 stainless steel. The reasoning here is similar to that described previously in our UWMAK-I design study.

The choice of a coolant was influenced by some of the problems we found in designing UWMAK-I. In particular, tritium recovery from liquid lithium at very low concentrations is difficult and suggested consideration of other approaches to breeding and recovering tritium. In addition, the temperature limitation of approximately 500°C due to the Li-stainless steel corrosion combined with the tritium extraction difficulties led us to eliminate liquid lithium as a possible coolant.

Based upon presently developed technology, the choice of a coolant lies between helium, a liquid metal or a fused salt. Each of these fluids must be circulated at rather high flow rates from the blankets to the external equipment for heat and/or tritium removal. The ability to transport tritium may be one determining factor in the choice of a coolant. Also, the MHD pressure drop associated with pumping conducting fluids across magnetic flux lines must be overcome by judicious design of the fluid flow channels or the development and utilization of non-conducting tubing. Simpler flow designs are possible, therefore, if helium is utilized, and chemical compatibility problems are reduced by the use of this inert gas. In addition, the neutronics interactions with helium are insignificant, except for the approximately 200 p.p.b. of ^{3}He normally in helium gas which would be rapidly transmuted* in an operating reac The utilization of helium does not perturb the neutronic behavior of the proposed blankets. For the reasons cited, helium is chosen as the coolant for this study. Using 316 stainless steel as the structural material virtually eliminated molten salt as a coolant.

The idea of low lithium inventory with rapid tritium recovery at reasonably low concentrations has the added merit of reducing the tritium inventory. This does not fix the choice of breeding material nor does it insure that adequate tritium production can be achieved in such a system. Adequate breeding with a small lithium inventory indicates the necessity of neutron multiplication (Be is used in UWMAK-II) which then must be combined with the use of lithium enriched in Li^{6} so that neutrons can be captured effectively even with a small Li inventory.

Of course, if liquid lithium is not used, another form of Li bearing compound is required and for reasons to be described, lithium aluminate ($LiAlO_2$) has been chosen. Tritium extraction from such compounds appears feasible and details of a proposed extraction method are given.

* He-3 has approximately 3000 barn (n,p) cross section for thermal neutrons

Given this basic set of design choices and overall philosophy, it is necessary now to develop a feasible design and to analyze it in all respects. This includes heat transfer, compatibility, neutronics analysis, structural analysis, radiation damage problems, tritium extraction, and so on. These questions are all addressed in this chapter. In Section IV-B, a study of potential materials for the various functions in the blanket is presented. A detailed discussion of helium compatiblity as a coolant with various structural materials is given in Appendix A at the end of the report. Section IV-C considers the survey studies carried out to evaluate the neutronic behavior of the proposed materials and to approximately determine the overall blanket layout. This is followed by the heat transfer analysis in IV-D and the description of the mechanical design in IV-E. A final neutronic analysis using three dimensional Monte Carlo calculations for the actual cellular geometry of the design is discussed briefly in Section IV-F. This section, as well as Sections IV-E and IV-J, contain some quite detailed drawings of the blanket design. The problems of tritium removal, handling, and leakage are assessed in Section IV-G. The analysis of radiation damage problems in UWMAK-II are given in Section IV-H while induced radioactivity, afterheat, and certain safety problems are analyzed in Section IV-I. Finally, a proposed manufacturing procedure is outlined in Section IV-J together with an estimate of fabrication costs.

IV-B. General Materials Considerations for Blanket and Shield Design

The concept of non-mobile breeder blankets permits a number of materials to be examined as blanket constituents. The blanket constituents can be classified according to their function, namely: coolant, structure, neutron multiplier, neutron moderator, and tritium breeder. The ultimate choice of a material for each function will depend upon its neutronics behavior, potential radiation damage, physical properties at operating temperatures and compatibility with other components. Also, each constituent must be compatible with the operation of the tritium removal system in which the tritium may exist in molecular or atomic form, or as tritium oxide.

1. Coolants

The potential coolants for fusion designs can be classified into two physical states, gaseous and liquid.* The gaseous coolants which may be considered are permanent gases, chiefly helium, metallic vapors, and perhaps steam or carbon dioxide. The liquid coolants which may be considered are water, high-boiling organic compounds, liquid metals and fused salts. Water is limited in its usefulness because of its low critical temperature, 375°C and the difficulty of using H_2O in the presence of large amounts of tritium. Also, the unknown radiation stability of the organic liquids make their use less certain at this time.

Based upon presently developed technology, the choice of a coolant lies between helium, a liquid metal or a fused salt. Each of these fluids must be circulated at rather high velocities from the blankets to external equipment for heat and/or tritium removal. The ability to transport tritium may also be a determining factor in the choice of a coolant. Also, the MHD pressuredrop associated with pumping conducting fluids across magnetic flux lines must be overcome by judicious design of the fluid flow channels or the development and utilization of non-conducting tubing.[1] Simpler flow designs are possible, therefore, if helium were utilized, and chemical compatibility problems are reduced by the use of this inert gas. In addition, the neutronics interactions with helium are insignificant, except for the approximately 200 p.p.b.[2] of ^3He which would be rapidly transmuted in an operating reactor; consequently, the utilization of helium does not perturb the neutronic behavior of the proposed blankets. For these reasons, helium is chosen as the coolant for this study.

* Solid coolants such as fluidized beds were briefly considered but considered too advanced for our present design philosophy.

2. Structure

The blanket structural materials which have been suggested in various reactor design studies[3,4] are: aluminum, stainless steel, niobium, vanadium, and molybdenum alloys. The choice of the structural material depends upon the fusion design parameters and the proposed operating temperatures. Aluminum appears limited in usefulness because of its low melting point, 660°C, unless special arrangement is made to preferentially cool the aluminum structure. The high helium production rates in Al (and the associated embrittlement) also makes the use of Al or Al alloys questionable. Excessive oxidation embrittlement of niobium[5] and probably vanadium alloys is predicted in even extremely pure helium, while the fabrication behavior of molybdenum is not completely established. For these reasons stainless steel is selected as the structural material, although vanadium, which has a single isotope, is considered in the neutronic parametric study. The maximum temperature of the stainless steel structure is limited to approximately 600°C by creep rupture life and radiation damage considerations.

3. Neutron Multipliers

The incorporation of beryllium in a blanket highly enriched with ^{6}Li is necessary in order to have a tritium breeding ratio greater than one with the possible exception of Li_2O. The chemical form of the Be in the fusion reactor may be metallic or a stable compound, such as BeO or Be_2C. The physical properties of each material,(Table IV-B-1,) their neutronic behavior, irradiation characteristics and chemical compatibility must be considered. A number of high melting intermetallic compounds[6] with compositions, MBe_{12} and MBe_{13}, are formed but information on their physical properties are insufficient for their consideration at this time.

The important neutronic reactions of Be are the (n,2n), (n,α) and (n,T) reactions. In UWMAK-II, these reactions will generate nearly $9cm^3$ (STP) He/yr and $3.6 \times 10^{-2} cm^3$(STP) T/yr per cm^3 Be (metallic).* The corresponding formation of tritium and He in BeO is approximately proportional to the density. However, BeO has a detrimental effect on neutron production, as discussed in the Neutronics Section. (IV-C)

The irradiation behavior of Be and BeO can be estimated based upon experimental data from fission reactor irradiations in which the total He production has been only 0.5 cm^3(STP) He/cm^3 Be. Under these conditions, the helium is insoluble and collects as bubbles at nucleation sites,

* 50% density factor

as discussed in Section IV-H on radiation damage, so that swelling was observed and stress-rupture values decreased.[7] This information indicates that in a fusion reactor blanket operating near 600°C, Be metal cannot be used as a structural member but must be supported in such a manner as to accomodate 10 to 30 vol. % swelling per year.

The escape of He from BeO compacts has been measured during irradiation at several temperatures by Carteret, Bareau and Elston.[8] The ratio of R/B, where

R = the quantity of He released from the solid unit time and
B = the quantity of He formed in unit time,

tended to become a constant, less than one, at each temperature after an initial induction period. For instance, R/B increased from 0.12 at 1020°C to 0.19 at 1350°C. They interpreted these results to mean that helium release is due partly to the diffusion of interstitial helium atoms, but that most of the helium nuclei remained in substitutional position. Because the helium atom is larger than the octahedral position in a BeO lattice, the interstitial helium atoms would presumably lead to expansion of the compacts. Swelling would be predicted to be especially important below 1000° where the helium release is probably small. Unfortunately, density changes were not measured on these compacts. Density changes for BeO single crystals have been obtained during irradiation in the 390° temperature range. Hickman and Walker[9] found that the expansion was highly anisotropic, decreased with temperature and was approximately 0.15% at 550°C. Based upon this information the volume expansion for BeO in a fusion reactor would be at least 1.5% in one year.

Although the quantity of tritium produced in beryllium is small, the fate of this tritium in both Be and BeO is of importance. Apparently, BeH_2 cannot be formed by direct combination of the elements.[10] The solubility of hydrogen in Be has been reported to be small, while the release via diffusion is moderately fast.[21] The diffusional release of tritium from irradiated BeO has been measured, and found to be very small.[11] For instance, the diffusion coefficient at 900°C is approximately $10^{-15} cm^2/sec$. As a consequence, the longest diffusion path in a BeO compact should be less than one μm in length, if the inventory of the tritium in the BeO is to be kept below 100 g. This is unrealistically low and therefore is a severe disadvantage of BeO as a fusion reactor neutron multiplier.

The chemical compatibility of BeO with stainless steel at high temperature should be excellent because of its high heat of formation compared with the oxides of the elements in steel.[12] Beryllium is not compatible with stainless steel, however, because of the intermetallic compound, $FeBe_{13}$, at 600°C formed in vacuum. At the same temperature and pressure, the experimental work by Vickers[13] suggests that the stainless steel can be protected by a protective layer of sintered Al_2O_3 or ZrO_2, such as might be applied by plasma spraying techniques.

Table IV-B-1

Potential Neutron Multipliers

Material	M. pt. °C	B. pt. °C	Be atoms $10^{22}/cm^3$
Be[a,b]	1283	2483	12.3
BeO[c]	2520	4260	7.3
Be_2C[d]	2400	2530	9.8

a. R. Hiltgren, R. L. Orr, P. D. Anderson and K. K. Kelley, Selected Values of Thermodynamic Properties of Metals and Alloys, p. 48, Wiley, New York (1963).

b. Handbook of Chemistry and Physics, 46th Ed., Chemical Rubber Co., Cleveland (1964)

c. Data on Chemicals for Ceramic Use, Bulletin No. 118, National Research Council, Washington (1949).

d. T. Ya Kosolapova, Carbides, pp. 67-69, Plenum Press, New York (1971).

4. Breeder Materials

The lithium compound selected as the tritium breeding material must satisfy many requirements. It must have properties exhibited by the other blanket constituents, such as: desirable neutronics and irradiation characteristics, chemical stability at operating temperatures and be compatible with the other blanket materials. In addition, the lithium compound must breed and release tritium. Any compound selected will eventually release tritium at the rate at which it is formed; however, the release must be at a sufficiently high rate so that the tritium inventory in the blanket is not excessive. Also, because nearly 55% of the nuclear heating is generated in the lithium region, the temperature of the lithium material may greatly exceed the average temperature in the blanket. Several classes of compounds are suggested, namely: metallic, salts and ceramics. The properties of these materials are listed in Table IV-B-2.

a. Lithium

Liquid lithium contained in steel capsules might be a potential breeding scheme. Tritium removal from sealed capsules is limited, however, because of the low permeability of tritium in stainless steel and the high solubility of tritium in the lithium. For instance, in order to keep the tritium inventory below 1 kg in the blanket, the liquid lithium would need to be encapsulated in nearly 10^{10} steel cylinders with a diameter of only 0.6mm and a wall thickness of 0.1mm. The utilization of such capsules is impractical.

Distillation of tritium from the lithium by the use of a porous plug in the capsule might be considered also; however, such a technique is not feasible because of the occurrence of a lithium-tritium azeotropic solution which is predicted at low tritium concentrations.[14] As a result, the vapor phase would be richer in lithium, while the tritium would concentrate in the capsule.

b. Intermetallic Compounds

Lithium forms intermetallic compounds melting above 600°C with Al, Bi, Pb, Si and Sn. Some of these compounds may be useful in specialized blanket designs; however, the radiation stability and the effects of the alloying elements upon the neutronic behavior of the blankets must be determined for each compound.

A major drawback to the utilization of the intermetallic compounds is the appearance of liquid phases at lower temperatures as the lithium atoms are transformed by nuclear reactions. For instance, when the high melting compound Li_3Bi, 1145°C, is subjected to neutron irradiation, its gross bismuth composition increases and a liquid phase is formed at 415°C by a peritectic reaction. This liquid would promote sintering of discrete particles and decrease the rate of tritium release.

Table IV-B-2

Potential Non-Mobile Breeder Materials

Material	M. pt. °C	Vapor Pressure	Li atoms $10^{22}/cm^3$
Li (liq.)[a]	180	1342°C(B. pt.)	4.2
LiAl	718	-	2.7
Li_3Bi[b]	1145	-	4.0
Li_2O[c]	1700	10^{-1} torr (1400°C)	8.2
LiOH[c]	471	5 torr H_2O(500°C)	3.7
$LiAlO_2$[e]	1700	Li_2O (1400°C)	2.3
Li_4SiO_4[f]	1256	Li_2O (1256°C)	4.8
Li_2C_2[g]	>1000	Li (1000°C)	4.1
LiF[d]	848	b. pt. (1693°C)	6.1
LiH[a,c]	686	24 torr H_2(686°C)	5.9

a. V. A. Moroni, E. J. Cairns, and F. A. Cafasso, "A Review of the Chemical, Physical and Thermal Properties of Lithium that are Related to Its Use in Fusion Reactors," Argonne National Laboratory, ANL-8001 (1973).

b. M. Hansen, Constitution of Binary Alloys, McGraw-Hill, New York (1958).

c. T. Kikuchi, Japan Atomic Energy Research Institute Memo - 5837 (1974).

d. W. A. Hart and O. F. Beumel, Jr., Comprehensive Inorganic Chemistry, Vol. I, A. F. Tnrutman-Dickenson, Ed., pp. 340-361, Pergamon Press, Oxford (1973).

e. D. W. Streckler and Rustum Roy, J. Am. Ceramic Soc., 44, 225 (1961).

f. F. C. Kracek, J. Phys. Chem., 34, 2645 (1930).

g. T. Ya. Kosolapova, Carbides, pp. 61-63, Plenum Press, New York (1971).

The compound LiAl has been proposed as a breeder blanket material. Examination of the phase diagram, Figure IV-B-1, indicates that because of the wide solid solubility region for this compound, the melting temperature, 718°C, would be lowered only ~10° by the transmutation of lithium atoms after two years of neutron irradiation. While the lowering of the melting temperature does not limit the usefulness of this compound, the effect of sintering does, however. Rapid sintering of alloys occurs at above 50% 0.5 times the melting temperature (in °K); consequently, discrete particles of this alloy could not be utilized above 150°C. Above this temperature, the particles would sinter, form a large clump and greatly increase the diffusional paths for tritium release.

c. Non-Metallic Compounds

An initial survey of the non-metallic compounds as shown on Table IV-B-2 indicates that the oxide-bearing ceramics[15] have the highest melting points, except for the carbide which will be discussed later. The compound Li_2O has a high melting point and a high lithium atom density although its vapor pressure prohibits its use above ~1400°C. Its chemical properties are poorly suited for its large scale usage, however, because of its strong affinity for water and carbon dioxide. The reaction,

$$Li_2O + H_2O = 2LiOH$$

has calculated free energy change at 298°K of -22.7 kcal so that the equilibrium vapor pressure of H_2O at 298°K is $\sim 10^{-14}$ torr. Consequently, the dry powder would be difficult to fabricate without producing some LiOH which must be dehydrated at elevated temperature after assembly. This dehydration procedure would be very difficult for large blanket and would be made more difficult by the need to remain below the melting point of the hydroxide, 471°C.

Lithium oxide compounds with Al_2O_3 and SiO_2 have much lower affinity for carbon dioxide and water; consequently, these compounds could be fabricated in dryboxes. In the Li_2O-Al_2O_3 system (Fig. IV-B-2) only two compounds exist,[16] $LiAlO_2$ and $LiAl_5O_8$. The melting point of its lithium rich compound, $LiAlO_2$, has been reported between 1610° and 1700°C. Such determinations were difficult because of the vaporization of Li_2O which began ~1400°C, and caused a change in the composition of the sample. A eutectic liquid reported at ~1670°C between the compounds Li_2AlO_2 and $LiAl_5O_8$ would form as the lithium in the compound $LiAlO_2$ is transformed by the neutron irradiation. The appearance of this liquid and the vaporization of lithia limits the usefulness of the compound to <1400°C. Also, sintering of ceramic materials becomes appreciable at 0.8 times the melting point.[17] The desire to avoid excessive sintering of the ceramic compound, $LiAlO_2$, limits its usefulness above ~1300°C. (This limit may even be optimistic if extremely small particles sizes (~20μm) are to be maintained.

Lithium ortho-silicate, Li_4SiO_4, and meta-silicate, Li_2SiO_3, are stable compounds[18] which may be useful. (Table IV-B-2 and Fig. IV-B-3). The ortho-silicat has a high lithium atom density, a lithium content per gram-formula weight greater than the meta-silicate or the aluminates and is non-hydroscopic. The ortho-silicate melts, however, by a peritectic reaction with Li_2O, 1255°C, and the rapid vaporization of lithia at this temperature has been reported. Also, as the lithium in the ortho-silicate transforms as a result of neutron irradiation, a eutectic liquid forms at 1024°C between the ortho and meta-silicates; consequently, the useful temperature limit of the ortho-silicate is <1000°C.

Figure IV-B-1

Li_2O–SiO_2 PHASE DIAGRAM

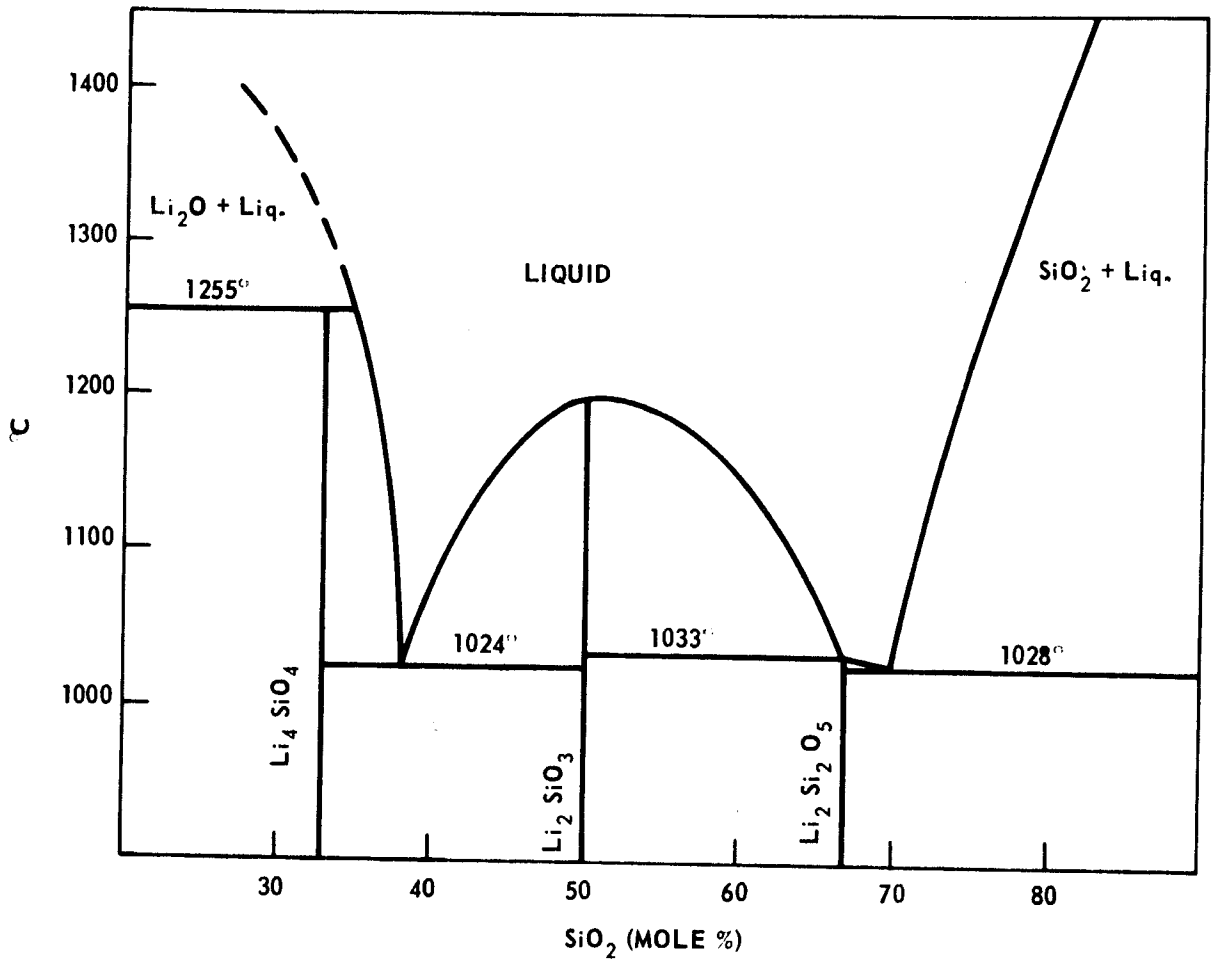

Figure IV-B-2

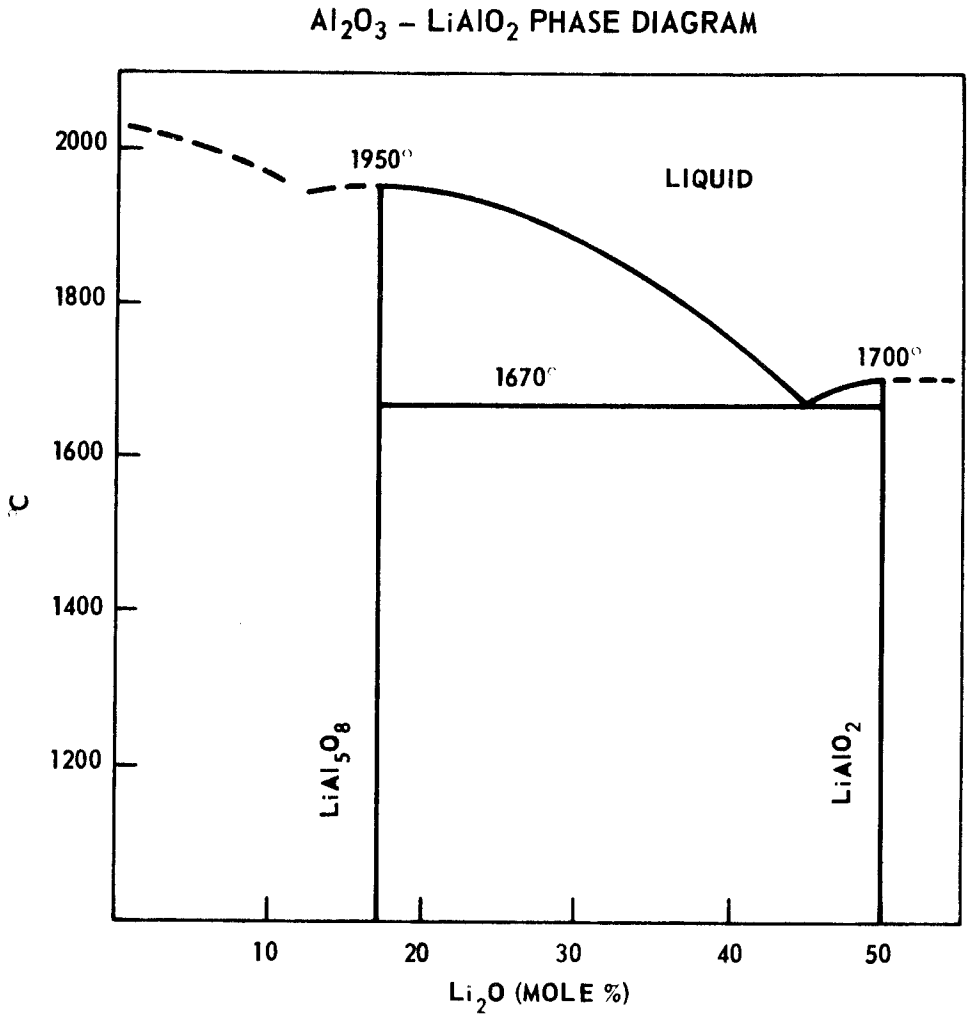
Al_2O_3 – $LiAlO_2$ PHASE DIAGRAM
2000
1800
1600
1400
1200
°C
1950°
LIQUID
1700°
1670°
$LiAl_5O_8$
$LiAlO_2$
10
20
30
40
50
Li_2O (MOLE %)

Figure IV-B-3

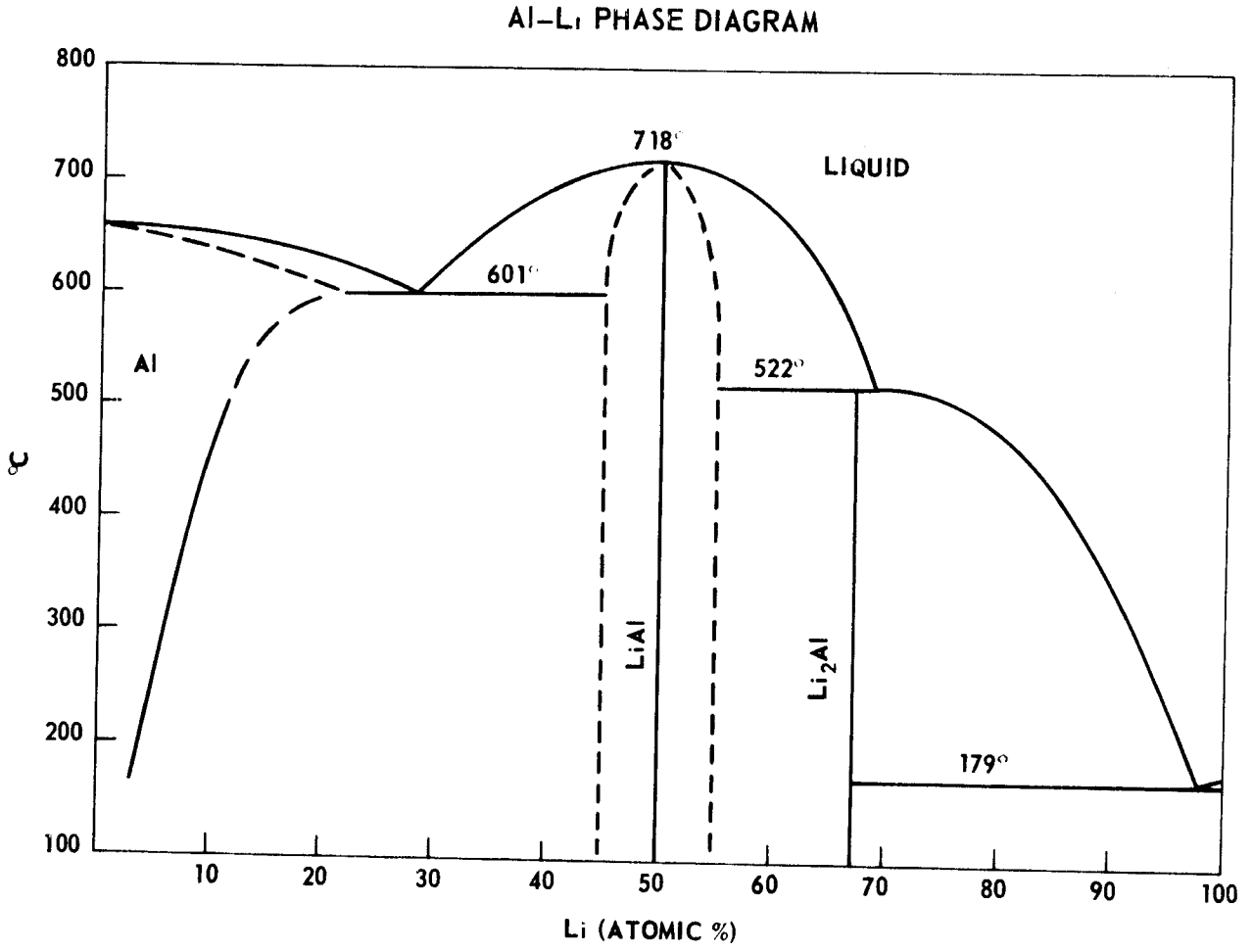
Al–Li PHASE DIAGRAM
800
700
600
500
400
300
200
100
°C
718°
LIQUID
601°
Al
522°
LiAl
Li2Al
179°
10
20
30
40
50
60
70
80
90
100
Li (ATOMIC %)

In addition to the oxide ceramics, the carbide of a metal is often a stable compound. Lithium forms a single carbide Li_2C_2, which reacts readily with water to yield actylene.(19) Although the detailed crystal structure of this compound has not been reported yet, it probably exists as a salt in which the carbon atoms form a dimer, similar to CaC_2 so that it is not a stable high temperature compound. This behavior was demonstrated in the study of the Li-Li_2C_2 system in which the trend of the melting point data indicated that the melting point of Li_2C_2 would be much greater than 1000°C; however, at temperatures >800°C in a vacuum, the lithium readily vaporized. Also, reported polymorptic transformation temperatures at 410, 440, and 560°C may limit its usefulness to even lower temperatures.

The lithium halide salt, LiF, has a high lithium atom density but its relatively low melting and boiling points probably limit its usefulness. Also, the tritium which is generated in a fluoride salt would be released as molecular TF which may cause potentially serious corrosion problems if released into the helium coolant. Consequently, a low temperature fused salt mixture would have to be circulated to external equipment for removal of the TF, as has been proposed previously.(20)

Lithium hydride or deuteride have many desirable neutronic characteristics as a potential tritium breeding material or neutron moderators. Their low melting point and high hydrogen pressure, Table IV-B-2, pose serious limitations on their usefulness, however. Perhaps these undesirable characteristics could be overcome by clever design of the blanket modules and the accompanying tritium extraction system.

Summary

This brief survey of the physical properties and predicted irradiation behavior of several lithium-bearing materials indicates that $LiAlO_2$ is preferred for a non-mobile fusion reactor breeder blanket. It is predicted to be amenable to large scale fabrication, useful in the 1300-1400°C temperature range and compatible with stainless steel and other blanket materials. Its undesirable characteristics are its low thermal conductivity, its low lithium atom density and the introduction of neutronically undesirable atoms into the breeding zone (see the Neutronics Section IV-C).

References for Section IV-B

1. D. K. Sze and W. E. Stewart, "Use of Electrical Insulation in Lithium - Cooled Fusion Reactor Blankets", Proceedings of the First Topical Meeting on the Technology of Controlled Nuclear Fusion, Conf-740402, USAEC (1974).

2. Chemical and Engineering News, p. 14, June 3, 1974.

3. J. Powell, A. Aronson, P. Bezler, F. Miles and W. Winsche, "Minimum Activity Blankets Using Aluminum Structure", Proceedings of the First Topical Meeting on the Technology of Controlled Nuclear Fusion, Conf-740402, USAEC (1974).

4. B. R. T. Frost, "Refractory Metals - Alloys and Properties", Fusion Reactor First-Wall Materials, WASH-1206, USAEC (1972).

5. J. H. DeVan, "Compatibility:, Fusion Reactor First-Wall Materials, ibid.

6. M. Hansen, Constitution of Binary Alloys, McGraw-Hill, New York (1958).

7. J. R. Weir, "The Effect of High Temperature Reactor Irradiation on Some Physical and Mechanical Properties of Beryllium", The Metallurgy of Beryllium, pp. 395-409, Chapman and Hall, London (1963).

8. Y. Carteret, J. Bareau and J. Elston, Brit. Ceramic Soc. Proc., 1967, No. 7, pp. 363-373.

9. B. X. Hickman and D. G. Walker, ibid, pp. 381-389.

10. W. M. Mueller, J. P. Blackledge and G. G. Libowitz, Metal Hydrides, pp. 550-551, Academic Press, New York (1968).

11. K. T. Scott and L. L. Wassell, Brit. Ceramic Soc. Proc., 1967, No. 7, pp. 375-380.

12. K. A. Gschneidner, Jr., N. Kippenhan and O. D. McMasters, "Thermochemistry of the Rare Earths", IS-RIC-6, Iowa State University (1973).

13. W. Vickers, "The Compatibility of Beryllium with Various Reactor Materials", The Metallurgy of Beryllium, (Chapman & Hall, London 1963) pp. 335-349.

14. J. S. Watson, "An Evaluation of Methods for Recovering Tritium from the Blankets or Coolant Systems of Fusion Reactors", ORNL-TM-3794, Oak Ridge National Laboratory (1972).

15. W. A. Hart and O. F. Beumel, Jr., Comprehensive Inorganic Chemistry, Vol. I, A. F. Troutman-Dickenson, (ED), pp. 340-361, Pergamon Press, Oxford (1973).

16. D. W. Strickler and Rustum Roy, J. Am. Ceramic Soc., 44, 225 (1961).

17. E. Ryshkowitch, Oxide Ceramics, p. 68, Academic Press, New York (1960).

18. F. C. Kracek, J. Phys. Chem., 34, 2641 (1930).

19. T. Ya Kosolapova, Carbides, pp. 61-63, Plenum Press, New York (1971).

20. E. Greenspan and W. G. Price, Jr., "Tritium Breeding Potential of the Princeton Reference Fusion Power Plant", Proceedings of the First Topical Meeting on the Technology of Controlled Nuclear Fusion, op. cit.

21. P. M. S. Jones and R. Gibson, J. Nucl. Materials 21, 353 (1967).

IV-C. Neutronics and Photonics

IV-C-1. General Survey Studies of Low Li Inventory Blankets

As explained in the introduction, to minimize the lithium inventory in CTR blankets, it is necessary to use highly enriched Li and Be (except for Li_2O). Clearly, employing a large amount of beryllium allows significant reduction in the lithium volume. However, the magnitude of beryllium reserves and resources is questionable at present. The known resources[1] of the U.S. is believed to be limited to 2×10^4 metric tonnes. An 8 cm thick layer of beryllium in a toroidal reactor with minor and major radii of 5 and 13 meters consumes about 2% of these resources. Thus, the question of beryllium resources needs to be investigated thoroughly as it is crucial for minimizing the lithium inventory in CTR blankets in addition to its well recognized importance for increasing energy multiplication in almost all conceptions of fusion blankets.[2] Indications are that world prospective resources may be larger than 0.6 megatons. If this proves to be true, then a few hundred fusion reactors can utilize moderate amounts of beryllium without exhausting a large fraction of the reserves. In any event, a prudent neutronics design at present should minimize the amount of beryllium incorporated into CTR blankets.

Several lithium and beryllium compounds were discussed in the previous section from material considerations rather than neutronics. In this section, we evaluate the neutronics behavior of most of these compounds.

Table IV-C-1 described several designs for which the neutronics analysis was carried out. One-dimensional cylindrical geometry with a plasma radius of 250 cm and an inner first wall radius of 300 cm was assumed. All the neutron and gamma transport calculations were carried out with the ANISN[3] program in the S_8-P_3 approximations. All neutron and gamma multigroup cross sections were processed using SUPERTOG[4] and SMUG[5] from ENDF/B-III[6]. The gamma production cross sections were processed from ENDF/B-III with LAPHANO[7]. Neutron kerma factors and partial group cross sections were processed with MACK[8] from ENDF/B-III. The energy group structure used in all cases consists of 46 neutron groups and 43 gamma groups.[9]

All the designs described in Table IV-C-1 have the common feature of low lithium inventory, i.e., the total thickness of the lithium region is less than 5 cm. Design 2, as shown schematically in Fig. IV-C-1, consists of a 1 cm vanadium first wall, a 1 cm region of 90% Li plus 10% V, a 12 cm thick region of 90% metallic beryllium plus 10% vanadium, and regions consisting of 2 cm of 90% Li plus 10% V, 2 cm of 90% Be plus 10% V, and 57 cm graphite. All composition percentages in Table IV-C-1 are by volume. Design 1 is the same as design 2 except the 1 cm lithium-vanadium region behind the first wall is removed. The amount of beryllium is decreased from 14 cm in design 2 to 9 cm in design 3 and 5 cm in design 4. All designs except design 5 utilize lithium enriched to 90% in ^6Li. The effect of reducing the lithium enrichment from 90 to 60% ^6Li, but using roughly the same optical thickness of ^6Li as in design 4,

Table IV-C-1

Description of Several Designs with Low Lithium Inventory for Which Neutronics Analysis was Carried out

$Z_{O_{N_E}}$ *	Design 1		Design 2		Design 3		Design 4	
	t†	Composition[a]	t	Composition	t	Composition	t	Composition
3	1	Vanadium	1	Vanadium	1	Vanadium	1	Vanadium
4	5	90% Be + 10% V	1	90% Li + 10% V	1	90% Li + 10% V	1	90% Li + 10% V
5	5	90% Be + 10% V	10	90% Be + 10% V	5	90% Be + 10% V	5	90% Be + 10% V
6	2	90% Be + 10% V	2	90% Be + 10% V	2	90% Be + 10% V	0.0	----------
7	2	90% Li + 10% V	2	90% Li + 10% V	2	90% Li + 10% V	2	90% Li + 10% V
8	2	90% Be + 10% V	2	90% Be + 10% V	2	90% Be + 10% V	0.0	----------
9	57	graphite	57	graphite	57	graphite	57	graphite

ZONE *	Design 5		Design 6		Design 7	
	t	Composition	t	Composition	t	Composition
3	1	Vanadium	1	Vanadium	1	Vanadium
4	1.5	90% Li[a] + 10% V	1	90% $Li_2Al_2O_4$ + 10% V	1	90% Li_2O + 10% V
5	5	90% Be + 10% V	5	90% Be + 10% V	5	90% Be + 10% V
6	0.5	90% Li[a] + 10% V	0.0	----------	0.0	----------
7	2	90% Li[a] + 10% V	2	90% $Li_2Al_2O_4$ + 10% V	2	90% Li_2O + 10% V
8	0.5	90% Li[a] + 10% V	0.0	----------	0.0	----------
9	57	graphite	57	graphite	57	graphite

ZONE *	Design 8		Design 9		Design 10	
	t	Composition	t	Composition	t	Composition
3	1	Vanadium	1	Vanadium	1	Stainless Steel
4	1	90% $Li_2Al_2O_4$ + 10% V	1	90% LiAl + 10% V	1	90% $Li_2Al_2O_4$ + 10% SS
5	5	90% BeO + 10% V	5	90% Be + 10% V	5	90% Be + 10% SS
6	2	90% BeO + 10% V	0.0	---------	0.0	----------
7	2	90% $Li_2Al_2O_4$ + 10% V	2	90% LiAl + 10% V	2	90% $Li_2Al_2O_4$ + 10% SS
8	2	90% BeO + 10% V	0.0	---------	0.0	----------
9	57	graphite	57	graphite	57	graphite

*In all designs: Zone 1 (central section of the cylindrical geometry) is the plasma region with an outer radius of 250 cm; and zone 2 is a vacuum gap of 50 centimeter.

† t is the thickness of the zone in centimeters.

a all composition percentages are by volume and lithium is enriched to 90% in Li-6 in all designs except design 5 for which lithium is enriched to 60%.

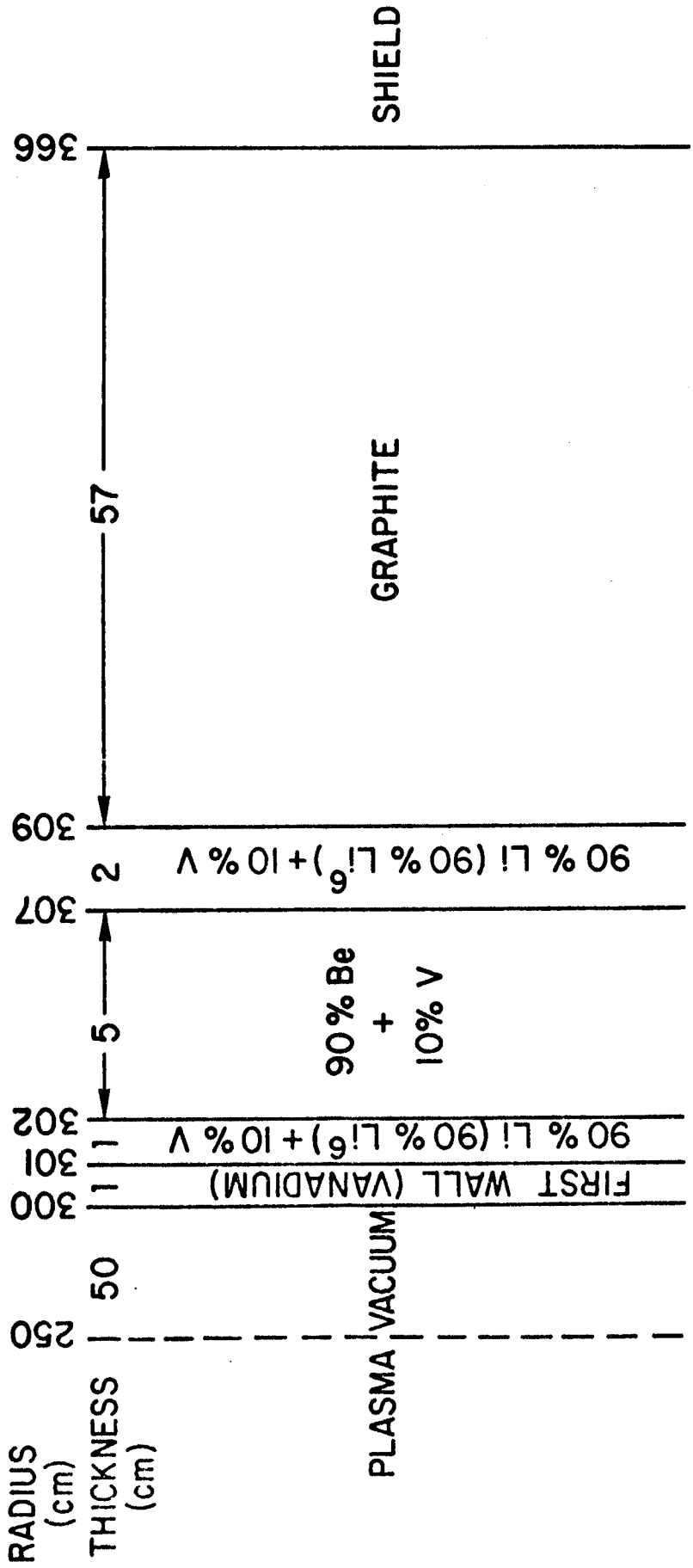

Figure IV-C-1
A Schematic of a Blanket Design with Low Lithium Inventory
(Design No. 4)

is shown by design 5. Designs 4, 6, 7, and 9 compare the performance of Li, $Li_2Al_2O_4$, Li_2O, and LiAl, respectively. Design 8 is the same as design 6 but metallic beryllium is replaced with beryllium oxide with approximately the same amount of Be. Vanadium is employed as the first wall and structure in designs 1 through 9 to simplify the neutronics data preparation and analysis. The effect of stainless steel is brought up in design 10 which is obtained by 1 to 1 volume substitution of stainless steel for vanadium in design 6.

Table IV-C-2 summarizes the most important neutronics results for the designs described in Table IV-C-1. Comparing the neutronics results for designs 2, 3 and 4 we find that the tritium breeding ratio and energy multiplication are quite sensitive to the amount of beryllium. These three designs employ 2.7 cm of 90% enriched lithium and approximately 5 cm of beryllium is the minimum for such designs to have a tritium breeding ratio of ~1.15. The tritium breeding ratio and energy per fusion reaction increases rather rapidly as the amount of berryllium is increased up to about 8 cm; then the rate of increase becomes slower as additional amounts of beryllium are employed. It can also be seen from Table IV-C-1, design 1, that the removal of the 1 cm enriched lithium layer behind the first wall in design 2 causes the tritium breeding ratio to drop by more than 35% despite the 5% increase in the Be (n,2n) reaction rate. The energy production, however, increases by about 2 MeV per D-T neutron. The reason for this can be explained by the strong competition of the $V(n,\gamma)$ with the $^6Li(n,\alpha)t$ reaction in a neutron spectrum greatly softened by the Be(n,2n) reaction. The angular distribution of the secondary neutrons emerging from the Be(n,2n) reaction is nearly isotropic and, therefore, a large fraction of these neutrons stream back in the direction of the first wall. The removal of the lithium-6 layer from behind the first wall increases the capture rate in vanadium from 0.2 to 0.6 reactions per D-T neutron. The Q-value for the $V(n,\gamma)$ reaction is about 70% larger than the Q-value in the $^6Li(n,\alpha)t$ reaction.

The results in Table IV-C-2 for designs 4, 6, 7 and 9 compare the neutronics performance of Li, $Li_2Al_2O_4$, Li_2O and LiAl as breeding materials. Since the comparison is on the basis of equal volumes of each compound, the amount of lithium varies greatly from design to design as can be seen by comparing the number of lithium atoms per unit volume in these compounds as given in Table IV-C-3. The tritium production in these compounds is affected mainly by two factors: 1) the lithium nuclide number density per unit volume in the compound, and 2) the presence of other elements such as oxygen and aluminum. The first factor simply means that the larger the lithium optical thickness the larger is the tritium breeding ratio. However, for the same amount of beryllium, the increase in the tritium breeding ratio as the lithium concentration is increased beyond 2×10^{22} atoms/cm^3 in the three centimeter lithium compound layer is modest as this amount of highly enriched lithium already represents several mean free paths for tritium production. The presence of oxygen and aluminum, on the other hand, has two opposite effects on the breeding ratio. Some of the high energy neutrons streaming into the breeding zones are slowed down by inelastic scattering. This prevents most of these neutrons from having a chance of inducing an (n,2n) reaction if they stream back into the beryllium region, thus reducing the blanket neutron multiplication. However, these neutrons as

Table IV-C-2

Summary of the Neutronics Results for the Designs Described in Table III

Design Number	1	2	3	4	5	6	7	8	9	10
^{6}Li (n,α)t	0.928	1.469	1.370	1.150	1.159	1.077	1.183	0.979	1.093	0.988
^{7}Li (n,n'α)t	0.001	0.004	0.005	0.006	0.035	0.003	0.010	0.002	0.003	0.003
Tritium Breeding Ratio	0.929	1.473	1.375	1.156	1.194	1.080	1.193	0.981	1.096	0.991
Neutron Heating*	13.71	15.82	14.94	13.46	13.49	12.74	13.67	11.89	12.85	
Gamma Heating	7.97	3.74	2.68	2.31	2.37	2.94	2.30	3.82		
Total Heating	21.68	19.56	17.62	15.77	15.86	15.68	15.97	15.71		
Neutron Leakage*	0.03	0.03	0.06	0.09	0.08	0.07	0.07	0.04	0.08	0.07
Be (n,2n)†	1.002	0.947	0.746	0.505	0.491	0.469	0.468	0.364	0.485	0.423
(n,2n)[a] in V or SS	0.124	0.128	0.124	0.118	0.122	0.115	0.114	0.118	0.117	0.069
(n,γ)[a] in V or SS	0.629	0.195	0.072	0.021	0.023	0.033	0.014	0.068	0.030	0.026

* in units of MeV per D-T neutron
† all reactions are given in units of reactions per D-T neutron
a-Vanadium in designs 1 through 9 and stainless steel in design 10.

they are slowed down will have a greater probability of inducing a $^{6}Li(n,\alpha)t$ reaction. In addition, the presence of oxygen and aluminum results in some parasitic capture. Nevertheless, the optical thickness of oxygen and aluminum in any of the compounds considered in the designs presented here is only a small fraction of a mean free path for collision by high energy neutrons. All the factors considered above which have opposite effects on the breeding ratio cause the variation of the ratio to be rather small from one compound to another. It is interesting to note that since the variation in the lithium concentration is very large (it varies by a factor as large as 4; see Table IV-C-3) the tritium breeding ratio is higher for the compounds with higher lithium nuclide number density.

Inspection of the results for designs 4 and 5 show that varying the enrichment of lithium in ^{6}Li while keeping the optical thickness of ^{6}Li the same does not significantly change the neutronics characteristics of the system. If the lithium enrichment and thickness are varied, however, such that the optical thickness of ^{7}Li is close to one average mean free path or more, the change in the results is more pronounced.

Although metallic beryllium is less favorable from a materials point of view than beryllium oxide or beryllium carbide, it is desirable from a neutronics standpoint not to introduce any elements other than beryllium into the neutron multiplication regions in the blanket. Neutron interactions in such elements compete with the (n,2n) reaction in beryllium decreasing the efficiency of beryllium utilization. Design 8 which utilizes BeO produces a breeding ratio about 8% smaller than that of design 6 which employs metallic beryllium although the amount of Be in the former is slightly larger than that in the latter. Thus the amount of beryllium required per blanket is larger when beryllium compounds are used. This is undesirable if beryllium resources are as limited as present studies indicate. It should be noted, however, that beryllium burn-up is approximately the same in beryllium and beryllium compounds for the same neutron multiplication. Another disadvantage of using beryllium compounds, although not of great importance in this case, is the associated increase in the physical thickness of the blanket.

Designs 1 through 9 utilize vanadium as first wall and structure. Design 10, however, is the same as that of design 6 except for replacing vanadium with stainless steel on an equal volume basis. Although the (n,γ) reaction rate in vanadium is greater than in stainless steel the breeding ratio is smaller in design 10 than in design 6. Stainless steel is more effective than vanadium in slowing down the high energy neutrons and therefore, it reduces the rate of neutron multiplication in beryllium. In addition, the (n,2n) reaction rate in vanadium is larger than that in stainless steel.

In designs 4 through 10, the tritium breeding required is achieved by about 3 cm of highly enriched lithium and lithium compounds and 5cm of Be plus structure in addition to a 1cm first wall. The average energy carried away with the neutrons leaking out of zone 8 in these designs (see Table IV-C-1) is 3 to 4 MeV per D-T neutron.

TABLE IV-C-3

POTENTIAL NON-MOBILE BREEDER MATERIALS

Material	M. pt. °C	Vapor Pressure	Li atoms $10^{22}/cm^3$
		(Metallic)	
Li (liq.)[a]	180	1342°C (b. pt.)	4.2
Li Al[b]	718	--	2.7
Li_3 Bi[b]	1145	--	4.0
		(Non-Metallic)	
Li_2O[c]	1700	600 torr (1400°C)	8.2
LiOH[d]	471	17 torr H_2O (500°C)	3.7
$LiAlO_2$[e]	1700	Li_2O (1400°C)	2.3
Li_4SiO_4[f]	1256	Li_2O (1256°C)	4.8
Li_2C_2[g]	>1000	Li (1000°C)	4.1
LiF[d]	848	b. pt. (1693°C)	6.1
LiH[a,c]	686	24 torr H_2 (686°C)	5.9

a. V. A. Maroni, E. J. Cairns and F. A. Cafasso, "A Review of the Chemical, Physical and Thermal Properties of Lithium that are Related to Its Use in Fusion Reactors", Argonne National Laboratory, ANL-8001 (1973).

b. Ref. 12.

c. Handbook of Chemistry and Physics, 46th Ed., Chemical Rubber Co., Cleveland (1964).

d. Ref. 21, and calculations from.

e. Ref. 22.

f. Ref. 24.

g. Ref. 25.

Therefore, an additional region is required beyond the neutron multiplication and tritium production zones in order to: 1) extract the kinetic energy remaining with the neutrons, and 2) moderate and reflect a fraction of the neutrons into the tritium breeding zones thus increasing the tritium production density which in turn allows reduction of the lithium inventory and/or the amount of beryllium required. We employed graphite to perform these functions in all designs (see zone 9 in Table IV-C-1). Some of the alternatives were eliminated on the basis of material performance. Some others were excluded on the basis of their undersirable neutronics characteristics. For example, the strong neutron absorption in boron prevents adequate tritium breeding with reasonable beryllium inventories if boron carbide (B_4C) is used instead of graphite. Similarly, the parasitic capture in stainless steel constituents reduces significantly the tritium breeding ratio when it is used in zone 9. Although graphite has several disadvantages[10] regarding its behavior under irradiation, it seemed a reasonable choice for the type of designs considered in this study.

It should be noted that an additional zone of about 1 cm of highly enriched lithium behind the graphite can increase the tritium production significantly thus increasing the breeding ratio or allowing a smaller amount of beryllium to be used. This has two disadvantages, however. First, segmenting the tritium breeding region into several zones may complicate the tritium extraction system. Another disadvantage is related to the high lithium burn-up in the designs considered here, as will be discussed later, requiring replacement of the breeding zones every few years depending on the magnitude of the wall loading. Thus, an additional breeding zone outside the bulky graphite region makes the replacement schemes more difficult.

IV-C-2 UWMAK-II Blanket and Shield Design Studies

A schematic of the UWMAK-II blanket and shield is given in Fig. IV-C-2. While the reactor is toroidal in geometry with a minor plasma radius of 5 meters and a major radius of 13 meters, the neutron and gamma transport calculations were carried out in cylindrical geometry using the same calculational techniques described in the previous section. Based upon the discussion given in section IV-B and other considerations such as fabricability and the presence of qualified technology, stainless steel is chosen as the material for the first wall, structural components, and helium coolant tubing. The first-wall thickness was determined from considerations which included hoop and thermal stresses, sputtering, blistering, and corrosion problems. The physical thickness of the first wall is 2 cm but 50% of the volume is occupied by the helium coolant. Since helium does not perturb the transport calculations to any measurable degree, a density factor of 0.5 for stainless steel in the 2 cm wall was used (see Fig. IV-C-2).

The stainless steel required for the structural components and coolant tubing was estimated as 10% of the physical volume of the blanket and shield. The blanket is conceived as composed of cells, each 20 cm wide and 90 cm deep; and the stainless steel cell walls are about 7 mm thick. The lithium aluminate

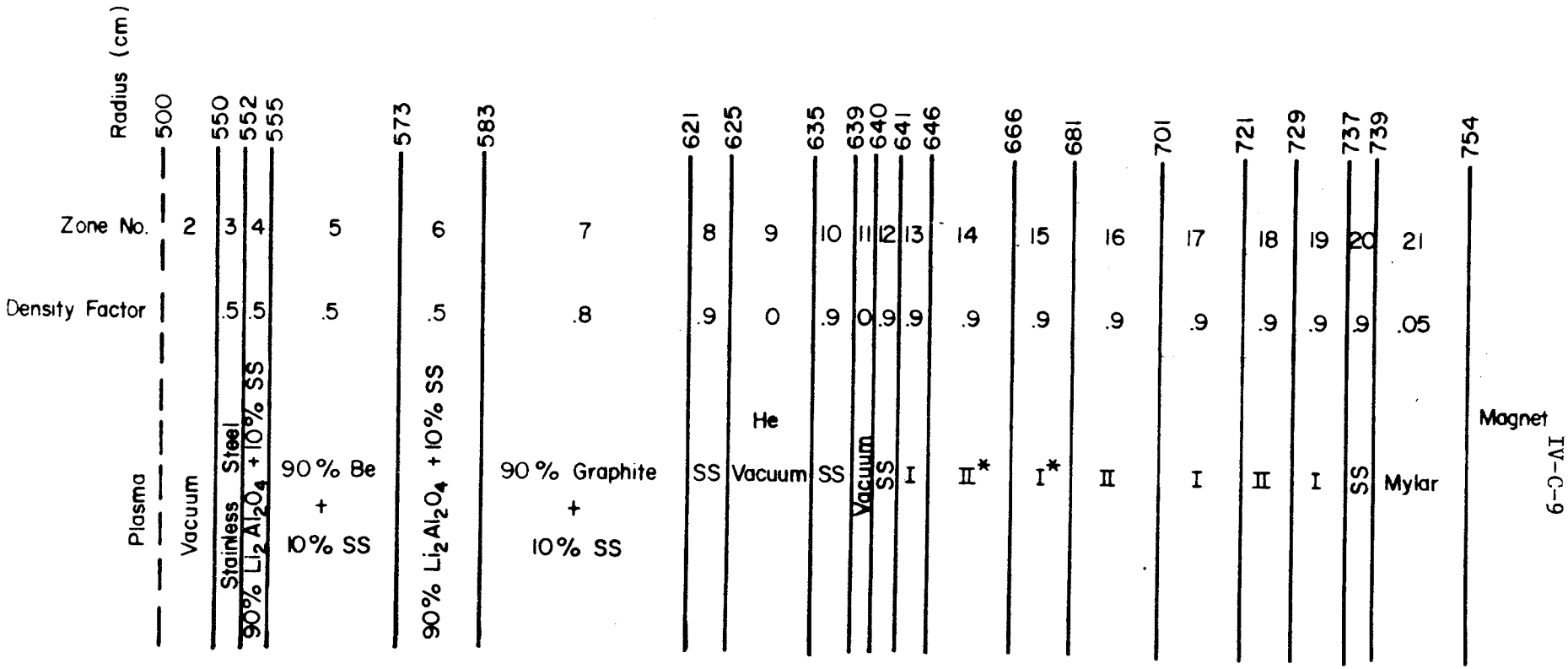

Material I is a mixture of 90% B_4C + 10% SS and Material II is a mixture of 90% Pb + 10% SS

Figure IV-C-2 **A Schematic of UWMAK-II Blanket and Shield**

and beryllium will be packed in pins with an average stainless steel wall of 0.75mm. Obviously, the neutronics for such a system can best be predicted by three-dimensional calculations. However, for the approximate one-dimensional calculation, the stainless steel structure must be homogenized with the other blanket and shield constituents. Since most of the neutrons in the beryllium and lithium aluminate regions of the actual system will not suffer any interaction in the stainless steel structure, a homogenization scheme based on the actual volume percentage of the structure in each zone would overestimate the neutron interaction rate in stainless steel, thus underpredicting the actual reaction rates in beryllium and lithium aluminate. At the time, no studies of detailed cells were available and to compensate for the above effect, we homogenized 50% of the structure in the inner region of the blanket with beryllium and lithium aluminate and placed the rest of the structure in the outer regions (with the stainless steel in zone 8 and 10 of Fig. IV-C-2 for the one-dimensional calculations.)

Zones 4 and 6 in Fig. IV-C-2 are the tritium production zones. They are 3 and 10 cm thick and the lithium is enriched to 90% in ^{6}Li. Lithium aluminate was chosen as the breeding material for the reasons discussed earlier. Due to the slow tritium diffusion predicted (Fig. IV-C-3, see also section IV-G), the lithium aluminate must be fabricated as very small pellets. Thus a large void fraction exists in the lithium aluminate and a 50% packing fraction appears reasonable.* Zone 5 is an 18 cm thick region of 90% beryllium plus 10% stainless steel. A density factor of 0.5 is used in this zone in order to accommodate the swelling resulting from excessive helium production in the beryllium.

Zone 7 is 38 cm of 90% graphite plus 10% SS. The graphite serves as moderator for the high energy neutrons streaming out of the neutron multiplication and tritium production zones and reflects some of the neutrons back into these zones. Because of the potential radiation induced growth in graphite, and because of space required for coolant, a density factor of 0.8 is used in that zone.

The headers for the primary helium coolant are idealized in the one-dimensional model by zones 8, 9, and 10. The 8 cm of stainless steel in zones 8 and 10 serve also as a neutron reflector and they extract the greater part of the useful kinetic energy remaining with the neutrons and photons.

Zone 11 is a 1 cm vacuum gap and it serves as a thermal barrier between the high temperature blanket (about 600°C) and the low temperature shield (approximately 200°C). Zones 12 through 20 comprise the magnet shield. The shield composition and dimensions resulted from optimizing the total cost of the shield, magnet, and the helium refrigerators required to cool the superconducting magnet to about 4°K, using the optimization technique described in reference 11. Excluding zones 12 and 20, the shield is 96 cm and consists of alternating zones of lead and boron carbide on an equal volume basis with 10% of the total volume occupied by stainless steel for structural purposes. The 1 cm of stainless steel in zone 12 is a structural support for the heavy weight of the shield. Zone 20 which is 2 cm of stainless steel is a part of the magnet

* This low density is also required to accomodate helium gas swelling in the $LiAlO_2$ (see Section IV-H-5).

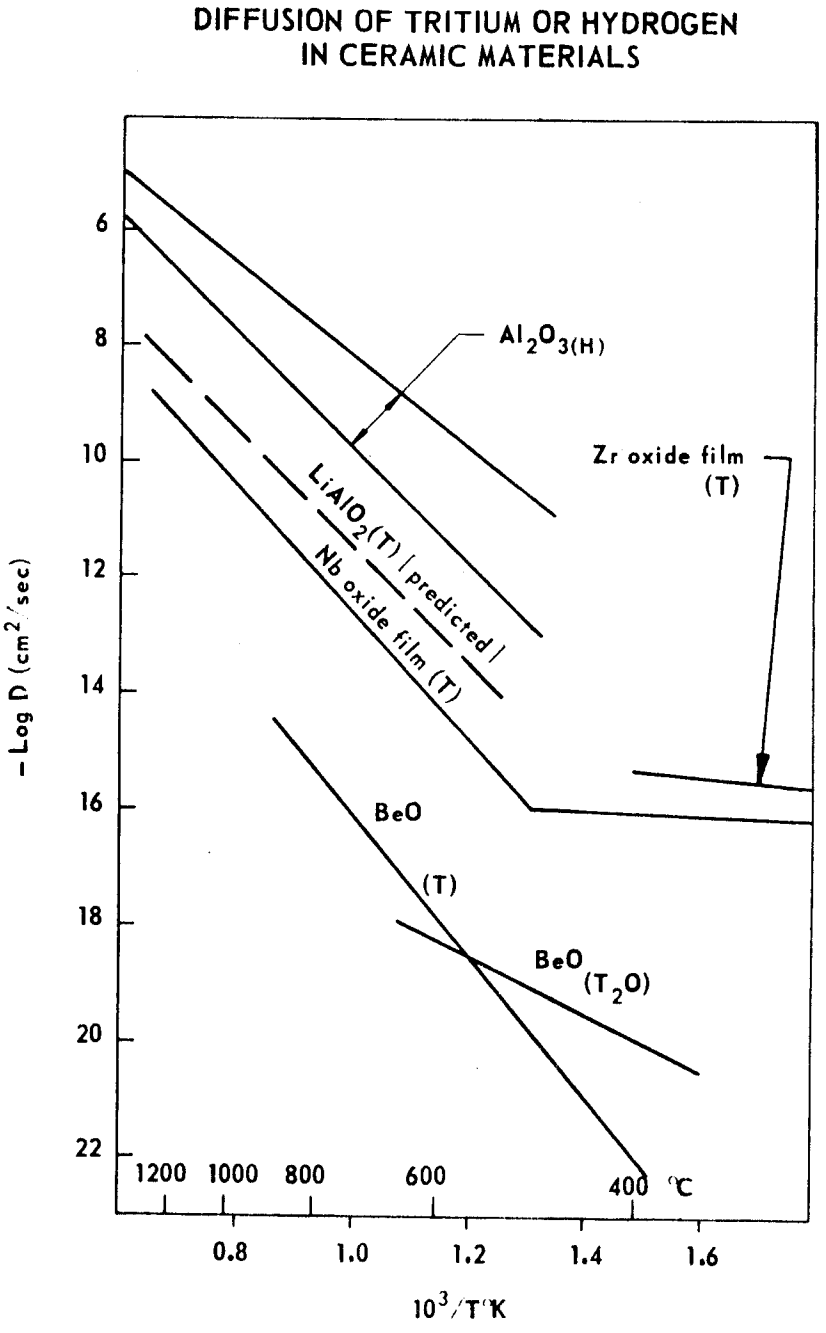

Figure IV-C-3

Diffusion of Tritium or Hydrogen in Ceramic Materials

and it represents the dewar for the cryogenic system. Zone 21 is thermal insulation for the magnet and cryogenic systems, about 95% of this zone is vacuum in order to prevent heat transfer by conduction. The mylar superinsulation reduces the thermal radiation losses.

We turn our attention now to a discussion of the results for the UWMAK-II reactor just described. The neutronics results in particular are presented in detail as they provide the basic input to other areas of the reactor design.

Neutron heating is given by material and zone in Table IV-C-4. In Table IV-C-5, the neutron and gamma heating and the gamma energy production are tabulated by zone. The results in these tables are given in units of MeV per DT neutron. Several observations are in order. The neutron heating in ^{6}Li alone is one-third of the total nuclear heating in the system, the average heating rate per unit volume in the first wall is 9.95 watts/cm^3/(MW/m^2). The maximum power density in the blanket is in the lithium aluminate-stainless steel region behind the first wall. The average power density in this region is 17.81 watts/cm^3/(MW/m^2) compared with 6.39 in the lithium aluminate-stainless steel mixture in zone 6 and 4.29 watts/cm^3/(MW/m^2) in the beryllium-stainless steel zone. The nuclear heating in the shield is only 1.2% of the total nuclear heating in the blanket and shield, i.e., about 50 MW for the 5000 MW(th) reactor. Thus, extracting this amount of energy at high efficiency is not necessary but its removal is crucial to insure the physical integrity of the lead containing shield. (The melting point of Pb is 327°C).

A summary of the results for the tritium breeding, nuclear heating, energy leakage from the magnet shield, and radiation damage parameters in UWMAK-II is given in Table IV-C-6. For purposes of comparison, we listed in this table the same parameters for the University of Wisconsin First Conceptual Reactor Design, UWMAK-I[11] The UWMAK-I blanket consists of a 0.4 cm stainless steel first wall, 51 cm of 95% natural lithium plus 5% stainless steel, and a 15 cm stainless steel reflector. The major differences between UWMAK-I and the UWMAK-II blanket presented here is the lithium inventory which is 1.4 x 10^6 kg in UWMAK-I while it is only 4.1 x 10^4 kg in UWMAK-II.* This also results in a much lower tritium inventory as discussed later in this section.

Table IV-C-6 shows that the contribution of ^{7}Li to tritium production is very small and that the tritium breeding ratio of 1.18 comes almost entirely from the ^{6}Li (n,α)t reaction. This is in contrast to reactors operating on a high energy spectrum in natural lithium in which about 40% of the tritium breeding comes from the ^{7}Li(n,n'α)t reaction as shown for UWMAK-I in Table IV-C-6. It is important to note that 0.01 tritium atoms per DT neutron are produced in the Be (n,t) reaction (see Table IV-C-7). While this amount of tritium is not crucial from a breeding point of view, it is extremely important to extract it as it represents a production rate of approximately 6 grams per day in a 5000 MW(th) reactor and allowing it to accumulate in the beryllium would increase the tritium inventory in the blanket significantly (i.e. 1-2 kg per year if not extracted.)

---

* Although this is highly enriched with Li^6 and the total amount of Li that must be mined from the ground is 5.6 x 10^5 kg for the initial loading and if it must be replaced every two years with the first wall, then 7.8 x 10^{6}kg must be mined for the lifetime of the plant. The original 1.4 x 10^{6}kg of Li in UWMAK-I will last for the lifetime of the plant.

Table IV-C-4

Neutron Heating in UWMAK-II by Material and Zone
(in units of MeV per D-T neutron)

Zone	Composition	Cr	Ni	Fe	Be	^{6}Li	^{7}Li	O	Al
1	Plasma								
2	Vacuum								
3	Stainless Steel	0.0823	0.1293	0.3794					
4	90% $Li_2 Al_2 O_4$ + 10% SS	0.0095	0.0153	0.0439		2.7297	0.0206	0.3566	0.1988
5	90% Be + 10% SS	0.0290	0.0488	0.1334	3.9784				
6	90% $Li_2 Al_2 O_4$ + 10% SS	0.0064	0.0110	0.0292		3.4098	0.0171	0.2650	0.1374
7	90% C + 10% SS	0.0104	0.0181	0.0471					
8	Stainless Steel	0.0021	0.0034	0.0092					
9	Helium	-	-	-	-	-	-	-	-
10	Stainless Steel	0.0012	0.0019	0.0054					
11	Vacuum	-	-	-	-	-	-	-	-
12	Stainless Steel	2.25 (-4)*	3.46 (-4)	9.80 (-4)					
13	90% B_4C + 10% SS	7.92 (-5)	1.26 (-4)	3.47 (-4)					
14	90% Pb + 10% SS	1.24 (-4)	1.70 (-4)	5.26 (-4)					
15	90% B_4C + 10% SS	1.34 (-5)	1.92 (-5)	5.71 (-5)					
16	90% Pb + 10% SS	2.91 (-6)	3.90 (-6)	1.22 (-5)					
17	90% B_4C + 10% SS	3.21 (-7)	4.57 (-7)	1.36 (-6)					
18	90% Pb + 10% SS	1.69 (-8)	2.64 (-8)	7.29 (-8)					
19	90% B_4C + 10% SS	6.77 (-9)	1.11 (-8)	2.94 (-8)					
20	Stainless Steel	8.32 (-9)	1.42 (-8)	3.66 (-8)					
Sum by Material		0.1413	0.2285	0.6495	3.9784	6.1395	0.0377	0.6216	0.3362

*2.25×10^{-4}

Table IV-C-4 (Contd.)

Zone	C	^{10}B	^{11}B	Pb	Sum by Zone
1					0.0
2					0.0
3					0.5910
4					3.3744
5					4.1896
6					3.8759
7	0.8453				0.9209
8					0.0147
9					0.0
10					0.0085
11	-	-	-	-	0.0
12	-	-	-	-	1.551 (-3)
13	2.92 (-3)	9.92 (-2)	8.76 (-3)	-	1.114 (-1)
14	-	-	-	8.55 (-4)	1.675 (-3)
15	5.89 (-4)	1.61 (-2)	1.86 (-3)	-	1.864 (-2)
16	-	-	-	2.18 (-5)	4.081 (-5)
17	1.48 (-5)	4.30 (-4)	4.78 (-5)	-	4.947 (-4)
18	-	-	-	1.14 (-7)	2.30 (-7)
19	2.73 (-7)	5.09 (-6)	8.49 (-7)	-	6.26 (-6)
20	-	-	-	-	5.91 (-8)
Sum by Material	0.8488	0.1157	0.0107	0.0009	13.109

Table IV-C-5

Neutron and Gamma Heating, Gamma Energy Production, and Total Heating in UWMAK-II by Zone (in units of MeV per D-T neutron)

Zone	Thickness (cm)	Density factor	Composition	Neutron Heating	Gamma Heating	Gamma Energy Production	Total Heating
1	500	0.0	Plasma	0.0	0.0	0.0	0.0
2	50	0.0	Vacuum	0.0	0.0	0.0	0.0
3	2	0.5	Stainless Steel	0.5910	0.8116	1.1858	1.4026
4	3	0.5	90% $Li_2 Al_2 O_4$ + 10% SS	3.3744	0.3908	0.6881	3.7652
5	18	0.5	90% Be + 10% SS	4.1896	1.2492	1.0289	5.4388
6	10	0.5	90% $Li_2 Al_2 O_4$ + 10% SS	3.8759	0.6289	0.5535	4.5048
7	38	0.8	90% C + 10% SS	0.9209	1.3990	1.1453	2.3199
8	4	0.9	Stainless Steel	0.0147	0.2695	0.2394	0.2842
9	10	0.0	Helium	~0.0	~0.0	~0.0	~0.0
10	4	0.9	Stainless Steel	0.0085	0.1263	0.0861	0.1348
11	1	0.0	Vacuum	0.0	0.0	0.0	0.0
12	1	0.9	Stainless Steel	1.551 (-3)*	1.74 (-2)	1.04 (-2)	1.895 (-2)
13	5	0.9	90% B_4C + 10% SS	1.114 (-1)	1.89 (-2)	4.55 (-3)	1.303 (-1)
14	20	0.9	90% Pb + 10% SS	1.675 (-3)	4.57 (-2)	1.32 (-2)	4.738 (-2)
15	15	0.9	90% B_4C + 10% SS	1.864 (-2)	5.51 (-4)	7.00 (-4)	1.915 (-2)
16	20	0.9	90% Pb + 10% SS	4.081 (-5)	4.47 (-4)	3.2 (-4)	4.878 (-4)
17	20	0.9	90% B_4C + 10% SS	4.947 (-4)	1.47 (-5)	1.75 (-5)	5.097 (-4)
18	8	0.9	90% Pb + 10% SS	2.30 (-7)	4.48 (-6)	2.21 (-6)	4.710 (-6)
19	8	0.9	90% B_4C + 10% SS	6.26 (-6)	3.73 (-7)	4.45 (-7)	6.633 (-6)
20	2	0.9	Stainless Steel	5.91 (-8)	2.44 (-7)	3.01 (-7)	3.031 (-7)
Sum (in MeV per D-T neutron)				13.109	4.958	4.958	18.067

*to be read as 1.551×10^{-3}

TABLE IV-C-6: Summary of Tritium Breeding, Nuclear Heating, Energy Leakage, and Radiation Damage Parameters in the UWMAK-II Design

(Results for UWMAK-I are shown for comparison)

Parameter	UWMAK-II	UWMAK-I
^{6}Li (n,α) t	1.1801	0.8835
^{7}Li (n,'α) t	0.0034	0.6037
Tritium Breeding Ratio	1.1835	1.4872
Neutron Heating	13.1088	12.43
Gamma Heating	4.9563	4.13
Total Heating (in units of MeV/DT neutron)	18.0651	16.56
Neutron Energy Leakage to the magnet	0.884×10^{-6}	1.5×10^{-5}
Gamma Energy Leakage to the magnet (in units of MeV/DT neutron)	0.137×10^{-6}	0.321×10^{-6}
Total Nuclear Radiation Load to the magnets (Watts)	256	3840

TABLE IV-C-7: Summary of Results for Some Nuclear Reactions of Interest in UWMAK-II

Parameter	UWMAK-II
Reaction Rates in Beryllium (in units of reactions/D-T neutron)	
(n, 2n) 2α)	0.5928
(n, γ)	0.0024
(n, p)	3.97×10^{-5}
(n, t)	0.0105
(n, α)	0.0532
(n, γ) reaction rate (reactions/DT neutron)	
Chromium	0.0337
Nickel	0.0284
Iron	0.1081
Aluminum	0.0017
Oxygen	4.0×10^{-6}
Lithium-6	5.2×10^{-5}
Lithium-7	5.0×10^{-6}
Beryllium	0.0024
Graphite	0.0007
Sum over (n,γ) reaction in the blanket	0.1751

The total energy deposition in the blanket and shield of the UWMAK-II design is shown in Table IV-C-6 to be about 18 MeV which is 1.5 MeV higher than that in the UWMAK-I. This can be explained on the basis of the additional (n,2n) reactions in Be and the increase in the exothermic reactions in the highly enriched lithium in the UWMAK-II.

It can also be noted from Table IV-C-6 that the nuclear radiation load to the magnet in UWMAK-II is only 256 watts which is more than an order of magnitude lower than that in UWMAK-I. The reasons for the better attenuation in the UWMAK-II shield are as follows. The cost optimization for UWMAK-II is based on a price of 3$/kg for B_4C while 15$/kg was assumed in UWMAK-I calculations. The lower price was used as it appears to be more realistic at present. Thus, the optimum shield of UWMAK-II is 96 cm of 50% Pb plus 50% B_4C in contrast to 75 cm of 70% Pb plus 30% B_4C in UWMAK-I. The 50% Pb plus 50% B_4C mixture is more efficient in total energy attenuation than the 70% Pb plus 30% B_4C mixture.

It can be seen from Table IV-C-7 that about .66 beryllium atoms are burned per DT neutron. Thus the burn-up rate for beryllium is 0.09% per year per (MW/m^2). This rate has a small effect on the neutronics behavior of the blanket, especially if the Be is reprocessed every two years. The Be inventory in UWMAK-II is 4.33×10^5 kg. Thus 1.09×10^4 kg of beryllium are burned in UWMAK-II if the reactor is operated for 30 years with a neutron wall loading of 1.16 MW/m^2(80% PF). This again raises the question of the availability of beryllium resources, which is discussed in detail in Chapter VII.

The tritium inventory in the blanket of UWMAK-II and its potential leakage into the steam cycle have been estimated and summarized in Table IV-C-8 based upon the breeding material selected and the blanket design shown in Fig. IV-C-7. (This is discussed in greater detail in section IV-G.) The decision to utilize the ceramic compound, $LiAlO_2$, as the tritium breeding material was made because of its good high temperature properties, as compared to the other lithium compounds, as is also discussed in Section IV-G. Additionally, the design criterion was to prevent,

TABLE IV-C-8: Tritium Breeding and Recovery

	UWMAK	
	II	I
Coolant	Helium (10^6 moles)	Lithium (2×10^8 moles)
T_2 Breeder	$^6LiAlO_2$	Li
Li in Blanket, kg (initial load)	4.1×10^4*	1.4×10^6
Coolant Temperature, Max. (°C)	650	483
Tritium Inventory in Breeder		
Solubility	7 g	8.7 kg
Diffusion (10 μm path) **	120 g	0
Total	127 g	8.7 kg
Tritium Pressure in Breeding Zone (torr)	10^{-4}	5.0×10^{-10}
Tritium pressure for diffusion into steam from sodium (torr)	1.6×10^{-14}	3.8×10^{-11}
Tritium Generation Rate, g/Sec	1×10^{-2}	1.22×10^{-2}
Additive to Coolant	O_2 (10^{-2} torr)	none
Tritium Species in Coolant for Recovery	T_2O	T(Li)
Extraction Bed	Molecular Sieves	Yttrium Metal
τ (Coolant transit time) sec	1	254
Fraction coolant to bed	0.7%	4%
Intermediate Heat Exc.	sodium	sodium
Tritium Leakage to Steam, Ci/day	1.0	10

* 90% Enriched in Li^6

**Assuming a uniform 900°C Temperature Across the $LiAlO_2$

if possible, the contamination of the helium coolant by fine particles of the tritium-breeding materials. Details on the design to accomplish this are given in section IV-G.

The question of lithium burn-up in the UWMAK-II design is important. From the neutronics results discussed above, ^6Li is burned at a rate of 1.34% per year per (MW/m^2). The lithium inventory is 4.1 x 10^4 kg of lithium enriched to 90% in ^6Li. Thus, 5.6 x 10^5 kg of natural lithium would be enriched to supply the initial loading of the UWMAK-II reactor. The 480 kg of ^6Li consumed per year per (MW/m^2) would come from 7,500 kg of natural lithium. It is of interest to compare the lithium utilization in this system with other designs employing natural lithium such as UWMAK-I. The percentage burn-up rate of ^6Li in UWMAK-I is nearly 19 times that of ^7Li. Thus, in terms of resources, ^6Li consumption is the crucial factor as in UWMAK-II although the efficiency of lithium resources utilization is different. If the UWMAK-I blanket is redesigned to produce the same breeding ratio as UWMAK-II, the rate of the $^6Li(n,\alpha)t$ reaction would be approximately .7 reactions per DT neutron compared with 1.18 in UWMAK-II. Hence the rate of consumption of ^6Li in UWMAK-II is about 70% larger than in UWMAK-I. In addition to the relatively inefficient utilization of lithium resources in UWMAK-II type of reactors,* the large amounts of ^7Li generated from lithium enrichment is a potential problem. One way to alleviate this problem is to employ some of this ^7Li as reflector-moderator instead of graphite in the reactor. However, tritium will inevitably be produced in ^7Li resulting in a large tritium inventory in the blanket which negates the principal purpose for building the UWMAK-II type of reactor.

It is also important to note that ^6Li burn-up in the UWMAK-II blanket is not uniform; it varies significantly from one position to another. This can be seen clearly in Fig. IV-C-4 where the reaction rates for the $^6Li(n,\alpha)T$ and the $^9Be(n,2n)$ reactions are shown. The average ^6Li burn-up rate is 2.5 and 1% per year per (MW/m^2) in zones 4 and 6, respectively. A maximum burn-up rate of 7.8% per year per (MW/m^2) occurs in the portion of zone 4 adjacent to the beryllium region (see Fig. IV-C-2). An important point is that the chemical change and the heat generation rates in the lithium aluminate will be very large at those positions where the lithium burn-up is highest. The use of a high melting compound such as lithium aluminate is a necessity at these positions.

The effect of Li burn-up on the tritium breeding ratio is an interesting question which we have studied using variational methods described previously[12,13]. The sensitivity study employs the Roussopolous principle,

$$I_R(\phi,\phi^+;L) = (\Sigma,\phi) + (\phi^+,S) - (\phi^+,L\phi) \qquad (1)$$

for the functional, (Σ,ϕ), which is the tritium production rate in this case. In this equation, ϕ and ϕ^+ are neutron fluxes satisfying the transport equation and its adjoint, respectively[12],

$$L\phi = S \qquad (2)$$

$$L^+\phi^+ = \Sigma. \qquad (3)$$

Σ is the macroscopic cross section for tritium production,

* See comments on page IV-C-12.

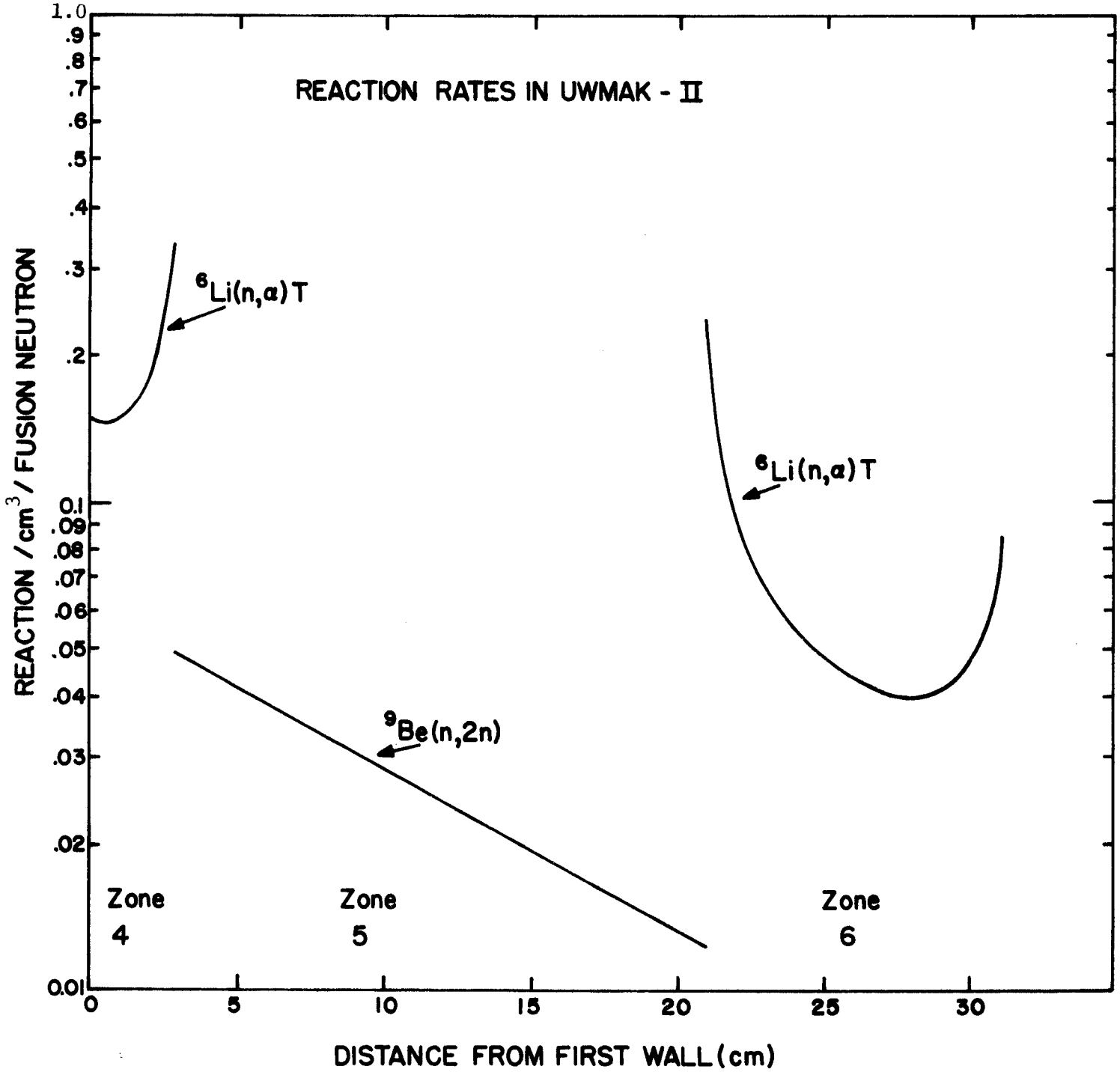
REACTION RATES IN UWMAK - II
REACTION /cm³ / FUSION NEUTRON
DISTANCE FROM FIRST WALL (cm)
⁶Li(n,α)T
⁶Li(n,α)T
⁹Be(n,2n)
Zone 4
Zone 5
Zone 6
1.0
.9
.8
.7
.6
.5
.4
.3
.2
.1
.09
.08
.07
.06
.05
.04
.03
.02
.01
0
5
10
15
20
25
30

FIGURE IV-C-4

$$\Sigma = N_7{}^7\sigma(n,n'\alpha) + N_6{}^6\sigma(n,\alpha). \tag{4}$$

The reference points for forward fluxes and adjoint fluxes were both chosen at the beginning of life conditions for UWMAK-II, and denoted by ϕ_o and $\phi^+{}_o$ respectively. For completeness, we have also carried out similar calculations for the UWMAK-I system. Now the change of tritium production macroscopic cross section (adjoint source) due to burn-up is

$$\Sigma = \Sigma_o + \delta\Sigma \tag{5}$$

where $\delta\Sigma = (\delta N_7)\delta_t + (\delta N_6)\delta_t$, where δN_7 and δN_6 are concentration changes of ^{7}Li and ^{6}Li in the blankets due to burn-up. The perturbed transport operator L accounting for burn-up can be written as

$$L = L_o - \delta L \tag{6}$$

where δL is the perturbation due to concentration changes of ^{6}Li, ^{7}Li and ^{9}Be caused by burn-up.

Since $(\phi^+{}_o,S) = (\Sigma_o,\phi_o)$, Equation (1) can be rewritten as

$$I_R(\phi_o,\phi^+{}_o;L) = (\phi^+{}_o,S)\left[1 + \frac{(\delta\Sigma,\phi_o)}{(\phi^+{}_o,S)} + \frac{(\phi^+{}_o,\delta L\phi_o)}{(\phi^+{}_o,S)}\right] \tag{7}$$

where $(\delta\Sigma,\phi_o)/(\phi^+{}_o,S)$ is the fractional change in the breeding ratio due to <u>concentration</u> changes of ^{6}Li and ^{7}Li. This is just the fractional change from zeroth order perturbation theory. The second term, $(\phi^+{}_o,\delta L\phi_o)/(\phi^+{}_o,S)$ can be interpreted as the fractional change in the breeding ratio due to the <u>flux</u> change induced by burn-up and manifested through the perturbation δL. The error made in using Equation (7) rather than direct calculations is second order in $\delta\phi_o$ and $\delta\phi^+{}_o$. For the results to be given, we have used the $S_4 - P_3$ approximation and slab, rather than cylindrical, geometry. The geometric effect is small.

The results are summarized in Table IV-C-9 for UWMAK-II and in Table IV-C-10 for UWMAK-I. We see from Table IV-C-9 that one year burn-up of ^{6}Li has two effects. The decrease in the ^{6}Li(n,α)T macroscopic cross section by itself would cause a decrease in the breeding ratio of about -1.95%. (Column 1.) Nonuniform burn-up is accounted for. On the other hand, the change in the tritium breeding ratio caused by the flux change, and accounted for by the term $\frac{(\phi^+,\delta L\phi)}{(\phi^+,S)}$, is <u>positive</u> and equal to +2.47%. (Column 2.) The net effect is therefore also positive and equal to 0.52%.

The effects of changes in the ^{7}Li and ^{9}Be concentrations are small as shown in the table and the overall net effect of one year burn-up of Li is to actually cause the breeding ratio to increase slightly. We conclude from this that while lithium is being consumed, the tritium breeding ratio will not change much over the two year lifetime now planned for the rods containing Be and lithium aluminate in the UWMAK-II blanket.

TABLE IV-C-9

Sensitivity of Tritium Breeding to Burn-up of Li and Be in UWMAK-II (in %/MW/m^2 of Wall Loading)

Lithium Enriched to 90% Li-6 and One Year of Burn Up

Type of Perturbation and Response	1 $\frac{(\delta\Sigma,\phi)}{(\phi^+,S)}$	2 $\frac{(\phi^+,\delta L\phi)}{(\phi^+,S)}$	3 Net Effect*
Burn-up of ^{6}Li on T Production from ^{6}Li	-1.95	+2.47	+0.52
Burn-up of ^{6}Li on T Production from ^{7}Li	0	negligible	negligible
Burn-up of ^{7}Li on T Production from ^{6}Li and ^{7}Li	negligible	negligible	negligible
Burn-up of ^{9}Be on T Production from ^{6}Li	0	-0.02	-0.02
TOTAL of Above Effects	-1.95	+2.45	+0.50**

*Using nonuniform burn-up.

**Therefore, the breeding ratio will <u>increase</u> by ∿1/2% after one year of operation. Initial breeding ratio is 1.19.

For comparison, we show in Table IV-C-10 the effects of one year burn-up in the liquid lithium cooled blanket design of UWMAK-I. Again, the direct effect of decreasing the ^{6}Li and ^{7}Li macroscopic cross sections is negative (column 1), but the effect of the flux change is positive (column 2). The overall net effect of one year of burn-up is to <u>decrease</u> the breeding ratio by 0.14%. This, however, causes no difficulty since the initial breeding ratio is 1.49.

TABLE IV-C-10

Sensitivity of Tritium Breeding to Burn-up of Li in UWMAK-I (in %/MW/m^2 of Wall Loading) - Natural Lithium and One Year of Burn Up

Type of Perturbation and Response	1 $\frac{(\delta\Sigma,\phi)}{(\phi^+,S)}$	2 $\frac{(\phi^+,\delta L\phi)}{(\phi^+,S)}$	3 Net Effect
Burn-up of ^{6}Li on T Production from ^{6}Li	-0.470	+0.342	-0.128
Burn-up of ^{6}Li on T Production from ^{7}Li	0	+0.014	+0.014
Burn-up of ^{7}Li on T Production from ^{6}Li	0	-0.004	-0.004
Burn-up of ^{7}Li on T Production from ^{7}Li	-0.025	+0.008	-0.017
TOTAL of Above Effects	-0.495	+0.360	-0.135

REFERENCES FOR SECTION IV-C

1. J. Cameron, University of Wisconsin - Private communication (1974).

2. M. A. Abdou and C. W. Maynard, "Neutronics and Photonics Study of Fusion Reactor Blankets", Proceedings of the First Topical Meeting on the Technology of Controlled Nuclear Fusion, CONF - 740402, USAEC (1974). Vol. II.

3. W. W. Engle, Jr., "A Users Manual for ANISN", K-1693, Oak Ridge Gaseous Diffusion Plant (1967).

4. R. Q. Wright et. al., "SUPERTOG: A Program to Generate Fine Group Constants and P_n Scattering Matrices from ENDF/B", ORNL-TM-2679, Oak Ridge National Laboratory (1969).

5. J. R. Knight and F. R. Mynatt, "MUG, A Program for Generating Multigroup Photon Cross Sections", CTC-17, Computing Technology Center, Union Carbide Corporation, Nuclear Division (1970).

6. M. K. Drake, Ed., "Data Formats and Procedures for the ENDF Neutron Cross Section Library", BNL-50279, Brookhaven National Laboratory (1970).

7. D. J. Dudziak et al., "LAPHANO: A Po Multigroup Photon-Production Matrix and Source Code for ENDF", LA-4750-MS, Los Alamos Scientific Laboratory (1972).

8. M. A. Abdou, C. W. Maynard and R. Q. Wright, "MACK: A Computer Program to Calculate Neutron Energy Release Parameters (Fluence-to-Kerma Factors) and Multigroup Neutron Reaction Cross Sections from Nuclear Data in ENDF Format", UWFDM-37, University of Wisconsin (1973); also issued as ORNL-TM-3994, Oak Ridge National Laboratory (1973).

9. M. A. Abdou, "Calculational Methods for Nuclear Heating and Neutronics and Photonics Design for CTR Blanket and Shields", PhD Thesis, University Microfilms Inc., 74-8981, also issued as Reports UWFDM-66 and UWFDM-67, University of Wisconsin, Nuclear Engineering Department (1973).

10. W. J. Gray and W. C. Morgan, "Projection of Graphite Behavior: Comparison of Results for Four Conceptual Fusion Reactor Designs", to be published.

11. B. Badger, M. A. Abdou, R. W. Boom, R. G. Brown, T. E. Cheng, R. W. Conn, J. M. Donhowe, L. A. El-Guebaly, G. A. Emmert, G. R. Hopkins, W. A. Houlberg, A. B. Johnson, J. H. Kamperschroer, D. Klein, G. L. Kulcinski, R. G. Lott, D. G. McAlees, C. W. Maynard, A. T. Mense, G. R. Neil, E. Normand, P. A. Sanger, W. E. Stewart, T. Sung, I. Sviatoslavsky, D. K. Sze, W. F. Vogelsang, L. J. Wittenberg, T. F. Yang, and W. D. Young, "UWMAK-I, A Wisconsin Toroidal Fusion Reactor Design", Nucl. Engr. Dept. Report UWFDM-68 (The University of Wisconsin, Nov. 1973) Vol. I; (May 1974), Chapter V.

12. R. W. Conn and W. M. Stacey, Nuclear Fusion 13, (1973).

13. E. T. Cheng and R. W. Conn, Trans. Am. Nucl. Soc. 18, 27 (1974).

IV-D Heat Transfer Analysis

IV-D-1. General Discussions

This section is concerned with the thermal hydraulics of the UWMAK-II blanket system. The thermal energy is distributed mainly in three zones in the reactor, namely, the blanket, the shield and the divertor. About 84% of the energy is deposited in the blanket, which has to be extracted at as high a temperature as possible to obtain high thermal efficiency of the system. The main effort of this section will, therefore, concentrate on the blanket.

The blanket of D-T tokamak reactor serves the following functions:

1. Provide mechanical integrity for the torus,
2. Convert neutron energy to thermal energy,
3. Breed tritium.

316 stainless steel is chosen as the structural material to provide mechanical integrity for the blanket in UWMAK-II. The reasons for using SS-316 over the refractory metals were discussed in section IV-B. A 316 SS first wall requires special attention to minimize its thermal stress.

Pressurized helium is the choice for the coolant. Helium is chemically and neutronically inert and provides some of the best heat transfer characteristics among gases. The use of an electrically non-conducting gas as the coolant avoids magnetohydrodynamic problems so that the thermal design aspect of helium cooled fusion reactor closely resembles that of a HTGR. It is well known that large coolant circulating power is required for a gas cooled reactor. The design criterion is, therefore, to achieve a system with minimum pumping power while providing adequate heat transfer.

Natural lithium is the most efficient breeding material. However, to circulate lithium involves magnetohydrodynamic problems and corrosion problems. The maximum interface temperature of lithium and stainless steel must be 500°C to avoid excessive corrosion of stainless steel by lithium. Consequently, the maximum coolant exit temperature will be significantly lower than 500°C, which will result in lower plant thermal efficiency. This is one of the reasons that a high melting point solid lithium compound is used as the breeding material. For obtaining adequate breeding ratios, a layer of beryllium is added in the blanket for neutron multiplication.

The average heating load on the divertor collector plates is 2.85 MW/m^2. This extremely high heating load is a result of the trapped particle mode scaling assumption use in the plasma analysis. The heat transfer problems associated with this system are discussed in section II-B-4 which deals with the divertor.

The energy received in the shield in only 52 MW. The cooling scheme is the same as that in UWMAK-I[1] and will not be repeated here.

IV-D-2. Blanket Design Considerations

The unique features of the UWMAK-II blanket design are:

1. Low first wall temperature.
2. Uncoupling the hoop stress and thermal stress in the first wall.
3. Containing breeding material inside cans to separate tritium from the primary coolant.
4. Keeping a high pressured blanket for safety reasons.
5. Redundancy in first wall design.

The cross section of the blanket is shown on Fig. IV-D-1.

The first wall of the blanket is subject to the maximum stress. Therefore, it is advantageous to keep the temperature of the first wall low. This design directs the coolant toward the first wall before it enters the blanket. This automatically causes the blanket to be made of either U-shaped or hexagonal-shaped module cells. We decided to use U-shaped module cells because it is easier to fabricate.

A large U-shaped blanket module requires a thick first wall to reduce the hoop stress. This thick stainless steel first wall will cause large thermal stress and to uncouple these two stress components, a bank of small tubes, called radiation shield tubes from here on, are located outside of the U-shaped module. The U-shaped module has a thick wall to contain the high helium pressure. The small radiation shield tube has a thin wall facing the plasma which reduces the thermal stress. The coolant will be fed from the supply headers to the radiation shield tubes to cool the first wall. The coolant will then enter the blanket.

A difficult question is how to suspend the breeding material in the blanket. For the following reasons, it is decided that the breeding material will be contained in a fuel rod type structure.

1. To prevent radioactive dust from entering coolant and leaving the reactor.
2. To prevent tritium from being distributed in the primary coolant. The fuel rod container also serves the purpose of the intermediate heat exchanger.
3. To prevent direct contact of potentially harmful atoms (i.e. O_2, N_2) with the breeding material if there is a leak.

The assembly of the breeding rods is shown on Fig. IV-D-2. A number of fuel rods are connected to a manifold so that the tritium can be vented to a tritium recovery ststem. Some tritium will, however, diffuse through the wall of the fuel rods to the primary coolant. A tritium recovery system is, therefore, still required for the primary coolant. (See section IV-G.)

Various designs have pressurized helium contained in tubes. This results in a low pressure blanket and reduces the amount of structural material in the blanket. This allows higher tritium breeding ratios while reducing induced radioactivity. However, it is our belief that the blanket should be designed to stand the coolant pressure so that a leak in coolant

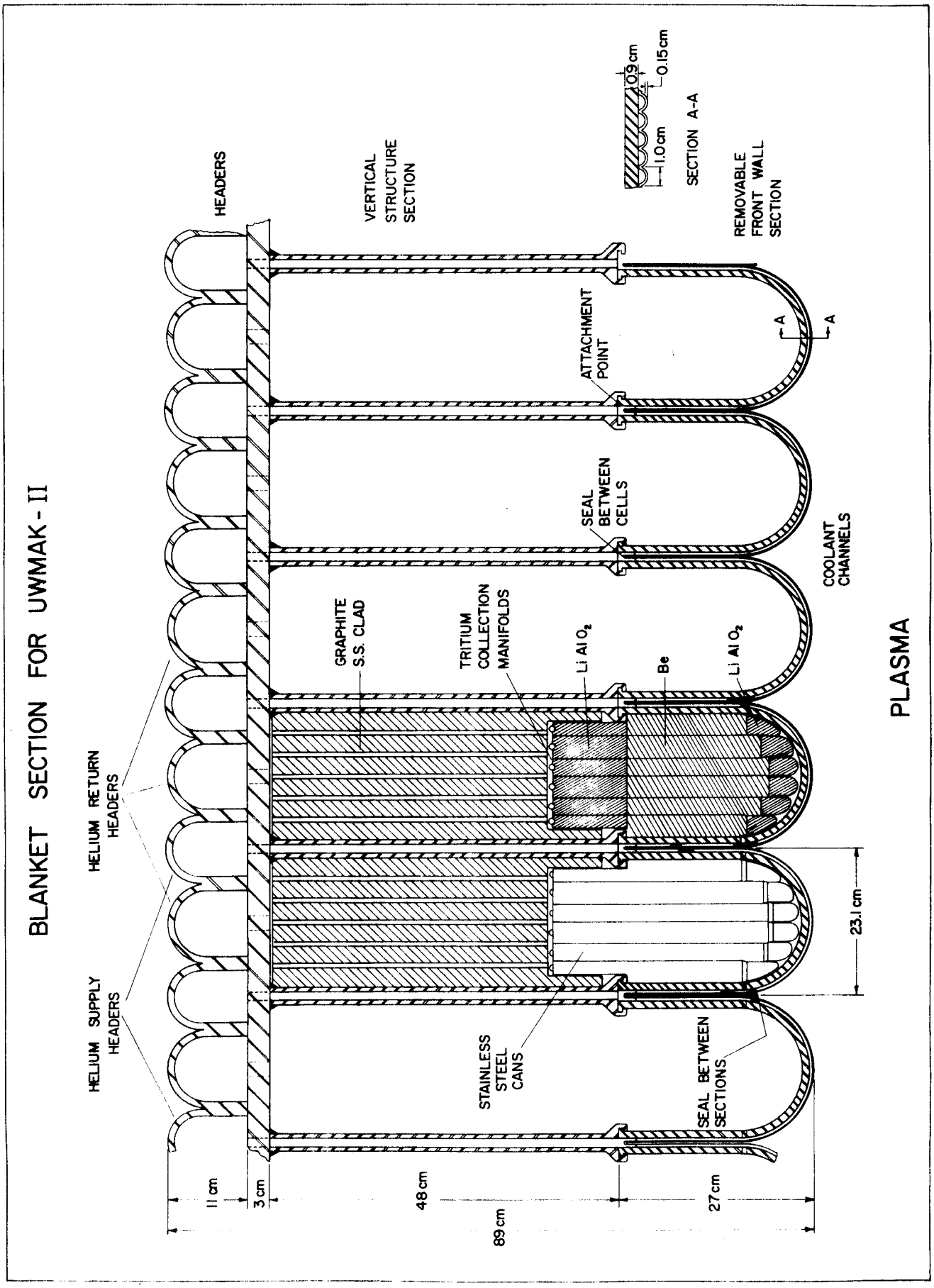
BLANKET SECTION FOR UWMAK-II
HEADERS
VERTICAL STRUCTURE SECTION
SECTION A-A
0.9 cm
0.15 cm
1.0 cm
REMOVABLE FRONT WALL SECTION
ATTACHMENT POINT
A
A
SEAL BETWEEN CELLS
COOLANT CHANNELS
GRAPHITE S.S. CLAD
TRITIUM COLLECTION MANIFOLDS
Li Al O2
Be
Li Al O2
HELIUM RETURN HEADERS
HELIUM SUPPLY HEADERS
23.1 cm
STAINLESS STEEL CANS
SEAL BETWEEN SECTIONS
PLASMA
11 cm
3 cm
48 cm
27 cm
89 cm

Figure IV-D-1

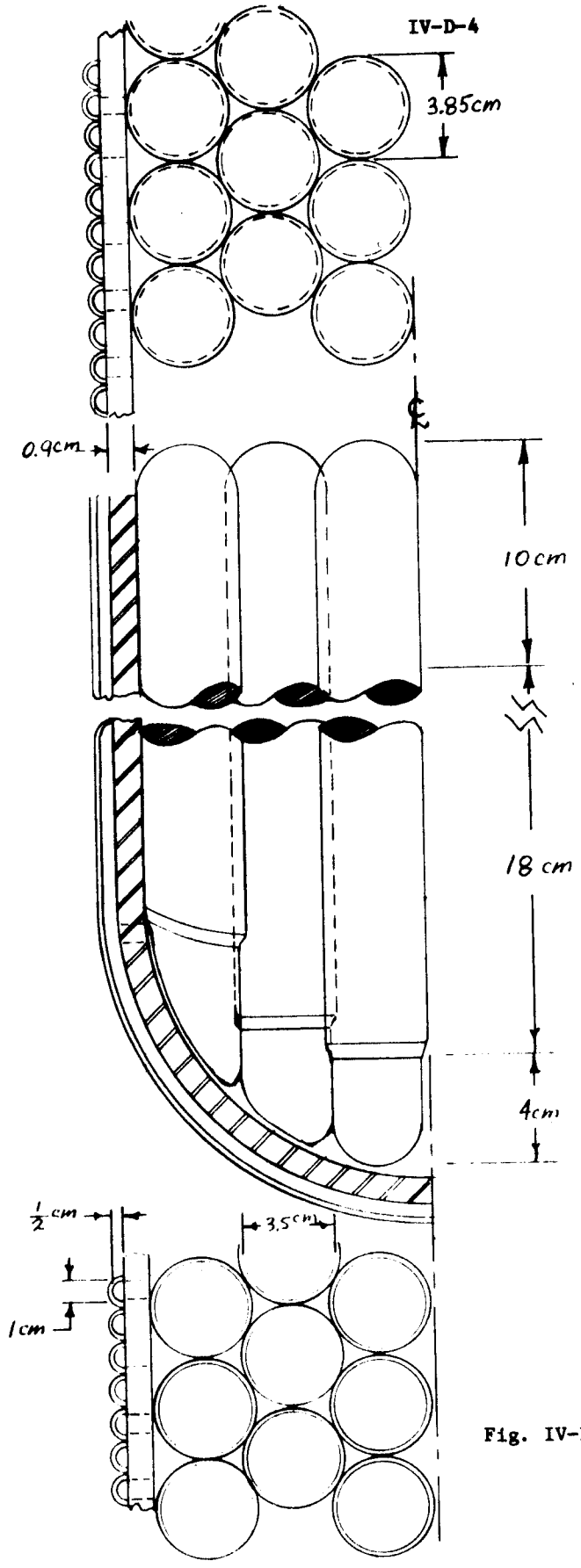

Fig. IV-D-2. Breeding Rods Assembly

tube will not cause a catastrophic accident. Such a philosophy automatically implie a larger fraction of structural material in the blanket but H is safer from the point of view of accidents.

Redundancy of the first wall design has been a major concern. It is inconceivable that the reactor will be shut down every time a leak occurs on the first wall. It may be desirable to keep the reactor in operation with a number of leaks, evan at somewhat reduced power level, until the time for a scheduled maintenance. In UWMAK-II, we provide a basic design upon which all calculations are based. Two design modifications are suggested for the redundancy of the first wall. One uses a double walled first wall concept. The other uses a second band of radiation shield tubes supplied by a multiple header. This will be discussed in more detail later.

IV-D-3. General Design Guidelines and System Description

The thermal hydraulic design is carried out under the following rules:

1. Maximum pumping power does not exceed 10% of the power output of the reactor, or 500 MW_{th}.
2. Maximum first wall temperature $\leq$ 600°C.
3. Maximum structural temperature $\leq$ 700°C. This will probably limit the coolant exit temperature to 650°C.
4. Maximum stress in structure $\leq$ 10,000 psi. ($6.9 \times 10^7 N/m^2$)
5. Maximum temperature in the breeding material is 200°C below its melting point.

The equations used for thermal hydraulic design in this study are given on Table IV-D-1.

The reactor is divided into twenty-four modules, one for each magnet. The cross section view of each module is shown on Fig. IV-D-3.* The blanket section of each module can obviously be divided into three distinctive sections. The inner blanket zone is located between the divertor and the axis of the torus. Since the magnets are in contact with each other near the machine centerline, the only way to supply and discharge the coolant of this section is from the top and bottom of the torus. The outer blanket zone is located furthest away from the machine centerline. The magnets in this region are far apart so that there is no space limitation. The upper and lower blankets are the zones between the divertor slots and these receive only a small fraction of the total heat. However, penetrations directly from the top are not too difficult.

The inner blanket presents the most critical design problems. The space available between the magnets to introduce the coolant for the section is very limited. This limited space is further to be shared by vacuum pumping and structure requirement to support the inner blanket and shield. Therefore, the supply and discharge channels for the coolant for each module are limited to a half meter diameter tube. The coolant is fed by the supply channel and must be distributed both toroidally and poloidally. The supply channel will change the direction toward the toroidal direction. It will then connect to a set of poloidal headers. The poloidal header will open to a bank of radiation shield tubes at the edge of the U-shaped blanket cells. This bank of tubes will direct the coolant toward the first wall.

* Figure IV-D-4 has been deleted.

Table IV-D-1

Equations Used

1.	$Q = VA\rho C_p(T_{out} - T_{in})$	Heat carried by coolant
2.	$Q = hA(T_{coolant} - T_{wall})$	Heat transfer to coolant channel
3.	$\frac{hD}{k} = 0.023\ (\frac{Dv\rho}{\mu})^{0.8}\ (\frac{C_p\mu}{k})^{0.4}$	Calculation of heat transfer coefficient
4.	$\Delta p = \frac{2f\rho v^2 L}{g_c D}$	Pressure drop in coolant channel
5.	$f = 0.0014 + 0.125\ (\frac{DV\rho}{\mu})^{-0.32}$	Friction factor calculation
6.	$T_i' = T_i + [\sum_j C_{ij}(T_j - T_i)/(V\rho C_p)_i + Q_i/\rho C_p]\Delta\theta$	Finite difference equation for temperature calculations
7.	$\Delta\theta \leqslant (V\rho C_p)_i / \sum_j C_{ij}$	Maximum time step of iteration
8.	$E = V\Delta p$	Pumping power required to circulate the coolant

Nomenclatures:

A	Area of coolant flow, or area of heat transfer
C_{ij}	Conductance between finite zones i and j
C_p	Specific heat
D	Diameter of coolant channel (= 4 R_H)
E	Pumping power required to circulate the coolant
f	Friction Factor
h	Heat transfer coefficient
k	Thermal conductivity of coolant
L	Length of coolant channel
Δp	Coolant pressure drop
Q	Heat transferred into coolant
Q_i	Heat generated in finite zone i
T	Temperature
v	Coolant velocity
V	Coolant volumetric flow rate
V_i	Volume of finite zone i
ρ	Density
μ	Viscosity
R_H	Hydraulic Radius

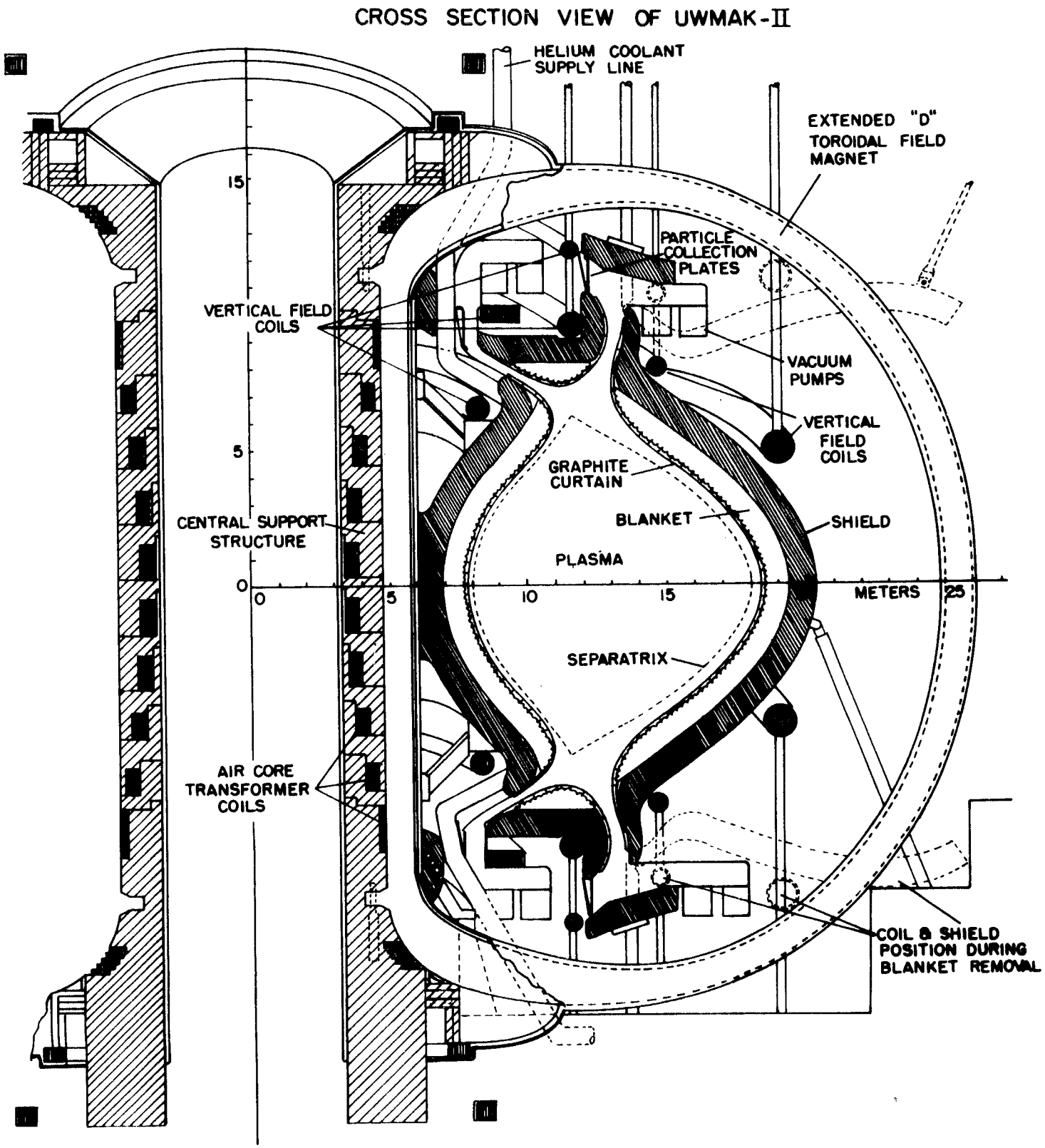
CROSS SECTION VIEW OF UWMAK-II
HELIUM COOLANT SUPPLY LINE
EXTENDED "D" TOROIDAL FIELD MAGNET
PARTICLE COLLECTION PLATES
VERTICAL FIELD COILS
VACUUM PUMPS
VERTICAL FIELD COILS
GRAPHITE CURTAIN
BLANKET
SHIELD
CENTRAL SUPPORT STRUCTURE
PLASMA
SEPARATRIX
AIR CORE TRANSFORMER COILS
COIL & SHIELD POSITION DURING BLANKET REMOVAL
15
5
0
0
5
10
15
METERS
25

Figure IV-D-3

The coolant will then enter the blanket and flow in the voids among the breeding rods. It will cool the cans containing graphite and then exit through the discharge headers and the discharge channel. Each poloidal header is 10 cm tall and 10 cm wide.

The breeding region contains three zones. The first 3 cm is $LiAlO_2$. The next 18 cm is beryllium, which is followed by another 10 cm of $LiAlO_2$. The heat deposition rate in the first Li zone is much higher than the rest of the blanket. To obtain better heat transfer and prevent the rod wall being overheated, special care has to be taken. The outside diameter of the rod is 3.75 cm, but reduces to 3.5 cm for the first breeding zone. The coolant is introduced perpendicular to the rods in this zone so that much better convection heat transfer is obtained. For the rest of the blanket, the coolant will flow in the void between the rods.

The blanket designs for the other parts of the blanket are identical to the inner blanket and because space is available, the outer blanket region can be divided into numerous coolant units. As a compromise between pumping requirements and easy fabrication and assembly, the outer blanket is divided into three coolant units.

IV-D-4. Pressure Drop and Heat Transfer Calculations

The pumping power is the product of the volumetric flow rate and the pressure drop of the coolant, as shown on Table IV-D-1. The volumetric flow rate is very large, because of the small ρC_p of a gas coolant. For this reason, a high pressure gas coolant minimizes the power required to circulate the coolant.

The pressure of helium is chosen to be 750 psi. We considered a case of 1000 psi pressure helium but found that the breeding ratio is significantly reduced because of the thick first wall required withstand the higher pressure. The physical properties of helium, as well as that of stainless steel, $LiAlO_2$ and beryllium, at the temperature and pressure of interest are given in Table IV-D-2.

The coolant temperature rise through the reactor is chosen to be 200°C. With this information together with a total thermal wall loading of 1.77 MW/m^2, the flow rate through each channel can be calculated. The pressure drop can then be calculated through each section of the reactor by using Equation 4. Detailed pressure drop calculations throughout the reactor are given in Table IV-D-3. The helium pressure drop in the helium to sodium heat exchanger is estimated to be 12 psi. The total pumping power required is 294 MW_{th} a high but acceptable value. The important results from the pressure drop calculations are summarized on Table IV-D-4 at the end of this section.

The temperature distribution in the blanket is of vital importance. It has effects on both mechanical design of the blanket and radiation damage to the structural material. The coolant exit temperature is determined by the structural material properties at high temperature. An exit temperature of 650°C is picked because the mechanical properties of 316 SS deteriorate rapidly when this temperature is exceeded. The coolant inlet temperature is 450°C.

Table IV-D-2

Thermal Properties of Various Materials

	He	$Li_2Al_2O_4$	Be	316 SS
Thermal Conductivity, $\frac{cal}{sec\text{-}cm\text{-}^\circ C}$	$.662 \times 10^{-3}$	4.14×10^{-3}	.287	4.78×10^{-2}
Density, $\frac{g}{cm^3}$	2.88×10^{-3}	2.52	1.82	7.82
Specific Heat, cal/g-°C	1.24	.35	.7	0.11
Viscosity, Centipose	.038	-	-	-
Prandt No.	.72	-	-	-
Melting Point, °C	-	1700	1285	~1500

Table IV-D-3

Pressure Drop Calculations

	D,m	L,m	G, $\frac{kg}{m^2 - sec}$	v,m/sec	Re x 10^{-6}	f x 10^3	$\Delta p(\frac{kg}{m^2})$
Hx to header	0.5	50.0	340.	118.	4.43	2.5	3,195
Poloidal header	0.1	25.0	286.	99.	.185	3.5	5,386
Header to first wall	0.01	1.5	106.	37.	.017	7.0	2,257
First wall to header	0.002	1.0	23.	8.	.001	20.0	1,655
Heat exchanger	-	-	-	-	-	-	9,029
TOTAL							21,522 (= 30.6 psi)

Coolant volumetric flow rate = 5 x 10^6 m^3/hr

$V\Delta p$ = 1.07 x 10^{11} kg - m/hr = 294 MW

The flow rates of the coolant at any location of the blanket are calculated by energy balance. The coolant to wall heat transfer coefficients are calculated by using Equation 3 given in Table IV-D-1. The energy deposition rate in the blanket is obtained from neutronics calculation, as shown on Fig. IV-D-5 and this information supplies the input for calculating the structure temperature by using Equation 2 in Table IV-D-1.

The temperature distribution in a typical rod has to be calculated numerically. A finite difference numerical computer program has been set up to perform these calculations. Using the heating rate shown on Fig. IV-D-5 as input, the temperature distribution is iteratively calculated for each time step by using Equation 6. The maximum allowable time step for the iterative calculation is defined by Equation 7 to insure the stability of the iteration process. .0001 degree is used as the convergence criterion for each iteration.

The coolant temperature and the temperature of the structure along the coolant flows directly in the blanket is shown on Fig. IV-D-6. The maximum temperature on the first wall is 550°C, which limits the maximum first wall stress to 10,000 psi. The maximum structure temperature in the blanket reaches 686°C in the interior of the blanket. This is not, however, stress bearing structure so that the high temperature is acceptable.

The size of the rods is chosen so that the maximum temperature in the interior of the rod would be comfortably below the melting point of the material contained inside. One of the reasons of picking $LiAlO_2$ as the breeding material is that it has a high melting temperature. The steady state temperature distribution for a typical rod is shown on Fig. IV-D-7. Part "a" of this figure shows the geometry of the finite difference division of the rod, while part "b" shows the temperature for each zone. The maximum temperature in the $LiAlO_2$ zone is only 1100°C, which is well below its melting temperature.

The important results from the heat transfer calculations are summarized on Table IV-D-4. From that table it can be concluded that a reasonable thermal hydraulic blanket design has been furnished. The pumping power requirement is high, but this appears to be a penalty one has to pay for using helium as the coolant for a power reactor.

REFERENCES

1. B. Badger et al., "UWMAK-1, A Wisconsin Toroidal Fusion Reactor Design", UWFDM-86, University of Wisconsin, Nuclear Engineering Department (1973).

Fig. IV-D-5. Heat Deposition Rate in the Blanket

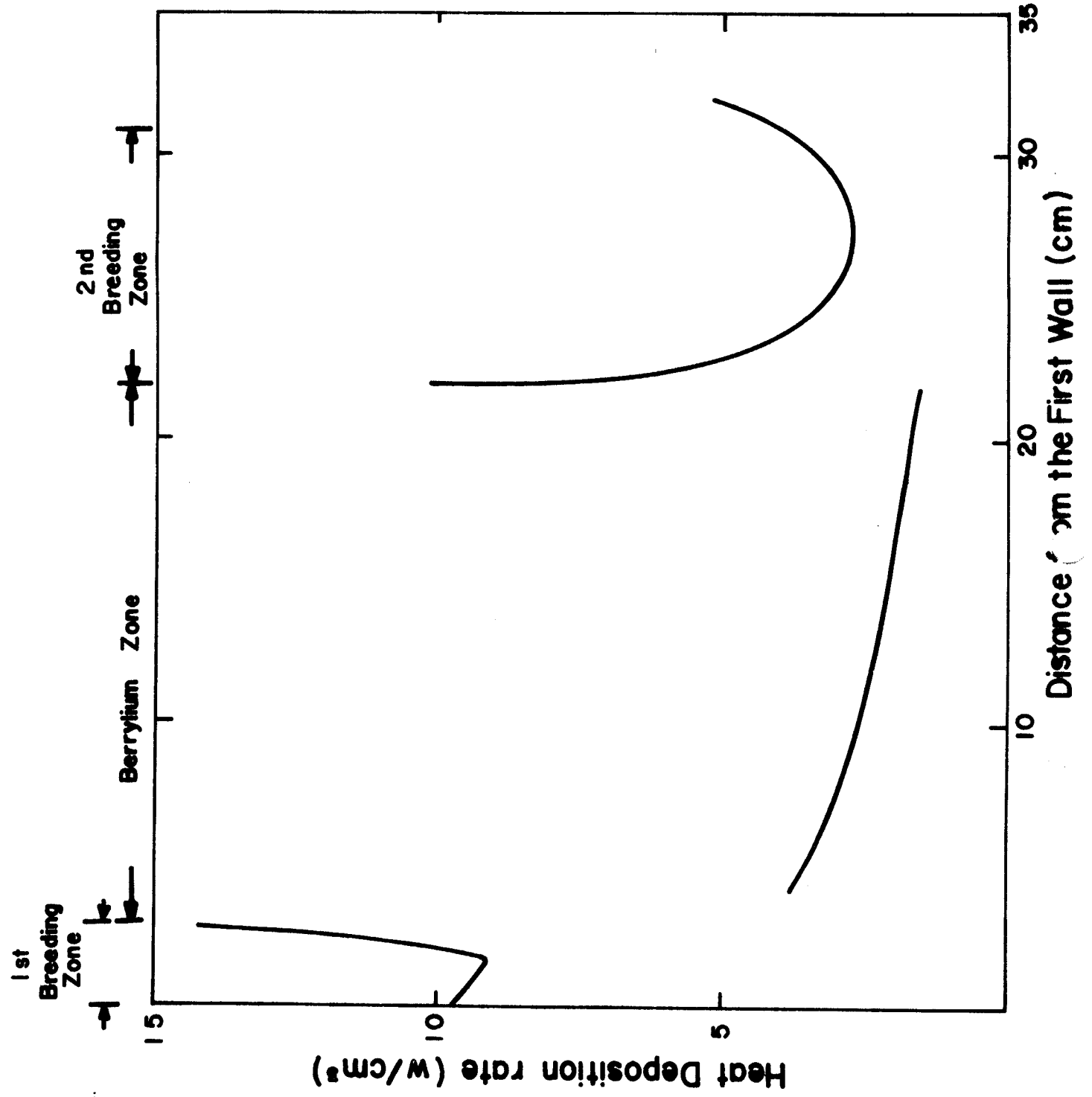

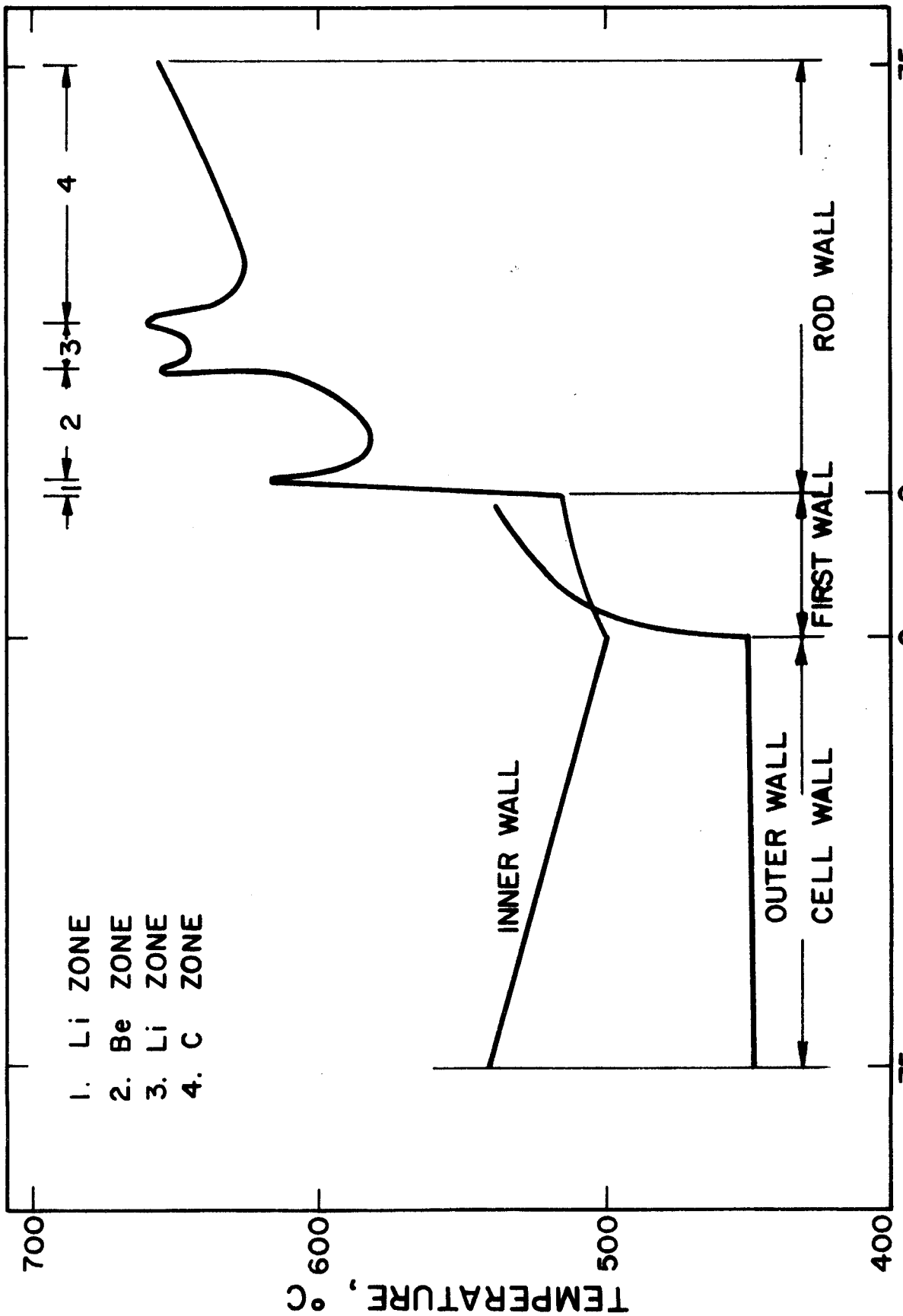

Figure IV-D-6 Structure Temperature in the Blanket

PLASMA

567	566	563	559	553	546	538	529	521	514
900	893	881	861	835	800	757	703	637	557
1097	1087	1067	1036	994	941	875	796	702	593
1049	1042	1028	1005	974	933	879	811	725	616
603	603	602	602	600	599	597	596	594	592
595	594	594	594	593	592	591	590	588	587
590	590	590	589	589	588	587	586	585	584
587	587	587	587	586	585	585	584	583	582
586	586	586	585	585	584	584	583	582	581
586	585	585	585	584	584	583	583	582	581
586	586	585	585	585	584	584	583	582	581
587	586	586	586	586	585	585	584	583	583
588	588	587	587	587	586	586	585	585	584
589	589	589	589	588	588	587	587	586	586
591	591	591	590	590	590	589	589	588	587
593	593	592	592	592	591	591	591	590	589
595	595	594	594	594	594	593	593	592	591
597	597	597	597	596	596	596	595	594	594
600	600	600	599	599	599	598	598	597	597
603	603	603	603	603	602	602	601	601	600
608	608	608	608	607	607	606	606	605	604
615	615	615	614	614	613	612	611	610	609
935	930	921	907	887	860	826	782	726	655
947	941	928	909	884	852	812	766	712	651
909	903	891	874	850	821	786	745	699	646
875	870	859	844	823	798	767	731	690	645
853	848	839	825	806	783	755	723	686	644
842	837	829	816	798	776	750	720	685	646
838	834	826	813	796	775	750	720	686	648
844	840	831	819	802	780	755	725	691	653
852	848	840	828	812	791	766	735	700	660
787	785	780	773	763	751	735	714	689	658

Fig. IV-D-7. Temperature of the Breeding Rods.

Table IV-D-4

Summary and Comparison of UWMAK-I and UWMAK-II

	I	II
Breeding material	Li	$LiAlO_2$
Neutron multiplier	None	Be
Reflector	SS	C
Moderator	Li	C
Coolant, primary	Li	He
Coolant, secondary	Na	
Coolant inlet temperature	283°C	450°C
Coolant exit temperature	483°C	650°C
Maximum first wall temperature	500°C	550°C
Maximum structure temperature	500°C	
Maximum blanket temperature	500°C	1097°C
Maximum first wall pressure	300 psia	750 psia
Maximum first wall stress	13,000 psi	10,000 psi
Coolant flows rate	5,600 kg/sec	4,303 kg/sec
Maximum coolant pressure drop	400 psi	30.6 psi
Pumping power required	22 MW_e	294 MW_{th}

1 psi = 6.9×10^3 N/m^2

IV-E. Mechanical Design Considerations

The blanket in UWMAK-II consists of three major parts, the removable front wall cells containing the breeding material, the vertical structure which connects the front wall cells to the headers, and the helium gas supply and return headers. These parts are shown distinctly in Fig. IV-E-1.

The very high pressure of the helium coolant in UWMAK-II makes the design of the front wall of the blanket somewhat complex. A single wall structure capable of containing the coolant pressure would have such large thermal stresses as to make it impossible to design.

A solution to the problem can be found in the use of a composite front wall. It is made of a thin material (0.15 cm) facing the plasma and enclosing small semi-circular tubes 1.0 cm in diameter, attached to a thicker (0.9 cm) backing material. The insert in Fig. IV-E-1 shows a section of the composite wall. Coolant gas from the supply headers passes through channels in the vertical structure and then traverses the front wall through the semi-circular tubes before emerging into the blanket region. This maintains the front wall as the coolest part of the front wall structure. It also means that the thermal stresses associated with the surface wall loading appear across the material only and are minimized. The pressure stresses are carried by both components of the front wall and are also kept low by appropriately selecting the thickness of the backing material. Major constraints are fabrication, material quantity and neutronic considerations.

The removable part of the blanket is made up of semi-cylindrical cells, 23.1 wide, 27.0 cm high and varying in length from 0.6 m to 1.5 m. Since these cells are oriented in the toroidal direction, their length depends on their location in the blanket (that is, they are longer on the outside of the torus and shorter on the inside).

The junction between the removable front wall cells and the vertical structure serves both as the attachment between the two structures as well as a gas distribution manifold. Every other tube is closed off to permit countercurrent flow of gas across the front wall to reduce thermal gradients. At this point, the thin component of the front wall is straightened out so that it can be welded to the adjacent cell as can be seen in Figs. IV-E-1 and IV-E-2. This will constitute the seal between cells. Five cells welded together make up a section as shown in Fig. IV-E-2. These sections have skirts attached to them which protrude slightly beyond the flat portion of the cell wall. Welding the skirts of adjacent sections from the plasma side provides the seal between sections (see Fig. IV-E-1 and IV-E-3(c)).

The vertical structure which connects the front wall to the headers is continuous for each module, has an effective thickness of 1.2 cm and has 1.0 cm diameter holes spaced 2.0 cm apart built into it. As can be seen from Fig. IV-E-1, it terminates in a latching concept which allows front wall sections to be slid in and become attached to the vertical structure. This point of attachment also acts as a manifold which distributes the flow between adjacent cells.

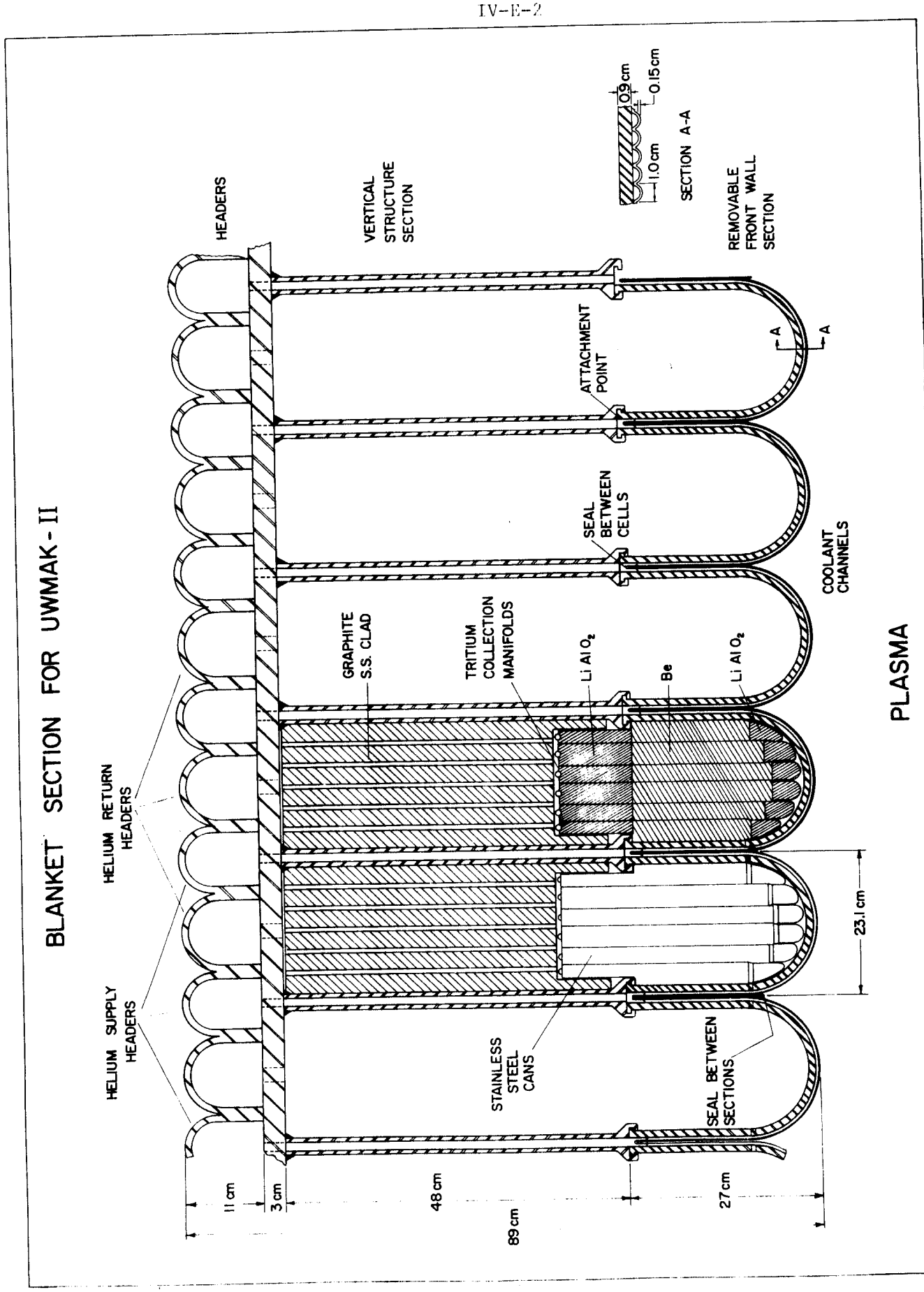
BLANKET SECTION FOR UWMAK-II
HELIUM SUPPLY HEADERS
HELIUM RETURN HEADERS
HEADERS
VERTICAL STRUCTURE SECTION
SECTION A-A
0.9cm
0.15cm
1.0cm
REMOVABLE FRONT WALL SECTION
ATTACHMENT POINT
SEAL BETWEEN CELLS
COOLANT CHANNELS
GRAPHITE S.S. CLAD
TRITIUM COLLECTION MANIFOLDS
Li Al O2
Be
Li Al O2
PLASMA
23.1 cm
STAINLESS STEEL CANS
SEAL BETWEEN SECTIONS
11 cm
3 cm
48 cm
27 cm
89 cm

Figure IV-E-1

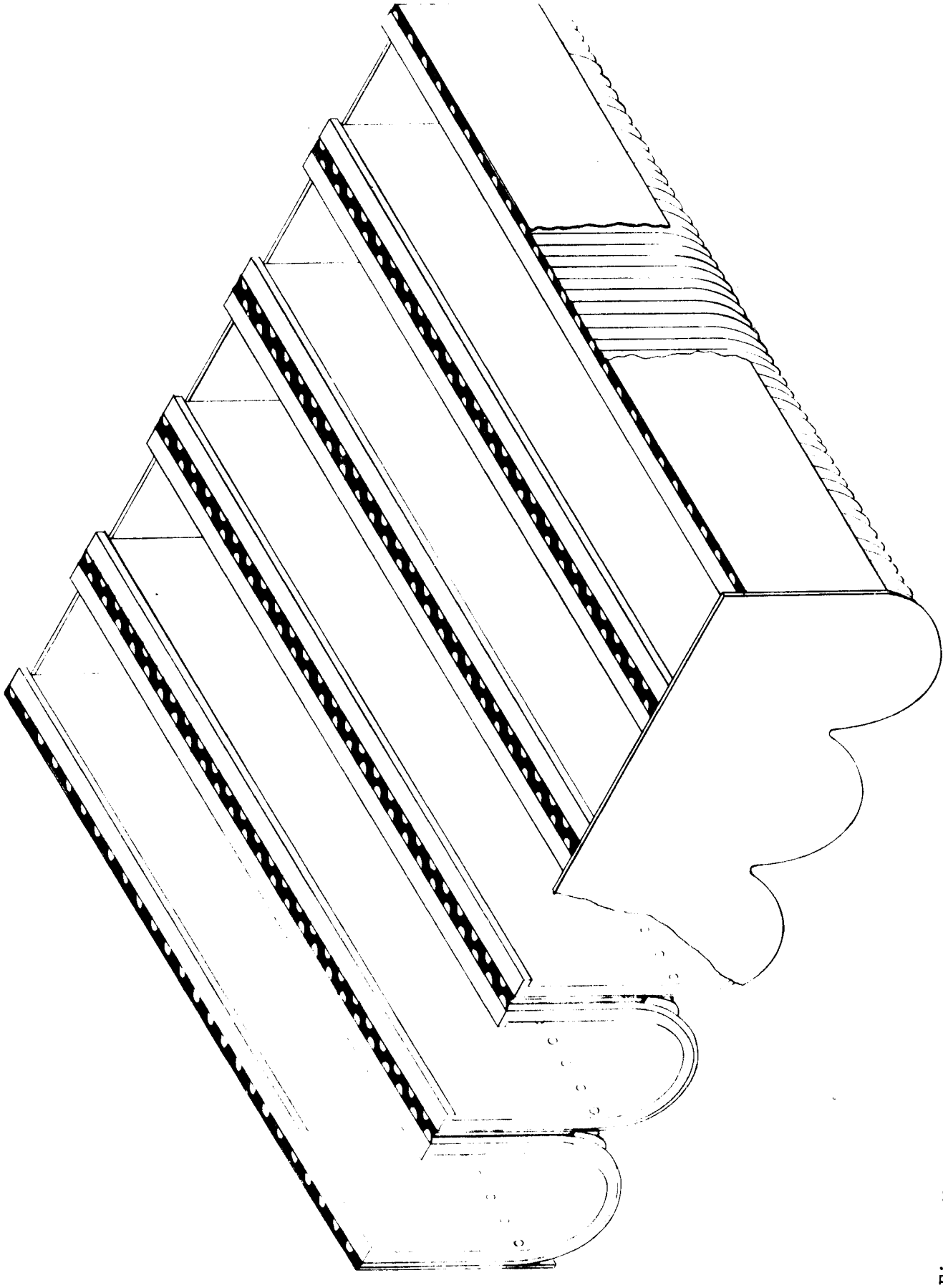

Figure IV-E-2 -- Isometric View of a Blanket Section

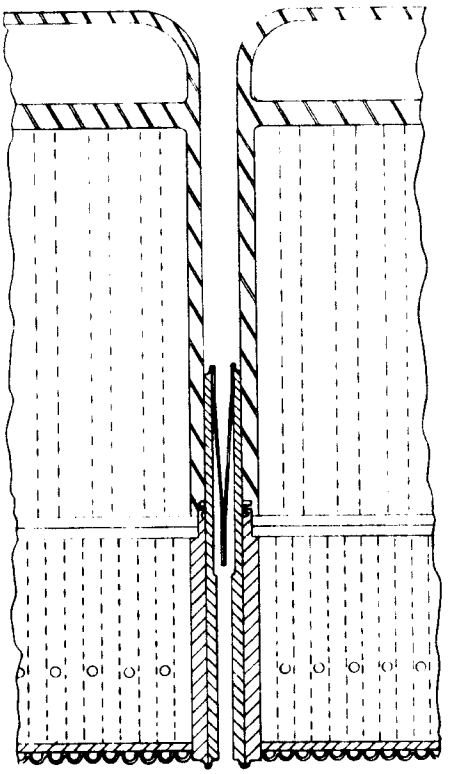

(a)

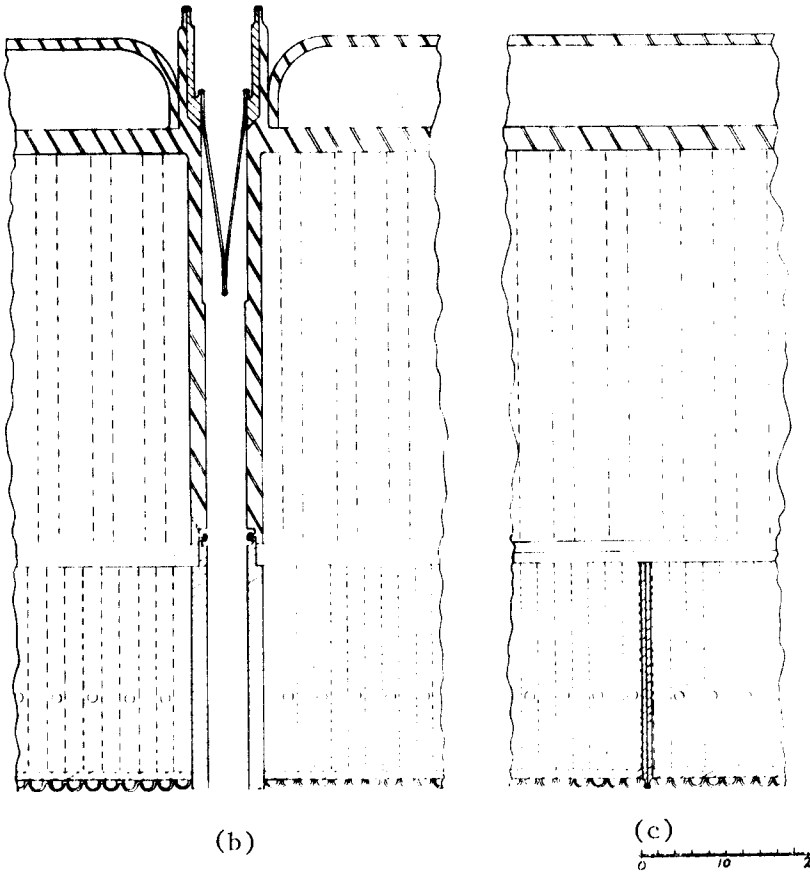

(b) (c)

Expansion Joints Between Modules (a) Inner Blanket (b) Outer Blanket (c) Joint Between Sections.

Figure IV-E-3

On the other end, the vertical structure is welded to the bottom plate of the headers. This bottom header plate has holes in it to allow the cooling gas to enter the vertical structure from the supply header. After the gas traverses the front wall and the blanket region, it exits through more holes in the plate to a return header. In Fig. IV-E-1, each header located directly above a vertical structure is a supply header and the intervening ones are return headers.

IV-E-1. Blanket Stresses

In calculating the front wall stresses, one has to keep in mind that the thermal stress affects only the thin component of the front wall. Thermal stress in a plate heated from one side is

$$\sigma_{th} = \pm \frac{\alpha}{2} \frac{E}{(1-\nu)} \Delta T$$

where α = coefficient of expansion

E = Modules of elasticity

ν = Poisson's ratio

ΔT = temperature difference across the plate

When the surface wall loading W_s and the neutron wall loading W_n is included the equation becomes

$$\sigma_{th} = \pm \frac{\alpha}{2} \frac{E}{k(1-\nu)} \left(W_s t + \frac{W_n}{2} t^2\right)$$

where k = thermal conductivity

t = plate thickness

For 316 SS at 550°C, the values used are

$$\alpha = 18 \times 10^{-6} {}^\circ C^{-1}$$

$$k = 0.2 \text{ watts cm}^{-1} {}^\circ C^{-1}$$

$$E = 23.2 \times 10^6 \text{ psi}$$

$$\nu = 0.3$$

$$t = 0.15 \text{ cm}$$

$$W_s = 3.42 \text{ watts/cm}^2$$

$$W_n = 11.6 \text{ watts/cm}^3$$

The calculated maximum thermal stress

$$\sigma_{th} = \pm 960 \text{ PSI } (6.62 \times 10^6 \text{ N/m}^2)$$

This stress is compressive on the side facing the plasma and tensile on the side facing the coolant.

The pressure stresses can be divided into two groups. The hoop and longitudinal stresses in the cell itself which are carried by both components of the front wall and the hoop stress in the semi-circular cooling tubes which effects the thin component of the front wall more than the thick.

The hoop stress in a cylindrical structure is expressed as

$$\sigma_h = \frac{pr}{t}$$

where p = pressure

r = internal radius

t = wall thickness

The effective thickness of the composite front wall is 1.05 cm, the internal radius 10 cm and the coolant pressure 750 psi (5.18×10^6 N/m^2) producing a hoop stress in the cell of σ_{hc} = 7143 psi(49.2×10^6 N/m^2). The longitudinal stress in the cell is equal to one half of the hoop stress, σ_{lc} = 3572 psi(24.6×10^6 N/m^2).

The cooling tubes are open ended and will thus only have a hoop stress equal to σ_{ht} = 2500 psi(17.25×10^6 N/m^2).

The highest tensile stress in the front wall structure is in the thin component on the side facing the coolant. The stress is perpendicular to the cell and its magnitude is the sum of $\sigma_{hc} + \sigma_{th}$ = 8103 psi(55.9×10^6 N/m^2). The corresponding stress on the side facing the plasma is also tensile and equal to $\sigma_{hc} - \sigma_{th}$ = 6183psi (42.66×10^6 N/m^2). In a direction parallel to the cylindrical cell the maximum tensile stress is equal to the sum of $\sigma_{lc} + \sigma_{ht} + \sigma_{th}$ = 7030 psi(48.5×10^6 N/m^2) and is also on the inside. On the outside, the stress is $\sigma_{lc} + \sigma_{ht} - \sigma_{th}$ = 5112 psi(35.27×10^6 N/m^2).

Radiation damage in the vertical structure is lower than in the front wall and its temperature is lower since it acts as the conduit for the cooling gas. It also is prudent to minimize the amount of steel in this region because it competes with the blanket material for neutron capture, thus reducing the breeding ratio. For these reasons, it was decided to use a higher design stress in the vertical structure. Its effective thickness is 1.2 cm and it supports the force of the coolant pressure on one cell producing a tensile stress of 12,500 psi (86.25×10^6 N/m^2). The hoop stress in the coolant passages of the vertical structure is only 625 psi(4.31×10^6 N/m^2) and it is not additive to the main stress since it is perpendicular to it.

Although the blanket structure will be in an evacuated environment during reactor operation, it will nevertheless be subject to atmospheric loading during testing periods and also in the event of a failure in the back-up vacuum system. The vertical structure welded to the header structure provides the stiffness needed to withstand an atmospheric loading.

IV-E-2. Overall Support of the Blanket

The blanket and shield configuration in UWMAK-II is not continuous but is made up of many different regions (See Fig. IV-E-4). Before we can describe the support of the blanket, we will define these regions.

The part of the blanket lying between the inner top and inner bottom divertor slots will be referred to as the inner blanket, similarly the part lying between the outer top and bottom divertor slots will be called the outer blanket. Those regions falling between the divertor slots will be called central blanket regions.

The complete toroid is divided into 24 equal modules. Each blanket region is further divided into sections which will be discussed later. Table IV-E-1 gives the mass distribution in the blanket.

Table IV-E-1

UWMAK-II Blanket (Weight in Metric Tons)

	Inner	Outer	Central
Removable Front Wall (S.S.)	222.18	460.78	115.43
Vertical Structure and Headers (S.S.)	616.83	1277.60	320.00
Cans for Breeder and Moderator (S.S.)	182.00	392.00	84.00
Be and $LiAlO_2$ x 1.8	225.00	486.00	104.00
Graphite	567.00	1174.00	147.10
Total in Reactor	1813.81	3790.88	770.76
Total per Module	75.57	157.95	32.1
			Or 16.05 each

From Fig. IV-E-4, it can be seen that supporting the inner blanket and shield region is not very straightforward. The extended divertor slot, the cooling lines, transformer and divertor coils fill up most of the available space on the top leaving no room for support structure.

To alleviate this problem, it was decided to modify the toroidal magnet dewar in such a way as to make it possible to support the various components on it. The toroidal magnet dewar which surrounds the straight legs of the

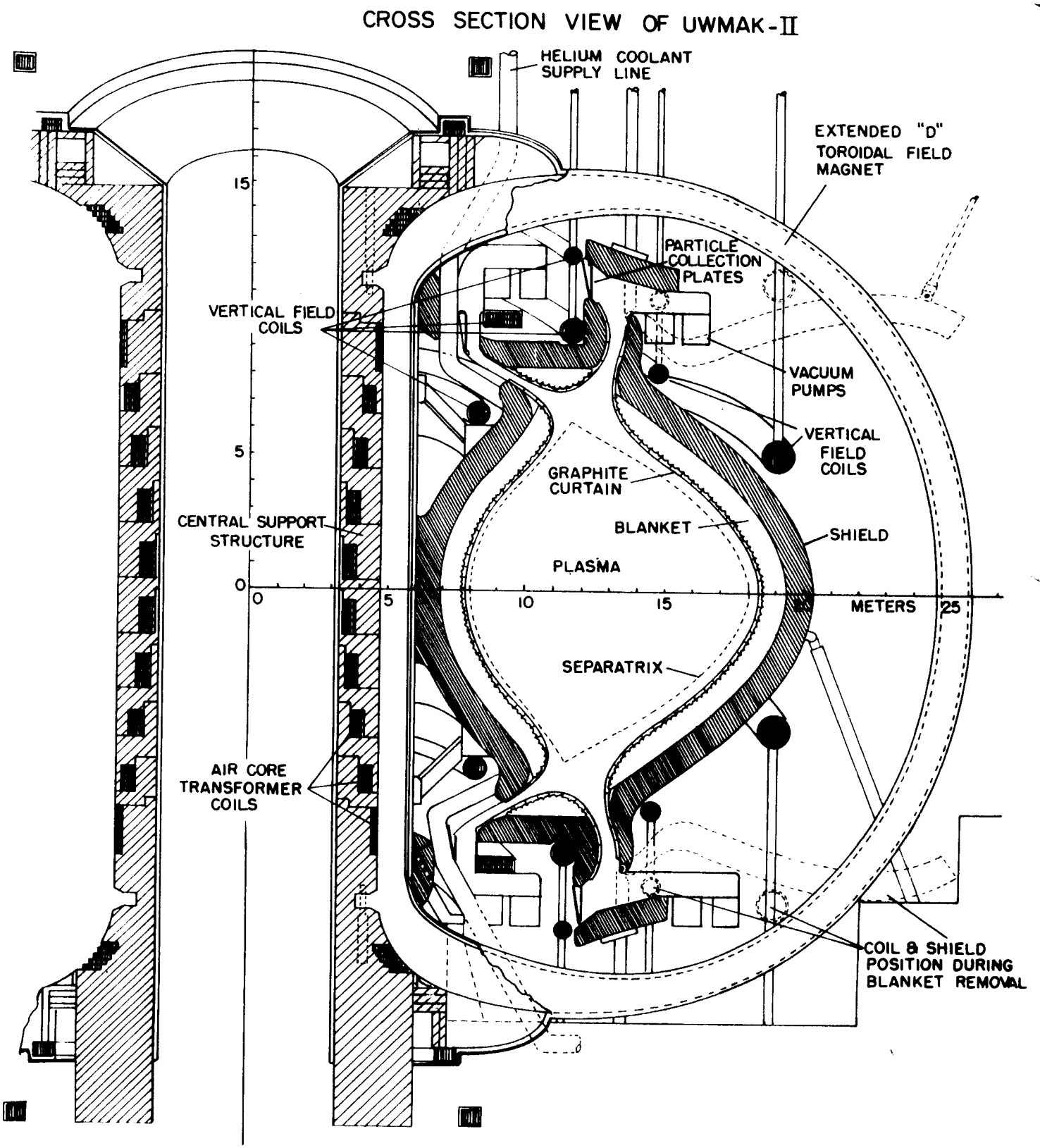
CROSS SECTION VIEW OF UWMAK-II
HELIUM COOLANT SUPPLY LINE
EXTENDED "D" TOROIDAL FIELD MAGNET
PARTICLE COLLECTION PLATES
VERTICAL FIELD COILS
VACUUM PUMPS
VERTICAL FIELD COILS
GRAPHITE CURTAIN
CENTRAL SUPPORT STRUCTURE
BLANKET
SHIELD
PLASMA
SEPARATRIX
AIR CORE TRANSFORMER COILS
COIL & SHIELD POSITION DURING BLANKET REMOVAL
15
5
0
0
5
10
15
20
METERS
25

Figure IV-E-4

torroidal magnets is now a continuous heavily reinforced cylinder surrounding all the magnets. Details of this dewar will be covered in the magnet section.

The inner shield is directly supported on this dewar and provides the base for the support of the inner blanket. Because of the difference in temperature between the blanket and shield, a non-rigid attachment will have to be provided between them. In addition, expansion joints between modules are provided. Expansion gaps of 1.94 cm and 4.6 cm between inner and outer blanket modules respectively have to be provided. Fig. IV-E-3 shows a possible scheme for providing expansion joints between modules. The single convolution welded bellows attached to flanges surrounds the toroid in the poloidal direction. In the inner blanket region (Fig. IV-E-3(a)) the flanges are designed to be attached to the blanket module by means of a weld from the plasma side while on the outer blanket region the weld is external (Fig. IV-E-3(b)). In some places, the expansion joint is permanently attached to structure which is not normally removed during front wall replacement. Blanket regions will also need welds to permanent structures in the toroidal direction.

The central blanket is similarly attached to the central shield which in turn is supported on structure extending between the toroidal magnets to massive roof beams on top and to the ground on the bottom.

In the case of the outer blanket, the situation is somewhat different. The outer shield has been designed to open up clam-shell wise making the outer blanket accessible from the outside. The back legs of the extended D toroidal magnets are far enough apart as to allow a module of the outer shield to swing out between them. A small wedge at the outer perifery of the shield between modules will have to be removed before hand to make this possible.

Each half of an outer shield module weighs 330 MT and an outer blanket module an additional 158 MT. The structure needed to support this load as well as resist the large bending moments produced when the shield is in the open position will have to be quite massive. However, there is room in this region for such structure. Ultimately, the load is transferred to the roof beams by means of supports extending between the magnets.

The outer blanket modules will be attached to reinforced plates which also make up the wall of the outer divertor slots. These plates are an integral part of the structure which supports the outer shield. As mentioned previously, welding outer blanket modules in the poloidal direction to the expansion joint and in the toroidal direction to the outer divertor plate constitutes the vacuum seal in the plasma toroid.

IV-E-3. Shield Design

General Description

The shield in UWMAK-II is made up of alternate layers of 90% B_4C-10% steel and 90% lead, 10% steel, divided up such as to provide maximum shielding of the toroidal magnets.

It appears that the construction of the shield can be in the form of preshaped 'H' beams welded together with the resulting spaces filled with either B_4C or lead depending on the location of the shield. The nomenclature used in the blanket section also applies to the shield with the addition of two more shielding units, namely the inner divertor slot shield and the outer divertor slot shield.

Table IV-E-2 gives the main distribution in the shield.

Table IV-E-2

UWMAK-II SHIELD (WT in MT)

	Inner Shield	Outer Shield	Inner Div. Slot Shield	Outer Div. Slot Shield	Central Shield
Structure (S.S.)	774.65	2,350.82	86.53	653.84	576.92
B_4C	956.80	2,903.65	106.89	807.61	712.59
Pb	3,453.82	10,481.11	385.83	2,915.18	2,572.22
Total in Reactor	5,185.32	15,735.25	579.25	4,376.63	3,861.72
Total per module	216.05	655.60	24.13	182.35	160.90

Shield Supports

In all cases, except the outer, the shields are continuous in the toroidal direction. The outer shield is segmented in the poloidal direction with the seams falling at the central plain of each toroidal magnet.

The inner shield and both top and bottom inner divertor slot shields are supported directly on the reinforced cylinder which constitutes the dewar for the toroidal magnet straight sections. As shown in Fig. IV-E-4, upper and lower braces are used to distribute the load from the inner shield on the cylinder. Shear restraint will have to be provided at the bearing point between the shields and the cylinder. This can be in the form of interlocking ledges.

As mentioned in the blanket section, the central shield is supported on structure extending between the toroidal magnets to the main roof beam on top and to the ground on the bottom. Similar supports are used both for the top and bottom outer divertor slot shields.

The outer shield is the heaviest of all the shield sections. However, only the top half, is supported from above while the bottom half is supported from below on the ground. In both cases, a continuous toroidal ring is provided just inside the toroidal magnets with connecting supports extending between the magnet to the roof beam or to the ground. Since the vacuum pumps are only located underneath the toroidal magnets, the space between the pumps will be devoted to the extensions on which the hinges for the outer shield will be attached. Obviously, the whole support structure will have to be reinforced against the huge bending moments introduced when the shield is in the open attitude as shown by the dotted lines in Fig. IV-E-4. In the closed attitude, the two halves will be locked together and a support rod will be provided to brace the shield on the ground.

IV-E-4. Front Wall Replacement

The neutron radiation damage to the front wall will necessitate its periodic replacement every two years (See Section IV-H).

In order to make the blanket accessible, the following functions would have to be performed:

1 - The outer divertor slot vacuum pumps will have to be disconnected and removed.

2 - The two outermost vertical field coils, both upper and lower, will have to be retracted.

3 - The helium supply and return lines are disconnected.

4 - The outer shield halves are swung open. (Figure IV-E-4)

The back side of the outer shield is now exposed. Rails can be placed radially between the magnets and a special counter balanced carriage designed to support the outer blanket can be rolled in. While the carriage supports the outer blanket, remotely controlled plasma cutting torches will burn away the seal wall between adjacent modules as well as the top and bottom seals to the support plates. The outer blanket module can now be rolled out on the carriage to a service area for front wall replacement.

Once the outer blanket is removed it makes the remaining inner and central blanket regions accessible. These regions can now be also disconnected and removed to service areas.

In the service areas the blanket modules will be mounted on fixtures which will make them easily accessible to remote control tools. At this point, the graphite curtain will be removed and the end flanges will be cut off with plasma torches. The last operation which will be performed before the sections can be removed is to burn off the welds which seal the sections to each other. This will free the sections to be pulled out of their sliding attachment.

A section of the front wall consists of five cells which makes it 115 cm wide, As mentioned previously, the length of a section varies from 60 cm to 150 cm depending on its location in the blanket. In order to simplify fabrication as well as to make the assembly of the blanket easier, it was decided to make the sections flat. This necessarily means that the toroidal and poloidal curvature of the front wall is broken up into a series of straight lines.

In Fig. IV-E-5(a), half of a blanket module is shown as it would appear if it were viewed from the center of the plasma. Fig. IV-E-5(b) shows the same blanket modules spread out on one plane. The squares and trapzoids outlined by the heavy lines represent sections. It is obvious from the figure that the cells run in the toroidal direction. In order to make it possible for the sections to be removed from either side of the module there can be only be one break along its width. This break is represented by the line in the center of each blanket module. The outer blanket is the widest and will have two rows of sections on each side, for a total of 68 sections. The inner blanket and the central blanket will have only one section on each side of the break for a total of 30 and 12 sections respectively.

To complete the front wall replacement, new front wall sections loaded with fresh breeding material will be assembled on the vertical structure and welded to each other. A new graphite curtain is attached. Refurnished blanket modules are then returned to the reactor and reinstalled. At the same time, new expansion joints will be provided.

The front wall including the breeding material weighs ~688 kg/m^2 which makes the weight of the largest section ~1180 kg. There are 2640 sections in the reactor weighing a total of 2270 MT.

It is significant to note that in UWMAK-I design, recycling the front wall necessitated the removal of 12 modules weighing 3600 MT each. In UWMAK-II, there are 24 modules weighing only 265 MT each of which the heaviest piece weighs 175 MT. Clearly, the handling problem has been simplified considerably.

It is conceded that it may be slightly more time consuming to remove and replace front wall sections in UWMAK-II than in its predecessor. However, on balance the total time required to complete the job is about the same. It is estimated that 6 weeks will be needed to replace the front wall by three shifts of working around the clock in several hot cells. This represents a down-time of 6% if done once every two years. In any case, reserve modules could be available to place into the reactor if the replacement of the first wall took an excessive amount of time.

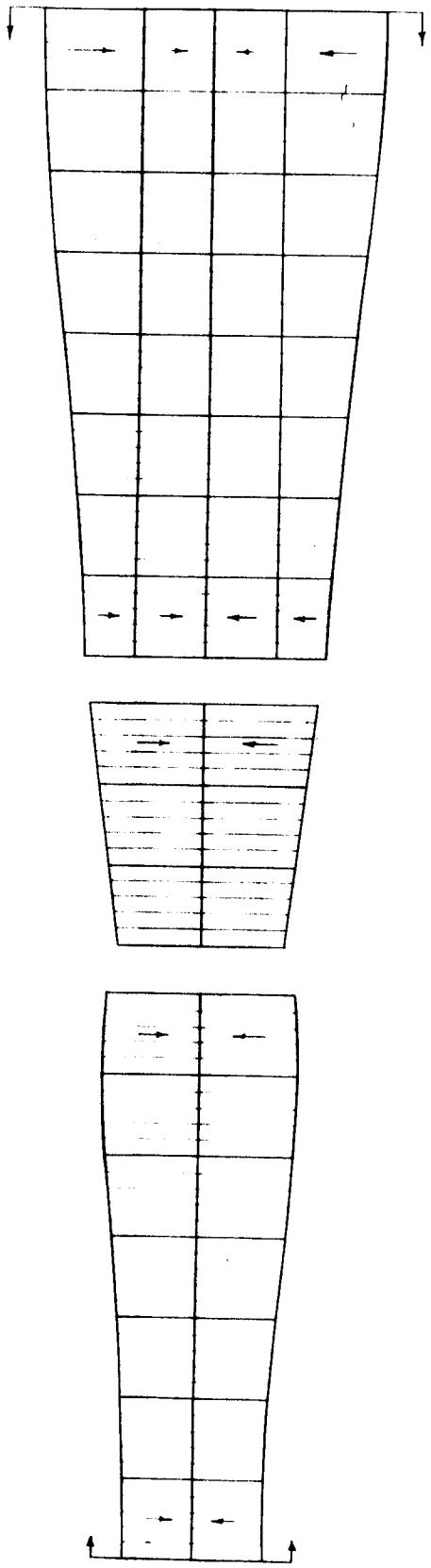

(b)

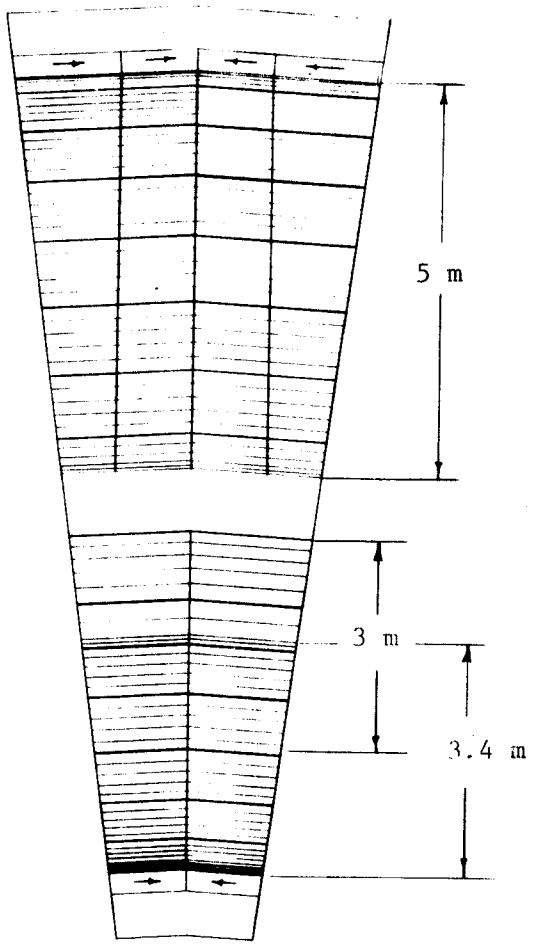

(a)

Front Wall (a) As Viewed From Plasma Center and (b) If Rolled Out on a Flat Plane

Figure IV-E-5

IV-F. Final Neutronics Analysis by Monte Carlo of the UWMAK-II Design

In this section, three dimensional models for Monte Carlo calculations are used for neutronics studies of the gas cooled blanket concept adopted for the UWMAK-II design. The results provide a refined iteration of the initial design developed using one dimensional transport calculations. This section is a summary of work reported in full in reference 1. As in our earlier Monte Carlo work, the Morse computer program[2] was employed with the same 46 group cross section library used in the one dimensional survey studies[3] Horizontal and vertical cross sections through one of the blanket cells are shown in Figures IV-F-1 and IV-F-2. On the basis of these figures, two model cells for calculations were developed. The first is referred to as a microcell model. It gave a gross blanket breeding ratio for the reference design as 1.148 ± 0.038 compared to the one dimensional 1.18 result. However, the present model contains more $LiAlO_2$ and Be.* The difference can be explained in terms of neutron escape by streaming and strong parasitic absorption of slow neutrons by the stainless steel cans. This will not be pursued here as it was noted that the model does not include the effect of the stainless steel in the lateral structure (coolant inlet to the first wall.) For this reason, the macrocell model was set up for further studies.

IV-F-A. Macrocell Model

In this three-dimensional model, a unit cell was chosen as shown in Figures IV-F-3 and IV-F-4. Lithium aluminate is contained in stainless steel cans 0.09 cm thick in two regions: VIII and XI. Beryllium also is contained in stainless steel tubes in regions IX and X. Region V represents the first wall tubing, and region VI represents the stainless steel gas coolant inlet tubing and support structure. Type 316 stainless steel was considered to consist of the following materials with their corresponding atomic densities:

316 Stainless Steel (100% density factor)	Chromium	0.01455 atoms/(barn·cm)
	Nickel	0.00938 "
	Iron	0.06141 "

These atomic densities are further modified by appropriate density factors (to be introduced later) for the different stainless steel zones.

The lithium aluminate (with 90% enriched lithium-6) atomic densities were taken as:

$LiAlO_2$ (90% enriched Li^6) (50% density factor)	3-Li-6	0.01887 atoms/(barn·cm)
	3-Li-7	0.00210 "
	Oxygen	0.04194 "
	Aluminum	0.02097 "

*50% density factors were used in the one dimensional calculations whereas the density of the $LiAlO_2$ itself (excluding space for coolant channels) is 90% in the 3-D calculations and the density used for the Be was 60%.

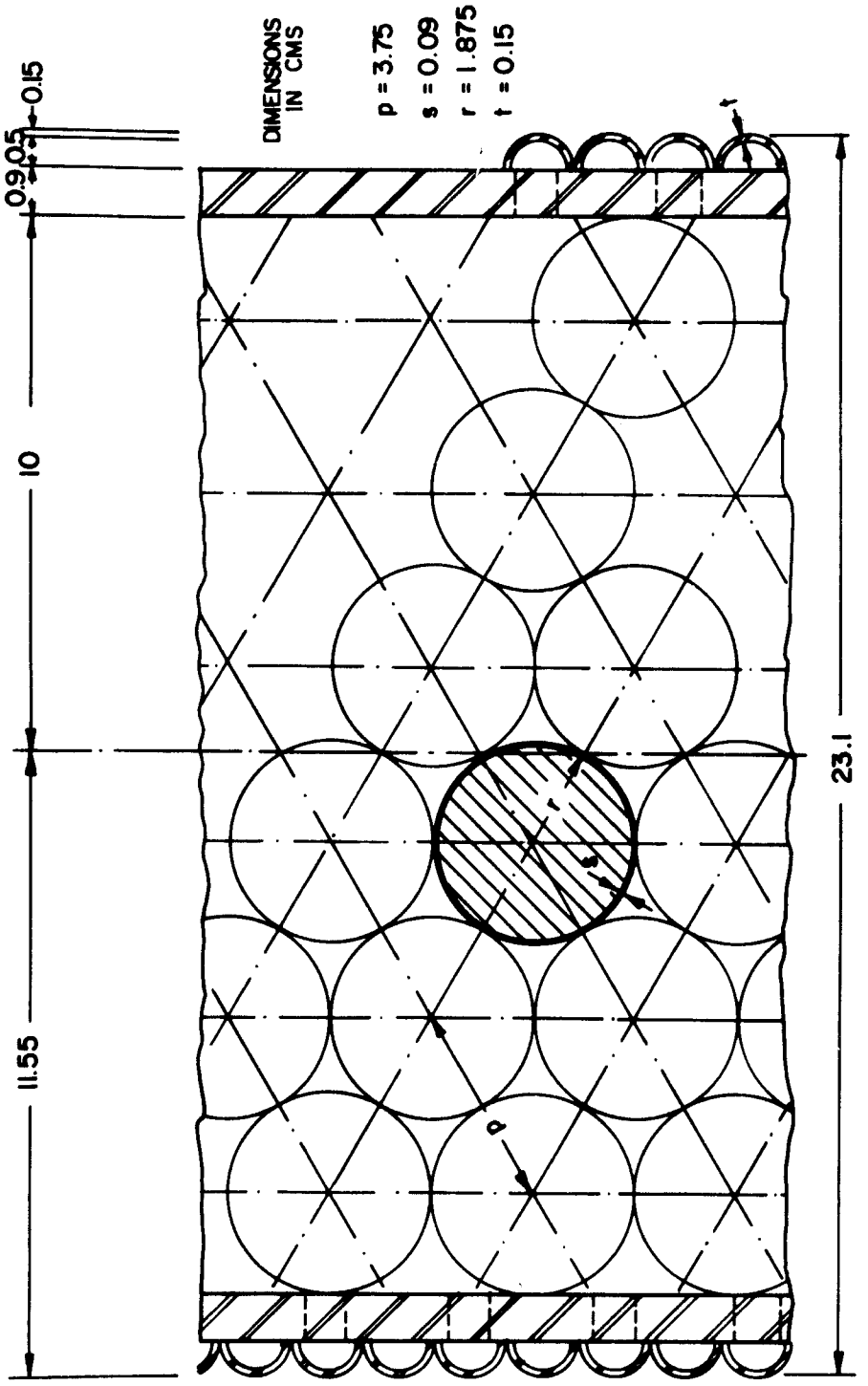

Horizontal cross-section through solid breeder cell

FIGURE IV-F-1

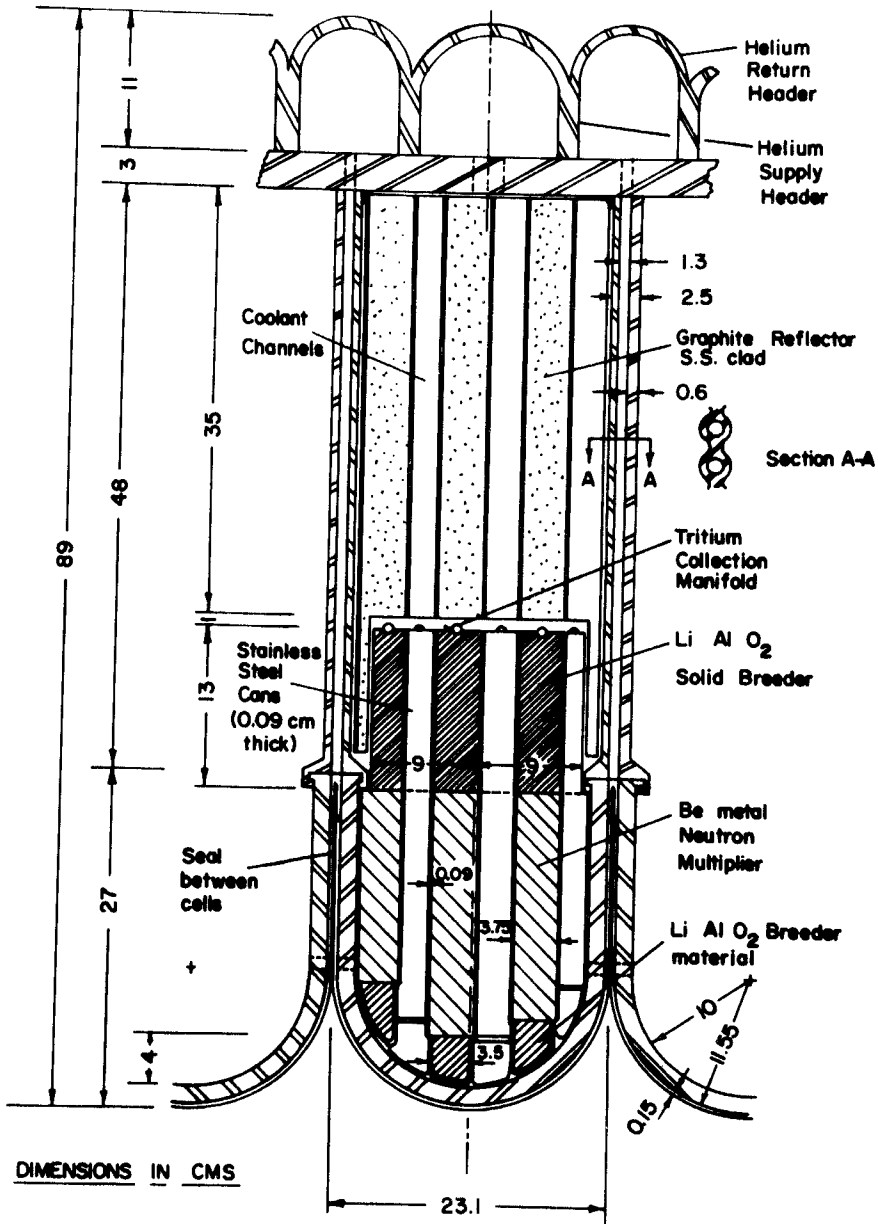

Vertical Section through solid blanket cells

FIGURE IV-F-2

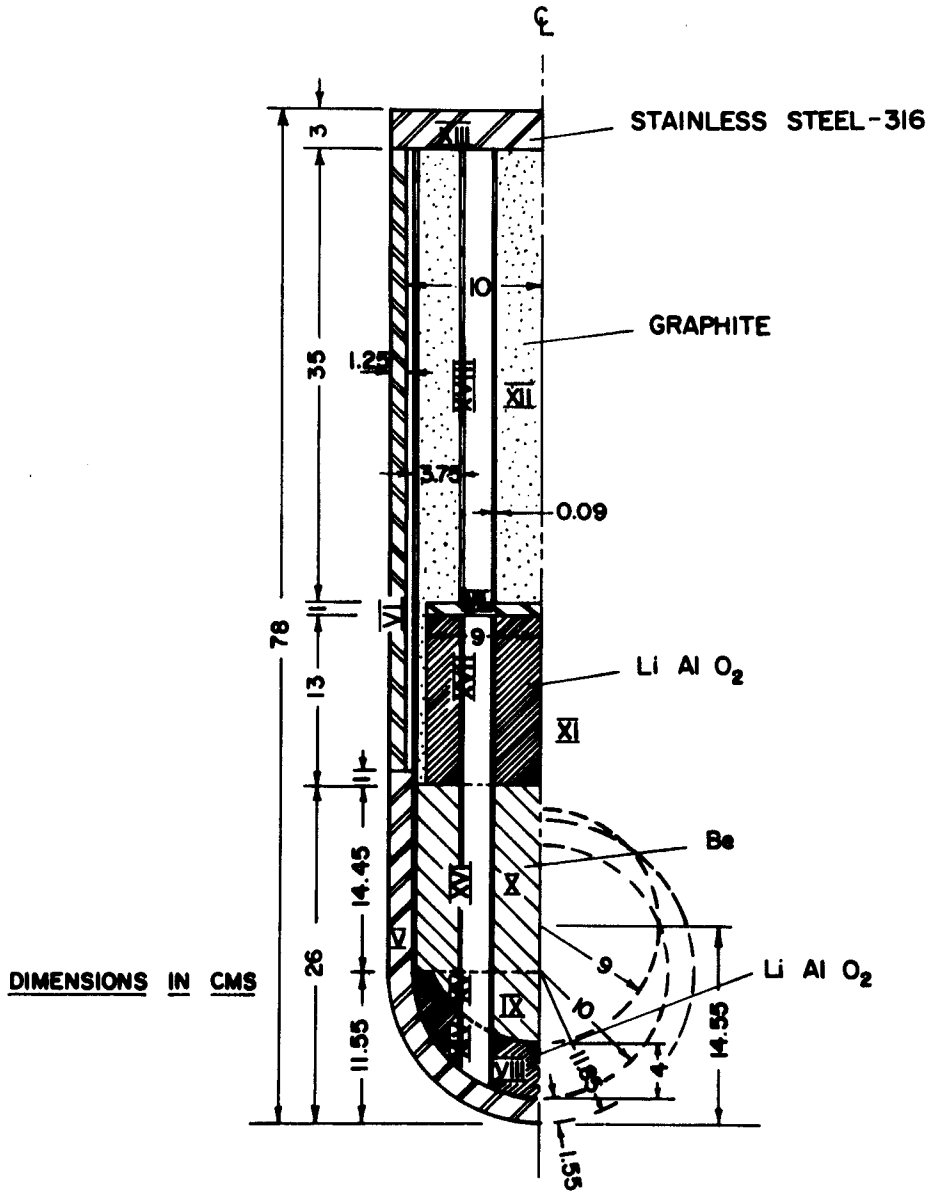

Vertical cross section through macrocell model

FIGURE IV-F-3

Region	Composition	Density factor
V	S.S. 316	0.68
X	Be	0.60
XVI	S.S. 316	0.95

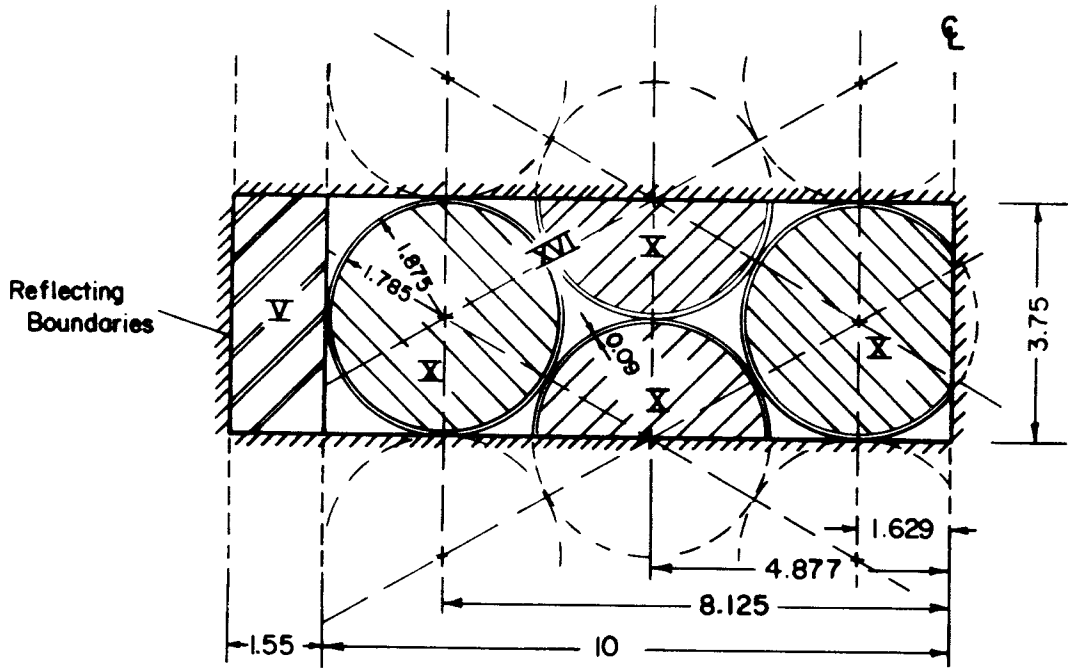

DIMENSIONS IN CMS

Horizontal section through macrocell model (Be zone)

FIGURE IV-F-4

The beryllium and graphite atomic densities adopted are:

Graphite (90% density factor)	Carbon 0.0723 atoms/(barn·cm)
Beryllium (90% density factor)	Beryllium 0.01112 atoms/(barn·cm)

The He coolant, having a very low density (1.663×10^{-4} gm/cm^3 (20°C, 1 atm), and a very small cross section, was considered as a vacuum.

These number densities were adopted from a previous discrete ordinate one-dimensional calculation.[3] The atomic densities of materials in these zones were adjusted to account for the actual amounts of materials in these regions. Regions VII and XIII represent the tritium collection manifold and coolant inlet and outlet ports respectively. Region XII is graphite contained in stainless steel tubing. Region compositions and atomic densities are displayed in Table IV-F-1. Such a geometry represents adequately the actual blanket configuration shown in Figures IV-F-1 and IV-F-2.

The geometry module of the MORSE code was used to represent that geometry and an output of the PICTURE routine showing a section through the lithium aluminate and beryllium zones showing the cladding and first wall stainless steel zones is shown in Figure IV-F-5.

Russian Roulette was used for particles reaching 1/1000 of their original weight,* and results of calculations are given in the form

$$\theta \pm S$$

where S is the estimated standard deviation and θ the estimated mean value. This corresponds to a 68.2% confidence interval. If a 95.4% confidence interval is required, the form $\theta \pm 2S$ should be used.

The blanket breeding ratio (gross) in different zones is displayed in Table IV-F-2. This blanket design was chosen on the basis of a sensitivity study and yields a blanket breeding ratio (gross) of 1.060 ± 0.022. The escape probability for neutrons was 0.04. The blanket breeding ratio (gross) is satisfactory, but the neutron escape requires more shielding and cooling at the back of the breeding cells.

IV-F-B. Sensitivity Studies

Important neutronics phenomena were uncovered in these studies. Numerical results show that solid gas cooled blankets behave basically as a heterogeneous system, and that three-dimensional computations are important for adequate design of such systems. Near optimal designs can be achieved by suitable material configurations and compositions. The neutron economy is highly affected by the large amount of structural materials present.

* See J. Spaniu and E. Gelbard, "Monte Carlo Principles and Neutron Transport Problems" (Addision-Wesley, Mass., 1969):

TABLE IV-F-1

Scalar neutron flux in unit cell, and region compositions: Reference Design.

Region	Composition	Density Factor	Volume(cm^3)	Scalar Neutron Flux per source neutron $n/(cm^2$ sec. source)
V	S.S. 316	0.68	188.181	0.168503 ± 0.003065
VI	S.S. 316	0.50	225.000	0.024422 ± 0.002157
VII	S.S. 313	0.18	33.750	0.026970 ± 0.001845
VIII	$LiAlO_2$(I)	0.90	123.515	0.184739 ± 0.003865
IX	Be (I)	0.60	108.931	0.188082 ± 0.005409
X	Be (II)	0.60	423.123	0.137390 ± 0.003619
XI	$LiAlO_2$(II)	0.90	345.670	0.040779 ± 0.001715
XII	Graphite	0.90	1062.552	0.019336 ± 0.001385
XIII	S.S. 316	0.95	129.937	0.004588 ± 0.000895
XIV	S.S. 316	0.95	11.908	0.195810 ± 0.005626
XV	S.S. 316	0.95	9.786	0.194349 ± 0.007181
XVI	S.S. 316	0.95	40.281	0.138271 ± 0.003142
XVII	S.S. 316	0.95	31.065	0.044182 ± 0.002649
XVIII	S.S. 316	0.95	103.140	0.021404 ± 0.001818

2,3 Stainless Steel 316 Clad
= $LiAlO_2$
+ Beryllium
0 Reflecting boundaries

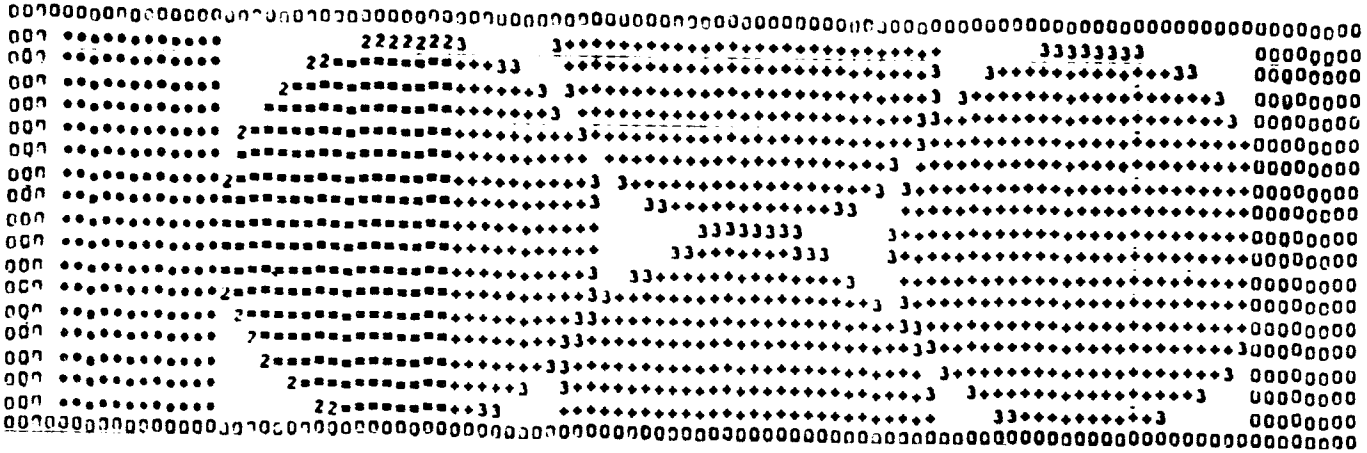

FIGURE IV-F-5

A PICTURE Routine Output Showing a Horizontal Cross Section Through the $LiAlO_2$ and Be Zones in a Unit Cell.

TABLE IV-F-2

Tritium Production per (D-T) Reaction Estimate by the Macrocell Model

Reference Design

$N(Li^6) = 0.018873$ $[\frac{\text{atoms}}{\text{barn}\cdot\text{cm}}]$ (90% d.f.)

$N(Li^7) = 0.002097$ $[\frac{\text{atoms}}{\text{barn}\cdot\text{cm}}]$ (90% d.f.)

escape probability = 0.039686

$N(Be^9) = 0.074130$ $[\frac{\text{atoms}}{\text{barn}\cdot\text{cm}}]$ (60% d.f.)

$\Delta t_2(LiAlO_2) = 13$ cm

$\Delta t_1(LiAlO_2) = 4$ cm

Number of histories = 2000

Zone / Contribution by	First Lithium Aluminate Zone	Beryllium Zone	Second Lithium Aluminate Zone	Total Contribution
Li^6	0.569021 ± 0.011602	---	0.481243 ± 0.009836	1.050264 ± 0.021438
Li^7	0.003244 ± 0.000085	---	0.000840 ± 0.000073	0.004084 ± 0.000158
Be^9	---	0.005592 ± 0.000334	---	0.005592 ± 0.000334
Total Contribution	0.572265 ± 0.011687	0.005592 ± 0.000334	0.482083 ± 0.009909	1.059940 ± 0.021930

The neutron escape probability from the blanket to the shield is sensitive to the quantity of neutron multiplier Be, the thickness of the graphite reflector and the quantity of lithium aluminate breeding material. The escape probability not only decreases with additional graphite, as would be expected, but also with the addition of Be which shows that beryllium also acts as a strong moderator and reflector, in addition to acting as a neutron multiplier. Neutrons slowed down in the Be may be scattered back to the first breeding zone, or forward to the second lithium aluminate zone where they interact with the Li^6 for tritium production (a beneficial result). However, these moderated neutrons do not contribute to further neutron multiplication in the Be and have a probability of being parasitically absorbed in the stainless steel structure and lost with respect to the breeding process. The behavior of the neutron escape probability is shown in Figure IV-F-6. This is defined as:

$$\text{Neutron escape probability} = \frac{\text{Total weight of neutrons escaping blanket}}{\text{Total weight of neutrons impinging on 1st wall}}$$

The first lithium aluminate zone and the beryllium zone see two neutron currents - an incoming one from the plasma, and a reflected one from subsequent material layers.

Each material layer has a reflection and a transmission coefficient for neutrons of different energies. Added to the reflector action of the graphite, the Be multiplier also reflects neutrons back to the first breeding zone, and the second breeding zone reflects some neutrons back to the first lithium aluminate zone across the Be zone. These reflected neutrons do not contribute much to the (n,2n) reaction in Be, but are further slowed down in Be. If their energy was initially low, they eventually get completely slowed down in the beryllium and then absorbed in the stainless steel.

The above remarks were inferred from estimates of the tritium atom production per (D-T) reaction for different cases of lithium aluminate, graphite and beryllium thicknesses. The sensitivity study involved a variety of cases in which the Be density was varied for different reflectors and breeding zone thicknesses. A summary of some of these results is given in Figure IV-F-7.

Figure IV-F-7 compares the different cases. It is interesting to notice the following: (1) Tritium production in the second breeding zone falls off with the addition of Be. This is due to the reflecting action of Be, since neutrons are reflected to the first breeding zone where the tritium production increases with Be addition.

(2) For the second breeding zone, tritium production is larger for greater $LiAlO_2$ content, and decreases with addition of Be (Be reflection action).

(3) Tritium production increases in the first breeding zone with Be addition, but with different slopes depending on the thickness of the second $LiAlO_2$ zone and the graphite reflector thickness. This might suggest that the graphite zone acts preferentially as a reflector for the fast neutrons reaching it, and that the second breeding zone reflects a part of the slow neutrons reaching it

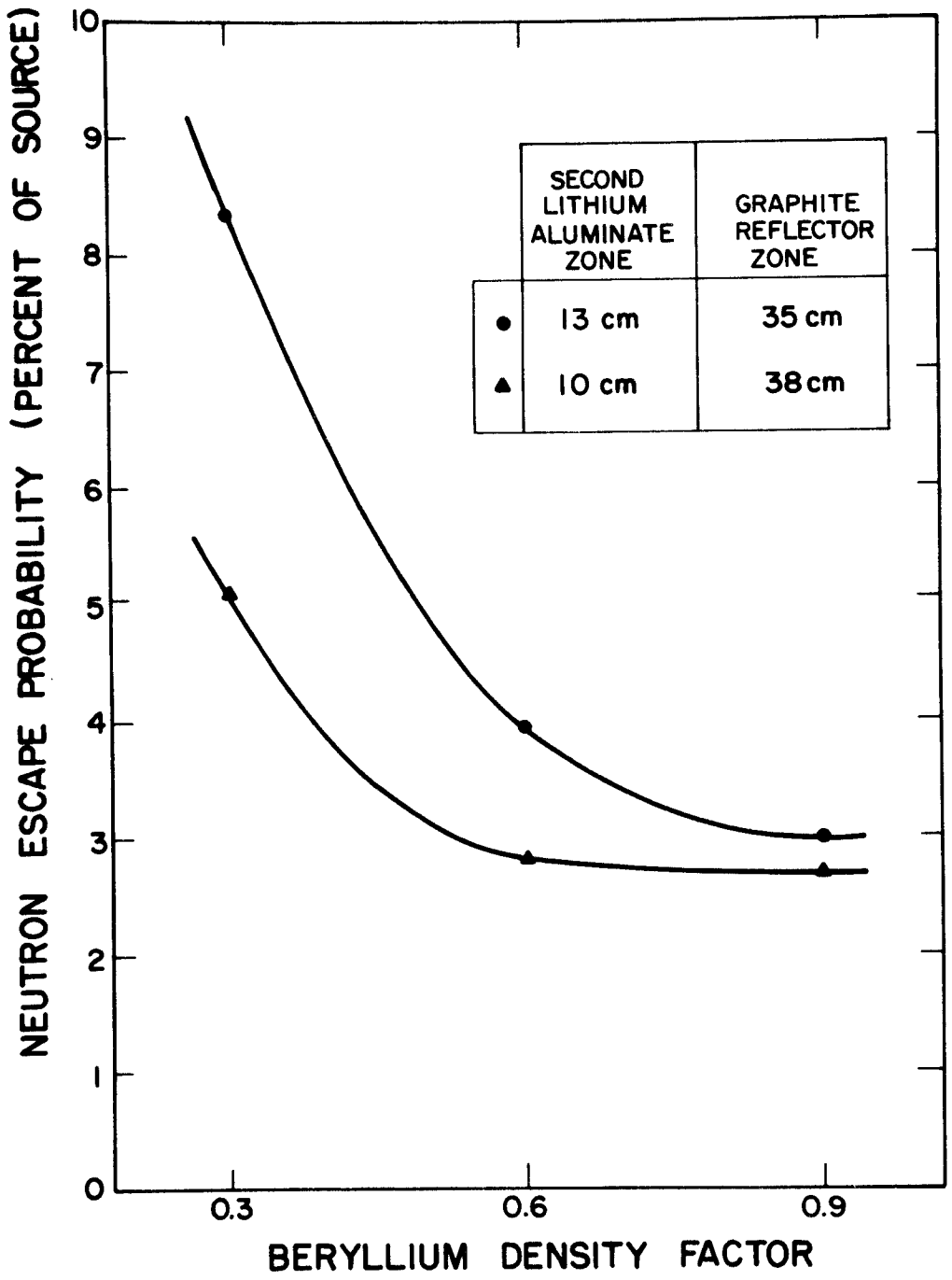

Figure IV-F-6 - Neutron Escape Probability Variation for Different Blanket Parameters

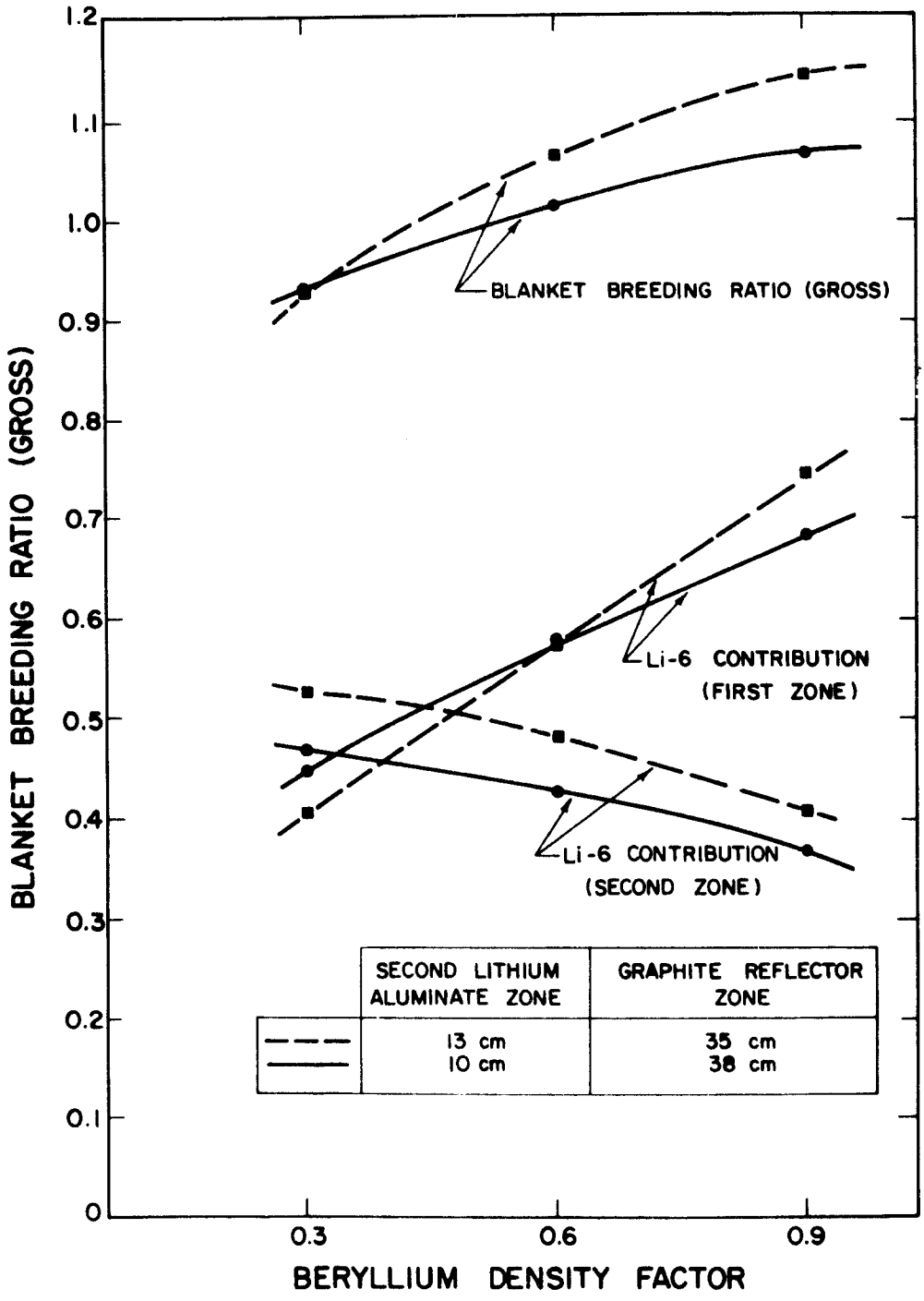

Figure IV-F-7 - Comparison of Tritium Production for Sensitivity Study Cases

Since that effect depends on the capture in the structure and does not contribute much to the blanket breeding ratio, this point was not investigated further.

(4) In the cases treated, the blanket breeding ratio (gross) increases with Be addition. However, the slope of the tritium production from the first zone may be such that the total blanket breeding ratio may reach a maximum for a given thickness of the first breeding zone, then fall with further Be addition.

For the chosen reference design, a blanket breeding ratio of $1.060 \pm .002$ was estimated corresponding to a neutron escape probability of 3.96%. With a 30% Be increase, a value of $1.140 \pm .028$ with a neutron escape probability of 8.3%, and another of 1.073 ± 0.041 with an escape probability of 5.1% can be attained. The escaping neutrons must be accounted for in the magnet shield design, or an extra breeding zone can be added to make use of them. Neutron spectra in different regions were obtained and as an example, the spectra in the stainless steel structure is shown in Figure IV-F-8.

IV-F-C. Comparison with Previous Calculations

Table IV-F-3 shows a comparison with blanket calculations from previous studies, Particularly, the one-dimensional computation (ANISN-discrete ordinates) yields a tritium production/(D+T) reaction of 1.1835. Our iterated blanket design yields a value of 1.060 ± 0.022. It should be emphasized that the materials compositions are basically different in the one-dimensional and the three-dimensional computations: adopting exactly the materials compositions used in the one-dimensional computation would yield a tritium production per (D-T) reaction of less than one.

Compared with the UWMAK-I design (liquid lithium breeder-coolant), the solid gas cooled blanket shows that nearly all the contribution to breeding is from Li^6 in the slow neutron energy range, whereas in liquid breeder-coolant blankets, a large contribution from Li^7 and fast neutrons is present.

IV-F-D. Conclusions and Recommendations

Gas cooled blankets behave basically as a heterogeneous system. A blanket breeding ratio (gross) greater than one is possible by adequate optimally chosen designs which include beryllium as a neutron multiplier. Three-dimensional computations seem to be a necessity for such optimizations after one-dimensional preliminary studies.

A substantial escape of neutrons is noticed at the back of the blanket and must be accounted for in the shield design. In the present configuration, if the structural walls were shielded against neutrons scattered from the Be and breeding zones by a layer of breeding material in a sandwich type layered design, a better neutron economy with a larger breeding ratio can be achieved, with a minimal size for the blanket.

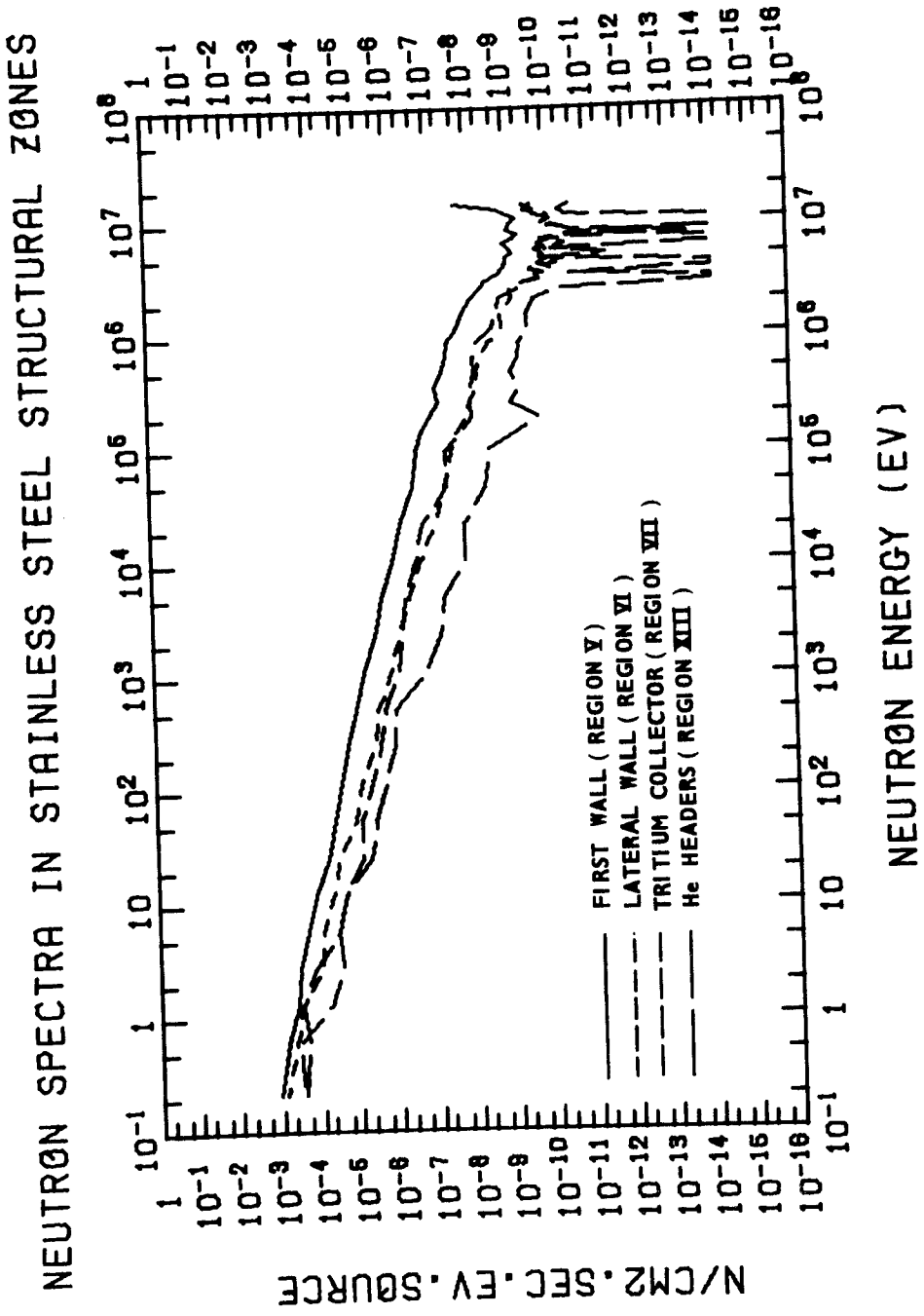
NEUTRØN SPECTRA IN STAINLESS STEEL STRUCTURAL ZØNES
N/CM2.SEC.EV.SOURCE
NEUTRØN ENERGY (EV)
FIRST WALL (REGION V)
LATERAL WALL (REGION VI)
TRITIUM COLLECTOR (REGION VII)
He HEADERS (REGION XIII)

Figure IV-F-8

TABLE IV-F-3

Comparison of one-dimensional ANISN and MORSE-Monte-Carlo estimates for blanket breeding ratio (gross) for the UWMAK-I and UWMAK-II conceptual designs

UWMAK-I : Liquid lithium (natural) breeding and coolant material, (also acting as moderator).

UWMAK-II: Solid $LiAlO_2$ (90% enriched in Li^6) breeder, He coolant, S.S. 316 structure, graphite reflector, with metallic Beryllium as neutron multiplier.

	UWMAK-I ANISN	UWMAK-I, Monte-Carlo (Unit Cell)	UWMAK-II ANISN	UWMAK-II Morse Microcell Model (1500 histories)	UWMAK-II Morse Macrocell Model (2000 histories)
$Li^6(n,\alpha)t$	0.883481	1.025940 ± 0.021127	1.1801	1.136213 ± 0.037104	1.050264 ± 0.021438
$Li^7(n,n'\alpha)t$	0.603706	0.483825 ± 0.021534	0.0034	0.004234 ± 0.000149	0.004084 ± 0.000158
Be(n,t)	---	---	---	0.007645 ± 0.000355	0.005592 ± 0.000334
Total Tritium production per source neutron	1.487187	1.509765 ± 0.042661	1.18	1.148092 ± 0.037608	1.059940 ± 0.021930

References for Section IV-F

1. M. H. Ragheb, C. W. Maynard, "Three Dimensional Neutronics for a Fusion Reactor Non-Mobile Gas Cooled Solid Blanket," UWFDM-92, Nucl. Eng. Dept. Univ. of Wis. (Feb. 1975).

2. E. A. Straker et al., "The MORSE Code - A Multigroup Neutron and Gamma Ray Monte Carlo Transport Code," ORNL-4585, Oak Ridge National Laboratory (1970).

3. R. W. Conn, G. L. Kulcinski, M. Abdou, R. W. Boom, G. A. Emmert, Y. Eyssa, M. Hilal, J. Kesner, W. Lue, C. W. Maynard, A. Mense, J. Scharer, T. Sung, I. Sviatoslavsky, D. Sze, W. Vogelsang, L. Wittenberg, T. Yang, W. Young, "Major Design Features of the Conceptual D-T Tokamak Power Reactor, UWMAK-II," IAEA-CN-33/G1-2; Proceedings of the Fifth IAEA Conference on Plasma Physics and Controlled Nuclear Fusion Research, Tokyo, Japan, Nov. 11-15, 1974.

IV-G. Tritium Removal

IV-G-1. Release Rate

A review of the plant design reveals that during operation significant quantities of tritium will be present in the following systems:

- the blanket
- the helium coolant
- the tritium extraction beds
- the plasma
- the divertor
- the fuel injectors
- the fuel reprocessing equipment.
- vacuum pumps

Many of these sytems are composed of a large number of individual pumps, valves, pipes, flanges, etc. Permeation and leakage of tritium from this multitude of components is inevitable. Because tritium is by far the most mobile of all the radioactive constituents in a fusion power plant, it will be necessary to design high integrity systems and back them with tritium scanvenger systems which will contain the tritium leakage within the reactor building so that the tritium release to the environment will be minimal.

The need for equipment, which will provide the containment, control and monitoring at the concentrations and quantities of the tritium required in a fusion power plant is being analyzed and some preliminary systems are being tested.(1) Further treatment of this subject is beyond the scope of this report; however, the activity and literature(2) devoted to this subject is increasing.

Nearly all of the tritium handling equipment described above will be housed in a reactor hall which will be hermetically sealed from the environment.(3) All gases and liquids which may exit from the reactor hall will be scavenged for traces of tritium - bearing material before being discharged to the environment. Because the hermetic seal is at ambient temperature where diffusion is very slow, and the scavenging systems are very efficient, several environmental studies(4) agree that tritium release from the reactor hall should be extremely small, <1 Ci/day.

The tritium escape route which appears to be the most difficult to control is permeation through the heat exchanger which will permit the transfer of tritium from the helium coolant to the steam system. Recovery of very dilute tritiated water from the steam system at a reasonable cost is beyond present technology. Tritiated water in the steam is transferred to the environment through several pathways, such as leakage in the steam generator, permeation, condenser blow-down, etc. The release of this tritiated water to the environment would therefore have to be controlled at rates compatible with radiation release guidelines. In addition, the controlled disposal of the steam generator water at the end of plant life would be necessary. It has been recently suggested to us by workers at Battelle Northwest Laboratories that we might consider using the contaminated water to make concrete which could then be buried until the tritium has decayed to acceptable levels.

Experience with LWR's indicated that a steady-state condition is eventually established in which the rate of release of tritiated water is equal to its leakage into the steam system,(5) which in this case would be by permeation through the helium-steam heat exchanger. The rate of release of tritiated water can only be regulated, therefore, by control of the permeation of tritium through this heat exchanger.

The tritium permeation rate through the heat exchanger is determined by its concentration in the helium, i.e. partial pressure of T_2, temperature and characteristics of the heat exchanger, such as surface area, wall thickness, and materials of construction. The characteristics of the heat exchanger and its operating temperature are set by the heat exchanger manufacture and the power plant engineers; consequently, these parameters are somewhat inflexible. The tritium systems designer does have some flexibility to control the tritium concentration in the helium coolant. Because the rate release of tritium from the helium coolant is small compared with its accumulation in the coolant, the concentration of the tritium is primarily controlled by the tritium removal system. If the extraction system is designed so that it is not rate limited, then its efficiency is determined by the equilibrium tritium partial pressure for the selected extraction system. The extraction systems for the removal of tritium from the helium will be discussed in Section IV-G-3, after the tritium inventory is considered.

The size of the tritium inventory in the blanket is of concern, also, and is another parameter which the tritium system designer has some flexibility to control. The tritium inventory should be kept to a minimum for at least two reasons. The first is related to the fact that tritium fuel must be supplied from an external source until tritium from the breeder material can be extracted at a rate sufficient to fuel the reactor. This approach to self-sufficiency for tritium fuel will occur after a shorter operating time as the tritium inventory is reduced. The second reason to keep the tritium inventory small is a desire to minimize the total radioactive material in the plant. This would be important if the tritium in the blanket might escape during some abnormal condition. The tritium inventory considerations will be discussed in Section IV-G-2.

IV-G-2. Tritium Inventory Considerations

The lithium compound used as the breeder must not only have the desirable physical properties, as discussed in the blanket section, but it must also release the tritium so that the total tritium inventory is minimal. For any lithium compounds, a steady-state will be approached in which the rate of tritium release will equal the generation rate; consequently, the factors which affect this steady-state condition are of importance. The rate of approach to the steady-state condition is dependent upon kinetic considerations, such as diffusion of tritium in the compound. On the other hand, the solubility of the tritium in the compound is determined by the thermodynamic equilibrium constant at the compound temperature and the tritium partial pressure in the extraction system. Both diffusion and solubility will be considered, therefore,

for each lithium-bearing material. Finally, the proposed tritium extraction system for the breeding cycle will be considered because it will determine the tritium partial pressure in equilibrium with the breeder materials.

When liquid lithium was utilized as a breeder and coolant, the rate of diffusion of the tritium in the lithium was not important because mechanical mixing quickly redistributed the tritium. The important consideration in that case was the partial pressure of tritium in the recovery system and the equilibrium solubility of tritium. It was necessary to employ a recovery system which had a tritium partial pressure of $<10^{-10}$torr in order to keep the solubility <5 ppm (wt), which gave a tritium inventory of nearly 9 kg because of the large lithium inventory.

a. Diffusion of Tritium

For the solid lithium-bearing compounds considered in this study, tritium diffusion will not be as rapid as in the case of liquid lithium and each compound will have to be evaluated. The relationship between the tritium concentration and its diffusion coefficient in the solid breeder material can be estimated by use of Jost's solution(6) to the photo-chemical generation of a gaseous molecule in a cylindrical vessel with the diffusion of the molecule to the walls of the cylinder where its concentration is zero. For this case, the average concentration of the generated species, τ, is given by the relationship,

$$\tau = \frac{1}{3} \frac{\overset{\circ}{\tau}\ \delta^2}{D}$$

where

$\overset{\circ}{\tau}$ = tritium generation rate,

δ = path length, and

D = diffusion coefficient.

This relationship will be used to evaluate the average tritium concentration in several breeder blankets for UWMAK-II in which $\overset{\circ}{\tau} \sim 10^{-2}$g/sec.

If the tritium in the intermetallic compound, LiAl, is in solid solution so that the interstitial diffusion coefficient is similar to that of hydrogen in steel at 500°C, then D is $\sim 10^{-5}$ to 10^{-6} cm^2/sec. For particles with $\delta = 10^{-1}$cm, the total tritium inventory in this compound is only ~15 grams.

The diffusion of tritium in the non-metallic compounds is more difficult to estimate because few measurements have been published on either hydrogen or tritium diffusion in ceramic materials. The relevant data are summarized in Figure IV-G-1. If the diffusion of tritium in $LiAlO_2$ is similar to the diffusion of hydrogen in Al_2O_3, then the measured values for the latter system may be utilized although wide variations exist between the two reported experiments.(7,8) Also, in the few cases where tritium diffusion has been measured in zirconia,(9) beryllia(10) and niobia, the diffusion coefficients are much lower than for hydrogen in alumina. While this difference may truly reflect enhanced diffusion in alumina, a difference in experimental techniques should be noted.

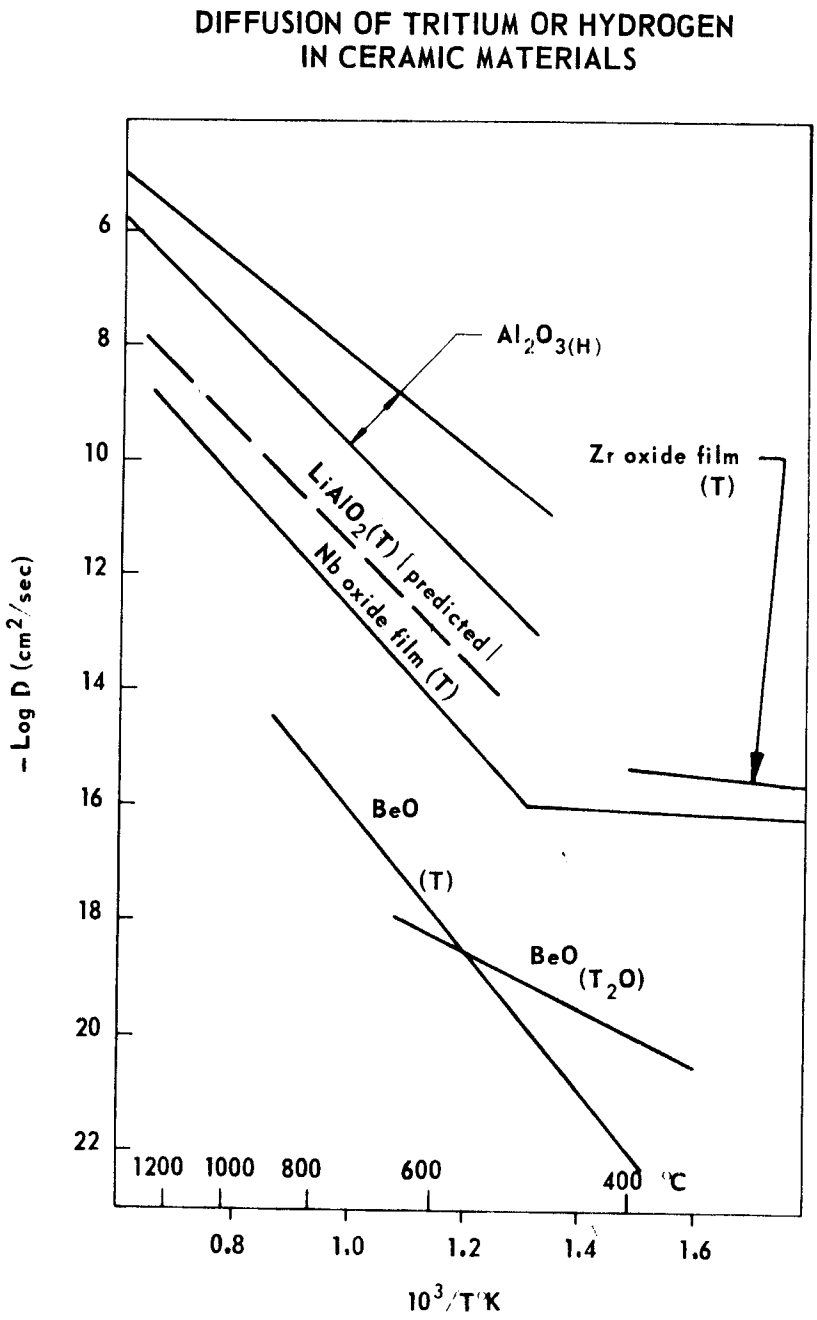
DIFFUSION OF TRITIUM OR HYDROGEN
IN CERAMIC MATERIALS
- Log D (cm²/sec)
6
8
10
12
14
16
18
20
22
Al2O3(H)
Zr oxide film
(T)
LiAlO2(T) [predicted]
Nb oxide film (T)
BeO
(T)
BeO
(T2O)
1200
1000
800
600
400 °C
0.8
1.0
1.2
1.4
1.6
10³/T°K

Figure IV-G-1

In the measurements on alumina, a differential hydrogen pressure was maintained across the ceramic specimens; consequently, any porosity in the specimen would contribute to an apparently higher diffusion coefficient. In the experiments involving tritium, the tritium was either generated within the specimens by nuclear transformations or injected into the specimens by nuclear recoil energy. The diffusion coefficients were measured as the tritium migrated to the surfaces of the specimens and probably followed lattice diffusion processes more closely than the hydrogen gas permeation experiments of alumina. For this reason, a conservative diffusion rate for tritium in $LiAlO_2$ of Li_2SiO_4 is proposed, as shown in Figure IV-G-1.

Based upon the predicted diffusion coefficients for tritium in $LiAlO_2$, an approximate tritium inventory due to diffusion can be calculated from Jost's relationship once the temperature has been established. Because of the low thermal conductivity predicted for $LiAlO_2$, one must integrate the inventory across the approximately parabolic temperature profile in a $LiAlO_2$ rod. If we investigate the case of the highest centerline temperature (1097°C) and apply this to all the rods along their entire length we find that the lowest T_2 inventory is ~120 grams if the diffusion length is 10μm. This can be met with the utilization of crushed powders approximately 20μm in diameter or by the fabrication of porous ceramic bodies with a nominal 20μm between interconnected pores.

In the diffusion and subsequent release of tritium from a ceramic compound, as additional factor must be considered. In the experimental determination of the diffusion and subsequent release of tritium from beryllia,[10] (see Fig. IV-G-1) an appreciable quantity of molecular T_2O was evolved, between 3 and 12% of the total tritium, particularly below 750°C. The evolution of the T_2O followed a faster diffusion rate at these lower temperatures. The quantity of T_2O evolved at the higher temperatures of the present reactor should be small; however, tritium oxide together with molecular tritium will probably be released from all of the oxide-bearing breeder compounds. The tritium extraction system must be capable of processing both T_2 and T_2O, therefore.

b. Solubility of Tritium

An estimation of the solubility of tritium in LiAl was made based upon the assumption that a Sievert's relationship exists similar to that for hydrogen in lithium, i.e.,

$$P_{H_2} = K_{s(LiAl)} C^2_{H(LiAl)}$$

where P_{H_2} = hydrogen gas pressure,

$K_{s(LiAL)}$ = Sieverts' constant for hydrogen in LiAl

and $C_{H(LiAL)}$ = Solubility of hydrogen in LiAl

Recent experimental measurements,[11] regarding the release of tritium from irradiated LiAl pellets at temperatures from 300 to 600°C and concentrations in the range of 1 appm, indicate that the Sieverts' constant at 500°C is no larger than 2×10^7torr/(atom fraction)^2. If the tritium pressure is kept below 10^{-4}torr, the approximate tritium solubility in a LiAl blanket is only 130 grams. It can be seen that the tritium solubility in LiAl is the predominant effect in the assumulated tritium inventory as compared to the hold-up by diffusion when particles <0.1 cm are utilized. The solubility of tritium in the non-metallic compounds is more difficult to estimate because only the solubility of hydrogen in one oxide, ZnO, has been measured over a wide temperature and pressure range.[12] The results are somewhat difficult to interpret for the present application because the solubility relationships were found to depend upon the concentration of hydrogen in the oxide. At high hydrogen solubilities i.e., high temperature and high hydrogen pressure the solubility follows the solid line in Fig. IV-G-2. At low hydrogen solubilities i.e., low temperature and low pressure, the solubility followed a 1/2 power hydrogen pressure dependence, as might be expected for the dissolution reaction,

$$H_2 \text{ (gas)} \rightarrow (2H^+ + e)_{ZnO}$$

as shown by the dashed-line in Fig. IV-G-2. Because the tritium solubility in the breeder blanket material would be low, although the temperature is high, the latter values for the hydrogen solubility in ZnO where used for the tritium solubility in $LiAlO_2$. The low solubility data (dashed-line) can be approximately expressed by the equation,

$$S = \frac{2.1 \times 10^6 \text{cm}^3}{\text{cm}^3 \cdot \text{atm}^{1/2}} \; P_{(\text{atm})}^{1/2} \left(\exp - \frac{36.7 \times 10^3 \text{cal/mole}}{RT}\right)$$

Based upon chemical considerations, Hickman[13] suggests that ZnO is a more receptive host for hydrogen than alumina; consequently, the solubility of tritium in an aluminate or silicate should be no greater than the solubility of hydrogen in ZnO. If the tritium pressure in the present breeder blanket is $<10^{-4}$ torr and the temperature ~900°C, then the tritium solubility in the total $LiAlO_2$ is only 7g, which is less important than the retention caused by the slow diffusion of tritium.

c. Tritium Inventory at Higher Density for the Breeding Material.

The previous estimates of the tritium inventory in the $LiAlO_2$ assumed this ceramic was in the form of crushed powders (approximately 20 μm diameter) which was packed into stainless steel tubes so that the bulk density was 50% of the theoretical density. Additional calculations of the breeding ratio for the present blanket design indicates (see Neutronics Section) that it may be necessary to load this ceramic to nearly 90% of its theoretical density. This requirement could cause a significant increase in the tritium inventory in this ceramic, as discussed below.

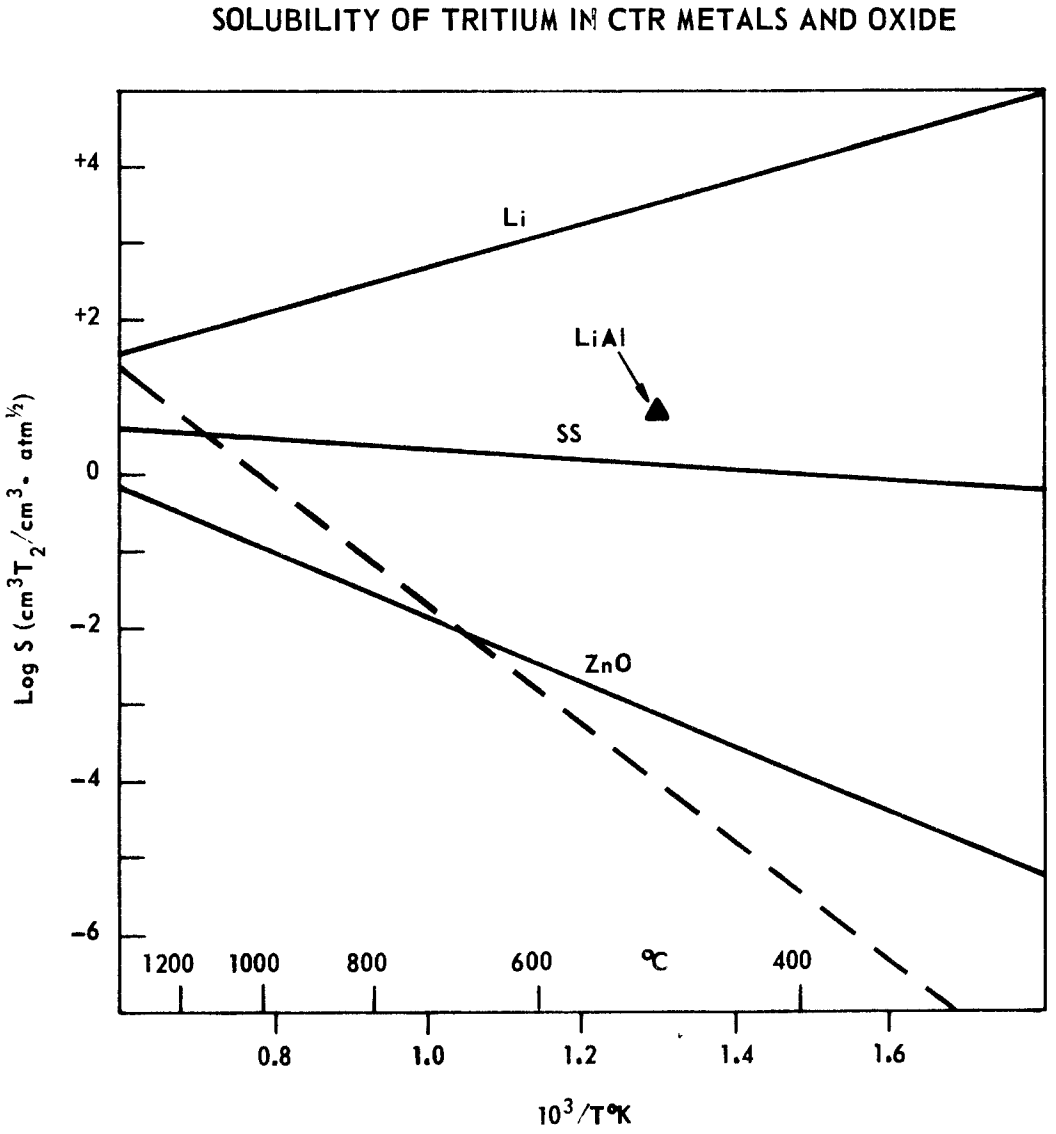
SOLUBILITY OF TRITIUM IN CTR METALS AND OXIDE
+4
+2
0
-2
-4
-6
Log S (cm³T₂/cm³· atm½)
Li
LiAl
SS
ZnO
1200
1000
800
600
400
°C
0.8
1.0
1.2
1.4
1.6
10³/T°K

Figure IV-G-2

The random packing of spherical particles of nearly the same size yields a maximum packing density of only 64% of the theoretical density.(22) The random packing of two sizes of spherical particles, in which the diameter of the larger particle is ten times greater than the smaller particle, gives an 83% maximum packing density. In order to achieve 90% packing density, three sizes of spheres must be used whose diameters are in the ratio 45:6:1.

Spherical ceramic particles are chosen for this study because the previous calculations have shown that the slow diffusion of tritium from this ceramic is the principal cause for tritium retention. When spherical particles are utilized the average concentration of tritium in the sphere, τ, can be estimated from the following relationship,(23)

$$\tau = \frac{\dot{\tau} R^2}{15 D}$$

where $\dot{\tau}$ = tritium generation rate, 10^{-2} g/sec

R = radius of the sphere

D = diffusion coefficient.

Increasing the density of the ceramic from 50 to 90% of theoretical will undoubtedly alter the temperature distributions calculated previously. However, if as a first order approximation, we assume the same temperature distribution as found in the 50% density case then we find that to keep the inventory to less than 1 kg requires particle radii of less than 30 microns. (Actually if one accounts for the axial temperature distribution the maximum radius is reduced even further.)

For these reasons, three sizes of spherical particles were selected so that 90% of theoretical density would be obtained. The accumulated tritium inventory is compared with that of LiAl and liquid lithium in Table IV-G-1. Note that the temperatures are 500°C for Li and LiAl and 700-1100°C for $LiAlO_2$. The tritium inventory in both solid breeder materials, $LiAlO_2$ and LiAl, are nearly the same and one order of magnitude less than for liquid lithium.

The lower inventory in the solid breeders may be unrealistic, however, because under the stresses of heat and radiation in the reactor, the ceramic fuel particles will undergo many structural changes. They will swell because of the retained helium, crack, and begin to sinter so that their original sizes are not retained. In the extreme case, the particles may sinter completely, as UO_2 fuel particles in a fission reactor, in which case all the voids migrate to the center and a hollow tube of ceramic is retained in contact with the cladding.(24) If this should occur with the $LiAlO_2$, then the maximum path length for tritium diffusion increases from 50^2 μm to 6000 μm and the tritium inventory increases to 10^4 kg due to the slow diffusion of tritium. A similar increase in the retention of tritium would occur with LiAl but it would not be as severe because of the more rapid diffusion coefficient for tritium.

Clearly, much more experimental evidence must be obtained on the behavior of these solid breeding materilas in simulated reactor environments, before this assessment can be completed. Perhaps some coating might be applied to these particles to retard their tendency to sinter. Alternatively, the particles may be removed rather frequently from the reactor, the tritium removed, the particles reconstituted and rapidly returned to the reactor. These concepts were not be fully evaluated at the time of this report.

Table IV-G-1

Tritium Inventory in Potential Breeder Materials
(5000 MW(th) Reactor)

	$LiAlO_2$	LiAl	Li
P_{T_2} (torr)	10^{-4}	10^{-4}	10^{-8}
Temp. (C)	900	500	500
Wt. Li (kg)	9×10^4 *	1×10^5 *	1.4×10^6 *
Theoretical Density, %	90	90	100
Particle Size, μm (%)	30 (65) 4 (24) 1 (11)	1000 (65) 120 (24) 20 (11)	Liq.
Tritium Retention (g)			
Solubility	15	215	7000
Diffusivity	710	5	0
TOTAL	725	220	7×10^3

* Initial loading also and does not represent replacement over the reactor lifetime or the amount to be mined from the ground due to the higher enrichment in Li-6.

d. Tritium Extraction System for Breeding Cycle

The utilization of a finely powdered ceramic material has some major impacts upon the design of the blanket and the tritium extraction system.

The first implication is the fact that a bed of finely crushed powders cannot be cooled directly by the circulation of main helium coolant through the bed because the pressure drop would be excessively large; consequently, the bed is cooled only by the conduction of heat to the surface of the bed. Secondly, the introduction of powder or porous ceramic bodies introduces the possibility that because of irradiation induced dimensional changes and thermal cycling, a large amount of fine dust will be generated. If this dust enters the helium coolant, then it could be transported throughout the reactor into the heat exchanger. For these reasons, the breeder material and the beryllium, which is used for neutron multiplication and also generates tritium, were placed inside stainless steel tubes approximately 3.5 cm diameter with a wall thickness of 0.75 mm and nearly 30 cm long. These tubes would be closed at the end facing the plasma and connected at the other end to a small gas plenum attached to a tritium extraction system external to the reactor. Alternatively, the exhaust ends of these tubes could be closed by the use of a porous metal plug. This plug would retain the ceramic powder inside of the tube but permit the tritium to diffuse into the helium coolant where it would be extracted. Such a technique would increase the tritium inventory within the tubes, increase the partial pressure of tritium in the helium coolant and subsequently increase the permeation of tritium through the primary heat exchanger. The design philosophy chosen was to minimize the tritium contamination in the helium coolant and extract the tritium directly from the tubes to a separate recovery system.

Conceptually, the tritium gas could be removed from these tubes into a separate collector system either (a) a flowing helium stream of (b) by continuous pumping with a vacuum system.

(a) The case of the flowing helium extraction system will be considered initially. The partial pressure of tritium within the tubes can be estimated from the following relationship;

$$\dot{T} = N \times n \times \delta$$

where $\dot{T}$ = tritium generation rate (1.67×10^{-3} moles/sec)
N = mole fraction tritium in the helium
n = moles of helium in tubes
δ = cycles of helium through the tubes/sec (~ 2 sec^{-1})

also, $N = P_{T_2}/P_{He}$

where P_{He} = helium pressure in tubes

P_{T_2} = tritium partial pressure

and $n = \frac{P_{He} V}{RT}$

where V = volume He in tubes ($5 \times 10^8 cm^3$)

R = gas constant ($82\ cm^3 \cdot atm \cdot deg^{-1} \cdot mole^{-1}$)

T = blanket temperature (900°K)

Substitution of these equations into the first equation shows

$$P_{T_2} = \frac{\dot{T} \times RT}{\delta \times V} \simeq 1 \times 10^{-4} \text{torr, regardless of the value of } P_{He}.$$

The value of P_{He} is determined by the permissible heat loss from the system and the extraction techniques for removal of the tritium. For this calculation, it will be assumed that all the helium would be circulated through an oxidizer and extraction system with a 94% efficiency so that the residual tritium pressure is 6×10^{-6}torr. In the oxidizer, the tritium is converted to tritiated water. This helium stream is then circulated over molecular sieves at 100°C to remove the water. A regenerator will be used to reheat this helium before it is returned to the reactor, but some heat loss, λ, will occur. The quantity of heat that will be lost from the reactor by the extraction system will be,

$$Q = m\, C_p (T_2 - T_1) \lambda$$

where m = helium flow rate, moles/sec

C_p = heat capacity of helium, 5 cal/mole·deg

T_2 = reactor coolant exit temperature, 600°C

T_1 = cooling bed temperature, 100°C

In these calculations, the conservative assumption will be made that the regenerator is only 75% efficient, i.e. $\lambda = 0.25$ and Q is <50 MW (1% of reactor power; therefore,

$$m = 1.9 \times 10^4 \text{moles He/sec.}$$

Because it makes 2 cycles/sec, the number of moles, $n = \frac{m}{2}$ also since $n = \frac{PV}{RT}$, for the previous values of V and T,

$$P_{He} = 1.4 \text{ atm (the pressure of helium inside the tubes)}$$

(b) The case of the tritium being removed from inside the breeder tubes by vacuum pumps will be considered next. For the entire blanket tritium generation rate is,

$$\dot{T} = 10^{-2} \text{ g/sec} = 28.4 \text{ torr} \cdot \text{liters (STP)/sec.}$$

If the pressure is maintained at 10^{-4} torr, then the speed of the vacuum pump, V_s, must be

$$V_s = \frac{28.4 \text{ torr}\cdot\ell/\text{sec}}{10^{-4}\text{torr}} = 2.84 \times 10^5 \ \ell/\text{sec}.$$

As discussed in the divertor section, presently available cryopumps designed for hydrogen can pump 5×10^3 ℓ/sec; therefore, approximately 60 pumps would be required for the whole blanket which would be conveniently be divided into 60 sections.

The ability of the vacuum system to keep each individual tube at 10^{-4}torr is of concern and will be estimated by use of the relationship for molecular flow,[14]

$$Q_{T_2} = F(P_2 - P_1) \text{ where } Q_{T_2} = \text{the quantity of tritium}$$

flow through a tube, and F = flow conductance of the tube. For a cylindrical tube, $F = 30.5\ (a^3/\ell)(T/M)^{1/2}$ liters/sec,

where a = radius of the tube

ℓ = length of the tube

T = temperature of gas (900°K)

M = molecular weight of gas (T_2 = 6 g/mole)

P_1 = pressure of the vacuum system (10^{-4}torr)

P_2 = pressure inside the individual tubes.

Let us assume $P_2 \sim 1.1 \times 10^{-4}$torr and the length of the tube ℓ, is sufficiently long to lead through the graphite region, 40 cm, where it will be connected to a larger plenum; therefore, F, must be at least as large as

$$F = \frac{Q_{T_2}}{(P_2 - P_1)} = \frac{28.4 \text{ torr}\cdot\text{liters/sec/reactor}}{3.43 \times 10^6 \text{ tubes/reactor}} \times \frac{1}{(1.1\times10^{-4} - 1.0\times10^{-4})\text{torr}}$$

$$F = 0.828 \text{ liters/sec/tube};$$

The radius of the tube required is therefore

$$a^3 = F\ (M/T)^{1/2}/30.5 = 8.87 \times 10^{-2}\text{cm}^3; \text{ therefore,}$$

$$a = 0.45 \text{ cm (the radius of the conductance tube, 40 cm long)}$$

Because the amount of tritium which will diffuse out of the helium is minor, all of the tritiated water must be absorbed. The size of the molecular sieve bed is determined by the bulk density of the dessicant, 40 lbs/cu ft, the fact that the dessicant will hold only 0.5 g (H_2O) per 100 g, and the accumulation of tritium in the helium occurs at the rate of 47.4 g/day forming 7.9 g-moles T_2O. The weight of molecular sieve required for one day, W, is

$$W = (7.9 \text{ moles } H_2O)\left(\frac{18\text{g } H_2O}{\text{mole } H_2O}\right)\left(\frac{100\text{g dessicant}}{0.5\text{g } H_2O}\right) = 28.4 \text{ kg}$$

The volume of the bed is then,

$$\text{vol} = \frac{(28.4 \text{ kg})(2.2 \text{ lg/kg})}{(40 \text{ lb/cu ft})(35.3 \text{ cu ft/m}^3)} = 0.044 \text{ m}^3 \sim 44 \text{ liters.}$$

The possible power loss through this regenerator can be approximated by the relationship,

$$Q = m\, C_p (T_2 - T_1)\lambda$$

where

m = He mass flow through regenerator, (moles/sec)

C_p = heat capacity of He (5 cal/mole-deg)

T_2 = temperature in He return (360°C)

T_1 = temperature in T_2O absorbant bed (95°C)

λ = heat loss in regenerator; therefore,

$Q = [0.007 \times 10^6 \text{ moles He/sec}][5 \text{ cal/mole He} \cdot \text{deg}][360° - 95°]\lambda$

$Q = 38.7\lambda$ MW. If $\lambda = 25\%$, $Q = 9.7$ MW or 0.2% of the total reactor power lost in this extraction system.

In summary, this tritium removal system based upon the oxidation of tritium to form tritiated water which is absorbed on a molecular sieve dessicant appears successful for the following reasons:

(1) the tritium leakage to the steam is low, 0.8 Ci/day

(2) the He flow required to the dessicant bed is small, 0.7% of the total flow

(3) the size of the dessicant bed is small, 0.044 m^3 and its cost should be low.

These calculations indicate that it is reasonable to assume that the tritium pressure inside the breeder tubes can be kept at 10^{-4}torr either by dilution with flowing helium at 1.5 atm pressure or by the use of a cryogenically pumped vacuum system. For the vacuum system, an off-gas tube of ~1 cm diameter must be connected to each breeder tube.

IV-G-3. Tritium Extraction from Helium Coolant

a. Tritium Escape into Steam System

Before a suitable tritium extraction can be proposed, the magnitude of the problem must be considered. This assessment will consist of (1) limits on the permissible concentration of tritiated water in the steam and (2) estimates of the potential release of tritium from the reactor to the steam system. Then, suitable extraction system(s) can be proposed which will limit the tritium escape to permissible concentrations.

A guide to the permissible tritium release can be obtained from the Environmental Assessment for UWMAK-I.[15] For both UWMAK-I and II, the reactor heat will be transferred from a coolant through a type of steel heat exchanger into a steam generator. Because both reactors are 5000 MW(th) designs, the steam-water flows will be nearly the same and condenser coolant water will circulate through a closed-cycle cooling tower with an assumed 12,000 gpm blowdown.

Nearly 10 Ci/day of T_2O were released in UWMAK-I which would result in a tritium concentration of 1.5×10^{-4} $\mu Ci/cm^3$ the condenser blow-down water. The proposed release from UWMAK-I is 30 times the lowest practical limit. Although the guidelines for fusion reactors have not been set, a diminuation in the tritium concentration from UWMAK-I either by dilution or more efficient tritium extraction appears advisable.

The magnitude of the potential release from UWMAK-II can be assessed based upon the assumption that the permeation of tritium from the breeder tubes to the helium coolant will come to a steady-state with the tritium permeating from the helium to the steam. This flow can be estimated by use of the permeability equation,[16]

$$V_{T_2} = \frac{\lambda \cdot A}{\sqrt{3}\ \sigma} \left[P_2^{1/2} - P_1^{1/2}\right]$$

A = area, cm^2

σ = thickness, mm

V_{T_2} = volume of tritium permeating $(cc(STP)h^{-1})$

λ = permeating constant $[cc\ H_2(STP) \cdot mm \cdot h^{-1} \cdot cm^{-2} \cdot atm^{-1/2}]$

P_2 = tritium partial pressure upstream, (atm)

P_1 = tritium partial pressure downstream, atm, and the term $\sqrt{3}$ is used to adjust the hydrogen diffusion rate for the mass of the tritium atom. For steady-state cases, the volumes of tritium permeating into and out of the helium coolant are equal and the tritium pressure in the steam system is considered to be zero. Rearrangement of the terms, gives the equation for the tritium pressure in the helium coolant, as follows

$$P_{T_{2(He)}}^{1/2} = \frac{A_B \lambda B}{\sigma_B} \left[\frac{A_s \lambda_s}{\sigma_s} + \frac{A_B \lambda_B}{\sigma_B} \right]^{-1} P_{T_{2(B)}}^{1/2}$$

$P_{T_{2(He)}}$ = tritium pressure in helium coolant

$P_{T_{2(B)}}$ = tritium pressure in breeder tubes (10^{-4}torr)

A_B = total wall area of breeder tubes ($3.3 \times 10^8 cm^2$)

λ_B = permeability stainless steel breeder tubes at 600°C [8×10^{-2}]

σ_B = thickness of breeder tubes (0.75 mm)

A_s = total wall area of steam generator tubes ($8.3 \times 10^8 cm^2$)

λ_s = permeability of stainless steel steam generator tubes ~450°C [1.3×10^{-2}]

σ_s = thickness of steam generator tubes (4 mm)

Therefore, $P_{T_{2(He)}} = 9.94 \times 10^{-5}$torr $= 1.3 \times 10^{-7}$ atm

The volume of T_2 permeating into the steam is

$$V_{T_2} = \frac{\lambda_s A_s}{\sigma_s \sqrt{3}} \times \frac{24h}{day} [P_{T_{2(He)}}]^{1/2} = 1.35 \times 10^4 cc(STP)/day$$

$$V_{T_2} = 3.6 \text{ g } T_2/day = 3.6 \times 10^4 \text{ Ci/day}$$

This leakage rate is completely unacceptable compared with the self-imposed guideline of 10 Ci/day; therefore, an extraction system must be introduced in to reduce the tritium concentration in the helium coolant.

The tritium in the helium coolant might be extracted by use of an active metal absorber, such as Zr, Ti or Y, as was accomplished for UWMAK-I. However, no experience is available regarding the stability of these beds in a large gas-cooled system. The active metal surfaces might be rapidly poisoned by impurities in the helium, such as oxygen, nitrogen and carbon dioxide. Excessive oxidation of niobium systems in helium coolant loops has been reported[17] and the free energies of formation of[18] these active metal oxides are much larger than that for niobium oxide. This information tends to confirm the concern for the rapid poisoning of the active metal absorbers.

An extraction system which is not easily poisoned can be provided when oxygen is admitted to the helium system. The radiation present within the helium coolant passageways of an operating reactor should be sufficiently reactive so that the following equilibrium is quickly established (or a catalyst may be used),

$$T_2 + 1/2\ O_2 = T_2O$$

The equilibrium constant for this reaction,

$$k = \frac{P_{T_2O}}{P_{T_2}(P_{O_2})^{1/2}}$$, where P_{T_2O}, P_{T_2} and P_{O_2} are the partial pressure

of the respective species, has been estimated[19] to be $6.3 \times 10^{11}\text{torr}^{-1/2}$ at 525°C, approximately the median temperature of the helium in the blanket.

If the partial pressure of oxygen is maintained at 10^{-2} torr and the T_2O is continuously removed so that its partial pressure is $\sim 10^{-3}$ torr, then the partial pressure of tritium can be calculated to be,

$$P_{T_2} = \frac{P_{T_2O}}{k(P_{O_2})^{1/2}} = \frac{10^{-3}\ \text{torr}}{6.3 \times 10^{11}\text{torr}^{-1/2}(10^{-2}\text{torr})^{1/2}} = 1.6 \times 10^{-14}\text{torr}.$$

If this is the only tritium pressure in the helium coolant to cause permeation, then the tritium leakage to the steam system is only 0.8 Ci/day. Possible effects of O_2 in the helium have been considered by Westerman.(20) This permeation rate could be reduced if the oxide coating in a SS-steam generator reduces tritium diffusion, or if a duplex steam generator tube is developed.

The continuous absorption of T_2O on molecular sieves is proposed in order to maintain the T_2O vapor pressure below 10^{-3}torr. A portion of the helium coolant flows through a regenerator (Fig. IV-G-3) into a molecular sieve bed maintained ~95°C. Such an absorption bed operating at 95°C has an equilibrium vapor pressure of 5×10^{-4}torr (H_2O) when it has absorbed 0.5g H_2O per 100g of dessicant.(21) If the vapor pressure of T_2O on this dessicant is similar to that of H_2O and the dessicant is recycled whenever the vapor pressure of T_2O exceeds 5×10^{-4}torr, then the fraction of helium which must flow through the dessicant can be calculated as follows, (based upon a total helium pressure of 50 atm)

$$\dot{N}_{T_2} = \dot{N}_{He} \left(X_{T_2O_{(in)}} - X_{T_2O_{(out)}}\right)$$

and

$$\dot{N}_{He} = N_{He}\, f/\tau$$

where $\dot{N}_{T_2}$ = accumulation of tritium in helium by permeation through breeder tubes (7.9 g-moles/day)

$\dot{N}_{He}$ = flow rate of He through bed (g-moles/day)

$X_{T_2O_{(in)}}$ = mole fraction of T_2O, into bed (2.632×10^{-8})

$X_{T_2O_{(out)}}$ = mole fraction of T_2O, out of bed (1.315×10^{-8})

N_{He} = total helium in systems (~10^6 moles)

f = fraction He flowing through bed

τ = time for circulation of He through entire system (~1 sec)

therefore,

$$f = \frac{\dot{N}_{T_2} \cdot \tau}{\left(X_{T_2O_{(in)}} - X_{T_2O_{(out)}}\right) N_{He}}$$

$$f = \frac{(7.9 \text{ g-moles } T_2O/\text{day})\ (1\text{sec})}{\left(1.315 \times 10^{-8} \frac{\text{moles } T_2O}{\text{mole He}}\right)(10^6 \text{ moles He})(8.6 \times 10^4 \text{ sec/day})}$$

$f = 0.007 = 0.7\%$ of helium flowing through bed on each cycle through the reactor

COOLANT FLOWS FOR UWMAK-II

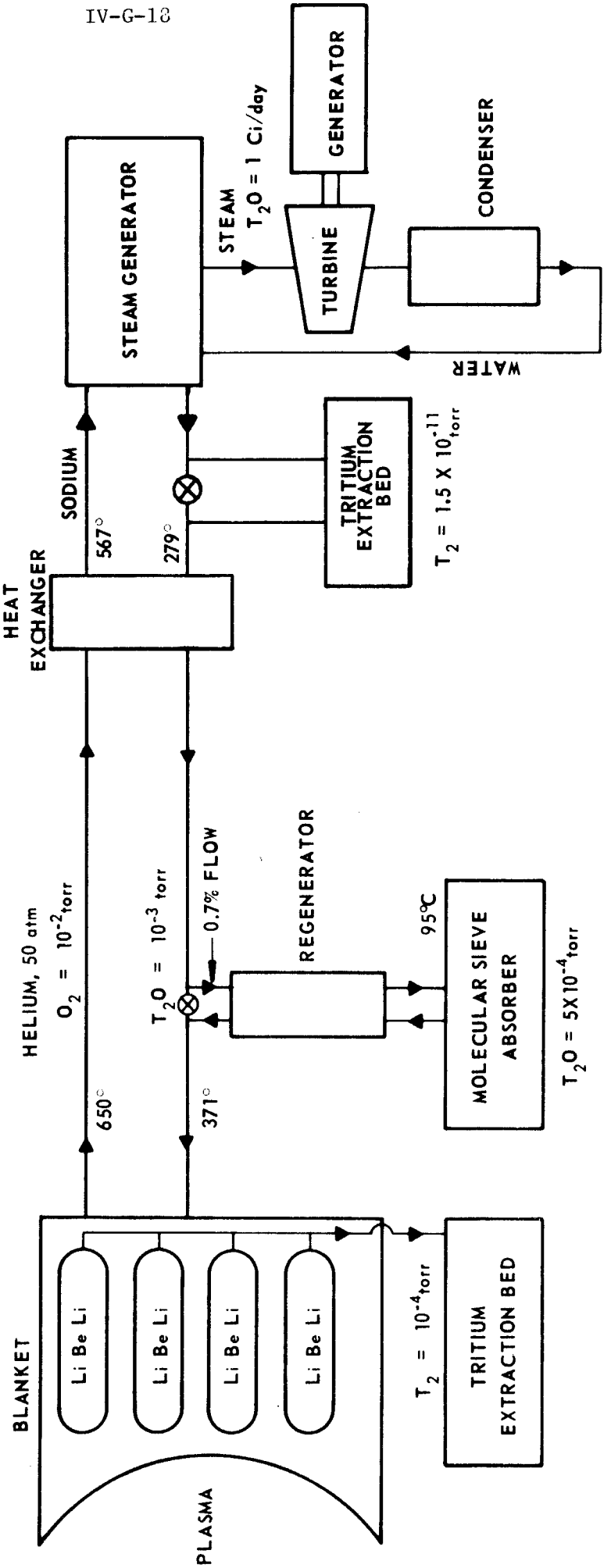

Figure IV-G-3

b. Tritium Permeation Through the Sodium Intermediate Heat Transfer System

The previous discussion was based upon a simple heat transfer system in which the primary helium coolant circulated through the steam generator. This simple configuration was used to assess the tritium extraction system required and the potential tritium release rate to the steam cycle. Heat storage and safety evaluating suggest the desirability to include a sodium intermediate heat transfer system between the helium coolant and the steam generator. The effect of the sodium system up on the tritium release rate to the steam will now be evaluated.

In the helium coolant, the technique which provides for oxidation of tritium to T_2O by the addition of oxygen will be retained so that a low partial pressure of tritium is maintained, i.e., 1.6×10^{-14} torr. If this partial pressure of T_2 were maintained in the sodium, the tritium permeation to the steam would be the same as for the helium-to-steam system, ~1 Ci/day. For several reasons, such as leakage, corrosion, etc., the tritium partial pressure in the helium may rise and its corresponding pressure in the sodium would increase and lead to increased tritium permeation into the steam. In order to limit the tritium partial pressure (and concentration) in the sodium, and retard the amount of hydrogen entering from the steam (which will be discussed later), it is necessary to insert a tritium extraction bed in the sodium system.

Two potentially useful extraction techniques were considered for the application and placed on the sodium return line from the steam generator where the sodium temperature is ~280°C. One technique required further cooling of the sodium to ~115°C and cold-trapping of the NaT which produced a tritium partial pressure[19] of 5.8×10^{-5} torr. Alternatively, the tritium was extracted on a yttrium bed to form YT_2, as utilized in UWMAK-I,[3] which yielded a tritium partial pressure ~1.5×10^{-11} torr at 280°C. The yttrium extraction bed was chosen, therefore, because it produced the lowest tritium pressure and did not require further cooling of the sodium which would impair the thermal efficiency of the power plant. The concentration of tritium in the sodium in only 4×10^{-10} at. fraction, therefore, which is well below the saturation calue, 1.8×10^{-4} at. fraction at 280°C.

An estimation of the tritium permeation through the sodium-steam heat exchanger can be made based upon the following assumptions: The partial pressure of tritium in the sodium upon exit from the yttrium bed is in equilibrium with the YT_2 bed at 280°C, i.e. 1.5×10^{-11} torr, a Sieverts; type relationship[19] exists for the sodium so that the tritium concentration in the sodium is 3.9×10^{-4} at. ppm. This concentration is maintained while the sodium is heated by the helium coolant and passed into the steam generator, which has an average sodium temperature of 423°C. At this temperature, the tritium partial pressure in the sodium is 1.25×10^{-11} torr and provides the driving force for tritium permeation through the steam generator tubing. The permeation of tritium into the steam can be calculated from the realtionship,[19]

$$\Phi = \frac{\sqrt{3} \times 0.65 \times 10^{-2} \text{ g·cm} \times A}{\text{day·cm}^2\text{·torr}^{1/2} \times \sigma} \left[P_2^{1/2} - P_1^{1/2}\right] \exp - \frac{16,\ \text{cal/mole}}{RT}$$

where A = total surface area of the steam generator tubing, $1.02 \times 10^{8}\ cm^{2}$

σ = wall thickness of the tubing, 0.24 cm

P_2 = tritium pressure in the sodium, 1.25×10^{-11} torr

P_1 = tritium pressure in the steam, zero

T = avg. steam generator temp., 400°C.

Based upon the use of average temperatures for the heat exchangers, $\Phi = 1.17 \times 10^{-4}$ g/day or 1.2 Ci.day. The goal of $\leq$ 1 Ci/day tritium release to the steam appears to be obtainable.

An additional hydrogen isotope permeation reaction must be considered, however, in steam power systems, namely the diffusion of hydrogen from the steam into the sodium. The hydrogen pressure in the steam exists from the equilibrium,

$H_2 + 1/2\ O_2 = H_2O$, which may be catalyzed by the oxidation of the steel heat exchanger. Although the equilibrium constant[19] for this reaction is very large in favor of the formation of water, at the steam temperature (500°C), i.e.

$$K = P_{H_2O}/P_{H_2} \times P_{O_2}^{1/2} = 6.3 \times 10^{11}\ \text{torr}^{-1/2},$$

the pressure of the steam in the superheater is high, 3690 psia; consequently, the partial pressure of hydrogen is significant, as shown by the following calculation:

because, $P_{O_2} = 1/2\ P_{H_2}$,

$$K = \frac{P_{H_2O}}{P_{H_2} \times P_{O}^{1/2}} = \frac{P_{H_2O}}{P_{H_2}(1/2\ P_{H_2})^{1/2}} =$$

$$P_{H_2} = \left[\frac{\sqrt{2}\ P_{H_2O}}{K}\right]^{2/3} = \left[\frac{\sqrt{2} \times 3690\ \text{psia} \times 760\ \text{torr/atm}}{15\ \frac{\text{psia}}{\text{atm}} \times 6.3 \times 10^{11}\ \text{torr}^{-1/2}}\right]^{2/3}$$

$$\underline{P_{H_2} = 5.6 \times 10^{-5}\ \text{torr.}}$$

The independent movement of hydrogen isotopes in opposite directions through a metal membrane has been confirmed;(25) consequently, it is reasonable to expect that hydrogen will permeate through the steel steam generator into the sodium at the same time that tritium is permeating out of the sodium into the steam. Based upon the hydrogen partial pressure, 5.6×10^{-5} torr, in the steam and the size and temperature of the superheater, nearly 0.16 moles H_2/day, permeates into the sodium plus an additional 0.11 moles H_2/day, through the pre-heater at a lower hydrogen pressure, 2.44×10^{-5} torr. Consequently, nearly 0.27 moles/day or 2.2×10^{21} atoms/sec of hydrogen enter the sodium. At the same time, approximately 1.78×10^{14} atoms/sec of tritium permeates from the helium into the sodium, based upon the pressure of tritium in the helium, 2×10^{-14} torr. If symbols are defined as follows,

S^T_{Na} = source term for tritium into the sodium, 1.78×10^{14} atoms/sec

S^H_{Na} = source term for hydrogen into the sodium, 2.2×10^{21} atoms/sec,

then is it noted that the source term for hydrogen is much larger then for tritium; because the yttrium bed can hardly distinguish between hydrogen and tritium atoms the composition of the hydrogen isotopes on the yttrium bed as well as the sodium upon exit from the bed will be in the ratio of S^T_{Na}/S^H_{Na}. Both hydrogen isotopes follow a Sieverts' relationship, i.e.

$$C_H = K_s P^{1/2}_{H_2}$$

where C_H = concentration of hydrogen in the sodium

K_s = Sieverts' constant

P_{H_2} = hydrogen partial pressure over YH_2, 1.5×10^{-11} torr (280°C).

The partial pressure of T_2 over the sodium can be estimated from its composition in the sodium, i.e.

$$C_T = K_s P^{1/2}_{T_2} \quad \text{where,}$$

C_T = composition of tritium in sodium = $S^T_{Na}/S^H_{Na}\ C_H$

K_s = Sieverts' constant

P_{T_2} = tritium partial pressure.

Substitution of these equations gives,

$$K_s P^{1/2}_{T_2} = C_T = \frac{S^T_{Na}}{S^H_{Na}} C_H = \frac{S^T_{Na}}{S^H_{Na}} (K_s P^{1/2}_{H_2}).$$

Because K_s for tritium and hydrogen are nearly the same, the above equation reduces to,

$$P_{T_2}^{1/2} = S_{Na}^{T}/S_{Na}^{H} P_{H_2}^{1/2}$$

This relationship shows that the previous calculation for the tritium permeation from the sodium to the steam, i.e. 1.2 Ci/day, should be multiplied by the ratio S_{Na}^{T}/S_{Na}^{H} so that

$$\phi = 1 \times 10^{-7} \text{ Ci/day}$$

This analysis agrees with some recent tritium transport measurements[26] from EBR-II in which it was shown that the tritium permeation from the hot reactor vessel, piping, etc., is nearly ten times greater than the leakage to the steam system because of the hydrogen "swamping" of the tritium in the sodium.

Based upon this latter information, the yttrium bed in the sodium will need to contain only 24 grams in order to accomodate all of the hydrogen permeating per day from the steam system. Also, some of their hydrogen will permeate back into the helium coolant, eventually into the main tritium extraction system and isotopically dilute the tritium in this system. These results suggest that hydrogen isotopic separation system will be required for all of the products collected on the several tritium extraction beds.

A schematic diagram of the reactor heat transfer cycle, Figure IV-G-3, indicates the extraction beds required for the tritium breeding and recovery system. The parameters for this system are given in Table IV-G-2. The tritium inventories for the various components of this system are summarized in Table IV-G-3.

IV-G-4. Divertor Tritium Recovery System

The tritium and deuterium leakage from the plasma is very large, nearly 950 g T/H and 630 g D/h. These very energetic fuel particles will impinge upon a flowing lithium surface which will absorb their kinetic energy. The liquid lithium serves also as a pump for approximately 96% of the (D+T) particles. Based upon the lithium flow rate across the divertor plates, 4.94×10^6 kg/h, the combined (D+T) concentration will increase nearly 1×10^{-6} at. fraction during each pass of the lithium through the divertor. This lithium at 325°C transits a sodium-cooled heat exchanger which cools the lithium to 200°C. A knowledge of the solubility of Li(D+T) in liquid lithium at 200°C is of importance because of the proposed high concentration of these fuel particles in the lithium.

In the absence of experimental data, two methods are available for an estimation of the solubility of LiH in Li. One method combines the Li-H plateau pressures as a function of temperature with the Sieverts' relationship for the solubility of hydrogen in liquid lithium as a function of hydrogen pressure. When these relationships which are measured at high temperatures are extrapolated to lower temperatures, 195°C, the solubility of LiH[27] is calculated to be 1.2×10^{-2} at. fraction H in Li, consequently, the hydrogen isotope concentrations in the divertor lithium should not be a problem as their combined concentration

is much below this saturation value. Conversely, Messer's data[28] indicate that at temperature below the monotectic temperature, 685°C, the solubility of LiH in Li follows a different relationship, which indicates that LiH will precipitate when the concentration exceeds 5×10^{-5} at. fraction H at 200°C. If this latter value is correct, then the lithium in the divertor will be saturated after 50 transits through the divertor and Li(D+T) would precipitate in the intermediate heat exchanger. For this reason a highly efficient extraction system is required in order to remove the hydrogen isotopes from the lithium in the divertor.

A cold-trap for the removal of the Li(D+T) from the Li is not practical because it would need to operate at 190-195°C which is too close to the exit temperature, 200°C, from the intermediate heat exchanger. A yttrium metal bed is suggested, therefore, as was utilized in the sodium system of the heat transfer cycle. The yttrium bed was placed initially on the high temperature stream, 320°C, of the lithium as it came from the divertor, because the rate of reaction and the diffusion of the hydrogen isotopes into the yttrium would be more rapid than at 200°C, the exit temperature from the heat exchanger. Although the hydrogen pressure above YH_2 is low, 3.2×10^{-10} torr, at 320°C, the concentration of hydrogen in the lithium would be 4×10^{-5} at. fraction, which is nearly the saturation value at 200°C, noted above from Messer's data. For this reason, the yttrium bed was placed on the exit from the heat exchanger, although it is recognized that the temperature, 200°C, may be too low for equilibrium operation of the bed and needs experimental verification. Based upon a 200°C operation temperature for the yttrium bed, the hydrogen isotope pressure is 2.7×10^{-5} torr and the concentration of these isotopes in the lithium is approximately 1.2×10^{-6} at. fraction. During one transit of the divertor, the lithium receives an additional 1×10^{-6} at. fraction (D+T) so that a combined concentration of 2.2×10^{-6} at. fraction (D+T) reaches the heat exchanger. Precipitation of Li(D+T) in the cold end of the heat exchanger should not occur as the hydrogen isotope concentration is 1/25 of the saturation value at 200°C.

The amount of yttrium required to absorb one day's accumulation of D+T, and from Y(D+T)2 is calculated to be,

$$\text{wt Y} = \frac{\text{at}\cdot\text{wt}\cdot\text{Y}}{2} \text{ [g}\cdot\text{at. D+T/day]} = 676 \text{ kg}$$

At an assumed efficiency of 20%, the total weight of yttrium required is 3400 kg.

The tritium permeation from the divertor lithium-to-sodium-steam systems would be the same as for the UWMAK-I system.[16] Because the temperatures are low, the permeation rates are small, only 2×10^{-4} Ci/day of tritium would be transferred to this steam system which could be used to heat the feed water in the borders of the power plant.

The tritium inventory in the various components of the divertor system are included in Table IV-G-3.

Table IV-G-2

Parameters of Tritium Breeding and Recovery Systems For UWMAK I and II

	UWMAK II	UWMAK I
Coolant	Helium (10^6 moles)	Lithium (2×10^8 moles)
T_2 Breeder	$^6LiAlO_2$	Li
Li in Blanket, kg	9×10^4 (a)	1.4×10^6
Coolant Temperature, Max. (°C)	650	483
Tritium Inventory in Breeder (g)	725 (b)	7000
Tritium Pressure in Breeding Zone (torr)	10^{-4}	5×10^{-10}
Tritium pressure for diffusion into steam (torr)	1.25×10^{-11}	3.8×10^{-11}
Tritium Generation Rate, g/sec	1×10^{-2}	1.22×10^{-2}
Additive to Coolant	0_2 (10^{-2} torr)	none
Tritium Species in Coolant for Recovery	T_2O	T(Li)
Extraction Bed	Molecular Sieves	Yttrium Metal
τ (coolant transit time) sec	1	254
Fraction coolant to bed	0.7%	4%
Intermediate Heat Exc.	sodium	sodium
Tritium Leakage to steam, Ci/day	1.0	10
Heat Exchanger, coolant - steam	SS	SS
Area, cm^2	1.0×10^8	3.2×10^8
Thickness, mm	2.40	1.65
Temperature, avg. °C	400	296

(a) Initial charge only, does not include replacement or reflect the fact that it is enriched to 90% Li-6.

(b) Minimum, could greatly exceed this if excessive sintering were to take place.

Table IV-G-3

Equilibrium Tritium Inventories for UWMAK-I and II

Location	UWMAK (grams)	
Breeder	II	I
Lithium Bearing Material	725 (a)	7,000
Coolant External to Breeding zone	0.2	1,650
Recovery Beds (12 hr cycle)	420	500
total in breeder system	1145	9,150
Divertor		
In Lithium	8	8
Recovery bed (4 hr cycle	3500	1,230
Vacuum system (4 hr cycle)	125	50
total in divertor system	3658	1,288
Fuel System		
(1 day supply)	12,850	8,400
total in reactor area	17.7 kg	18.8 kg

(a) minimum value if no sintering takes place.

References for Section IV-G

(1) "Tritium Technology Related to Fusion Reactor Systems" Symposium, Monsanto Research Corp, October, 1-2,(1974).

(2) T. B. Rhinehammer and P. H. Lamberger, Tritium Control Technology, USAEC Document, WASH-1269 (Jan.1974).

(3) B. Badger, M. A. Abdou, R. W. Boom, R. G. Brown, T. E. Cheng, R. W. Conn, J. M. Donhowe, L. A. El-Guebaly, G. A. Emmert, G. R. Hopkins, W. A. Houlberg, A. B. Johnson, J. H. Kamperschroer, D. Klein, G. L. Kulcinski, R. G. Lott, D. G. McAlees, C. W. Maynard, A. T. Mense, G. R. Neil, E. Normand, P. A. Sanger, W. E. Stewart, T. Sung, I. Sviatoslavsky, D. K. Sze, W. F. Vogelsang, L. J. Wittenberg, T. F. Yang and W. D. Young, "UWMAK-I, A Wisconsin Toroidal Fusion Reactor Design", UWFDM-68, University of Wisconsin-Madison, (1974).

(4) T. A. Coultas, J. E. Draley, V. A. Maroni and R. A. Krakowski, "An Environmental Inpact Study of a Reference Theta-Pinch Reactor (RTPR)", Proceedings of the First Topical Meeting on the Technology of Controlled Nuclear Fusion, CONF - 740402, USAEC (1974).

(5) J. M. Smith and R. S. Gilbert, "Tritium Experience in Boiling Water Reactors," in Tritium, Messenger Graphics, pp 57-68, Phoenix, Arizona, (1973).

(6) W. Jost, Diffusion in Solids, Liquids and Gases, p. 60, Academic Press, New York (1960).

(7) E. W. Roberts and J. P. Roberts, Bull. Soc. Franc. Ceram., (1967) No. 77, pp. 3-13.

(8) V. K. Hauffe and O. Hoeffgren, Berichte Bunsen-Gesell, Physikal. Chem., 74, 537 (1970).

(9) P. M. Abraham, J. Davis, C. W. Pennington, T. S. Elleman and K. Verghese, "Diffusion of Gases in Solids; Tritium Diffusion in Stainless Steel, Zircaloy-2 and Niobium;" ORO-3508-9, North Carolina State University (1973).

(10) K. T. Scott and L. L. Wassell, Brit. Ceramic Soc. Proc., (1967), No.7, pp. 375-380.

(11) J. Powell, A. Aronson, P. Bezler, F. Miles and W. Winsche, "Minimum Activity Blankets Using Aluminum Structure", Proc. First Topical Meeting on the Technology of Controlled Nuclear Fusion, op. cit.

(12) D. G. Thomas and J. J. Lander, J. Chem. Phys., 25, 1136 (1956).

(13) R. G. Hickman, "Some Problems Associated with Tritium in Fusion Reactors", Proc. Tech. Controlled Thermonuclear Fusion and Eng. Aspects of Fusion Reactors, CONF - 721111, USAEC (1974).

(14) S. Dushman, Scientific Foundation of Vacuum Technique pp. 90-100, Wiley, New York,(1949).

(15) P. G. Lorenzini, "Environmental Assessment of UWMAK-I", private communication, (1974).

(16) "UWMAK-I" op. cit, Tritium Consideration Chapter.

(17) J. H. DeVan, "Compatibility", Fusion Reactor First-Wall Materials, WASH - 1206, USAEC (1972).

(18) K. A. Gschneidner, Jr., N. Kippenhan and O. D. McMasters, "Thermochemistry of the Rare Earths", IS-RlC-6, Iowa State University (1973).

(19) V. A. Maroni, "An Analysis of Tritium Distribution and Leakage Characteristics for Two-Fusion Reactor Reference Designs", CEN/CTR/TM-9, Argonne National Laboratory (1974).

(20) R. E. Westerman, "Compatability of Stainless Steel with Oxygen - Contaminated Helium" UWFDM-117, University of Wisconsin, Oct. (1974).

(21) Linde Molecular Sieves Data Sheet, Union Carbide Corporation, New York, (1974).

(22) R. K. McGreary, J. Am. Ceramic Soc., 44, 513 (1962).

(23) W. A. Stark, Jr., Nuclear Tech., 26, 35 (1975).

(24) R. B. Holden, Ceramic Fuel Elements, pp. 63-75, Gordon and Breach, New York, 1966.

(25) F. J. Smith, J. D. Redman, R. A. Strehlow, in "Tritium Tech. Related to Fusion Reactors," Monsanto Res. Corp. Oct. 1974.

(26) R. Kumar, "Tritium Transport in an LMFBR," ANL-8089, Argonne National Laboratory, 1974.

(27) K. Natesan and D. L. Smith, Nuclear Technology, 22, 138 (1974).

(28) C. E. Messer, et al , J. Am. Chem. Soc., 62, 220 (1958).

IV-H. Radiation Damage

IV-H-1. Introduction

The general effects of D-T neutron and charged particle irradiation to CTR materials have been discussed in several recent papers and conferences.[1-6] A previous review in UWFDM-68[7] outlined the problems expected in that reactor and the reader is referred to that report for more detail on how the various forms of radiation interact and effect the solid components of a fusion device. No attempt will be made to duplicate that information here other than to say that we have essentially all of the problems identified in UWMAK-I in addition to a few which are unique to solid breeding blankets. Outside of the plasma physics problems, it still appears that the most severe CTR technological problem that must be solved before commercialization of fusion power is the degradation of the materials performance in the environment of neutrons, charged particles and photons released from the D-T reaction.

IV-H-2. The Scope of Radiation Damage Problems in UWMAK-II

The radiation damage problems in UWMAK-II can be broken up into seven convenient categories, working from the plasma outward:

1. Curtain (carbon)
2. Structure (316 SS)
3. Breeder ($LiAlO_2$)
4. Neutron Multiplier (Be)
5. Reflector (carbon)
6. Shielding (Pb, B_4C)
7. Magnet Materials (Cu, NbTi, mylar insulation)

The operating environments for each of these areas is given in Table IV-H-1.

The carbon curtain, which is closest to the plasma experiences the most severe environment in terms of temperature and neutron bombardment. Its temperature will vary from ~1200°C during the burn to ~650°C during the recycle period between burns. The curtain will also accumulate neutron fluences of ~$2.6 \times 10^{21} cm^{-2} yr^{-1}$ (E>13.5 MeV) and ~$1.1 \times 10^{22} cm^{-2} yr^{-1}$ (E>1 MeV) at the upper temperature. The stainless steel structure will operate at a much lower temperature (T<660°C) and will be subject to a wide variation of fluences in the blanket, shield and toroidal field magnets.

The breeder material will also be subject to high fluences of neutrons as well as high internal heating rates (3-14 watts/cm^3). Large temperature gradients will exist across the lithium ceramic rod, operating at 640-1100°C resulting in thermal gradients of ~225°C/cm. Similar neutron fluences will be incident on the Be multiplier but the thermal gradients should be much less (<5°C/cm) because of the much higher thermal conductivity of Be.

The graphite reflectors will suffer moderate damage in the temperature range of 600-700°C while accumulating neutron fluences of up to $3.7 \times 10^{21} n/cm^2/yr$ (E>1 MeV). Dimensional instability is the major concern here.

Table IV-H-1

Summary of the Environment for the UWMAK-II Solid Materials

Function	Material	Distance From First Wall-cm	Temperature Range °C	Neutron Fluence $n/cm^2/yr \times 10^{21}$ (a) > 13.5 MeV	Neutron Fluence > 1 MeV	Neutron Fluence Total	Maximum Nuclear Heating Watts/cm^3	Other
Curtain	C	-2	650-1200	2.4	11	14		1200°C during burn, 650°C during recycle
Structure	316 SS	0-89 (Blanket)	450-660	0.0017-2.4	0.14-11	0.18-14	12	4500 cycles yr^{-1}, 5 watts/cm^2
		89-189 (Shield)	50-200	1.3×10^{-8}-1.7×10^{-3}	1.6×10^{-6}-0.14	1.8×10^{-6}-0.18	0.08	High pressure He cooling
		204-302 (Magnet)	-269	$<1.3\times10^{-8}$	$<1.6\times10^{-6}$	$<1.8\times10^{-6}$	2×10^{-4}	Liquid He Temperature
Breeder	$LiAlO_2$	2-4.5	640-1100	1.5-1.8	9.8-10	12-13	9-14	Large thermal gradient across breeder pins
		23-32	690-950	0.22-0.37	3.7-5.4	4.8-7.1	3-10	Large thermal gradient across breeder pins
Neutron Multiplier	Be	5-22	580-615	0.39-1.3	5.4-9.8	7.1-9.8	2-4	
Reflector	C	32-70	655	5.8×10^{-3}-0.22	0.35-3.7	1.0-4.8	0.3	
Shielding	Pb,B_4C,SS	89-189	50-200	1.3×10^{-8}-1.7×10^{-3}	1.8×10^{-6}-0.16	1.8×10^{-6} - 0.18	0.08	High pressure He cooling
Magnet Materials	Cu,NbTi	204-302	-269	$<1.3\times10^{-8}$	$<1.8\times10^{-6}$	$<1.8\times10^{-6}$	2×10^{-4}	Warm up to room temperature every few years

(a) 80% Plant Factor

The damage to the Pb in the temperature range of 50-200°C at fluences of up to 1.6 x 10^{20} n/cm^2/yr is not expected to be severe, especially since the Pb is not structural material. However, one point which was not investigated here and should be looked into in the future is the neutron induced swelling in Pb in this temperature fluence range. The operating environment for the B_4C is essentially the same as for UWMAK-I except that the UWMAK-II shield is thicker and provides more attenuation of neutron damage. The neutron flux leaking to the UWMAK-II magnet is far less than that of UWMAK-I and hence, the damage was found to be much smaller, almost to the point of no concern.

We will provide more quantitative detail in the following sections on the level of damage to be expected in each of the items listed in Table IV-H-1. However, we will not go into the qualitative detail of damage mechanisms for stainless steel, B_4C, and the magnet materials as that has been adequately covered in UWFDM-68, Volume I.(7)

IV-H-3. Bulk Radiation Damage to Carbon Curtain*

The neutron spectrum to the carbon curtain is given in Table IV-H-2 along with the displacement cross sections determined by Morgan.(8) This information reveals that the carbon curtain will suffer radiation damage equal to 8.6 displacements per atom per year (assuming a 80% plant factor). This corresponds roughly to 1.2 x 10^{22}n/cm^2 per year from a fission reactor.(9)

Carbon is also subject to internal helium atom formation via the following reactions.

$$^{12}C(n,\alpha)^{9}Be \qquad \text{(reaction 1)}$$

$$^{12}C(n,n')3He^{4} \qquad \text{(reaction 2)}$$

The cross sections for both reactions are listed in Table IV-H-3. The appropriate calculations reveal that 2211 appm (of helium) is produced per year of operation. Approximately 18% of that helium comes from reaction 1 and 82% from reaction 2. However, we were forced to use the full (n,n') cross section (excluding the first excited state) for reaction 2 because the (n,n') cross section to higher exctied states is not given separately from the (n,n')3He^4 reaction. Hence, our helium production numbers represent a maximum and if future neutronic measurements can determine the exact value of the (n,n')3He^4 cross section, the helium production rates may be reduced.

Two other calculations on carbon were performed: radioactivity production via the reaction

$$^{13}C(n,\gamma)^{14}C$$

and the afterheat resulting from the decay of the ^{14}C. The half life of the ^{14}C is ~5600 years and it decays by weak beta emission (E_{max} ~156 keV). The production rate of carbon-14 is 0.108 appm per year which corresponds to

---

* Surface effects have been covered in Chapter II-A-3.

Table IV-H-2

Data for Displacement Damage in Carbon Curtain

Neutron Group No.	Carbon Displacement Cross Section(8) barns	$n/cm^2/sec$*		dpa/yr/energy group
1	1254.2	9.53	E13	3.77
2	1378.1	4.67	E12	0.20
3	1364.3	2.30	E12	0.099
4	1014.8	2.66	E12	0.085
5	1107.2	2.88	E12	0.10
6	1038.0	2.31	E12	0.076
7	1703.8	1.94	E12	0.10
8	788.8	1.97	E12	0.049
9	996.5	1.94	E12	0.061
10	829.7	1.89	E12	0.049
11	914.7	1.82	E12	0.053
12	1047.2	1.85	E12	0.061
13	1512.3	1.91	E12	0.091
14	1518.6	1.99	E12	0.095
15	1855.2	2.10	E12	0.12
16	1100.8	2.37	E12	0.082
17	1427.5	2.66	E12	0.12
18	844.6	3.56	E12	0.095
19	867.8	1.37	E13	0.38
20	915.5	1.88	E13	0.54
21	985.4	1.81	E13	0.56
22	1013.3	2.00	E13	0.64
23	997.1	2.04	E13	0.64
24	941.9	1.77	E13	0.53
25	863.0	2.18	E13	0.59
26	763.0	1.68	E13	0.40
27	647.1	1.59	E13	0.33
28	560.2	1.85	E13	0.33
29	547.0	3.27	E13	0.56
30	358.0	2.81	E13	0.32
31	193.5	2.84	E13	0.17
32	99.4	2.66	E13	0.083
33	49.5	2.66	E13	0.041
34	24.6	2.22	E13	0.017
35	12.0	1.65	E13	0.0062
36	5.8	1.36	E13	0.0025
37	2.8	1.03	E13	0.00091
38	1.4	7.27	E12	0.00032
39	0			10.8 dpa/year
40	0			
41	0			or 8.64 dpa/year (80% plant factor)
42	0			
43	0			
44	0			
45	0			
46	0			

* Instantaneous flux for 1.16 MW/m^2, E13 = x 10^{13}

Table IV-H-3

Data for Calculating Helium Production Rates in the UWMAK-II Carbon Curtain

Neutron Group No.	Neutron Flux/Group $n/cm^2/sec$ (a)		$^{12}C(n,\alpha)^{9}Be$ barns	$^{12}C(n,n')3He^{4}$ barns (b)	appm He/year per group
1	9.53	E13	0.143	0.711	2569
2	4.67	E12	0.164	0.546	105
3	2.30	E12	0.185	0.342	38.1
4	2.66	E12	0.140	0.176	27
5	2.88	E12	0.126	0.068	18
6	2.31	E12	0.0464	0.015	4
7	1.94	E12	0.0523	0.0006	3
8	1.97	E12	0.0033		2
9	1.94	E12	0.0006		0.04
				Total/year	$\cong$ 2764
				or	2211 (80% plant factor)

(a) For 1.16 MW/m^2, E13 = x 10^{13}

(b) 3 times the (n,n') cross section excluding the inelastic cross section to the first excited level.

$\sim 4.1 \times 10^4$ dps/cm^3 after one year of irradiation. This is equal to ~1.4 micro curie per cm^3 of carbon curtain. Assuming 1.4×10^6cm^3 of curtain in UWMAK-II, shows that the total radioactivity produced in the carbon curtain after 1 year of irradiation is ~2 curies! (therefore, the impurities in the carbon will undoubtedly be the determining factor in total radioactivity). The afterheat associated with the above radioactivity is ~1.3 milliwatt.

The major question now becomes what will the displacement damage and high helium production do to the carbon curtain at 1200°C? This is a difficult question because, to our knowledge, no carbon cloth has been irradiated, even in fission reactors, to fluences of 10^{22}n/cm^2. There is also very little information on carbon or graphites of any kind at 1200°C and 10^{22}n/cm^2. It is risky to extrapolate the behavior of solid graphite to small fibers formed in a completely different manner, However, to illustrate the problems that might be faced, we will use information gathered together by Gray and Morgan.(9) They have conservatively set lifetime of the graphite equal to the time required for the graphite to go through its initial shrinkage phase and then expand back to its original dimension. The actual lifetime would be higher than this because one could allow some expansion to take place, especially in the weave structure.

The data used by Gray and Morgan is shown in Figures IV-H-1 and IV-H-2. The length change for two representative bulk graphites, Type NC8 and Type 9640, are shown as a function of irradiation temperature and equivalent full power days in UWMAK-II. The conversion from the actual fission neutron data to full power days at 1.16 MW/m^2 is, 1 full power day = 4.2×10^{19}n/cm^2 (fission).* The full power day limitations on the two types of graphite are given in Table IV-H-4. From this information it may be inferred that irradiation in the 1150-1350°C temperature range would give a minimum lifetime of 340 full power days for the NC8 graphite and 320 full days for the Type 9640 graphite. However, the slope of the length change curves with exposure time is shallow enough that less than 5-10% expansion may occur after 584 full power days, a time which is equivalent to 2 years at an 80% plant factor. Since the first walls will have to be changed after that time in any case, we feel that a two year lifetime on the carbon curtain at 1200°C is reasonable. It should be pointed out that if the cloth acts similar to the data in Figures IV-H-1 and IV-H-2, a 30 year lifetime (8760 full power days) is probably out of the question.

The uncertainty of the carbon cloth lifetime points out some critical experiments that could be performed in the near future in fission reactors. However, it should be noted that fission reactor experiments cannot duplicate the high helium contents. We do not know how some 5500 appm of helium in the carbon after 2 years will effect the properties.

---

* This conversion only applies to the carbon curtain. Different values should be used for carbon farther back into the blanket.

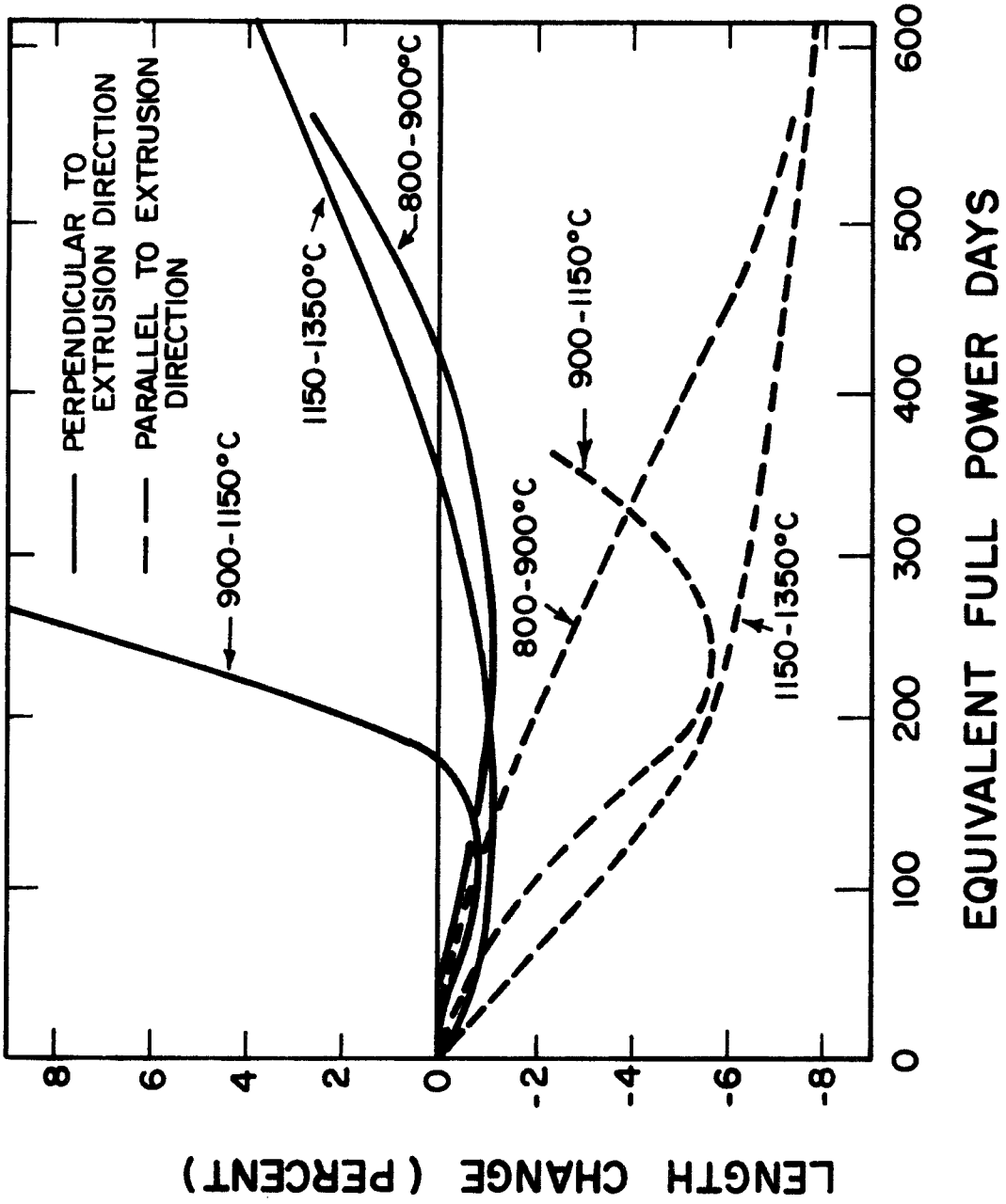

FIGURE IV-H-1 - Length Changes of Type NC8 Graphite [9]

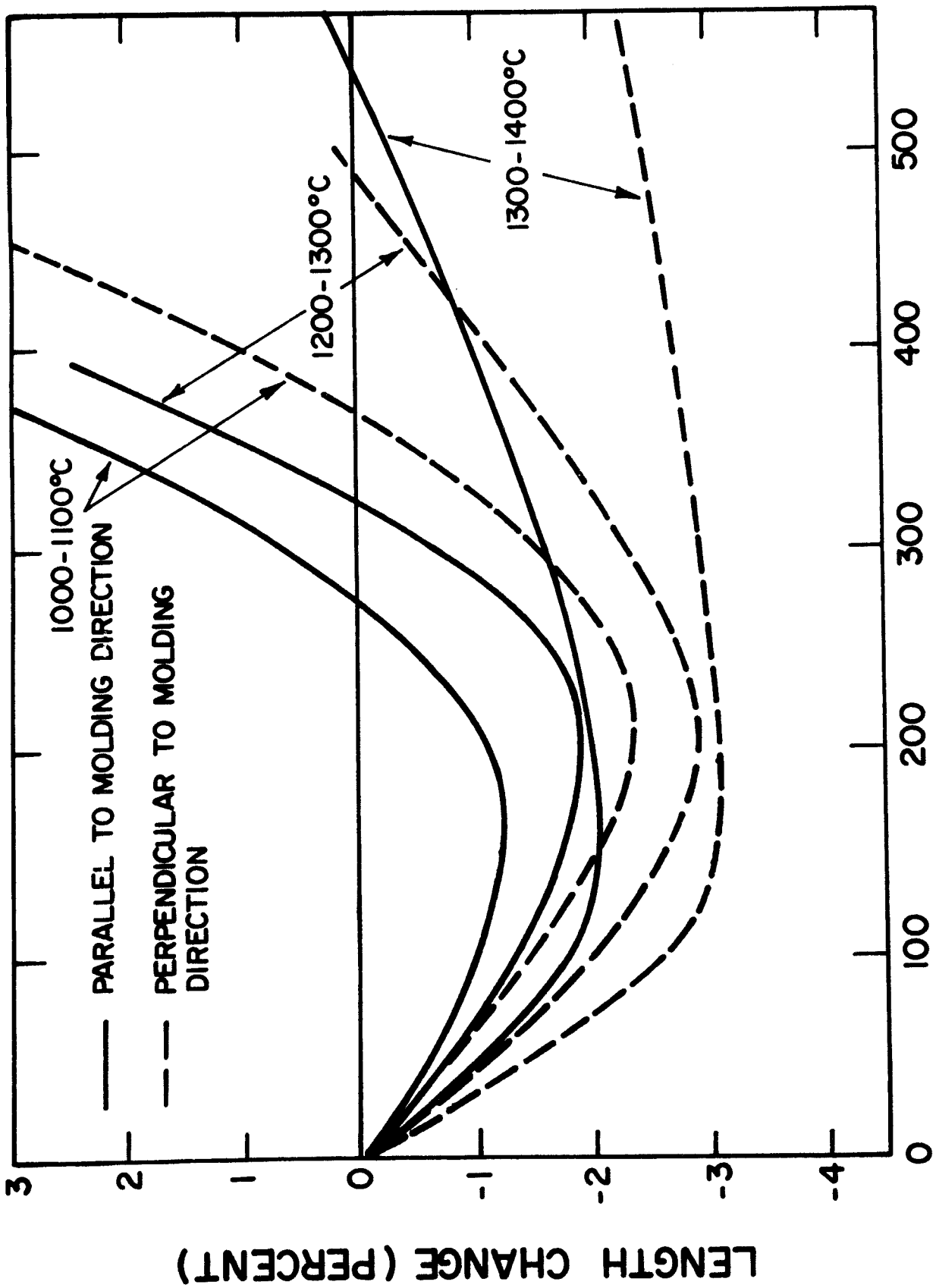

FIGURE IV-H-2 - Length Changes of 9640 Type Graphite [9]

Table IV-H-4

Minimum Expected Lifetime of Nuclear Graphite[a]

	Full Power Days[b]			
	Type NC8		Type 9640	
Temperature °C	Parallel[c]	Perpendicular[c]	Parallel[d]	Perpendicular[
800-900	>615	415		
900-1150	~400	120		
1000-1100			270	370
1150-1350	>615	340		
1200-1300			320	490
1300-1400			540	>570

(a) Approximate time required for graphite to pass through the initial shrinkage phase and return to its original dimensions.

(b) 2 years operating at 80% plant factor is 584 days

(c) To extrusion direction

(d) To molding direction

IV-H-4. Radiation Damage to 316 Stainless Steel Structural Material

There are three primary measures of radiation damage to metals in fusion reactors:

- . displacement of atoms from their equilibrium position
- . transmutation of the atoms from one element to another, sometimes associated with the production of gas atoms.
- . sputtering of atoms from the surface of the metal

These primary effects of irradiation can sometimes lead to secondary responses in the metal such as

- . production of voids
- . production of bubbles and blisters
- . increase in yield strength
- . decrease in ductility
- . change in creep rates

The details of these processed for 316 SS have been reviewed elsewhere,[7] only the information that pertains directly to 316 SS in UWMAK-II will be quoted here.

IV-H-4-a. Displacement and Gas Production Rates in UWMAK-II

The displacement cross section used for this work has been derived elsewhere[10] and is given in Table IV-H-5. Neutron spectral information, as described earlier in this chapter was used to calculate the displacement and helium gas production rates as a function of distance from the first wall. The results are summarized in dpa/year and appm He/year for 20 positions from the first wall to the inside surface of the toroidal field magnets (Table IV-H-6 and Figure IV-H-3). The composition of the 316 SS used here is given in Table IV-H-7.

Table IV-H-5

Displacement Cross Sections Used For 316 SS Damage Calculations in UWMAK-II (10)

Neutron Energy Group	Cross Section-Barns	Neutron Energy Group	Cross Section-Barns
1	2226	23	394
2	2078	24	376
3	1992	25	297
4	1955	26	193
5	1913	27	198
6	1904	28	182
7	1897	29	122
8	1848	30	70.9
9	1763	31	79.3
10	1702	32	26.4
11	1661	33	15.7
12	1621	34	5.41
13	1559	35	3.63
14	1491	36	0.97
15	1409	37	0.143
16	1376	38	0.203
17	1296	39	0.291
18	1274	40	0.423
19	1072	41	0.615
20	791	42	0.887
21	631	43	1.29
22	468	44	1.89
		45	2.71
		46	5.31

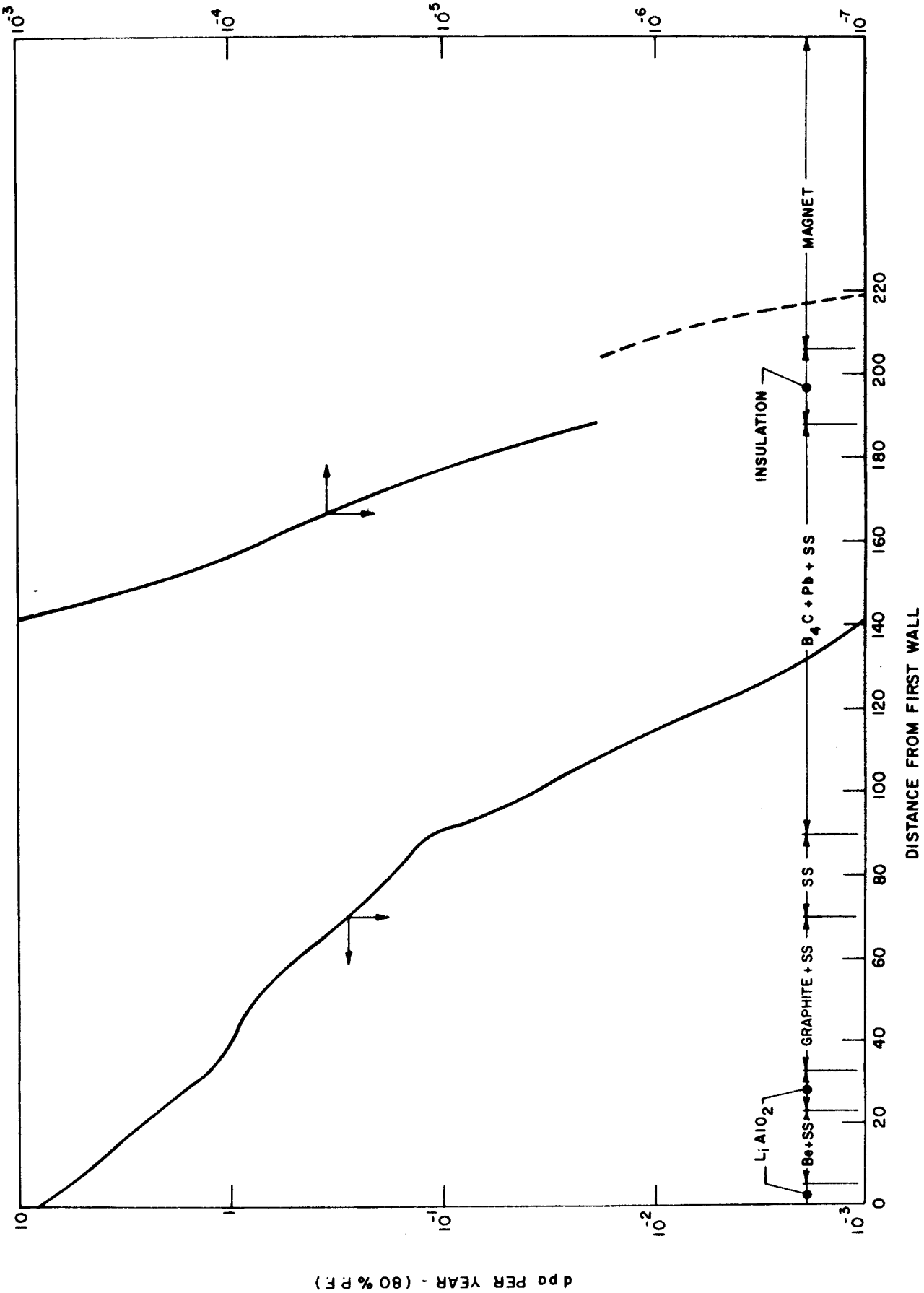

FIGURE IV-H-3 - Displacement Rate in 316 Stainless Steel in UWMAK-II Blanket and Shield

Table IV-H-6

Summary of Displacement Rates and Helium Gas Production in 316 SS as a Function of Distance from the First Wall of UWMAK-II (1.16 MW/m^2, 80% Plant Factor)

Interval	Distance From First Wall-cm	Zone	dpa/yr	appm He/yr[b]	T_{min} °C	T_{max} °C
3	0	First Wall	8.58[a]	187[b]	450	567 (c)
6	1.5	First Wall	7.4	154	450	567 (c)
9	3	I-$LiAlO_2$ (middle)	6.71	133		593 (d)
13	5	Be-$LiAlO_2$ Interface	5.91	109		592 (d)
19	12.7	Be (middle)	3.90	60.8		584 (d)
27	23	II-$LiAlO_2$-Be Interface	2.26	30.9		609 (d)
39	28	II-$LiAlO_2$ (middle)	1.77	22.6		646 (d)
51	33	C-II $LiAlO_2$	1.24	16.7		658 (d)
86	51.5	C (middle)	0.75	4.50		655 (d)
123	71	Header-C	0.266	1.05		650 (d)
141	90	Shield-Blanket	0.117	0.33		650
149	93.3	1st B_4C Zone (middle)	0.0756	0.25	50	200
175	105.5	1st Pb Zone (middle)	0.0256	5.87 E-2	50	200
215	123.	2nd B_4C Zone (middle)	4.21 E-3	0.87 E-2	50	200
255	140.5	2nd Pb Zone (middle)	9.67 E-4	1.18 E-3	50	200
300	160.6	3rd B_4C Zone (middle)	6.66 E-5	1.26 E-4	50	200
334	175	3rd Pb Zone (middle)	1.23 E-5	2.22 E-5	50	200
351	182.6	3rd B_4C Zone (middle)	4.61 E-6	1.0 E-5	50	200
365	188.5	Outside Shield	1.92 E-6	5.1 E-6	50	200
368	204	Inside Magnet	1.81 E-6	2.81 E-6		-269

(a) Note on the scale of displacement cross sections used for UWMAK-I this would be ~16.9 dpa per year at 100% plant factor, however the present numbers reflect the current displacement damage models.

(b) On the basis of 62.6 at. % Fe, 19.5 at. % Cr, 13.4 at. % Ni only, total amount including all impurities approximately 13% higher.

(c) Cell wall

(d) Rod wall temperatures

Table IV-H-7

Typical Chemical Analyses of Commercial 316 Stainless Steel[(a)]

Element	ppm Weight	ppm Atomic
Al	500	1000
As	300*	230*
B	10	52
Co	500*	500*
Cr	180,000	195,000
Cu	1,000	900
Fe	626,000	626,000
Mn	20,000	20,000
Mo	20,000	12,000
Nb	500*	300*
Ni	140,000	134,000
P	200	400
S	100*	200*
Si	7,000	14,000
Ta	200*	60*
Ti	100	100
V	2,000	2,200
C	600	2,800
H	?	
N	100	400
O	<200	<700

* Not considered for transmutations in this work

(a) Note that these are slightly different than for UWMAK-I

IV-H-4-b. Transmutation Rates in UWMAK-II 316 Stainless Steel

The similarity in the neutron spectra for UWMAK-I and UWMAK-II allows us to approximate the transmutation rates for UWMAK-II by using UWMAK-I values. The net change values, in appm/MW-year/m^2, are summarized in Table IV-H-8. These transmutation rates result in the compositional changes given in Table IV-H-8 and IV-H-9.

The conclusions of this work are the same as for UWMAK-I in that increases in Mn, Ti and V may tend to make a harder and stronger alloy while reductions in Ni do not appear to have any serious effect on the stability of the austenitic phase. There appears to be no significant problems if the first wall is changed every 2 years.

Table IV-H-8

Summary of Major Metallic Transmutation Rates in UWMAK-II for 316 Stainless Steel[a]

Element	Original Concentration appm	Net Change-Amys appm/MW-year/m^2	Absolute Change[b] appm 2 years	10 years	30 years
Fe	626,000	-1,220	-2,260	-11,300	-34,000
Cr	195,000	+ 24	+ 45	+ 220	+ 670
Ni	134,000	- 177	- 339	- 1,640	- 4,930
Mn	20,000	+1,160	+2,150	+10,800	+32,300
Si	14,000	- 12	- 22	- 110	- 330
Cu	900	- 5.6	- 10	- 52	- 156
Al	1,000	- 0.6	- 1	- 6	- 17
B	52	- 0.1	- 0.2	- 0.9	- 2.8
Co	500	+ 0.3	+ 0.6	+ 2.8	+ 8.4
Nb	300	- 0.5	- 0.9	- 4.6	- 14
P	400	- 0.1	- 0.2	- 0.9	- 2.8
Ti	100	+ 45	+ 8.4	+ 418	+ 1,250
V	2,200	+ 177	+ 329	+ 1,640	+ 4,930
C	2,800	- 3.4	- 6.3	- 32	- 95
O	700	- 0.4	- 0.7	- 3.7	- 11
N	400	- 0.5	- 0.9	- 4.6	- 14
Be	N	+ 1.6	+ 3.0	+ 15	+ 45
Mg	N	+ 12	+ 11	+ 56	+ 167
Na	N	+ 0.5	+ 0.9	+ 4.6	+ 14
Zr	N	+ 0.5	+ 0.9	+ 4.6	+ 14

N = Negligible

(a) UWMAK-I Spectrum, first wall, 1.16 MW/m^2

(b) 1.16 MW/m^2 and 80% plant factor (note - UWMAK-I values were for 100% plant factor)

Table IV-H-9

Summary of Most Important Transmutation Effects in 316 SS First Wall of UWMAK-II*

Element	Original Composition - at %	Final Composition - at %		
		2 years	10 years	30 years
Fe	62.6	62.4	61.5	59.2
Ni	13.4	13.4	13.2	12.9
Mn	2.0	2.2	3.1	5.2
Ti	0.01	0.02	0.05	0.14
V	0.22	0.25	0.38	0.71

*1.16 MW/m^2 and 80% plant factor

IV-H-4-c. Sputtering Effects on UWMAK-II Carbon Curtain and 316 Stainless Steel First Wall

The flux, energy and types of particles striking the carbon curtain and stainless steel first wall in UWMAK-II are given in Table IV-H-10. The mechanisms by which these particles can erode a surface have been explained elsewhere[11-12] and applied to the UWMAK-I system.[7]

The rate at which a solid member is eroded by an energetic particle beam is given by:

$$\frac{\Delta x}{t} = \sum_{\mu} S_{\mu} \phi_{\mu} \frac{A_w}{N_o \rho}$$

where S_{μ} is the sputtering yield in atoms per particle for a particular bombarding particle μ

ϕ_{μ} is the flux of bombarding particles of the type μ

A_w is the atomic weight of the struck material

N_o is Avogadro's number

ρ is the density of the struck material

The values of S_{μ} are given in Table IV-H-10 along with the individual and total wall erosion rates. Note that the effective erosion rates due to blistering of carbon have been estimated from data on metallic elements[13]* and that neutrons are presumed to strike both sides of the metallic wall (all the ions are intercepted by the curtain). Both pessimistic[14] and optimistic[15] values of S_n are used for 316 SS and carbon.

The results of Table IV-H-10 reveal the following interesting points.

1. The magnitude of the wall erosion depends very heavily on the neutron sputtering coefficient. Use of the pessimistic values can result in erosion rates of ~100 microns per year whereas optimistic values result in <0.1 micron per year removal rates.

2. Even with low neutron sputtering coefficients, the major inner (carbon) wall erosion mechanism will be sputtering which is about three times the erosion rate due to blistering. The erosion would be equally divided between neutron sputtering and charged particle sputtering. Of course, there is no charged particle sputtering of blistering on the steel wall because of carbon liner.

3. The charged particle sputtering is dominated by tritium and deuterium with helium contributing ~2% and the refluxing carbon atoms contributing less than 5%.

---

* This assumption will probably result in an overestimate of blistering rates but will be used until experimental data is available.

Table IV-H-10

Summary of Erosion Rates in UWMAK-II

Particle	Mean Energy KeV	Flux $cm^{-2}sec^{-1}$	Carbon Curtain Sputtering Coefficient	Carbon Curtain Erosion mm/year(a)	316 SS Sputtering Coefficient	316 SS Erosion mm/year(a)
Physical Sputtering						
D	18	1×10^{13}	5×10^{-3}	1.1×10^{-4}	---	0
T	18	1×10^{13}	7×10^{-3}	1.6×10^{-4}	---	0
He	18	5×10^{10}	~0.1	1.1×10^{-5}	---	0
He	~100	--	0.01	--	---	0
neutron(b)	10-15 MeV	1×10^{14}	10^{-4}-0.2	4.6×10^{-4} 9.2×10^{-2}	10^{-4}-0.2	6×10^{-5} 1.2×10^{-1}
neutron(b)	0.1-10 MeV	2.5×10^{14}	10^{-2}	11×10^{-4}	10^{-2}	7.5×10^{-4}
C	18	2.4×10^{10}	0.4	2.2×10^{-5}	---	0
			Subtotal	1.4×10^{-3} to 9.3×10^{-2}		8×10^{-4} to 1.2×10^{-1}
Blistering						
D	18	1×10^{13}	~0.01(c)	2.2×10^{-4}	---	0
T	18	1×10^{13}	~0.01(c)	2.2×10^{-4}	---	0
He	18	5×10^{10}	~1(c)	1.1×10^{-4}	---	0
He	~100	--	~3(c)	--	---	0
			Subtotal	5.5×10^{-4}		0
			Total	2×10^{-3} to 9.3×10^{-2}		8×10^{-4} to 1.2×10^{-1}

a) 80% Duty Factor
b) Include both sides
c) Estimated as maximum for data on metals.(16)

4. Even though the flux of helium atoms is ~0.5% of the flux of D or T atoms, it could contribute approximately 20% of the erosion due to blistering. However, it should be pointed out again that the S values for blistering of carbon are relatively unknown and further experimental work in this area is required.

In summary, erosion of the carbon curtain even at the maximum estimated sputtering and blistering coefficients amount to approximately 100 microns per year which is not large compared to the ~2000 micron initial thickness.* Therefore, one does not expect a severe problem from thinning if the lifetime of the curtain is approximately two years. The same conclusion can be drawn for the stainless steel first wall which has an initial thickness of approximately 1500 microns. If the lower neutron sputtering values are valid, then erosion rates of 1 micron per year could be accomodated even for a full 30 year reactor lifetime.

* However, the removal and redeposition of this much radioactive material (~1 tonne/year) in the rest of the chamber or vacuum pumps could be a problem.

IV-H-4d. Void Induced Swelling in 316 Structure of UWMAK-II

It is well known that neutron irradiation of 316 SS in the 300 to 650°C temperature region to damage levels of ≥5 dpa will produce voids and induce swelling[17-19]. The details of the swelling in this steel have been covered elsewhere and we will not repeat them here.[7,17-19] Our purpose is to present what we think may be the swelling characteristics of 316 SS in this reactor and to infer what the useful lifetime might be for UWMAK-II operation.

It must be emphasized at the beginning, that while the blanket of UWMAK-II will be originally made out of 20% cold worked material, subsequent welding of the helium coolant tubes and vacuum enclosures will result in the loss of the cold working in the heat effected zones. Therefore, the blanket will be a mixture of annealed and cold worked material at intervals as small a 1 cm apart (such as on the outer coolant tubes). This is probably a highly undesirable situation and indicates that better fabrication techniques are required. Such an analogy will also apply to other complex alloys which rely on second phase precipitation for their desirable properties, i.e., after the blanket modules are fabricated the metallurgical state of the structure may be quite variable and a simple approach of assuming constant materials properties may not be valid.

Having recognized the nature of the problem, we will illustrate the potential dilemma by calculating the swelling induced in 316 SS for both the cold worked and annealed state. One can then draw his own conclusions about which is the more severe design constraint and appreciate the nature of swelling gradients which could exist in an engineering structure.

Scientists working on the LMFBR program have determined the effects of temperature and damage level on swelling in 316 SS[20]. They have proposed the following empirical formula to fit available data.

$$\frac{\Delta V}{V_o} = R \left[\phi t + \frac{1}{\alpha} \mathrm{Ln} \left\{ \frac{1 + \exp[\alpha(\tau - \phi t)]}{1 + \exp[\alpha\tau]} \right\} \right] \qquad (1)$$

where $\frac{\Delta V}{V_o}$ = fractional volume change

ϕt = fluence, 1 unit = 10^{22} n/cm^2 (E > 0.1 MeV)

T = neutron Irradiation Temperature in °C

and the R, α, and τ parameters depend on the microstructure as follows:

20% Cold Worked

$$R = \beta \exp[-88.5499 + 0.531072T - 1.24156 \times 10^{-3}T^2 + 1.37215 \times 10^{-6}T^3 - 6.14 \times 10^{-10}T^4]$$

where β = multiplicative factor to describe the confidence limits

β = 0.0133 for Maximum Swelling

β = 0.01 for Nominal Swelling

β = 0.005 for Minimum Swelling

$$\alpha = -1.12 + 6.89 \times 10^{-3} T$$

$$\tau = \exp[-16.7382 + 0.130532T - 3.8108 \times 10^{-4} T^2 + 5.51979 \times 10^{-7} T^3 - 3.26491 \times 10^{-10} T^4]$$

Annealed

$$R = \beta \exp[-49.8592 + 0.195283T - 1.87409 \times 10^{-4} T^2]$$

$$\alpha = -1.117 + 6.889 \times 10^{-3} T$$

$$\tau = \frac{1}{(7.98769 - 2.98448 \times 10^{-2} T + 2.87279 \times 10^{-5} T^2}$$

$$\beta = 0.01$$

Examples of the temperature dependence for swelling in both types of materials are given in Figure IV-H-4 .

The above equation was modified to treat the displacement damage calculations in UWMAK-II on the following basis,(7)

$$4.7 \text{ dpa} = 10^{22} \text{n/cm}^2 \quad (E > 0.1 \text{ MeV}) .$$

Such a modification does not take into account the higher PKA energies produced by the 14 MeV neutrons nor does it account for the production of large amounts of helium gas. While there is no data on the first assumption, it has recently been found that high helium generation rates together with displacement damage does induce more swelling than the displacement damage alone.(21) Unfortunately, the data is too meager to draw any major conclusions at this time.

A schematic of the modified UWMAK-II blanket cell used for swelling calculations is shown in Figure IV-H-5. A rectangular representation was used to calculate the damage rates and the temperatures at various points in the cell were determined from the previous heat transfer calculations (see Section IV-D). The swelling was then calculated at 21 different points in the cell for irradiation times of 1, 2, 4, 6, 8, 10 and 30 years (an 80% plant factor was used). Some of the results are given in Table IV-H-11 and plotted in Figures IV-H-6 and IV-H-7 The nominal swelling value (β = 0.01) was used for the cold worked material.

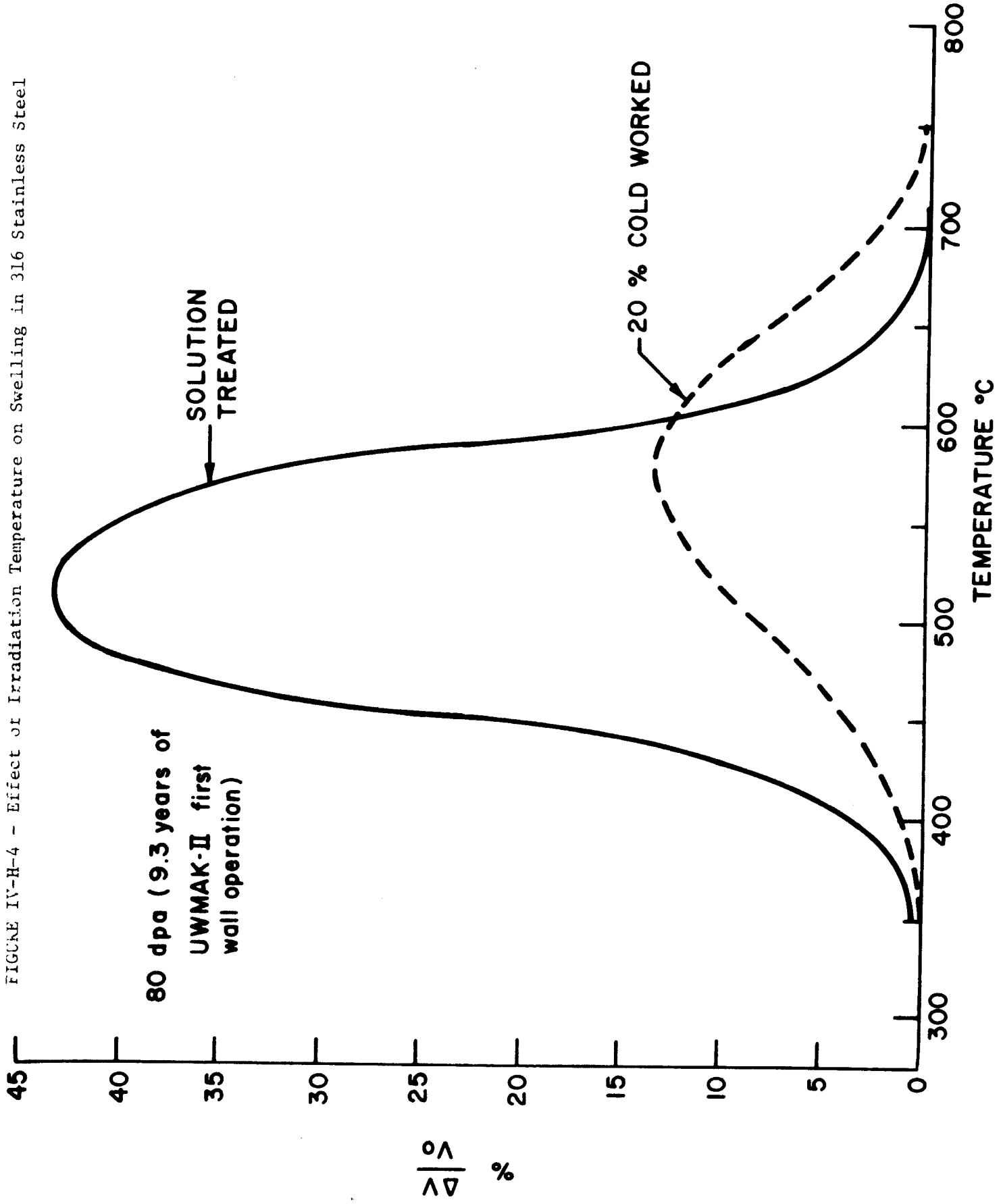

FIGURE IV-H-4 - Effect of Irradiation Temperature on Swelling in 316 Stainless Steel

Fig. IV-H5 SCHEMATIC OF UWMAK-II CELL USED TO CALCULATE SWELLING IN 316 STAINLESS STEEL STRUCTURE

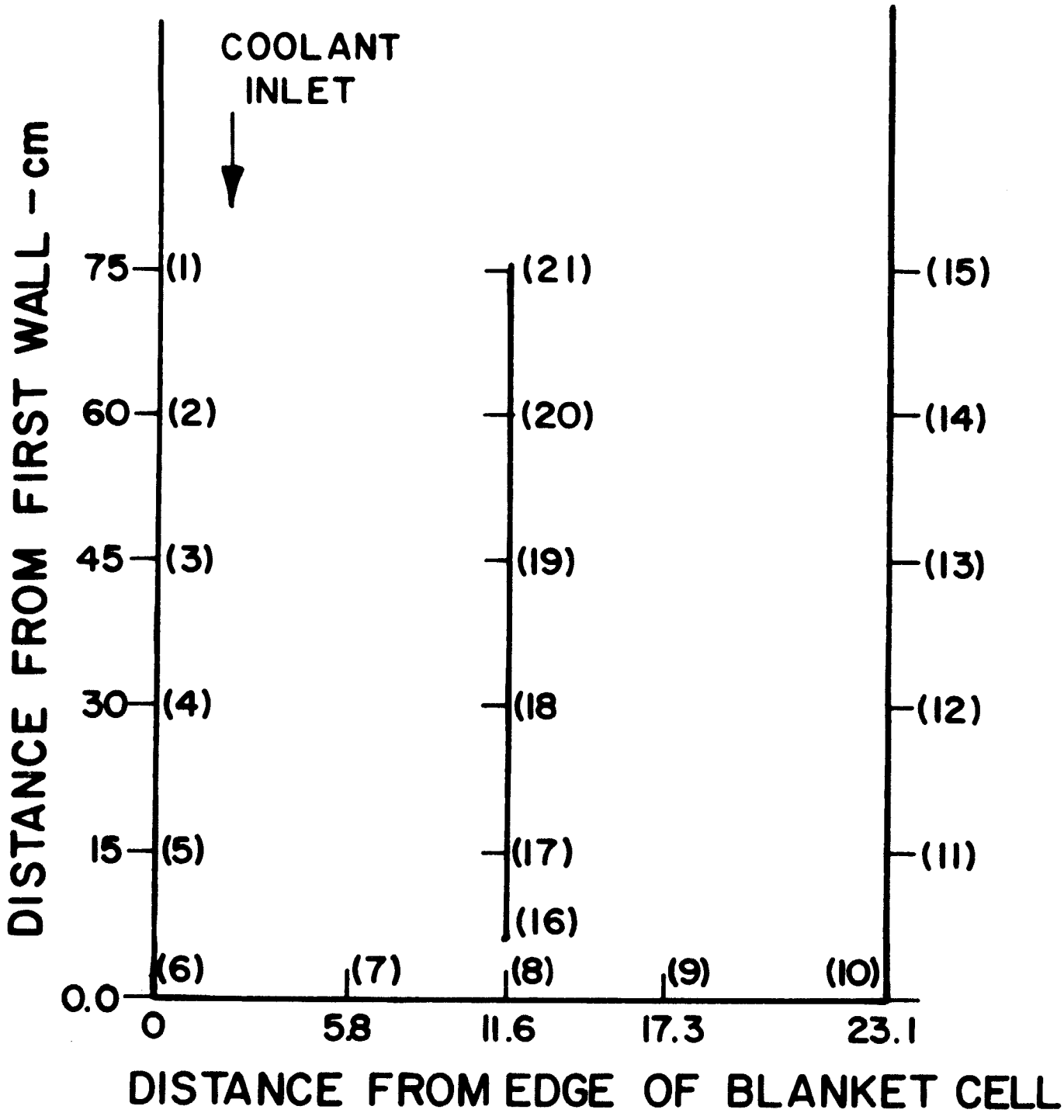

Figure IV-H-6
Calculated Swelling in 316 SS Solution Annealed Structure in UWMAK-II

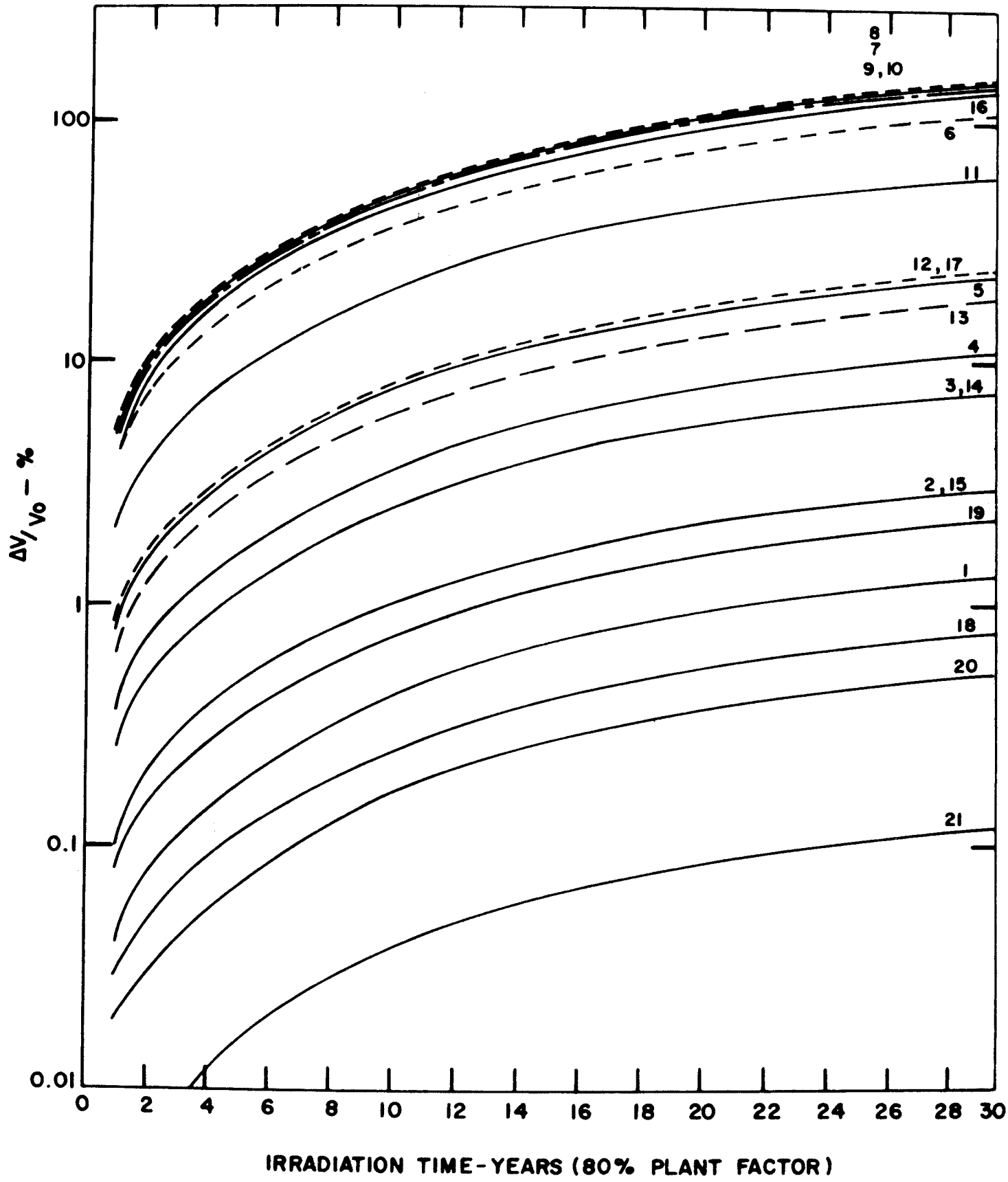

FIGURE IV-H-7
Calculated Swelling in 316 SS - 20% Cold Worked Structure in UWMAK-II. See Figure IV-H-8 for Data Point Identification.

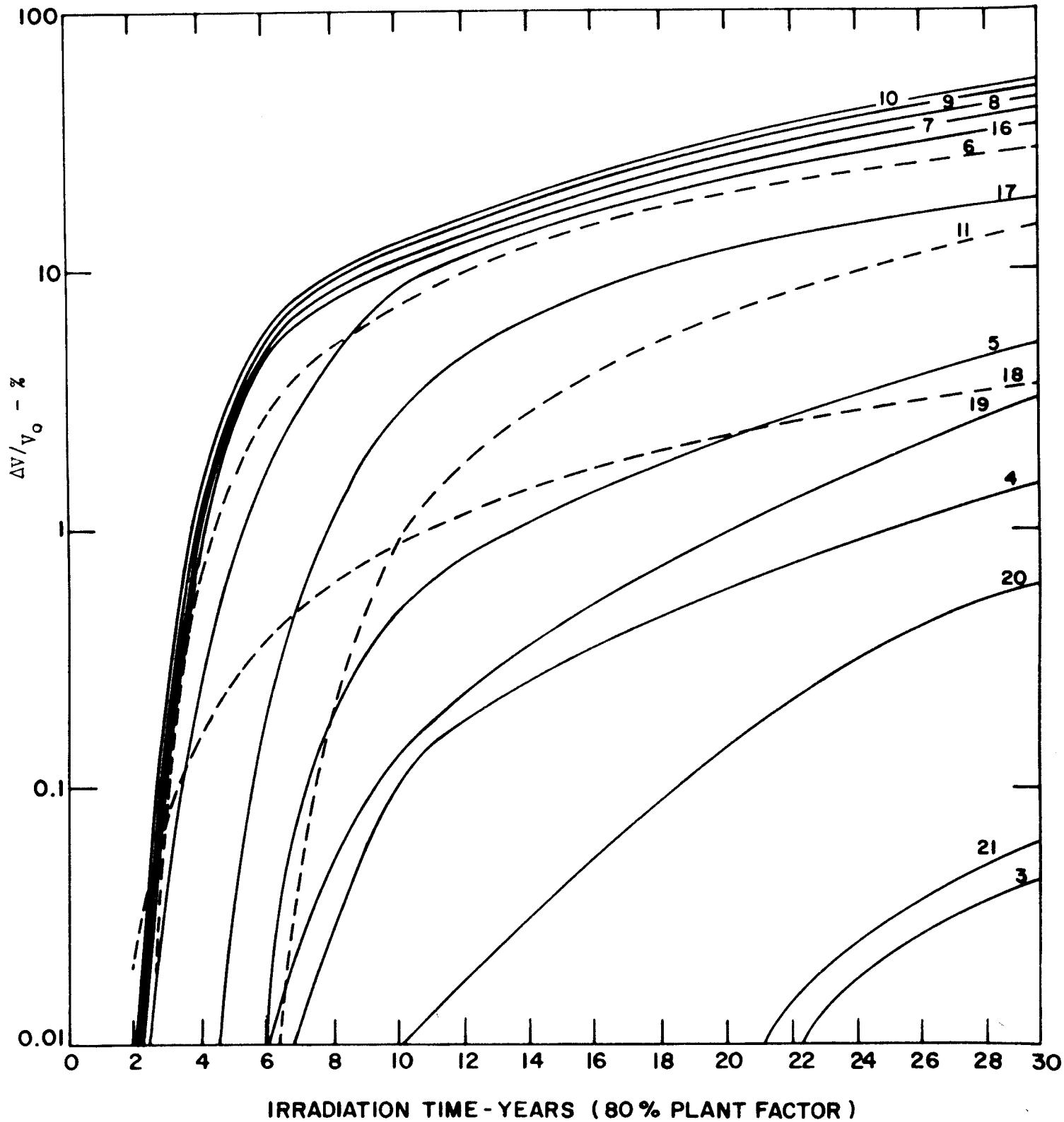

Table IV-H-11

Summary of Swelling Data for UWMAK-II 316 Stainless Steel Structure

			$\Delta V/V_o$(%)							
			Solution Annealed				20% Cold Worked			
Data Point*	T°C	dpa/yr	1yr	2yr	10yr	30yr	1yr	2yr	10yr	30yr
1	450	0.18	0.04	0.08	0.42	1.3	<0.01	<0.01	<0.01	<0.01
2	450	0.46	0.10	0.21	1.0	3.1				↓
3	450	1.1	0.25	0.50	2.5	7.5				0.43
4	450	1.6	0.36	0.73	3.6	10.9			↓	1.5
5	450	3.4	0.77	1.5	7.7	23.2			0.50	5.2
6	481	8.6	3.7	7.4	37.2	111			7.1	28.8
7	512	8.6	4.9	9.9	49.5	148			10.4	42.3
8	520	8.6	5.0	10.0	50.2	151			11.2	45.3
9	532	8.6	4.9	9.8	49.1	147			12.3	49.1
10	540	8.6	4.7	9.4	47.0	141			12.9	50.1
11	523	3.4	2.0	4.0	19.9	59.6			0.96	14.7
12	565	1.6	0.89	1.8	8.9	26.8			<0.01	3.1
13	505	1.1	0.61	1.2	6.1	18.4			↓	0.59
14	505	0.46	0.25	0.51	2.5	7.6				<0.01
15	505	0.18	0.10	0.21	1.0	3.1				<0.01
16	515	7.4	4.3	8.6	43	129			8.5	36.7
17	590	3.4	0.81	1.6	8.1	24.4		↓	3.1	17.6
18	660	1.6	0.03	0.05	0.25	0.75		0.02	0.92	3.7
19	624	1.1	0.08	0.15	0.75	2.75		<0.01	0.13	3.3
20	642	0.46	0.02	0.03	0.17	0.52		↓	0.01	0.64
21	658	0.8	<0.01	0.01	0.04	0.12	↓		<0.01	0.06

* See Figure IV-H-5

The calculations reveal that there is no detectable (<0.01%) swelling in the entire UWMAK-II cell after two years of irradiation for the 20% CW 316 SS. After three years, swelling is first noticed on the first wall and by 10 years it should be detectable as far back as 50 cm from the first wall. The swelling approaches 10% after ten years and may be between 30-50% if the cold worked structure were irradiated for 30 years (assuming no recovery of cold work). The swelling is slightly higher on the return leg of the helium coolant loop compared to the inlet because of the higher temperature (505 vs 450°C). The cans containing the breeder and neutron multiplier also suffer significant swelling, approaching 10% in the first breeding zone after 12 years and 30% for a 30 year exposure.

The swelling gradients in the steel are also worth noting. For example, critical areas will certainly be the inlet side of the first wall where both the temperature and damage are rising steeply. Gradients of 1 to 3% per cm could occur in this region after 10 years of irradiation, The same is true of the cans holding the $LiAlO_2$ and Be.

In contrast to the cold worked material, the annealed 316 SS swells quite readily. The first wall may experience >10% swelling in 3 years, >30% after 8 years and >100% after 20 years of irradiation. These numbers are also the same for the end of the cans closest to the plasma. Even the regions 15-30 cm from the first wall may swell more than 10% in ~15 years of irradiation showing that the first wall is not the only component with a finite reactor lifetime. If one uses 10% as an arbitrary limit on swelling, then one must go back as far as 30 cm before the material could remain below the limit during the reactor's lifetime.

The swelling gradients within a solution annealed structure are also quite severe, Again, approximately 0.5% $\Delta V/V_o$ per cm could be present after as little as 2 years irradiation and as much as 1or2% per cm after 10 years and 30 years respectively. The effect of such non-uniform swelling on dimensional stability (i.e, warping, bending, buckling, etc.) must be examined closely in any structure which must contain high pressure coolants and maintain vacuum tightness.

An even more severe problem may exist if, as stated before, there exists regions of cold worked metal immediately adjacent to annealed metal. For example, if the outer coolant tubes are welded every cm and if the heat effected zone extends 2.5 mm on each side of the weld zone, then we could have alternate 0.5 cm strips of annealed and cold worked metal. After one year of irradiation, the swelling in the annealed sections could be ~5% whereas the cold worked material will have no detectable swelling. Hence, swelling gradients of ~10%/cm would exist. This may increase to approximately 20% per cm after 2 years to 80% per cm after 10 years and 200% per cm after 30 years. Obviously, these last numbers are not meaningful because one would have to change the wall long before that time. Even after a two year exposure, the gradients may induce strains which the embrittled metal (see Section IV-H-4e) cannot withstand without fracturing. The possibility that such strains could be relieved by irradiation induced creep should also be closely examined.

It is worthwhile at this point to examine some recent data by Wiffen and Bloom with respect to swelling in 316 SS which contains high (several thousand atomic parts per million) helium contents.[21] If one accounts for the difference in displacement models (our dpa cross sections are one half of theirs) then the following values were measured.

			% $\Delta V/V_o$ - 316 SS			
			annealed		20% cold worked	
T°C	(dpa) present	appm He	meas[21]	Eq. 1	meas[21]	Eq.1
379	48	4020	6.7	~0.5	1.6	0.17
456	53	4820	8.7	~13	0.8	1.7
528	57	5450	8.3	~25	2.6	6.5
535	26	1930	3.5	~12	0.52	<0.01
574	29	1790	3.3	~ 8		0.42
602	59	5940	8.0	~ 8	3.3	~8
679	60	6090	14.1	~ 0.26	16.8	~3

The agreement between measured and calculated swelling in annealed 316 SS is good to within a factor of 2 to 3 over the 450 to 600°C range with the calculated values overestimating the swelling. On the other hand, there appears to to be large unaccountable swelling in the low (380°C) and high (680°C) temperature ranges. This is probably due to helium bubble swelling. The underestimate of swelling in the mid-temperature range may be due to enhanced nucleation by the helium bubbles.

The calculated swelling in the 316 SS cold worked samples is also higher than that measured in all cases except at the temperature extremes. This could also be due to the finite swelling due to helium bubble formation or it could be due to lack of sufficient data points to form a statistically meaningful data base. It is almost certain that at high temperatures (679°C) the large discrepancy is undoubtedly due to helium bubble growth. Such is also the case for 26 dpa samples because that fluence is below the threshold for void formation without large amounts of helium.

The tentative conclusion is that the calculated values will probably be representative of the measured values in the mid-temperature range even considering that about 200 appm helium will be generated per year. The swelling above 600°C will probably be dominated by bubble growth and must be calculated separately. Fortunately, the only point in the UWMAK-II cell which will reach that temperature only contains approximately 20 appm per year of irradiation (~600 appm maximum).

In summary, if the entire cell would be made of 316 SS and retain its 20% cold working, then one might anticipate first wall lifetimes of ~12 years or more depending on the effect of stress on swelling. On the other hand, if the cell is made of annealed 316 SS, then lifetimes of as little as 3 years (with a 10% swelling limit) might be expected. A major question exists about the effect of mixed zones of annealed or cold worked metal on the swelling gradients and hence the integrity of the first wall. If values of 10% $\Delta V/V_o$ per cm are too much for the metal to accomodate (especially without creep relaxation) then wall lifetimes in the UWMAK-II could be as low as 1 year or less from swelling.

IV-H-4e. Effect of UWMAK-II Environment on the Mechanical Properties of 316 SS

It is well known that high temperature neutron irradiation of 316 SS (or any metal for that matter) causes an increase in the yield strength, decrease in ductility and decreased rupture life.[22-24] The latter two properties are particularly important since the UWMAK-II reactor must accomodate significant stresses and strains during the ~4500 burn cycles it will undergo per year of operation.

Effect of Irradiation on the Yield Strength of 316 SS

The increase in yield strength is most predominant at lower temperatures (<550°C) and results from the blocking of dislocation motion by lattice defects (i.e., interstitial loops, voids, second phase particles, etc.). This effect has been treated in UWMAK-I[7] and the same general conclusions can be drawn for UWMAK-II.

- Solution treated material will be strengthened by factors of 5-6 after 2 years of irradiation at T < 550°C and factors of 2 when irradiated for the same time in the 550-650°C temperature range. (See Figure IV-H-8).

- Cold worked 316 SS will be slightly softened by irradiation in the 500-700°C temperature region (Figure IV-H-9). However, since the metal initially is stronger than the solution treated material (due to the 20% cold work), the effect is less pronounced than for the annealed material.

The general effect of the hardening will extend all the way back into the blanket and because of the possible initial mixture of annealed and cold worked material, it will tend to make the yield strength of the blanket structure more uniform than it was before irradiation.

Effect of Irradiation on the Stress Rupture Properties of 316 SS

The rupture life of a reactor component is particularly important for a system where even one failure in a large system (i.e. vacuum vessel) could result in a complete shutdown of the plant. There are both safety and economic implications associated with such an event. Therefore, it is vital that reactor designers can predict the lifetime of a given component under given stress, temperature and irradiation conditions.

The traditional way of describing this lifetime is given by

$$t_r = A\sigma^B \qquad (2)$$

where t_r is the rupture life

σ is the true stress

A,B are temperature dependent constants

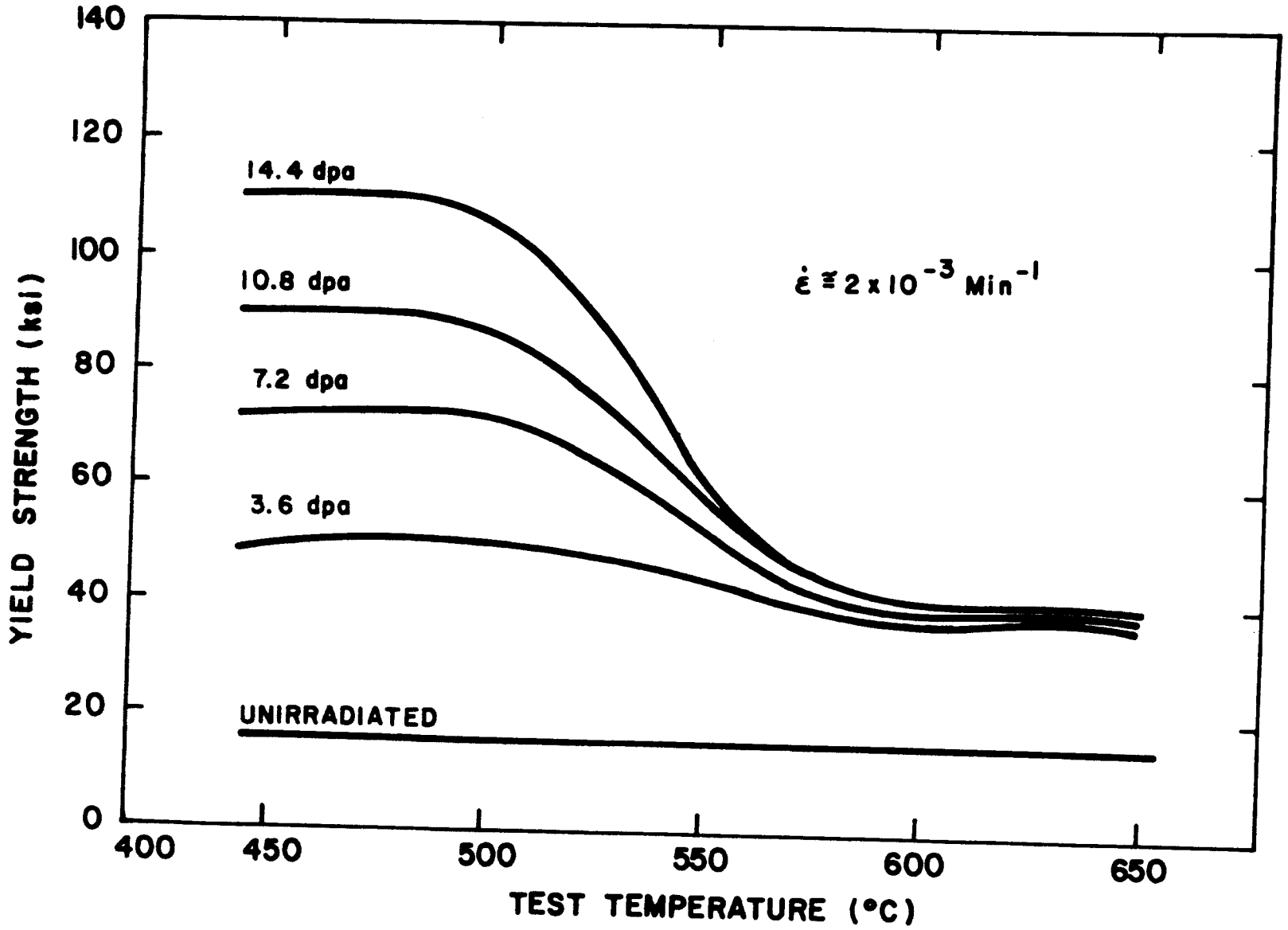

Figure IV-H- 8 Parametric dpa Plots for Yield Strength of Annealed (ST) Type 316 Stainless Steel Irradiated (EBR-II) vs Temperature. Irradiation within ~50°C of Test Temperature.

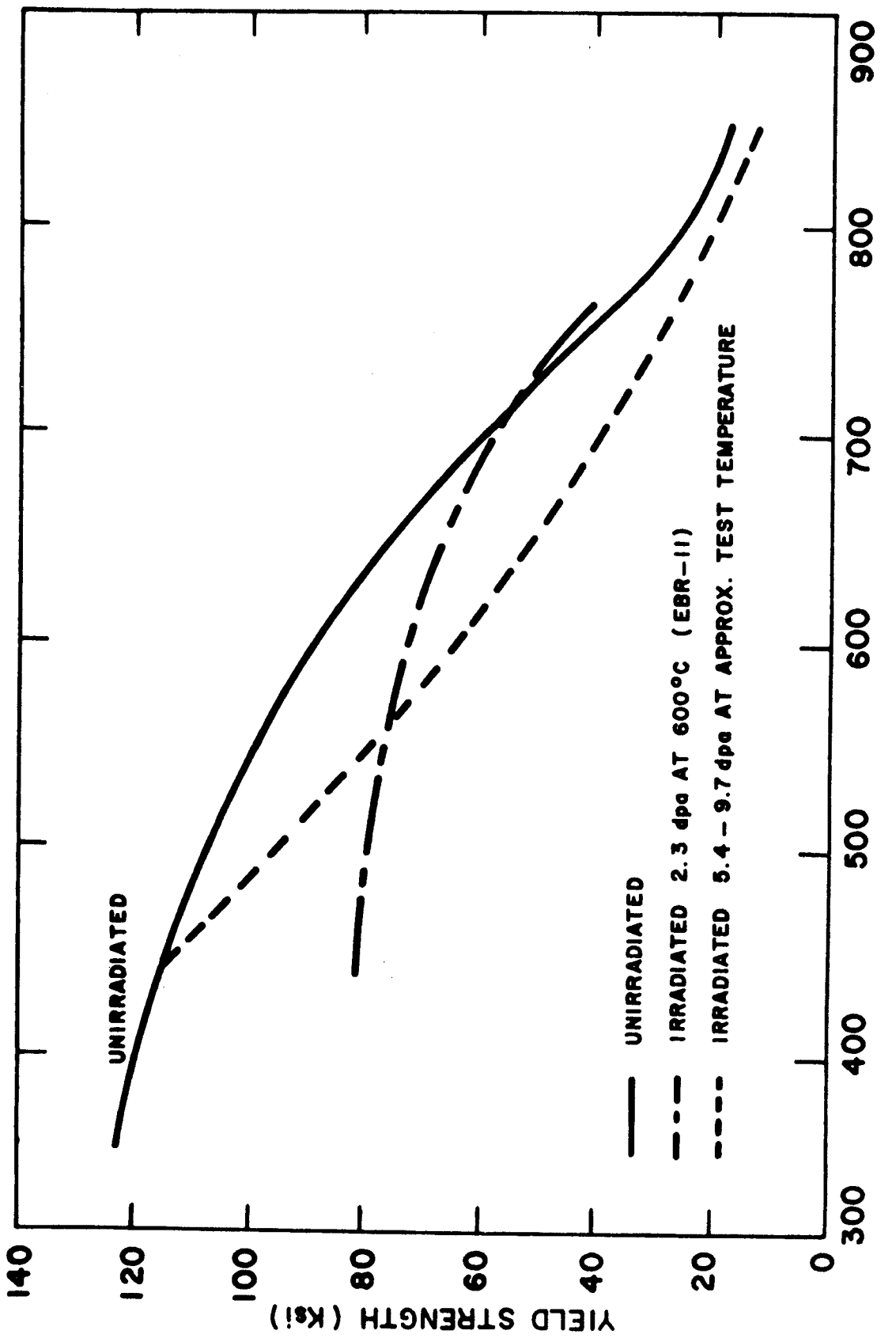

Figure IV-H-9 Yield Strength Versus Test Temperature for Unirradiated and Irradiated 20% CW Type 316 Stainless Steel[23]

This formula has been modified to include irradiation effects by Lovell [24];

$$t_r = A \left[\frac{t_i}{t_n}\right] \sigma^B \qquad (3)$$

where t_i = rupture time after irradiation

t_n = unirradiated value.

He has measured the ratio of (t_i/t_n) for 316 SS irradiated up to fluences as high as $7 \times 10^{22} n/cm^2$ ($E > 0.1$ MeV), or 33 dpa, at temperatures of 538°C, 593°C, 649°C, and 760°C. The fluence dependence of (t_i/t_n) is given in Figure IV-H-10

In general, the effects of irradiation are more pronounced at the lower temperatures and the threshold for reduction of rupture life increases from ~0.5 dpa at 538°C, to ~5 dpa at 593°C and ~15 dpa at 649°C. There is no clear cut threshold at 760°C, but this temperature is well within the helium embrittlement stage and the threshold is probably a function of the constantly increasing helium content.

The initial decrease in rupture life at 539°C is probably due to the combined effects of matrix strengthening and grain boundary embrittlement by helium. The matrix strengthening (by voids, dislocation loops, etc.) forces the deformation to be absorbed by the grain boundaries. If helium bubbles are present at these grain boundaries, plastic deformation will cause them to grow, initiate cracks, and accelerate the fracture of the component. The rupture life continues to decrease with increasing matrix hardening and helium atom generation until the primary and secondary creep strains are so greatly reduced that very little strain develops, and the rupture life increases with increasing fluences at high exposure levels.

The increased thresholds at 593°C and 649°C is primarily due to the reduced matrix hardening at those temperatures. However, eventually the high temperature promotes the collection of helium at the grain boundaries so that even very small amounts of helium (<0.3 appm He) can cause a reduction in rupture life.

Lovell has derived the following emperical relationships which can be used to calculate actual rupture lives from equation 3;

$$A = \exp\left\{18 + 0.02893\ (T - 461.6)\exp\left[-\frac{1}{84}\left(\frac{T - 461.6}{655}\right)^{8.4}\right]\right\}$$

$$B = -5.4 - 0.014633\ (T - 916)\exp\left[-\frac{1}{4}\frac{(T-916)^4}{265}\right]$$

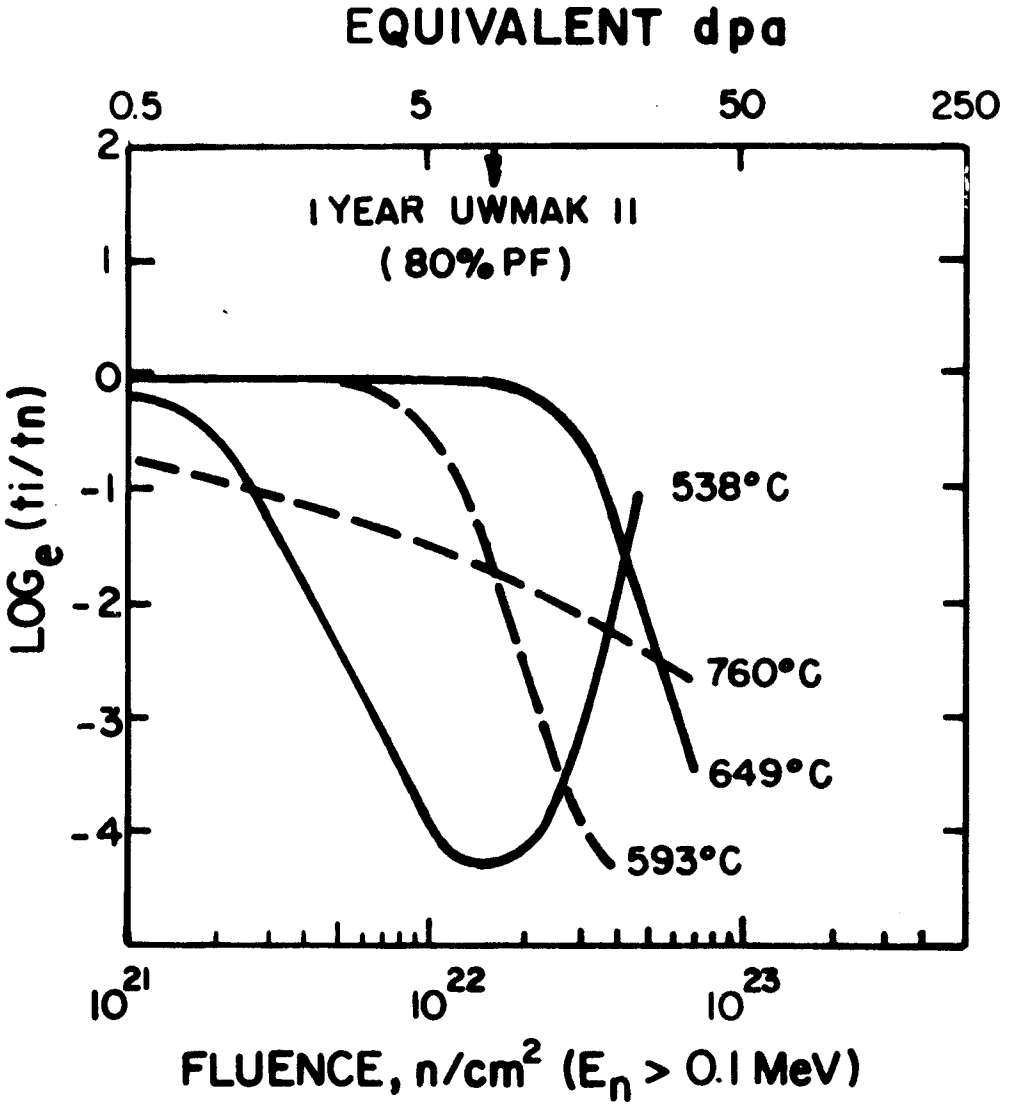

Figure IV-H-10 Calculated versus measured fluence parameter

$$\left(\frac{t_i}{t_n}\right) = \exp\left\{-\frac{3.3}{\exp\left(-\frac{1}{m}\right)}\left[G - \ln(\phi t)\exp\left[-\frac{1}{m}\left|\frac{G-\ln(\phi t)}{1.3}\right|^m\right]\right]\right\} \qquad (4)$$

where $G = 42.9 + 0.0095T$

$$m = 0.015408\,(T-870)\exp\left[-\frac{1}{4}\left(\frac{T-870}{300}\right)^4\right]$$

T in °F, ϕt in units of n/cm^2 ($E > 0.1$ MeV), σ in ksi

The limits of the above expressions are 338-760°C, stress to ultimate strength and fluence to $7 \times 10^{22} n/cm^2$ ($E_n > 0.1$ MeV).

Figures IV-H-11 and IV-H-12 show how the 10,000 hr (1.43 years of actual UWMAK-II operation or 1.14 calendar years) rupture life varies with both temperature and fluence. Note that between 650-700°C, irradiation to ~16.5 dpa (~2 years of actual UWMAK-II irradiation) has little effect on the rupture life but that t_r is reduced by almost a factor of 2 at 540°C or 760°C.*

At this point, we might relate the experimental information to the actual conditions in UWMAK-II. It has been previously shown that the highest tensile stress is in the front wall structure, specifically in the thin component on the side facing the plasma. This stress was calculated to be 8.1 ksi (not including that induced by swelling gradients, etc.) We will now use the modified formula to calculate the rupture life at a temperature of 540°C, highest temperature on the first wall. From Figure IV-H-10 we see that after an exposure of 1 year (8.6 dpa or $\sim 1.8 \times 10^{22} n/cm^2$) the ratio of t_i/t_n is ~1%. Coupling this with values for A and B, we find the following values for rupture life at 540°C.

σ-ksi	t_r-years
8	284
10	69
12	21
14	7.3
16	3

The question now is now much of a safety factor will be required for fusion reactors. Or stated another way, how much of "stress factor" is reasonable to assign to local thinning, temperature inhomogeneities, higher helium generation, swelling gradients, machining imperfections, etc. It is probably not unreasonable to apply a factor of 50-100% to the calculated stresses in order to assure high vacuum integrity. Such a factor would

---

* Bloom and Wiffen[25] note that irradiation to 3.4 dpa at 550°C and concurrent generation of 48 appm He reduces the creep rupture life of 316 SS by a factor of 50.

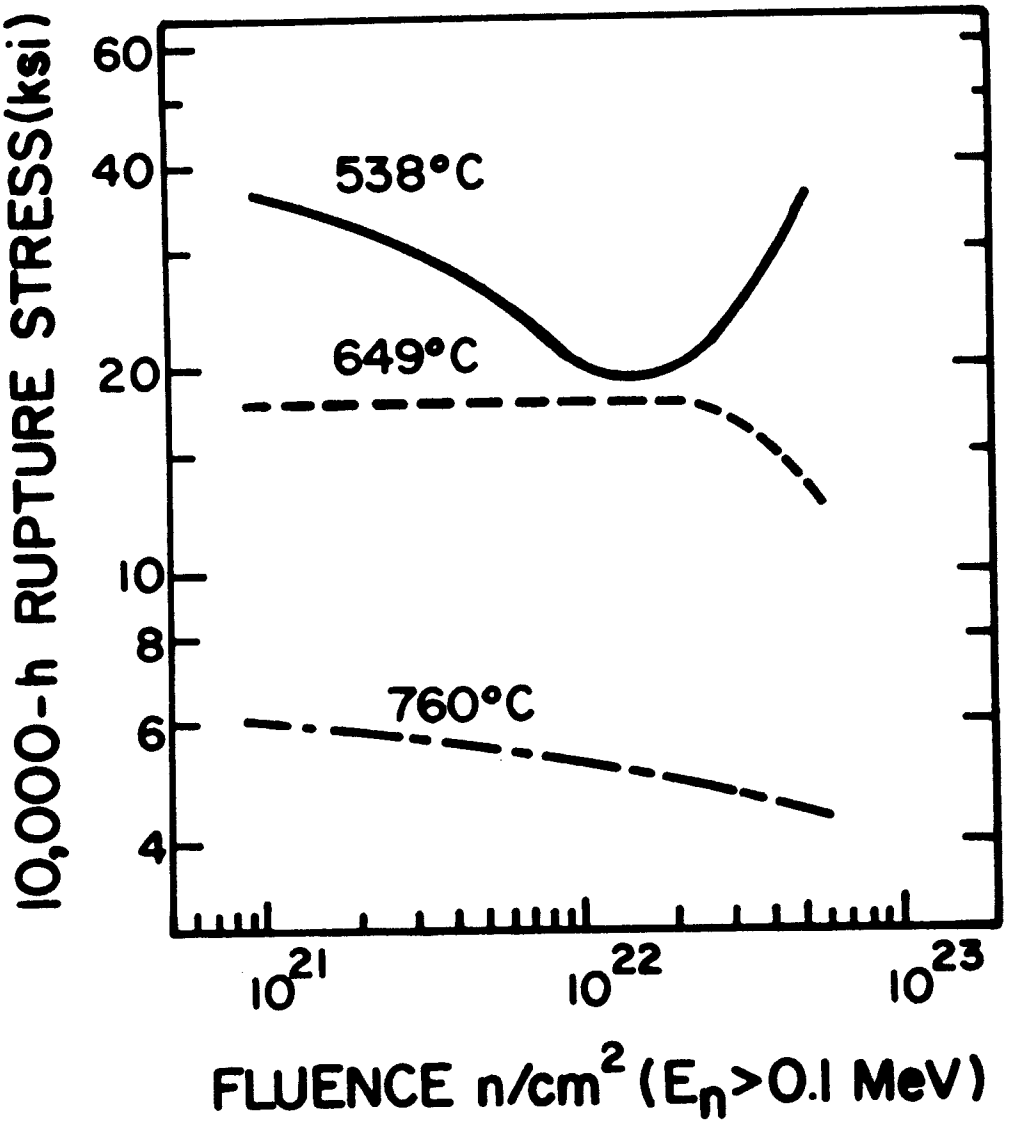

Figure IV-H-11 Calculated 10,000-h rupture stress

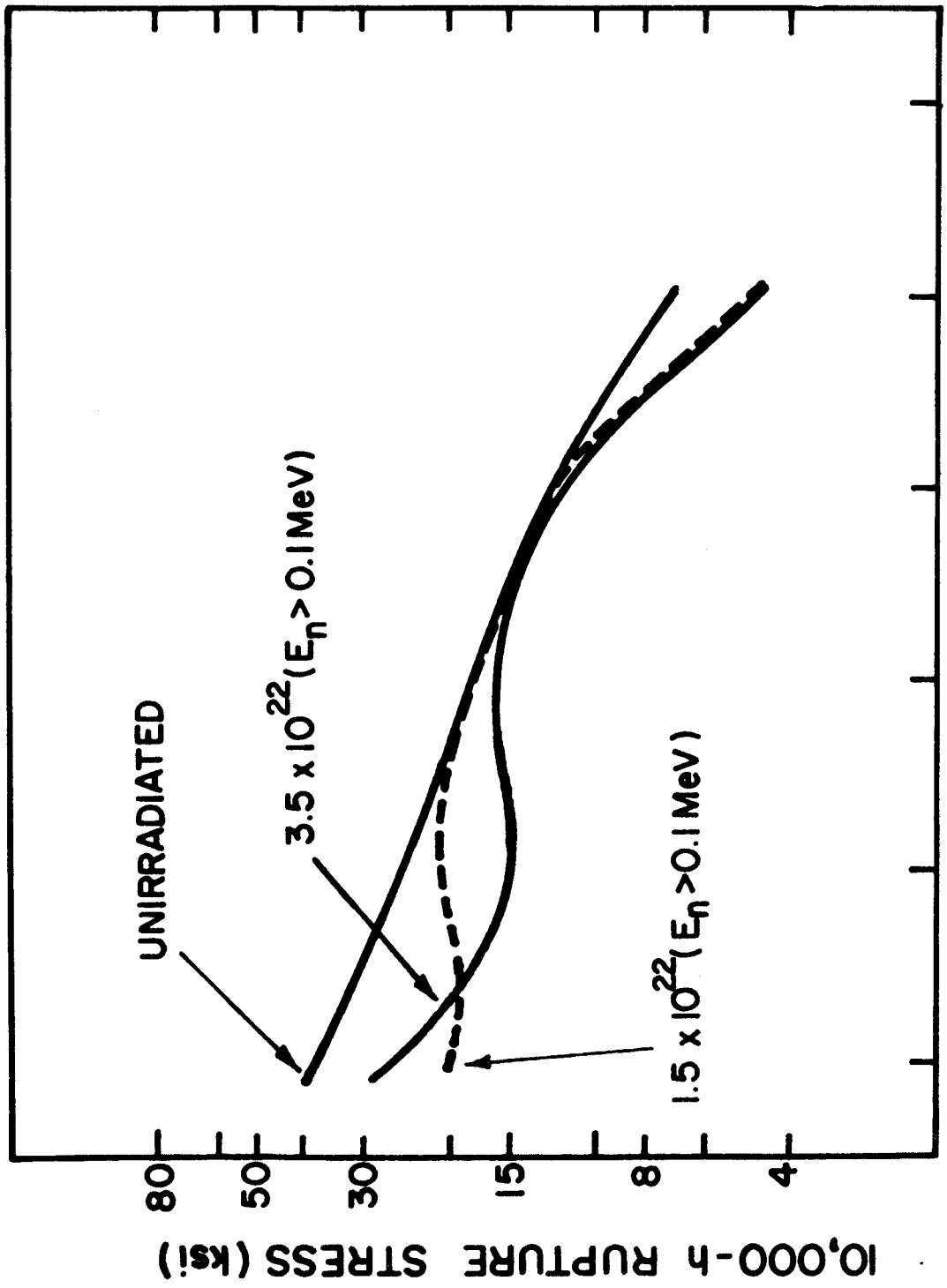

Figure IV-H-12 Calculated 10,000 h-rupture stress

place the minimum rupture life between 3 and 21 years, again less than the lifetime of the plant.

Another problem may occur in the cans holding the breeder and neutron multiplier. Here the temperature can approach 660°C (1220°F) and damage will accumulate at the rate of 1.77 dpa per year ($3.8 \times 10^{21} n/cm^2$, E >0.1 MEV equivalent). The predicted rupture life of these cans after 10 years of irradiation would be ~1 year at ~16 ksi. Whether or not such stresses could arise from swelling of the Be or $LiAlO_2$ is a question which should be closely examined.

Effect of Irradiation on the Ductility of 316 SS

An extremely important feature of any large structure which is subject to varying thermal and mechanical loads is the ability to elastically deform without failing. Probably the most graphic example of this phenomenon is the flexing of the wings on a jet aircraft during take-off and landing.

The reactor vessel of UWMAK-II will also be required to expand and contract during the approximately 4500 reactor pulses per year. It is difficult to give a quantitative number for the minimum strain that must be available for reactor operation until the details of the blanket design have been fully described. However, one might expect that value of a few percent are not unreasonable given the changes of temperature (300-400°C) which might occur during major shutdowns and pressure changes of several thousand psi which might occur between burn cycles as the coolant flow is greatly reduced to maintain relatively constant blanket temperatures. Superimposed on these strains would be those associated with swelling gradients in the structural material.

The ductility considerations in UWMAK-II are even more severe than in a typical LMFBR cladding where the minimum uniform elongation ductility design limit is ~0.4%.[26] Even with this design feature, an LMFBR may have a small but finite number of failures, e.g. the clean up system will be designed to remove a limited amount of fission products from the coolant. It is not sure that UWMAK-II can operate with a single failure in its vacuum vessel liner and therefore one might be tempted to reduce the number of potential failures by raising the minimum allowable uniform elongation to approximately 1% or more. Such values will have to be decided upon in more detailed reactor designs. For UWMAK-II, we will choose a minimum uniform ductility design value of 0.5% fully realizing that we may be too liberal and that safety-economic considerations might require values of 1% or more.

Prediction of the ductility of steel components after irradiation have very little theoretical foundation. The basic mechanism of ductility loss are known and discussed elsewhere[27] as well as in the previous section on rupture life. Considerable experimental data exists for fast reactor spectra and the effect of displacement damage in EBR-II (and the associated helium production rates ~0.1 appm He per dpa) on the uniform elongation of 316 SS is shown in Figure IV-H-13. Extrapolation of such data to 0.5% would predict that, at 530°C,

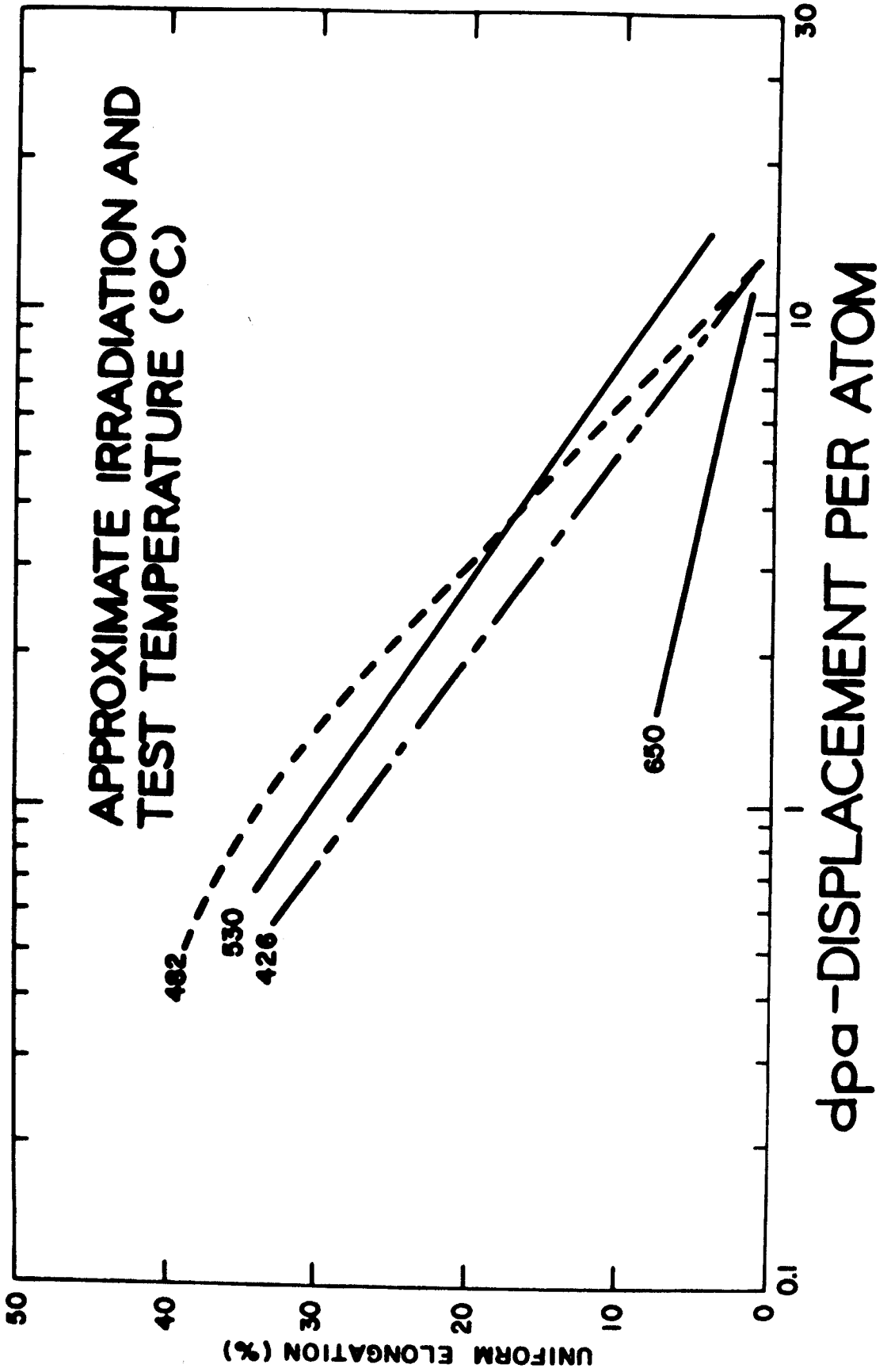

Figure IV-H-13 Design Curves for the Effect of Irradiation on Uniform Elongation of 316 SS[23]

the first wall in UWMAK-II would last approximately 2-3 years before it fell below the minimum allowable ductility. However, because ductility is so much of a function of helium content, such lifetimes are considered to be a maximum value in the high helium production environment of UWMAK-II. This point is amply demonstrated by recent work of Bloom and Wiffen.(25)

They irradiated both annealed and cold worked 316 SS in HFIR to produce high helium contents and high displacement values. The results of their work are summarized below in Table IV-H-12 where the total and uniform elongation at failure are quoted as well as what fraction this represents of the unirradiated control ductility (total elongation). This information is also plotted in Figure IV-H-14 along side similar data from EBR-II. The general trend of the data for annealed 316 SS is a drastic reduction in total elongation even at the lowest test temperature of 350°C. The irradiated total elongation values for 350 and 450°C test temperatures are 1-2% of the unirradiated control values. Such damage levels (38-49 dpa) correspond to 4.5 to 5.8 years of UWMAK-II operation. Irradiation and testing in the 575-600°C region to 59 dpa and 5940 appm He results in a further reduction in the total elongation. Since the uniform elongation is usually less than the total elongation in solution treated material, it is expected that ductility limit would be reached in a shorter time than the 5 to 7 years indicated here.

The reduction in ductility of the cold worked material is not quite so pronounced. The ductility is only reduced by ~24% after 49 dpa and 4020 appm He at a 380°C irradiation temperature. Further reduction takes place at higher temperatures (42% at 455°C and 86% at 530°C) such that by 530°C (57 dpa and 5450 appm He), the total elongation is only 0.7%, only 0.2% above the design limit.

The next three higher temperature data points are perhaps the most disturbing of the ORNL data. One specimen irradiated and tested at 575°C (only 30°C more than the maximum UWMAK-II first wall temperature) displayed only 0.5% uniform and total elongation after 3.4 dpa and 48 appm He. This corresponds to approximately 5 months of UWMAK-II irradiation for that dpa level and only 3 months of irradiation to accumulate that much helium. The next data point came from a sample irradiated to a factor of 17 higher in dpa and a factor of 126 higher in helium. Both the total and uniform elongation in that sample were 0.2%, well below our design limit. The lack of linearity in this region is demonstrated by the fact that a sample irradiated at the same temperature (600°) and tested at 575°C but to only 2.6 dpa (33 appm He) had already reached the design limit of 0.5%. The degree of scatter in the data is demonstrated by another sample irradiated to 28 dpa (1660 appm He) at 605°C and tested at 575°C. This sample showed ~1.5% elongation. However, going to higher temperatures (680°C irradiation) higher dpa values (60) and higher helium contents (6090 appm) resulted in a sample with zero ductility, a situation which clearly cannot be tolerated.

The percent total elongation associated with 316 SS specimen irradiated in EBR-II are also plotted in Figure IV-H-14. The data for 5.6 to 14 dpa (0.7 to 1.7 equivalent years of UWMAK-II displacement damage but only ~1 month of equivalent helium generation). Even accounting for the reduced displacement damage, one clearly sees the effect of helium content on ductility, especially at higher temperatures. There is no question but that higher helium contents at roughly

FIGURE IV-H-14

Effect of Irradiation and Test Temperature on the Total Elongation of Annealed (Solid Line) and 20% Cold Worked (Dotted Line) 316 SS. EBR-II Data for 5.6 to 13.6 dpa (<11 ppm He) while HFIR data for 38 to 60 dpa (3000 to 6000 ppm Helium). Reference 25.

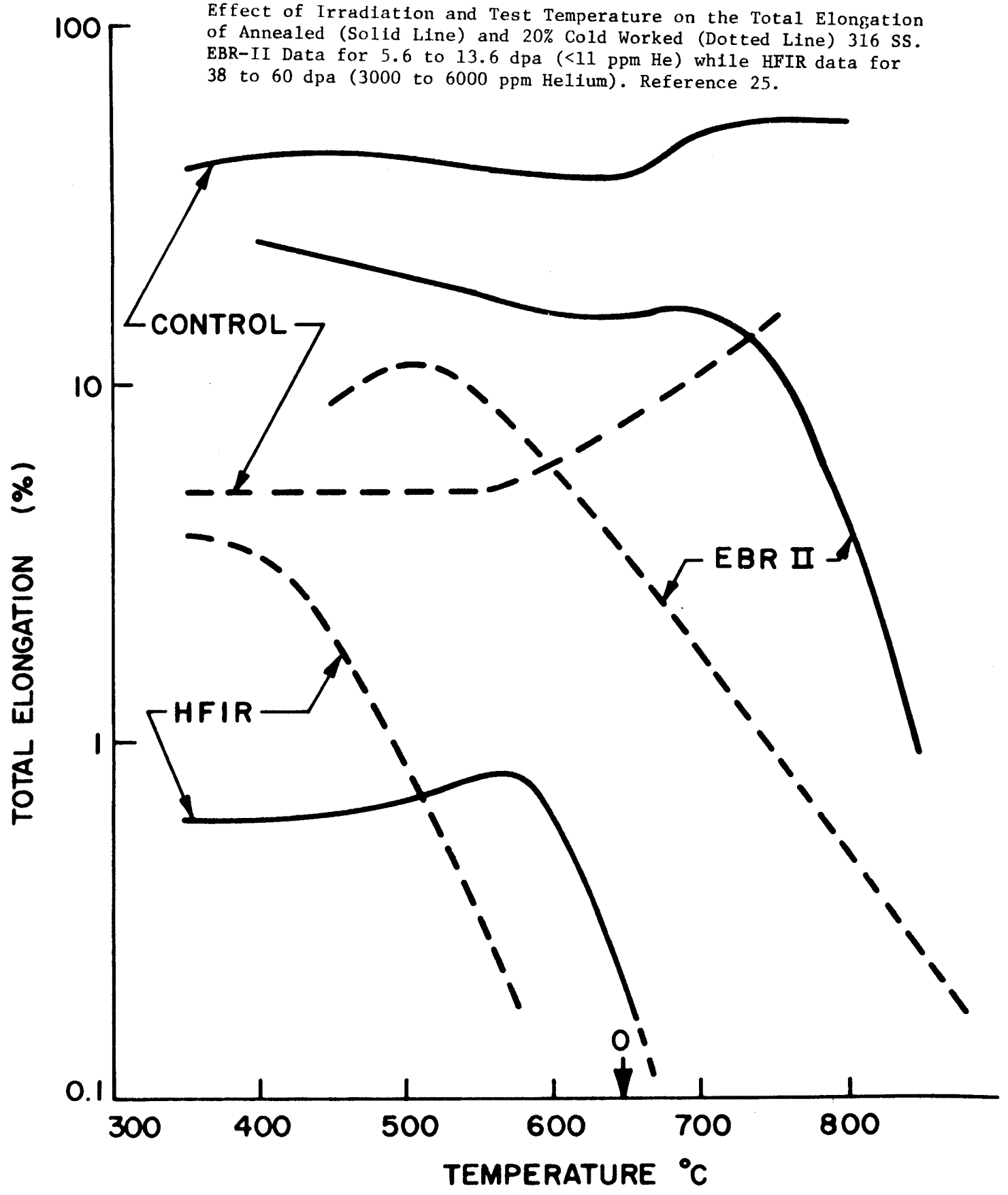

equivalent displacement values cause a serious degradation of the mechanical properties.

The major question is "How does one use the meager experimental data to predict a useful lifetime for the 316 SS components of UWMAK-II? We will address this question in two parts; the first wall and the can wall for breeder material.

The temperature of the first wall ranges from 481 to 540°C and it accumulates damage at the rate of 8.6 dpa and 187 appm He per year. Prudent engineering would require that we take the worst data point at that condition and then apply a reasonable safety factor to arrive at the time required to change the first wall before any failures occur. Following this philosophy for displacement damage, we find that the useful wall life is a maximum of 6.6 years at 530°C and a minimum of 0.3 to 0.4 years at 575°C and 600°C irradiation temperatures respectively.(Tbl.IV-H-13) Other data would predict 3 to 10 years lifetime. Similar analyses for the helium content (associated with that displacement damage in HFIR) reveals lifetimes of 0.2 to 29 years. Obviously, there is no clear cut answer for the first wall lifetime.

In order to derive a number for first wall lifetime that can be used in the economic analysis, we will use the following (admittedly arbitrary) logic.

1. EBR-II data predicts ~3 year lifetime at 530°C (Figure IV-H-13)
2. HFIR data predicts a lifetime of 6.6 years at 530°C (Table IV-H-12)
3. HFIR data predicts a lifetime of 0.4 years at 575°C (Table IV-H-12)
4. HFIR data predicts a lifetime of 0.3 years at 600°C (Table IV-H-12)

An average value over the 530-600°C temperature range is 2.6 years and allowing a 30% safety factor gives a first wall life of approximately 2 years. Pessimists could argue that the real value should be less than 0.4 years (when safety factors and perhaps higher minimun uniform elongation values are used) and optimists may claim that HFIR data right at the 530°C indicates a value of 6.6 years. However, temperature uniformity cannot always be assured and hot spots of 45°C could easily occur requiring 575°C data to be used. In any case, more experimental and theoretical work is needed to clarify this point and we shall use 2 years for the first wall lifetime in UWMAK-II.

Table IV-H-13

Maximum First Wall Lifetime Irradiated by Experimental Data on 316SS (20% CW)

$T_{irr} - T_{test}$ °C	Yrs due to displacement damage only	due to He Generation only
530-500	6.6	29
575-575	0.4	0.3
600-575	0.3	0.2
600-575	~3	~11
605-575	~10	~27

The next point to consider is how long will the breeder cans last. Perhaps the most critical point here is that part of the can which operates at 660°C. At that temperature most of the cold work will be annealed out and the component should behave as a well annealed alloy. Data from Table IV-H-12 shows that irradiation and testing or this material in the 650-685°C temperature range results in either zero of 0.2% uniform elongation after 30 and 32 years respectively. It is difficult to extrapolate such data back to a 0.5% uniform elongation limit but linear extrapolation would reveal a maximum lifetime of 9 years for one of the specimens. Hence, since the breeder cans must be replaced every time the first wall is changed because of swelling in the Be and $LiAlO_3$ (see Section IV-H-5 and IV-H-6) then one should also have to replace the cans because of the ductility loss at 660°C. Here again, more data is urgently required.

IV-H-5. Radiation Effects to $LiAlO_2$

The reasoning behind the choice of $LiAlO_2$ as the solid breeder for UWMAK-II has been discussed in IV-H-B. The lithium has been enriched to 90% Li-6 and the $LiAlO_2$ has been assumed to be fabricated at 50% of theoretical density with 20 micron diameter particles. The geometry and temperature distribution within the center fuel rod is given in Table IV-H-14.

It can be seen that the maximum temperature in the center of a rod in the first breeding zone is 1097°C and temperature gradients as high as 226°C per cm exist to the outside of the rod. The temperatures are somewhat lower in the second breeding zone with maximum temperature of 947°C and the thermal gradients range from 56°C cm^{-1} to 135°C cm^{-1}.

The production of helium via the Li-6 $(n,\alpha)T$ reaction is also included in Table IV-H-14. The helium generated by the Li-7 $(n,n'\alpha)T$ reaction is less than 0.6% of the Li-6 value and has been neglected in these calculations. The helium generation rate at an 80% plant factor ranges from 1.095 to 1.825 x 10^{21} atoms per cm^3 per year in the first breeding zone and from 0.2956 to 1.241 x 10^{21} atoms per cm^3 per year in the second breeding zone. These numbers can be converted to more meaningful quantities by the following factors

$$\frac{10^{21} \text{ He atoms}}{\text{cm}^3 \text{ of } LiAlO_2} = \frac{37.2 \text{ cm}^3 \text{ of gas (STP)}}{\text{cm}^3 \text{ of } LiAlO_2}$$

$$\frac{10^{21} \text{ He atoms}}{\text{cm}^3 \text{ of } LiAlO_2} = 85{,}840 \text{ appm of } LiAlO_2 \text{ molecules at 50\% DF} *$$

There is essentially no experimental data on helium induced swelling in $LiAlO_2$ so we will have to resort to a simple theoretical model to calculate swelling.

Let us assume for the time being that the mobility of the helium atoms is high enough such that once a gas atom is produced, it can migrate to a nucleation site and form a bubble. We will also assume no helium is lost by release to the coolant. In the presence of the large flux of vacancies produced by irradiation, the bubble will grow with an equilibrium gas pressure P of

$$P = \frac{2\gamma}{r} \qquad (5)$$

where

γ is the surface energy
r is the radius of the bubble.

* DF = Density Factor

Table IV-H-14

Summary of Operating Conditions and Helium Generation in the Breeding-Neutron Multiplying Zones of UWMAK-II

cm from First Wall	Material	Centerline Temperature °C	Temp. inside °C Cladding	ΔT °C	ΔT/ΔX °C-cm^{-1}	Helium atom Generated per cm^3/year x 10^{21}
0	Steel	567	514	53	30	
1	90% $LiAlO_2$	900	637	263	151	0.18
2	(50% DF)	1097	702	395	226	0.19
3	10% Steel	1049	725	324	186	0.35
4		603	594	9	5.2	0.14
5		595	588	7	4	0.13
6		590	585	5	2.9	0.12
7		587	583	4	2.3	0.12
8	90% Be	586	582	4	2.3	0.11
9	(50% DF)	586	582	4	2.3	0.10
10	10% Steel	586	582	4	2.3	0.089
11		587	583	4	2.3	0.080
12		588	585	3	1.7	0.076
13		589	586	3	1.7	0.073
14		591	588	3	1.7	0.065
15		593	590	3	1.7	0.061
16		595	592	3	1.7	0.056
17		597	594	3	1.7	0.052
18		600	597	3	1.7	0.050
19		603	601	2	1.1	0.044
20		608	605	3	1.7	0.041
21		615	610	5	2.9	0.039
22		935	726	209	120	0.29
23	90% $LiAlO_2$	947	712	235	135	0.11
24	(50% DF)	909	699	210	120	0.079
25		875	690	185	106	0.065
26	10% Steel	853	686	167	96	0.058
27		842	685	157	90	0.052
28		838	686	152	87	0.053
29		844	691	153	88	0.064
30		852	700	152	87	0.11
31	Steel	787	689	98	56	

If we assume that the bubble radius is small (<1000 Å) then we must use a VanderWaals equation to describe the volume, V, occupied by a bubble which contains m' atoms. Neglecting the attractive terms we find

$$P(V - m'b) = m'kT \tag{6}$$

where

b is the VanderWaals constant
k is Boltzmann's constant
T is the temperature °K

The volume induced by a density of bubbles, ρ, which have radius r and contain m' atoms is

$$\left(\frac{\Delta V}{V_o}\right)\% = 100\ N\left[\frac{rkT}{2\gamma} + b\right] \tag{7}$$

where

$N = \rho m'$ number of atoms cm^{-3}
ρ = bubbles cm^{-3}
m' = atoms per bubble of radius, r

$$m' = \frac{8\pi\ \gamma r^3}{3(kTr + 2\gamma b)}$$

Hence, given the amount of gas produced per cm^3 at some temperature T in a solid with surface energy γ, we can calculate the volume change provided we specify either the bubble density or the bubble size.

The calculated effect of temperature, bubble size and irradiation time on the helium gas induced swelling in $LiAlO_2$ is shown in Figure IV-H-15. The curves depict two helium concentrations, 3.5×10^{20} atoms/cm^3 of $LiAlO_2$ and 7×10^{20} atoms/cm^3. These numbers correspond to one and two years of irradiation to the first breeding zone respectively. They also correspond to 6 or 12 years respectively in the $LiAlO_2$ at the back side of the second breeding zone.

The results in Figure IV-H-15 show that an absolute minimum of 4-5% swelling will occur in the $LiAlO_2$ of the first breeding zone after one year of irradiation. However, if the helium atoms collect into bubbles and grow by absorbing vacancies, then the swelling could be much worse. Swelling of as much as 10% could occur if the bubbles attained diameters of 500 Å and if they grew to 6000 Å diameter the specific volume of the $LiAlO_2$ could double in one year. These constraints are even more severe if we look at the two year irradiation case. This level of helium will induce 10% swelling values for 200 Å diameter bubbles and 100% swelling for 3000 Å diameter bubbles. Such bubble diameters are probably quite realistic given the fact that 1097°C represent approximately 70% of the melting point of $LiAlO_2$ and that large (226°C per cm) temperature gradients exist.

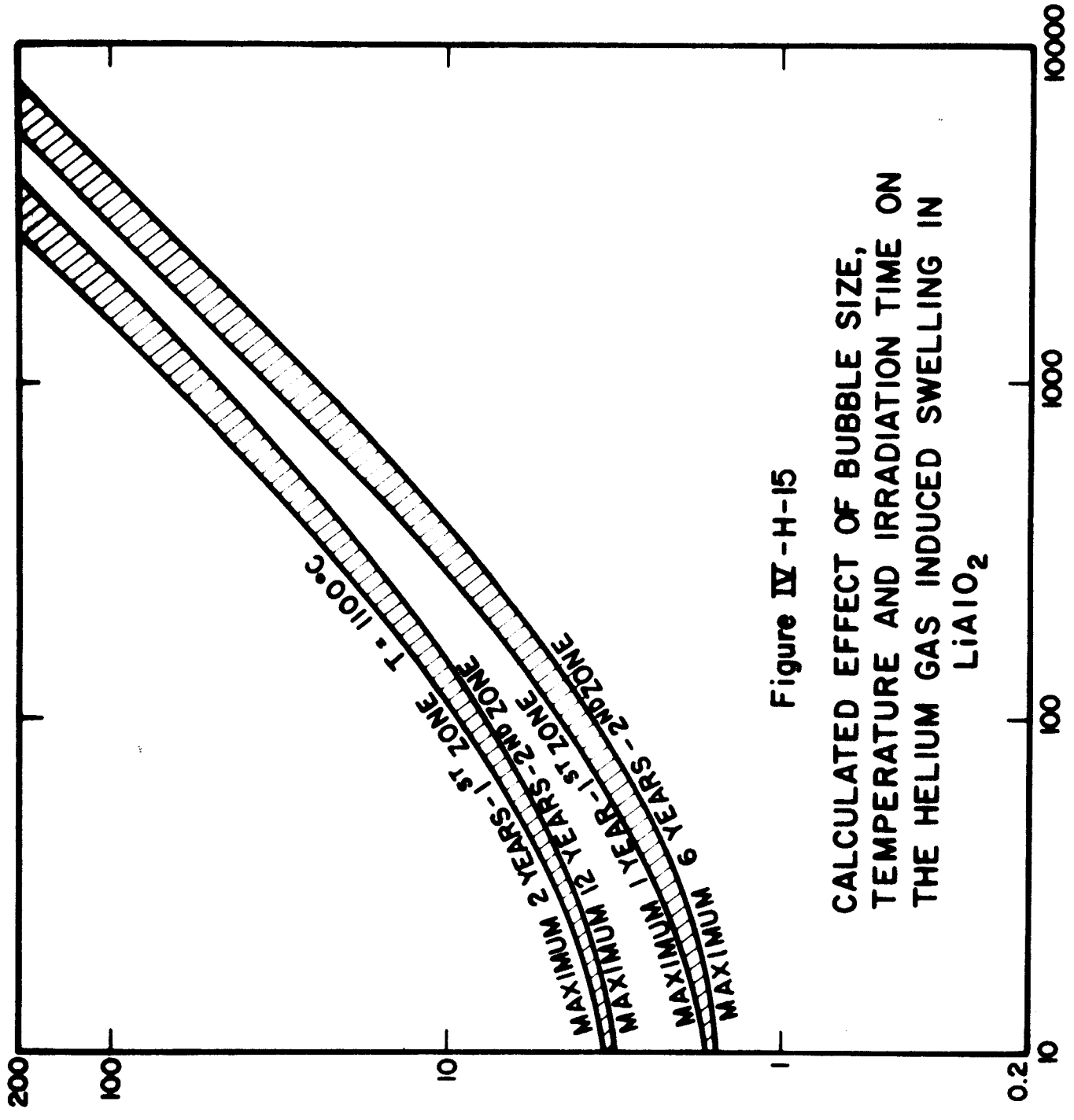

Figure IV-H-15

CALCULATED EFFECT OF BUBBLE SIZE, TEMPERATURE AND IRRADIATION TIME ON THE HELIUM GAS INDUCED SWELLING IN $LiAlO_2$

The previous analysis assumes no helium atom release either by individual atom or bubble migration, or by intersection of the bubbles with the surface of the particles. While the diffusivity of helium in the $LiAlO_2$ ceramic is unknown, it probably is very low in the presence of all the lattice defects being generated by displaced atoms and the fissioning of the Li atoms. Helium-vacancy complexes probably would determine the rate at which gas atoms diffuse through the matrix. It is also questionable that we will be able to maintain a 20 micron diameter particle size in the face of UWMAK-II operating conditions.[28] It is quite possible that thermal or irradiation induced sintering might take place so that the average particle size will greatly increase (with other consequences such as increased tritium inventories) thus reducing the possibility of helium leakage. In any case, our calculations here represent a worst case and future experimental work is required to clarify the exact helium retention rate.

In summary, the helium generation problem in $LiAlO_2$ is so large that significant swelling will occur in as little as one year of irradiation. The 50% void fraction could easily be filled by the expanding $LiAlO_2$ if the He gas bubbles were as large as 1000 Å after two year, or 500 Å after 4 years of irradiation. Further irradiation beyond this point would place a stress (and associated strain) on the wall which could result in failure of the cladding. This would in turn release tritium into the helium coolant stream and could result in increased T_2 leakage to the environment. The results here indicate that the use of $LiAlO_2$ for long times in high temperature environments should be closely examined.

IV-H-6 Radiation Damage to Beryllium Neutron Multiplier in UWMAK-II

The major problem of irradiated Be is the production of helium atoms. There are five possible reactions which can produce helium, four of which operate in UWMAK-II. Table IV-H-15 lists the reactions and their relative and absolute helium production rates in two extreme positions of the neutron multiplier. The amount of gas atoms produced per cm^3 of Be (50% DF) per year at 80% plant factor is also given in table IV-H-15.

As anticipated, the major source of helium comes from the (n,2n) reaction (~95%) and less than 5 percent comes from the (n,α) reaction and subsequent burning of the Li-6 atom produced. The concentration of helium in the 50% dense Be ranges from 2430 appm to 926 appm, after one year of irradiation. The maximum of these numbers corresponds to 5.2 cm^3 of helium gas produced per cm^3 of Be.

We can get an idea of the anticipated swelling in the beryllium by using the same calculational model as for $LiAlO_2$. The results are given in figure IV-H-16 for an average irradiation temperature of 600°C and the minimum swelling is included to illustrate the gradient in He production through a typical rod. Maximum values of swelling are given for 1, 2 and 10 years assuming a surface energy of 1000 ergs/cm^2. The volume increase due to the production of helium atoms alone approaches 0.6 per year. This means that in the absence of significant bubble formation the 50% void space should be sufficient to accomodate ~80 years of operation or the entire plant lifetime. However, if the helium atoms form bubbles larger than 20 Å in diameter the swelling could be substantially more. The high operating temperature (56% of the melting point) and displacement rates will probably promote bubble agglomeration. The temperature gradients are quite low <5°C cm^{-1} so that driving force will probably be inconsequential.

If the bubble size increases to 2000 Å diameter one could find as much as 2% swelling after one year or 20% swelling after 10 years of irradiation. The entire void space would be filled after one year of the bubble size reached 5000 Å. The critical value after two years is reduced to 2500 Å diameter. It should be noted in this respect that irradiation at 650°C to only 0.25 cm^3 of He/cm^3 of Be produced helium bubbles which ranged from 500-20,000 Å in diameter [29]. Therefore it is not unreasonable to expect that swelling values of 50 to 100% per year of UWMAK-II irradiation might occur in the neutron multiplier. This means that the Be should also be changed out every 2 years when the first wall and $LiAlO_2$ is recycled.

Table IV-H-15

Summary of Helium Production in UWMAK-II

Beryllium

1. $Be^9(n,2n)\ Be^8 \xrightarrow{<10^{-14}s} 2He^4$

2. $Be^9(n,\alpha)\ He^6 \xrightarrow{0.82s} Li^6 + n \rightarrow T + He^4$

3. $Be^9(n,d)\ Li^8 \xrightarrow{0.86s} Be^8 \xrightarrow{<10^{-14}s} 2He^4$

4. $Be^9(n,p)Li^9 \xrightarrow{0.17s} n + 2He^4$

5. $Be^9(n,T)\ Li^7 + n \rightarrow He^4 + T + n$

Reaction #	E_{th} MeV	Region Closest to Plasma		Region Furthest from Plasma	
		appm/year[a]	%	appm/year[a]	%
1	1.85	2306	95.1	870	94.3
2[b]	0.67	95	3.9	50	5.0
3	16.29	0	0	0	0
4	14.26	0.2	0.008	0.06	0.0001
5[b]	11.60	25	1.0	6.3	0.7
		~2430		~ 926	

(a) 80% plant factor

(b) assuming the Li atom captures a neutron during the lifetime of the Be in the reactor.

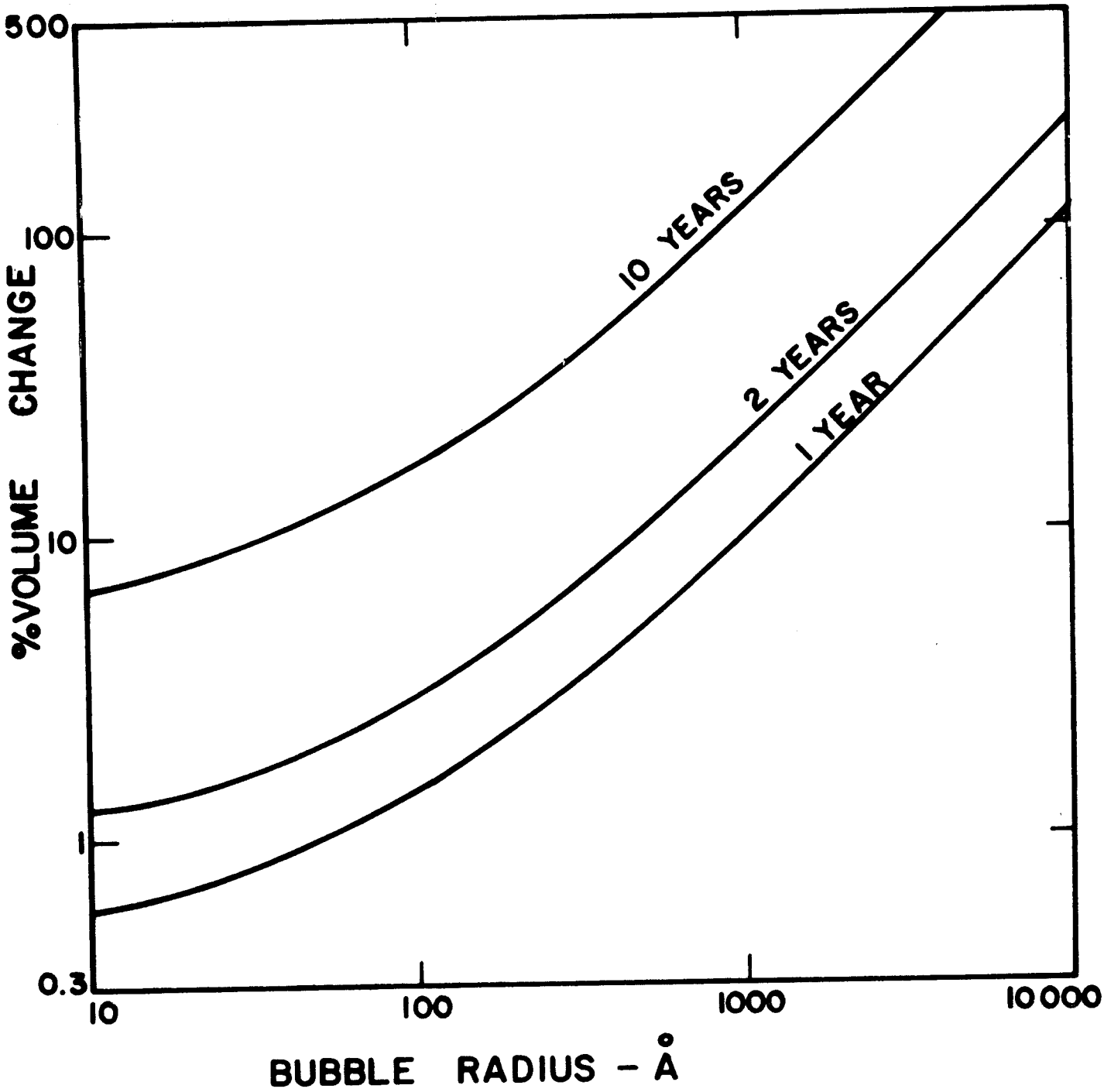

FIGURE IV-H-16
Maximum Calculated Swelling in UWMAK-II Beryllium at 600°C

IV-H-7 Radiation Damage to UWMAK-II Graphite Reflector

The graphite in the reflector zone is expected to operate in the temperature range of 655°C and will suffer displacement damage ranging from 1.8 dpa per year (80% P.F.) at the surface closest to the plasma to 0.24 dpa per year at the back edge of the reflector. We can get a feeling for the dimensional changes in graphite subjected to this fluence by using the data of Gray and Morgan.[9] The appropriate conversion factor is now

$9.3 \times 10^{18} n/cm^2$ (fission) = 1 full power day to the graphite reflector closest to the plasma.

$1.2 \times 10^{18} n/cm^2$ (fission) = 1 full power day to the graphite at the back side of the reflector.

Figure IV-H-17 shows how the dimensional stability of NCR graphite might be for up to 2000 full power days (6.9 years at 80% plant factor) at the front of the reflector and up to 18,000 full power days (62 years of UWMAK-II operation) at the back of the reflector. We will use the criteria of Gray and Morgan that state the useful lifetime is determined by the fluence required for the graphite to pass through the initial contraction stage and come back to zero dimension change. This conservative design limit says that if irradiation at 655°C is similar to 400-500°C irradiation, then the maximum useful operation time for the reflector is between 6 and 7 years. However, a slight amount of expansion could be tolerated and it seems reasonable to expect a 10 year useful lifetime. It is doubtful that a full 30 years could be realized but since the rest of the blanket will probably have to be changed every 10 years because of embrittlement and swelling, the graphite reflector could also be changed at that time.

IV-H-8 Radiation Effects to UWMAK-II Shielding

There are three materials to consider in the UWMAK-II shield --

316 SS structure
Pb gamma shielding
B_4C neutron absorber.

The problems in the structure are expected to be minimal because of the low temperature (50-200°C) and low dpa value (~0.004 dpa per year maximum). This latter value is roughly equivalent to a fast neutron exposure of $2 \times 10^{20} n/cm^2$ per year ($E > 0.1$ MeV). Hence, both the maximum temperature ($0.26\ T_m$) and the maximum damage are below the threshold for void formation[18] and even significant hardening to occur.

The effect of neutron irradiation on the properties of Pb is virtually unknown. The UWMAK-II operating temperature range corresponds to 40 to 60% of the absolute melting temperature. Hence, it is possible that voids could form or if significant amounts of He were generated, bubbles could form. However, maximum damage levels of <0.004 dpa (the dpa cross section for Pb is unknown but probably smaller than for 316 SS because of the reduced energy transfer to the heavier Pb atoms) are probably too low to induce significant void formation. The threshold for helium generation is also >14.1 MeV so that insufficient amounts of helium are generated to cause bubble formation. Therefore, a preliminary assessment might conclude that there would be no significant problem with Pb in the UWMAK-II environment.

Figure IV-H-17 Length Changes of Type NC8 Graphite at 400-500°C

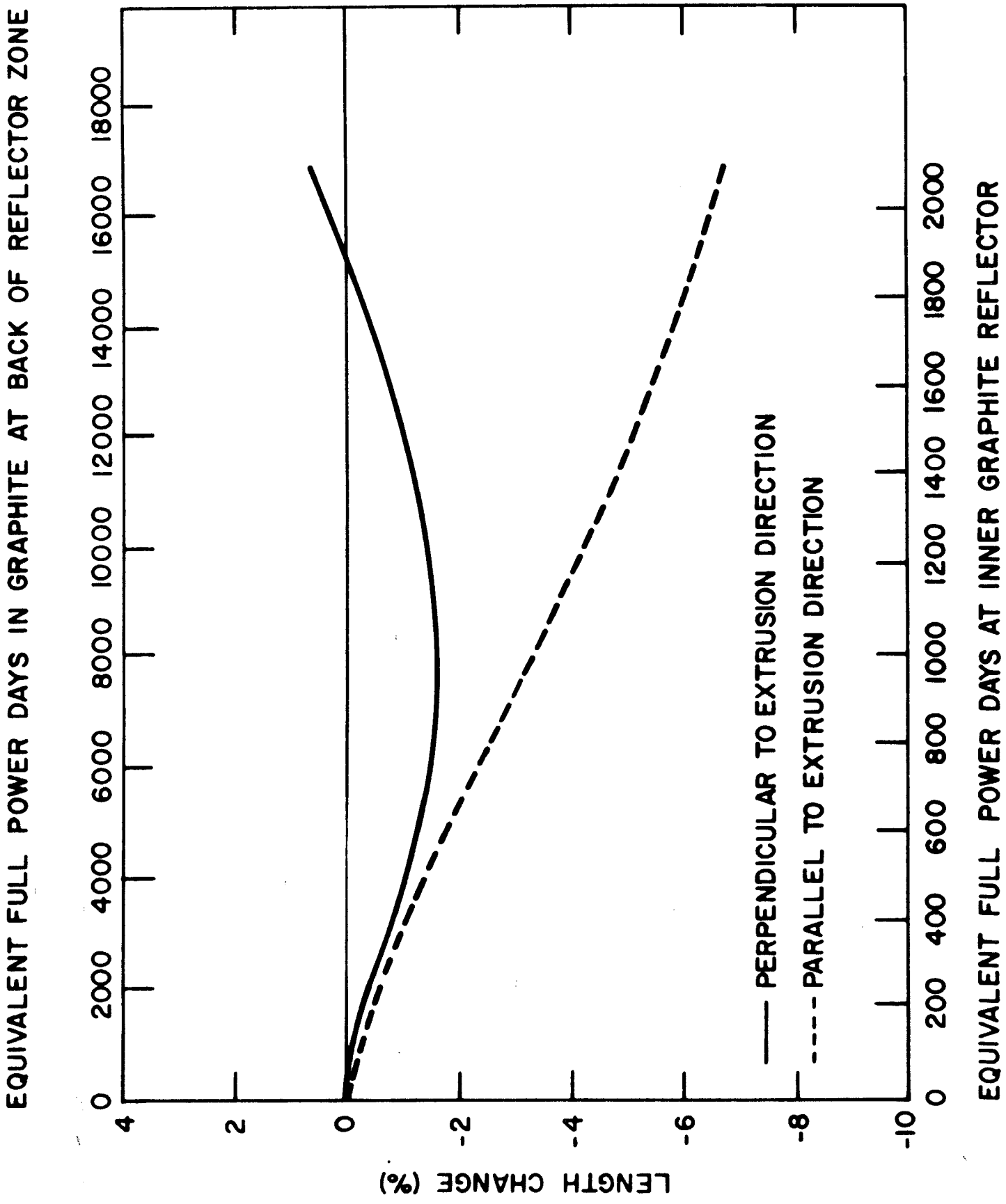

The only major problem with the B_4C is the production of helium via the $B^{10}(n,\alpha)Li^7$ reaction.* The maximum amount of helium produced in the B_4C is 0.358×10^{20} atoms/cm^3 per year of UWMAK-II operation.

Hence, over the 30 year lifetime, the maximum helium generation is 10.7×10^{20} atoms/cm^3 of B_4C. Previous analysis (Figure IV-H-18) shows that the amount of swelling to be expected from this much helium is <1% if the irradiation takes place below 300°C. Therefore, there should be little if any noticeable dimensional change in the B_4C even if irradiated for the full lifetime of the reactor.

It is worthwhile to note here that a significant amount of tritium will be produced in the following reactions.

$B^{10}(n,T)2He$	(91%)
$B^{11}(n,T)Be^9$	(9%)

The total amount of tritium generated per year via these two reactions is 1100 curies or 3.3×10^4 curies in 30 years of UWMAK-II operation. The maximum concentration of this tritium activity will be approximately 1 curie/cm^3 of B_4C and such an activity is probably tolerable even in the event of a rupture of the shield due to some as of yet undefined accident.

In summary, there appears to be no obvious reasons that, at least from the radiation damage standpoint, the shield will not last the entire projected plant lifetime.

IV-H-9 Radiation Damage to UWMAK-II Superconducting Magnet

We will use as our model for these calculations the configuration of the toroidal coils at the midplane on the inside of the torus. There are other vertical field coils on the outside of the torus between the shield and the TF coil but the radiation damage in these coils should be typical of our model. We will briefly analyze five areas of potential damage --

316 SS support structure
Mylar super insulation
Epoxy electrical insulators
Cu stabilizer
NbTi filaments

The 316 stainless steel in the magnets will operate all the way from ~4°K to 300°K. The maximum displacement rate is $\sim 2 \times 10^{-6}$ dpa per year of operation, which corresponds to an equivalent fission spectrum fluence of $\sim 5 \times 10^{15}$ n/cm^2 (E > 0.1 MeV). Such a low fluence is not expected to cause significant mechanical property changes in steel. The threshold for observable damage in metals at low temperature appears to be on the order of approximately 5×10^{16} n/cm^2 or greater (E > 1 MeV).(31)

The critical parameters for the thermal insulation between the shield and the TF magnet is the total radiation dose received in Rads from both neutron and photon

---

*The $B^{11}(n,\alpha)2He^4$ reaction contributes <0.1% of the total helium generated.

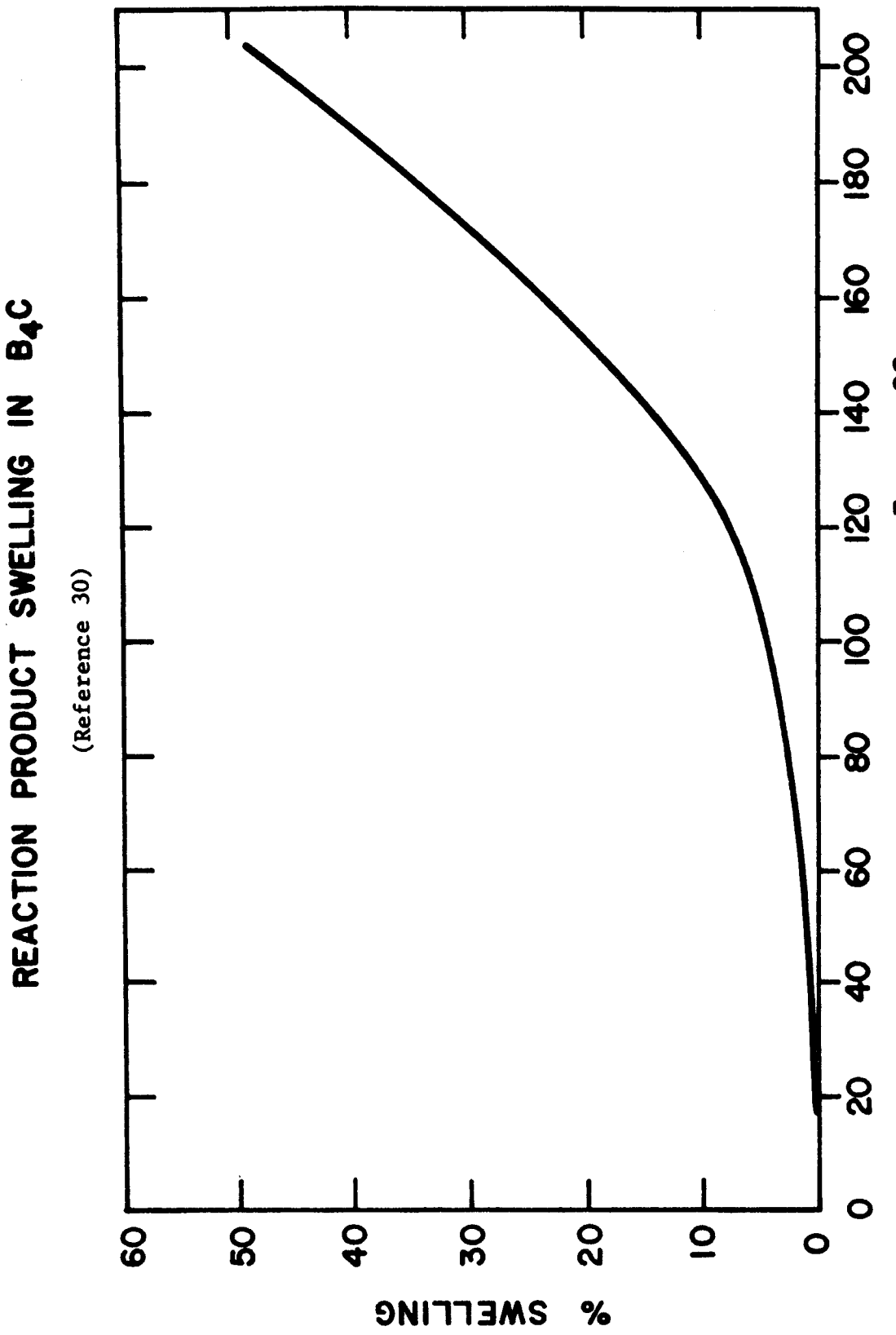

Figure IV-H-18

irradiation. We can calculate the maximum dose received by the mylar if we assume all of the energy leaking from the shield in the form of neutrons and gamma rays is absorbed in the 15 cm thick region of mylar (5% density). Calculations show that 0.137 eV/DT neutron "leaks" from the shield in the form of gamma rays and 0.884 eV/DT neutrons comes from neutrons. The total leakage is then 1.021 eV/DT neutron or 7.25×10^{-8} eV/eV. Since our power level is 5000 MW, then approximately 256 watts is available for radiation damage to the mylar. If the energy is deposited uniformly in the 2.9×10^{7} of mylar, then the density of damage is 9.1×10^{-6} watts per cm^3 of mylar. Using the density of mylar to be ~ 1 g/cm^3, we find that the maximum exposure level is 0.9 Rad/sec, 23 MRad/year (80% P.F.), or 690 MRad/30 year of operation.

The above calculations are likely to be too high by a factor of 10 because the mean free path for 1 MeV gamma rays is ~10 cm in mylar and the mean free path for scattering of 1 MeV neutrons in mylar is also on the order of 10 cm. Hence, only approximately 10% of the energy of the average photon and neutron will be absorbed in the mylar and we will assume that the following energy deposition rates are correct for UWMAK-II.

0.09 Rad/sec

2 MRad/year

60 MRad/30 years of operation

Previous analysis of the radiation damage resistance of mylar has produced a threshold for observable degradation of the mechanical properties at 30 MRad and that a reasonable design limit would be when the irradiated mylar has its unirradiated tensile strength degraded by 25% (~120 MRads). On the basis of the previous analysis, we would expect to slightly exceed the threshold for damage in 30 years. Therefore, it appears that the irradiation of the super insulation in UWMAK-II is not a serious problem.

Next we turn our attention to the organic electrical insulating material, glass fiber reinforced epoxy. The threshold for observable damage in this material is 8000 MRads and a 25% property degradation occurs at 50,000 MRads.[7] Obviously, even if we took the worst case and allowed all of the energy leaking from the shield to pass through the mylar and be entirely deposited in the epoxy, we would not exceed the threshold for damage in 30 years of operation.

The next component of the magnet to consider is the copper stabilizer. The object of this material is to be able to temporarily carry the current normally conducted by the NbTi filaments. The copper should have as low an electrical resistance as possible in order not to generate excess heat due to I^2R losses. Radiation damage in copper at low temperature tends to increase its electrical resistance so that for any given design there is a critical damage level above which the passing of the current from the NbTi to the copper will result in an excess of heat being generated. Obviously, one would like to stay below that level of damage in 30 years of operation. It was previously determined that the threshold for 10% resistivity increase above that of normal OFHC copper at 4.2°K, is approximately 5×10^{-5}dpa (Figure IV-H-19) and that was used as a design limit.

Present analysis of the displacement rate in the magnet reveals that it is $<8 \times 10^{-7}$ dpa per year of operation. This calculation assumes that the displacement

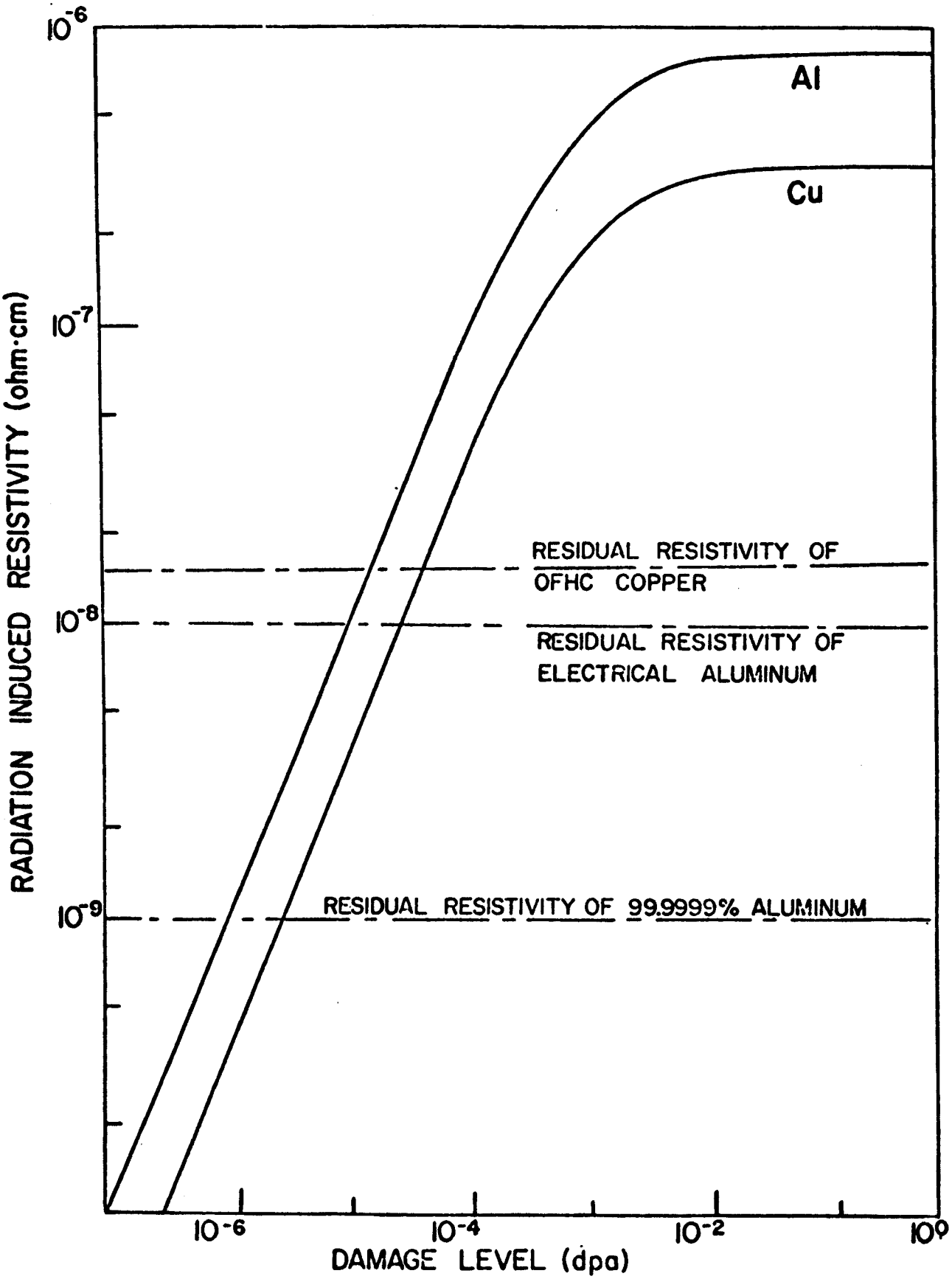

Figure IV-H-19 Radiation Induced Resistivity of Copper and Aluminum

cross sections of copper are the same as those in the steel. This means that one could theoretically operate the UWMAK-II TF coils for over 60 years before they would need to be annealed to remove the damage. It also means that no design modifications such as increasing the stabilizer thickness on the inside of the TF coils is required as in UWMAK-I.[7] The increased effectiveness of the UWMAK-II blanket and shield has greatly reduced the radiation damage problems in that system.

The last area to consider is any potential degradation of the NbTi superconducting properties. It is generally accepted that one of the most sensitive properties of superconducting magnets is the critical current density. Previous studies on NbTi[32] (Figure IV-H-20) have shown that damage levels of 10^{-3} dpa are required before as much as a 10% drop in J_c/J_{co} is observed. At damage levels of 10^{-5} dpa, essentially no change in critical current has been observed. Therefore, since our displacement rate is in the neighborhood of $<10^{-6}$ dpa per year, one would not expect significant effects even after 30 years (3×10^{-5} dpa). Again, the design of the blanket and shield to reduce the heat deposition in the S/C TF coils has about completely eliminated radiation damage to the magnet components.

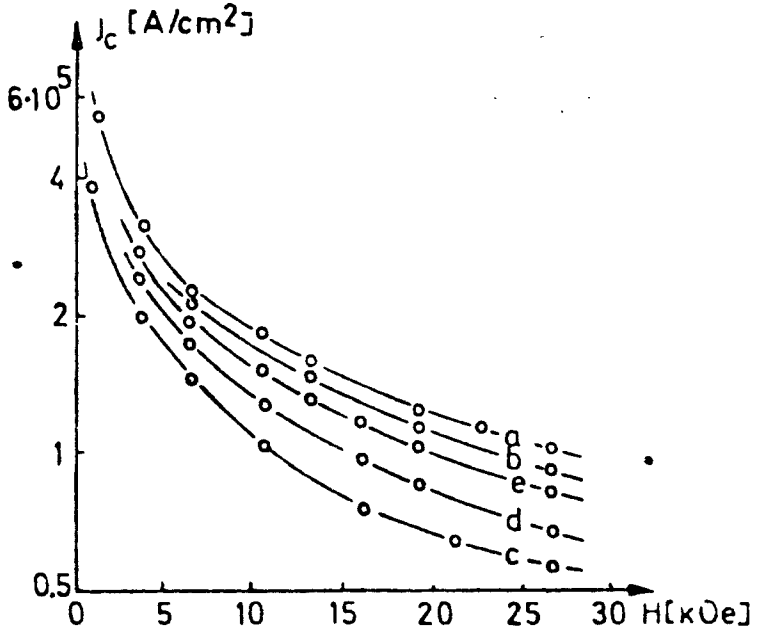

Critical current density j_c versus applied transverse magnetic field H for Nb-50wt%Ti at 5.3K. Curve a unirradiated, b irradiated with 3.2×10^{18} neutrons /cm² (E>0.1 MeV), c irradiated with 7.5×10^{18} n/cm², d annealed at 100 K, e annealed at 270 K (after Soell ref.2).

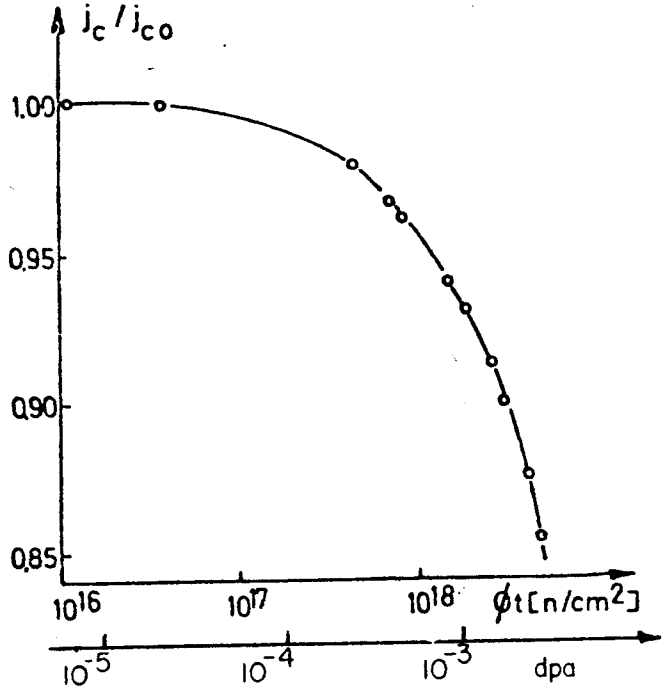

Relative Change of the critical current density jc of a Nb-50wt% Ti sample at zero field (H=0) as a function of the neutron dose $\phi \cdot t$. j_{co} is the current density before the irradiation (after Soell ref. 2).

Figure IV-H- 20 The effect of fast neutron irradiation at cryogenic temperature on the critical current of Nb-50 w/o Ti. The conversion to dpa was made using a typical thermal reactor spectrum.

References

1. Proceedings of the International Working Sessions on Fusion Reactor Technology, June 28-July 2, 1971, Oak Ridge National Laboratory, Oak Ridge, Tenn., CONF-710624, p. 137-222.

2. G. L. Kulcinski, "Bulk Radiation Damage Problems to First Wall Materials", p. 479-492, in "Fusion Reactor Design Problems," Special Supplement, Nuclear Fusion (1974).

3. See Nuclear Technology, Vol. 22, Nos. 1 & 2, (April-May 1974) for a collection of over 20 articles pertaining to Materials Problems in Fusion Reactors.

4. D. G. Martin, p. 399 in "Proceedings of British Nuclear Energy Society on Nuclear Fusion Reactors," held at Culham, England, Sept. 1969. See also article by M. T. Robinson, p. 364.

5. G. L. Kulcinski, "Radiation Damage by Neutrons to Materials in DT Fusion Reactors," IAEA-CN-33/53-1, to be published in the Proceedings of the 5th IAEA Conference on Plasma Physics and Controlled Nuclear Fusion Research, Tokyo, Japan, Nov. 1975. See also UWFDM-116, Nov. 1974.

6. G. L. Kulcinski, "The Need for Neutron Radiation Damage Information from the Viewpoint of the Fusion Reactor Designer," to be published in the Proceedings of the Int. Conf. on Radiation Test Facilities for the CTR Surface and Materials Program, Argonne, Ill., July 1975. See also UWFDM-132, July 1975.

7. Chapter VI in "UWMAK-I, A Wisconsin Toroidal Fusion Reactor Design", UWFDM-68, Nov. 1973.

8. W. C. Morgan, J. Nucl. Mat. 51, 209, 1974.

9. W. J. Gray and W. C. Morgan, BNWL-B-288, June 1973.

10. G. L. Kulcinski, D. G. Doran and M. A. Abdou, to be published in ASTM-STP publication of Gatlinburg Conf. on Radiation Effects, June 1974, See also UWFDM-15.

11. R. Behrisch, Nuclear Fusion 12, 695, 1972.

12. M. Kaminsky, IEEE Trans. Nucl. Sci., 18, 208, 1971.

13. M. Kaminsky, Proc. Int. Working Session on Fusion Reactor Technology, Oak Ridge National Laboratory, Oak Ridge, Tenn., 1971 USAEC Report # CONF-719624 (1971) p. 26.

14. M. Kaminsky and S. K. Das, Nucl Tech. 53, 162, 1974.

15. O. K. Harling, M. T. Thomas, R. L. Brodzinski, and L. A. Rancitelli, Phys. Rev. Lett. 34, 1340, 1975.

16. S. K. Das and M. Kaminsky, p. 1 in "Fifth Symposium on Engineering Problems of Fusion Research," Princeton, N. J., Nov. 1973, Published by IEEE, No. 73CH0843-3-NPS.

17. H. R. Brager and J. L. Straalsund, J. Nucl. Mat. 46, 134, 1973.

18. E. E. Bloom and J. O. Stiegler, J. Nucl. Mat., 36, 331, 1970.

19. A. L. Bement, Jr., "Void Formation in Irradiated Austenitic Stainless Steel", p. 1 in Adv. in Nuclear Sci., 7, 1972.

20. Nuclear Systems Handbook, Vol. 1, Property Code 3304(E-1) Page 1.0. Part I, Group I, Sections 4 and 5, 1974.

21. F. W. Wiffen and E. E. Bloom, Nucl. Tech., 25, 113, 1975.

22a. R. L. Fish and J. J. Holmes, J. Nucl. Mat., 46, 113, 1973.

22b. E. E. Bloom, p. 93 in "Irradiation Embrittlement and Creep in Fuel Cladding and Core Components," BNES, London 1973.

23. P, Soo and J. McAndrew, WARD-3045T2C-3 Nov. 1972.

24. A. J. Lovell, Nucl. Tech, 26, 279, 1975.

25. E. E. Bloom and F. W. Wiffen, ORNL-TM-4861, May 1975.

26. J. J. Holmes, private communication.

27. R. L. Fish, J. L. Straalsund, C. W. Hunter, and J. J. Holmes, p. 149 in "Effects of Radiation on Substructure and Mechanical Properties of Metals and Alloys," ASTM-STP-529, 1973.

28. J. S. Hirschorn, to be published.

29. B. S. Hickman, p. 72 in "Studies in Radiation Effects," Vol. 1, Gordon and Breach, New York, ed. by G. J. Dienes, 1966.

30. R. G. Gray and L. R. Lynam, WAPP-261, 1963.

31. M. Kangilaski, p. 122 in "Radiation Effects Design Handbook," Section 7, Structural Alloys, NASA-CR-1873, 1971.

32. M. Soell, S. L. Wipf, and G. Vogel, "Change in Critican Current of Superconducting NbTi by Neutron Irradiation," Applied Superconductivity Conf., Annapolis, Md., 1972.

IV-I. Radioactivity, Afterheat and Safety Considerations

IV-I-1. Introduction

The structure in the blanket, shield, and magnet regions is exposed to the neutron flux originating in the plasma and therefore will become radioactive. This radioactivity may present afterheat and safety questions. This problem is of course, not unique to UWMAK-II but occurs in any reactor using the D-T reaction. In the earlier report reviewing the design of UWMAK-I,[1] the radioactivity aspects were treated in detail for that design. This work will review the same areas for UWMAK-II pointing out from time to time significant differences between the two designs. Qualitatively the differences should not be too great especially on an overall basis and should be largely attributable to differences in the quantities of activating material used. For example the first wall of UWMAK-II is thicker than that of the UWMAK-I design.[2] Information will be presented first for the basic design specifically using 316 SS as the blanket structural material. We will then present a comparison with Nb-1Zr or V-20Ti substituted for the blanket structure. The reactions considered and methods of calculation are the same as reported in UWMAK-I.[2] However the cross sections used for many of the present calculations came from a set generated by Pearlstein[3] rather than those used in the earlier report which were often based on a minimum amount of reported data. Whenever comparisons are made with UWMAK-I, both results have been calculated using the revised cross sections.

The representation of the blanket is the same as that taken for the neutronics calculations given in section IV-C and is shown again in Fig. IV-I-1. The fluxes used in the calculation are also taken from the neutronics work. To reduce the labor somewhat, each region of that blanket and shield have been divided into one or more subregions and the average flux for that region used for the calculations. The neutron flux is assumed to be constant during the life of the plant as in the earlier calculations. The energy of the decay products is assumed to be deposited at the site where they are produced which is a very good assumption for the beta particles but does not allow for gamma transport, which should be an important effect. Although most of the results shown are for a ten year operating time, calculations were made for operating times up to twenty years.

IV-I-2. Radioactivity Calculations

The radioactivity of the blanket is shown in Fig. IV-I-2. Also shown in this figure is the radioactivity for the first wall and the total radioactivity of UWMAK-I, all for a 10 year operating time.* The rapid decrease at a short time is due to the decay of He^5. It is seen that for decay times longer than ~1 minute, the first wall contributes over 50% of the activity and that the activity of the blanket is greater for UWMAK-II than UWMAK-I. However the shapes of the curves for the two designs are quite similar. The increase of activity in UWMAK-II over UWMAK-I is due primarily to the increase in thickness of the 1st wall, which is the equivalent of 1 cm thick in II but only 0.4 cm in I. However, although the total activity of the first wall is greater in UWMAK-II than in UWMAK-I, the specific activity is lower. This is illustrated in Table IV-I-1 in which the total and specific activity of the first wall is compared in both designs. It is seen that although the total activity is greater in II by a factor of 2.1, the specific activity of II is only 0.42 that of I. Also shown in Table IV-I-1 is the inventory of isotopes contributing greater than 1% of the activity of shutdown. The major contributor is ^{55}Fe in both cases. Furthermore, the percentage contribution of each isotope is very nearly the same for both designs which accounts for the similarity in the shape of the decay curves for the two designs.

* All times reported in this Chapter are for 100% plant factor.

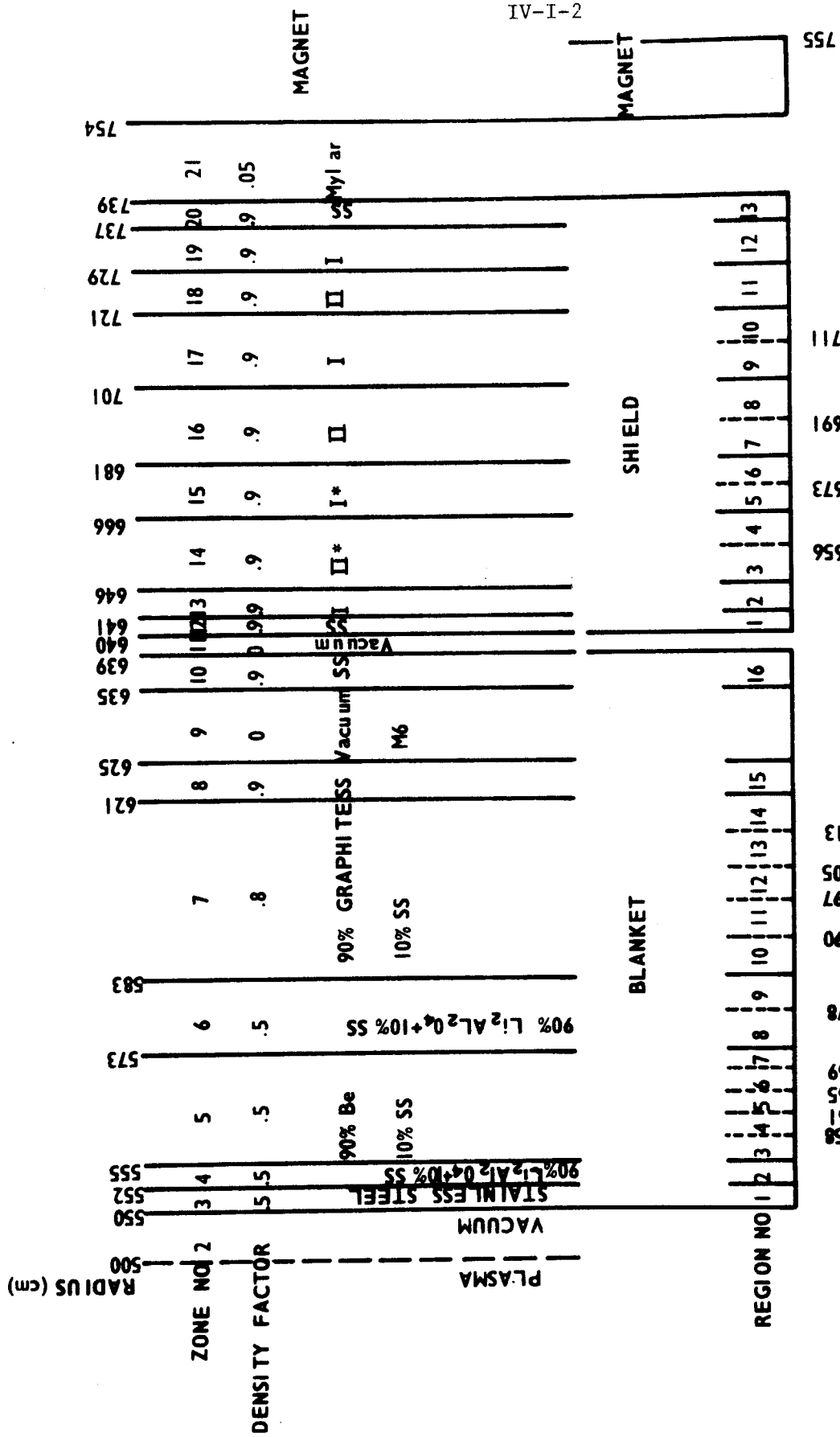

UWMAK - 2 BLANKET, SHIELD AND MAGNET STRUCTURE
FIG. IV--I -1

FIG. IV-I-2

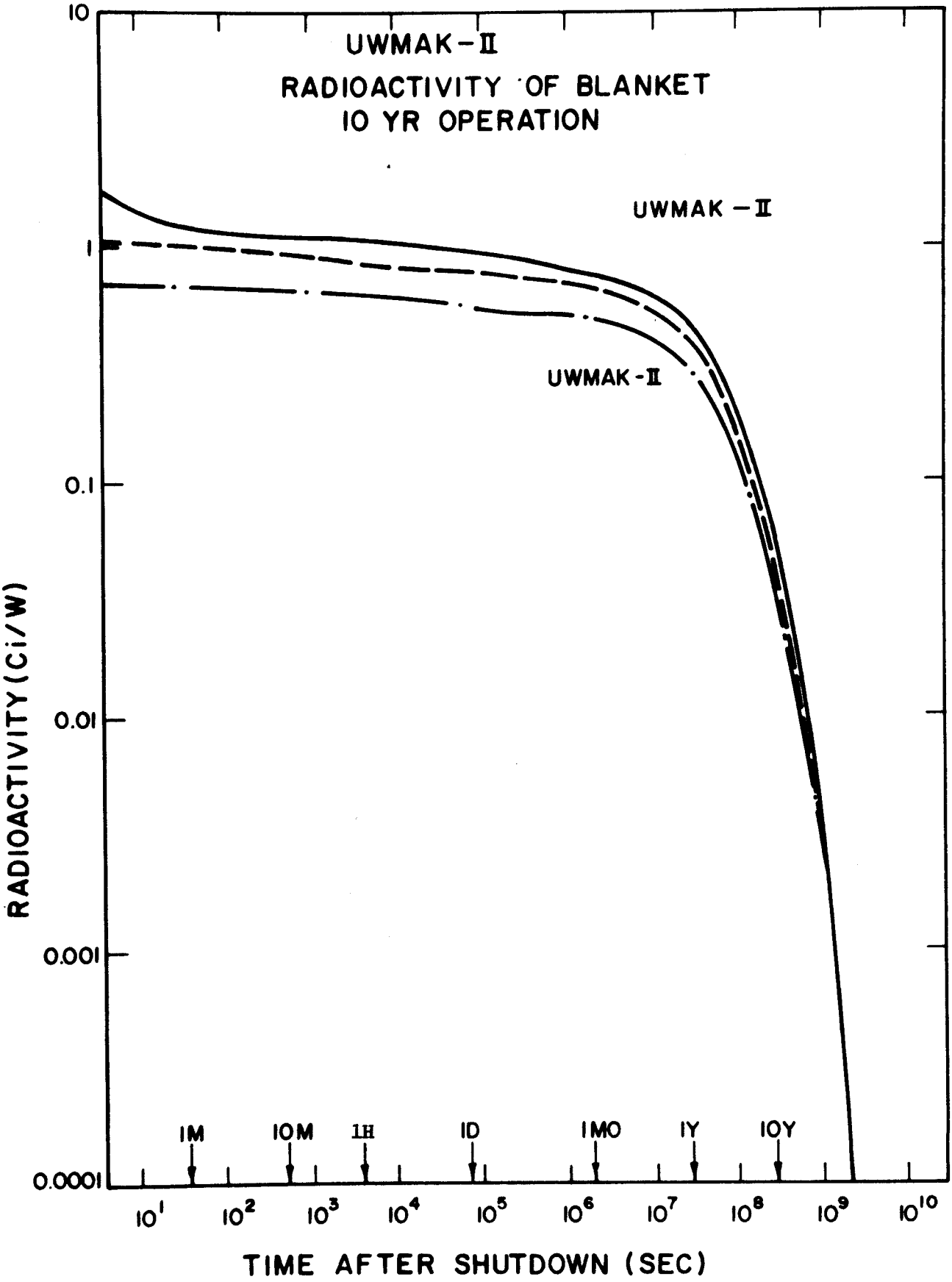
UWMAK-II
RADIOACTIVITY OF BLANKET
10 YR OPERATION
UWMAK-II
UWMAK-II
RADIOACTIVITY (Ci/W)
10
1
0.1
0.01
0.001
0.0001
1M
10M
1H
1D
1MO
1Y
10Y
10^1
10^2
10^3
10^4
10^5
10^6
10^7
10^8
10^9
10^{10}
TIME AFTER SHUTDOWN (SEC)

TABLE IV-I-1

First Wall Radioactivity
At Shutdown (10 yr. Operation)

	UWMAK-I			UWMAK-II			RATIO $(\frac{II}{I})$
Total Activity	$0.606 + 20^{dps}$			$0.127 + 21^{dps}$			2.1
Specific Activity	$0.537 + 13^{dps/cm^3}$			$0.225 + 13^{dps/cm^3}$			0.42
	dps/cm^3*		percent	dps/cm^3*		percent	
^{55}Fe	0.267	10(13)**	49.7	0.113	10(13)	50.2	0.42
^{56}Mn	0.783	10(12)	14.8	0.324	10(12)	14.4	0.41
^{51}Cr	0.533	10(12)	9.9	0.230	10(12)	10.2	0.43
^{58}Co	0.385	10(12)	7.4	0.159	10(12)	7.1	0.40
^{54}Mn	0.375	10(12)	7.0	0.153	10(12)	6.8	0.41
^{52}V	0.174	10(12)	3.2	0.708	10(11)	3.2	0.41
^{57}Co	0.132	10(12)	2.5	0.560	10(11)	2.5	0.42
^{60}Co	0.872	10(11)	1.6	0.366	10(11)	1.6	0.42
^{60m}Co	0.716	10(11)	1.3	0.305	10(11)	1.4	0.43
^{28}Al	0.544	10(11)	1.0	0.222	10(11)	(.99)	.41

* Radioactive Nuclides (> 1% of Spec. Rad.)

**dps/cm^3

The nature of the spatial dependence of the radioactivity is illustrated in Table IV-I-2 which shows the radioactivity of each zone of the blanket as a function of time after shutdown. As expected the first three zones contribute over 85% of the activity with the first wall being clearly the biggest contributor followed by the breeding region by virtue of its large size.

Figures IV-I-3 and IV-I-4 are a comparison of radioactivity in a UWMAK-II type blanket using Nb-1Zr or V-20Ti as alternate structural materials to stainless steel. In the calculations, the SS in zones 3,4,5, and 6, i.e. the 1st wall and breeding regions, were replaced on a one to one volume basis by either Nb-1Zr, or V-20Ti.* The same neutron flux was used for all cases. These curves indicate a qualitative behavior very similar to that seen in UWMAK-I, i.e. the radioactivity of the Nb-1Zr systems is significantly higher at shutdown than either the SS or V-20Ti systems but in the 1-50 yr time span is lower than that of SS. At long times, however, the presence of long-lived Nb produces a residual activity greater than either of the other two systems. V-20Ti on the other hand while initially about the same as SS drops off much more rapidly until the activity of the SS in the rear of the blanket region starts to dominate. A comparison of the 2 yr and 10 yr operating time curves shows the tendency of the V-20Ti activity to saturate while both the SS and Nb-1Zr systems do not, especially at longer times.

The importance of various isotopes in the alternate systems is shown in Table IV-I-3 and IV-I-4 while the spatial dependence within the 1st wall and breeding region is shown in Tables IV-I-5, IV-I-6, and IV-I-7. Note that as with the SS systems at shutdown virtually all of the radioactivity comes from the breeding region while after a year of decay over 40% of the activity comes from the remainder of the blanket for Nb-1Zr and over 75% from the remainder of the blanket for the V-20Ti systems.

The radioactivity and afterheat in the shield region is shown in Figure IV-I-5 for a 10 year operation. The primary source of this activity is the SS structure in the shield and thus the shape of the curves is somewhat similar to that of the blanket. Both the activity and afterheat are quite low. As is expected, since the shield is designed to alternate neutrons, the major part of the activity comes from that part of the shield closest to the plasma. For example, ~95% of the activity comes from zones 13 and 14, i.e. the SS wall and the first B_4C-10% SS region.

The neutron flux through the magnets was not available at the time of publication. To obtain an idea of the problem with induced activity in the magnet, the calculation was made for 1 cm of magnet material using the leakage flux from the outside of the shield. The results are shown in Figure IV-I-6. The decay has a shape expected of steel which is the major constituent of the magnet. Both the activity and heating levels are quite low, the heating being only ~75 watts at shutdown and the radioactivity is approximately 100 curies.

IV-I-3. Biological Hazard Potential

The activities of the radionuclides may be expressed in terms of the "Biological Hazard Potential" (BHP) i.e. the amount of air required per kilowatt of thermal power to dilute the radioactive isotope to its maximum permissible concentration. The use of BHP requires no judgement as to a mode of release or whether it is possible to distribute the material in air but does, however, present a

* However, the stainless steel in the graphite and breeder zones was retained.

TABLE IV-I-2

RADIOACTIVITY OF EACH ZONE (10 Yr. Operation)

Time After Shutdown	T = 0		1 Minute		1 Hour		1 Day		1 Year		100 Years	
TOTAL	Ci 0.871 10(10)	%	Ci 0.622 10(10)	%	Ci 0.541 10(10)	%	Ci 0.453 10(10)	%	Ci 0.236 10(10)	%	Ci 0.436 10(6)	%
ZONE 3	0.344 10(10)	34.5	0.341 10(10)	54.8	0.311 10(10)	57.4	0.271 10(10)	59.8	0.152 10(10)	64.4	0.283 10(6)	63.5
4	0.984 10(9)	11.3	0.770 10(9)	12.4	0.555 10(9)	10.3	0.370 10(9)	8.2	0.166 10(9)	7.0	0.317 10(5)	7.1
5	0.325 10(10)	37.3	0.114 10(10)	18.3	0.105 10(10)	19.4	0.828 10(9)	18.3	0.397 10(9)	16.8	0.664 10(5)	15.2
6	0.631 10(9)	7.2	0.497 10(9)	8.0	0.323 10(9)	6.0	0.203 10(9)	4.5	0.828 10(8)	3.5	0.178 10(5)	4.1
7	0.271 10(9)	3.1	0.269 10(9)	4.3	0.254 10(9)	4.7	0.229 10(9)	5.1	0.900 10(8)	3.8	0.123 10(5)	2.8
8	0.932 10(8)	1.1	0.924 10(8)	1.5	0.868 10(8)	1.6	0.777 10(8)	1.7	0.294 10(8)	1.2	0.434 10(4)	1.0
10	0.361 10(8)	0.4	0.357 10(8)	0.6	0.326 10(8)	0.6	0.277 10(8)	0.6	0.120 10(8)	0.5	0.242 10(4)	0.6

FIG. IV-I-3 UWMAK-II
RADIOACTIVITY, 2 YR OPERATION

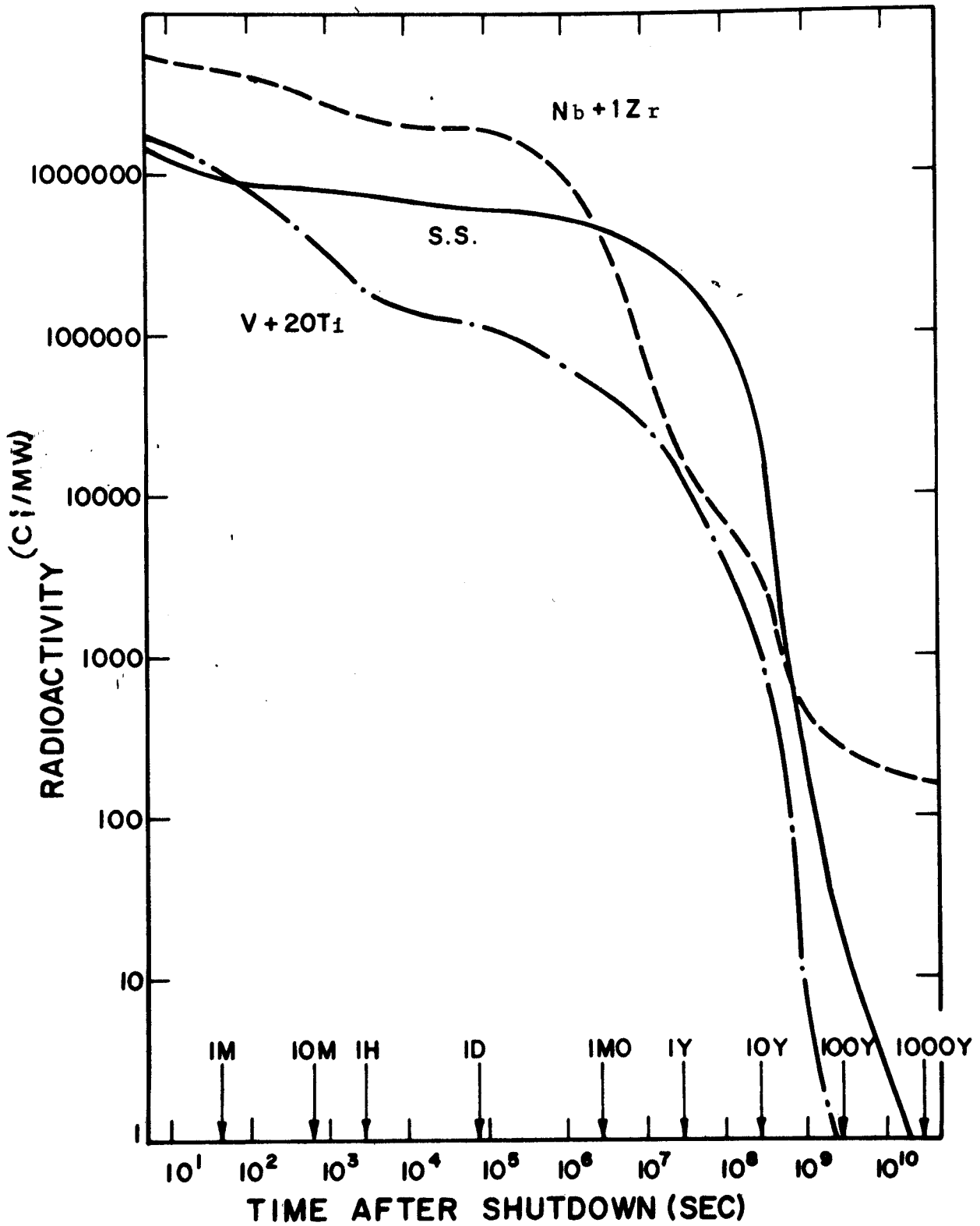

FIG. IV-1-4 UWMAK-II
RADIOACTIVITY
10 YR OPERATION

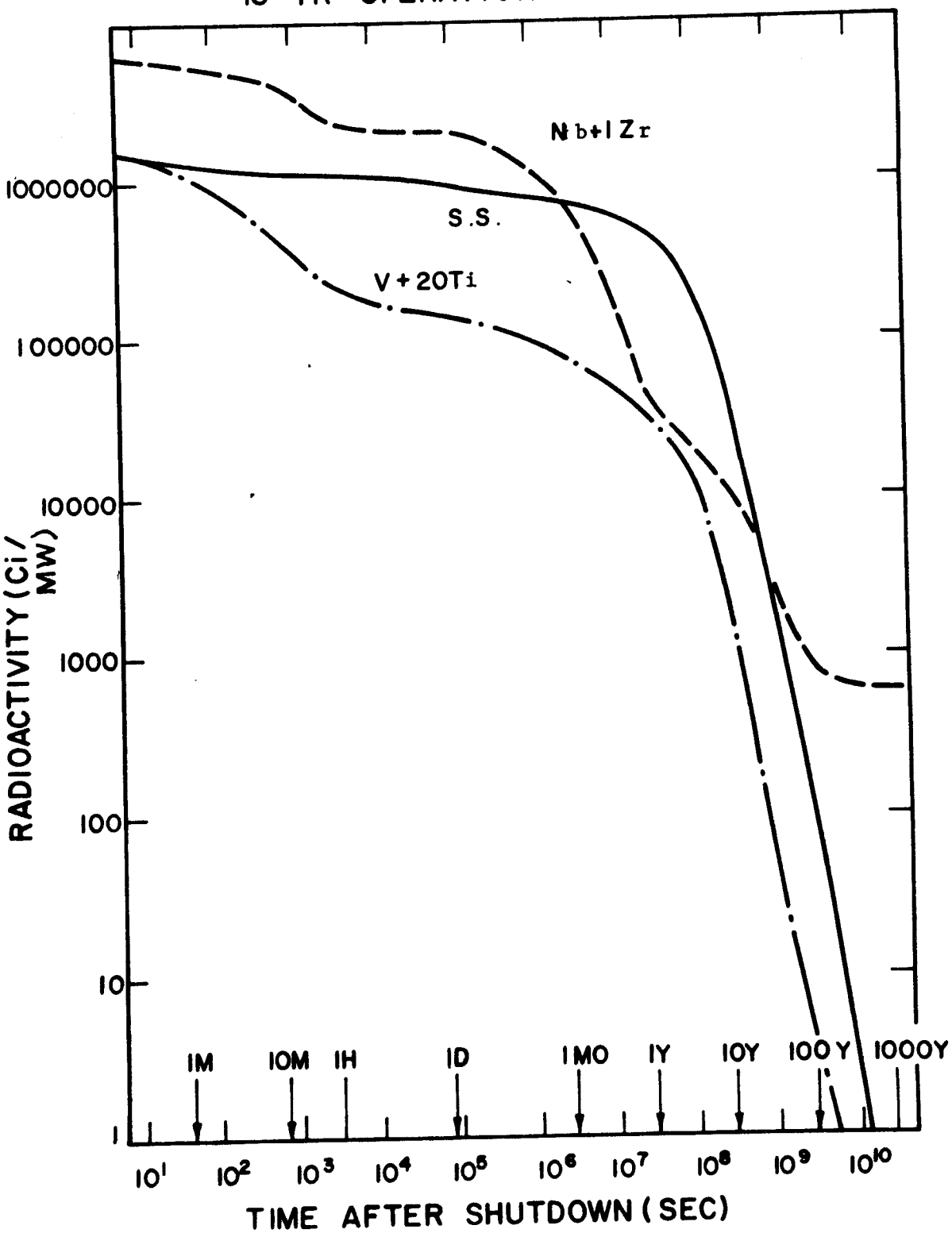

TABLE IV-I-3

Nb - 1Zr 1st Wall Radioactivity

10 Yr Operation

	AFTER SHUTDOWN TIME		
	t=0	1 H	1 Yr
TOTAL	0.475 10(21) dps	0.310 10(21) dps	0.153 10(19) dps
SPEC.	0.840 10(13) dps/cm^3	0.547 10(13) dps/cm^3	0.271 10(11) dps/cm^3
	%	%	%
Nb 92m	0.329 10(13) 39.1	0.328 10(13) 60	
Nb 94m	0.291 10(13) 34.6		
Nb 95m	0.112 10(13) 13.3	0.111 10(13) 20.3	
Nb 95	0.993 10(12) 11.8	0.993 10(12) 18.2	0.901 10(9) 3.3
Nb 93m			0.251 10(10) 92.6
Nb 94			0.881 10(9) 3.3

TABLE IV-I-4

UWMAK-II

V -20 Ti 1st Wall Radioactivity

	TIME AFTER SHUTDOWN					
	t=0		1 Hr		1 Yr	
TOTAL	0.706 10(20) dps		0.936 10(19)		0.111 10(19)	
SPEC.	0.125 10(13)		0.166 10(12)		0.196 10(11)	
	dps/cm^3	%	dps/cm^3	%	dps/cm^3	%
V 52	0.924 10(12)	73.9				
Ti 51	0.157 10(12)	11.6				
V 49	0.343 10(11)	2.7	0.342 10(11)	20.6	0.159 10(11)	81.1
Ca 45	0.129 10(11)	1.0	0.128 10(11)	7.7	0.278 10(10)	14.2
Sc 46	0.163 10(11)	1.3	0.162 10(11)	9.8	0.832 10(9)	4.2
Sc 47	0.111 10(11)	.9	0.110 10(11)	6.6		
Sc 48	0.900 10(11)	7.2	0.886 10(11)	53.4		

TABLE IV-I-5

Radioactivity of Each Region

10 Yr Operation

SHUTDOWN TIME

	S S		Nb - 1 Zr		V - 20 Ti	
TOTAL	0.871 10(10) Ci		0.310 10(11) Ci		0.938 10(10) Ci	
REGION	Ci	% of Total*	Ci	% of Total*	Ci	% of Total*
1	0.344 10(10)	39.5	0.128 10(11)	41.2	0.191 10(10)	20.4
2	0.984 10(9)	11.3	0.230 10(10)	7.4	0.898 10(9)	9.6
3	0.751 10(9)	8.6	0.256 10(10)	8.3	0.980 10(9)	10.4
4	0.664 10(9)	7.6	0.267 10(10)	8.6	0.105 10(10)	11.2
5	0.737 10(9)	8.5	0.338 10(10)	10.9	0.137 10(10)	14.6
6	0.606 10(9)	7.0	0.280 10(10)	9.0	0.118 10(10)	12.6
7	0.487 10(9)	5.6	0.193 10(10)	6.2	0.852 10(9)	9.1
8	0.362 10(9)	4.2	0.121 10(10)	3.9	0.435 10(9)	4.6
9	0.269 10(9)	3.1	0.898 10(9)	2.9	0.309 10(9)	3.3
		95.4		98.4		95.8

* Does not add to 100% because of neglect of isotopes which contribute <1%.

TABLE IV-I-6

Radioactivity of Each Region

10 Yr Operation

1 Hr. AFTER SHUTDOWN

	S S		Nb - 1 Zr		V - 20 Ti	
TOTAL	0.541 10(10) Ci		0.168 10(11) Ci		0.111 10(10) Ci	
REGION	Ci	% of Total*	Ci	% of Total *	Ci	% of Total *
1	0.311 10(10)	57.4	0.837 10(10)	49.8	0.253 10(9)	22.8
2	0.555 10(9)	10.3	0.125 10(10)	7.4	0.255 10(9)	23.0
3	0.263 10(9)	4.9	0.121 10(10)	7.2	0.191 10(8)	1.7
4	0.225 10(9)	4.2	0.127 10(10)	7.6	0.154 10(8)	1.4
5	0.239 10(9)	4.4	0.157 10(10)	9.3	0.152 10(8)	1.4
6	0.187 10(9)	3.5	0.123 10(10)	7.3	0.115 10(8)	1.0
7	0.135 10(9)	2.5	0.739 10(9)	4.4	0.879 10(7)	.8
8	0.186 10(9)	3.4	0.486 10(9)	2.9	0.929 10(8)	8.4
9	0.137 10(9)	2.5	0.336 10(9)	2.0	0.689 10(8)	6.2
		93.1		97.9		66.7

* % of t=0 value

TABLE IV-I-7

Radioactivity of Each Region

10 Yr Operation

1 Yr AFTER SHUTDOWN

	S S		Nb - 1 Zr		V - 20 Ti	
TOTAL	0.236 10(10) Ci		0.210 10(9) Ci		0.170 10(9) Ci	
REGION	Ci	% *	Ci	% *	Ci	% *
1	0.152 10(10)	64.4	0.414 10(8)	19.7	0.310 10(8)	18.2
2	0.166 10(9)	7.0	0.585 10(7)	2.8	0.268 10(7)	1.6
3	0.582 10(8)	2.5	0.522 10(7)	2.5	0.158 10(7)	.9
4	0.100 10(9)	4.2	0.481 10(7)	2.3	0.115 10(7)	.7
5	0.103 10(9)	4.4	0.556 10(7)	2.6	0.998 10(6)	.6
6	0.785 10(8)	3.3	0.471 10(7)	2.2	0.683 10(6)	.4
7	0.572 10(8)	2.4	0.386 10(7)	1.8	0.483 10(6)	.3
8	0.480 10(8)	2.0	0.387 10(7)	1.8	0.428 10(6)	.3
9	0.348 10(8)	1.5	0.322 10(7)	1.5	0.297 10(6)	.2
		91.7		37.2		23.2

* % of t=0 value

FIG. IV-I-5

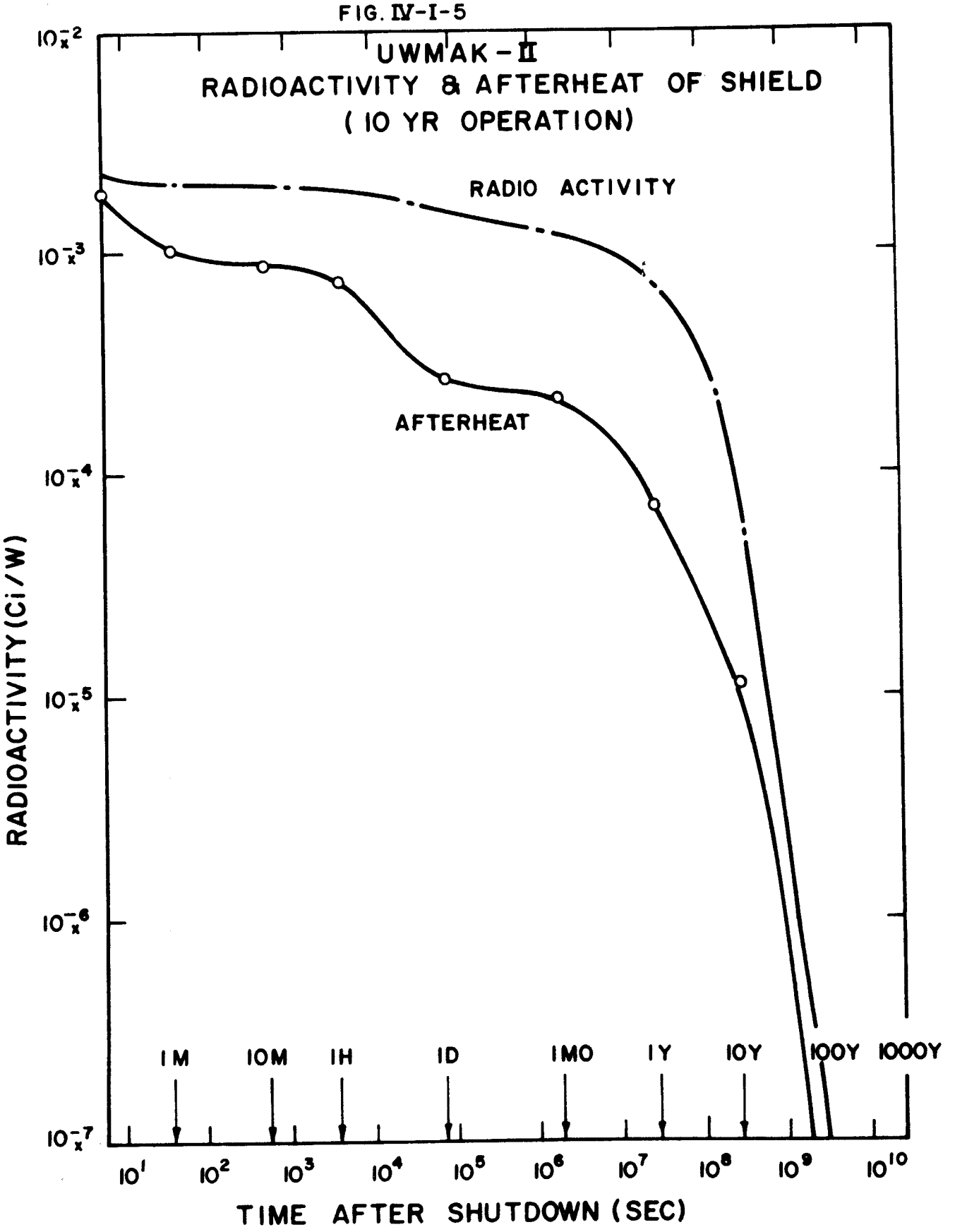
UWMAK-II
RADIOACTIVITY & AFTERHEAT OF SHIELD
(10 YR OPERATION)
RADIO ACTIVITY
AFTERHEAT
RADIOACTIVITY (Ci/W)
10^{-2}_x
10^{-3}_x
10^{-4}_x
10^{-5}_x
10^{-6}_x
10^{-7}_x
1M
10M
1H
1D
1MO
1Y
10Y
100Y
1000Y
10^1
10^2
10^3
10^4
10^5
10^6
10^7
10^8
10^9
10^{10}
TIME AFTER SHUTDOWN (SEC)

FIGURE IV-1-6

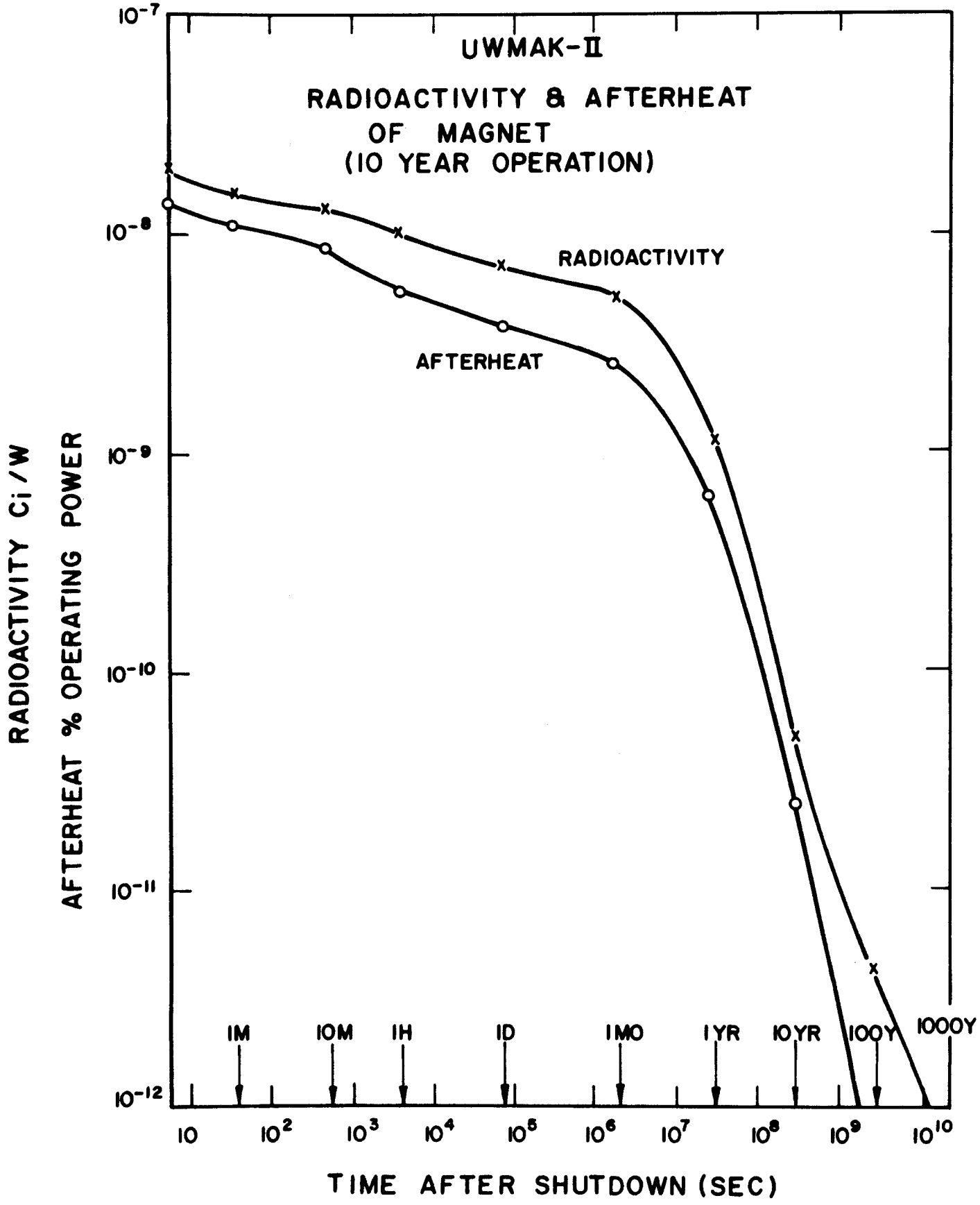
UWMAK-II
RADIOACTIVITY & AFTERHEAT
OF MAGNET
(10 YEAR OPERATION)
RADIOACTIVITY
AFTERHEAT
RADIOACTIVITY Ci/W
AFTERHEAT % OPERATING POWER
10^-7
10^-8
10^-9
10^-10
10^-11
10^-12
1M
10M
1H
1D
1MO
1YR
10YR
100Y
1000Y
10
10^2
10^3
10^4
10^5
10^6
10^7
10^8
10^9
10^10
TIME AFTER SHUTDOWN (SEC)

first attempt to include the maximum biological effects of the radioactive structure.

The BHP calculated for the first wall of UWMAK-II at shut down for two years of operation is shown in Table IV-I-8. The results are qualitatively quite similar to that of UWMAK-I and differ quantitatively primarily because of the greater amount of material in the first wall in UWMAK-II. The primary contribution to the BHP came from only five isotopes, Mn-54, Ni-57, V-49, Fe-55 and Mn-56 with Mn-54 and Ni-57 alone making 75% of the contribution. Tables IV-I-9 and IV-I-10 show the BHP calculated for the alternate materials, Nb-1Zr and V-20Ti. As in the case for UWMAK-I the BHP for the Nb-1Zr system is much greater than that of the 316SS system due primarily to the large contribution of Nb-92m to the MPC value. V-20Ti also follows the trends shown in UWMAK-I by having a BHP less than that of SS (~55%).

The change in BHP with time after shutdown is shown in Figures IV-I-7 and IV-I-8. The results are somewhat similar to those of activity or decay heat in that the SS system shows a relatively slow initial drop requiring about two years to be reduced by an order of magnitude. The V-20Ti system, however, by the end of two years has been reduced well over an order of magnitude and by ten years is down four orders of magnitude. The BHP of the Nb-1Zr system is significantly larger due to the contribution of Nb-92m and remains high at long times because of the Nb-94 (t 1/2 ~ 20,000 years). As discussed previously, Nb-92m is an unevaluated isotope and thus the MPC is set at 1 x 10^{-10} μCi/ml of air. An evaluation of this isotope, which could result in an upward revision of the MPC, would change the above results but an increase of a factor of 100 would be necessary to make the BHP of the Nb-1Zr system comparable to that of SS. The long lived residual activity would remain unaltered, however. The BHP of the shield is also shown on Fig. IV-I-7. Its BHP is significantly lower than that of the blanket and since the activity comes primarily from steel, the curve has the same qualitative shape as that of a SS blanket.

IV-I-4. Afterheat Calculations

The afterheat for the UWMAK-II blanket is shown in Figure IV-I-9 along with the afterheat of the first wall and the total afterheat of UWMAK-I. Because of the larger amounts of steel in UWMAK-II, the afterheat is significantly higher being over a factor of two greater at shutdown and as much as 30% higher for times the order of minutes after shutdown. The general shape of the curves and the qualitative results are similar, however. The first wall is still the major contributor and its contribution which may be as high as 40% of the total, decays away with a time dependence similar to that of the total.

TABLE IV-I-8

Biological Hazard Potential of 316 SS
First Wall at Shutdown for 2 Year Operation

Isotope	Specific Activity dps/cm^3	Activity Ci/kw_{th}	Biological Hazard Potential km^3 of air/kw_{th}
Mg-27	1.09 10(8)	0.03	1.11 10(-3)
Al-28	2.22 10(10)	6.79	0.226
Al-29	3.56 10(8)	0.11	3.46 10(-3)
Al-30	4.19 10(8)	0.13	4.27 10(-3)
V-49	3.08 10(9)	0.94	9.43
V-52	7.08 10(12)	216.5	0.72
Cr-49	1.24 10(9)	0.38	1.27 10(-2)
Cr-51	2.32 10(11)	70.95	0.18
Cr-55	8.46 10(9)	2.59	8.63 10(-2)
Mn-54	1.17 10(11)	35.78	35.8
Mn-56	3.26 10(11)	99.09	3.33
Mn-57	4.75 10(9)	1.45	4.84 10(-2)
Fe-53	2.22 10(9)	0.68	2.27 10(-2)
Fe-55	5.11 10(11)	156.26	5.21
Fe-59	3.36 10(8)	0.10	2.05 10(-2)
Co-57	4.81 10(10)	14.7	0.15
Co-58	1.61 10(11)	49.2	1.65
Co-60m	3.09 10(10)	9.45	0.32
Co-60	1.18 10(10)	3.6	0.36
Co-61	8.60 10(8)	2.63	8.77 10(-3)
Ni-57	1.02 10(10)	3.12	31.1
Ni-63	8.31 10(7)	0.03	1.27 10(-2)
Ni-65	4.00 10(7)	0.01	4.69 10(-4)
TOTAL	2.10 10(12)	675.3	89

TABLE IV-I-9

Biological Hazard Potential of Nb-1Zr
First Wall at Shutdown for 2 Year Operation

Isotope	Specific Activity dps/cm^3	Activity Ci/kw_{th}	"Biological Hazard Potential" km^3 of air/kw_{th}
Nb-92m	3.61 10(12)	1103.9	1110
Nb-93m	6.85 10(9)	2.09	0.52
Nb-94m	3.20 10(12)	978.5	32.6
Nb-94	2.39 10(8)	0.07	0.73
Nb-95m	2.97 10(11)	90.82	90.8
Nb-95	2.70 10(11)	82.57	4.13
Zr-89	7.46 10(9)	2.28	22.8
Zr-95	1.21 10(9)	0.37	9.3 10(-2)
Y-88	3.75 10(7)	0.01	0.12
Y-90	4.94 10(10)	15.11	3.78
Y-91	4.08 10(8)	0.13	0.13
Sr -89	2.23 10(8)	0.07	0.22
Sr -90	1.14 10(5)	4 10(-5)	1.16 10(-3)
TOTAL	7.45 10(12)	2.28 10(3)	1.20 10(4)

TABLE IV-I-10

Biological Hazard Potential of V-20 Ti

First Wall at Shutdown for 2 Year Operation

Isotope	Specific Activity dps/cm^3	Activity Ci/kw_{th}	"Biological Hazard Potential" km^3 of air/ kw_{th}
Ca-45	1.23 10(10)	3.76	3.77
Sc-46	1.61 10(10)	4.92	0.62
Sc-47	9.05 10(9)	2.77	0.14
Sc-48	9.12 10(10)	27.87	4.65
Sc-49	1.53 10(9)	0.47	1.56 10(-2)
Ti-45	1.39	0.42	4.21
Ti-51	1.59 10(11)	48.71	1.62
V-49	7.84 10(9)	2.40	24.0
V-52	9.40 10(11)	287.4	9.59
TOTAL	1.24 10(12)	378.7	48.6

FIGURE IV-I-7

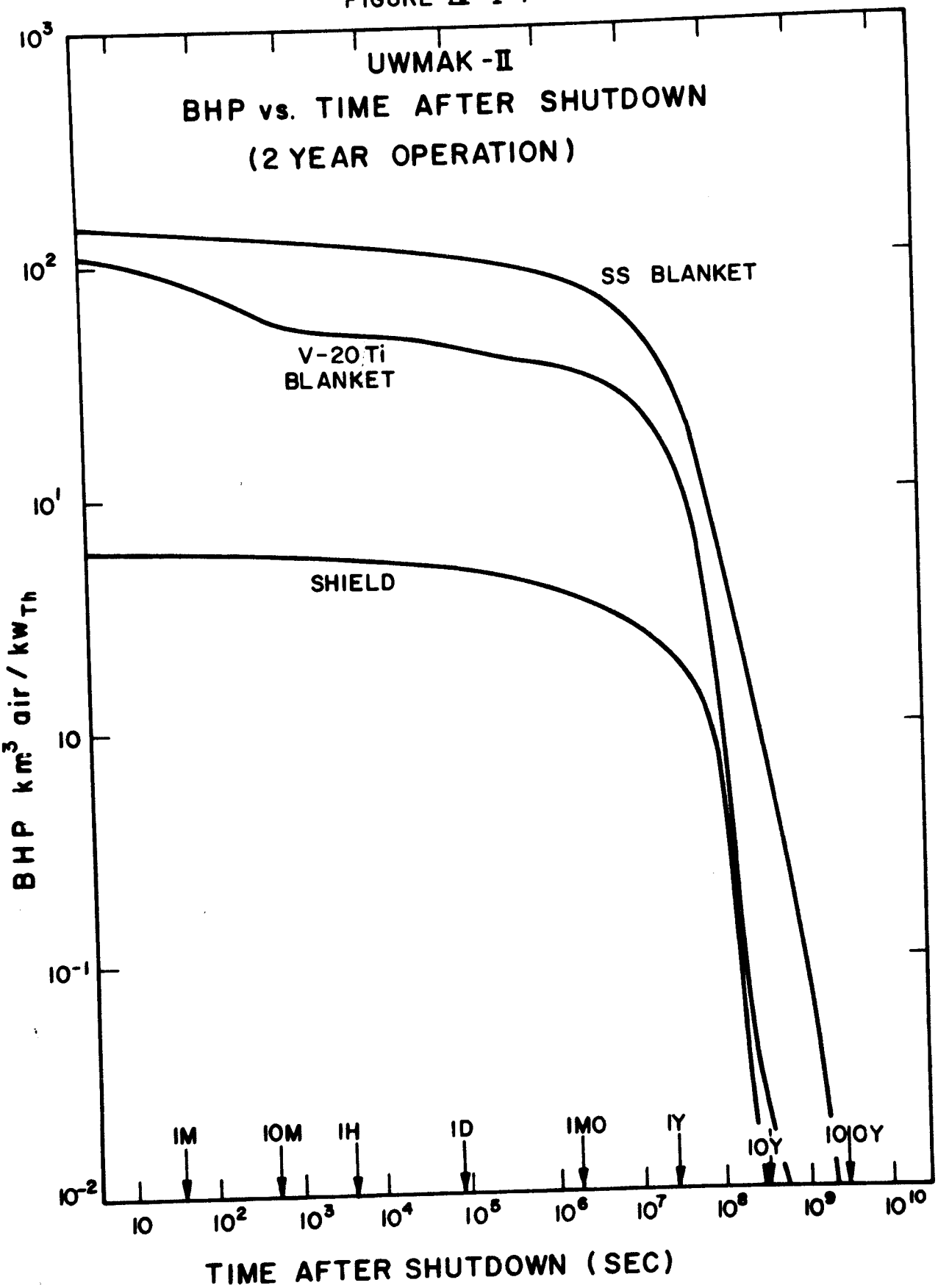
UWMAK-II
BHP vs. TIME AFTER SHUTDOWN
(2 YEAR OPERATION)
SS BLANKET
V-20Ti
BLANKET
SHIELD
BHP km³ air / kW_Th
TIME AFTER SHUTDOWN (SEC)
1M
10M
1H
1D
1MO
1Y
10Y
100Y

FIG. IV-I-8

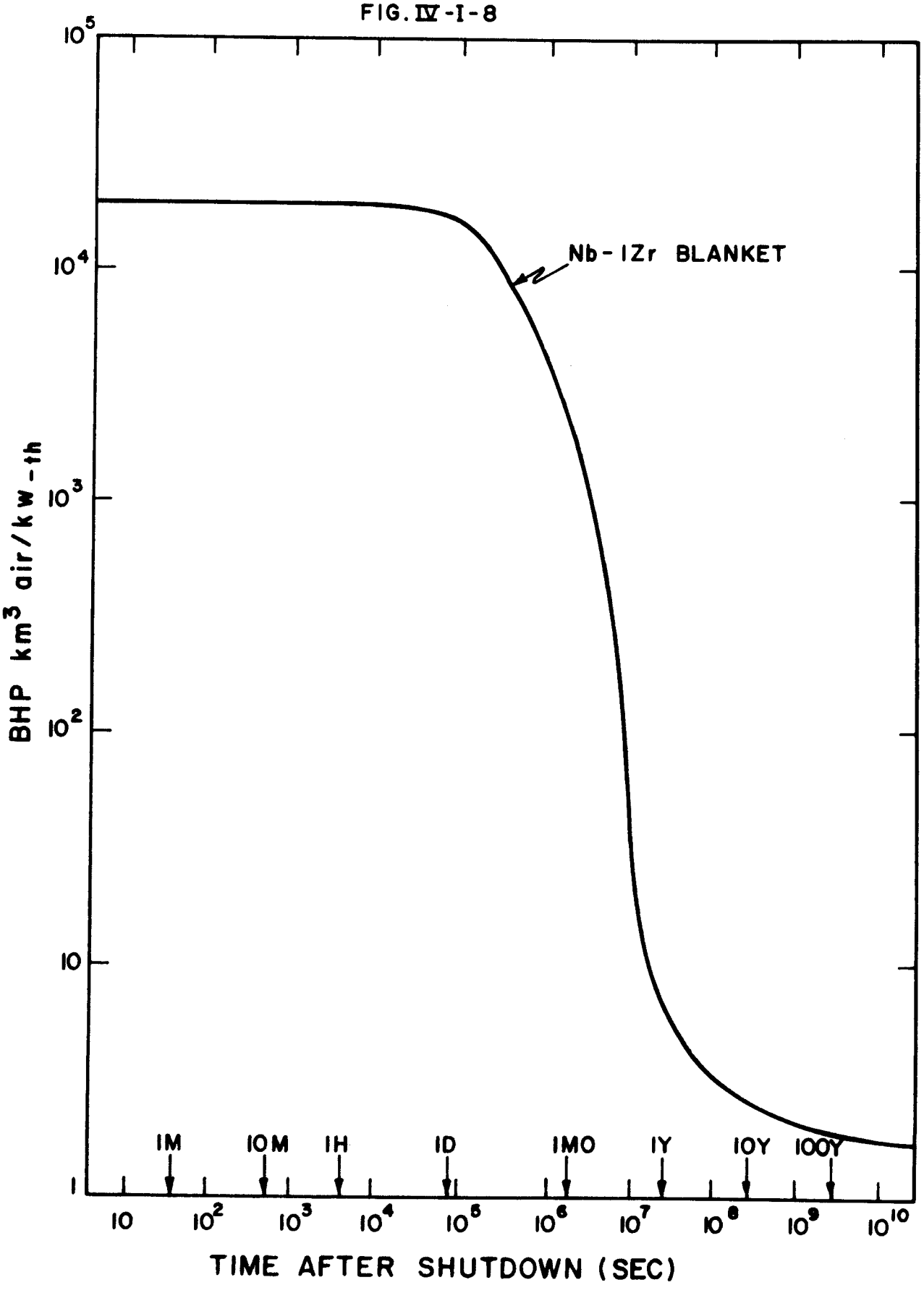
Nb-1Zr BLANKET
BHP km³ air/kW-th
TIME AFTER SHUTDOWN (SEC)
1M
10M
1H
1D
1MO
1Y
10Y
100Y

FIG. IV-I-9

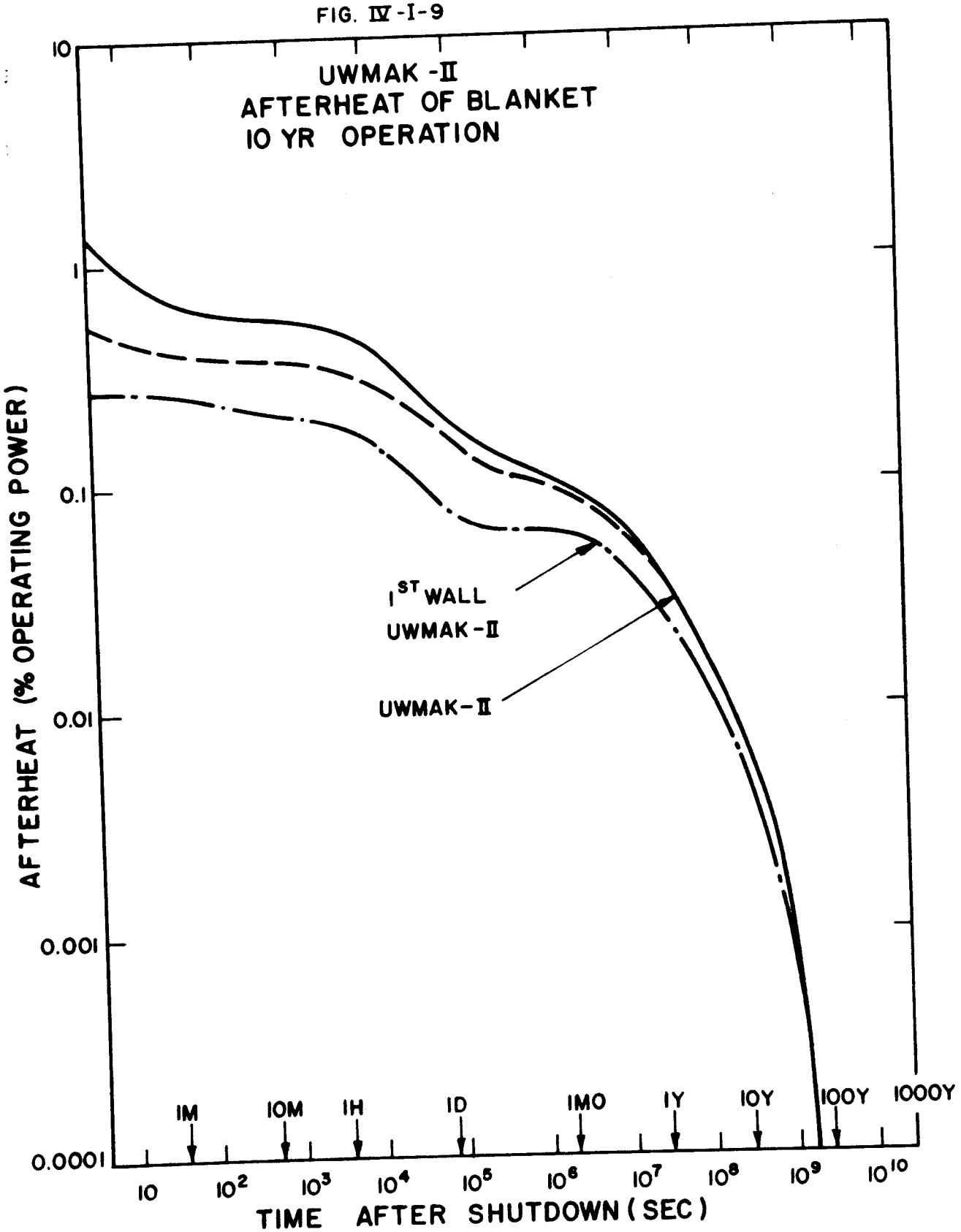
UWMAK -II
AFTERHEAT OF BLANKET
10 YR OPERATION
AFTERHEAT (% OPERATING POWER)
10
1
0.1
0.01
0.001
0.0001
1ST WALL
UWMAK-II
UWMAK-II
1M
10M
1H
1D
1MO
1Y
10Y
100Y
1000Y
10
10^2
10^3
10^4
10^5
10^6
10^7
10^8
10^9
10^10
TIME AFTER SHUTDOWN (SEC)

The afterheat for the alternate systems is shown in Figure IV-I-10 and IV-I-11. Once again the results are qualitatively similar to that obtained in UWMAK-I with the afterheat of the V-20 Ti systems, while having an initially higher value, decaying away much more rapidly than either of the other two systems.

IV-I-5. Emergency Cooling of the First Wall

The thermal flux near the first wall region is the maximum within a fusion reactor. The stress caused by the internal pressure in the blanket and the thermal flux from the plasma is also high. In addition, the radiation damage to the structural material of the first wall is most severe. Therefore, it is critical to keep the first wall within a reasonable temperature during a loss of flow accident or after the reactor is shut down.

For a helium cooled fusion reactor, loss of flow accident is essentially the same as a loss of coolant accident. Assuming the coolant stops during the operation of the reactor, the first wall can reasonably be assumed to be isolated from the rest of the system. Therefore, all the energy received by the radiation shield wall, i.e. from radiation, particles, and local neutron and gamma heating, will convert to thermal energy and raise the temperature of the wall. The energy received there is 4.2 watts/cm^2. The temperature response of the radiation shield wall is linear, as shown in Fig. IV-I-12. The temperature there will rise at a rate of 8.8°C/sec. This means it takes 11.8 seconds for the wall temperature reaches 650°C. It is expected that the plasma can be quenched in less than 10 seconds meaning that 650°C is a maximum temp.

It may be recalled that for the UWMAK-I design, the first wall temperature will rise 100°C in about 10 seconds. Therefore, it appears the temperature response of the first wall is approximately the same for a lithium cooled blanket and a helium cooled blanket. The similarity, however, is misleading. Due to completely different plasma assumptions, the surface heating loadings are 22.6 watts/cm^2 and 3.42 watts/cm^2, respectively, for UWMAK-I and UWMAK-II. If the plasma behaves as is assumed in the UWMAK-I design, the temperature of the UWMAK-II first wall will increase at a rate of 45°C/sec. In this case, the plasma has to be quenched within a few seconds. This will present a more serious problem.

After a reactor is shutdown, the structure will still be heated by the afterheat from the radiation decay. Calculations should be made to determine the temperature response of the blanket so that:

FIG. IV-I-10

UWMAK-II

AFTERHEAT (2 YR OPERATION)

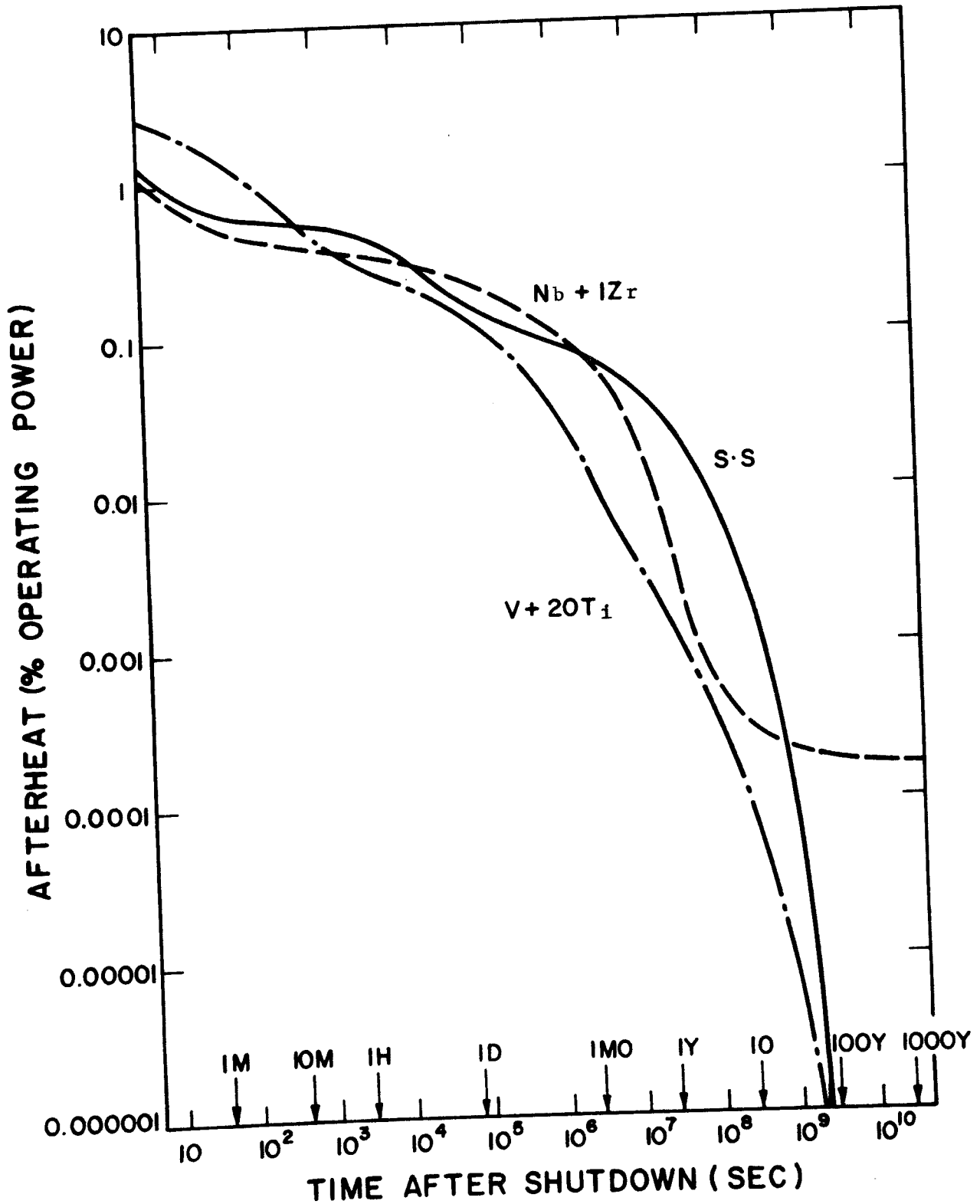

FIG. IV-I-11

UWMAK-II
AFTERHEAT (10YR OPERATION)

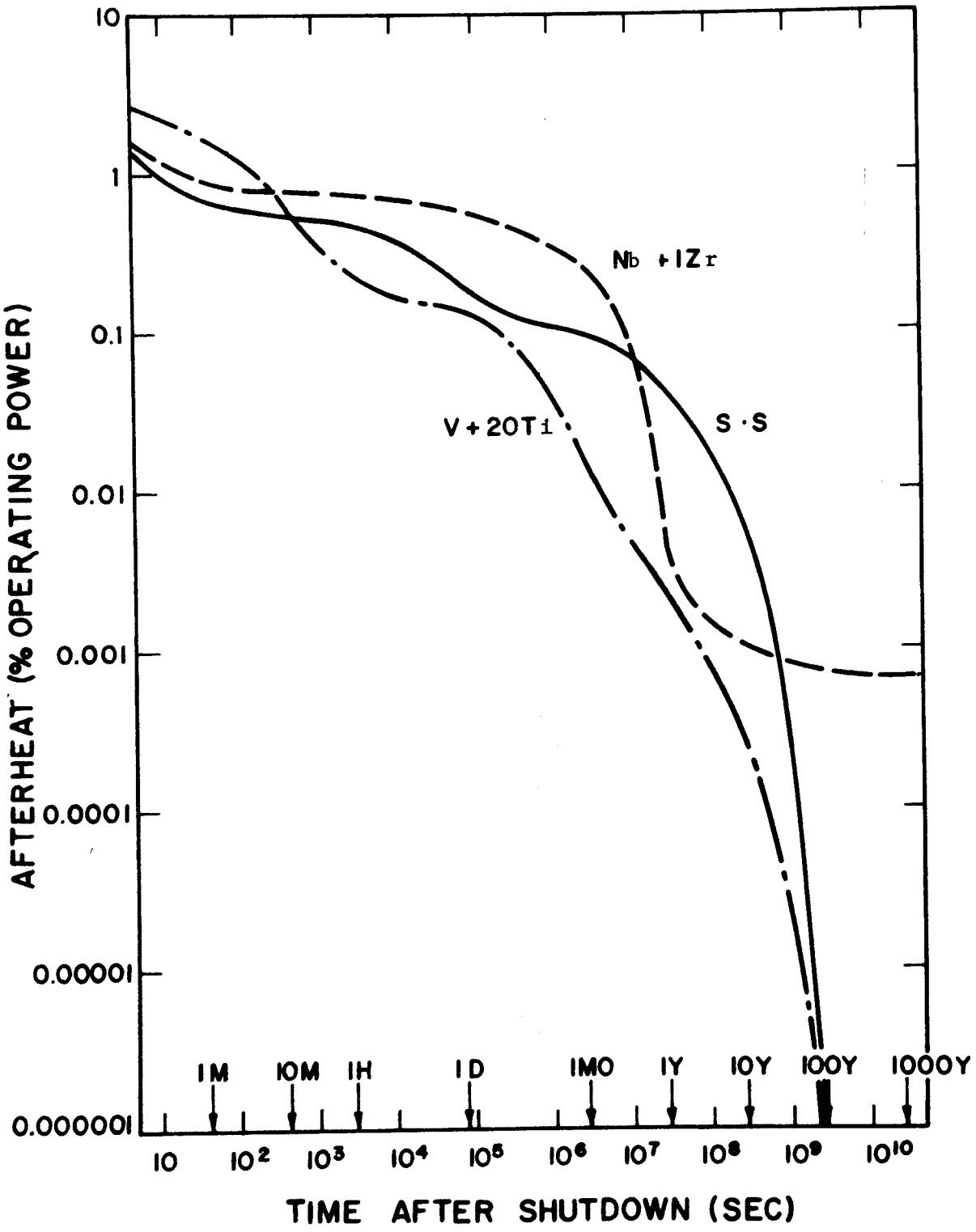

Fig. IV-I-12. Temperature Response of F.W. with Loss of Flow Accident

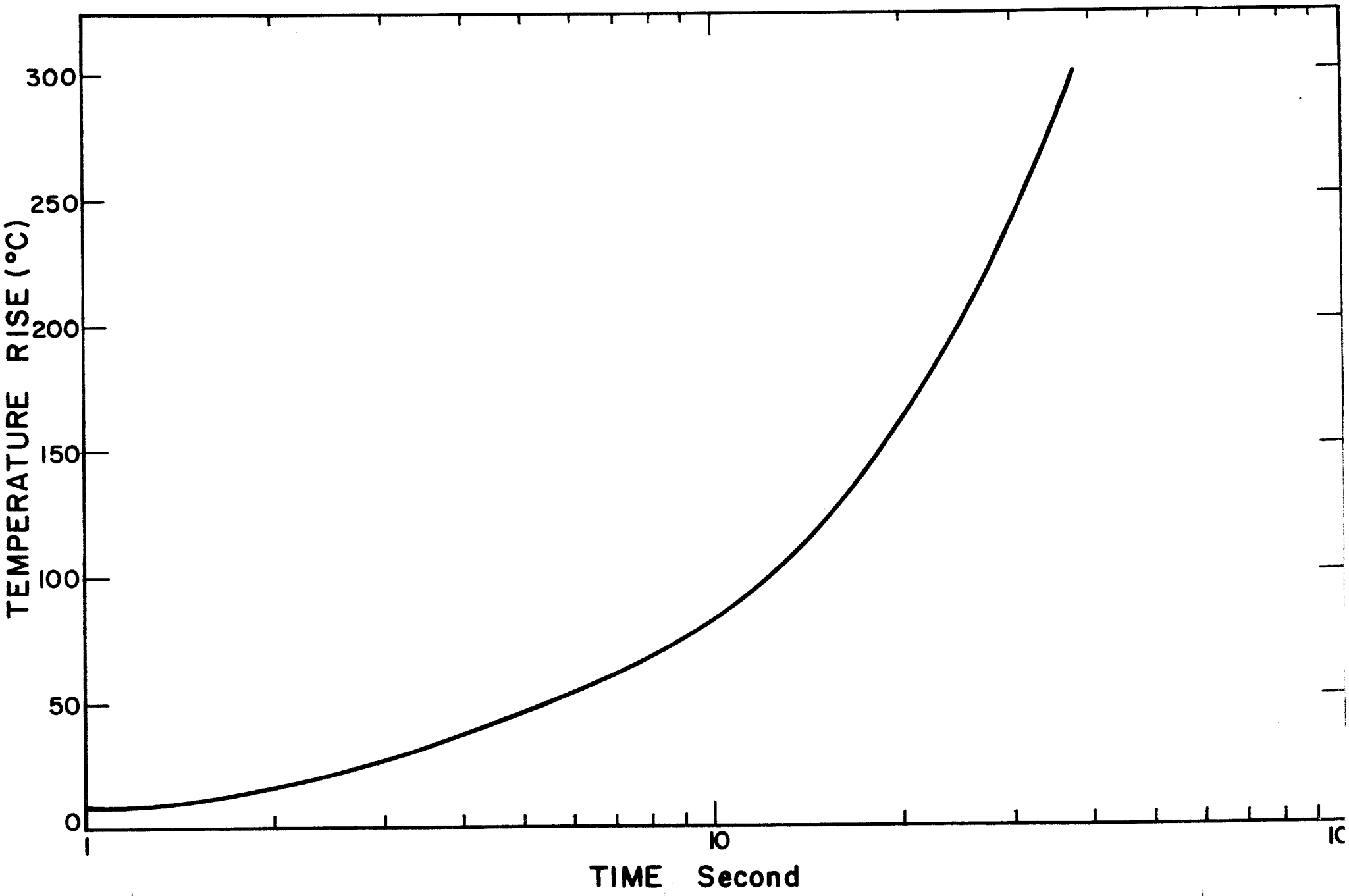

a. The structure in the blanket will not be overheated and cause irreversible damage due to precipitation of helium bubbles at the grain boundaries.
b. The blanket will be below a certain temperature so that it can be moved apart for service.

The heat transfer from the first wall toward the shield is very poor. Therefore, the residual heat of the blanket has to be carried away by the helium coolant. If no cooling is provided, the first wall temperature will increase 250° to (~700°C) in two days, which will probably damage the first wall.

After the blanket has been cooled by helium for 1 day following a reactor shutdown, the afterheat decreases by an order of magnitude. It is then safe to take the reactor apart without excess heating. The thermal radiation will be capable of dissipating the afterheat. The first wall will not exceed 150°C afterward.

First Wall Design Considerations:

The first wall area of UWMAK-II is 3300m^2 (actual). This first wall is scheduled to be replaced every two years. However, with thousands of welds under severe radiation, high temperature, and high stress conditions, it is inconceivable that the first wall will last the designed life time without leaks. Considering the difficulties involved in taking apart a tokamak, it is impracticle to fix the first wall everytime there is a leak. The advantage is obvious if the reactor can be kept in operation even if there is a leak, or even if it will be operated in reduced power. A redundant first wall is almost a must if a tokamak is ever to be a viable power generating reactor.

Two proposals are made for the first wall redundancy. The design modifications are being added on to the basic blanket design just described. This is perhaps the first time this problem has been examined in detail and the present designs certainly leave much to be desired.

The first proposal is to use a double walled vacuum structure. The first wall design is then as shown on Fig. IV-I-13. The two walls facing the plasma are in close contact with each other, and the gap in between is filled with helium at 1 atm. The temperature difference between the two walls is small and therefore so is the stress caused by the temperature gradient. Thus, during normal operation, the two walls behave as one wall.

If there is a crack on one of the walls, the stress will be high around the crack. This stress concentration will not be carried over to the other wall since they are separate. Each wall will be designed so that it can stand the stress by itself. Therefore, unless two failures occur on the same radiation shield tube, the first wall can stand any number of local leaks.

The advantage of this proposal is obvious. The design is simple and the fabrication is easy. The additional structural material required for the first wall, which has an significant effect on breeding

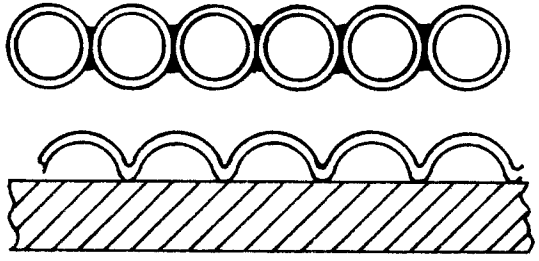

Fig. IV-I-13. Double Walled First Wall Design

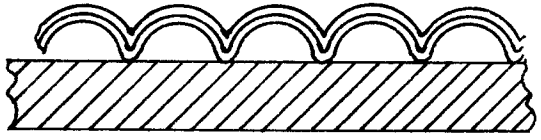

Fig. IV-I-14. Sacrificial First Wall Design

ratio, is minimum. A large number of leaks can occur during the life of the first wall as long as no two leaks occur on the same tube.

There are, however, drawbacks on this scheme. The leaking of the first wall will most likely occur on an imperfect weld in the first wall. The design just described does not provide redundancy with respect to welding. In addition, if there is a crack on one of the walls, the other wall has to carry the stress which was shared by the two walls. Therefore, another crack is much more likely to occur on the same tube than the other tubes. The second proposal is to add a complete bank of tubes in between the first wall and the basic design and the plasma, as shown on Fig. IV-I-14. We will call this a sacrificial wall. Each adjoining tube of this wall will be fed through different headers, so that they can be numbered, as shown on the drawing. The space between the sacrificial wall and the original first wall is vacuum tight and capable of standing the full coolant pressure.

In the basic design, in order to obtain high thermal efficiency, the first wall is operated at a high temperature near its stress limit. With this design, it is possible that the sacrificial wall can be operated at a lower temperature. This will move the operation condition further away from stress limitations. The original first wall will have a high temperature but will be subjected to a much lower stress because the thermal flux which causes the thermal stress is being absorbed by the sacrificial wall. Therefore, it is possible to design both walls with a much higher safety factor and the possibility of leaks decreases. If there is a leak on the sacrificial wall, say on tube 1, the header feeding tube 1 will be closed off and tube 1 will be cooled by conduction by adjoining tubes. The part of tube 1 facing the plasma will be hot and the other part of tube 1 will be relatively cool, thus achieving mechanical integrity of the sacrificial wall. If there is a leak on the first wall, the coolant will fill the space between the first wall and the sacrificial wall and nothing has to be done until the next shutdown period.

Two major drawbacks still exist. The fabrication of such a system is very difficult and certainly will tax the ingenuity of the industry. The other is more serious. About 1 cm of additional structural material will be required for the sacrificial wall and that will probably reduce the breeding ratio below 1.0.

Since this is the first attempt to construct a redundant first wall, it is hoped that future studies will result in a more acceptable system.

IV-J. Fabrication Procedures and Cost Estimates for UWMAK-II Blanket

A key part to any reactor design study is the fabrication of the various components. In this study, economics was the main concern and as such we examined those techniques which may be slightly advanced but which are within state-of-the-art capabilities. In other words the manufacturing techniques that are described have a high probability of success and represent the lowest cost.

In the performance of this fabrication/cost study, it was necessary to establish certain ground rules so that the costs could be compared to other studies. These ground-rules are presented in Table IV-J-1. This table contains two key points. The first is that it is assumed several pre-production reactors have been built, tested and the design proven-out. Consequently, no engineering development is included in the cost numbers. The second point is that all direct labor and material costs are based on 1974 dollars.

Before we can develop a manufacturing approach and its associated costs, it is necessary to identify the various forms of the material used in the reactor. By material form, we mean the condition the material is in when it is procured from a material supplier. Reactor studies usually develop a list of materials and quantities to be used but do not specify whether the material is in the form of sheet, tubing, extrusions, forgings or castings. To establish this, a series of tradeoff studies were carried out on various material forms which could be used in the blanket, front wall and header regions. These tradeoff studies consist of selecting various sub-components, such as the front wall, gas manifolds, gas headers, canning pins, and examining the various methods for fabricating them.

An example of this is the selection of a forging for the front wall. The obvious way to produce this component would be to corrugate a sheet and weld it to the thicker plate. Closer examination of that process, however, reveals that, because the corrugations are fairly rigid and the plates are not constantly flat, leak proof welds would be difficult to produce. On the other hand, die forged blanks are flat and the coolant channels and close outs can be formed in one operation.

A schematic diagram of a manufacturing flow plan to construct a complete blanket section is shown in Fig. IV-J-1. The initial material form chosen for each component part of the module is specified on the figure.

From Fig. IV-J-1, it can be seen that die forged blanks were selected for use in the helium flow channels in the front wall cells to reduce machining time. The cover plates and fillet plates are welded to these forgings using high speed multihead E.B. welding. The forming and machining operations are accomplished on automated lines prior to welding the five cells together to form a section. Welding consistency and cost were the major considerations for choosing to do the forming after the welding rather than joining pre-curved details. End plates are welded on all sides as called for in the design of a front wall section.

Table IV-J-1

UWMAK-II R.O.M. Cost Estimate of Blanket Modules

Conditions and Assumptions

1. This estimate is for the manufacture and assembly of the blanket section for UWMAK-II. It does not include the protective carbon cloth liner.

2. The blanket structure is 316 stainless steel with beryllium for neutron multiplication and lithium aluminate for tritium breeding.

3. Production rate is 25 reactors per year plus spares. A reactor consists of 2,857 modules with 5 cells per module.

4. All modules and headers are straight (flat) and identical.

5. The blanket front wall section is removed and replaced every two (2) years; refurbishment of the main support structure is not included. This includes replacement of $LiAlO_2$ and the Be tubes.

6. The Be is in green compact form, 1/2 normal density within the stainless tubes. Cost of Be is $100/lb for nuclear grade material while the $LiAlO_2$ is $15/lb.

7. Several pre-production reactors have been built, tested and proven-out; no engineering effort is included in the cost.

8. All production facilities and equipment and raw materials are assumed to be available to support peak production rates.

9. Special tools and equipment are included.

10. Tool maintenance not included.

11. Quality assurance and control practices are the same as current aerospace industry standard.

12. No product support effort is estimated.

13. Direct labor and material costs are in 1974 dollars.

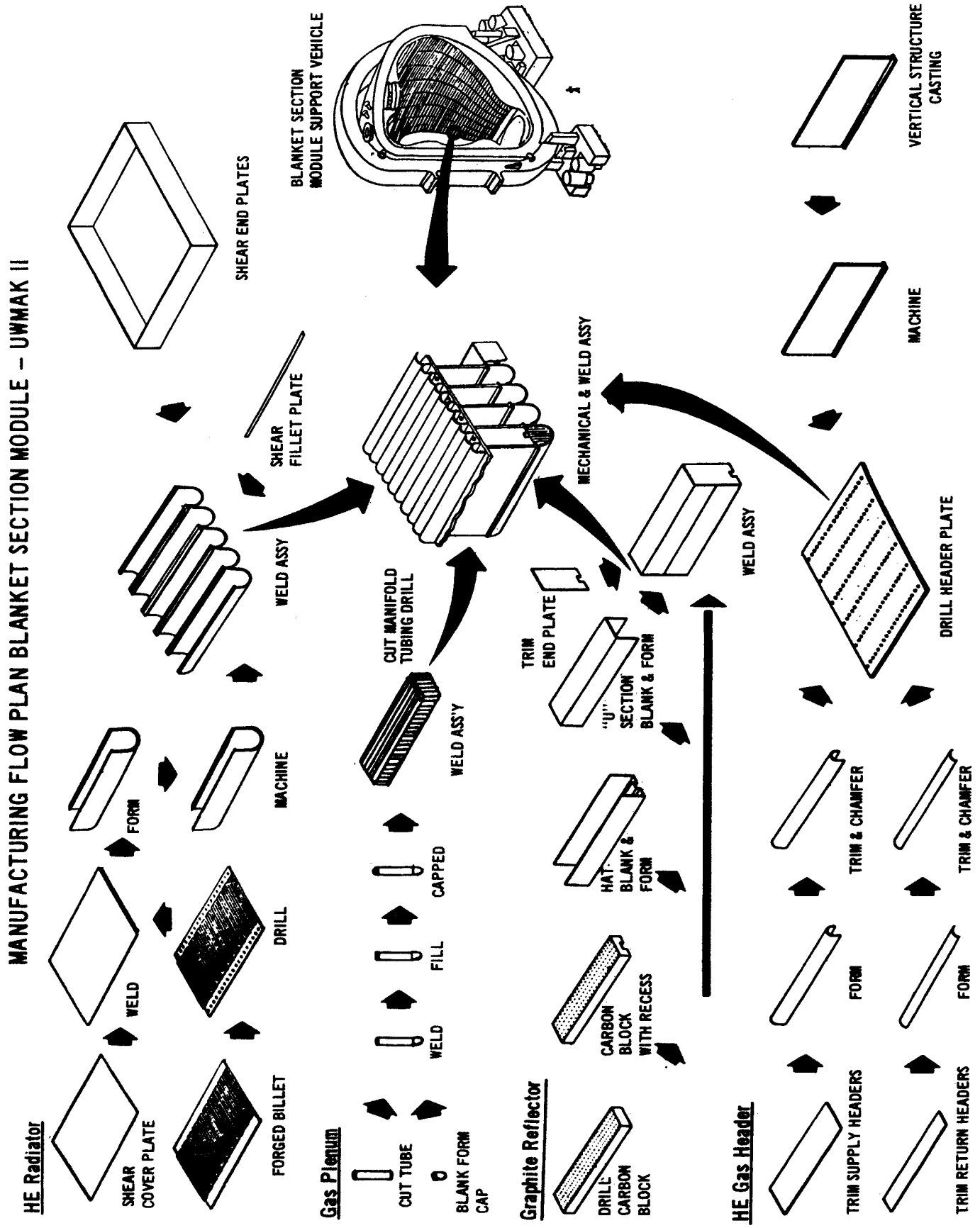
MANUFACTURING FLOW PLAN BLANKET SECTION MODULE – UWMAK II
HE Radiator
SHEAR COVER PLATE
FORGED BILLET
WELD
DRILL
FORM
MACHINE
Gas Plenum
CUT TUBE
BLANK FORM CAP
WELD
FILL
CAPPED
WELD ASS'Y
CUT MANIFOLD TUBING DRILL
WELD ASSY
SHEAR FILLET PLATE
SHEAR END PLATES
BLANKET SECTION MODULE SUPPORT VEHICLE
Graphite Reflector
DRILL CARBON BLOCK
CARBON BLOCK WITH RECESS
HAT BLANK & FORM
"U" SECTION BLANK & FORM
TRIM END PLATE
MECHANICAL & WELD ASSY
WELD ASSY
HE Gas Header
TRIM SUPPLY HEADERS
TRIM RETURN HEADERS
FORM
FORM
TRIM & CHAMFER
TRIM & CHAMFER
DRILL HEADER PLATE
MACHINE
VERTICAL STRUCTURE CASTING

Figure IV-J-1

The ends of the breeding material cans are blanked round from 316 stainless sheet coil stock and draw formed into the desired shape using high rate transfer dies. These are then automatically welded to pre-cut tubes. The possibility of cold extruding these cans in half sections and welding them was considered. This method is not presently considered feasible because of the thin wall and the depth of the half section, but would be cost effective if developed. Following welding, the cans are automatically filled with lithium aluminate and beryllium particles. They are then capped, sealed by welds, and finally joined (welded) to the pre-drilled tritium collection manifold.

The graphite reflector is divided into four blocks to allow multi-spindle deep hole drilling of the coolant channels. These blocks are completely clad in a jacket made from coiled stainless steel sheet stock. Detailed parts for the cladding are made on progressive dies. Stainless tubing is used to line the coolant channels after which the graphite reflector is assembled automatically using multihead T.I.G. welders to form a sealed container. The possibility of plating the reflector in one piece could provide considerable savings in assembly but the thickness of the plating that could be economically produced would have to be studied.

The vertical structure is produced from a machined casting. The helium conduits running the entire length make it impractical to drill. A casting may be produced by coring these holes with stainless steel tubes filled with ceramic. This method will require some development work because the cores are thin and extremely long.

The headers are welded to the header plate with multihead M.I.G. welders. The helium supply headers are welded in place first and the return headers are then welded to the supply headers to close out the assembly. The helium supply headers are slightly shorter in length than the header plate to provide access for welding in the field. The procedure for assembly in the field is welding of the header assemblies using fixtured automatic M.I.G. welding with the weld sequence being the same as was used to build up the headers initially. The graphite reflectors, gas plenums and front wall helium radiator cells are then installed. The final step is to weld the end plates to provide a sealed unit. Inspection will consist of a combination of x-ray and ultrasonic checks on all welds with proof pressure and leak checks on pressure systems.*

Once the manufacturing flow plan is developed, it is possible to establish a cost to manufacture the front wall, blanket and headers. This cost is roughly $150 M and a detailed breakdown is given in Table IV-J-2. From this table, it can be seen that the starting material cost increases the fabrication cost by a factor of 7. This is because extensive automated equipment is used and this significantly reduces the labor effort required for fabrication. A second item is the fact that the beryllium represents roughly 60% of the blanket cost. If the beryllium is to be refurbished after two years, then it will have to be reprocessed in order to maintain realistic operating costs. An estimate of the costs associated with procuring the automated equipment and tooling has also been made. This cost would be $160 M and does not represent costs associated with construction of facilities.

---

* It should be noted that all of the above techniques make the use of a uniformly 20% cold worked structure possible. The heat effect zones will have lost the cold working and the forging will not give the desired cold working.

In conclusion, the approach for fabricating the front wall, blanket, and headers represents minimal extension of the state of the art and should have a high probability for success. The use of Be dominates the total cost of the system and if it must be recycled, more extensive work on an appropriate facility must be performed.

TABLE-IV-J-2

UWMAK II REACTOR R.O.M. COST/MATERIAL SUMMARY

Item	No. of Units Req.d. per Reactor	Wt. of Mat'l. (Tonne) Per Reactor	Raw Material Cost ($)		Manufacturing Cost ($)		Total Item Cost ($)	
			Per Unit	Per Reactor	Per Unit	Per Reactor	Per Unit	Per Reactor
1. Front Wall Section	2,857	227	2,528	7,222,500	556	1,587,750	3,084	8,810,250
2. Tubes ~ $LiAlO_2$ and Be {Be / $LiAlO_2$ / S.S.}	2,142,750	410 483 2,541	44 1.62 1.38	94,280,953 19,130,472 2,956,994	1	2,748,125	48	119,116,504
3. Tube Tritium-Manifold Assy.	85,710	39	3	262,300	4	323,625	7	585,925
4. Tube Installation	2,857	-	1	2,900	22	63,125	23	66,025
5. Graphite Block Assy. {C / S.S.}	14,285	1,589 113	192 106	2,742,700 1,514,200	163	2,330,750	461	6,587,650
6. "T" Slot Helium Manifolds	14,285	94	1,022	14,599,300	83	1,190,875	1,105	15,790,175
7. Headers	2,857	1,722	1,212	3,462,700	1,069	3,053,375	2,281	6,516,075
8. Assembly	2,857	-	22	62,900	2,651	7,572,500	2,673	7,635,400
TOTAL/REACTOR		SS 5563 Be 410 C 1589 $LiAlO_2$ 483	$146.238 M		$18.870M		$165,108,042	

V. Energy Conversion System

V-A. Introduction

The energy conversion system has four functions. They are:

- Remove the thermal energy generated in the blanket, divertor and shield
- Maintain the temperatures of equipment and materials within prescribed limits under normal and abnormal conditions
- Convert the thermal energy generated to electrical energy
- Reject waste heat to the atmosphere

The system must satisfy these functions subject to technical, economic, safety and environmental constraints. The concepts presented in this section are preliminary, without benefit of optimization and consideration of a broad spectrum of alternatives. In addition, they have been subject only to first order analyses. However, the design selected is believed to represent a technically feasible and reasonably economic design. Further, it provides a basis for evaluating the UWMAK-II design and the engineering problems of this type of fusion power plant.

The system design is based on using technology under development for gas-cooled and liquid metal-cooled fission reactors wherever it is a reasonable application. The selections made are based on technology expected to be available and demonstrated on an early commercial basis in the late 1980's to the mid-1990's. New technology areas that are not currently under intensive development were only briefly evaluated. The reason for this approach was twofold:

- This will provide a conservative basis for fusion power evaluation
- Extensive evaluations of new technology were not within the scope of this study

The coolants selected for the reactor primary systems are:

- Blanket - Helium
- Divertor - Lithium (both particle collector and coolant)
- Shield - Helium

The energy conversion concept must be designed to interface with these coolants.

The cyclic nature of the Tokamak reactor operation imposes unique design problems on the energy conversion system. In the UWMAK-II, energy is generated in the reactor for 90 minutes (burntime); the reactor is then shut down for 5 1/2 minutes (downtime) for recharge. The total cycle time of 95 1/2 minutes is called the burn cycle. The ratio of the burntime to total burn cycle period is defined as the duty factor. Thus, the UWMAK-II reactor has a duty factor of 0.94. To be a viable electricity-producing machine for electric utilities, energy must be produced at a nearly uniform rate which imposes a requirement for an energy storage system.

OVERALL ENERGY CONVERSION SCHEMATIC

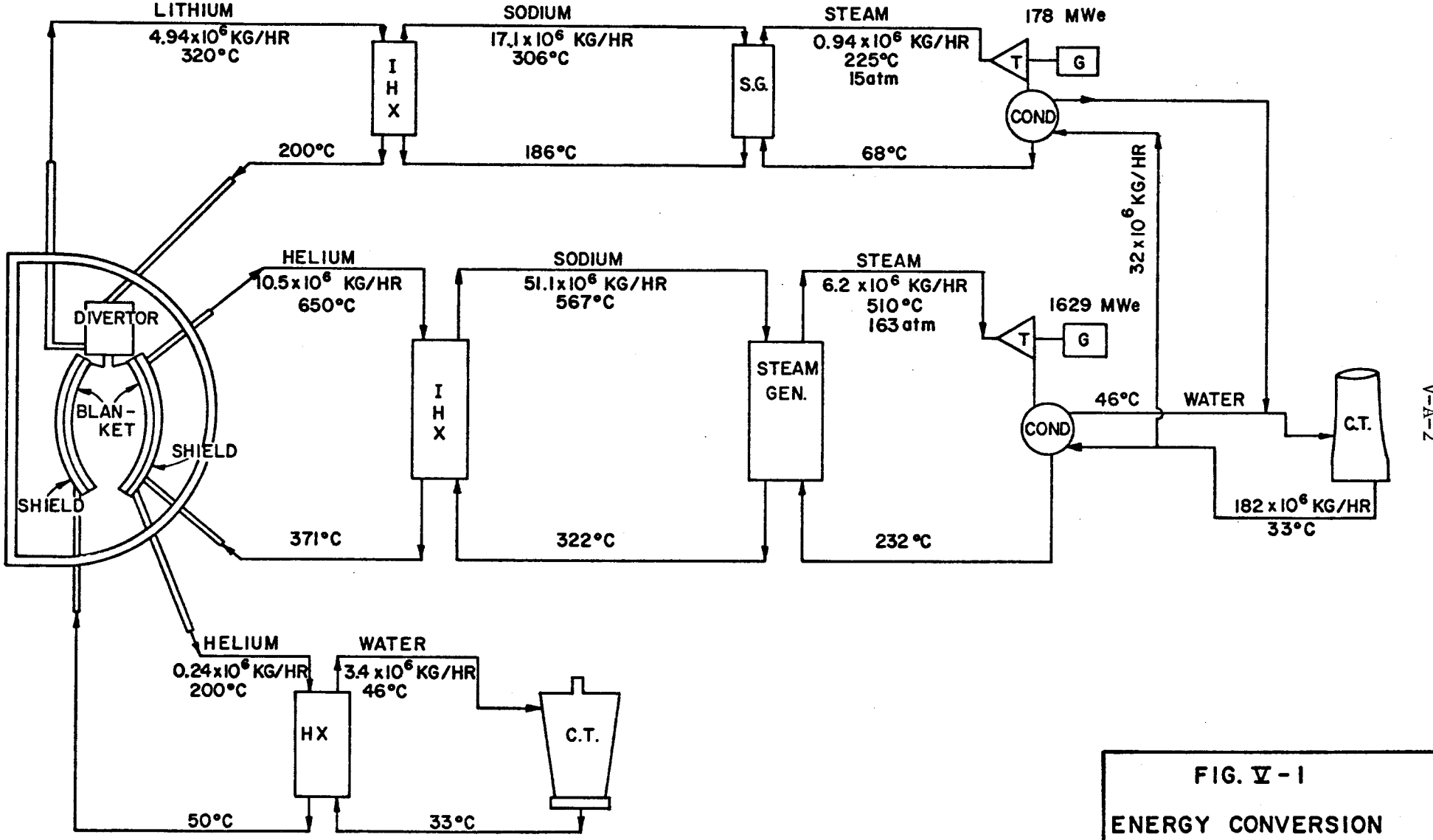

FIG. V-1
ENERGY CONVERSION
SCHEMATIC

A one-line block diagram of the UWMAK-II energy conversion system is shown in Figure V-1 and the key parameters are listed in Table V-1. There are three separate heat removal systems:

. Blanket system

. Divertor system

. Shield cooling system

The blanket is the major source of thermal energy where approximately 85% of the fusion reaction energy is captured. This energy is removed by the circulation of helium gas.

In the divertor, about 14% of the reaction energy is recovered in liquid lithium which acts as both a coolant and particle collector medium. The remaining 1% of the total reaction energy is captured in the neutron shield and is removed by the circulation of helium gas.

As may be seen in Figure V-1, the energy removed from the blanket by the circulating helium is transferred to a circulating intermediate liquid sodium system. intermediate sodium system in turn transfers the energy to the blanket steam cycle. A similar arrangement is used for the divertor. The lithium coolant transfers the divertor thermal energy to an intermediate sodium system which in turn transfers the energy to the divertor steam cycle. A common condenser cooling water system is provided for both the blanket and the divertor steam cycles.

Thermal energy from the shield is at relatively low temperature. Since this energy has to be removed in case of reactor shutdown (normal or emergency), a separate cooling water system with cooling towers is used to reject this energy to atmosphere. Although recovery of this energy for generating electricity is possible, it has not been considered in this study.

In addition to the cooling and heat transfer functions of the blanket and divertor heat removal systems, a large thermal energy storage device is needed to deliver thermal energy to the steam cycle at a uniform rate. A total of about 427 MWh (1.46×10^9 Btu) of thermal energy must be stored; 365 MWh for the blanket and 62 MWh for the divertor. The intermediate sodium system serves this purpose by storing hot sodium during the 90 minute energy generating period. During the 5.5 minutes when energy is not being generated by the reactor, this stored hot sodium supplies energy to the steam cycle. In addition to energy storage, the intermediate sodium system helps to minimize tritium permeation into the steam cycle. (See Chapter IV, Section G).

Figure V-2 shows the overall energy balance of the blanket and divertor heat removal systems during reactor operation and during reactor downtime. During reactor operation, the blanket generates 4232 MWt. Of this, 243 MWt goes to the energy storage system and 11 MWt (net) goes to non-recoverable losses in the helium circulators leaving 3978 MWt transferred to the steam cycle. During the reactor downtime, 3978 MWt it supplied to the steam generators by the energy storage system. The divertor generates 716 MWt during reactor operation;

Table V-1

Key Energy Conversion System Parameters

PARAMETER	BLANKET	DIVERTOR	SHIELD	TOTAL
Thermal Power, MWt (during reactor burntime)	4232	716	52	5000
Thermal Power, MWt (average continuous)	3989*	675	49	4712
Net Electrical Power, MWe	1541	168	--	1709
Plant Efficiency, %	38.6	24.9	--	36.4
Primary Cooling System				
Coolant	Helium	Lithium	Helium	
Flow rate, Kg/hr (lb/hr) x 10^6	10.5(23.2)	4.94(10.9)	0.24(0.53)	
Hot leg temp, °C(°F)	650(1202)	320(608)	200(392)	
Cold leg temp, °C(°F)	371(700)	200(392)	50(122)	
Intermediate Cooling System				
Coolant	Sodium	Sodium	--	
Flow rate, Kg/hr (lb/hr) x 10^6	51.1(112.7)	17.1(37.7)	--	
Hot leg temp, °C(°F)	567(1052)	306(583)	--	
Cold leg temp, °C(°F)	322(612)	186(367)	--	
Steam System				
Turbine Throttle Conditions				
Pressure, atm (psia)	163(2400)	15(220)	--	
Temperature, °C(°F)	510(950)	225(438)	--	
Flow rate, Kg/hr (lb/hr) x 10^6	6.2(13.6)	0.94(2.1)	--	
Condenser Pressure				
mm HgA	51	51	--	
in HgA	2.0	2.0	--	
Cooling Water System				
Water flow rate, Kg/hr (lb/hr) x 10^6	150(330)	32(71)	3.4(7.6)	
Hot water temp, °C(°F)	46(115)	46(115)	46(115)	
Cold water temp, °C(°F)	32.8(91)	32.8(91)	32.8(91)	

*Includes non-recoverable losses of 11 MWe in the He circulator.

ENERGY BALANCE SCHEMATIC

DURING REACTOR BURNTIME 90 MINUTES

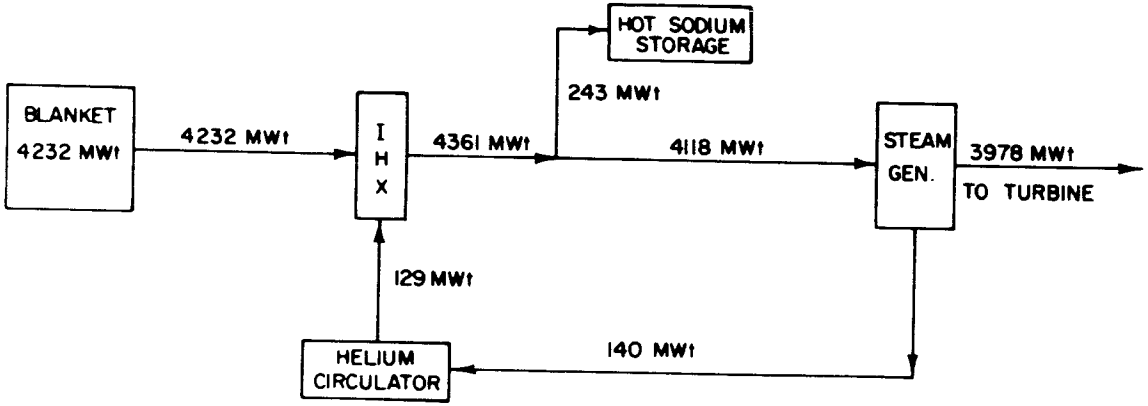

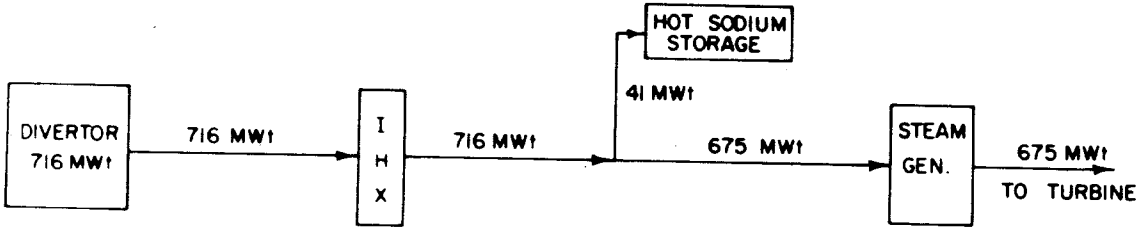

DURING REACTOR DOWNTIME 5.5 MINUTES

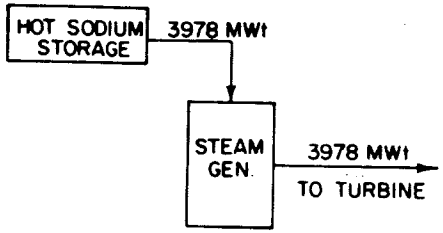

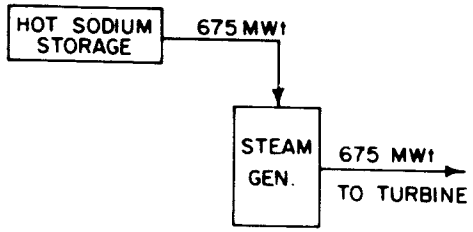

Figure V-2

41 MWt goes to the energy storage system, leaving a net of 675 MWt supplied to the steam generator. During the reactor downtime, 675 MWt is supplied by the energy storage system.

V-B. Selection of the Energy Storage System

In the previous section, the use of the intermediate sodium system for energy storage was briefly discussed. The background and rationale for selecting the system is described in this section.

UWMAK-II, like other tokamak designs, has the inherent characteristic of discontinuous energy generation. The operating cycle for UWMAK-II is:

- 90 minutes reactor operation (burntime)
- 5.5 minutes reactor shutdown (downtime)
- 95.5 minutes total cycle period (burn cycle)

Consequently, to maintain constant plant output as desired for electrical generation, the energy conversion system is required to operate according to the following scheme:

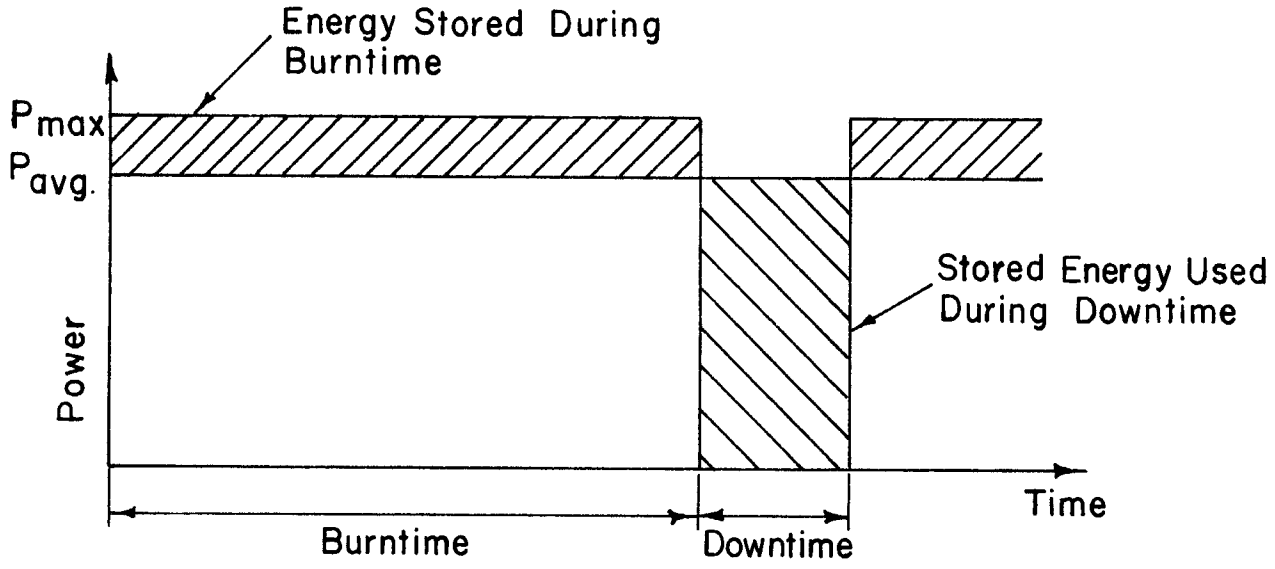

The reactor generated energy at a rate p_{max}; the conversion unit converts energy at a rate p_{avg} while the difference ($p_{max} - p_{avg}$) is stored in a storage device during the burntime. The stored energy is then used during the reactor downtime at the rate p_{avg}. Thus,

Total energy stored during burntime = total energy used during downtime

$$(P_{max} - P_{avg}) \times \text{Burntime} = P_{avg} \times \text{Downtime}$$

$$P_{avg} = P_{max} \times \frac{\text{Burntime}}{\text{Burntime + Downtime}} = 0.94\ P_{max}$$

To select the storage system, various thermal, mechanical and electrical storage schemes were evaluated. The energy storage concepts were classified by basic types as shown in Table V-2. The following criteria were established to screen these concepts and select those to be evaluated further.

- Sufficient storage capacity must be provided to maintain uniform power output during downtime.
- Energy to turbine-generator must be supplied at a uniform rate.
- Low electrical energy requirements for stored energy system.
- Size and complexity of the system should be minimized.
- Steam conditions at turbine throttle must remain nearly the same throughout the cycle.
- Materials used should be reasonably avaiable.
- Flow reversal through any portion of the system is not desirable.
- The system should be based on minimum extrapolation of present day technology.

All the concepts were evaluated against these criteria and very few appeared to meet all of them. Several were immediately discarded because of the large number of key criteria not met. A summary of this initial screening is provided in Table V-2. The ones examined in more detail were:

- Electrical and mechanical energy storage.
- Thermal energy stored as heat of vaporization.
- Thermal energy stored in solids.
- Thermal energy stored as heat of fusion.
- Thermal energy stored in liquids.

The advantages and disadvantages of each of these concepts are summarized in Table V-3.

Based on the preliminary qualitative evaluation of energy storage methods, liquid sodium was selected as the storage medium for UWMAK-II because:

- It meets all the criteria established for the storage system.
- It is an established technology and there is broad knowledge of characteristics and behavior of systems under the conditions required for UWMAK-II.
- The extensive development program for LMFBR's will provide tested system components and operating experience with large heat transfer systems by the 1990's.
- It will establish a technically and economically conservative basis to evaluate advanced systems against in future studies.

Table V-2: Criteria for Energy Storage System

Category / Concept \ Criteria	Adequate Energy Storage Capacity	Steady Turbine Output	Minimizes Electrical Energy Use	Minimizes Size and Complexity	Constant Steam Properties	Available Materials	No Flow Reversal	Available Technology
Electrical/Mechanical								
1. Superconductors	Projected as Feasible	No	No	No	No	Yes	-	For Small Units Only
2. Batteries	Yes	No	No	Lead-acid batteries occupy large area	No	Yes	-	Lead-acid Only
3. Compressed Gasses	Yes	No	No	Yes	No	Yes	-	Yes
4. Pumped Storage	Yes	No	No	No	No	Yes	-	Yes
5. Flywheels (Super-flywheel)	Projected as Feasible	No	No	No	No	Yes	-	For Small Units Only
Solids								
1. Fluidized Metals	Possibly	Yes	Yes	No	No	No	Yes	No
2. Material Masses	Yes	Yes	Yes	Volume depends on material. Least Complex	Yes	Yes	Yes	Yes
Heat of Vaporization								
1. Vaporized Metals	Yes	Yes	Yes	No	Yes	Possibly	Yes	No
2. Steam	Yes	Yes but add'l. storage volume required	Yes	No	Yes but add'l. storage volume required	Yes	-	Yes
Liquids								
1. Pumped Liquid Metal	Yes	Yes	Yes	No	Yes	Yes	Yes	Yes
2. Stagnant Liquid Metal	Yes	Possibly	Yes	Least Complex Large Volume	Yes	Yes	Yes	Yes
Heat of Fusion	Potentially	Yes	Yes	Yes	Yes	Yes but extensive research required	Yes	Only on Small Scale

Table V-3

Summary of Energy Storage System Evaluation

Concept	Advantages	Disadvantages	Comments
Electrical and Mechanical Storage		•Turbine operation is not maintained during downtime •Most concepts would require major development	•Alternating loading and unloading of turbine is unacceptable and overrides any advantages
Thermal Energy-Heat of Vaporization	•High storage potential per pound •Technology and experience available for water/steam •Steam permits direct use in turbine without additional heat exchanger •Minimizes degradation of system temperatures •No intermediate loop required	•Water/steam appear to be only suitable material •Large high pressure storage volume required •Special turbines required •Maintenance of constant turbine output requires storage of extra steam to maintain pressure or a displacement type accumulator	
Thermal Energy-Solids	•Simple in concept •Simple operation •Minimizes degradation of system temperatures •No intermediate loop required	•Large material volumes •Extra piping probably required for headering storage units •Special design required to maintain constant outlet temperature •Further design, analysis and R&D required to confirm feasibility •Energy storage system must be in containment	•Although simple in concept, a practical device may be complex
Thermal Energy-Heat of Fusion	•Simple in concept •Simple operation •High storage potential per pound •Constant system outlet temperature •Minimizes degradation of system temperatures	•Heat transfer during melting and freezing not well understood •Material compatability with most of candidate substances may be a problem •Technology relating to large high-temperature application is not being developed	•This concept has great potential. As it is a relatively new technology application, advances in technology could be rapid.

Table V-3 (continued)

Concept	Advantages	Disadvantages	Comments
Thermal Energy-Heat of Fusion (continued)	•Probably smallest volume of all the concepts •No intermediate loop required	•A large development program would be required •Energy storage system must be in containment	
Thermal Energy-Stagnant Liquid Sodium	•Same as storage in solids	•Same as storage in solids •Larger sodium volume than circulating sodium system •Energy storage system must be in containment	
Thermal Energy-Circulating Liquid System	•Feasibility proven •No serious technical problems •Good technical and economic design bases •Intermediate system can be outside containment •Systems and components developed for LMFBR can be used	•Intermediate loop required •Reduced steam temperatures due to ΔT's for intermediate systems	

The concepts which appear to offer the most promise of yielding improved systems in the long run are graphite solid storage and heat of fusion. Both of these systems offer significant potential advantages in simplification, but considerable further study would be required to establish their practicality, identify the problems in detail and evaluate the overall economics.

The results of the evaluation are summarized in the following paragraphs.

1. Electrical and Mechanical Energy Storage Concepts. Any energy storage system that requires periodic unloading and reloading of turbine-generator units during the burn cycle creates difficulties in the operation of these units due to the fluctuating temperatures. Unloading and reloading of large turbine-generator units may take as long as 30 minutes and would constitute an unacceptable constraint on both the plant and the energy storage system. All the electrical and mechanical energy storage concepts suffer from this shortcoming.

Therefore, because of the turbine operating problems, these concepts were eliminated from further consideration. As a result, we are left with the thermal energy storage concepts which, at least theoretically, would make it possible to maintain energy supply to the turbine-generators at a uniform rate throughout the burn cycle.

2. Thermal Energy Storage Concepts. Following general types of thermal energy storage have been considered:

- Heat of vaporization
- Heat in solid materials
- Heat of fusion
- Heat in liquid metals

All these concepts are in current use in some form or another but none have been developed for the power level or rate of recovery required by UWMAK-II.

a. Heat of Vaporization

Steam was the logical medium to consider under this category since it could be directed to the turbine through existing piping and would not require an additional heat exchanger. Further, since water has a relatively high heat of vaporization, it appeared that it could be stored in a relatively small volume. It was proposed that steam be stored in vessels at 238 atm (3500 psia) and 566°C (1050°F). A percentage of the steam generated during the 90 minute burntime would be diverted to these vessels. The energy stored would then be recovered during the downtime by drawing steam from the storage vessels through a throttle valve. This throttle valve would deliver the steam at 163.3 atm (2400 psia) and 510°C (950°F) to the turbine throttle, bypassing the helium circulator.

While this approach was satisfactory in theory, it presented two problems which made its usefulness for this application appear somewhat doubtful.

- The minimum vessel volume for steam storage would be about 19,500 m^3 (686,000 ft^3) (e.g., 160 vessels, each measuring 3.05 m (10 feet) in diameter and 16.8 m (55 feet) long.)
- The main turbine would require unique design features to permit the stored steam to be bled into successive stages as the pressure in the storage vessels decreased below normal operating pressure.(1) This design would result in a steadily decreasing generator output unless significantly more steam were stored to insure a minimum inlet pressure of 163 atm (2400 psia).

As a result of these factors, the storage of energy in the form of steam was not considered further in this study. However, the development of a constant pressure displacement type accumulator(2) might well make this concept attractive.

Other materials, such as liquid metals, could be considered as media for energy storage in this fashion. However, none of these were considered since there were no readily available materials identified with boiling points compatible with UWMAK-II parameters. In addition, use of such materials would require an extensive research and development effort.

b. Solids

The concept considered in this category was heat storage in a solid mass placed in the helium coolant system. Two materials compatible with the helium atmosphere were investigated; stainless steel and graphite.

Two operational concepts were considered. Figure V-3 is the flow diagram for heat storage with bypass flow. During reactor operation, a small bypass flow is circulated through the heat exchanger/storage unit. During energy recovery, the reactor is isolated and full system flow is put through the unit, recovering the stored energy.

Figure V-4 is the flow diagram for placement of the energy storage unit directly in the main helium-circulation line. This is the simpler of the two concepts as there are fewer valves and helium lines required than for the bypass concept. The disadvantage is that there is full helium flow (or lithium in the case of the divertor system) through the unit during the reactor burntime as well as during downtime. Consequently, an economic penalty will be incurred in pumping power due to the higher pressure drop. Further analysis will be required to select the best concept, but the flow scheme is not an important factor in the assessment of the concept.

To avoid degradation of outlet temperature during recovery of the energy from the storage media, the unit would require a variable mass distribution along its length. This variation would be such that a temperature distribution similar to that shown in Figure V-5 could be achieved.

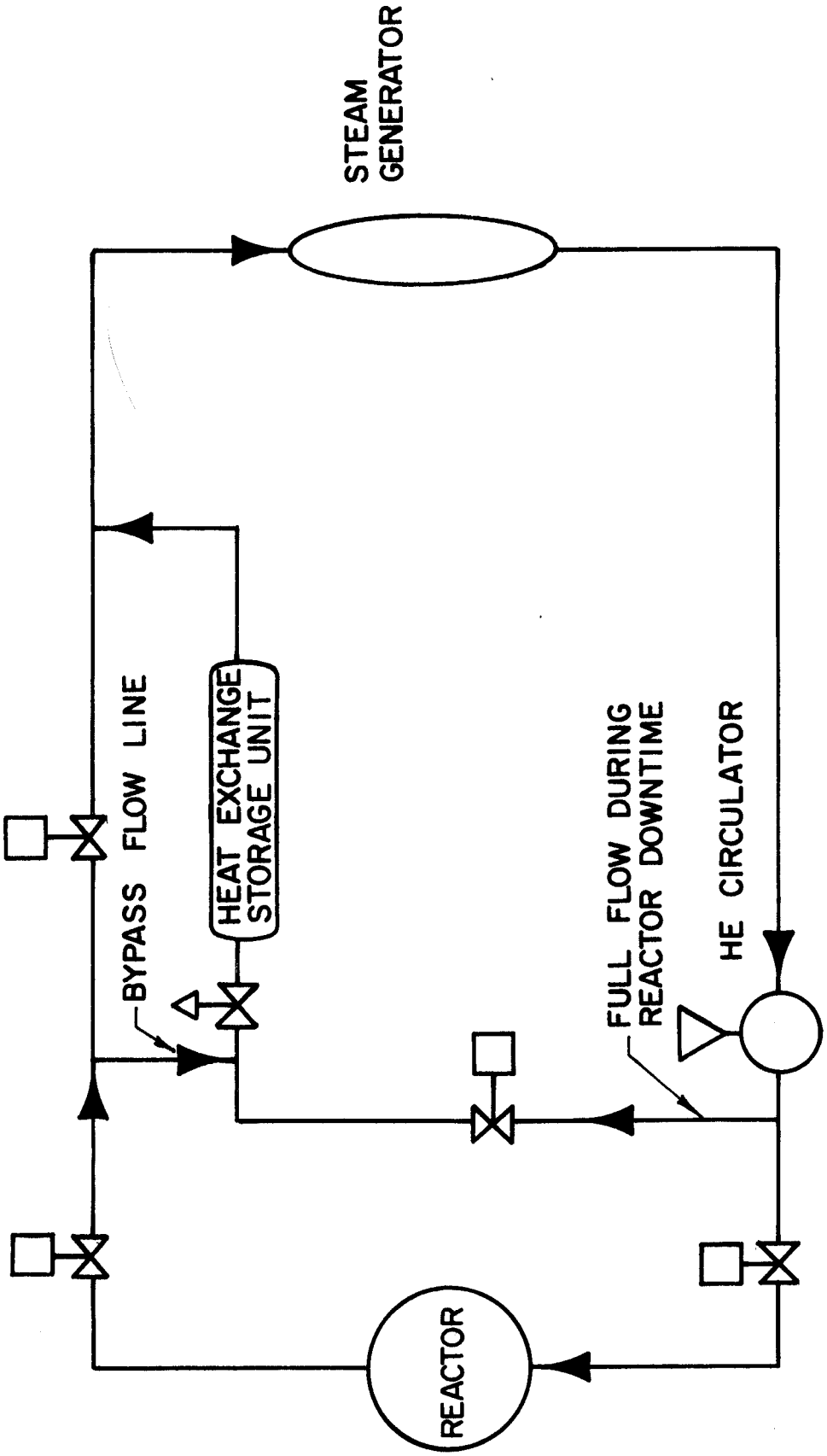
STEAM GENERATOR
BYPASS FLOW LINE
HEAT EXCHANGE STORAGE UNIT
FULL FLOW DURING REACTOR DOWNTIME
HE CIRCULATOR
REACTOR

Figure V-3

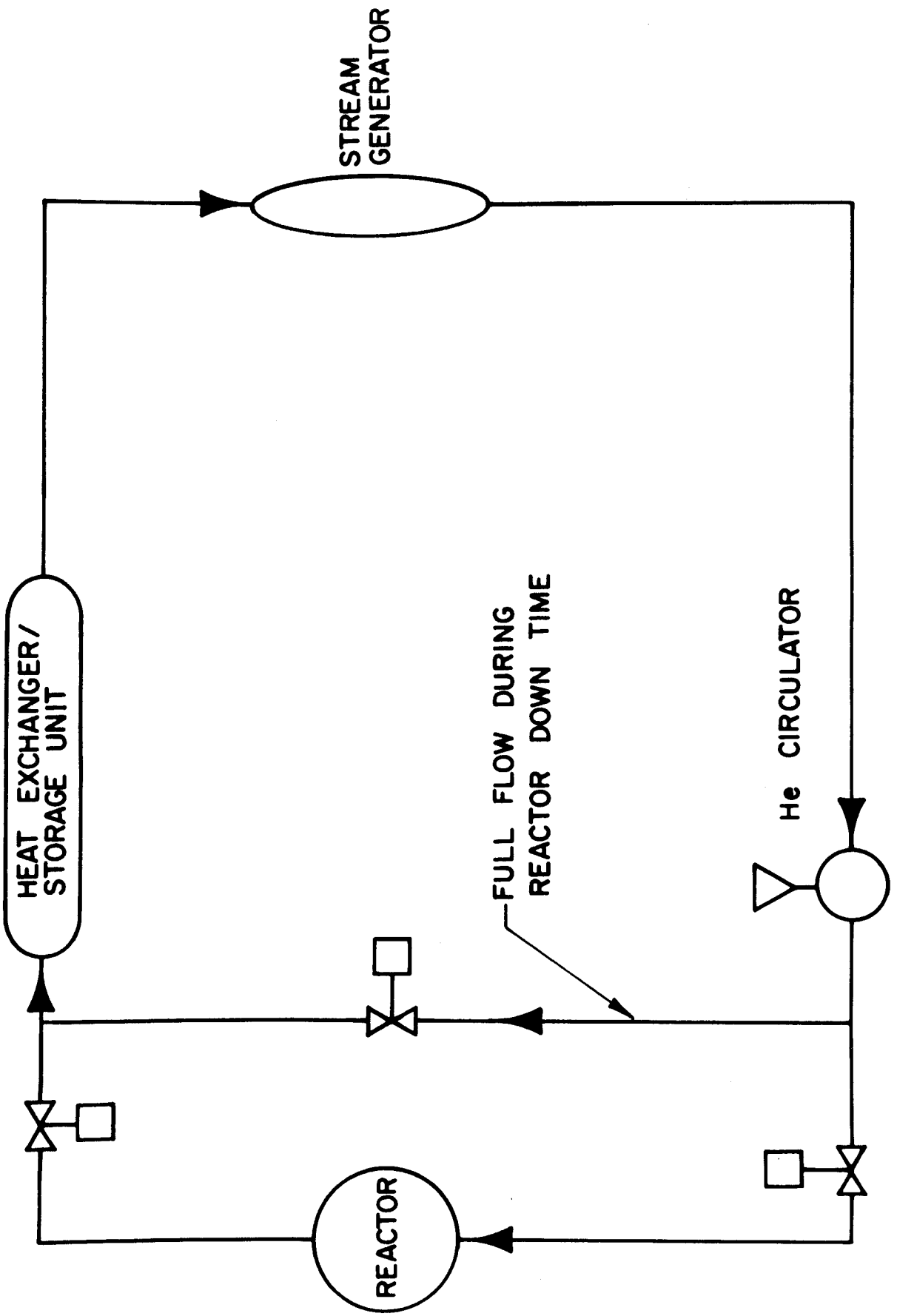
STREAM GENERATOR
HEAT EXCHANGER/ STORAGE UNIT
FULL FLOW DURING REACTOR DOWN TIME
He CIRCULATOR
REACTOR

Figure V-4

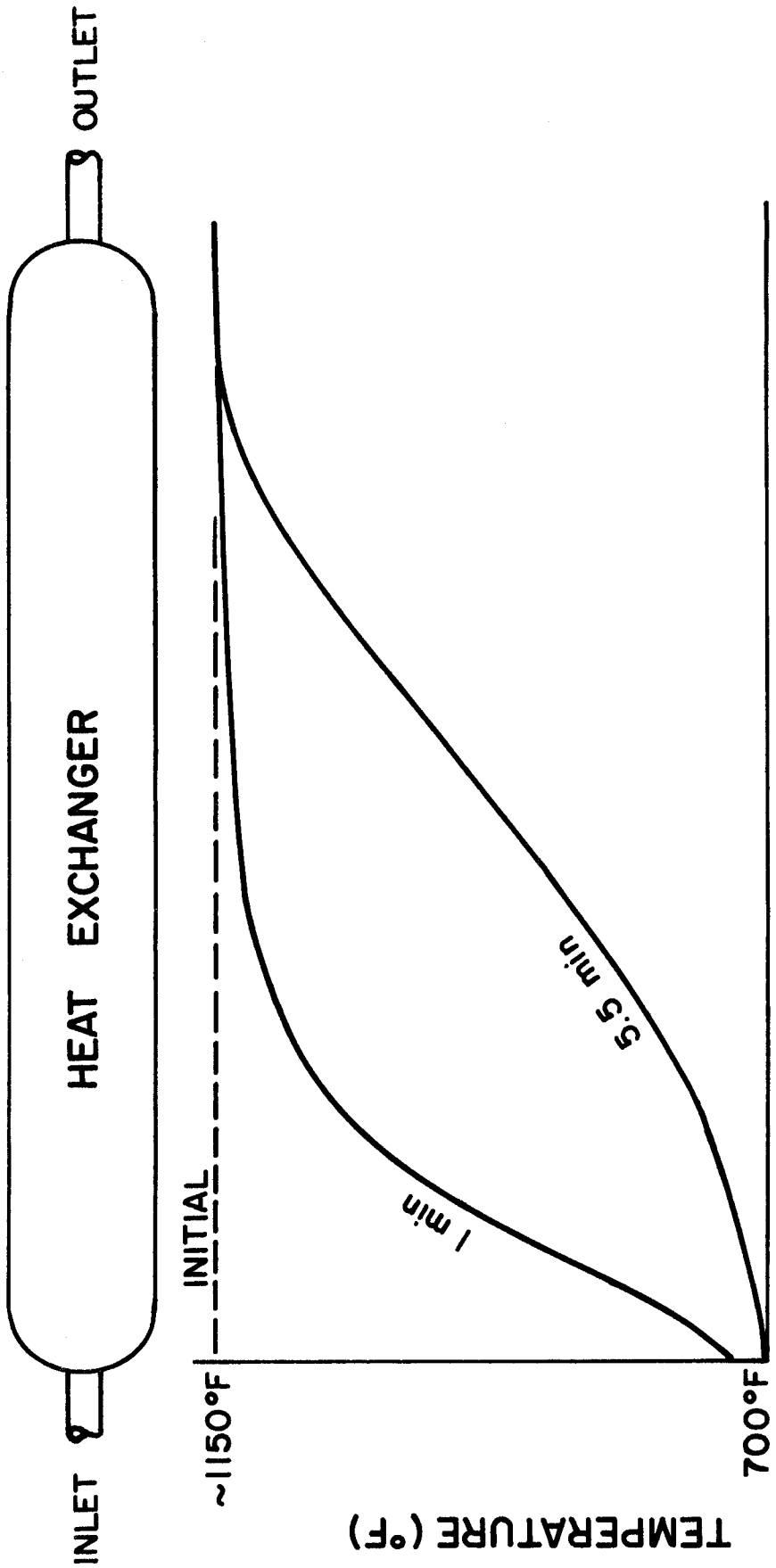
OUTLET
HEAT EXCHANGER
INLET
INITIAL
~1150°F
1 min
5.5 min
700°F
TEMPERATURE (°F)
LENGTH

Figure V-5

Rough estimates of the material quantities required to store the blanket energy were made. The concept was not considered for the divertor system because of the requirement to use an intermediate system with the lithium primary coolant in the divertor. The circulating sodium concept appears most attractive for the divertor system because of this.

The following table gives the estimated material quantities. The quanitity given in the "Theoretical" column is the mass required to store the 365 MWh needed without regard to the effectiveness of the system. The "Estimated Exchanger Requirements" column is a first approximation of the amount of energy storage material that might be required for a practical system. It is based on the assumption that the temperature distribution in the storage device at the end of the energy recovery cycle will be linear. The result of this assumption is that only one-half of the energy available for transfer is used, i.e., twice the theoretical quantity is required. The estimated volume includes an allowance of 50% for gas-side heat transfer space,

Material	Theoretical Quantity, 10^3 MT(T)	Estimated Exchanger Requirements	
		Quantity, 10^3 MT(T)	Volume, M^3 (ft^3)
Graphite	3.4 (3.7)	6.8 (7.5)	6200 (220,000)
Stainless Steel	10.4 (11.5)	20.9 (23)	4000 (141,000)

This concept appears feasible, but several problems and uncertainties have been identified including:

- The concept of variable material distribution to achieve a constant outlet temperature has not been analyzed to establish feasiblity and determine design constraints.
- The design of a practical unit that can deliver energy at the required rate from a solid material may be a limitation. Excessive heat transfer surface might be necessary to obtain the required heat transfer rates.
- The quantities of materials and volumes would be large and would likely have to be inside reactor containment or a separate containment building provided because the primary coolant flows through them.
- In the bypass regeneration concept (Figure V-4), it may be difficult to obtain proper helium flow distribution during energy storage because of the low flow rate.

c. Liquids

In evaluating this sub-category, two different concepts were examined:

- Stagnant sodium heat storage.
- Pumped sodium heat storage.

Sodium was chosen as the heat transfer medium to be studied in this concept because of the existing body of experience with sodium systems, and its applicability to the temperature range of interest.

d. Stagnant Sodium System

In the stagnant system, when the reactor is operating, a portion of the primary helium is passed through a heat exchanger containing a mass of stagnant sodium. Then, when the reactor is shut down, the stored heat is recovered by circulating the helium through the heat exchanger with the heat exchanger now acting as the heat source.

The same scheme can be used in this approach as was used for the solids energy storage (Figure V-3 and V-4). The total mass of sodium for blanket energy storage is 8400 MT (9300 T) and the volume, allowing 50% for gas passages is 15,000 M^3 (530,000 ft^3). Again, with this flow scheme, the mass would have to be distributed to maintain a constant outlet temperature from the storage device during operation as indicated in Figure V-5.

The important considerations in the evaluation of the stagnant sodium storage system are:

- Obtaining proper distribution of sodium mass and helium flow to maintain the desired temperatures during energy recovery.
- The larger volume of sodium required as compared to the circulating system because the full system ΔT is not available to release energy.

e. Circulating Sodium System

Figure V-6 shows the pumped sodium concept. The system contains an intermediate sodium loop similar to the UWMAK-I design. However, since helium rather than lithium is the primary coolant, the IHX's are significantly larger for UWMAK-II.

The system has two storage tanks; one for cold sodium and one for hot sodium. During the operating cycle, cold sodium is pumped into the cold leg and mixed with the cold leg sodium flow. It is heated in the IHX, and a portion of the total sodium flow is discharged to the hot-sodium tank. There it remains, maintained at 567°C (1052°F) by flow recirculation or by electrical topping heaters, until the down cycle of the reactor. At that point, the hot sodium is pumped through the steam generators, where steam continues to be generated, and back into the cold sodium storage tank.

While there are several disadvantages to this system, all are acceptable, particularly when compared with the other systems discussed previously. These disadvantages include:

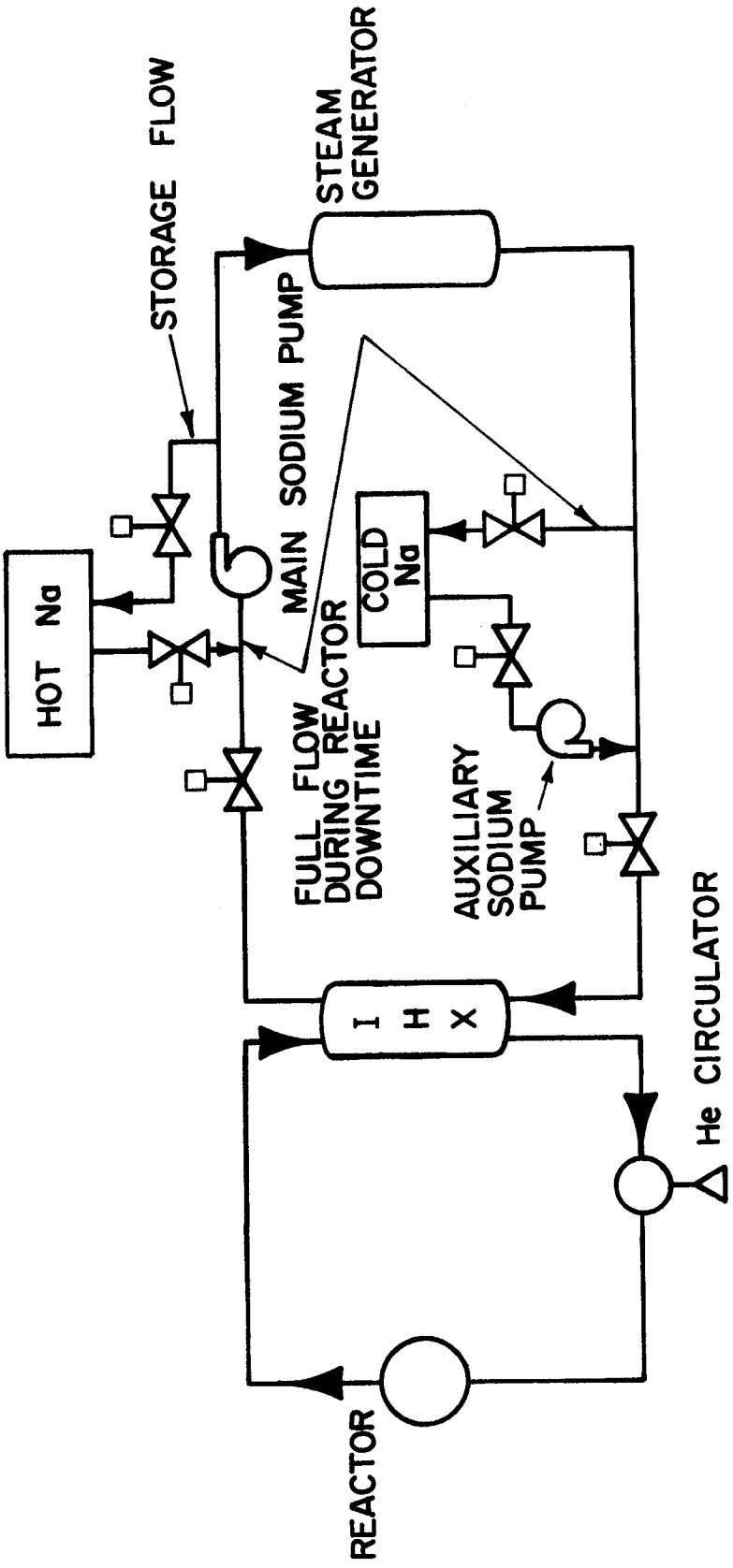
STEAM GENERATOR
STORAGE FLOW
MAIN SODIUM PUMP
HOT Na
COLD Na
FULL FLOW DURING REACTOR DOWNTIME
AUXILIARY SODIUM PUMP
I H X
He CIRCULATOR
REACTOR

Figure V-6

- An additional intermediate sodium system is required.
- Due to the presence of the intermediate loop, steam parameters at the steam generator outlet are lower than in a helium-to-steam loop
- Sodium/helium heat transfer surface area requirements are large.

The major factors favoring the use of a pumped sodium energy storage system for the UWMAK-II reference design are:

- There are no apparent serious technical problems or feasibility questions.
- There is a major national program directed to the development of systems and components similar in size and performance levels for the LMFBR.
- The system meets criteria established for the energy storage system (Table V-2).
- It acts as an additional barrier to the escape of tritium.

f. Heat of Fusion

A search of the literature revealed that little has been done in the way of development of large-volume, high-temperature energy storage systems using the latent heat of fusion. However, the concept appeared to be very attractive for several reasons:

- The system would require no intermediate loop.
- The system would require no additional pumps.
- The outlet temperature of the heat exchanger bed would be essentially constant.
- This concept would likely result in the smallest quantity of material and volume of any of the thermal storage systems.

Prompted by these potential advantages, a system was proposed utilizing a molten salt with a melting point of approximately 627°C (1160°F) as the storage medium. The flow schemes are the same as those shown for energy storage in solids (Figures V-3 and V-4).

Inquiries of the Molten Salt Data Center, Renselaer Polytechnic Institute and Holifield National Laboratory, Oak Ridge, Tennessee, resulted in the identification of a eutectic of LiF-NaF with a melting point of 652°C (1205°F), adjusted to 627°C (1160°F) by the addition of a small amount of KF. The heat of fusion of this material is between 167 and 222 kcal/kg (300-400 Btu/lb).

Rough calculations show that theoretically, 2040 tons of this eutectic would be needed to store the necessary heat.

However, there was at least one potential problem with this particular material; its density decreases by 1/3 on melting. As a result, the solid phase would remain at the bottom of the mixture against the heat transfer surface

during both the operating and down cycles, reducing the effectiveness of convective heat transfer in the liquid. The degree of the volume change would make it extremely difficult to eliminate this problem since the eutectic must be stored in a containment which would allow this expansion to take place and must, therefore, have at least 30% void space. A recent article[3] has proposed the use of certain semiconductors such as silicon, germanium, gallium arsenide, etc., for such applications. If any of these prove usable, they should eliminate the problem just discussed since they contract on melting, allowing the solid material to float, leaving the liquid in contact with the heat exchange surface. While many of these semiconductors melt at extremely high temperatures (e.g., silicon at 1412°C (2574°F)) and are therefore unusuable, germanium sulfide melts at a more useful temperature 590°C (1094°F). However, it is corrosive to most ferrous metals.

Although the use of the latent heat of fusion for heat storage is certainly promising from a purely theoretical viewpoint, it cannot be considered current technology in any sense. Consequently, it was not selected for use in UWMAK-II.

Some of the concerns and uncertainties of this concept are:

- The heat transfer during phase change does not appear to be well understood.
- Compatibility with structural materials may be a problem at these high temperatures. Many of the materials are highly corrosive and reactive.

V-C. Blanket Energy Transport and Conversion

An overall schematic diagram of the blanket energy conversion system is shown in Figure V-7. The system consists of four identical circuits operating in parallel. Each circuit has in series a primary helium system, an intermediate sodium system and a steam generation system. The primary helium is circulated through the blanket where it absorbs the energy being generated and transports it to the intermediate heat exchanger (IHX). The energy is transferred in the IHX to the intermediate loop sodium. The intermediate loop includes the sodium storage used for energy levelizing during the downtime while the reactor is being recharged. Energy is transported by the sodium to the steam generators to generate steam to operate the turbine-generator.

The selection of four heat transfer circuits was based on the size of systems planned for development for gas-cooled and sodium-cooled fission reactors. In their large High Temperature Gas-cooled Reactor (HTGR) studies, General Atomic Company (GAC) is considering loops of about 400 MWe capacity. Studies of commercial Liquid Metal Fast Breeder Reactors (LMFBR) for operation in the mid-1990's are also considering capacities in the range 400 MWe to 500 MWe per loop. Thus, proven technology and equipment should be avaiable for the design selected for the UWMAK-II energy conversion system. In addition, the current state of knowledge for both HTGR's and LMFBR's provides a good basis for engineering and cost estimating.

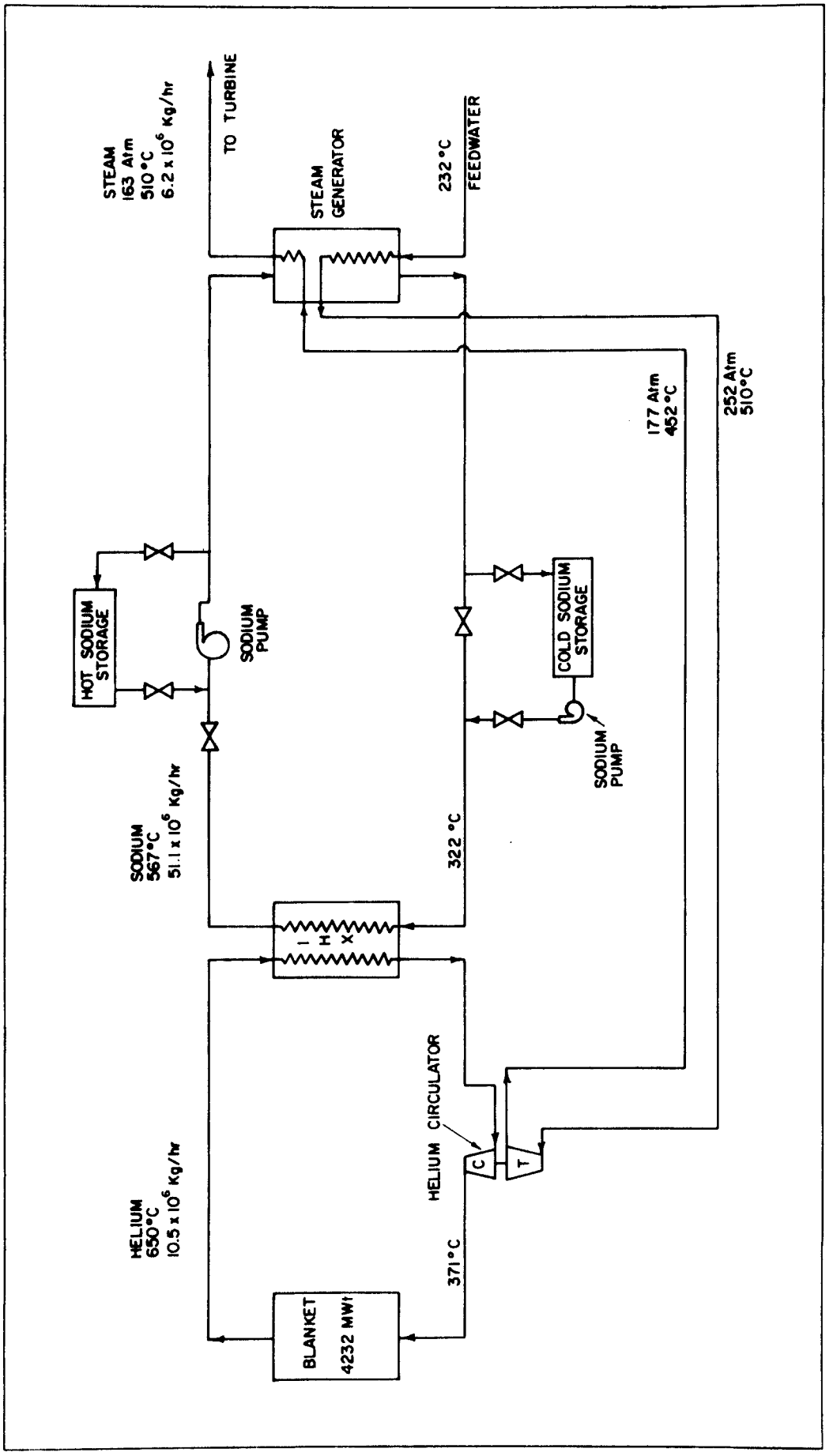
STEAM
163 Atm
510°C
6.2 x 10⁶ Kg/hr
TO TURBINE
STEAM GENERATOR
232°C
FEEDWATER
177 Atm
452°C
252 Atm
510°C
HOT SODIUM STORAGE
SODIUM PUMP
COLD SODIUM STORAGE
SODIUM PUMP
SODIUM
567°C
51.1 x 10⁶ Kg/hr
322°C
I
H
X
HELIUM CIRCULATOR
C
T
HELIUM
650°C
10.5 x 10⁶ Kg/hr
371°C
BLANKET
4232 MWt

Figure V-7.

V-C-1. Primary Helium System

The primary cooling cycle consists of four helium loops. The principal components in each loop are the helium circulator, the helium-to-sodium heat exchanger and the helium piping. The heat exchanger is also referred to as the intermediate heat exchanger (IHX). The helium circulators are driven by steam turbines, the steam being supplied from the steam generators. Approximately 2.6×10^6 kg/hr (5.8×10^6 lb/hr) helium is circulated in each loop to remove 1058 MWt. Helium enters the blanket at 371°C (700°F) and leaves at 650°C (1202°F). Hot helium then flows through the intermediate heat exchanger. Cold helium enters the circulator which maintains an average pressure of 51 atmospheres (atm) (750 psia) within the blanket. The circulator turbine receives steam at 252 atm (3700 psia), 510°C (950°F) and exhausts at about 177 atm (2600 psia).

The characteristics of the conceptual IHX's are shown in Table V-4. There is no industrial experience in the design of a helium to sodium heat exchanger of comparable capacity. However, no major technological problem is foreseen. Experience gathered from the design of HTGR and LMFBR steam generators will provide the basis for the design of IHX.

Each IHX unit is 21 meter (69 ft) in height and 3.2 m_2(10.5 ft) in diameter having a total heat transfer area of 10,800 m^2 (116,500 ft^2) based on the tube outside diameter. High pressure helium flows through the tubes while sodium flows in the shell. Hot helium enters the unit at the top and the cooled helium is discharged at the bottom. Cold sodium enters near the bottom and the heated sodium is discharged at the top. A single stage axial flow helium circulator is mounted at the bottom of the IHX unit and receives cold helium.

Materials used for the heat exchanger surface as well as for the shell are consistent with the current industrial practice as used in the heat exchanger design for gas cooled and liquid metal cooled fission reactors. The material selected for tubes is Incoloy-800 and that for the shell is 316 SS. These materials are compatible with helium and sodium and the system operating temperatures.

V-C-2. Intermediate Sodium System

The intermediate cycle consists of 4 identical sodium loops. The principal components in each loop are the sodium circulation pump, the steam generator, the hot and cold sodium storage tanks and sodium piping. The circulation pumps are electric motor driven.

Approximately 12.8×10^6 kg/hr (28×10^6 lb/hr) liquid sodium is circulated in each loop through the intermediate heat exchanger during the 90 minute burntime. To maintain average uniform flow rate through the steam generator, a fraction of hot sodium flow from IHX is stored in the hot sodium storage tank. Flow rate through the steam generator is approximately 12.1×10^6 kg/hr (26.6×10^6 lb/hr). This flow rate is maintained during the 5.5 minute downtime by drawing sodium from the hot storage tank. Cold sodium from steam generator is stored in the cold storage tank during this downtime and is pumped back to the loop during the burntime. Cold sodium enters the IHX at about 322°C (612°F) and leaves at about 567°C (1052°F).

Table V-4

Intermediate Heat Exchanger Characteristics

Number of IHX's	Four
Type	Shell and Tube
Primary Helium	Tube
Intermediate Sodium	Shell
Helium Inlet Temperature, °C(°F)	650 (1202)
Helium Outlet Temperature, °C(°F)	371 (700)
Sodium Inlet Temperature, °C(°F)	322 (612)
Sodium Outlet Temperature, °C(°F)	567 (1052)
Primary Helium Flow Rate kg/hr (lb/hr)	2.6×10^6 (5.8×10^6)
Intermediate Sodium Flow Rate, kg/hr (lb/hr)	12.8×10^6 (28×10^6)
Duty, MWt	1093
Surface Area, m^2(ft^2)	10,800 (116,500)
Number of Tubes	9100
Effective Tube Length, m(ft)	15.2 (50)
Tube Diameter, cm(in)	2.54 (1)
Shell Diameter, m(ft)	3.2 (10.5)
Overall Heat Transfer Coefficient, Kcal/ hr-m^2-°C(Btu /hr-ft^2-°F)	1464 (300)
LMTD, °C(°F)	42 (107)
Material - Tube	Incoloy 800
- Shell	316 SS

Table V-5

Steam Generator Characteristics

Number of Loops	4
Number of Modules/Loop - Preheater	1
Superheater	1
Resuperheater	1
Type	Shell and Tube
Intermediate Sodium	Shell
Steam/Water	Tube
Sodium Flow Rate, kg/hr (lb/hr)	12.1×10^6 (26.6×10^6)
Water/Steam Flow Rate, kg/hr (lb/hr)	1.5×10^6 (3.4×10^6)
Preheater Module (each)	
Sodium Inlet Temperature, °C(°F)	465 (870)
Sodium Outlet Temperature, °C(°F)	322 (612)
Feedwater Inlet Temperature, °C(°F)	232 (450)
Steam Outlet Temperature, °C(°F)	399 (750)
Duty, MWt	604
Surface Area, m^2(ft^2)	4650 (50,000)
Number of Tubes	3500
Effective Tube Length, m(ft)	26.7 (87.5)
Tube Diameter, cm (in)	1.59 (5/8)
Shell Diameter, m(ft)	2.13 (7)
Overall Heat Transfer Coefficient, kcal/hr-m^2-°C (Btu/hr-ft^2-°F)	1434 (294)
LMTD, °C(°F)	60 (140)
Materials	2 1/4 Cr - 1 MØ
Superheater Module (each)	
Sodium Inlet Temperature, °C(°F)	546 (1014)
Sodium Outlet Temperature, °C(°F)	465 (870)
Steam Inlet Temperature, °C(°F)	399 (750)
Steam Outlet Temperature, °C(°F)	510 (950)
Outlet Steam Pressure, atm (psia)	252 (3700)
Duty, MWt	338
Surface Area, m^2 (ft^2)	3005 (32,350)
Number of Tubes	3500

Table V-5 (continued)

Effective Tube Length, m(ft)	17 (56.5)
Tube Diameter, cm(in)	1.59 (5/8)
Shell Diameter, m(ft)	2.13 (7)
Overall Heat Transfer Coefficient, Kcal/hr-m^2-°C (Btu/hr-ft^2-°F)	1952 (400)
LMTD, °C(°F)	32 (89)
Material	321 SS
Resuperheater Module (each)	
Sodium Inlet Temperature, °C(°F)	567 (1052)
Sodium Outlet Temperature, °C(°F)	546 (1014)
Steam Inlet Temperature, °C(°F)	452 (846)
Steam Outlet Temperature, °C(°F)	510 (950)
Outlet Steam Pressure, atm(psia)	163 (2400)
Duty, MWt	88
Surface Area, m^2(ft^2)	846 (9100)
Number of Tubes	2500
Effective Tube Length, m(ft)	6.9 (22.5)
Tube Diameter, cm(in)	1.59 (5/8)
Shell Diameter, m(ft)	1.83 (6)
Overall Heat Transfer Coefficient, Kcal/hr-m^2-°C (Btu/hr-ft^2-°F)	1220 (250)
LMTD, °C(°F)	56 (132)
Material	321 SS

The characteristics of the conceptual steam generator unit are shown in Table V-5. Current steam generator design practice for LMFBR provides the basis for the design of the unit. A modular concept is used with 3 modules for each loop. The modules are characterized as follows:

Module	Temperature Range (Water/Steam Side)
Preheater	<750°F
Superheater	>750°F
Resuperheater	>800°F

Each of the preheater and superheater modules has a heat transfer area of 4650 m^2 (50,000 ft^2) and 3005 m^2 (32,350 ft^2), respectively and they are 28 m (92 ft) and 18 m (60 ft) high. respectively. Each module is 2.13 m (7 ft in dia.). The resuperheater module has a heat transfer area of 846 m^2 (9100 ft^2). It is 8 m (26 ft) high and 1.83 m (6 ft) in diameter.

The preheater modules are 2 1/4 Cr-1 Mo ferritic steel alloy (ASME-T22). The superheater and resuperheater modules use 321 SS.

V-C-3. Steam Cycle

The steam cycle is illustrated schematically in Figure V-9. The turbine-generator selected for the blanket steam cycle is a cross-compound 3600/1800 rpm unit with throttle steam conditions of 163 atm (2400 psia) and 510°C (950°F). These conditions are consistent with present day turbine generators (fossil plants, HTGR, LMFBR). The 3600 rpm shaft of the unit is driven by two double-flow high pressure (HP) and two double-flow intermediate pressure (IP) turbines. The 1800 rpm shaft is driven by three double-flow low pressure (LP) turbines.

Steam generators deliver a total of about 6.2×10^6 kg/hr (13.6×10^6 lb/hr) superheated steam at 252atm (3700 psia),510°C (950°F) to helium circulator turbines. Exhaust from these full-flow turbines enters the resuperheater section of the steam generators and is resuperheated to 510°C (950°F) for expansion in the turbine-generator. Seven feedwater heating stages are used with a steam turbine driven feedwater pump.

V-C-4. Cooling Water System

A closed loop cooling cycle with evaporative type cooling towers is used for cooling the condenser. A cooling water flow of approximately 150×10^6 kg/hr (330×10^6 lb/hr) is required. The cycle is shown in Figure V-8. This cooling tower also is used for divertor steam cycle cooling water. A hyperbolic cooling tower is used.

V-D. Divertor Energy Transport and Conversion

An overall schematic diagram of the divertor energy conversion system is shown in Figure V-9 . A single circuit is used for this system which consists of a primary lithium loop in series with an intermediate sodium loop and a steam generation system. The lithium is circulated through the divertor where it collects particles removed from the reactor and cools the structure. The energy absorbed by the lithium is transferred to the intermediate sodium in the IHX. As in the blanket system, the intermediate loop includes the sodium storage used for energy levelizing. Energy is transported by the sodium to the steam generators to generate steam to operate the turbine-generator.

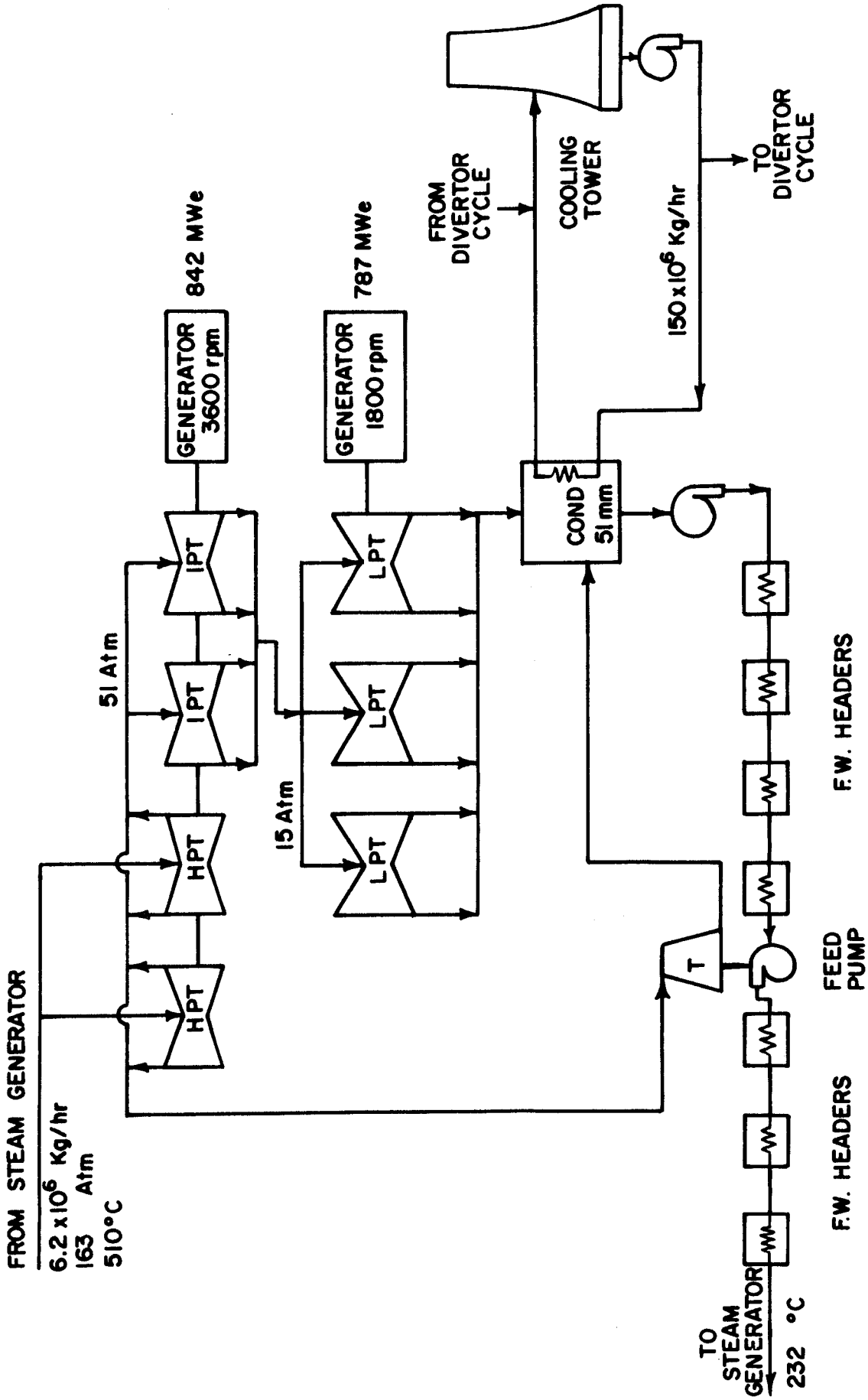

NET CYCLE HEAT RATE = 8331 $\frac{Btu}{Kwh}$ (2099 $\frac{kcal}{Kwh}$)

Figure V-8

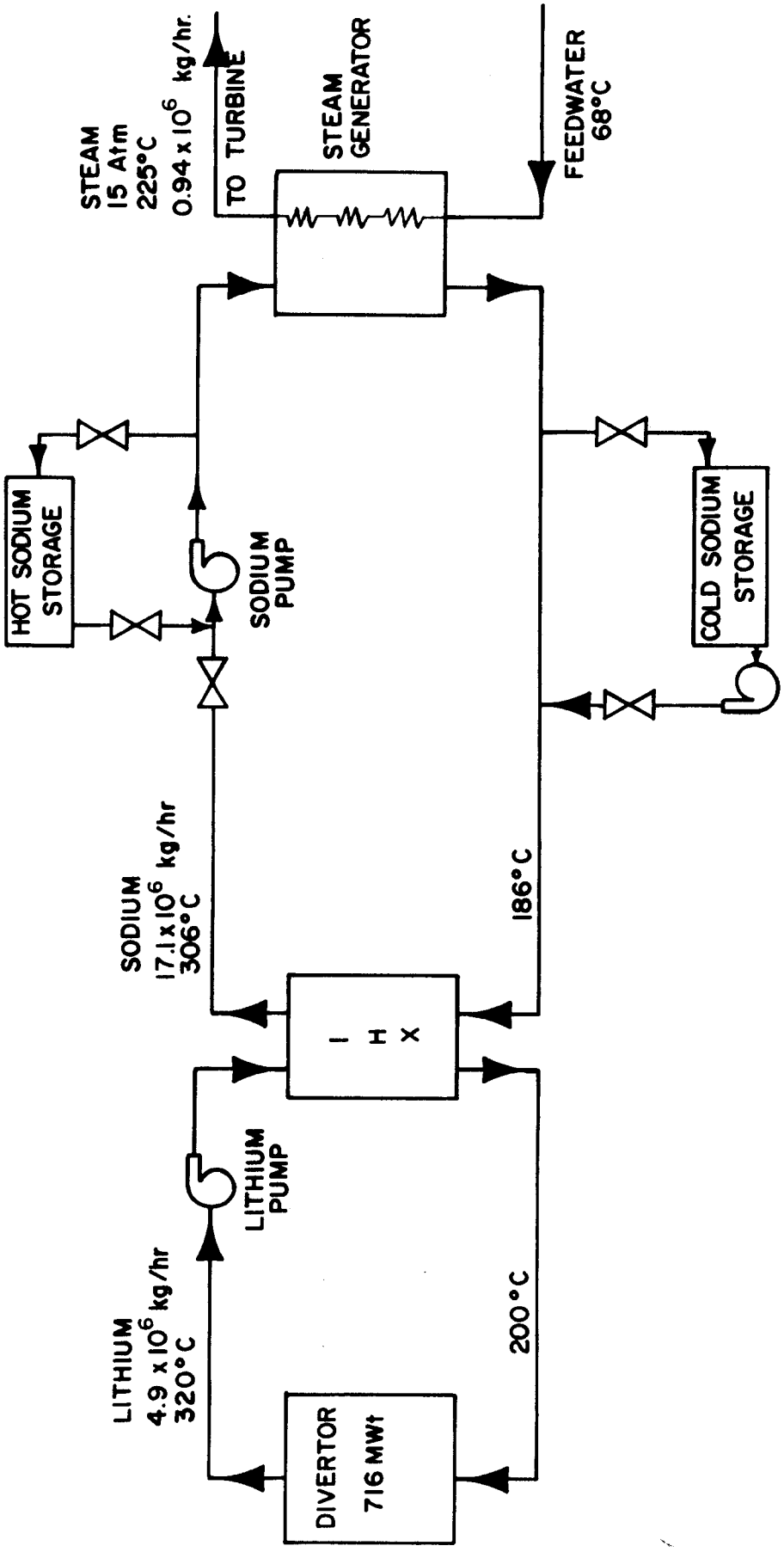
STEAM
15 Atm
225°C
0.94 x 10^6 kg/hr.
TO TURBINE
STEAM GENERATOR
FEEDWATER
68°C
HOT SODIUM STORAGE
SODIUM PUMP
COLD SODIUM STORAGE
SODIUM
17.1 x 10^6 kg/hr
306°C
186°C
I - H X
LITHIUM PUMP
LITHIUM
4.9 x 10^6 kg/hr
320°C
200°C
DIVERTOR
716 MWt

Figure V-9

Although a single circuit as selected for the divertor system is within the technology expected to be available, other considerations may affect this choice as more detailed engineering studies of fusion power plants are made. The major considerations affecting the number of circuits are operational flexibility of the plant and economics.

V-D-1. Primary Lithium System

The primary cooling cycle consists of one lithium loop. The principal components in the loop are the lithium pump, the lithium-to-sodium heat exchanger and the lithium piping. The heat exchanger is also referred to as the intermediate heat exchanger (IHX). The lithium pump is electric motor driven.

Approximately 4.94×10^6 kg/hr (10.9×10^6 lb/hr) lithium is circulated in the loop to remove 716 MWt. Lithium enters the divertor at 200°C (392°F) and leaves at 320°C (608°F). The lithium pump is located in the hot leg to take suction from the divertor where lithium flow is maintained by gravity. Hot lithium is circulated through the IHX and transfers its energy to the intermediate sodium system.

V-D-2. Intermediate Sodium System

Similar to the primary cycle, the intermediate cycle consists of one sodium loop. The principal components in the loop are the sodium circulation pump, the steam generator, the hot and cold sodium storage tanks and sodium piping. The circulation pump is electric motor driven.

Approximately 17.1×10^6 kg/hr (37.7×10^6 lb/hr) liquid sodium is circulated in the loop through the intermediate heat exchanger during the 90 minute burntime. To maintain average uniform flow rate through the steam generator, a fraction of hot sodium flow from IHX is stored in the hot sodium storage tank. Flow rate through the steam generator is approximately 16.1×10^6 kg/hr (35.5×10^6 lb/hr). This flow rate is maintained during the 5.5 minute downtime by drawing sodium from the hot storage tank. Cold sodium from steam generator is stored in the cold storage tank during this downtime and this is pumped back to the loop during the burntime. Cold sodium enters the IHX at about 186°C (367°F) and leaves at about 306°C. (583°F).

V-D-3. Steam Cycle

The steam cycle is schematically illustrated in Figure V-10. The turbine-generator selected for the divertor steam cycle is a double-flow 1800 rpm unit with inlet steam conditions of 15 atm (220 psia) 225 °C (438°F). These conditions were selected since they are consistent with those of the LP unit of a light water reactor plant turbine. Steam flow of about 0.94×10^6 kg/hr (2.1×10^6 lb/hr) enters the turbine and exhausts to the condenser after expansion. One stage of feedwater heating is used. No separate feed pump is condensate pump is needed as the condensate pump is adequate to deliver the feedwater to the steam generator at the required pressure.

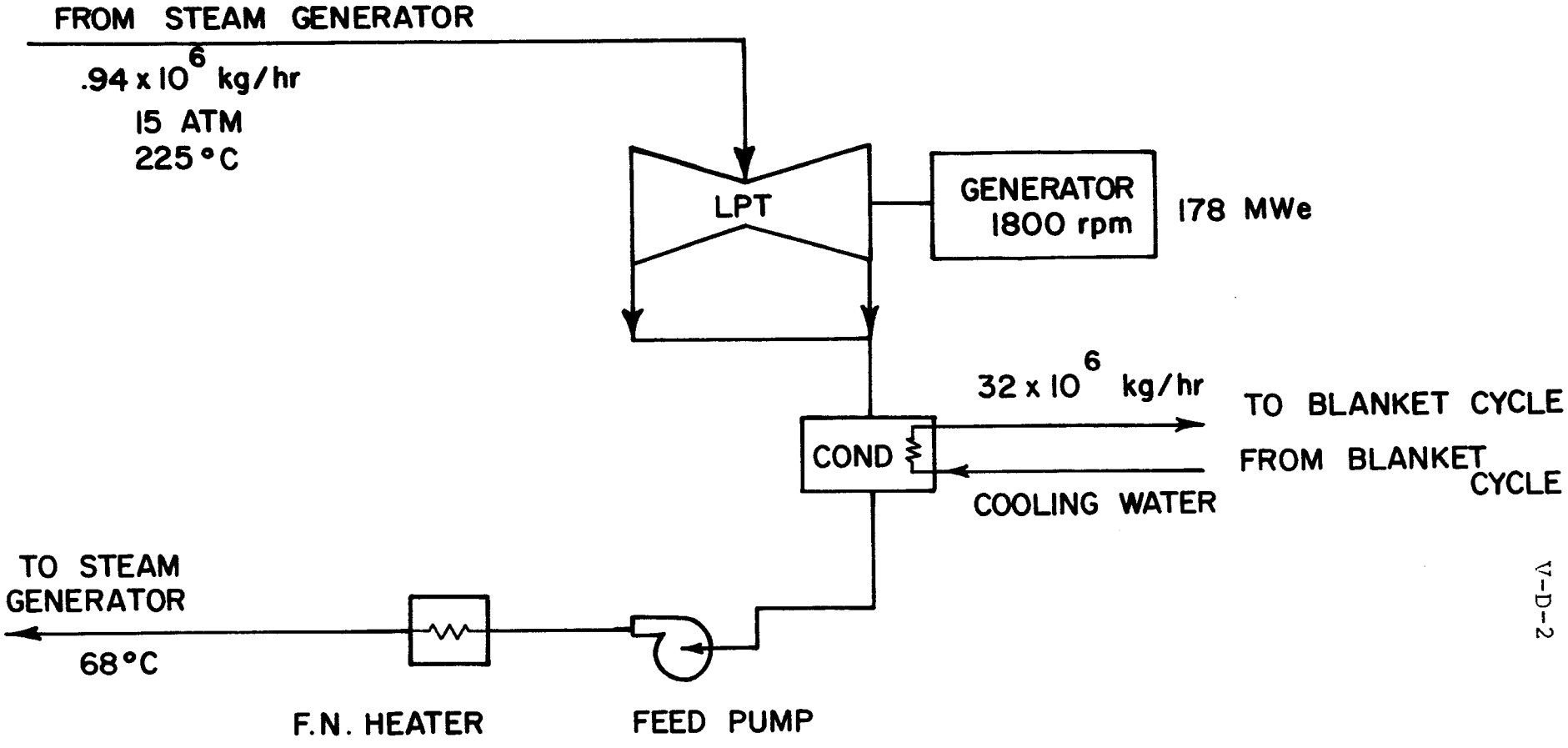

NET CYCLE HEAT RATE = 12,943 $\frac{\text{Btu}}{\text{Kwh}}$ (3262 $\frac{\text{Kcal}}{\text{Kwh}}$)

Figure V-10

V-D-4. Cooling Water System

A closed loop cooling water cycle provides condenser cooling. A common cooling tower is used for both divertor and blanket cooling water cycle. This is schematicall shown in Figures V-8 and V-10. A cooling water flow of about 32.4 x 10^6 kg/hr (71 x 10^6 lb/hr) is needed. The cycle is shown in Figure V-10.

V-E. Shield Energy Rejection

As mentioned previously, the removal and rejection of energy deposited in the neutron shield is accomplished in two steps. A schematic arrangement of the system is shown in Figure V-11. This is a reactor safety-related system because the system is also used to remove the reactor afterheat. Removal of afterheat is needed after reactor shutdown, normal or emergency to avoid damage to the reactor. Questions of redundancy and/or backup cooling requirements have not been addressed in this study.

V-E-1. Primary Helium System

The primary cooling system consists of one helium loop. The principal components in the loop are the helium circulators, the helium-to-water heat exchanger, and the associated helium piping. The helium circulator is electric motor driven.

Approximately 0.24 x 10^6 kg/hr (0.53x10^6lbs/hr) helium is circulated in the loop to remove 52 MWt. Helium enters the shield at 50°C (122°F) and leaves at 200°C(392°F) Hot helium then flows through the heat exchanger and transfers its energy to the cooling water. Cold helium enters the circulator which maintains an average pressure of 51 atm (750 psia) within the shield.

V-E-2. Cooling Water System

A closed loop cooling water cycle with evaporative type cooling tower is used for rejecting the energy to the atmosphere. Since this is a safety-related system, the cooling tower is not made common with the blanket and divertor cooling tower. A cooling water flow of approximately 3.4 x 10^6 kg/hr (7.6 x 10^6 lb/hr) is required for removing the shield energy. This cycle is shown in Figure V-11.

V-F. Auxiliary Power

The total station power requirement is anticipated to be 98 MWe. This requirement consists of:

Nuclear Island (Cryogenerators, Vacuum System, Fueling and Heating, Magnets)	38 MW
Balance of Plant (Sodium System, Cooling Water System, and Other Auxiliaries)	60 MW
Total	98 MW

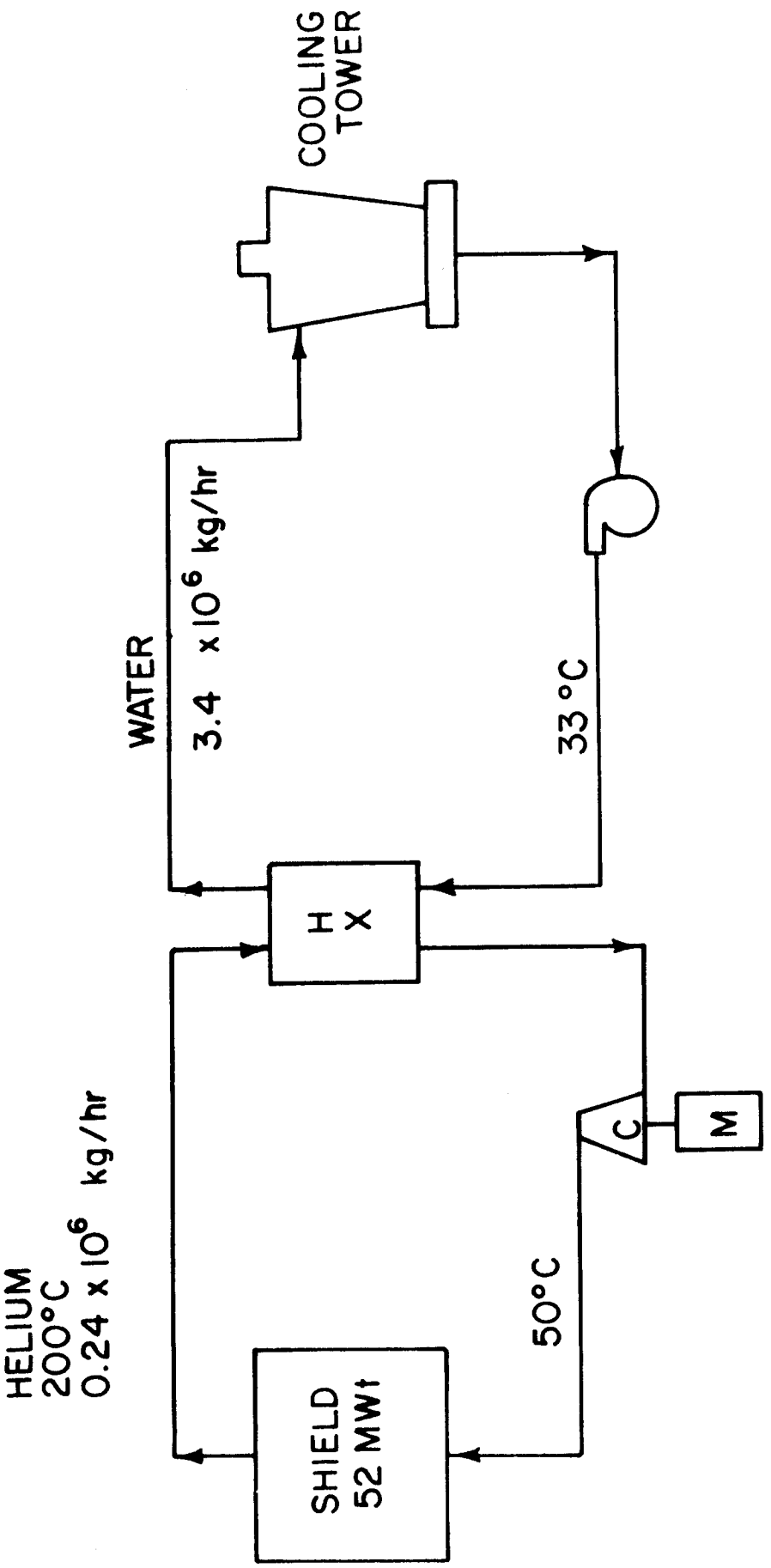
COOLING TOWER
WATER
3.4 x10^6 kg/hr
33 °C
HX
HELIUM
200°C
0.24 x10^6 kg/hr
C
M
50°C
SHIELD
52 MWt

Figure V-11

This total amounts to about 5.4% of gross generation. Blanket helium circulators and main feedwater pumps, which would normally consume approximately 200 MW, are steam driven.

V-G. Plant Performance

Table V-6 lists the overall plant power parameters and efficiency of UWMAK-II.

Table V-6

Summary of Power Level and Efficiency of UWMAK-II

Reactor Power (Periodic)	5000 MW
Reactor Power (Average Continuous)	4712 MW
Gross Generation (Continuous)	1807 MW
Auxiliary Power (Continuous)	98 MW
Net Generation (Continuous)	1709 MW
Plant Efficiency	36.3%
Plant Heat Rate	2371 kcal/kWhr 9408 Btu/kWhr

References for Chapter V

1. Gilli, P. V., Beckman, G., "Steam Storage Adds Peaking Capacity to Nuclear Plants,"Energy International, Aug. 1973.

2. Gilli, P. V., Beckman, G., "The Nuclear Steam Storage Plant - An Economic Method of Peak Power Generation," World Energy Conference, Detroit 1974.

3. Van Vechter, J. A., "An Economically and Ecologically Viable Alternative to Pumped Water Storage." An Edited Version of the paper was published in Electrical World, Aug. 15, 1974.

VI. Plant Design

VI-A. Introduction

Only recently have the plant design requirements for fusion reactors begun to receive engineering attention. There is little prior work to provide guidance for the design of many of the facilities for fusion plants. Those areas unique to the UWMAK-II fusion plant have been emphasized in this study while aspects which are similar to a fission plant have been extrapolated from fission plant design practices. The UWMAK-II design is developed to the detail required for a conceptual cost estimate.

The objectives of the conceptual plant design study for the UWMAK-II reactor are to:

- Identify the major buildings and structures needed to contain the plant equipment.
- Define the functional interrelationships among various buildings and structures.
- Develop a technically feasible, operable, and maintainable plant design.
- Identify areas in which there are significant technical or cost uncertainties.
- Provide a basis for conceptual cost estimate.

Bechtel has developed a generic plant design concept for fission reactor facilities and this has served as a basis for similar aspects of the UWMAK-II plant. Conceptual design studies were performed for the Containment Building, Reactor Auxiliary and Service (Hot Cell) buildings, and the primary coolant system arrangement even though no generic design basis is available for these items. The building design effort was confined to the major structures (Containment Building, Service and Auxiliary buildings, and Heat Exchanger Building). Only superficial consideration was given to piping and equipment design and arrangement.

The generic plant layout is based on the concept of identifying system functions and functional interrelationships and assigning these into modules. The modules form the framework for the following buildings and their functions:

- A Reactor Containment Building containing the reactor and other components of the nuclear island.
- A Reactor Service Building containing equipment for servicing radioactive components.

- A Reactor Auxiliary Building containing safety-related equipment and other equipment closely associated with that located within the Containment Building.

- A Heat Exchanger Building containing the heat exchange and transport equipment. (It also contains the thermal energy storage equipment for UWMAK-II).

- A Turbine Building containing the energy conversion equipment.

- A Control Building containing the central plant control equipment.

- A Diesel Generator Building containing the emergency diesel generators.

- A Radioactive Waste Building containing processing equipment for radioactive wastes.

Other major buildings and features unique to the UWMAK-II plant are:

- A Reprocessing Building containing the equipment and facilities for processing the spent first wall of the blanket.

- A Fabrication Building containing the equipment for fabrication and installation of the new first wall on the already irradiated blanket sections.

- A railroad tunnel for storage and handling of blanket sections with spent and rebuilt first walls.

- A harmonic filter and inverter area associated with the Inductive Energy Supply System.

VI-B. Plant Arrangement

VI-B-1. General

A principal aim of this portion of the study is to develop a conceptual plant design that will meet the requirements for operation and maintenance. Space is provided for necessary equipment and functions; allowance is also made for unidentified equipment and for "design growth".

The general plant arrangement and the internal arrangement of some of the buildings are patterned wherever possible after the generic concept developed by Bechtel for fission reactor plants. The greatest effort was devoted to those areas unique to the UWMAK-II, such as the Containment Building, the Heat Exchanger Building, and the Reactor Auxiliary Building. Other buildings such as the Control Building and the Turbine Building are similar to those in other nuclear plants, and their arrangements can be adopted readily to this plant.

The general plant arrangement is shown in Drawings VI-M-1 and VI-M-2. The major features of the arrangement include the following:

- The Containment Building is centrally located relative to the other buildings.
- The Auxiliary Building, Service Building, Radwaste Building, Reprocessing Building, and the Fabrication Building are arranged around the Containment Building. This arrangement seems to have some advantage in handling blanket sections and large volumes of radioactive wastes.
- The peninsular arrangement of the Turbine Building orients the turbine-generator axis such that any missiles generated by the machine will not strike the Containment Building.
- Access corridors run the length of the Turbine Building and continue in the Control Building and the Auxiliary Building to provide accessibility to all equipment.

A brief description of these features and of the various buildings is given in the following sections.

VI-B-2. Containment Building

VI-B-2-a. Function

The Containment Building houses the entire nuclear island and the blanket handling facilities. The building is designed to:

- Provide a protective barrier against leakage of radioactive material from the nuclear island to the environment under all postulated accident conditions.
- Contain internal pressure in the event the reactor helium coolant depressurizes into the containment and/or the liquid helium is discharged into the containment.
- Protect the reactor against missiles and detrimental environmental conditions.

In addition, the Containment Building must accomodate fuel injection equipment, plasma heating equipment, and primary coolant piping, and provide sufficient space for equipment handling and other maintenance operations.

VI-B-2-b. Equipment Location

Location of major equipment, piping and supporting structures within the Containment Building is shown on arrangement drawings VI-M-3, VI-M-4 and VI-M-5.

The major equipment items located within the building in addition to the reactor are: primary helium and lithium piping, fuel injection and plasma

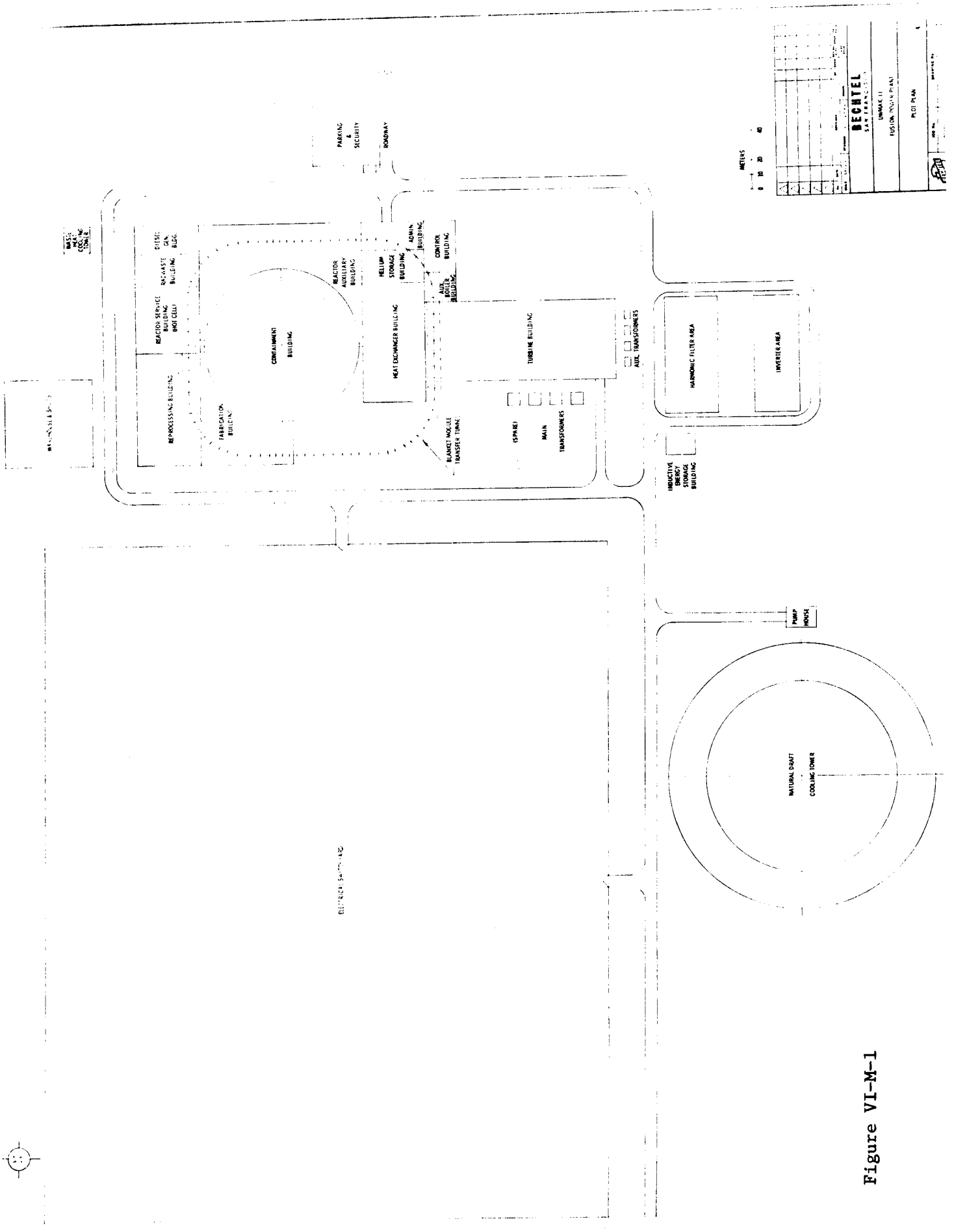
BECHTEL
SAN FRANCISCO
UWMAK II
FUSION POWER PLANT
PLOT PLAN
METERS
0 10 20 40
PARKING & SECURITY
ROADWAY
MASS WATER COOLING TOWER
DIESEL GEN. BLDG.
RADWASTE BUILDING
REACTOR SERVICE BUILDING
SHOT CELL
REACTOR AUXILIARY BUILDING
HELIUM STORAGE BUILDING
ADMIN BUILDING
CONTROL BUILDING
AUX. BOILER BUILDING
CONTAINMENT BUILDING
REPROCESSING BUILDING
FABRICATION BUILDING
HEAT EXCHANGER BUILDING
BLANKET MODULE TRANSFER TOWER
TURBINE BUILDING
(SPARE)
MAIN TRANSFORMERS
AUX. TRANSFORMERS
HARMONIC FILTER AREA
INVERTER AREA
INDUCTIVE ENERGY STORAGE BUILDING
PUMP HOUSE
NATURAL DRAFT COOLING TOWER

Figure VI-M-1

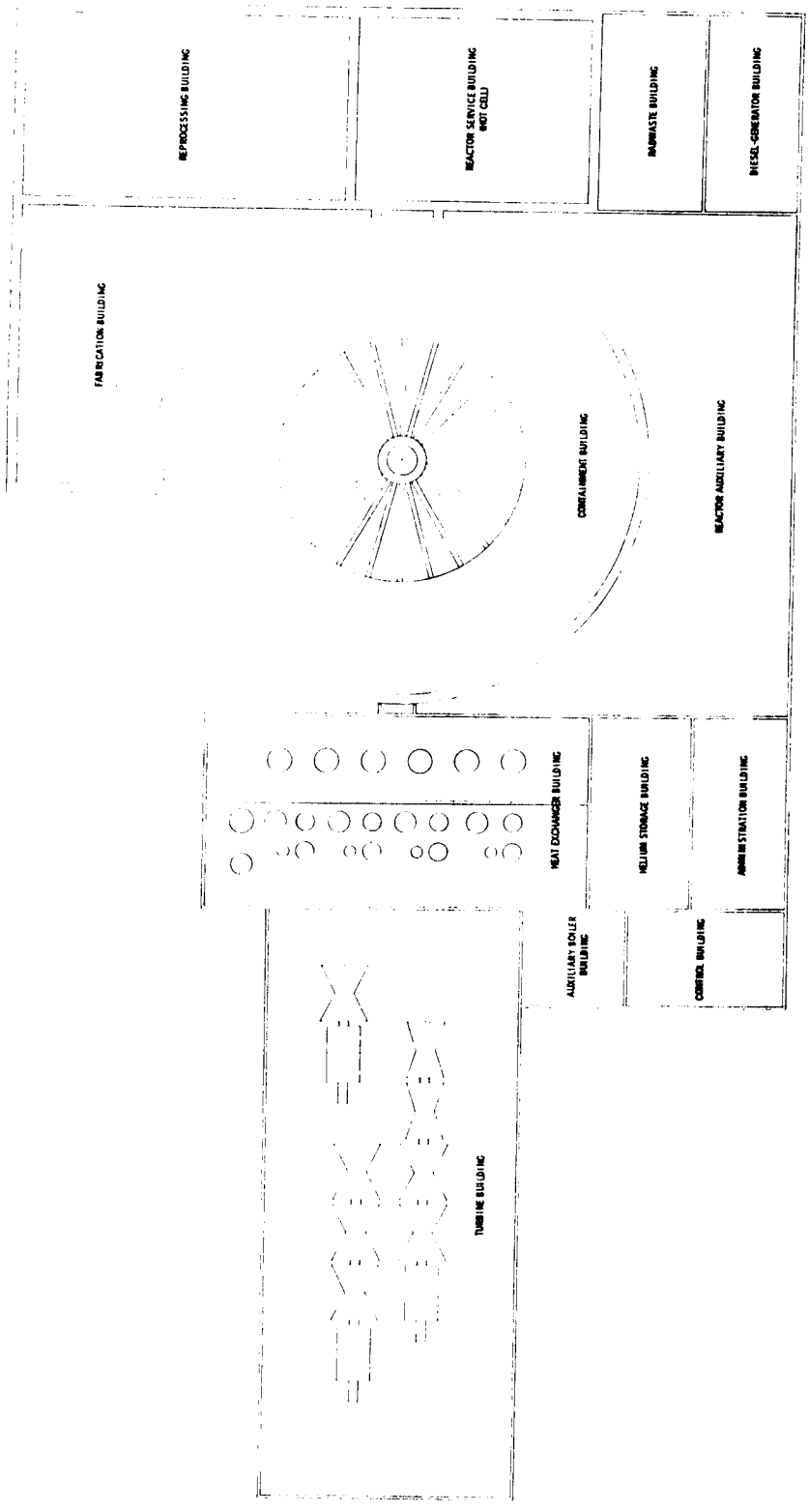
REPROCESSING BUILDING
REACTOR SERVICE BUILDING (HOT CELL)
RADWASTE BUILDING
DIESEL-GENERATOR BUILDING
FABRICATION BUILDING
CONTAINMENT BUILDING
REACTOR AUXILIARY BUILDING
HEAT EXCHANGER BUILDING
HELIUM STORAGE BUILDING
ADMINISTRATION BUILDING
AUXILIARY BOILER BUILDING
CONTROL BUILDING
TURBINE BUILDING
BECHTEL
METERS

Figure VI-M-2

heating equipment, and heating and ventilation equipment and the machines for handling the blanket sections.

The main primary system piping for carrying coolant from the blanket, divertor and shield to the intermediate heat exchanges (IHX) and back are shown in two plan and one elevation views in Drawings VI-M-3, VI-M-4, and VI-M-5. The helium from the blanket outlet headers is fed through risers to the hot leg ring header above the reactor. To conserve material, the ring header has two different sized sections. A common duct transports the helium from the ring header to the four helium-to-sodium IHX's in the Heat Exchanger Building. The cold helium from the IHX's is carried back by another common duct to the cold leg ring header (which has two different sized sections also) from where it is fed to the blanket sections by 24 risers. The cold leg headers are located below the floor slab.

The piping is insulated on the inside using silica insulation and on the outside using conventional insulation. The purpose of the internal insulation is to maintain the piping at low temperature to permit selection of more economical material. Expansion joints are used to accomodate the thermal expansion of pipes and reduce thermal stresses.

The hot lithium from the divertor is pumped to the hot leg ring header. A common pipe then transports it from the ring header to the lithium-to-sodium IHX. The cold lithium from the IHX flows to the cold leg ring header and then back to the divertor. A similar arrangement is used for the shield coolant (helium) flow path. The hot helium from the shield flows to the hot leg ring header and a common duct conveys it to the helium-to-water IHX. The cold helium from the IHX is pumped to the cold leg ring header and then back to the shield.

A steel support structure is located on the inside surface of the containment dome. All the hot leg piping is supported from this structure which also carries ventilation ducts and electrical cable trays. The structure serves as a support for the pipe whip restraints required for high-energy piping systems.

IV-B-2-c. Equipment Handling

Space is provided within the Containment Building to carry out a number of equipment handling operations. The removal of blanket sections is expected to be a major operation and a special machine capable of reaching and handling all the 96 blanket sections is needed. A conceptual sketch of this special Blanket Handling Machine is depicted in Drawing VI-M-5. Two such machines are used (to reduce the reactor downtime) - one for removing the irradiated sections and the other for installing the rebuilt sections.

The handling machines travel on a circular track installed on the Containment Building floor. The circular track runs in an annular region between the reactor and the Containment Building wall. Radial tracks between the toroidal magnets enable the machines to travel into the reactor and reach the blanket sections. The irradiated (or spent) sections are removed and transferred to the Hot Cell through an equipment hatch. The rebuilt sections are brought from the Fabrication Building through another equipment hatch.

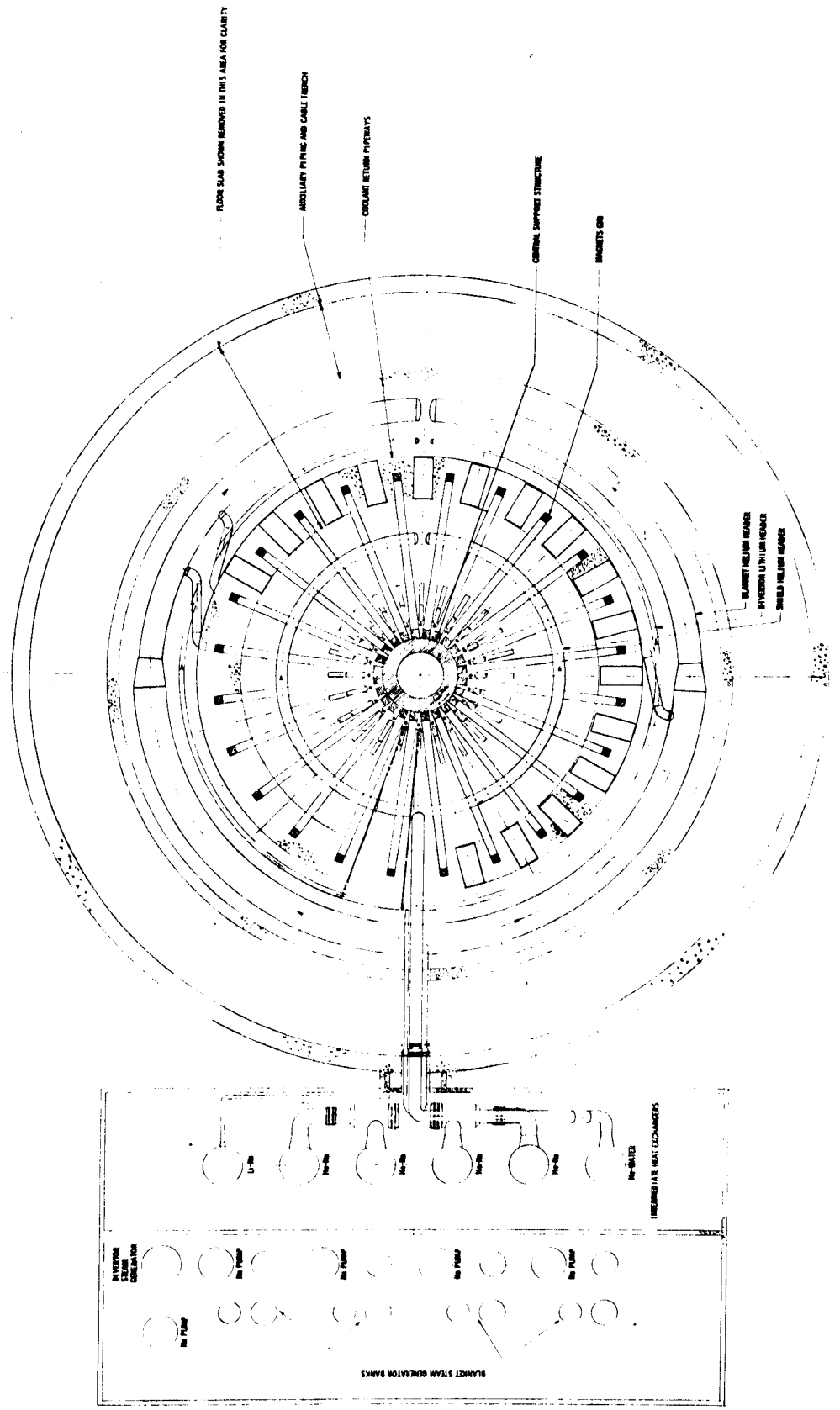
FLOOR SLAB SHOWN REMOVED IN THIS AREA FOR CLARITY
AUXILIARY PIPING AND CABLE TRENCH
COOLANT RETURN PIPEWAYS
CENTRAL SUPPORT STRUCTURE
MAGNETS OMI
BLANKET MANIFOLD HEADER
DIVERTOR MANIFOLD HEADER
SHIELD MANIFOLD HEADER
BLANKET STEAM GENERATOR BANKS
DIVERTOR STEAM GENERATOR
No PUMP
No-WATER
INTERMEDIATE HEAT EXCHANGERS
N

Figure VI-M-3

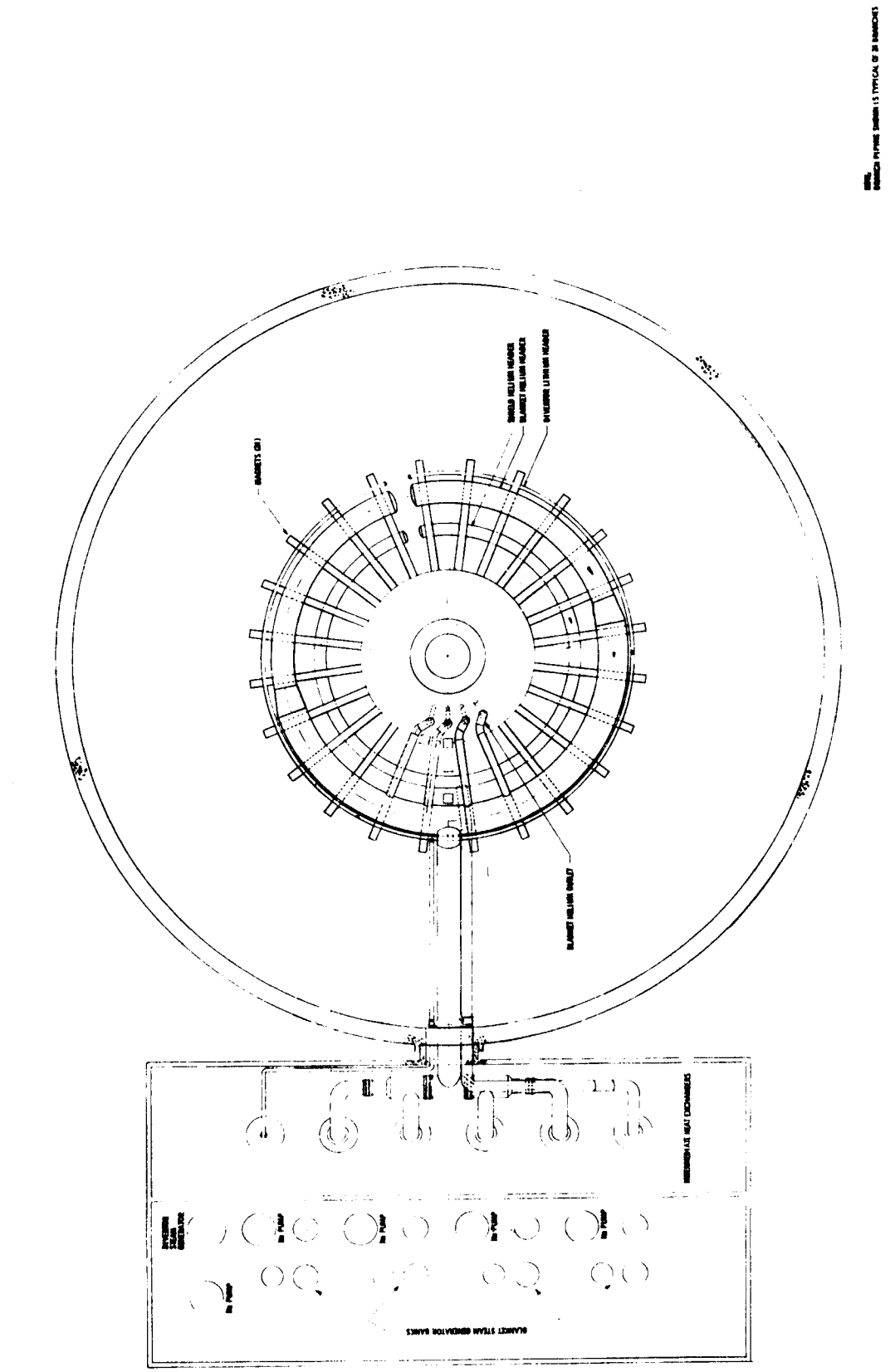

Figure VI-M-4

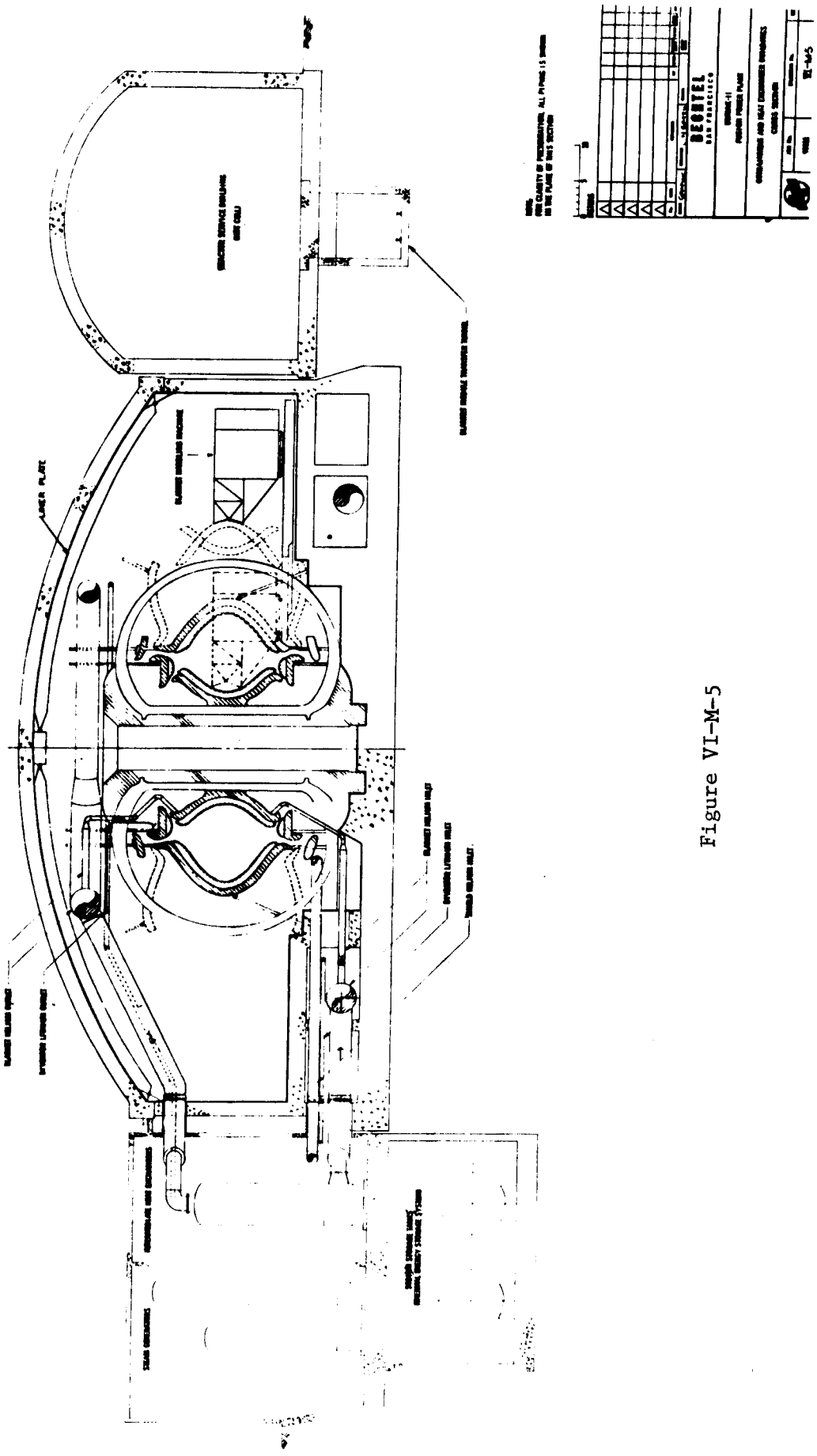

Figure VI-M-5

The handling machines are also intended to be used to handle all other heavy pieces of equipment within the Containment Building as well as in the Hot Cell.

VI-B-2-d. Penetrations

A large number of pipes and electrical and instrumentation cables must penetrate the containment wall. Most of these penetrations are through the wall of the Containment Building into the Reactor Auxiliary Building. Separate penetration zones are needed to separate mechanical (piping) penetrations from electrical penetrations. The helium and lithium piping penetrations are located on the wall of the Containment Building adjacent to the Heat Exchanger Building. There are no electrical penetrations on this wall.

Personnel access to the Containment Building is through a personnel airlock located in the Reactor Auxiliary Building. A large equipment hatch between the Containment Building and the Reactor Auxiliary Building is used for transfer of fuel handling, plasma heating and other large equipment. The Containment Building is inaccessible during reactor operation.

VI-B-3. Reactor Service Building (Hot Cell)

The Reactor Service Building or the Hot Cell is located adjacent to the Containment Building. The functions of the building are to receive the spent blanket sections and remove the front wall from these sections. An overhead crane is provided to handle the blanket sections. This crane receives the sections from the handling machine which can enter the Hot Cell to deliver the blanket sections. During normal operation, the machine is used in the Hot Cell. Once the front wall is removed, the Overhead Crane in the Hot Cell transfers the blanket sections to the underground railroad cars. The railroad cars carry the blanket sections to the Fabrication Building for rebuilding the front wall on these sections. The spent front wall removed in the Hot Cell is then transferred to the Reprocessing Building for the recovery of tritium and beryllium.

The Hot Cell also can be used for maintenance work on other equipment such as the blanket handling machines and other radioactive or contaminated components.

The equipment needed in the Hot Cell is not yet defined. Additional studies are needed to determine this before a conceptual design of the Hot Cell can be prepared.

VI-B-4. Reactor Auxiliary Building

The auxiliary building is wrapped around the east side of the Containment Building and contains the equipment that must be located close to the reactor. The location of the building relative to the Containment Building is shown in the Drawing VI-M-6. It contains the majority of the cryogenic equipment, equipment for tritium extraction from helium and lithium, lithium and helium clean-up systems equipment, blanket tritium recovery equipment, etc.

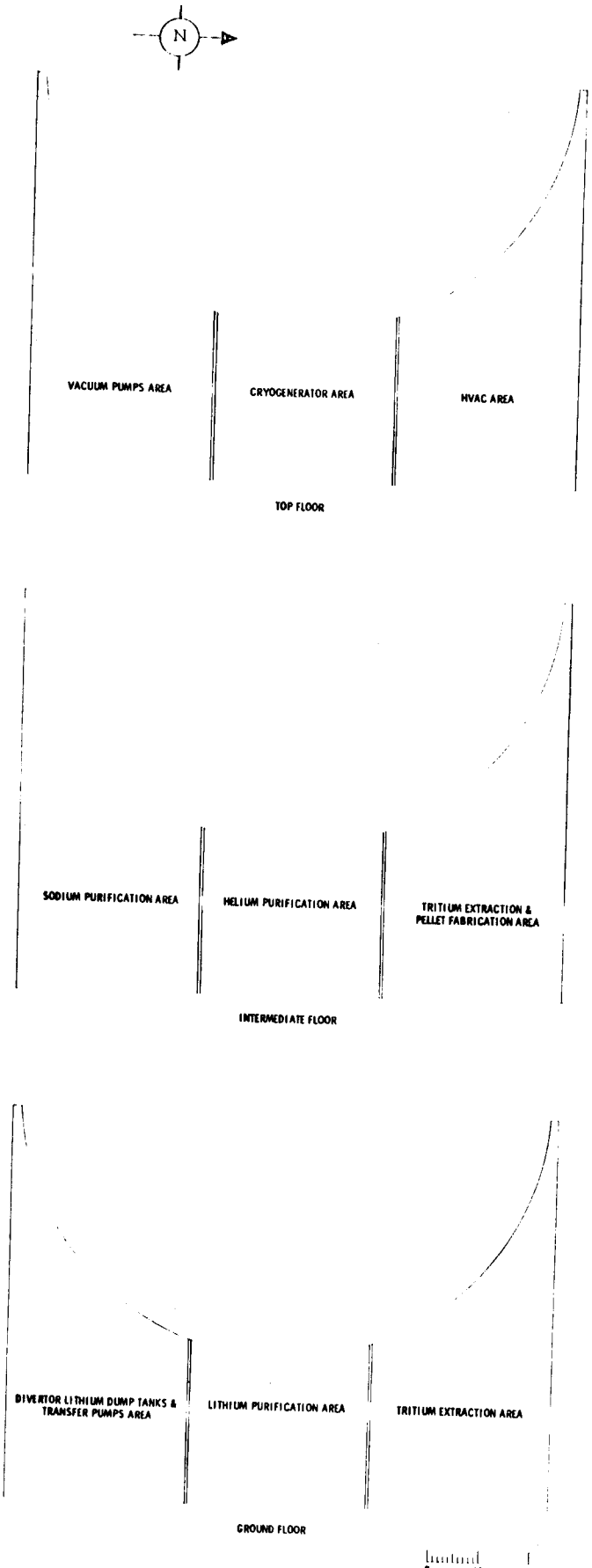
N
VACUUM PUMPS AREA
CRYOGENERATOR AREA
HVAC AREA
TOP FLOOR
SODIUM PURIFICATION AREA
HELIUM PURIFICATION AREA
TRITIUM EXTRACTION & PELLET FABRICATION AREA
INTERMEDIATE FLOOR
DIVERTOR LITHIUM DUMP TANKS & TRANSFER PUMPS AREA
LITHIUM PURIFICATION AREA
TRITIUM EXTRACTION AREA
GROUND FLOOR
0
10
20
METERS

Figure VI-M-6

A separate floor is provided to locate the equipment for the containment clean-up system and for the fans, blowers, chillers, filters, and associated equipment required for the heating, ventilating and air conditioning (HVAC) systems of the Auxiliary Building.

Other equipment necessary for proper functioning of the plant is located in this building. A data acquisition instrument room is also provided.

The requirements for the equipment to be located in this building have not been established. As a result, only approximate areas for various equipment are indicated on Drawing VI-M-6.

VI-B-5. Heat Exchanger Building

The building contains the following heat exchanger, thermal energy storage components and the associated equipment:

- Helium to sodium heat exchangers (IHX) for the blanket cooling system.
- Lithium to sodium heat exchanger (IHX) for the divertor cooling system.
- Helium to water heat exchanger (IHX) for the shield cooling system.
- Steam generators for the divertor cooling system.
- Hot and cold sodium storage tanks for thermal energy storage system.

Drawings VI-M-3, VI-M-4, and VI-M-5 show the arrangement of this building.

The Heat Exchanger Building is divided into two separate areas: intermediate heat exchanger (IHX) area and steam generator area. The IHX area is connected to the Containment Building through a penetration zone through which all the primary helium and lithium piping pass. Separation of the IHX area from the steam generator area provides containment and a protective barrier against leakage of radioactive material from the primary system under accident conditions (helium or lithium pipe break) and protection from tornados and missiles.

The hot helium duct enters the IHX area and then branches out to supply the four IHX's (for the blanket cooling system) as shown in Drawings VI-M-3, VI-M-4 and VI-M-5. Hot helium enters near the top and cold helium leaves through the bottom of the IHX and enters the helium circulators which are built integral to the heat exchangers. After leaving the circulators, the four cold helium lines join the common return duct which then enters the Containment Building to join the ring header.

The shield coolant duct enters the IHX area and connects to the shield IHX at the top. The cold helium header leaves the circulator (located at the bottom of the IHX) and enters the Containment Building to connect to the distribution ring header. The arrangement for the lithium piping is similar. However, the lithium circulation pump is in the lithium hot leg and is located near the divertor.

The steam generator area of the Heat Exchanger Building contains all the steam generator modules for the blanket and the divertor energy conversion cycles. Space is provided for location of all associated piping and instrumentation. The hot and cold sodium storage tanks for thermal energy storage are located on a floor below the heat exchanger floor (see Drawing VI-M-5). (The thermal storage system is described in Chapter V.) Only superficial consideration has been given to the design of this building; detailed analysis and study are needed to develop the design further.

VI-B-6. Turbine Building

The Turbine Building houses the turbine generators and the associated energy conversion equipment. Communication corridors run the length of the building at various levels. These corridors provide access to equipment for operation and maintenance and serve as major accessways to convey the control cable trays to the central control room and piping to other areas of the plant.

An overhead crane is provided for equipment handling and to permit disassembly of the turbine-generator for maintenance. Equipment hatches allow access to the feed pumps and condensate pumps with the overhead crane. The crane capacity is determined by the weight of the generator rotor. A truck access and loading bay is provided. Access to the control room from the upper communication corridor is possible.

VI-B-7. Control Building

The Control Building contains a central control room, cable spreading rooms, switchgear, auxililary panels, and M-G sets. It also houses the heating, ventilating and air-conditioning equipment for the entire building. The building will be provided with an area from where all access to potentially radioactive areas of the plant is controlled. Facilities for monitoring levels of radioactivity, and showers and change facilities for controlling radioactive contamination are provided in this area. The following facilities are also located in the Control Building.

- Radiation Chemistry Lab
- Clean Chemistry Lab
- Counting Room
- Contamination Laundry
- Health Physics Office
- First Aid Facilities

The Control Building is located at a distance of 100 M away from the center of the Containment Building to minimize the effect of the magnetic field on the control instruments. The building structure serves as the magnetic barrier.

VI-B-8. Other Buildings and Facilities

Other buildings and facilities shown in the general arrangement drawings, VI-M-1 and VI-M-2, are described briefly in the following paragraphs.

VI-B-8-a. Reprocessing and Fabrication Buildings

These two buildings are wrapped around the west-south-west side of the Containment Building. The Reprocessing Building contains all the equipment for handling and recovering tritium and beryllium from the irradiated front wall which is separated from the spent blanket section in the Hot Cell. The function of the Fabrication Building is to receive the bare (without the front wall) blanket sections and to rebuild the front wall on these sections. The rebuilt blanket sections are then returned to the Blanket Module Transfer Tunnel (described later in this section) for storage. The type of equipment and nature of its operation together with the environment, shielding, and other requirements for these buildings are not yet determined; additional studies are needed to establish these.

VI-B-8-b. Radwaste Building

All equipment for processing solid, liquid and gaseous radioactive wastes are located in this building. Solid radwastes generated from the spent front walls are transferred to this building from the Reprocessing Building for processing and disposal.

VI-B-8-c. Blanket Module Transfer Tunnel

The Radwaste Building, the Hot Cell, the Reprocessing Building and the Fabrication Building are connected by an underground railroad tunnel surrounding the Containment Building. It serves to transport radioactive components, materials and wastes between these buildings, and to store spent and rebuilt blanket sections.

VI-B-8-d. Inductive Energy Storage Building

This building houses the superconducting solenoid magnets to store electrical energy for charging and discharging of divertor and transformer coils during the reactor burn cycle. The building is located more than 100 M away from the center of the Containment Building to minimize the effect of interactions of the magnetic fields generated by the inductive field coils and the toroidal field coils.

VI-B-8-e. Helium Storage Building

This building contains the cylinders used for storage of purified helium when the blanket and shield primary systems are depressurized. The cylinders are stacked in racks within this building. The building is designed to withstand the consequences of any potential cylinder failure. The helium purification equipment, transfer compressor and associated equipment are located in the Reactor Auxiliary Building.

VI-B-8-f. Administration Building

This is a two-storey office building located adjacent to the Control Building at the front (east) side of the plant. It contains offices, other administrative facilities, a lunchroom, and a locker room.

VI-B-8-g. Warehouse and Shop Building

A permanent warehouse and shop building is part of the plant supporting facilities. Depending on the services available in the vicinity of the plant site, it might contain, for example, an electrical shop, an instrument shop, a dismantling room, a tool room, and welding area. Because of the special nature of many of the components of the plant (e.g., magnets, cryogenerators, vacuum pumps), some of the shops are likely to be more elaborate than those in fission plants.

VI-B-8-h. Diesel-Generator Building

This building houses the emergency diesel generators and their associated diesel oil storage tank, day tanks, and the exhaust silencers. In the event of an off-site power failure, they will automatically start and be up to speed and voltage and ready to assume load in about 10 seconds. The generators are self-cooled and are equipped with static excitation systems. Helium cryogenerators and vacuum pumps are the major essential loads that will require the bulk of on-site diesel power. The building design provides for protection of the diesel-generator equipment from tornados and missiles.

VI-C. Civil/Structural

VI-C-1. General

Conceptual civil/structural design was performed for major structures of the plant to determine their technical feasibility and to provide information required for the conceptual cost estimate. Emphasis has been placed on the Reactor Containment Building which is significantly larger than for fission power plants. The design criteria are the following:

- Plant Location - The plant is assumed to be located in the State of Wisconsin.

- Seismic Load - The seismic activity in the State of Wisconsin is low. The plant buildings and structures are designed according to AEC Regulatory Guide 1.60 and the Uniform Building Code (UBC), as appropriate.

- Wind Load - The State of Wisconsin is located in an area designated as Zone I in the AEC Regulatory Guide 1.76 titled "Design Basis Tornado for Nuclear Power Plants". In Zone I tornados with maximum wind speed of 360 mph could occur.

. Snow Load - During winter, the State is subjected to heavy snow fall. Snow loading (live load) of 185 kgf/m^2 (40 psf) has been adopted (as per UBC).

. Soil Condition - The soil in the area is composed of dense sandy-silt laminated with silty-sand. The allowable soil bearing pressure of 48.8 tons/m^2 (5 ton (U.S.)/ft^2) has been assumed (based on information supplied by the University of Wisconsin).

VI-C-2. Plant Structure

The major structural design effort has been devoted to the Reactor Containment Building. Less detailed consideration has been given to the Reactor Service (Hot Cell) Building and the Heat Exchanger Building. These buildings, however, are also of major concern, but the scope of this study limited the design effort on these structures.

VI-C-2-a. Reactor Containment Building

The Reactor Containment Building is a fully reinforced, concrete structure consisting of a base mat foundation, a cylindrical wall and a spherical dome. The cross section view of this building is shown on Drawing VI-M-5.

The spherical dome has an inside radius of 84M (276 ft) and a rise of 16 M (53 ft) above the spring line (interface with the cylinder wall). The thickness of the dome and wall is 185 cm (6 ft) and is based on shielding requirements as determined by the University of Wisconsin. The central angle subtended by this dome is 73.50 deg. The ratio of thickness to radius (h/r) for the dome is 1/42, thus requiring an analysis based on non-shallow thin-shell theory. The theoretical buckling load for this shell was found to be larger than the combined loading (dead load + live load), thus no buckling will occur. The reinforced concrete edge (ring) beam is 350 cm (11 ft) deep by 250 cm (8 ft) wide.

The dome is a composite structure made up of 12 three-hinged arches, the containment liner and the concrete shielding. The arches are box girders fabricated from steel plates. The midpoint hinge for the arches is provided by a central ring at the crown to which the individual half segments of the arches are attached. The use of a ring avoids congestion at the crown. The cylindrical wall of the Reactor Containment Building acts as a buttress for the arches.

The containment liner plate is laid on top of the arches and the concrete shielding is poured over the liner. Thus, the arches support the wet concrete during the construction and using the containment liner as part of the formwork minimizes the forming required for the concrete.

The hangers for the primary piping and the magnet coil supports are attached to the arches. For leak tightness, the building containment liner is a stiffened 6.5 mm (1/4 in) thick plate. An indicated above, this liner plate serves also as a formwork while the containment concrete is being poured.

The cylinder wall is 185 cm (6 ft) thick, has an inside diameter of 100 M (328 ft) and rises 29 M (95 ft) above the base mat.

The wall is tapered (between the floor slab and the base mat) to a thickness of 300 cm (10 ft) at the base to carry the large bending moment if the containment should ever be pressurized as a result of an accident (15 psig internal pressure is assumed based on the information supplied by the University of Wisconsin). There are penetrations in the containment wall to permit transfer of radioactive materials into the adjacent Fabrication and Reactor Service (Hot Cell) buildings and for pipes leading to the Heat Exchanger Building.

The Building foundation is a reinforced concrete mat 500 cm (16 ft - 5 in) thick, which is needed to support the building and the equipment. Two concentric ducts above the base mat carry piping to and from the Heat Exchanger Building. The top slab of these rectangular ducts is the operating floor of the Reactor Containment Building. The cylinder wall and the dome are constructed of 352 kgf/cm^2 (5000 psi) concrete and reinforced with reinforcing bars. The base mat consists of 457 kgf/cm^2 (6500 psi) concrete, reinforced with several layers of rebars and is sized to accomodate all loads without exceeding the allowable pressure on soil.

Only preliminary consideration could be given to the actions of lateral forces (wind and seismic forces) on the structure. These indicate that the structure would be able to withstand their actions without loss of stability.

VI-C-2-b. The Reactor Service (Hot Cell) Building

The Reactor Service (Hot Cell) Building contains radioactive material from the reactor. The building, shown in Drawing VI-M-5, is 50 M (164 ft) in length by 40 M (131 ft) in width by 24 M (79 ft) in height to the springline elevation (interface with the shell roof).

The roof of the building is a shell of radius 25 M (82 ft) so that the ratio of its radius to length is half. Its rise to the inside is 6.5 M (21 ft - 6 in). The walls and the roof are of 185 cm (6 ft) thick reinforced concrete construction (determined by the University of Wisconsin on the basis of shielding requirements). There are two intermediate stiffening arches between the end diaphragms of the shell. The longitudinal walls, in addition to carrying weight from the shell, act as buttresses for the shell and the arches. An overhead bridge crane serves the entire building and is mounted on brackets attached to the walls.

The foundation of the building is 2 M (6 ft 8 in) thick reinforced concrete mat resting on sound soil.

VI-C-2-c. The Heat Exchanger Building

The superstructure of this building, as may be seen in Drawing VI-M-5, consists of two separate areas - one for the intermediate heat exchangers and the associated equipment, and the other for the steam generators and the thermal energy storage system equipment. The substructure of the building houses the hot and cold sodium storage tanks and the associated equipment for the thermal

energy storage system. The IHX's and the associated equipment are located in a separate compartment to provide protection from missiles and tornados and to provide containment for helium gas and lithium in case of accidental release into the Heat Exchanger Building. The superstructure of the building is 80 M (262 ft) long, 40 M (131 ft) wide and 33 M (108 ft) high.

The IHX area of the superstructure is of reinforced concrete construction, and the walls of the roof are 61 cm (2 ft) thick. The roof is supported on transverse beams spaced 5 M (16 ft - 6 in) apart. For leak tightness, the building is lined with a stiffened 6.5 mm (1.4 in) thick liner plate.

The steam generator area of the superstructure is a steel framed structure with trusses supporting the roof. The roofing is of built-up material on metal decking and sides are of insulated metal siding. The floor is a 50 cm (1 ft - 8 in) thick reinforced concrete slab spanning between transverse beams spaced 5 M (16 ft - 6 in) apart. Two longitudinal beams, 13 M (42 ft - 8 in) apart carry the load from the transverse beams. Columns are located 10 M (32 ft - 10 in) apart and transfer the loads from the longitudinal beams to the base mat.

The substructure is 20 M (66 ft) deep. The walls are of reinforced concrete counterfort-type retaining walls. These are 150 cm (5 ft) thick and are spaced at 3 M (10 ft). The base slab is 250 cm (8 ft) thick and rests on sound soil.

VI-D. Conclusions

The present study is an initial assessment of the problems associated with the plant design for tokamak-type reactor plants in general and the UWMAK-II reactor plant in particular. The design and analyses are relatively superficial and conceptual in nature. Many of the systems and associated equipment are not defined in detail and some of them probably have not yet been identified. Allowances have been made to accomodate these unknowns and uncertainties; but until further design and analysis is done, these uncertainties remain. On the basis of the present study. the following comments are in order.

- The plant layout including equipment and piping arrangement is preliminary. Further study is needed to detail and improve the arrangements. The primary piping arrangement is a critical aspect of the plant layout and can have a large impact on building costs. No consideration has been given to the arrangement of the reactor internal piping or its interface with the external primary piping systems.

- Use of large size piping for transporting high temperature helium gas may be of some concern. Internally insulated piping has been proposed; however, no stress analysis has been performed to substantiate the piping arrangement. Expansion joints are used to account for the large thermal expansions. Application of internal ceramic insulation and expansion joints is within the state-of-the-art; however, the feasibility of their use has to be investigated in this particular service.

- Reactor Maintenance problems, especially in regard to blanket removal, constitute another area where only preliminary consideration could be given. A conceptual blanket handling concept has been proposed, but studies are needed to evaluate the feasibility of the concept and

develop procedures and conceptual equipment designs. The problem of radioactive contamination of the plant and equipment has not been looked at and must be given a serious consideration.

- Analysis of the effects of magnetic fields (generated by toroidal field coils) on plant equipment and components is necessary. As a result, it may be necessary to consider relocation of some of the buildings and equipment. To avoid interference with the magnetic field, non-magnetic materials are needed for helium piping and the containment liner.

- The equipment requirements for the Hot Cell, Reprocessing Building and Fabrication Building have not been defined. Concepts for handling the blanket sections, disassembling and processing the irradiated front wall and fabrication and reassembling the new front wall must be developed. The building sizes and arrangements shown are preliminary and may change considerably after detail engineering is undertaken.

- The underground circular railroad arrangment shown for handling and storing spent and rebuilt blanket section is conceptual in nature. A careful study is needed to establish the feasibility of the concept and to study the trade-offs with other possible concepts.

- Details have to be worked out to determine an acceptable method of storing solid radioactive wastes. Several alternatives are possible such as: on-site storage versus burried vaults, air-cooled versus forced convection systems.

- The structures in this plant are significantly larger than those in fission power plants. All the structures are very massive because of shielding and other safety requirements. The conceptual design, as described, is considered to be a feasible design consistent with current technology and industry practice. However, some aspects of the design/analysis of the structures have to be investigated further before a method for their design can be established.

- In the Reactor Containment Building, the tie-rods which extend up to the dome preclude the use of overhead cranes for material handling. Special vehicles, possibly running on tracks, have to be built for this purpose, which will subject the floor slab to moving dynamic loads. A thorough analysis of the floor slab, subjected to moving loads, is needed.

- The dome has been analyzed on the assumption that its thickness is uniform throughout. The domes are usually thickened near the edges. This necessitates a finite element analysis to study the propogation of edge disturbances into the dome. Also, the dome and the metal arch ribs will act together to support the loading. An analytical procedure has to be developed to take this composite action into account to evaluate the strength of the dome.

. The phenomenon of instability of the dome and the cylinder has been studied on the basis of classical linear theory. However, it is also known that, due to imperfections and boundary conditions different from those used in linear theory, the buckling load of shells are significantly lower than those given by the classical theory. An estimate of this lower buckling load should be obtained by non-linear analysis in conjunction with realistic boundary conditions. At springline level, the arches will exert considerable thrust producing radial expansion of the cylinder. It is, therefore, necessary to evaluate the interactions between the arches, the dome and the cylinder.

. The long, narrow penetrations on the cylinder wall leading to the adjacent buildings requires thorough investigation. A "closed-form" solution (which could be used for designing the penetration) for this problem does not exist in literature. It is, therefore, necessary to investigate the effect of this opening in a pressurized shell by using finite element methods.

VII-A. Materials Resource Assessment for UWMAK-II

One of the main characteristics of circular, low β Tokamaks is that the plasma effectively uses about 5-10% of the available magnetic field energy, i.e. β total ~0.05-0.1. This implies a relatively low power density in the plasma, ~1 W/cc. An added difficulty is the relatively thick blanket and shield required to extract the kinetic energy from the 14 MeV neutrons and to shield equipment and personnel from the high radiation fields in a CTR. It follows that such a device will occupy a substantial volume if it is to produce 1000-2000 MW_e and this fundamentally explains the large size of the UWMAK reactor designs. Given this, an important problem is to ascertain the resource requirements posed by such devices and to compare these requirements with present estimates of materials reserves and resources.

Estimates of the materials requirements for UWMAK-II have been compiled, to establish the input information for the resource study. These are described in the next section. The section following this contains the results of the resource assessment. Estimates have been made of materials availability both inside and outside the United States, and at present prices, three times present prices, and ten times present prices. These estimates are then matched against the requirements of a $10^6 MW_e$ economy of UWMAK-II type reactors.

VII-A-1. Materials Requirements of UWMAK-II

The materials requirements of UWMAK-II have been divided into two major categories, the nuclear island and the balance of plant. The nuclear island is defined as all systems within the toroidal field coils plus the central support core and the transformer coils. Thus, He coolant piping from the reactor to the primary heat exchanger is part of the balance of plant whereas the headers feeding the blanket and the blanket itself are part of the nuclear island. The balance of plant includes everything else outside the toroidal field coils, including the primary containment structure around the reactor and the primary heat exchanger.

The materials requirements for the nuclear island are summarized in Table VII-A-1. These figures are based on a 30 year plant life and the estimates include the added requirements imposed by blanket replacement every two years. The composition used for the stainless steels to obtain these numbers are:

	Wt.%	
	316 SS	304 SS
Fe	62	66
Cr	18	20
Ni	14	12
Mn	2	2
Mo	2	-
Al	1	-
Cu	1	-

The largest requirements (greater than 10,000 metric tonnes (MT)) are for Fe, Pb, and Cu. Materials requirements that fall between 10^3 and 10^4 MT range include Al, B, C, Cr, and Ni. Of these, Cr will be a particular concern, as is discussed in the next section.

Table VII-A-1

Materials Requirements - UWMAK-II Nuclear Island

(Metric Tonnes)

ELE.	Initial Struc.[a]	1st Wall Sec. Replacement (14 Times)[b]	Canning[c] (14 Times)	Reflec. & Header Replac. (2 Times)	Blanket & Shield Support	Shield Structure	T.F. Magnets and Dewars	T.F. Magnet Bracing[d]	Ver. Field Coils	Ver. Field Coil Support[d]	Vacuum Pumps (d)	Storage	Total (MT)	MTonnes MWe (1710 MWe)	ELE.
Al	184	112	2338	44	-	44	193	1693	2	-	-	-	4766	2.79	Al
B	-	-	-	-	-	4280	-	-	-	-	-	-	4280	2.50	B
C	1307			2376	-	1207							4890	2.86	C
Cr	692	2011	1726	797	52	800	1818	514	48	58	9	-	8525	4.98	Cr
Fe	2385	6929	5940	2746	172	2754	6233	1683	167	191	29		29229	17.1	Fe
Mn	77	223	192	88	5	89	199	51	6	6	1		937	.55	Mn
Mo	77	223	192	88	5	89	179	51	6	6	1		917	0.54	Mo
Ni	538	1564	1344	620	31	622	1378	306	37	35	5		6480	3.78	Ni
Si							1	11					12	0.007	Si
Pb						19800							19800	11.6	Pb
Nb							119		26				145	0.085	Nb
Ti							62	18	13				75	0.054	Ti
Cu	38	112	96	44	3	44	8889	22	1444				10692	6.94	Cu
He	4					1	20		19			25	69	0.04	He
Li	50[e]+300[f]		630										980	0.57	Li
Be	433	552[g]											985	0.58	Be
Total Weight (MT)		11726	12554	6803	268	29730	19091	4353	1768	296	45	25	92782	54.3	

(a) 24 regular modules plus 2 spare blanket modules
(b) First 27 cm only
(c) Canning is the 316 SS needed to contain the breeding and neutron multiplying material as well as the graphite.
(d) 304 SS, includes central support structure
(e) 50 MT is the Li Inventory in the Blanket-This Li is enriched to 90% Li-6 and then requires 12 times this amount in natural Li.
(f) 300 MT is the Li Inventory in the particle collection stream of the divertor
(g) One additional loading plus makeup for burnup and reprocessing losses

The lithium requirements are 980 MT or 0.57 MT/MW_e. This is reduced by a factor of 2 compared with UWMAK-I, which was cooled with liquid Li, because a solid breeder concept is used in the UWMAK-II blanket design. However, this number could be reduced further if liquid lithium is not used as the particle collection material in the divertor. The lithium required for breeding in the blanket only amounts to ~50 MT or 0.03 MT/MW_e. But the lithium is enriched to 90% Li-6, which means that 600 MT has to be mined to provide it. Similarly, the 630 MT needed for replacement will require 7560 MT of natural lithium mined from the earth.

The other major material requirement for a solid breeder blanket using lithium aluminate is for beryllium. The Be requirements are 0.58 MT/MW_e or 985 MT for a 30 year plant life. This is a very large requirement and exceeds resource estimates for a 10^6 MW_e economy as is also discussed in detail in the next section.

The materials requirements for the balance of plant are listed in Table VII-A-2. By far the largest requirement is for Fe, 79000 MT or 46 MT/MW_e, although substantial amounts of Cr and Ni are also required.

The Nb, Ti, and Cu requirements are 7.5 MT, 23 MT, and 659 MT respectively. A reasonable fraction of the requirements are associated with the energy storage unit.

Finally, we note that the He requirement for the nuclear island and balance of plant amount to ~91 MT or 0.053 MT/MW_e. Of this, 79 MT of He is required for use at cryogenic temperatures in the superconducting TF, VF, and OH coils in the nuclear island and in the superconducting magnetic energy storage unit. The amount of He used as the blanket and shield coolant is approximately 11.8 MT which is 13% of the He requirements of the plant. 11.8 MT amounts to 5725 standard ft^3/MW_e.

VII-A-1-a. Nuclear Island Requirements

Table VII-A-1 gives the elemental material requirement for the UWMAK-II nuclear island. The table includes all the liquid helium in the plant although some of it may be external to the nuclear island as defined. However, only the gaseous helium contained within the blanket is included. Separate considerations will be given to the balance of plant.

It must be noted that the initial structure in the first wall includes 24 regular modules plus two spares. Thereafter, each replacement will consist of all 24 regular first wall modules, always keeping two spares in reserve for emergency use. On a regular schedule, six first wall modules will be replaced every six months, giving a two year turn around for the first 27 cm of the blanket. The figures in Table VII-A-1 allow for 14 replacements of the first wall over a projected 30 year plant life. Because radiation damage to the reflector and header area will be substantially reduced, they will be replaced every 10 years, or three times during the plant lifetime.

An important fact to note is that the amount of structure needed for blanket replacement in UWMAK-II is about 7% greater than in UWMAK-I if the reflector and header zones are included. If, however, these zones were excluded, then the increase in steel for UWMAK-II is a factor of 3 larger.

This is mainly due to the higher coolant pressure in UWMAK-II and to the large amount of steel needed for canning the solid breeder material, amounting to 45% of the steel in the first wall. Another reason is the fact that UWMAK-I has a stainless steel reflector.

The initial amount of stainless steel in the UWMAK-II blanket is 3,845 metric tonnes. Over the next 30 years, an additional 25,100 tonnes will be needed. This figure includes 4,427 tonnes needed for two replacements of the vertical structure and header zones.

The shield in UWMAK-II weighs a total of 29,730 tonnes, of which 4,433 tonnes is stainless steel, 5,487 is B_4C and 19,800 is lead. The blanket and shield support structure will require an additional 268 tonnes of 304 SS.

The toroidal and vertical field magnets require 8040 tonnes of stainless steel for structure and 1042 tonnes for dewars. These figures include materials for two spare toroidal magnets. Other materials needed are 200 tonnes of aluminum alloy bolts, 10,333 tonnes of Cu stabilizer, 220 tones of superconductor and 39 tonnes of liquid helium. An additional 25 tonnes of liquid helium is in storage and there is 4 tonnes of gaseous helium in the blanket and headers.

Finally, the values given under toroidal field magnet bracing include 1715 tonnes of aluminum for lateral support between magnets and 2550 tonnes of 304 SS for the central support structure. The vertical field coil supports require 296 tonnes of stainless steel and the vacuum pumps another 45 tonnes.

The total mass of material required for the UWMAK-II nuclear island over a 30 year life is 92,782 tonnes, made up of 50.2% stainless steel, 21.3% lead, 11.5% copper, 5.9% B_4C, 4% graphite, 3.4% $LiAlO_3$, 2% aluminum, 1% beryllium, 0.24% NbTi and 0.7% helium. During the anticipated lifetime of the reactor, the blanket will account for 40% of the total weight of the nuclear island, the shield for 32% and the magnets for 27.5%.

The last column gives the amount of elemental material required per MWe. The dominating elements are iron (17.1), lead (11.6) copper (6.24), chromium (4.98) and nickel (3.78) where the units are tonnes/MWe.

VII-A-1b. Balance of Plant Requirements

Two important differences can be noted immediately between the balance of plant materials in UWMAK-I and UWMAK-II. The first is that UWMAK-I has fourteen complete coolant loops while UWMAK-II has only six, consisting of four regular loops, one divertor loop and one spare. The second difference is that UWMAK-I needed 15 MWh of energy storage to drive the vertical field coils whereas UWMAK-II requries only 1 MWh. As will be evident, these two points will account for a substantial difference in the total amount of materials used.

Table VII-A-2 lists the elemental materials used in the balance of plant as completely as possible. Wherever appropriate, the values quoted in UWMAK-I were used because of identical situations between the two systems.

Table VII-A-2

UWMAK-II Balance of Plant Materials Requirements

(Metric Tonnes)

Element	Heat Exchanger			Piping			Thermal Flywheel (Na Tanks) (e)	Dump Tanks (Na) (e)	Pumps (Na) (e)	Building Liner (e)	Reinforcing Rods & Structure (g)	Turbine Generator Unit (h)	Energy Storage Unit	Misc.	Total (MT)	MTonnes / MW_e (1710 MW_e)	Element
	He-Na (a)	Na-Steam (b)	Regenerative (321) (c)	He (316) (d)	Na (304) (f)	Steam (321) (c)											
Al	1			19											20	.012	Al
Cr	135	278	8	349	184	30	938	712	540	320		30	81		3605	2.11	Cr
Fe	402	1584	27	1204	607	107	3095	2347	1783	1056	63479	2567	269		78527	45.92	Fe
Mn	7	28	1	39	18	3	94	71	54	32			8		355	.208	Mn
Mo	46	7		39											92	.054	Mo
Ni	310	152	5	271	110	18	563	427	324	192		59	49		2480	1.45	Ni
Na														9816(i)	9816	5.74	Na
Cu				19								295	362		676	.395	Cu
Nb													7.5		7.5	.004	Nb
Ti	19	6	0.2			1							4		7.5	.018	Ti
He	1			5.8									15		21.8	.013	He
Y													2.9(j)		2.9	.0017	Y
Zr													100(k)		100	.058	Zr
Concrete (m^3)											340000 m^3				340000 m^3	199 m^3 / MW_e	

(a) Shell 316 SS Tubes Incoloy 800 (4 regular, 1 spare, 1 divertor)
(b) Croloy 2 1/4 Cr. 1 Mo, and 321 SS (4 regular, 1 spare, 1 divertor)
(c) 321 SS (14 regular + 1 spare)
(d) 316 SS
(e) 304 SS
(f) 321 SS
(g) Low carbon steel
(h) Low alloy steel 21% Ni, 1% Cr and Cu
(i) Secondary loop
(j) Tritium extraction bed for divertor loop
(k) Liquid Na cleanup system

There are 5 (4 regular and 1 spare) He-Na heat exchangers which have a 316 SS shell and Incoloy-800 tubes. Another heat exchanger of similar construction is used in the divertor Li-Na loop.

There are 6 (4 regular, 1 divertor and 1 spare) steam generators which have shells made of 2 1/4 Cr 1 Mo alloy and tubes of 321 SS. The regenerative heat exchangers of which there are 15 (14 regular and 1 spare) are also of similar construction.

Under the piping column is included all fluid routing from the blanket to the steam turbine and back. These include the large supply and return helium manifolds located above the reactor. The helium pipes are 316 SS, the Na pipes are 304 SS and the steam pipes 321 SS.

In the thermal flywheel, dump tanks, pumps and building liner columns, all the components are 304 SS.

Reinforcing rod material which is a low carbon steel was estimated at 2% by volume of the concrete in the building. It is interesting to note that the 340,000 m^3 of concrete used, although exactly equal to the figure quoted in UWMAK-I, was independently arrived at by a different Architectural and Engineering firm.

The turbine generator units are made of a 2% Ni 1% Cr alloy with additional Cu in the generators. Materials for the energy storage unit[7] are an order of magnitude lower than in UWMAK-I. This produces a significant difference in the total balance of materials.

In the miscellaneous column is included 9816 tonnes of Na needed for the secondary loop. This is a factor of two down from UWMAK-I, primarily because of the smaller number of loops. Yttrium is still needed in the tritium extraction bed for the divertor loop, but is down to 2.9 tonnes, still a rather large quantity. Finally, 100 tonnes of Zr is needed in the liquid metal cleanup system.

The total amount of material in the balance of plant is 95,733 tonnes, about 3/4 of that in UWMAK-I. A summary of the requirements for the total plant is given in Table VII-A-3. The total amount of materials (with the exception of concrete) is 185,816 tonnes, which is 87% of UWMAK-I. The important points to note are the following:

1 - By far the dominating element is Fe at 63% of the total plant.

2 - The second most used elements are:

Pb	11.6%
Cu	6.65%
Na	5.74%
Cr	5.51%
Ni	5.24%

3 - The third group amounting to less than 5% is:

C	2.86%
Al	2.80%
B	2.5%

4 - Each of the remaining elements constitutes less than 1% of the total. However, some of these elements, either due to small resources or to inadequate production capacity, may present a procurement problem.

Table VII-A-3

Summary of Elemental Requirements for UWMAK-II

Element	Nuclear Island	Balance of Plant	Total	Tonnes/MWe (1710)
Al	4766	20	4786	2.80
B	4280		4280	2.50
C	4890		4890	2.86
Cr	5825	3605	9430	5.51
Nb	145	7.5	153	0.089
Cu	10,692	676	11,368	6.65
He	69	22	91	0.053
Fe	29,229	78,527	107,756	63.02
Pb	19,800		19,800	11.6
Li	980		980	0.57
Mn	937	355	1292	0.75
Si	12		12	0.007
Mo	917	92	1009	0.59
Ni	6480	2480	8960	5.24
Na		9816	9816	5.74
Ti	75	30	105	0.06
Y		3	3	0.0017
Zr		100	100	0.058
Be	985		985	0.58
			185,816	108.66

Finally, Table VII-A-4 summarizes the need for various alloys and compounds in the UWMAK-II system. The most abundantly used alloy is the low carbon steel at 63,479 tonnes, constituting 34% of the total plant. The austentic stainless steels are next, with 316 SS at 26.7% and 304 SS at 6.7%, placing a severe burden on Cr and Ni resources. The resource problem is discussed in Section VII-A-2.

Table VII-A-4

Summary of Alloy Requirements for UWMAK-II Metic Tonnes

Alloy or Compound	Nuclear Island	Balance of Plant	Total	Tonne/MWe (1710)
316 SS	47,104	2,643	49,747	29.1
304 SS		12,548	12,548	7.3
321 SS		2,499	2,499	1.46
Croloy-2 1/4		687	687	0.40
Inconel 800		624	624	0.36
Low alloy steel 2% Ni 1% Cr		2,656	2,656	1.55
Low Carbon Steel		63,479	63,479	37.12
NbTi	258		258	0.15
B_4C	5,487		5,487	3.21
Concrete (m^3)		$(340,000)m^3$	$(340,000)m^3$	

VII-A-2. Availability of Metals

a. General Statement

The availability of metals for UWMAK-II in the year 2000 and beyond will be determined by:

1) The size of ore reserves
2) Mine production capacity
3) The ability of the United States to compete in world markets for those metals or ores that must be imported
4) Smelting and refining capacities
5) Manufacturing capacity for alloy production and production of final shapes

The following discussion is an appraisal of availability of metals for UWMAK-II in terms of the above factors. Any such appraisal, twenty-five years in advance of the time when the metals might begin to be acquired, is subject to many uncertainties. The appraisal seems to indicate, however, that the metals on the required list present a variety of problems of procurement, and it indicates clearly that some metals are likely to present much more difficult problems of procurement than others.

In Table VII-A-3, metal requirements currently calculated for UWMAK-II are listed, together with estimated U.S. reserves at present prices and 3X present prices, U.S. consumption and production of each metal in 1974, world reserves at present and 3X present prices, and world production of each metal in 1974. World consumption and world production of metals are approximately equal. The requirements assume a total generating capacity (2020 A.D.) of 10^6MWe, produced in individual reactors with nominal capacity of 1710 MWe. Requirements cover both nuclear island and balance of plant.

Details of resource estimates for metals other than Be are presented in the section of the UWMAK-I report on materials availability.

b. Metals for 316 SS

Metals required for 316 SS are iron, chromium, nickel, manganese, and molybdenum.

Iron

U.S. iron ore reserves at present prices are ample to sustain normal consumption plus UWMAK-II requirements well beyond the year 2020. The total requirement of 10^6MWe, if spread over the period 2000 to 2020, would require only a small percentage increase in U.S. production, not a serious matter. Present use of imported iron ore is a matter of industry history and economics, not limitation of reserves. With adequate forewarning, there should be no problem in achieving increase in steel production capacity.

Chromium

There are no U.S. reserves of chromium at present prices. At 3X present prices, domestic production of sufficient chromium would require tapping the chromite deposits of the Stillwater Complex, Montana. The present mine and mill would have to be restored, and additional milling

Table VII-A-3

Data Relating to Availability of Metals for UWMAK-II

(All quantities in metric tonnes x 10^6)

Element	Requirements for 10^6 MWe[1]	United States Reserves 1X[2]	United States Reserves 3X[3]	United States Production 1974[4]	United States Consumption 1974[4]	World: Ex-U.S.A. Reserves 1X[2]	World: Ex-U.S.A. Production 1974[4]	Element
Al	2.80	~2.00	>1,000.00	~0.40	~4.86		8.3	Al
B	2.50	10.1	Large	~0.18	~0.15	10.1	>0.15	B
Cr	5.51	0.00	1.53	0.00	~.73	~370.0	~2.0	Cr
Fe	63.02	2,000.00	>10,000.00	50.00[5]	80.0[6]	246,000.0	413.0	Fe
Mn	0.75	0.00	>10.00	0.00	~1.60	>2,000.0	~9.0	Mn
Mo	0.59	5.41	> 2.08	0.06	0.04	~13.0	0.21[7]	Mo
Ni	5.28	0.20	~16.00	0.015	0.20	~24.0	0.67	Ni
Si	0.007	Very large	.58	0.66	.58	Very large	1.28	Si
Pb	11.60	59.00	no data	0.68	~0.82	160.00	2.81	Pb
Nb	0.089	0.006	0.070	0.00	.001	7.00	~0.006[7]	Nb
Ti	0.067	34.00	~29.00	0.29	0.20	147.00	~0.077[7]	Ti
Cu	6.65	90.00	>100.00	~1.59	1.79	370.00	5.75	Cu
Li	0.57	0.50	3.90	~0.002	~0.003	>0.80	~0.002	Li
Be	0.58	.03	.005	0.002	0.002	>0.01	0.0002	Be
Na	5.74	Unlimited		?.200[8]	?0.200	Unlimited	no data	Na
Y	0.0017	0.0009	no data	?.00004	0.00009	0.036	0.0002	Y
Zr	0.058	10.00	no data	?.070[9]	.153[9]	>14.0	>0.475[7,9]	Zr

Notes:

[1] Based on 1710 MWe (nominal) per reactor.
[2] Reserves at present metal prices.
[3] Reserves at metal prices 3 times present prices.
[4] Primary metal only. Data, except data for lithium, from U.S. Bur. Mines, Commodity Data Summaries, 1975.
[5] Approximate iron content of domestically produced iron ore.
[6] Approximate iron content of iron ore consumed.
[7] Free World only.
[8] Sodium metal only. About 1 percent of total sodium minerals production.
[9] Zirconium content of Zircon ($ZrSiO_4$) concentrates. No data for U.S. metal production; Free World production (1974) 3750 short tons.

facilities might have to be constructed. There would have to be adjustment of American metallurgical practice to use the low grade concentrates that would be produced. Satisfactory procedures for controlling mine and mill wastes would have to be developed. The proposed copper-nickel mining operation, by Anaconda Copper Corporation, at the same site has met strong opposition from environmental groups. Finally, the chromium in ores of the Stillwater Complex would be adequate only if output were reserved for CTR. As the table indicates, the U.S. at present is totally dependent on foreign sources for chromite ore.

Another factor may become increasingly important as the present century wears on. There is a strong move toward creation of chromite smelting operations and alloy production facilities in the chromite-producing countries. By the end of the century, there may be no U.S. industry capable of producing the base alloys (ferrochromes) that enter into stainless steel production.

A final element in the future availability of chromium is the fact that most of the world's reserves and 3X resources are in Rhodesia and South Africa, which face an uncertain political future.

The future price of chromite will have a bearing on the possible development of U.S. low grade chromite resources (see section on chromite in the report on UWMAK-I). Since September, 1974, world prices for chromite have approximately doubled, partly because shipping charges have risen in response to increases in world petroleum prices, partly because the principal chromite producers, Russia, Turkey, South Africa, and Rhodesia, are setting prices in terms of what the market can be made to bear.

Nickel

U.S. reserves of nickel are small and will be largely or entirely depleted by the end of the century. Reserves at 3X present prices are largely in the Duluth Gabbro Complex in Minnesota. There are no mines in the Complex. There is only a small domestic smelting and refining capacity. Inasmuch as the target amount is four times U.S. annual consumption of nickel, a 20 percent increase in alloy production and fabrication facilities per year over present level will be required during the period 2000 to 2020, even in the unlikely event that U.S. consumption does not increase in the meanwhile.

World reserves of nickel at present prices are very large, and new reserves are being identified. Reserves are scattered widely over the world, outside North America, and this provides some assurance of future availability. There is as yet no new nickel cartel. The rapid progress of research and development of the deep sea nodule deposits gives promise of substantial additions to nickel supply from that source. U.S. mining organizations are actively involved.

Molybdenum

The present U.S. reserve position for molybdenum is very good. The U.S. is the world's largest producer. Reserve figures suggest an adequate supply to the end of the century at present prices and certainly at 3X prices. However, there is a question of possible rates of production, which may or may not be high enough to supply CTR requirements over and above "normal" market demand. The situation is analogous to that in copper (which see below) and should be watched. It should not be taken for granted that the supplies for CTR will be available in the period 2000-2020 A.D. Demand for molybdenum

is rising, and there is already concern over adequacy of future supplies.

Manganese

The U.S. has no reserves of manganese, being totally dependent on foreign sources for its supply of a metal that is vital to the steel industry. At 3X present prices, the UWMAK-II target amount could be met from domestic deposits, but a 5 to 10-year lead time would be necessary to achieve U.S. production from these deposits, since every domestic resource presents metallurgical problems.

The data for U.S. resources do not include Mn in the accumulated slags from open-hearth steel furnaces. These are a substantial resource that was considered as a possible source of manganese during World War II.

World reserves of manganese are very large relative to current demand. The figure for reserves at present prices given in the table is conservative. There may be that much in South Africa alone. Major Free World producers are Australia, Gabon, Brazil, and South Africa.

For the future, manganese presents the same problem as chromium, from the standpoint of future availability of a domestic metal-producing industry. The main first step in conversion of manganese ore is production of ferromanganese. This step is more and more being undertaken in the ore-producing countries. U.S. imports of ore are dropping, whereas imports of ferromanganese are rising. The price of imported ferromanganese has risen from $200 per ton in mid-1973 to about $450 per ton at the end of 1974.

Summary for 316 SS

Except for iron and possibly molybdenum, the metals for 316 SS present problems or possible problems of availability. In terms of domestic resources, chromium is an especially serious problem.

c. Aluminum

U.S. reserves of aluminum ore (bauxite) at present prices are small, but it appears likely that by the end of the century U. S. industry will be converted to use of clays, shales, and other lower grade sources of aluminum. Domestic deposits of such materials are enormous. Interest in conversion has recently been stimulated by (1) the formation of the Organization of Bauxite Exporting Countries, (2) abrupt increase in the prices of imported bauxite, and (3) a drive on the part of bauxite-producing countries toward establishment of local alumina plants and aluminum smelters. The sources of bauxite supply for U.S. alumina plants and smelters are thereby threatened.

d. Boron

The U.S. has about half the known world reserves of boron, is a major exporter of borates, and has large resources that would be economic at higher prices. Reserves are large relative to UWMAK-II requirements, but there could be a problem of rate of production. The target amount is more than 10X present annual U.S. production.

World reserves of boron minerals are large and could be greatly increased by future exploration if world demand should increase greatly.

e. Silicon

Reserves and resources of raw materials for silicon are for all practical purposes inexhaustible. High purity silica is another matter. Sources of silica essentially free of both Fe and Al require special search. Figures for reserves are unavailable.

f. Lead

U.S. reserves of lead are at the highest level in history, and chances of discovering additional reserves are considered good. Known reserves appear adequate to meet normal U.S. requirements at least until the end of the century, particularly with increased availability of recycled lead. Present partial dependence on imported metal ores is a matter of economics and availability of smelting, refining, and fabricating facilities.

The UWMAK-II requirement for lead, however, is a formidable one, equivalent to 4 times present world annual production, and 17 times U.S. 1974 production. An annual increase of 1.7 percent in U.S. annual lead consumption through 1980 is forecast (U.S. Bur. of Mines, 1975). World annual consumption has increased about 25 percent since 1965. To the extent that international competition for lead supply restricts the availability of lead to the United States, large increases in U.S. mining, smelting, and refining capacity would be required. This could be a major problem, but the dimensions of the problem by the end of the century are not readily foreseen. The U.S. lead industry presently is beset with serious environmental problems and problems of capital formation.

In any event, the development of world and U.S. lead-producing industries between now and the end of the century should be monitored. It is possible that the availability of lead could set a limit on the rate of development of generating capacity in the form of fusion reactors.

g. Niobium

Niobium reserves and resources are summarized in the UWMAK-I report. There are no U.S. reserves at present prices. The only sizeable reserves at 3X prices are in the Powderhorn Complex, Colorado (about 65 x 10^3 m.t.). World reserves are large, and important deposits exist in Canada, Brazil, and certain African countries. Access to supplies from these countries would ensure availability of Nb in adequate amounts for UWMAK-II.

h. Copper

U.S. and world copper reserves, like those of lead, are at the highest level in history. The question here is rate of production. A recent study (National Academy of Sciences, 1975)[1] concludes that if U.S. requirements for normal industrial purposes are to be met from domestic reserves, two medium-sized copper deposits (580,000,000 tons of 0.6 percent ore) must be discovered annually between now and the year 2000. The large requirement of copper for UWMAK-II, about 4.5 times U.S. 1974 production of new copper, is formidable, even if procurement is spread over a period of years.

i. Lithium

The recent drastic downward revision of estimates of reserves of Li in the brine of Silver Peak reduces reserves of Li at present prices below the UWMAK-II requirements. However, resources at 3X present prices are large, and the chances of discovering additional reserves in the United States, and in the world, are good. There seems no cause for alarm over lithium availability, but there should be a determined effort to discover additional reserves and to develop means of extracting Li from them. The problem of expanding the scale of Li production likewise requires attention.

j. Yttrium

Data for U. S. and world reserves of yttrium are so meager that no estimate can be given.

k. Zirconium

Zircon, the commercial source of zirconium, is in good supply as a byproduct of rutile and ilmenite from beach sand deposits. U.S. and world reserves of zircon are large and can be increased by further exploration. The UWMAK-II target amount could require an increase in metal-producing capacity, but reserves will be ample to support this.

l. Sodium

Common salt (NaCl), the source material of Na metal, is available in essentially unlimited amounts from rock salt deposits and both sea and salt lake brines. The UWMAK-II target amount would require, however, a substantial increase in metal-producing capacity.

m. Beryllium

Information on beryllium reserves and resources is very uneven in quality and is incomplete. During and after World War II, the U.S. Geological Survey and U.S. Bureau of Mines studied beryl-bearing pegmatites in every pegmatite district of the United States. These studies showed that the only sizeable resource of beryl in U.S. pegmatites (ca 36,000 m.t.) is in the tin-spodumene belt of the Piedmont of North Carolina and South Carolina. The grade of the ore, however, is only 0.4% beryl (.02% Be), the beryl is very fine-grained, and concentration of beryl at high levels of recovery is not possible. Any beryl produced would be a byproduct of the mining of spodumene for lithium. Even at 10X present prices, the feasibility of recovering Be from such deposits is dubious.

In the early 1950's, the U.S.G.S. sampled a wide variety of mineral deposits, mostly in the western states, for beryllium. The results were reported in Professional Paper 318.[2,3] No significant concentrations were found.

In 1959, prospecting with a beryllometer showed the presence of bertrandite [$Be_4Si_2O_7(OH)_3$] in tuffs of the west side of the Thomas Range, Utah, on either side of Spor Mountain. Beryllium is being produced from these deposits. The Bureau of Mines (Commodity Data Summaries, 1975, 17)[4] estimates beryllium in domestic bertrandite deposits at 28,000 tons. Most of this would be in the deposits at Spor Mountain. In addition, 4,500 tons of beryllium in ore averaging 0.2 percent Be are estimated by Sainsbury (1969) to be present in the central York Mountains, Alaska.[5] A modest amount of beryllium is probably present in deposits of Gold Hill, Utah.

Spor Mountain, Lost River, and Gold Hill are all examples of non-pegmatite, hydrothermal beryllium deposits. Most hydrothermal deposits are lacking in Be or have the metal in negligible concentrations. It is possible, however, that unusual hydrothermal deposits containing beryllium have been overlooked in the western states. Beryllium minerals, particularly if fine-grained, are very difficult to recognize. Intensive prospecting with the beryllometer is necessary to discover deposits of the Spor Mountain type. The chances of discovery are unpredictable. In our opinion, the figure of 250,000 tons of beryllium estimated for "undiscovered deposits" in the U.S. (Prof. Paper 820)[6] is meaningless.

There are no real data on world reserves of beryllium. Estimates are based on examination of past production and prediction that world reserves are adequate to sustain production at the same level for a period of years. Small mines in Brazil, Argentina, South Africa, and a few other countries supply the two hundred tons of world annual production of beryllium (in beryl) outside the United States. No large deposits are known.

Most of world production of beryllium has come from beryl in pegmatites. Bertrandite in significant quantities has been reported from the Aguachile area, northern Mexico, in fluorspar deposits associated with Tertiary rhyolitic intrusions, but no estimate of Be reserves or resources in the deposits has been made. In U.S.G.S. Professional Paper 820, (p. 32) world reserves (ex-U.S.A.) in pegmatite deposits are estimated at 600 short tons Be, in non-pegmatite deposits at 32,000 short tons. No basis for these figures is given.

It is clear that the 10^6 MWe target amount for the UWMAK-II Reactor is out of all proportion to the size of known U.S. and world reserves.

References for Section VII-A

1. National Academy of Sciences, 1975, Mineral Resources and the Environment, Chapter VI, Resources of Copper, p. 127-183.

2. Warner, L. A., Holser, W. T., Wilmarth, V. R., and Cameron, E. N., 1959, Occurrence of nonpegmatite beryllium in the United States. U. S. Geol. Survey, Prof. Paper 318, p. 198.

3. Materials Advisory Board, 1958, Beryllium. National Academy of Sciences, National Research Council, Division of Engineering and Industrial Research, p. 57. Report of Committee on Beryllium, E. N. Cameron, chairman.

4. U. S. Bureau of Mines, 1975, Commodity Data Summaries.

5. Sainsbury, C. L., 1969, Geology and ore deposits of the central York Mountains, western Seward Peninsula, Alaska. U. S. Geol. Survey, Bull. 1287, p. 101.

6. Griffiths, W. R., 1973, Beryllium. U. S. Geol. Survey, Prof. Paper 820, 85-93.

7. "Cryogenic Energy Storage System Design Report," Fermi National Laboratory Report FN-264, 8000.00 in collaboration with the University of Wisconsin, October 1974.

VII.B Economics

The primary measures of the practicality of a power plant design are the reliability and costs (both economic and environmental) of the electricity produced. Reliability is primarily a function of the plant design and the dependability of the fuel supply but will not be discussed in detail here because the design and operating details of UWMAK-II are not known well enough. We can only assume that the plant will be designed, built and operated such that it has adequate reliability. The reliability of the fuel supply is essentially 100 percent since it depends on purchase of relatively small amounts of readily-available deuterium and proper design and operation of the tritium recovery system within the plant. The purpose of the remainder of this section is to describe the economics of UWMAK-II and estimate the cost of the electricity produced.

The cost of electricity produced in a power plant is determined primarily by the operating costs, the fueling costs, the capital cost, the amount of electricity generated, and the financial conditions for the utility operating the plant. Each of these primary factors is addressed below.

First, the plant operating cycle is described. Because Tokamak reactors have a unique operating cycle in comparison to conventional power plants, it is important that the operating cycle is understood well enough that the plant factor and operating costs can be estimated. The second section determines the plant factors that appear attainable. It is desirable to have the plant factor as large as possible since the electricity production is essentially proportional to the plant factor, and the unit cost of electricity generally decreases as the plant factor increases. In addition, the plant factor should be high enough that the plant can be considered a reliable source of electricity during the seasonal peak periods of electricity consumption. In any case, the plant factor must be known before the electricity production and unit cost can be estimated.

The third section contains a description of the UWMAK-II capital costs and a presentation of the philosophy and basic assumptions used during development of the capital costs. The fourth and fifth sections contain estimates of the electricity unit costs. First, the annual operations, maintenance, and fueling costs are estimated. These costs are then combined with the annual return on capital to determine the annual electricity cost and the resultant electricity unit cost.

This description of the UWMAK-II reactor was prepared as a preliminary evaluation of the feasibility and costs for building and operating such a plant. Detailed designs and cost estimates were not made. The general reactor design was developed by first conceiving the physical conditions (temperature, ion densities, etc.) necessary for creating and maintaining

the fusion plasma. The general physical structures and equipment necessary for creating these conditions and controlling the products of the fusion reaction were then identified. General designs for these items were developed, but design details were developed only far enough that there was assurance that the primary structures could be built and that they would operate as required. In particular, in many cases, optimum designs were not developed.

Only general cost estimates were made. Most costs were developed by determining the total quantities of materials in a structure and then multiplying the weight by a standard unit cost for similar equipment with the same degree of fabrication. In some cases, where equipment or process designs were not available (for example the fuel pellet injectors) the cost estimate was based on costs for similar complex equipment items. The time and effort spent on estimating costs generally was proportional to the total cost of the item. Little time was spent on low cost items.

In general, the costs were overestimated in order to assure that the final costs would not be criticized for being optimistic. This also compensates for the possibility that significant costs may have been left out of the estimates.

VII-B-1. The UWMAK-II Operating Cycle

The UWMAK-II has a three phase operating cycle consisting of

1. The initial loading and heating to ignition and operating conditions;
2. The fuel burning period;

and 3. The plasma shutdown, reactor evacuation, and transformer reset period.

During operating periods* this cycle is repeated at about 95 minute intervals as shown on Figure VII-B-1. The operating conditions for each of the major equipment items throughout the operating cycle are as shown on Figure VII-B-2.

The equipment conditions listed at the upper left of Figure VII-B-2 are the base conditions created during the startup period at the end of an outage. At that time the reactor divertor system is at its normal

---

*An operating period is defined as a period of time in which the operating cycle is repeated without unscheduled interruption or pause between operating cycles.

One operating cycle

	Phase 1		Phase 2	Phase 3			
150 Sec. Transformer Coil Reset	10 Sec. Current Rise Time	20 Sec. Heating to Operating Conditions	90 Minute Burn Period	100 Sec. Plasma Current Decrease	50 Sec. Chamber Purge	150 Sec. Transformer Coil Reset	10 Sec. Current Rise Time

TIME

Fig. VII-B-1 - The UWMAK-II Operating Cycle

At end of Prestartup Period:

1. Lithium and sodium systems near operating temperatures by use of startup heaters.
2. All lithium and sodium and helium systems operating.
3. All vacuum systems operating, but cryopumps are valved off.
4. Reaction chamber at 10^{-5} torr.
5. All magnets at 4.2 K.
6. Divertor current off.
7. Transformer reset to startup current.
8. Neutral beams off.
9. Fuel injectors off.

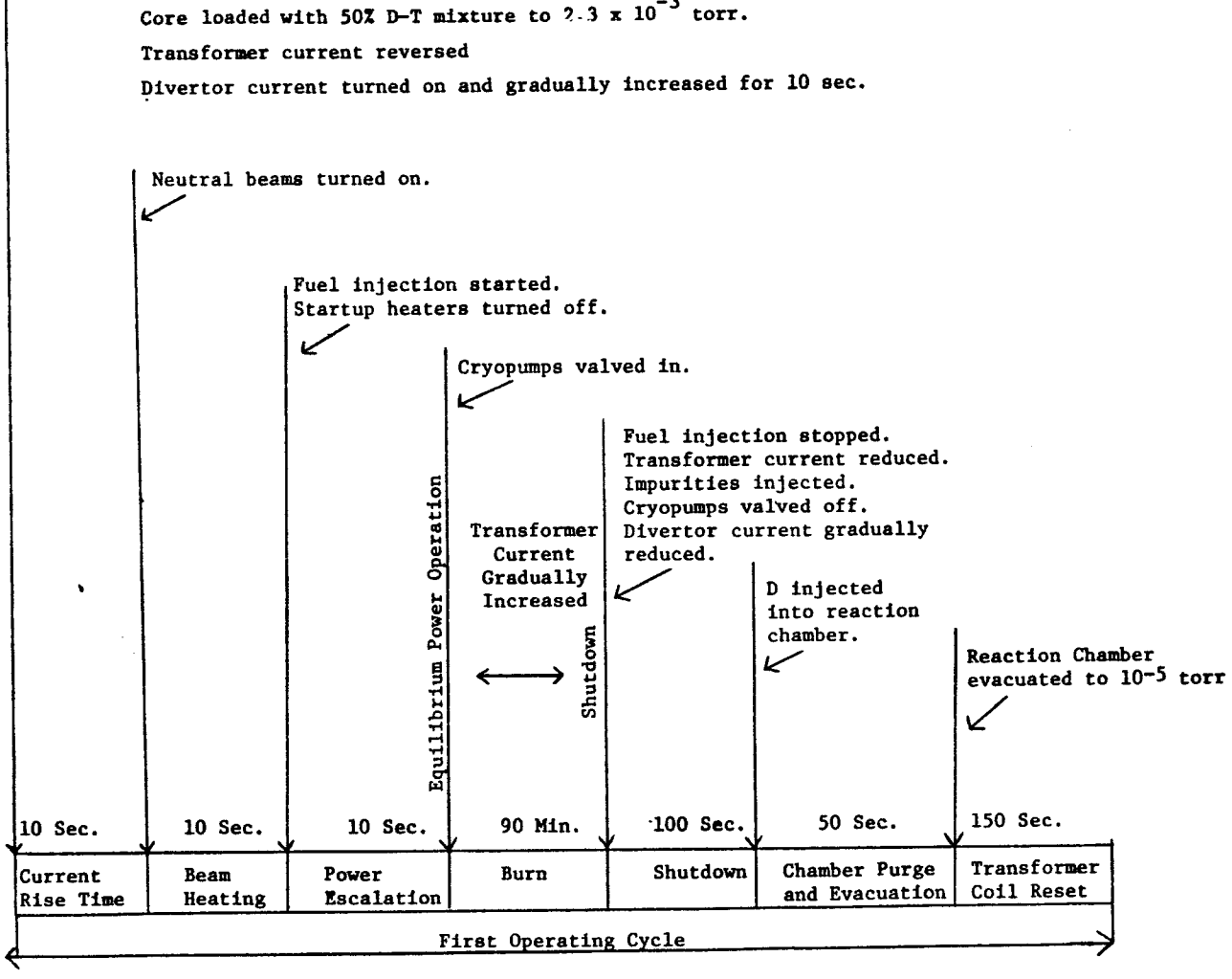

Figure VII-B-2

Equipment Operation During Operating Period

operating temperatures with all coolant and most vacuum systems operating. The cryogenic systems are holding the magnet coils at about 4°K. The Li and Na systems associated with the divertor are at the normal operating temperatures because startup heaters are used. The core has been evacuated to 1 x 10^{-5} torr by the vacuum system, and the currents in the transformer have been reversed in preparation for startup of the next cycle.

These initial operating conditions are repeated at the beginning of each cycle. However, after the first operating cycle following an outage, the Li and He systems are maintained at the normal operating temperatures by heat due to the fusion reaction. The startup heaters are shut off as soon as ignition occurs in the first operating cycle following an outage. They remain off during the rest of the operating period.

At the beginning of an operating cycle, the transformer current is reversed into the normal operating mode, and the chamber is loaded with a fuel mixture of 50% D and 50% T until the pressure reaches 2.3 x 10^{-3} torr. During the next 10 seconds, as the plasma current increases, the currents in the vertical field (or divertor) coils are increased at the same rate as the plasma current. The plasma temperature rises during this period as a result of ohmic heating to about 1.5 keV.

At 10 seconds, the neutral beams are turned on for a 10 second period to heat the plasma. Ohmic heating alone will not provide sufficient heating. At the end of 10 seconds, the beams are turned off and the plasma self heats in another 10 seconds until the stable operating conditions for plasma burn are achieved.

Fuel injection continues for the entire burn period. The fuel is assumed to be injected as solid (D+T) pellets. The cryopumps are valved into the vacuum system during the initial operation to assist in maintaining the desired vacuum.

The reactor system is designed to have about a ninety minute burn period. The transformer coils are designed to have adequate current capacity to maintain the plasma current during the burn phase. The use of a carbon curtain on the inner wall to retard the buildup of high Z impurities plus an effective "unload" divertor is expected to permit a ninety minute operation before the impurity level in the plasma becomes too high. (See Chapter II.)

The burn is terminated by cooling the plasma below the ignition temperature. This is done by shutting off the fuel injectors and injecting impurities which increase the heat transfer to the wall by radiation. At the same time, the cryopumps are isolated from the reaction chamber to avoid swamping them with impurities, the transformer and divertor currents are reduced and the plasma current is gradually reduced to zero over a 100 second period.

The reaction chamber is then purged with deuterium gas to reduce the concentration of impurities low enough that the subsequent evacuation to 1×10^{-5} torr will reduce the quantity of impurities to the desired amount at the beginning of the next burn period. The transformer coils are then reset over 150 seconds to the desired currents for the start of the next operating cycle.

VII-B-2. Fusion Reactor Plant Factor

The plant factor for a power plant is defined as the ratio between the actual power generation and the power generation that would occur if the plant operated 100 percent of the time at the design power level. The plant factor is always less than 100 percent because of (1) outage time for maintenance (and refueling, in some cases) and (2) operation at less than the design level during startup periods and periods of time when there is not a need for all the electricity which could be generated.

The plant factor for the UWMAK-II will be determined primarily by four factors:

1. The time required for wall replacement outages,
2. The amount of unscheduled outage time due to miscellaneous equipment failures and transmission system abnormal conditions,
3. The average length of the plasma burn, and
4. The length of the reactor rejuvenation time between plasma burns.

Each of these four factors will be briefly discussed and then a general correlation between these factors and the plant factor will be made.

A. The biennial wall replacements

The inner wall is designed to last two years before replacement is necessary to prevent failure. During each two year period, the inner wall in each of the twenty-four reactor segments will be replaced as described in Section IV-E.

The optimum schedule for replacing the wall segments is determined by making an economic balance of (1) the costs for keeping spare wall segments in inventory, (2) the costs for replacement of the segments, and (3) loss of income from sale of electricity during the outage periods. The cost of keeping spare segments in inventory is quite large and is directly proportional to the number replaced per outage. This cost decreases as the interval between outages decreases. Both the costs due to replacement of the segments and the loss of income from sale of electricity increase as the interval between outages decreases because the amount of outage time increases. (More time is required to prepare for the replacements and to prepare the reactor for operation after the replacements are completed.)

An economic balance for UWMAK-II shows that the optimum wall replacement interval is about six months. (See Table VII-B-1.) This interval would result in an outage during the spring and fall of each year when most utilities have minimum demand for electricity.

During the wall replacement outages, all routine major outage maintenance would be done. This includes such items as periodic inspection and maintenance of the turbine-generators, inspection and maintenance of large motors and pumps, etc. Also major equipment modifications would be done.

B. Unscheduled outage time

All power plants are plagued by numerous outages due to minor equipment failures, loss of transmission system, etc. In addition, it is probable that a segment of the fusion reactor occasionally will have to be replaced because of a failure in one of the heat transfer walls, the inner wall, the divertor system, or the magnets. If such a replacement is necessary, it probably could be done rapidly (in less than a week) because a spare segment would be kept ready for installation.* The failed segment would be simply moved to a storage cell, and the spare put in its place. The failed segment would be repaired during the subsequent reactor operating period.

An exact estimate of the amount of miscellaneous outage time cannot be made because the design of some of the equipment is not known at present. However, based on initial operating experience of nuclear power plants, a total miscellaneous outage time of four weeks per year appears reasonable. It should be noted that four weeks per year of outage time represents the average conditions for a debugged reactor system. The initial operating period for large nuclear reactors has required more than four weeks per year of miscellaneous outage time (or equivalent loss of time due to operations at less than design power level.)

C. The length of the burn period

The current design burn period is 90 minutes. If the burn is for a shorter time period, the plant factor is reduced because a larger fraction of the available reactor time is used for rejuvenation periods.

It is assumed that during the burn period, the average thermal power will equal the design power level of 5000 MWt. This is a reasonable assumption because the life of the inner wall is determined primarily by the total number of neutrons passing through the wall. Minor fluctuations of the thermal power level around the design level should not have a significant effect on the wall life as long as the average power level is 5000 MWt.

---

*A total of seven spare segments would be kept in inventory. During each wall segment replacement outage, six would be installed on the reactor. The seventh would be available to replace a failed segment during the one month following the replacement outage when one of the removed segments is being rebuilt.

Table VII-B-1

Wall Replacement Costs for UWMAK-II

Intervals Between Replacement Outages	Number Segments Replaced Per outage*	Annual Outage Time (days)	Annual Costs - millions of dollars			
			Segment Inventory Costs	Outage Costs	Loss of Income	Total
2 yrs.	24	20.5	24	0.58	8.8	33.4
1 yr.	12	23	12	0.66	9.9	22.6
6 mo.	6	28	6	0.8	12.0	18.8
4 mo.	4	33	4	0.94	14.2	19.1
3 mo.	3	38	3	1.09	16.3	20.4

Basis: Outage time = (1.5) (No. segments replaced) + (5) (No. outages)

Inventory cost = ($6,250,000) (No. segments replaced/outage) (0.16)

Outage Costs = (Annual outage time) ($28,500/day)

Loss of income is 10 mills/kwh. or $430,000 per day

*Equals number segments in inventory in order to perform outages. Does not include one additional segment in inventory to cover failures immediately following a replacement outage.

D. The length of the rejuvenation period

The rejuvenation period is essentially a non-productive time for heat generation. Any fusion reactions occurring during that period represent a minute fraction of the total heat generation. As explained in Section II-B-2, the rejuvenation period is estimated to last approximately 330 seconds. During the time when the fusion reaction is shut off, the reactor is evacuated, the reactor is refueled, and the fusion reaction is re-established. The various actions during this period will have to be controlled by automatic control systems because of the numerous sophisticated actions that are necessary in a short time period.

Experience or detailed design may demonstrate that the rejuvenation would require a different time period. However, a change in the length of the rejuvenation period will not have a significant effect on the plant factor if the burn period is as long as 90 minutes and the rejuvenation period does not increase significantly. (See Figure VII-B-4.)

E. The general plant factor correlation

The plant factor is defined as:

$$\frac{H_a}{H_t} \quad \text{, where}$$

H_a is the actual heat production during a time period, and H_t is the maximum possible heat production during the same time period. If it is assumed that UWMAK-II operates at the design power level throughout its burn periods, the annual heat production can be stated as:

$$H_a = (P_d) \quad \left(\frac{T_b}{T_b + T_r}\right) \quad (W_y - W_{uot} - W_{sot})$$

where

P_d is the design power level (MWt)

T_b is the average burn time (seconds)

T_r is the average rejuvenation time (seconds)

W_y is the number of weeks in a year,

W_{uot} is the number of weeks of unscheduled outage time in a year, and

W_{sot} is the number of weeks of scheduled outage time in a year.

The maximum possible heat generation is the amount of heat that would be generated if the reactor operated in the burn mode throughout the year. Therefore:

$$H_t = (P_d)(W_y)$$

The plant factor is then given by

$$\frac{H_a}{H_t} = \left(\frac{T_b}{T_b + T_r}\right) \left(\frac{W_y - W_{uot} - W_{sot}}{W_y}\right)$$

Figures VII-B-3, VII-B-4 and VII-B-5 present general correlations between the plant factor, the length of the burn, the length of the rejuvenation period and the length of the biennial wall replacement outages. The star represents the design conditions.

In general, the correlations show that a plant factor of about 80% can be achieved with reasonable values of the design parameters. To achieve 80% plant factor, the permissible values for each of the design parameters are about:

1. an outage time of 4 weeks each year for wall replacement
2. an outage time of 4 weeks each year for unscheduled maintenance
3. a 90 minute burn time, and
4. a rejuvenation period length of 330 seconds.

Throughout this analysis of plant factors, it has been assumed that the total electricity production will be proportional to the heat generation. This assumption is correct only if the design of the heat storage system is adjusted whenever the lengths of the burn and rejuvenation periods change so that the inlet steam conditions to the turbine generator are the same for all operating schedules. If the heat storage system design is not adjusted, a correction factor must be added to the plant factor equation to compensate for the changes in thermal efficiency as the lengths of the burn and rejuvenation period changes.

F. Summary

A plant factor of about 80% can be achieved for UWMAK-II with reasonable values of design parameters. To achieve this plant factor, it is necessary that the total outage time per year be no more than eight weeks when the rejuvenation time is about six percent of the total time for the reactor burn and rejuvenation. These conditions are satisfied by the design conditions of a 90 minute burn, a 330 second rejuvenation time, four weeks of unscheduled outage time per year, and four weeks of scheduled outage time per year for wall replacement.

VII-B-3. Capital Costs

The capital costs for UWMAK-II were estimated using standard preliminary capital cost estimating procedures. The primary guide for estimation of the capital cost was the document NUS-531 "Guide for Economic Evaluation of Nuclear Reactor Plant Design".(1) That document presents the general philosophy, procedures, and record tables for estimating all costs for a power plant.

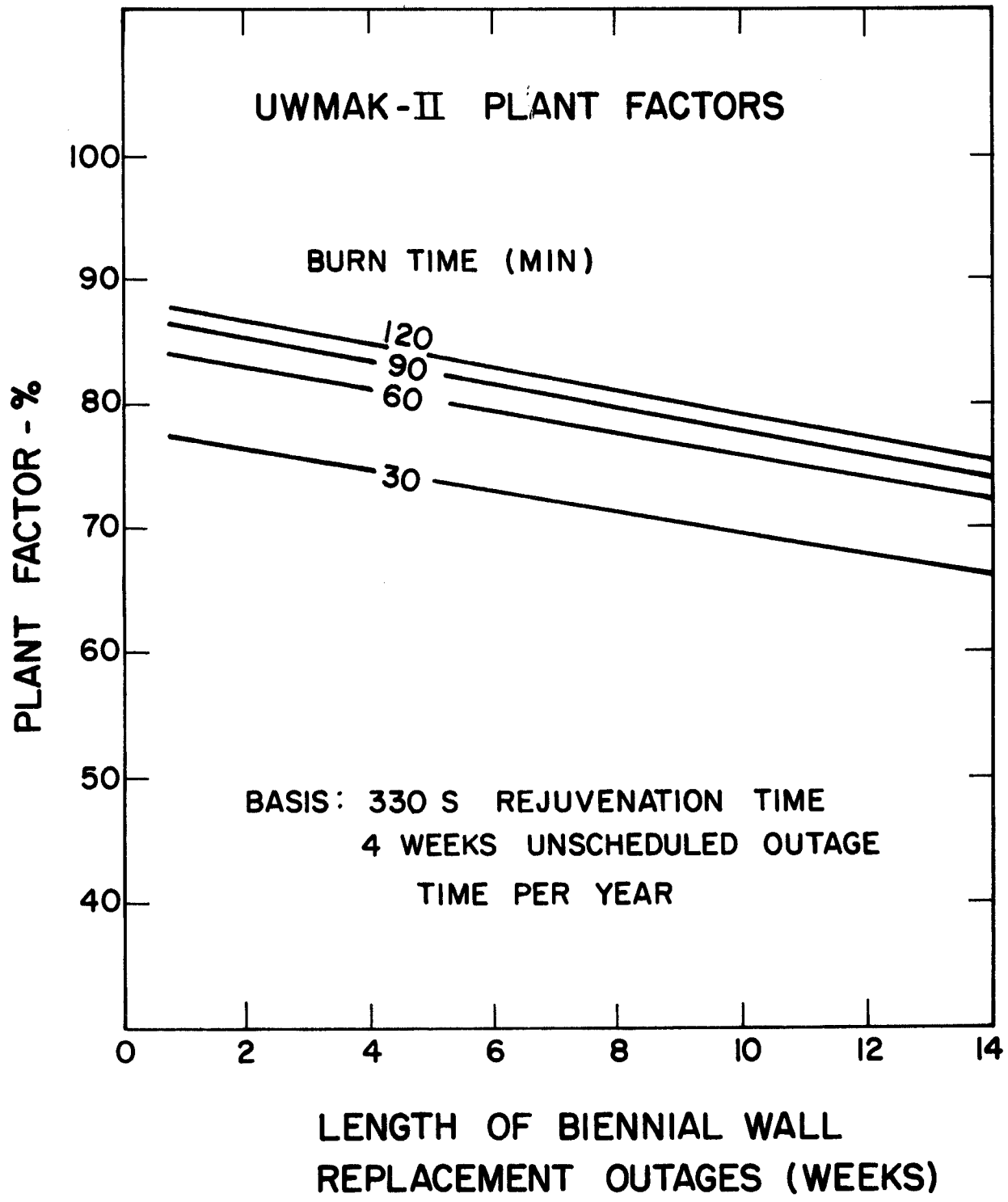

FIGURE VII-B-3

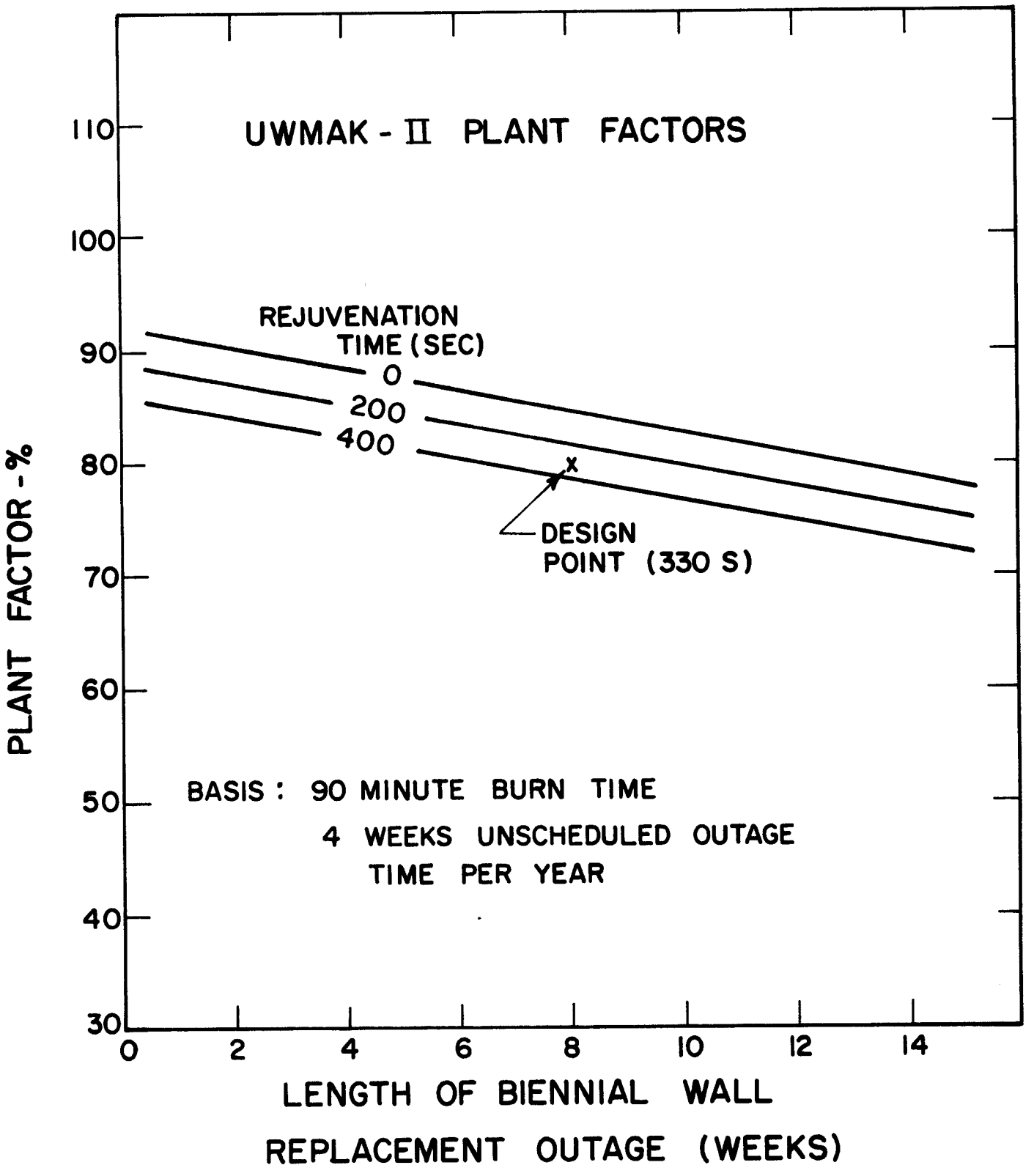

FIGURE VII-B-4

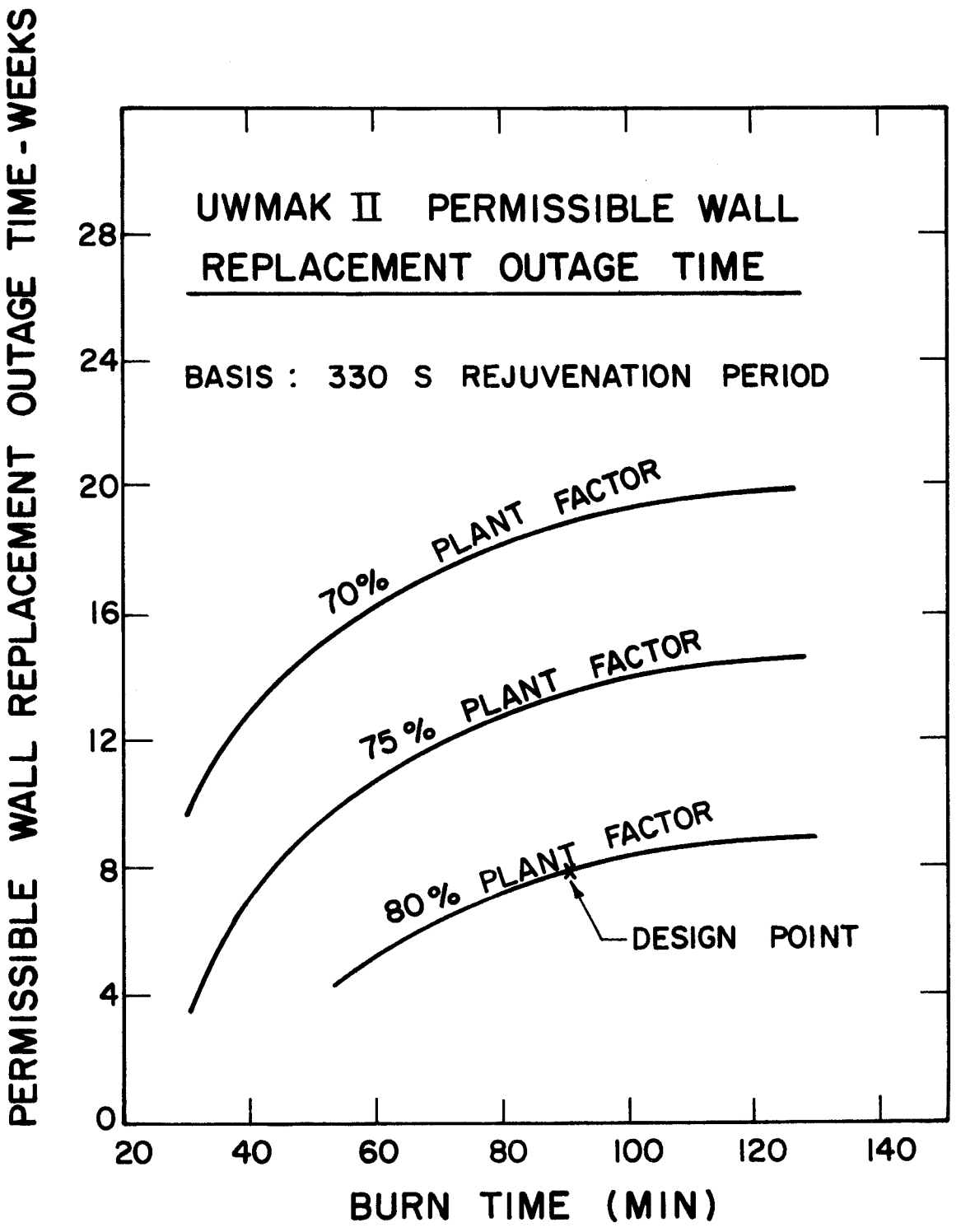

FIGURE VII-B-5

A conservative approach was used in estimating the capital costs. Past experience has demonstrated that advocates of new facilities frequently underestimate the capital costs because of optimism in design and failure to include sufficient contingency for unforeseen difficulties. In this analysis, the construction costs were deliberately overestimated whenever uncertainties existed. As an example, current maximum equipment sizes were used whenever there was any doubt that larger equipment could be produced. This eliminated the economies-of-scale that might be realized by use of larger equipment or increases in quantities manufactured.

No attempt was made to develop detailed designs for the numerous small support systems. It became apparent early in the effort that order-of-magnitude costs for such items would be adequate. Large errors in these costs would have an insignificant effect on the total capital costs because they cause a small fraction of the total costs.

Most of the costs were estimated by use of standard costs per unit of material. After development of a general design for a facility, the quantities of material needed for construction of that facility were estimated and then multiplied by the standard cost per unit of material to obtain the installed cost. The standard unit costs are presented in Table VII-B-2.

The estimated capital costs are presented in Tables VII-B-3 and VII-B-4. Table VII-B-3 presents the summarized costs by major plant components. Table VII-B-4 presents a breakdown of the costs in the greater detail developed during the cost estimating. The basis for each of the costs is presented in Appendix A.

Several reference documents were used to obtain quantity requirements and unit costs. These costs were adjusted as appropriate for differences in size and for cost escalation. The primary source of information was WASH 1230 (Vol. 1).[2]

References

1. NUS-531, "Guide for Economic Evaluation of Nuclear Reactor Plant Designs", NUS Corporation, January, 1969.

2. WASH-1230 (Vol. 1), "Pressurized Water Reactor Plant, 1000-MW_e Central Station Power Plants - Investment Cost Study", United Engineers and Contractors, June, 1971.

(Section VII-B-4 begins on page VII-B-36 because of the length of Table VII-B-4 summarizing cost data.)

Table VII-B-2

Standard Material Unit Costs

Material	Purchase Cost	Installed Cost
Deuterium	$40/kg	------
Helium	$1.22/1.	------
Lithium	$10/kg	------
Nitrogen	$0.25/1	------
Sodium	$0.55/kg	------
Tritium	No cost*	------
B_4C	------	$3/kg
Stainless Steel		
Sheet or bulk usage	$6.60/kg	$8.80/kg
Special shapes	------	$17.60/kg
Lead	------	$0.60/kg
Zirconium getter	------	$45/kg
Yttrium getter	------	$330/kg
Concrete	------	$206/$m^3$
Alloy Steel		
Structural	------	$4.40/kg
Special shapes	------	up to $13.20/kg
Nb-Ti	$33.00/kg	------
Copper	$1.10/kg	------
Copper matrix	$2.20/kg	------
Copper stabilizer	$3.30/kg	------
Copper conductor	------	$4.29/kg

*Mature industry assumed with a surplus of tritium

Table VII-B-3

Cost Data

(Prices are Present Day and Based on a 40 Hour Work Week)

Account Number	Account Title	Total
	DIRECT COSTS:	
Nondepreciating Assets:		
20	Land and Land Rights	$1,200,000
Depreciating Assets:		
26	Special Materials	5,820,000
	Physical Plant	
21	Structures and Site Facilities	161,590,000
22	Reactor Plant Equipment	775,179,000
23	Turbine Plant Equipment	160, ,000
24	Electric Plant Equipment	84,218,000
25	Miscellaneous Plant Equipment	19,110,000
	SUB-TOTAL Physical Plant	1,200,100,000
	INDIRECT COSTS (All Depreciating Assets):	
91	Construction Facilities, Equipment and Services	24,300,000
92	Engineering Services	48,500,000
93	Other Costs	90,800,000
	SUB-TOTAL	1,363,700,000
94	Interest During Construction	250,923,000
	TOTAL PLANT CAPITAL INVESTMENT	$1,614,620,000
	COST PER KILOWATT GENERATED	$944/kWe

Table VII-B-4

COST DATA

(Prices are Present Day and Based on a 40 Hour Work Week)

Account Number	Account Title	Total
20	Land and Land Rights	
201	Land and Privilege Acquisition	$1,200,000
202	Relocation of Buildings, Utilities, Etc.	
	TOTAL - ACCOUNT 20	$1,200,000
21	Structures & Site Facilities	
211	Site Improvements and Facilities	
.1	General Yard Improvements	
.11	Grading, General Excavation and/or Fill and Landscaping	
.12	Roads, Sidewalks & Parking Areas	
.13	Retaining Walls	
.14	Fences, Railings, and Gateways	
.15	Sanitary Sewer System:	
.151	Connection to Existing System	See Page 3
.152	Septic Tank	
.153	Distribution Box	
.154	Tile Field (Drainage)	
.155	Piping, Conduits, & Manholes	
.16	Yard Drainage & Storm Sewer System:	
.161	Connection to Existing System	
.162	Manholes, Catch Basins & Inlets	
.163	Outfall Structure	
.164	Piping, Conduits, Open Ditches	
.17	Roadway & General Yard Lighting	
.18	Cathodic Protection	
.2	Waterfront Improvements	
.21	Revetments	
.22	Levees	
.23	Breakwaters	
.3	Highway Access	
.31	Grading	
.32	Surfacing	

Account Number	Account Title	Total
21	Structures & Site Facilities (Cont'd)	
211	Site Improvements and Facilities (Cont'd)	
.3	Highway Access (Cont'd)	
.33	Culverts	
.34	Bridges, Trestles, and Causeways	
.35	Guards and Signs	
.36	Lighting	$8,000,000
.4	Railway Access	
.41	Grading	
.42	Bridges, Culverts & Trestles	
.43	Ballast, Ties, Rails & Accessories	
.44	Signals & Interlocks	
.45	Switches, Crossovers & Bumpers	
.5	Waterway Access Facilities	
.51	Dredging	
.52	Piers, Barge Docks, Etc.	
	TOTAL ACCOUNT 211	$8,000,000
212	Reactor Building Incl. Radwaste & Fuel Handling Areas	
.1	Basic Building Structures	
.11	Earth Work Including Dewatering, Walers Steel Sheeting	
.13	Substructure Up to Grade Incl. Concrete, Reinforcing, Forms	
.14	Superstructure	
.141	Concrete Work Incl. Floors, Exterior Walls, Interior Walls Piers, Col's. Reactor Area Concrete, Etc.	$39,000,000
.142	Structural & Gallery Steel	
.143	Exterior Metal Siding Walls	
.144	Roof Slabs, Roofing, Flashing Etc.	
.147	Doors & Windows & Wall Lauvers	
.148	Floor Finishes	
.149	Painting Incl. Special Coating	
.16	Structural Steel Stack	
	TOTAL .1	$39,000,000

Account Number	Account Title	Total
21	Structures & Site Facilities (Cont'd)	
212	Reactor Building Incl. Radwaste & Fuel Handling Areas (Con'td)	
.2	Building Service	
.21	Plumbing Below & Above Grade	$200,000
.22	Heating, Ventilation, Air-Conditioning	5,800,000
.23	Fire Protection System	150,000
.24	Electrical & Lighting	Incl. Acct. 24
.25	Elevator	100,000
	TOTAL .2	$6,250,000
.3	Containment Structures	
.31	Primary Containment Liners at Reactor Area	Included in 212.1
.32	Secondary Liner Plate Work for Walls, Floors, Roof	
.33	Penetrations (Mechanical & Electrical)	
	TOTAL .3	
	TOTAL - ACCOUNT 212	$45,250,000
213	Turbine Building Incl. Control Room, Heater Bay, Diesel Generator Area	
.1	Basic Building Structures	
.11	Earth Work	25,000,000
.13	Substructure	
.14	Superstructure Incl. Structural & Gallery Steel	
.2	Building Services	
.21	Plumbing	Incl. in .1
.22	Heating, Ventilation Air-Conditioning	1,300,000
.23	Fire Protection System	300,000
.24	Electrical & Lighting	Incl. Acct. 24
.25	Elevator	50,000
	TOTAL .2	$ 1,650,000
	TOTAL ACCOUNT 213	$26,650,000

Account Number	Account Title	Total
21	Structures & Site Facilities (Cont'd)	
214	Intake & Discharge Structures (Cooling Tower Building Work)	
.1	Circulating Water Cooling Tower Concrete Basins Incl. Outlet Structures	Incl. Acct. 232.3
.2	Earth Work	
.21	Circulating Water Pipe Excavation, Backfill, Disposal & Dewatering	Incl. Acct. 232.0
.22	Blow-down Pipe Excavation Backfill, Disposal & Dewatering	
.23	Make-up Pipe Excavation Backfill, Disposal & Dewatering	
.3	Make-up Pump House	
.31	Dredging River & Forebay Construction	$1,000,000
.32	Substructure	
.33	Superstructure	
.34	Structural Steel	
.35	Building Services	
.4	Retention Basin & Drain Line for Blow-Down	100,000
.5	Waste Heat Cooling Tower Building Work	
.51	Substructure	Incl. Acct. 232.3
.52	Superstructure	
.53	Structural Steel	
.54	Earth Work for Waste Heat Pipe	Incl. Acct. 232.0
.6	Protection Relief Slabs for Circulating Water, Blow-Down & Make-Up Pipe Lines	200,000
.7	Circulating Water Blow-Down Make-Up & Waste Heat Cooling Piping, Valves, Fittings, Etc.	Incl. Acct. 232.2
	TOTAL ACCOUNT 214	$1,300,000

ccount Number	Account Title	Total
21	Structures & Site Facilities (Cont'd)	
215	Reactor Auxiliaries Building Including Switchgear Bay and Heat Exchange Building	
.1	Basic Building Structures)	
.11	Earth Work)	
.13	Substructure)	$22,000,000
.14	Superstructure Including Gallery Steel)	
.2	Building Services	
.21	Plumbing	75,000
.22	Heating Ventilation & Air-Conditioning	1,100,000
.23	Fire Protection System	100,000
.24	Electrical & Lighting	Incl. Acct. 24
.25	Elevator	100,000
	TOTAL .2	$1,375,000
	TOTAL ACCOUNT 215.0	$23,375,000
216	Radioactive Waste Building	
.1	Basic Building Structures)	Incl. Acct. 215
.2	Building Services)	
217	Fuel Storage Building	
.1	Basic Building Structures)	Incl. Acct. 215
.2	Building Services)	
218	Miscellaneous Buildings	
A	Service Building	
.1	Basic Building Structures)	
.11	Earth Work)	
.13	Substructure)	4,500,000
.14	Superstructure Including Structural)	
	Steel)	
	TOTAL .1	$4,500,000

Account Number	Account Title	Total
21	Structures & Site Facilities (Cont'd)	
218	Miscellaneous Buildings (Cont'd)	
A	Service Building (Cont'd)	
.2	Building Services	
.21	Plumbing	Incl. .1
.22	Heating, Ventilation & Air-Conditioning	$900,000
.23	Fire Protection System	50,000
.24	Electrical & Lighting	Incl. Acct. 24
.25	Elevators	100,000
	TOTAL .2	$1,050,000
	TOTAL ACCOUNT 218-A	$5,550,000
B	Harmonic Filter Area	
.1	Basic Building Structures	
.11	Earth Work	
.13	Substructure	
.14		
	TOTAL .1	Incl. Acct. 24
.2	Services	
.23	Fire Protection System	
.124	Electrical & Lighting	
	TOTAL .2	Incl. Acct. 24
	TOTAL ACCOUNT 218-B	Incl. Acct. 24
C	Inverter Area	
.1	Basic Structures	
.11	Earth Work	
.13	Substructure	
.14	Structural Steel	
		Incl. Acct. 24
.2	Services	
.23	Fire Protection System	
.24	Electrical & Lighting	
	TOTAL .2	Incl. Acct. 24
	TOTAL ACCOUNT	Incl. Acct. 24

Account Number	Account Title		Total
21	Structures & Site Facilities (Cont'd)		
218	Miscellaneous Buildings (Cont'd)		
D	Inductive Coil Storage Building		
.1	Basic Building Structures	)	
.11	Earth Work	)	
.13	Substructure	)	
.14	Superstructure Incl. Structural Steel	)	
		)	
.2	Building Services	)	
.21	Plumbing	)	$790,000
.22	Heating Ventilation & Air-Conditioning	)	
.23	Fire Protection System	)	
.24	Electrical & Lighting	)	
	TOTAL ACCOUNT 218-D		$790,000
E	Helium Storage Building		
.1	Basic Building Structures	)	
.11	Earth Work	)	
.13	Substructure	)	
.14	Superstructure Incl. Structural Steel	)	
		)	
.2	Building Services	)	
.21	Plumbing	)	$100,000
		)	
.23	Fire Protection System	)	
.24	Electrical & Lighting	)	
	TOTAL ACCOUNT 218-E		$100,000
F	Miscellaneous Structures & Building Work		
.1	Gate House (Permanent)		25,000
.2	Visitor Center Building		Not Incl.
.3	Electrical Yard Foundations & Structures		Incl. Acct. 24
.4	Heating Boiler House		$200,000
.5	Hypochlorination Solution Tank Foundation		15,000
.6	Oil Separator Under-ground Vault		Incl. Acct. 24
.7	Foundation for Tanks (Water Storage)		150,000
.8	Berm & Foundation for Oil Storage Tanks		10,000

Account Number	Account Title	Total
21	Structures & Site Facilities (Cont'd)	
218 F	Miscellaneous Buildings (Cont'd) Miscellaneous Structures & Building Work (Cont'd)	
.9	Test Borings	$200,000
.11	Laboratory Material Testing & Structural Steel Inspection (Not Incl. Quality Control & Assurance)	75,000
.12	Temporary Construction Buildings, Field Office Building, Toilet & Wash Building for Construction Employees	Not Incl.
.13	Maintenance & Services for Various Contractors Scope of Work	
.131	Maintenance of Roads & Track	)
.132	Maintenance & Servicing of Sewage Plant & Lift Station	)
.133	Maintenance & Servicing Construction Employees Wash & Toilet Buildings	)
.134	Snow & Ice Removal Maintenance	) Not Incl.
.135	Guards Service	) in Acct. 91
.136	Switching & Handling of Railroad Cars on Station Property Incl. Necessary Yard Mobile Switching Equipment	)
.137	Traffic Flagman	)
.138	Miscellaneous Other Provisions	)
.14	Miscellaneous Yard Structures & Building Work	200,000
	TOTAL F	$875,000
218-G	Storage Tunnel	$4,000,000
218-H	Inner Wall Dissassembly Building	$20,000,000
218-I	Inner Wall Assembly Building	$20,000,000
218-J	Hot Cell	$4,900,000
	TOTAL ACCOUNT 218	$56,215,000
219	Ventilation Stack	800,000
	TOTAL ACCOUNTS 211 to 219 Inclusive	$161,590,000
	TOTAL ACCOUNT 21 STRUCTURES & SITE FACILITIES	$161,590,000

Account Number	Account Title	Total
22	Reactor Plant Equipment	
221	Reactor Equipment	
.1	Magnets and Central Support Structure	$182,800,000
.2	Shield	70,820,000
.3	Blanket	193,850,000
.4	Neutral Beam Injectors	80,000,000
.5	Equipment Foundation and Supports	2,050,000
.6	Vacuum Vessel Walls Between TF Coils	1,320,000
	TOTAL ACCOUNT 221	$530,840,000
222	Main Heat Transfer & Transport System	
.1	Primary Helium Coolant System	
.11	Pumps & Motor Drives Modular in He Systems & Non Modular	$4,000,000
.12	Piping	32,000,000
.13	Heat Exchangers (IHX and Clean-up Regenerative)	49,000,000
.14	Tanks	
.141	Dump and Make-up Tanks	Incl. in Acct. 226.3
.142	Tritium Extraction	6,000
.15	Thermal Insulation Piping & Equipment	Incl. in .12 and .13
.16	Tritium Extraction	6,100
.2	Divertor Lithium System	
.21	Pumping	$2,000,000
.22	Piping	5,000,000
.23	Heat Exchangers	4,000,000
.24	Tanks	Incl.in.14
.25	Clean-Up	1,340,000
.26	Tritium Extraction	1,340,000
.3	Direct Intermediate Sodium Loop System	
.31	Pumps & Motor Drives Modular & Nonmodular	31,300,000
.32	Piping	15,000,000
.33	Heat Exchangers (Steam Gen. & Clean-Up Regenerative)	25,300,000

Account Number	Account Title	Total
22	Reactor Plant Equipment (Cont'd)	
222	Main Heat Transfer & Transport Systems	
.3	Intermediate Sodium Loop Systems	
.34	Clean-Up System	$700,000
.36	Tanks	
.361	Sodium Dump Tanks	$20,000,000
.362	Hot Storage Tanks	
.363	Make-up Tanks	
.364	Clean-up Tanks	
.365	Tritium Extraction Tanks	
.37	Thermal Insulation Piping and Equipment	2,900,000
.38	Tritium Extraction	670,000
	TOTAL ACCOUNT 222	194,562,100
223	Auxiliary Heating Systems	
.1	Shield Cooling (He)	
.11	Pumping	372,000
.12	Piping	212,000
.13	Heat Exchangers	492,000
.14	Purification	36,000
.15	Tritium Extraction	30,000
.2	Magnet Cooling System	
.21	Cryogenic System	$19,300,000
.22	Piping	330,000
.23	Transport System	330,000
.24	Tanks	70,000
	TOTAL ACCOUNT 223	$21,172,000
224	Radioactive Waste Treatment & Disposal	
.1	Liquid Waste Processing & Equipment	180,000
.2	Gaseous Wastes and Off-Gas Processing System	0
.3	Solid Wastes Processing Equipment	90,000
.4	Wall Liner Disposal Equipment	60,000
	TOTAL ACCOUNT 224	$330,000

Account Number	Account Title	Total
22	Reactor Plant Equipment (Cont'd)	
225	Nuclear Fuel Handling & Storage Systems (Fuel Injection)	
.1	Used Fuel Purification System	$110,000
.2	Liquefaction	190,000
.3	Pellet Fabrication	340,000
.4	Pellet Injection	1,480,000
.5	Storage Equipment	100,000
	TOTAL ACCOUNT 225	$2,220,000
226	Other Reactor Plant Equipment	
.1	Inert Gas System	163,000
.2	Special Heating Systems	1,100,000
.3	Coolant Receiving, Storage & Make-up Systems	1,172,000
.4	Fluid Leak Detection	40,000
.5	Auxiliary Cooling Systems	2,300,000
.6	Maintenance Equipment	1,850,000
.7	Building Vacuum Systems	350,000
.8	Core Vacuum System	7,380,000
	TOTAL ACCOUNT 226	$14,355,000
227	Instrumentation and Control	
.1	Reactor & Process I & C Equipment	
.2	Automatic Monitoring & Computation Equipment	
.3	Radiation Monitoring Systems	11,700,000
.4	Isolated Indicating & Recording Gauges, Etc.	
.5	Control & Instrument Piping, Tubing, & Wiring	
	TOTAL ACCOUNT 227	$11,700,000

Account Number	Account Title	Total
22	Reactor Plant Equipment (Cont'd)	
228	Fossil-Fueled Boilers & Superheaters	
.1	Boiler and/or Superheaters)	
.2	Draft Systems)	Not Req'd.
.3	Fuel Handling Systems)	
.4	Ash Handling Systems)	
	TOTAL FOR ACCOUNT 22	$775,179,000
23	Turbine Plant Equipment	
231	Turbine-Generators	
.1	Turbine-Generators & Accessories Including:	
.11	Two(2) 778, 7MW 1800 RPM Tandem Compound Four(4) Flow Nuclear Steam Turbines with 43" Last Stage Blades)	
.12	Two(2) 865.2 MVA Generators @ .90P.F. and .50 SCR)	
.13	Non Standard Accessories)	
.14	Steam By-Pass System)	
.15	Live Steam Reheaters)	
.16	Piping, Valves & Hangers for By-Pass System	
.17	Thermal Insulation	
.2	Foundations	
.3	Standby Exciters	
.4	Lubricating System	
.41	Oil Conditioning Equipment)	
.42	Clean & Dirty Oil Storage Tanks)	
.43	Turbine Oil Transfer Pumps & Motors)	

Account Number	Account Title	Total
23	Turbine Plant Equipment (Cont'd)	
231	Turbine Generators (Cont'd)	
.5	Gas Systems	
.6	Reheaters	
.7	Shielding	
.8	Weather-Proof Housing	
	TOTAL ACCOUNT 231	$69,000,000
232	Heat Rejection Systems	
.1	Water Intake Common Facilities	
.11	Traveling Screens	
.12	Screen Wash Pumps	
.14	Piping	
.15	Chlorination	
.2	Circulating Water Systems	
.21	Circulating Water Pumps & Motor Drives	
.22	Circulating Water Piping, Valves & Fittings from Pumps to Condenser and to the Cooling Towers	
.23	Waste Heat Cooling Tower Circulating Water Piping	
.24	Cooling Tower Make-up Pipe Lines	
.25	Cooling Tower Blow-Down Pipe Lines	
.26	Trench Work for Circulating Water Piping Systems	
.3	Cooling Towers	
.31	Foundations & Basins	
.311	Mechanical Draft Towers	
.312	Waste Heat Tower Structure	
.313	Waste Heat Tower Circulating Water Pumps	
.33	Four(4) Mechanical Draft Cooling Towers	
.34	Mechanical Draft Waste Heat Cooling Tower	
.35	Waste Heat System Heat Exchanger	
.4	Other Systems Which Reject Heat to the Atmosphere	
	TOTAL ACCOUNT 232	$37,000,000

Account Number	Account Title	Total
23	Turbine Plant Equipment (Cont'd)	
233	Condensing Systems	
.1	Condensers	)
.11	Condensers Complete Including Shells, Tube Plates, Water Boxes, Hot Wells, Etc.	)
.12	Condenser Tubes	)
.13	Expansion Joints & Exhaust Stack Extensions	)
.14	Supervision of Erection	)
.16	Foundations	)
.2	Condensate System	
.21	Condensate Pumps Suction Piping, Valves, Etc.	
.22	Condensate Pumping Units Consisting of:	
.221	Condensate Pumps & Motor Drives	)
.222	Condensate Booster Pumps & Motor Drives	)
.3	Gas Removal System	
.31	Vacuum Pumps & Motor Drives	)
.32	Air Ejector Equipment	)
.33	Priming Ejectors	)
	TOTAL ACCOUNT 233	$23,000,000
.4	Turbine By-Pass System	
234	Feed Heating System	
.1	Regenerative Heat Exchangers	
.11	Four(4) Strings of H.P. Closed Feedwater Heaters	))
.12	Four(4) Strings of L.P. Closed Feedwater Heaters	))
.2	Pumps	
.21	Four(4) Turbine Driven Reactor Feed Pumps, Bedplates, Complete with Appurtenances	)))
.22	Two(2) Motor Driven Reactor Feed Pumps Bed-Plates complete with Motor Drives	))
.23	Four(4) Turbine Drives, for Reactor Feed Pumps	))
.24	Exhaust Ducts & Appurtenances to Main Condenser	))

Account Number	Account Title	Total
23	Turbine Plant Equipment (Cont'd)	
234	Feed Heating System (Cont'd)	
.2	Pumps (Cont'd)	
.25	Heater Drain Pumps & Motor Drives	
.26	All Other Miscellaneous Pumps & Motors	
.27	Foundations	
.3	Piping & Tanks	
.31	Piping Systems	
.33	Tanks	
.331	Condensate	
.332	Chemicals	
.333	Oil	
	TOTAL ACCOUNT 234	$23,000,000
235	Other Turbine Plant Equipment	
.1	Main Steam (or Other Vapor) Piping	
.11	Main Steam	
.12	Extraction	
.13	Condensate	
.14	Feedwater	
.15	All Other Miscellaneous Systems, Drips, Drains and Vents	
.16	Thermal Insulation	
.2	Turbine Auxiliaries	
.3	Auxiliaries Cooling System	
.4	Make-Up Treatment System	
.5	Chemical Treatment & Condensate Purification Systems	
.51	Filtration Equipment, Including Sand Filters, Aerators, Retention Tanks, Pumps, Etc.	
.52	Demineralizing Equipment, Including Anion & Cation Units, Decarbonator, Mixed Bed Units, Pumps Regeneration Units	
.53	Condensate Polishing Equipment Including Polishers, Anion & Cation Regeneration Equipment, Resin Mixing & Storage Vessels, Pumps, Tanks, Instruments, Controls	
.54	Chemical Feed Equipment Including Mixing Tanks, Pumps	

Account Number	Account Title	Total
23	Turbine Plant Equipment (Cont'd)	
235	Other Turbine Plant Equipment (Cont'd)	
.6	Central Lubrication Service System	
.61	Clean Oil Tank)	
.62	Dirty Oil Tank)	
.63	Turbine Oil Conditioning Equipment)	
	Including Pumps)	
.64	Turbine Oil Transfer Pumps & Motors)	
.65	Portable Oil Centrifuge & Filters)	
.66	Miscellaneous)	
	TOTAL ACCOUNT 235	$5,000,000
236	Instrumentation & Control	
.1	Process I&C Equipment)	
.2	Automatic Monitoring & Control Equipment)	3,000,000
.3	Isolated Indicating & Recording Gauges,)	
	Meters, and Instruments)	
.4	Control & Instrument Piping, Tubing, & Wiring	Incl. 235.1
	TOTAL ACCOUNT 236	$3,000,000
	TOTAL FOR ACCOUNT 23	$160,000,000
	Contingency	
	Spare Parts	150,000
	TOTAL FOR ACCOUNT 23	$160,150,000
24	Electric Plant Equipment	
241	Switchgear	
.1	Generator Circuits	536,000
.2	Station Service	3,756,000
	TOTAL FOR ACCOUNT 241	$4,292,000
242	Station Service Equipment	
.1	Station Service	549,000
.2	Low Voltage Unit Substations & Lighting Transformers	1,246,000
.3	Auxiliary Power Sources (Incl. Four(4) 5000KW Diesels)	3,370,000
.4	Main Power Transformers	3,362,000
	TOTAL FOR ACCOUNT 242	$8,527,000

Account Number	Account Title	Total
24	Electric Plant Equipment (Cont'd)	
243	Switchboards (Incl. Heat Tracing)	$2,786,000
244	Protective Equipment	95,000
245	Electrical Structures & Wiring Containers	1,150,000
246	Power and Control Wiring	
.1	Generator Circuits Wiring	677,000
.2	Station Service Power Wiring)	7,941,000
.3	Control Wiring)	
	TOTAL FOR ACCOUNT 246	$8,618,000
247	Diverter Coil Power Supply System	32,500,000
248	Poloidal Magnet Rectifiers	210,000
249	Electrical Installation	
.1	Contractor Furnished Material-Conduits, Lighting Fixtures, Etc.	1,640,000
.2	Construction & Erection Labor	24,400,000
	TOTAL FOR ACCOUNT 249	$26,040,000
	Contingency	Incl. Above
	Spare Parts	Incl. Above
	TOTAL FOR ACCOUNT 24	$84,218,000
25	Miscellaneous Plant Equipment	
251	Transportation & Lifting Equipment	
.1	Cranes, Hoists, Monorails & Conveyors	
.11	Two (2) 250 Ton/25 Ton Capacity Turbine Room Cranes	525,000
.12	Reactor Hall Crane	500,000
.13	Miscellaneous Hoists Cranes, Jibs & Trolleys for Equipment Maintenance	575,000
.14	One (1) 150 Ton/10 Ton Inductive Coil Storage Building Crane	300,000
.15	Blanket Storage Cell Trolleys	800,000
.16	Blanket rejuvenation equipment	10,000,000
.2-.6	Railway & Roadway Equipment, Watercraft Aircraft, & Vehicle Maintenance Equipment	50,000
	TOTAL ACCOUNT 251	$12,750,000

Account Number	Account Title		Total
25	Miscellaneous Plant Equipment (Cont'd)		
252	Air and Water Service Systems		
.1	Air Systems		
.11	Service Air Compressors & Motor Drives	)	
.12	Service Air Receivers	)	$460,000
.13	Instrument Air Compressors & Motor Drives	)	
.14	Instrument Air Receivers	)	
.15	Instrument Air Dryers	)	
.2	Water Systems		3,400,000
.3	Auxiliary Heating Boilers		1,800,000
	TOTAL ACCOUNT 252		$5,660,000
253	Communications Equipment		220,000
254	Furnishings & Fixtures		480,000
	SUB-TOTAL FOR ACCOUNT 25		$19,110,000
	TOTAL FOR ACCOUNT 25		$19,110,000
26	Special Materials		
261	Moderator		0
262	Reflector		0
263	Reactor Coolant		$2,760,000
264	Intermediate Coolant (Sodium)		2,850,000
265	Turbine Cycle Working Fluids		0
266	Other Materials		210,000
	TOTAL FOR ACCOUNT 26		$5,820,000

Account Number	Account Title	Total
91	Construction Facilities, Equipment and Services	
911	Temporary Facilities	$7,300,000
912	Construction Equipment	12,200,000
913	Construction Services	4,800,000
	TOTAL	$24,300,000
	Contingency	
92	TOTAL FOR ACCOUNT 91	
92	Engineering Services	
921	Plant Engineering	23,100,000
922	Plant Engineering	25,400,000
	TOTAL FOR ACCOUNT 92	$48,500,000
93	Other Costs	
931	Taxes and Insurance	$85,000,000
932	Staff Training and Plant Startup	900,000
933	Owner's G & A	4,900,000
	TOTAL FOR ACCOUNT 93	$90,800,000
94	Interest During Construction (@8%)	
941	Physical Plant and Associated (5 yrs) Indirect Costs	$252,230,000
942	Land and Land Rights (6 yrs)	704,000
943	Special Materials (1 yr)	466,000
	TOTAL FOR ACCOUNT 94	$253,400,000
	TOTAL PLANT CAPITAL INVESTMENTS	

VII-B-4. The Electricity Production Cost

The electricity cost for a power plant normally is determined by calculating three general types of costs:

1. The operation and maintenance cost,
2. The fuel cost, and
3. The annual return on capital.

a. The Operations and Maintenance Cost

The operations and maintenance (O & M) cost consists of the routine day-to-day expenditures for salaries, supplies, maintenance materials, process chemicals, etc. As a general rule, these costs are essentially constant from year to year.

Because the exact design for many of the UWMAK-II components is not known, an exact estimate of the O & M costs is not possible. However, a reasonable estimate can be made by use of known design features and experience at fission power plants.

The potential components of the O & M cost are:

a. Salaries,
b. Miscellaneous supplies and equipment,
c. Outside support services,
d. Miscellaneous costs,
e. General & Administrative,
f. Replacement inner walls,
g. Coolant make-up,
h. Working capital requirements.

Each of these items is briefly described and estimated below, and then the total O & M cost is determined.

Salaries

The size of the operating crew needed for a power plant depends on many factors such as the number of power plants at the site, the utility's personnel policies, the amount of automation, etc. Consequently, a set of operation conditions and policies must be assumed in order to permit estimation of the size of the operating crew. The following assumptions were used for UWMAK-II:

1. It is the only power plant at the site,
2. The design and operation has been debugged so that only routine technical assistance is needed,
3. The plant operates 24 hours per day, 365 days per year,

4. Five complete operating crews are used to provide full operating plus day crew and relief coverage,
5. The additional maintenance personnel needed for the wall replacement outages are provided by an outside independent maintenance contractor,
6. General and administrative services are provided by the utility's central administrative organization,
7. The plant operations are highly automated and computer controlled from the central control room,
8. Specialty services such as non-routine analysis, film badge processing, etc., are provided by outside contractors.
9. A special crew rebuilds the inner wall segments and assists in performance of wall replacement outages.

The plant is expected to have a typical utility organization as described in NUS-531. Each of the four functional groups - operations, maintenance, technical and clerical & services - is headed by a supervisor with full responsibility for his function. These four supervisors, in turn, report to an assistant superintendent and plant superintendent, who are responsible for overall plant safety and efficient operations.

The total normal operating staff for the plant is estimated to be 112 persons as shown in Table VII-B-5.* This staff varies from that in NUS-531 primarily in the operations and maintenance activities, where additional personnel are included because of the more numerous and more sophisticated equipment and instrumentation systems.

Based on an assumed average personnel cost of $12,000 per year, the total salary cost including fringe benefits is estimated to be $1,350,000 per year.

Miscellaneous supplies and equipment

This cost includes such items as ion-exchange chemicals, biocides for fouling protection, gases, routine maintenance materials, waste containers, etc. - the multitude of material items used by the personnel during routine day-to-day operations. Because of the larger operating staff and more sophisticated equipment systems, it is estimated that this cost would be about 50% higher than for a fission reactor or about $1,000,000 per year.

Outside support services

Two general types of outside support services probably will be needed for UWMAK-II. The first is the routine specialty services such as radioactive waste disposal, laundry, film-badge processing, etc. for which installation and staffing of facilities generally is more costly than use of outside help. Included in this category are personnel borrowed from other power plants.

---

*The normal operating staff performs all activities except rebuilding the inner wall segments. A special crew, described below, is responsible for rebuilding the segments and assisting in replacement of those segments.

Table VII-B-5

UWMAK-II Personnel

Position	Number persons Per Crew	Total Persons
Superintendents office		
Plant superintendent	---	1
Assistant	---	1
Secretary	---	1
Operations		
Operations supervisor	---	1
Shift supervisors	1	5
Senior control room operator	1	5
Control room operator	2	10
Equipment operator	1	5
Equipment attendant	1	4
Maintenance		
Maintenance supervisor	---	1
Mechanical Foreman	---	1
Electrical foreman	---	1
Instrument foreman	1	5
Mechanic	1	5
Mechanics helper	1	5
Welder	---	4
Machinist	---	4
Electrician	---	3
Electrician helper	---	3
Instrument mechanic	2	10
Instrument helper	1	5
Technical		
Technical supervisor	---	1
Plant Engineer	---	1
Instrument Engineer	---	1
Nuclear Engineer	---	1
Health Physicist	---	1
Chemist	---	1
Technicians	---	8
Clerical and Services		
Clerical & services supervisor	---	1
Typist	---	2
Storekeeper	---	1
Clerk	---	2
Yardman	---	1
Janitor	1	5
Messenger and handyman	---	1
Guard	1	5
Total	14	112

The total cost for the first type of outside services is estimated to be about $350,000 per year, based on fission reactor experience.

The second type of outside support services is the special maintenance force that is needed for replacing the inner wall. This requires a special crew trained to disassemble the reactor, move the irradiated segments to the storage cells, move rebuilt segments back to the reactor hall and then reassemble the reactor. It is expected that this will require 24 hours/day effort for four weeks per year with the associated higher costs for premium pay.

A crew of 96 men working each shift would expend about 30 man years of effort during each outage. If these men cost about 50% more than the average maintenance craftsmen because of special training, shift premiums, living expenses, and extra administrative costs, the total annual labor costs for these outages would be about $800,000.

Miscellaneous costs

The miscellaneous costs are the numerous relatively small costs that do not fit into the other cost centers listed here. It includes such items as office supplies, vehicle maintenance, public relations expenses, travel, rent, training, etc. Assuming that these costs would be about 50 percent larger than for a fission reactor of the same capacity yields an annual cost of about $200,000.

General and administrative costs

General and administrative costs are the charges for activities such as fringe benefit, administration, purchasing, division level management, etc. These usually average about 15 percent of the cost for salaries, supplies, and equipment, outside support services, and miscellaneous costs. This cost is calculated below on Table VII-B-6.

Rebuilding inner walls

This cost is shown as a separate item because it is unique for fusion reactors and because of its large size. The blanket sections are replaced each two years after a part, including the front wall, is removed and discarded. The tubes containing the $LiAlO_2$ and Be are opened, the $LiAlO_2$ and Be are removed, the tubes are discarded, the $LiAlO_2$ and Be is processed to restore the proper physical form (makeup material is added as needed) and placed in new tubes, these tubes are welded shut and connected to the tritium collection manifolds, and the blanket section is reassembled.

Because of the induced radioactivity in the stainless steel, this entire operation is done remotely in hot cells containing appropriate equipment for the necessary operations. No attempt is made to purify the $LiAlO_2$ and Be because there is no apparent benefit. The $LiAlO_2$ is discarded after one use.

The Be and LiAlO annual makeup costs are estimated to be $6,370,000 based on burnout of 370 kg/yr of beryllium, an annual processing loss of 0.5 percent, and replacement of all $LiAlO_2$.

The graphite has to be replaced each ten years. The annual cost is $3,300,000 since the whole blanket assembly is replaced.

The material costs for rebuilding the segements are assumed to be the same the original manufacture of those segments and is as follows:

Cost of Segment Materials

Item	Number	Unit Cost	Annual Cost
Helium radiator modules	1,430	3084	$4,410,000
Tube manifolds	42,855	7	293,000
Tubes	1,071,375	2.13	2,282,000
			$6,985,000

Because the activities required for rebuilding the segments are different than the normal power plant operational activities, it is assumed that the rebuilding is done by a special crew at the same costs as for the same activities when performed under non-radiation conditions. The costs are then:

Activity	Cost/Unit	Number Units	Annual Cost
Recover and prepare Be	$150/kg	215 MT	$32,300,000
Filling tubes	0.25	1,071,375	268,000
Connecting tubes to manifolds	23	1,430	33,000
Dissassemble modules	200	1,430	286,000
Reassemble modules	500	1,430	722,000
			$33,609,000

The total annual cost for rebuilding the modules is

Be, $LiAlO_2$ and Graphite	9,670,000
Components	6,985,000
Labor and equipment costs	33,609,000
	$50,264,000

Coolant makeup

The two coolants of importance for this reactor are lithium and helium.

Lithium is lost primarily because of leakage and adherence to components when they are removed or opened for maintenance. The loss rate due to reactions with neutrons is expected to be negligible. Because of the dangers resulting from leakage, losses will be kept as low as is economically possible and generally can be considered to have negligible cost.

Helium on the other hand is difficult to contain and continuous effort is necessary to prevent high leakage rates. The total inventory (cryogenic cooling) is about 700,000 liters (liquid) costing $854,000. A typical loss of 5% per year would cost $43,000/yr.

Because sodium costs only $0.25/lb and because leakage is kept to a low level for safety reasons the annual cost due to loss of sodium is considered to be negligible.

Working capital requirements

The working capital is the amount of money that must be on hand to pay day-to-day expenses or has been expended to purchase inventories of materials and supplies. The interest payment on the working capital generally is paid for in the annual return on capital and is not included in the O & M costs. Consequently, it will not be included in the O & M costs for UWMAK-II.

Total operations and maintenance costs

The total O & M costs are summarized on Table VII-B-6. The general and administrative costs were calculated during preparation of that table.

b. Fuel Costs

The UWMAK-II operates on a mixture of 50 percent D_2 and 50 percent T_2. Because the breeding ratio is greater than 1.0, a surplus of T_2 will exist after start of routine operation. The excess T_2 will have to be disposed of by sale to other fusion reactors which are just starting to operate, by storage, or by release to the atmosphere. In this study, it is assumed that a surplus of T_2 will exist so that it has essentially zero value. In that case, there is no fuel purchase cost for the T_2.

The D_2, on the other hand, will have to be purchased at the current market price of about $440 per kg ($200 per lb). The quantity of D_2 burned per year is about 140 kg. If a fifty percent loss occurs during the numerous recycles through the reactor, divertors, and fuel fabrications, the annual cost would be about $123,000.

Because the fuel pellets are fabricated on site, the cost for fabrication is included in the O & M costs. The fuel cost normally includes only the cost of the fuel as delivered to the site.

The total fuel cost is about $123,000 per year.

c. The Annual Return on Capital

Many of the costs for producing electricity can be related directly to the total capital cost for the plant. Examples are the real estate taxes, the interest on bonds, the dividends on stocks, insurance and unusual maintenance costs. Normal financial practice is to sum all such costs for a utility and then calculate a percent annual return on capital that will pay for these costs.

Table VII-B-6

UWMAK-II Operations & Maintenance Costs

Cost Item	Annual Cost
Salaries, including fringe benefits	$1,350,000
Miscellaneous supplies and equipment	1,000,000
Outside support services	1,150,000
Miscellaneous costs	200,000
Sub total	$3,700,000
General and Administrative (15% of above)	570,000
Replacement inner walls (annual share)	50,264,000
Coolant makeup (Li, Na, He(liq) He(gas))	43,000
Total annual cost	$54,577,000

The annual return on capital depends primarily on the financial structure of the utility and on the amount of taxes that it must pay. The normal range is from 12 to 18 percent for private utilities and from 6 to 9 percent for public utilities.

Assuming a typical 15 percent annual return on the capital cost for a private utility (see Table VII-B-7) results in an annual cost of approximately $242,193,000 for UWMAK-II.

d. The Total Electricity Cost

If the UWMAK-II operates at an eighty percent plant factor, the annual electricity production would be about 1.20×10^{10} kwh/yr. Summing the costs for that reactor results in the following total costs and unit cost for the electricity production.

Table VII-B-7

UWMAK-II Electricity Costs

Cost Item	Annual Cost	Unit Cost (mills/kwh)
Operations and Maintenance	$54,577,000	4.55
Fuel	123,000	0.01
Return on Capital	242,193,000	20.18
		24.74

VII-B-5. Summary and Critical Analysis

One benefit of a conceptual fusion power plant design study is the identification of major costs and potential methods for reducing the electricity unit cost. This provides the guidance required by the next generation of fusion power plant design studies. This section analyzes the UWMAK-II design and costs to determine potential methods for reducing the electricity unit costs.

The main cost estimates which result from this study are that the capital cost for UWMAK-II is about $950/kWe and that the electricity production costs are about 25 mills/kwh. A general analysis of the UWMAK-II costs reveals eight major cost parameters that contributed to the relatively high electricity costs:

1. Low inner wall neutron flux
2. Low thermal efficiency (~36%)
3. Use of beryllium as a neutron multiplier.
4. Short inner wall life
5. Intermittent reactor operation
6. High shield and magnet costs
7. High neutral beam injector costs
8. Use of stainless steel

Each of these cost parameters will be briefly discussed to demonstrate potential methods for reducing the electricity unit costs.

a. Low Inner Wall Neutron Flux

The power density in the reactor chamber currently is restricted to about 1 MW/m^2 to prevent the inner wall lifetime from becoming less than two years. The result is four weeks of outage time per year for wall replacement. If the reactor power density were increased, the amount of electricity produced probably would increase at a faster rate than the capital and operating costs until an optimum power density (resulting in the minimum electricity unit cost) would be reached. Several higher power densities should be investigated until the optimum power density is identified.

b. Low Thermal Efficiency

UWMAK-II has a thermal efficiency of 36 percent because stainless steel is used as the blanket structural material. This restricts the maximum permissible He coolant outlet temperature. The use of other structural materials could permit higher coolant temperatures and higher thermal efficiencies. Of course, the problem of having an established industry surrounding other metals, such as refractories, is a serious problem which led us to the choice of stainless steel in the first place.

c. Use of Beryllium Neutron Multiplier and Lithium Aluminate as a Stationary Breeding Material

The use of beryllium increases costs two ways: (1) A high initial capital cost, and (2) A high blanket replacement cost. The initial capital cost is about

$100,000,000 for beryllium, or about 7% of the direct capital costs. The corresponding return on capital is about 1.2 mills per kwh. Because of the high beryllium cost (and its scarcity as a resource) recovery and reuse of the beryllium is necessary whenever the inner wall sections are replaced. This recycling is estimated to cost about 3.3 mills per kwh for operating costs and return on capital investment. Total beryllium cost is about 4.5 mills per kwh.

Use of other neutron multipliers, particularly low cost ones that could be discarded after use, could result in a substantial electricity cost reduction. However, aside from fissionable materials, no element is as effective as Be because of its low (n,2n) threshold energy.

Use of a stationary breeding material (and the neutron multiplier) results in a total capital cost of about $200,000,000 (2.4 mills per kwh) plus an annual wall replacement cost of about $43,000,000 (3.6 mills per kwh). Mobile breeding materials would cost much less.

d. Short Inner Wall Life

Neutron damage to the stainless steel inner wall results in an estimated two year useful life for UWMAK-II conditions. The use of a better material could result in a longer life and less outage time for wall replacement. Alternatively, a higher average reactor power density can be employed. This is really a statement that much further work is required on alloy development.

e. Intermittent Reactor Operation

UWMAK-II has a ninety minute burn period followed by a 5.5 minute rejuvenation period. This rejuvenation period reduces the plant factor and results in the need for a sodium intermediate loop plus the thermal energy storage system. Continuous operation probably would make the sodium and thermal energy storage system unnecessary. A higher thermal efficiency would be possible and the capital cost would be decreased by approximately $120,000,000 (an electricity cost reduction of about 1.5 mills per kwh).

f. High Shield and Magnet Costs

The shield and magnets have a total construction cost of about $400,000,000. A substantial cost reduction might result from the use of less costly materials or development of more effective magnet designs. Also, since the sizes and costs of the shield and magnet are interrelated, several material and size combinations should be investigated.

g. High Neutral Beam Injector Costs

The neutral beam injectors cost $80,000,000 based on 200 MW of capacity and a cost of $0.40 per watt. Less costly designs should be developed and reactor startup methods using less neutral beam capacity should be investigated. In

particular, a comparison between neutral beam heating and RF, from both a physics and estimate cost standpoint, should be performed.

h. Use of Stainless Steel

Stainless steel is used as the primary structural material in the reactor because it is a non-magnetic material. Other, less costly, structural materials should be investigated. This is also suggested by the potential problem associated with Cr resources, as discussed in Section VII-A.

Appendix A

Basis for Capital Cost Estimates

Account Number	Account Title and Estimating Philosophy	Quantity	Unit Cost	Total Cost	Reference Document
20	Land and Land Rights Same as for a PWR	500 acres	$2400	$1,200,000	WASH 1230 (Vol. 1)
21	Structures and Site Facilities				
211	Site Improvements and Facilities			8,000,000	
212	Reactor Building	*			
213	Turbine Building	*			
214	Intake & Discharge Structures	*			
215	Reactor Auxiliaries Building	*			
218	Miscellaneous Building	*			
22	Reactor Plant Equipment				
221	Reactor Equipment of spare reflector elements included				
221.1	Magnets (see attachment)			$229,700,000	
--1.2	Shield				
	316 S.S.	4665 MT	8.80	$41,051,000	
	B_4C	5762 MT	3.00	$17,286,000	
	Pb	20,799 MT	0.60	$12,479,000	
				$70,816,000	
221.3	Blanket Estimated by McDonnell-Douglass			$193,750,000	
	Graphite Cloth			100,000	
221.4	Neutral Beam Injectors	200 MW	$0.40/watt	$80,000,000	
221.5	Equipment Foundations and Supports	2200 MT	$8.80/kg	$1,940,000	
	SS super insulation	622 m^2	$180/$m^2$	110,000	
221.6	Vacuum Wall	400 MT	$3.30/kg	$1,320,000	
222	Neon Heat Transfer by Transport System				
222.1 to 222.15		*			
222.16	Tritium Extraction				
	Molecular Sieve			$400	
	Pumps, Blowers, and Heaters			5,700	
				6,100	

*means information must be provided by others

222.21 to 222.24			*	
222.25	Clean-up			
	Zr.	15,000 kg	$45/kg	$690,000
	Filtration System	(design unknown)		649,000
				$1,339,000
222.26	Tritium Extraction	4,060 kg	$330/kg	1,340,000
222.31 to 222.33			*	
222.34	Clean-up Systems			
	Zr	10^4 kg	$45/kg	$450,000
	Filtration system			250,000
				$700,000
222.35 to 222.37			*	
222.38	Tritium Extraction	2030 kg	$330 kg	$670,000
223	Auxiliary Heating Systems			
223.1	Shield Cooling			
223.11	Pumping	12 pumps	$31,000	$372,000
223.12	Piping (Estimated pipe length and size)			$212,000
223.13	Heat Exchangers	12 units	$42,000	$492,000
223.14	Purifications(filter systems and tanks)			$ 36,000
223.15	Lithium extraction (yttrium cost)	80kg	$330/kg	30,000
223.2	Magnet Cooling Systems			
223.21	Cryogenic System	24 kw	$583,000/kw	$13,990,000
223.22	Piping (Estimated pipe length and size)			250,000
223.23	Transport systems (cryogenic pump costs			250,000
223.24	Tanks 200,000 liter tank			50,000
224	Radioactive Waste Treatment & Disposed			WASH 1230 (Vol. 1)
224.1	Liquid Radwaste System			
	Waste Holdup Tank			$33,000
	Sump tank			4,000
	Sump pump and motor			8,000
	Disposal pumps and motors			3,000
	Waste evaporator			132,000
				$180,000

224.2	Gaseous Rodwaste System - No special equipment required				
	Tritium extraction equipment and filters indicated in room ventilation costs.				
224.3	Solid Radwaste system - Same as for PWR			$90,000	WASH 1230(Vol. 1)
224.4	Wall liner disposal equipment	3 crushers		$20,000	$60,000
225	Fuel Handling & Storage Systems				
225.1	Used Fuel purification system 2-50 kg/day Cryogenic stills			$55,000	$110,000
225.2	Liquefication Heat exchange systems (50 kg/day)				$190,000
225.3	Pellet Fabrication 50 kg/day capacity				$340,000
225.4	Pellet Injection design uncertain				1,480,000
225.5	Storage equipment 200 kg gas and 200 kg liquid				100,000
226	Other Reactor Plant Equipment				
226.1	Inert gas systems - nitrogen only 4 times the capacity at a PWR			$163,000	WASH 1230 (Vol. 1)
226.2	Special heating systems Estimated pipe lengths, electric and steam capacity			$1,100,000	
226.3	Cooling receiving, storage and makeup systems				
	Helium tanks	1,200,000 ft^3		$973,000	"
	Pumps			150,000	
	Lithium	5,000 gallon tank		22,000	
	Sodium	2,500 gallon tank		27,000	
226.4	Fluid leak detectors	100	$400	40,000	
226.5	Auxiliary Cooling Systems	150% of PWR cost		2,300,000	
226.6	Maintenance equipment				
	Mobile lift machines	4	$250,000	$1,000,000	
	Portable grinders, welders, brazers, impact wrenches and other tools	8 sets	$100,000	800,000	
	Maintenance and inspection cab			50,000	
226.7	Building vacuum systems				
	10,000 cfm blower @ 12 psi head			100,000	
	1,000 cfm blower @ 30 torr head			10,000	
	tritium extraction system			240,000	
226.8	Core vacuum system				
	Cryopumps	192	$14,000	$2,690,000	
	Hy diffusion pumps	192	$8,500	1,640,000	
	Roots blowers	384	$5,443	2,090,000	
	Forepumps	96	$3,780	360,000	

	Piping			$600,000	
227	Instrumentations and Control	200% of PWR costs		$11,700,000	WASH 1230 (Vol. 1)
228	Fossil-Fueled Backers and Superheaters	none required			
23	Turbine Plant Equipment	*			
24	Electric Plant Equipment	*			
25	Miscellaneous Plant Equipment				
251.11	Turbine Hall 175/25 ton cranes	2	$262,000	$525,000	
251.2	Reactor Hall 200/35 ton remote	1	500,000	500,000	
251.3	Numerous miscellaneous items			575,000	
251.4	Inductive coil building crane (150/10 ton)		300,000	300,000	
251.5	Blanket storage cell trolleys	20	40,000	800,000	
251.6	Blanket rejuvenation equipment				
	Remote grinding, welding, cutting equipment plus Be and $LiAlO_2$ rejuvenation equipment			$5,000,000	
251.2-0.6	Mobile equipment			50,000	
252	Air and water service systems				
252.1	Air systems	150% of PWR		$460,000	
252.2	Water systems	150% of PWR		3,400,000	
252.3	Auxiliary heating boilers	150% of PWR		1,800,000	
253	Communications Equipment	125% of PWR		220,000	
254	Furnishings and Fittings	150% of PWR		480,000	
26	Special Materials				
261	Moderator	none required			
262	Reflector	none required			
263	Reactor Coolant and cryogenic systems				
	Helium	700,000 l	$1.22/l	$854,000	
	Lithium	190,000 kg	10/kg	1,909,000	
264	Intermediate Coolant (sodium)	5.2×10^6kg	$0.55/kg	2,850,000	
265	Turbine Cycle working fluids	no special fluids			
266	Other Materials				
	Deuterium	80 kg	$440/kg	$35,200	
	Nitrogen	688,000 l	0.25/l	172,000	
91	Construction facilities, equipment and services				
911	Design engineering	150% of PWR cost		$24,300,000	
92	Engineering Services				
921	Design engineering	200% of PWR cost		$23,100,000	
922	Other	150% of PWR cost		$25,400,000	

93	Other Costs			
931	Taxes and Insurance	10% of material costs		
932	Staff Training & Plant Startup	150% of PWR costs	$900,000	WASH 1230 (Vol. 1)
933	Owners G & A	150% of PWR costs	$4,900,000	
94	Interest During Construction			
941	Physical Plant	8% for 5 years		
942	Land and Land Rights	8% for 6 years	$704,000	
943	Special Materials	8% for 1 year	$466,000	

VIII. General Conclusions of the UWMAK-II Study

The general conclusions reached as a result of the UWMAK-II Tokamak conceptual reactor study are summarized by major subject areas. By and large, the conclusions described here are the major ones and are discussed in general terms so that specific numerical results are not usually given. For more specific details on the analysis which led to these conclusions, on other conclusions not presented in this section, and a more elaborate discussion of the conclusions themselves, the reader is referred to the individual chapters of the report. The subject areas were subdivided to follow the chapter and section headings within the report itself.

A. Plasma and Divertor

The analysis of the plasma and divertor in UWMAK-II led to the general conconclusions listed below:

1. The predictions of microinstability theory regarding trapped particle instabilities, which are crude but hopefully pessimistic, nevertheless do predict that reactor grade plasmas can be produced in systems like UWMAK-II. The average temperatures are in the optimum range of 10-20 keV and the equilibria are thermally stable against temperature fluctuations. The $n\tau_E$ values are adequate for ignition and the fractional burnup is generally about 5%. Should plasma scaling laws prove to be somewhat more optimistic than the trapped ion mode scaling, plasma $n\tau$ and fractional burnup values will increase but thermal stability may become a more difficult problem, as discussed in the UWMAK-I study.

2. The diffusivity and thermal conductivity increase inversely with density in the trapped ion regime. This influences neutral beam injection heating because one cannot lower the average density, for example, to 1-2 x $10^{13}cm^{-3}$, to improve beam penetration. The reason is that the transport induced particle losses increase too rapidly and prevent the plasma from reaching ignition. For UWMAK-II, this minimum density is about 4 x $10^{13}cm^{-3}$. In addition, the relatively high loss rates associated with trapped particle mode predictions implies that the neutral beams system must be in the 500 keV range (D°) for penetration and at the 100-200 MW level for rapid heating.

3. For heating only, a viable alternative is to heat a 50-50 D-T target plasma with neutral <u>hydrogen</u> (H°) beams of about 250 keV while simultaneously fueling the plasma with cold, D-T pellets. The hydrogen will not dilute the D-T mixture by more than 10% over the heating phase. This is subsequently reduced to negligible amounts in a few τ_p once the neutral beams are turned off. For such a heat up scenario, the requirements for a reactor system are 200-300 keV H° beams at the level of 10-15 MW per beam and 100-200 MW total injected energy.

4. Detailed MHD calculations including the plasma current distribution show that equilibria can be found that are stable against local flute modes and which have q(o) greater than 1 even with null points on the plasma boundary.

5. The design decision to use vertical field coils that are inside the toroidal field magnets is very attractive and can reduce the stored magnetic energy in the poloidal field by more than an order of magnitude (for example,

from 15 MW-hr in UWMAK-I to 1 MW-hr in UWMAK-II). When combined with "extended D" toroidal field magnet designs, this approach also allows adequate space for blanket module removal.

6. The analysis of mirror instabilities in the divertor zone plasma shows that particles should flow to the divertor at some fraction of the ion sound speed. The mirror microinstabilities imply that a shielding divertor will not be possible, especially if maintaining high (several keV) or intermediate (several hundred ev) edge temperature is also important.

7. The divertor zone is expected to ionize approximately 15% of the wall sputtered impurities. Ionized impurities should be swept to the collector plates due to ion-impurity viscosity as well as the electrostatic field along B field lines.

8. The use of a low Z liner together with a divertor may be essential for long burn times should impurities accumulate in the plasma. A low Z liner made of graphite or graphite fibers operating at ~1000°C appears to be compatible with the reactor environment and to have acceptably low chemical and physical sputtering removal rates.

9. The particle leakage rates predicted by trapped ion modes lead to unacceptably high heat fluxes in particles to the divertor. The estimate in UWMAK-II is ~700 MW in particles delivered to the divertor. Collecting this energy remains an essentially unsolved problem. If impurities do not accumulate with time, they enter near the plasma edge and will serve to radiate energy to the first wall. This will lower the energy leaving the plasma in charged particles and alleviate the collection problem to some extent. Details here remain to be worked out.

10. The problem of fueling, which was not analyzed in detail in this report, remains an important problem for reactors. Experiments are needed to provide guidance for the development of theoretical models. At the particle leakage rates anticipated, refueling by neutral beams is unacceptable from a power balance point of view even if relatively nonpenetrating beams in the 100 keV range are used. Cold particle fueling thus appears essential for long burn times.

B. Magnets

The magnet analysis and design has led to the following major conclusions.

1. The modified constant tension "D" shaped toroidal field (TF) magnets, in which the outer leg of the coil is extended several meters beyond the end of the blanket and shield into the low field region, produces a significant increase in space and eases the problem of blanket accessibility and removal. In addition, it allows the vertical field (VF) coils to be placed inside the TF windings. This reduces the stored magnetic energy in the poloidal field by more than an order of magnitude compared with VF coils outside "D" shaped TF magnets. The reduced costs of the VF coil systems tend to offset the increased cost of the "extended D" TF magnets such that the combined cost for the total OH, VF, and TF system is about the same as that for a constant tension "D" TF coil set with VF windings on the outside. The greatly increased space available allows design flexibility and easier blanket handling and therefore makes the "extended D" TF coils design a very attractive feature.

2. Magnetic fields of about 35-40 kG on axis are adequate for Tokamak power reactors with circular cross section plasmas that have neutron wall loadings of less than about 2 MW/m^2. Therefore, viable low aspect ratio machines require only NbTi as the superconductor.

3. All NbTi superconducting coils are designed for complete cryogenic stability using Cu as the stabilizer. This is the only viable design at the present time that has the potential for very high reliability in operation, a critical requirement in experimental and power reactors.

4. A shell structure built between the TF coils can be made to serve as both a secondary vacuum wall and as a lateral support structure to protect against the failure of one or two adjacent TF coils.

5. It appears feasible to set up a special rail to wind the divertor coils in place inside the TF magnet set.

6. Large ac losses in the poloidal field coils during a 10 second plasma current rise requires the use of a higher resistivity for part of the matrix for the conductors in the OH and VF coils.

7. The power supply for a 10 second current rise can be a superconductive inductor energy storage unit of about 1 MW-hr rating. This is within present technological capability for both the coils and the switching system and can follow the design developed by the University of Wisconsin and the Fermi National Accelerator Laboratory for the NAL energy storage system.

C. Blanket and Shield Design

Analysis of the blanket and shield design has revealed the following major conclusions.

1. A stainless steel blanket can be constructed to utilize helium cooling of a solid breeder material. The use of an outer bank of thin walled coolant channels is necessary to accomodate the high thermal stresses due to the high thermal expansion coefficient and low thermal conductivity of steel. The maximum stress can be maintained at $\lesssim$8 ksi barring structural inhomogeneities or inhomogeneities in the radiation environment.

2. A method for disassembling the shield and blanket structure has been developed that requires the heaviest component moved to be less than 175 metric tonnes. This is in contrast to ~3600 metric tonnes for UWMAK-I. However, the equipment for remote disassembly and assembly has not been fully described at this time.

3. A fabrication and reprocessing scheme has been developed for the complex geometry of solid breeding systems. The use of forgings, while economic, may not be compatible with the desire for highly cold worked structures from the radiation damage standpoint. Techniques for separating beryllium from nonmagnetic steel and $LiAlO_2$ need to be developed as well as remote Be metal processing equipment.

D. Radioactivity

There are two major components of the radiological problems for UWMAK-II, the tritium and induced structural activity. The following major conclusions can be drawn from the investigation of tritium.

1. The use of a neutron multiplier (e.g. Be) is essential if the breeding ratio is to exceed one. The use of Be produces a significant cost penalty both in initial capital investment of the Be and also in processing facilities.

2. Even with the use of a neutron multiplier, the lithium in $LiAlO_2$ must be highly enriched to allow a BR of greater than 1. This creates a false sense of a low inventory system. However, if one calculates the total amount of lithium that must actually be removed from the ground, and accounts for the fact that solid $LiAlO_2$ is probably not recyclable as liquid Li would be, then one finds that the total amount of Li mined for a reactor like UWMAK-II is actually 3 times that required for a reactor like UWMAK-I which used Li as both the coolant and breeder.

3. The tritium inventory in the $LiAlO_2$ is a very sensitive function of particle size and it has been necessary to postulate the use of very small (~20 micron diameter) particles to keep the inventory to an acceptable level. However, due to the low thermal conductivity, it is anticipated that the temperature in the solid breeder zone may exceed 1000°C. Such a high temperature will certainly promote sintering over a 10,000 to 20,000 hour time period and when coupled with radiation induced sintering may produce tritium inventories in the neighborhood of 10's of kg in the blanket. Hence sintering could negate the very reason for using a solid breeder material.

4. Due to the low thermal conductivity of $LiAlO_2$ and the subsequent high temperature gradients, the tritium concentration in the breeder will be a highly variable quantity. It has been calculated that the outer layer (~10%) of a breeder rod could actually contain 90% of the tritium and this may be 10 times that calculated by using the average temperature. The problem here is that to reduce this inventory would require raising the centerline temperature of a breeder rod, thus promoting more sintering which, in turn, might promote a higher inventory.

5. If the inventory of the partial pressure of tritium in the breeding zone can be kept to $<10^{-4}$ torr, then the tritium leakage to the steam cycle can be held to less than 1 curie/day by cleaning up the main helium coolant stream with oxygen and the secondary coolant stream with yttrium traps. We have not been able to completely assess the amount of tritium leaking out of the main coolant pipes to the building but it is assumed that this tritium can be easily recovered.

6. While considerable emphasis is placed on determining and lowering tritium in the blanket, very little attention is paid to the tritium flowing through the plasma chamber. Due to the low burnup, approximately 12 kg of unburnt tritium must be collected per day, extracted, purified and re-injected into the reactor. It appears that a one day turn around time is not unreasonable here and that the major inventory problem in UWMAK-II (as it was in UWMAK-I) is that tritium in the exhaust stream. We feel that more attention must be given to this aspect of the system because it can be much larger than the blanket inventory.

7. The tritium inventory is also very sensitive to the amount of T_2 which must be kept in reserve to counter the failure of processing or extraction equipment. For example, if the entire divertor T_2 processing equipment failed one day, we would have to have ~12 kg in reserve. This would amount to ~1 kg/day for the blanket system. How many days could (or should) one plan for such events under commercial operation? Ten days would amount to over a hundred kg of T_2, perhaps an unreasonable number. Hence, some thought should be given to the reserve quantities required due to equipment failure, in a mode which would not cause the release of tritium to the environment.

The basic conclusions of the induced radioactivity section of UWMAK-II are:

1. The radioactivity of UWMAK-II is slightly higher than UWMAK-I because of the higher fraction of steel used in the blanket. The general activity levels still approach 10^6 Ci/MW_{th} after two years of operation. The activity takes a relatively long time (~10 years) to decay by a factor of 10 meaning that remote maintenance of all the blanket modules is absolutely necessary.

2. Calculations of the biological hazard potential (BHP) reveal that it is ~10^2 km^3 of air/kw_{th} after two years of operation and decays in roughly the same manner as the radioactivity. However by 100 years after shutdown it has decayed to 10^{-3} km^3/kw_{th}. This indicates that long term storage facilities will have to be constructed to hold failed components or those steel components changed for precautionary reasons.

3. The afterheat of UWMAK-II represents ~1% of the thermal power level, or ~50 MW. However, this afterheat is spread out over a large mass and afterheat densities of <0.1 watt/g are present in the blanket. Such low values do not seem to present a significant problem even in the event of a loss of coolant.

4. The use of V-20 Ti or Nb-1 Zr would not significantly alter these results at shutdown, nor up to decay times of ~100 years. Thereafter the V-20 Ti system would decay somewhat faster while the Nb-1 Zr system would stay constant due to the Nb-94 activity ($t_{1/2}$ = 20,000 years). This means that there is currently no overwhelming reason to depart from 316 SS on the basis of radioactivity or afterheat for reasonable engineering materials. (We do not consider the use of aluminum alloys above 200°C as a technically feasible system.)

F. Radiation Damage

The analysis of the interaction of the solid materials in UWMAK-II with the D-T plasma environment has led to the following major conclusions.

1. The carbon cloth used to protect the plasma and first wall will have a finite lifetime if it is operated at ~1000°C. A rough estimate of its lifetime is ~2 years before run away swelling may occur. Experiments need to be performed to determine the influence of high helium contents (~4000 to 5000 appm He) on the dimensional stability.

2. A structure which uses cold working to reduce swelling must be very carefully designed to minimize the number of welded zones. The existence of annealed and cold worked zones in high flux positions will produce large swelling gradients that could induce unacceptable stresses or strains in one year or less

of UWMAK-II exposure. Radiation induced creep may reduce these stresses but the maximum dpa rate of 3.4×10^{-7} sec^{-1} is rather low compared to fast reactors where most of the current data originates and careful analysis of this effect is required.

3. The degree of safety factors on stress in the vacuum walls for fusion reactors must be determined. For example the lifetime of a component can not be determined by the average stress value because some parts of a component will be subject to higher values due to machining inhomogeneities, hot spots in the breeding material, coolant flow irregularities, etc. Such stress intensification could cause much shorter lifetimes, perhaps even below the minimum value determined by other factors such as swelling, high strain rate ductility or fatigue life. A careful assessment of the consequences of 50-100% increases in the calculated stress on wall lifetimes should be made in all future reactor designs.

4. The effect of high helium production and moderate dpa rates on the high strain rate ductility of 316 SS needs to be understood. Current data is somewhat ambiguous in that some data shows that low uniform elongation values are reached after a few months of typical UWMAK-II operation while other data indicates relatively no effect for 1 to 2 orders of magnitude increase in the damage level. Unfortunately all of the data shows that post irradiation ductility of 316 SS is reduced to uncomfortably low values in the 550-650°C region. It will be extremely important to determine how the application of cyclic stresses affect these ductility values and to that end, reactor tests need to be conducted as soon as possible.

5. This study could not determine the lifetime of the first wall based on fatigue considerations because there is simply no data and no acceptable theories available (even on post irradiation behavior). Such studies need to be designed to closely duplicate the actual temperature, stress, damage, and transmutation conditions in a fusion reactor for a wide range of materials.

6. The major problem with the use of $LiAlO_2$ as a breeder for tritium is the production of large amounts of helium gas. This requires that the initial density of the breeder be low to accomodate the swelling without imposing undue stresses on the container walls. Experimental information in this area is not presently available and must be determined before designers can use such a concept even in an experimental reactor.

Another factor in the use of solid breeders is the extent of radiation induced sintering. If this is large enough the diffusion path of the tritium may be considerably extended resulting in unacceptably large tritium inventories. These experiments must be done in situ, that is, the material must be irradiated at temperature, not simply irradiated at low temperature and then annealed out of reactor.

7. A major limitation to the use of Be as a neutron multiplier in a fusion reactor is also its tendency to produce large amounts of helium gas and the subsequent swelling induced by that gas. This requires a reduced density (hence increased thickness of the blanket and magnet systems) and produces a finite useful lifetime. The high cost of Be and its scarce availability means that one will have to find ways of reprocessing the radioactive Be (mainly due to impurities and contamination by tritium). In general, ways of avoiding the use of Be should be found whenever possible.

8. The radiation damage produced in graphite reflectors operated at 650°C may require that material to be changed every 10 years or so to avoid excessive growth. It would be highly desirable to develop graphite which can withstand equivalent fission neutron exposures of up to $10^{23} n/cm^2$ without entering the breakaway swelling region.

9. The design of the shield in UWMAK-II has reduced the radiation damage to the magnet materials (thermal and electrical insulator, stabilizer and superconducting elements) to a level far below the known threshold for serious consequences. However, continual monitoring of low temperature irradiation data is required to insure that such a design is indeed sufficient.

F. Power Cycle

The analysis of the power cycle produced a detailed conceptual design and the following conclusions.

1. A He-Na-Steam power cycle as utilized on UWMAK-II appears feasible but a He-Na primary heat exchanger would have to be developed. The gross efficiency of the cycle is about 38%. The use of four primary loops for the blanket coolant has clear economic advantages over the twelve loops (one for each main module) used in the UWMAK-I study.

2. The heat in the divertor is low grade but it is feasible to generate electricity through a Li-Na-Steam cycle. The efficiency is about 25%. Nevertheless, when combined with the high gross efficiency of the primary coolant power cycle, an overall plant efficiency of 36% is possible.

3. The cyclic nature of Tokamak reactor operation imposes unique design problems on the energy conversion system. It is necessary to devise a system that allows continuous turbine operation and power output. After a study of various alternatives, the use of liquid sodium from the intermediate loop as the energy storage medium in the form of a "thermal flywheel" provides the greatest number of advantages. For a 5000 MW(th) system with a cycle as in UWMAK-II, the energy stored in hot liquid metal amounts to about 430 MW hr and the continuous electric output is 1716 MW.

4. In addition to energy storage, an intermediate sodium loop helps to minimize tritium permeation into the steam cycle and allows the adaptation of fast reactor power conversion technology.

G. Plant Design Considerations

The present study is an initial assessment of the problems associated with the plant design for Tokamak-type reactor plants in general and the UWMAK-II reactor plant in particular. The design and analyses are conceptual in nature. Many of the systems and associated equipment are not defined in detail and some of them probably have not yet been identified. Allowances have been made to accomodate these unknowns and uncertainties, but until more detailed design and analysis is done, these uncertainties remain. On the basis of the present study, the following comments are in order:

1. The plant layout including equipment and piping arrangement is preliminary. Further study is needed to detail and improve the arrangements. The

primary piping arrangement is a critical aspect of the plant layout and can have a large impact on building costs. No consideration has been given to the arrangement of the reactor internal piping or its interface with the external primary piping systems.

2. Use of large size piping for transporting high temperature helium gas may be of some concern. Internally insulated piping has been proposed but no thermal stress analysis has been performed. Application of internal ceramic insulation is within the state-of-the-art, but the feasibility of using such pipe has to be investigated in this particular service.

3. Reactor maintenance problems, especially in regard to blanket removal, constitute another area where only preliminary consideration has been given. A conceptual blanket handling scheme is proposed but further studies are needed to evaluate the feasibility of the concept and develop procedures and conceptual equipment designs.

4. Analysis of the effects of magnetic fields (generated by toroidal field coils) on plant equipment and components is necessary. To avoid interference with the magnetic field or to avoid large transient stresses in the coolant system, non-magnetic materials are needed for helium piping and the containment liner.

5. The detailed equipment requirements for the Hot Cell, Reprocessing Building and Fabrication Building have not been defined. Concepts for handling the blanket sections, disassembling and processing the irradiated front wall and fabrication and reassembling the new front wall must be developed.

6. The underground circular railroad arrangement shown for handling and storing spent and rebuilt blanket section is conceptual in nature. A careful study is needed to establish the feasibility of the concept and to study the trade-offs with other possible concepts.

7. Details have to be worked out to determine an acceptable method of storing solid radioactive wastes. Several alternatives are possible such as: on-site storage versus off-site shipment, above-ground storage versus buried vaults, air-cooled versus forced convection systems.

8. The structures in this plant are significantly larger than those in fission power plants. All the structures are very massive because of shielding and other safety requirements. The conceptual design, as described, is considered to be a feasible design consistent with current technology and industry practice but may be subject to objections from environmentalists on the basis of aesthetic qualities.

H. Materials Resources

One benefit of a conceptual design is to provide a basis for estimating system requirements that might not be noticed otherwise. This is particularly true of materials requirements and the analysis of the materials requirements implied by a 10^6 MW_e economy of UWMAK-II type reactors together with a comparison of present and projected resources and production capacity has led to two specific conclusions.

1. Low β circular Tokamaks with low power density are large volume systems requiring large quantities of materials, particularly Fe, Pb, Cu, Na, Cr, and Ni. Except for Fe and possibly Mo, the metals for 316 SS present problems or possible problems of availability. In terms of domestic resources, chromium is an especially serious problem. The large requirement or copper for UWMAK-II type magnets in a well developed ($\sim 10^6$ MW_e) fusion economy is 4.5 times U.S. 1974 production of new copper and thus presents a serious procurement problem. Lead presents a similar problem of procurement. Niobium availability is likely to depend heavily on access to supplies of Nb from sources outside the U.S.

2. The use of lithium aluminate as a breeder requires the use of beryllium as a neutron multiplier. Information on beryllium reserves and resources is uneven in quality and is incomplete. Nevertheless, there have been extensive explorations and it is clear that the target amount of Be for a 10^6 MW_e system of UWMAK-II type reactors is out of all proportion to the size of known reserves both within the U.S. and in the world.

I. Economics

Another benefit of a conceptual fusion power plant design study is the identification of major costs and potential methods for reducing the electricity unit cost. This provides the guidance required by the next generation of fusion power plant design studies. The main cost estimates which result from this study are that the capital cost for UWMAK-II is about $950/kWe and that the electricity production costs are about 25 mills/kwh. A general analysis of the UWMAK-II costs reveals eight major cost parameters that contributed to the relatively high electricity costs:

1. Low First Wall Neutron Wall Loading

The 14 MeV neutron wall loading is currently restricted to about 1 MW/m^2 to prevent the inner wall lifetime from becoming less than two years. The result is four weeks of outage time per year for wall replacement. If the reactor power density were increased, the amount of electricity produced probably would increase at a faster rate than the capital and operating costs until an optimum power density (resulting in the minimum electricity unit cost) would be reached. Several higher power densities should be investigated until the optimum power density is identified.

2. Low Thermal Efficiency

UWMAK-II has a thermal efficiency of 36 percent because stainless steel is used as the blanket structural material. This restricts the maximum permissible He coolant outlet temperature. The use of other structural materials could permit higher coolant temperatures and higher thermal efficiencies. Of course, the problem of having an established industry surrounding other metals, such as refractories, is the serious problem which led us to the choice of stainless steel in the first place.

3. Use of Beryllium Neutron Multiplier and Lithium Aluminate as a Stationary Breeding Material

The use of beryllium increases costs two ways: (1) A high initial capital cost, and (2) A high blanket replacement cost. The initial capital cost is

about $100,000,000 for beryllium, or about 7% of the direct capital costs. The corresponding return on capital is about 1.2 mills per kwh. Because of the high beryllium cost (and its scarcity as a resource), recovery and reuse of the beryllium is necessary whenever the inner wall sections are replaced. This recycling of radioactive Be is estimated to cost about 3.3 mills per kwh for operating costs and return on capital investment giving a total beryllium cost of about 4.5 mills per kwh.

Use of other neutron multipliers, particularly low cost ones that may be discarded after use, could result in a substantial electricity cost reduction. However, aside from fissionable materials, no element is as effective as Be because of its low (n,2n) threshold energy.

Use of a stationary breeding material (and the neutron multiplier) results in a direct capital cost of about $200,000,000 (2.4 mills per kwh) plus an annual wall replacement cost of about $43,000,000 (.36 mills per kwh). Mobile breeding materials would cost much less.

4. Short Inner Wall Life

Neutron damage to the stainless steel inner wall results in an estimated two year useful life for UWMAK-II conditions. The use of a better material could result in a longer life and less outage time for wall replacement. Alternatively, a higher average reactor power density can be employed. This is really a statement that much further work is required on alloy development.

5. Intermittent Reactor Operation

UWMAK-II has a ninety minute burn period followed by a 5.5 minute rejuvenation period. This rejuvenation period reduces the plant factor and results in the need for a sodium intermediate loop plus the thermal energy storage system. Continuous operation would make the sodium and thermal energy storage system unnecessary if the T_2 leakage can be minimized and if one is willing to have radioactive primary coolant in contact with the steam. A higher thermal efficiency would then be possible and the capital cost would be decreased by approximately $120,000,000 (an electricity cost reduction of about 1.5 mills per kwh).

6. High Shield and Magnet Costs

The shield and magnets have a direct construction cost of about $400,000,000 or $235/kW$_e$. A substantial cost reduction might result from the use of less costly materials or development of more effective magnet designs, such as using strong Al alloys instead of SS for the coil former. Also, since the sizes and costs of the shield and magnet are interrelated, several material and size combinations should be investigated.

7. High Neutral Beam Injector Costs

The neutral beam injectors cost $80,000,000 based on 200 MW of capacity and a cost of $0.40 per watt. Less costly designs should be developed and reactor startup methods using less neutral beam capacity or alternate and possibly less expensive heating methods should be investigated. In particular, a comparison between neutral beam heating and RF, from both a physics and estimate cost standpoint, should be performed.

8. Use of Stainless Steel

Stainless steel is used as the primary structural material in the reactor because it is a non-magnetic material. Other, less costly, structural materials should be investigated. This is also suggested by the potential problem associated with Cr resources discussed earlier. However, no reasonable alloys appear to be ready for this role at the present time.

Appendix A

Compatibility of Stainless Steels with Oxygen-Contaminated Helium[+]

1. Introduction

Pressurized helium possesses several advantages as a CTR and blanket cooling medium: it is chemically inert, it is not activated by neutron irradiation, and it does not interact with magnetic fields. However, reactive gaseous impurities present in a helium coolant stream, such as O_2, N_2, CO, CO_2 and CH_4 maintain their chemical activity in the inert helium gas. The problems associated with the resulting gas-metal reactions must be recognized before nominally pure helium, or helium with intentional impurities added, is approved for use in an actual CTR system. As purposeful additions of O_2 to the primary helium coolant are being considered as a means of reducing T_2 activity, special consideration must be given to the long-term effect of a continuously replenished O_2 contaminant on the stainless steel structure.

2. Objectives

The primary objective of the present work is to estimate the extent of stainless steel corrosion and mechanical property degradation which will result from the use of oxygen-contaminated helium as the primary coolant in the UWMAK-II design. Secondary objectives, related to the concept of tritium control by O_2 additions to the helium coolant, involve estimation of the O_2 necessary to maintain the system's "normal"oxidation rate, and estimation of the potential release rate of nascent tritium by T_2O oxidation of the helium-steam heat exchanger tubing.

[+]Originally appeared as UWFDM-117, Nucl. Eng. Dept. Report, Univ. of Wisconsin (Oct. 1974) by R. E. Westerman, Battelle Northwest Laboratories.

3. Conclusion and Comments

- The metal loss rate due to oxidation of an austenitic stainless steel in helium contaminated with 0_2 at 10^{-2} Torr at 650°C is estimated to be ~3 x 10^{-5} cm/yr. Reduction of net metal cross-section by corrosion does not appear to be a matter of concern, though the foregoing value does not take into account possible enhancement of corrosion rates by radiation.
- The presence of 10^{-2} Torr 0_2 in the helium coolant should cause no significant deterioration in the long-term tensile, creep, and creep-rupture properties of an austenitic stainless steel at 650°C. Resistance to creep deformation is likely to be higher than in the case of a completely inert system. The 0_2 is likely to have a deleterious effect on fatigue life, however, especially if the fatigue is fixed-strain, rather than fixed-load, as in the former case no benefit is gained from oxidation strengthening.
- Low concentrations of N_2 present in the helium will most likely result in an increase in creep strength over values obtained in vacuo.
- Presence of reducing gases, such as H_2 and CO, can cause a decrease in creep strength, if the oxidizing power of the gas is such that selective oxidation of steel constituents occurs, e.g., oxidation of Cr, Ti, or Nb.
- Hydrocarbon impurities tend to carburize stainless steels, with an initial increase in creep strength but ultimate embrittlement.
- Presence of CO and CO_2 will generally carburize austenitic steels, causing an increase in creep strength and eventual embrittlement. Low partial pressures (i.e., a few micro-atmospheres) of CO and CO_2 should

be tolerable, however, as high-temperature gas reactor materials are generally performing well in such environments.

- At a pressure of 10^{-2} Torr, the impingement rate of O_2 molecules on the stainless steel surface at 650°C is a factor of $\sim 10^5$ greater than the oxygen supply required to maintain the steel's oxidation rate. This suggests that maintaining an O_2 pressure of 10^{-2} Torr is both adequate, to maintain the anticipated oxidation kinetics, and practical, from an operational standpoint.
- If the T_2O present in the primary system participates substantially and continuously in the "normal" stainless steel oxidation in the helium-steam heat exchanger there is a good possibility of finding unacceptable permeation of the heat exchanger tubing by the nascent T formed during the oxidation reaction. Conversely, protium from the steam side will tend to pass into the primary coolant by the same mechanism, contaminating the T_2O residing in the molecular sieve.
- Sulfur-bearing or carbonaceous materials (such as oil) must be rigorously excluded from the primary helium system.
- There are experimental data indicating that the mechanical properties of Nb-stabilized steels, such as Type 347, are superior to Ti-stabilized steels, such as Type 321, in contaminated helium environments of low oxidizing potential.

4. Corrosion Rates in Oxygen-Contaminated Helium

The oxidation rates of stainless steels under projected UWMAK-II primary coolant operating conditions (650°C, 10^{-2} Torr O_2) have not been determined experimentally and so must be estimated from available data. In order to estimate the oxidation rates, the small amount of quantitative experimental

data available will be evaluated for applicability, and the results extrapolated into the temperature and pressure range of interest. Though the hazards associated with extrapolation of corrosion data are well known, it appears to be a useful procedure in the present case, as extreme changes in the corrosion rate control mechanisms are not expected under the new (extrapolated) conditions.

The potentially important enhancement of oxidation rates by radiation has not been considered in this review.

4.1 Mechanisms

The mechanisms of oxidation of stainless steel in high-temperature gaseous environments are extremely complex and not at all well understood. Some qualitative generalizations are possible, though they are derived from the results of high-temperature work (> 700°C) and so may not accurately describe conditions existing at 650°C and below.

Caplan and Cohen[1] exposed specimens of Types 302, 330, and 309 stainless steels to dry air and wet air at temperatures in the range 871° - 1093°C. They continuously monitored the weight changes during oxidation, and analyzed the crystal structure of the scales formed by X-ray diffraction. The longest test reported was of ~1000 hr duration.

Moisture in the air greatly accelerated the oxidation rate of Type 302ss; the effect on Type 309 was much less marked. The weight gain vs time curves were not smooth in either gaseous environment but exhibited sharp "breaks", caused by a temporary loss of protection by the oxide scale. The two major scale constituents were found to be spinels, of the general form M_3O_4, capable of wide composition variability:

$(Fe, Ni, Mn)\ O \cdot (Fe, Cr, Mn)_2\ O_3$

and rhombohedral oxides, M_2O_3:

$(Fe, Cr, Mn)_2\ O_3$.

The scale composition was found to vary not only with depth, but from one area to another on the specimens. A further complicating factor was the profound effect of prior surface treatment on oxidation rates. An electropolished sample of Type 309ss showed a lower oxidation rate than an abraded sample, and specimens abraded and preheated in high purity helium showed still greater oxidation rates. The authors concluded that a realistic interpretation of the scaling observed would be impossible, because of the many unknown factors contributing to the oxidation process and the inherent complexity of commercial alloys.

Yearian, Randell and Longo[2] studied the films formed on commercial steels varying in Cr content from 5 to 26 percent after exposure in air and oxygen in the temperature range 700° -1160°C for times up to 100 hr. They concluded that for exposures resulting in metal loss rates < 10 mg/cm^2-day, the essential scale component is Cr_2O_3. (This finding is relevant to the UWMAK-II blanket-heat exchanger system.) This is accompanied by α Fe_2O_3 in an amount increasing with the iron content of the alloy and the rate of attack. When the alloy contains a few tenths percent Mn, the scale may include relatively large quantities of $MnCr_2O_4$, especially in the case of high Cr alloys and for low temperature oxidations in air.

Very high temperature data on the oxidation of Type 304Lss in steam and air have been reported by Bittel, Sjodahl, and White.[3] Temperatures were in the range 1000° to 1375°C; test durations were a matter of hours. The oxidation rates in steam were much greater than those in air at equivalent

temperatures. The rate control in steam is ascribed to diffusion through a Fe-Ni-Cr spinel layer. The protective oxide film for the air oxidation case was found to be essentially Cr_2O_3. They further found that the oxidation kinetics data for pure Cr reported by Hagel[4] agreed very well with their air oxidation results.

If a metal forms a protective film as it oxidizes, with diffusion through the oxide film exerting the rate control, parabolic oxidation kinetics are expected:

$$W^2 = Kt \qquad (1)$$

where: W = oxygen weight gain, mg/cm^2
K = parabolic rate constant, $(\frac{mg}{cm^2})^2\ sec^{-1}$
t = time in seconds.

These parabolic oxidation kinetics are found, incidentally, in the case of oxidation of pure chromium.

If the corrosion of a metal is not impeded by the thickening oxide scale, e.g., in the case of a cracked, porous, or non-adherent corrosion product, linear oxidation kinetics are frequently found, i.e.,

$$W = Kt. \qquad (2)$$

In this case "K" is a linear rate constant, of dimensions mg/cm^2-sec.

It is known that stainless steels generally exhibit oxidation rate behaviors lying somewhere between these two extremes,[5,6] with the behavior in any one instance dependent on the environment, the temperature, the particular alloy, its surface pretreatment, and the test duration. This variable behavior makes exact oxidation rates impossible to predict without recourse to experiment, as has been previously noted. However, the variable, unpredictable behavior becomes easier to understand with an appreciation of the complex reactions going on at the alloy surface.

4.2 Oxidation Rates Under UWMAK-II Conditions

The oxidation data most relevant to expected UWMAK-II conditions appear to be that of Eberle, Ely, and Dillon,[6] who have reported on the corrosion and mechanical property behavior of a number of candidate superheater materials. As part of their study they exposed specimens of a variety of stainless steels to laboratory air at 760°C for 1270 hr, then calculated the corrosion rates from weight change data. Their data are reproduced in Table I.

TABLE I

Corrosion Rates of Stainless Steels in Air[6]

760°C, 1270 hr test duration

Steel	Corrosion Rate, mils per year (mpy)
AISI 304	0.22
AISI 321	0.14
AISI 347	0.32
AISI 316	0.13
AISI 318	0.14

Average = $\frac{0.2 \text{ mpy}}{} = 5 \times 10^{-4}$ cm/yr

The data of Table 1 are expressed in terms of a linear rate (mils per year). No attempt was made on the part of the authors to determine the strict time-dependence of the weight gain (metal loss)* observed. Even if the time dependence were known, the short test duration (53 days) would not permit accurate long-term extrapolation of the observed data to anything approaching the projected life time of the UWMAK-II primary system. For this reason, a conservative approach will be taken to the foregoing data: The average value

*For 300 series stainless steels, 0.1 mil of metal $\approx$ 1.0 mg O_2/cm^2

of all the steels tested will be used, even though the corrosion rate for Type 316 is lower than the average; the corrosion rate law will be considered linear; and the corrosion rate exhibited for the first 53 days of the steel's exposure (the data of Table 1) will be considered representative of its long-term behavior, even though the rate is apt to slow down with increasing time. The last two assumptions are obviously closely related.

The corrosion rate of a steel will be substantially less at 650°C than at 760°C, if the mechanism of corrosion rate control does not change. If we make this reasonable assumption, we may estimate the corrosion rate at the lower temperature if the activation energy for the corrosion rate control process is known. Such an activation energy has not been reported for stainless steels for the temperature range and environments of interest. However, the 760°C corrosion rates reported for pure chromium[4] in 76 Torr O_2 lie within a factor of two, in terms of oxygen consumption, of the stainless steel data of Table 1. Because the mechanism of oxidation in both cases is thought to be diffusion of cations outward to the gas-metal interface through a metal-deficit lattice, the activation energy obtained for Cr oxidation should be approximately applicable to the stainless steel situation.

Consider the parabolic rate law for Cr:

$$W^2 = Kt, \quad \text{or} \quad W = K^{1/2}t^{1/2} \tag{3}$$

where $$K = 0.111 \exp(-59{,}000 \pm 1800/RT)\,(\text{gm-cm}^{-2})^2\,\text{sec}^{-1} \tag{4}$$

The instantaneous rate of oxidation may be found by taking the derivative of Eq. (3) with respect to time:

$$\frac{dw}{dt} = \frac{K^{1/2}}{2t^{1/2}} \quad \frac{mg}{cm^2\text{-sec}} \tag{5}$$

At any given time, the instantaneous oxidation rate is proportional to $K^{1/2}$. A temperature correction to $K^{1/2}$ may be determined which is applicable to the linear kinetics we have assumed:

$$\frac{\text{Oxidation Rate at 760°C}}{\text{Oxidation Rate at 650°C}} = \frac{K_{760}^{1/2}}{K_{650}^{1/2}} = \left(\frac{e^{-\frac{59,000}{(1033)(1.99)}}}{e^{-\frac{59,000}{(923)(1.99)}}} \right)^{1/2} = 5 \tag{6}$$

From Eq. (6) we find that a 5-fold reduction in oxidation rate could be expected in lowering the temperature from 760°C to 650°C. This reduces the assumed oxidation rate from 0.2 mpy (Table 1) to 0.04 mpy, or $\sim 10^{-4}$ cm/yr.

Determining the effect of reduced pressure on the oaidation rate involves a somewhat less certain extrapolation. Hagel notes that pressure effects predicted by theory are not at all well borne out in the case of Cr oxidation.[4] (Theory predicts a very small effect of pressure, but an even smaller effect is found.) Charlot and Westerman[7] studied the effect of oxygen pressure on the oxidation rate of Hastelloy X-280 over the pressure range 0.039 to 25 Torr at 1120°C. It was found that the <u>parabolic</u> oxidation rate constant is proportional to the one-fifth power of the oxygen pressure:

$$K \left(\frac{mg}{cm^2}\right)^2 \text{ sec}^{-1} \propto P_{O_2}^{1/5} \text{ Torr} \tag{7}$$

Because this alloy is believed to oxidize at a rate determined by the diffusion of cations through a Cr_2O_3 - rich layer[8] we can tentatively justify application of Eq. 7 to the oxidation of stainless steel.

It should also be noted that an oxygen pressure of 10^{-2} Torr at 650°C is sufficient to oxidize all of the principal metallic constituents of a 300 series stainless steel, thereby minimizing the possibility of selective

attack, which can occur in the presence of reducing species, such as CO or H_2.

If we utilize the same procedure as in Equations (5) and (6) we find that

$$\frac{\text{Oxidation rate in air (150 Torr } O_2)}{\text{Oxidation rate in } 10^{-2}\text{Torr } O_2} \propto \left(\frac{150 \text{ Torr}}{10^{-2}\text{Torr}}\right)^{1/10} = 3 \qquad (8)$$

By applying this factor of 3 to the one-atmosphere air data of 0.04 mpy we obtain a value of 0.01 mpy (3×10^{-5}cm/yr) for the metal loss rate of stainless steel at 650°C and 10^{-2} Torr pressure. This value is reasonable, but the approximations used and the assumptions made in obtaining the value must be recognized. It appears that there need be no concern that gross corrosion effects will significantly reduce the net metal section of any UWMAK-II structural component operating under the temperature-pressure conditions described, though it must be reiterated that radiation-enhancement of the oxidation rates has not been considered in this treatment.

4.3 Oxygen Demands

It is next necessary to determine the oxygen demands imposed on the contaminated helium to satisfy the oxidation rates described in the foregoing section. A stainless steel penetration rate of 0.01 mpy is approximately equivalent to 0.1 mg O_2/cm^2-yr, or 3×10^{-12}gm $O_2/sec\text{-}cm^2$. The impingement rate of O_2 molecules on the steel surface at 650°C and 10^{-2} Torr pressure is 2×10^{-7} gm O_2/cm^2-sec. There is a factor of 10^5 times more oxygen incident on the surface at 10^{-2}Torr than is required to maintain the expected oxidation rate, so that there appears to be no unusual oxygen transmission or makeup demands under the expected operating conditions.

If the area of the blanket tubing is assumed to be 4×10^8 cm^2, ~ 40 kg of oxygen/yr will be required to satisfy the oxygen consumption demands of the corroding stainless steel. This is a modest quantity, approximately equivalent

to the contents of 5 common (size H) cylinders.

4.4 T_2O as Oxidant

A legitimate concern in T control is the possibility that T_2O will enter into the stainless steel oxidation reactions, liberating nascent T which would be able to diffuse through the walls of the primary system.

It is expected that T_2O will be present in the system at a pressure of ~ 1×10^{-3} Torr. If the O_2 pressure is maintained at 10^{-2} Torr, a level greatly in excess of that required to maintain the "normal" oxidation rate (see Section 4.3), it will be at a pressure only ~ 10 times greater than that of the T_2O. (By the reasoning of section 4.3 it must be noted that the pressure of T_2O is also maintained at a level greatly in excess of that required to maintain "normal" oxidation of the stainless steel.)

Let us conservatively* assume that only T_2O enters into the corrosion of the primary helium coolant/steam heat exchanger and that all nascent T liberated from the reaction will permeate the heat exchanger walls. Assume that the heat exchanger material corrodes at the same rate as the primary system material, i.e., assume it is equivalent to a 300 series stainless steel. As the average temperature of the heat exchanger is only 460°C, we must compute the oxidation rates expected at this lower temperature by means of the same approximation technique used before [Eq. (6)]:

$$\frac{\text{Oxidation Rate at } 650^\circ\text{C}}{\text{Oxidation Rate at } 460^\circ\text{C}} \propto \left(\frac{e^{-\frac{59{,}000}{1.99 \times 923}}}{e^{-\frac{59{,}000}{1.99 \times 733}}} \right)^{1/2} = 64 \qquad (9)$$

*"Conservative" is always used herein in the sense of anticipating the most extreme, or worst, case.

The oxygen consumption rate at 460°C would then be expected to be approximately

$$3 \times 10^{-12} \frac{\text{gm } O_2}{\text{sec-cm}^2} \times \frac{1}{64} = 4.7 \times 10^{-14} \frac{\text{gm } O_2}{\text{sec-cm}^2} \qquad (10)$$

For each gram oxygen consumed in the corrosion reaction, 2/16 gm T will be liberated, or

$$\text{T liberation rate} = \frac{2}{16} \times 4.7 \times 10^{-14} = 5.8 \times 10^{-15} \frac{\text{gm T}}{\text{sec-cm}^2} \qquad (11)$$

If we multiply the value of Eq. 11 by the heat exchanger area, we obtain

$$5.8\text{x}10^{-15} \frac{\text{gm T}}{\text{sec-cm}^2} \times 8.3\text{x}10^{8}\text{cm}^2 \times 8.6\text{x}10^{4} \frac{\text{sec}}{\text{day}} = 0.42 \frac{\text{gm T}}{\text{day}} \qquad (12)$$

or

$$0.42 \frac{\text{gm T}}{\text{day}} \times 9600 \frac{\text{Ci}}{\text{gm T}} = \underline{4000 \text{ Ci/day}} \qquad (13)$$

While the result of Eq. 13 is based on rather conservative assumptions, the result is far higher than the 1.8 Ci/day estimated by Wittenberg on the basis of T permeation of heat exchanger tubing. It should be noted also that the assumption of preferential metal oxidation by the T_2O molecule in the presence of a preponderance of O_2 is not overly extreme, as this phenomenon is found in the oxidation of zirconium alloys in this temperature range.

It would appear that generation of T by steel oxidation remains an open question, and one that may eventually require a laboratory study for resolution. If T generation is found to be a problem under the test parameters described, a logical solution would be to increase the O_2 pressure and decrease the T_2O pressure. The latter could be accomplished by increasing the size and/or reducing the temperature of the molecular sieve bed.

Within the steam generator pressure tubing, the reaction between steam and the pressure tube alloy will constitute a continuous source of nascent protium. The protium will tend to permeate the pressure tubing and enter the primary coolant, where it will become oxidized and eventually reside, along with the T_2O, in the molecular sieve. While this does not constitute a material compatibility problem, it is worth considering if an attempt is made to evaluate the purity of the tritium oxide residing in the molecular sieve. It should also be taken into account in sizing the molecular sieve beds, so that sufficient capacity is assured.

5. Mechanical Properties

The effects of corrosive environments on the long-term mechanical properties of a structural material are of obvious concern to the system designer, as any degradation process must be anticipated and suitable allowance made, if necessary, to ameliorate the effect. This may be accomplished by environment control, material selection, increase in sectional area, design modification, or a combination of two or more of these factors. In general, a high-temperature corrosive attack consists of one or more of the following:

1) Surface reaction, with uniform or selective loss of alloy constituents;

2) Subsurface reaction, such as internal oxidation;

3) Contaminant solution effects.

In addition to the foregoing, undesirable changes in the metal microstructure may take place due to the operating temperature alone, such as precipitate coarsening, sensitization, sigma phase precipitation, etc. In this section the effect of various high-temperature environments on the mechanical properties of stainless steels will be reviewed and the results analyzed for applicability to the UWMAK-II reactor design.

Most of the available data concerning the effect of environment on the high-temperature mechanical properties of stainless steels consist of creep and creep-rupture studies. The data are found to be highly variable and difficult to interpret, as the results depend in an intricate manner on temperature, stress level, reactive gas(es) present, steel composition, specimen geometry, and specimen pretreatment.

The creep, stress-rupture, tensile, impact, and fatigue properties of Type 316 ss in air, helium, and sodium at 650°C have been reported by Kirschler and Andrews.[11] The creep rates in helium and sodium were slightly higher than in air. The stresses required to produce 1 per cent creep in helium and sodium in 10,000 hr were within 15 percent of the corresponding stress in air. The stress-rupture tests, to 4000 hr maximum time, showed no significant difference in rupture strengths in any of the three environments. In the cyclic strain tests the specimens fatigued in air withstood the least cycles before failing and the specimens in helium the most. At 1 per cent cyclic strain, the specimens in air failed in ~ 1500 cycles, while the specimens in helium withstood ~40,000 cycles. The fatigue test yielded the only results which were environment-sensitive.

LeMay, Truss, and Sethi[12] determined the creep properties of Type 347ss over the temperature range 604°-791°C in air, nitrogen, argon, and vacuum (5×10^{-6} Torr). They found the rupture life to be lower in air than in argon or vacuum over the entire temperature range. The elongation at fracture was higher in air than in the other environments in every test; the lowest elongation-at-fracture reported was 13 per cent and the lowest reduction-in-area 16 per cent. Both of these minimums came from tests in the argon environment. It is possible that selective oxidation and intergranular attack was taking place in the argon tests.

Eberle, Ely, and Dillon[6] performed tensile and impact tests on specimens of Types 304, 321, 347, 316, and 318 steels after exposure of 6950 hr to a 760°C superheater atmosphere, i.e., steam on one side and flue gas on the other. Both steam and flue gas are more corrosive towards these steels than air. The tube wall thicknesses ranged from 1 cm (Type 347) to 1.2 cm (all other steels). In both room-temperature and 732°C tensile tests, the alloys which had seen superheater service exhibited higher yield and ultimate strengths and lower ductilities than the control specimens. The lowest post-service room temperature ductility (elongation in 1.5 in.) was 22 percent, for Type 347ss; the lowest 732°C ductility was 57.3 percent, also for Type 347. The room temperature Charpy impact values (for half-width specimens) were found to be significantly reduced by the superheater exposure. Type 304 retained 44% of its pre-exposure impact strength, while Type 318 retained the least, only 20% (8.9 ft-lb). The authors concluded that "the remaining notch toughness appears to be adequate for superheater service if there is no further significant decrease."

McCoy[13] studied the creep-rupture behavior of Type 304 ss in Ar, CO, CO_2, H_2, N_2, O_2 and air at temperatures of 816° and 927°C. The environments listed in order of a decreasing strengthening effect at 816°C and 3,400 psi stress are CO (lowest strain rate), CO_2, N_2, air, Ar, H_2 and O_2 (highest strain rate). The results are similar at 927°C and 1200 psi stress, except that Ar and H_2 environments yielded higher strain rates than the O_2 environment. McCoy pursued the effect of O_2 pressure on creep rate by exposing specimens to Ar-O_2 mixtures at 1 atm total pressure at 816°C. He found a maximum creep rupture life and a minimum creep rate at ~10 ppm O_2 in Ar. These effects were considered "inexplicable". Exposure of the specimens to the CO-CO_2 environments resulted in carburization and hardening of the specimens, hence the increase

in creep strength. Nitrogen is thought to strengthen the steel through a hardening mechanism near the sample surface.

The puzzling effect of 0_2 on creep strength was investigated in more detail by Rodriquez,[14] who again exposed Type 304 ss specimens to Ar-0_2 mixtures at 815° and 927°C. At concentrations of 0_2 in the range 0 to 70 ppm, the creep rate decreases with increasing 0_2 content at 815°C and 3400 psi stress. For 0_2 concentrations between 70 and 250 ppm, the rate increases to a maximum value. The creep rate again decreases at 0_2 concentrations above ~250 ppm, with the creep rate in pure 0_2 approximating the low rate found at ~70 ppm. At 927°C and 2000 psi stress the data follow the same trend. Metallographic analysis showed no evidence of internal oxidation and no increase of oxygen in the bulk samples with increasing oxygen level in the environment. The surface crack densities were found to increase with oxygen concentration in the environment, as reported by McCoy. The average crack depth attained a maximum value at ~250 ppm oxygen, i.e., the level corresponding to maximum creep rate. Rodriquez explains the oxygen pressure dependence of creep rate on the basis of the properties of the oxide scale formed in the different environments, i.e., a hard, tenacious scale will produce a higher creep strength than a weak, easily spalled layer.

Smith, Shahinian, and Achter[15] determined fatigue crack growth rates in Type 316ss at 500° and 800°C as a function of 0_2 pressure. Crack growth rates showed a sharp increase with 0_2 pressure in an intermediate pressure range (10^{-3} to 1.0 Torr), but little change at pressures outside this range. At 500°C, 1 Torr 0_2 pressure reduced the fatigue life by a factor of ~100 compared with that in vacuum; at 800°C the effect was somewhat smaller. A model in which the rate of fresh metal surface production equals

the rate of surface coverage by gas molecule adsorption explains the 500°C results, but at 800°C the model does not fit the experimental data. The authors note that oxidation strengthening, leading to increased fatigue resistance, can take place at the higher temperature. Smith and Shahinian[16] found that the rate of strain hardening of Type 316ss during cyclic straining prior to crack initiation is dependent on O_2 pressure, with a pressure as low as 5×10^{-4} Torr causing hardening at 500°C. A pressure of 10^{-3} Torr initiated hardening at 800°C.

The high-temperature gas-cooled reactor concept has been resonsible for a great deal of research work on the effect of contaminated helium on mechanical properties of stainless steels and superalloys.[17-20] While most of the helium atmospheres used in the studies are contaminated with CO and H_2, rather than O_2, the temperatures are in the appropriate range, and the relatively low oxidizing power of the atmospheres used could represent a possible transient condition in a CTR system.

Weinberg and Scoffin[17] exposed tensile and impact-tensile specimens of Types 321H, 347, 304 and 403 stainless steels and Inconel to impure helium at 650° and 760°C for times to 3000 hr. Two helium impurity levels were used: 200-300 ppm CO with 200-300 ppm H_2, and 2000-3000 ppm CO with 2000-3000 ppm H_2. Oxidation rather than carburization appeared to be the major corrosion process. Both carburization and decarburization were observed. None of the materials studied exhibited a large change in mechanical properties after the 650°C exposure. After the 760°C exposures only moderate changes in mechanical properties were observed for all materials except Type 321ss which exhibited a large decrease in ductility after 1500 hr in the high-impurity environment.

In general, however, control specimens encapsulated in vacuo and held at the test temperatures were affected as greatly as the specimens exposed to the impure helium environments.

Wood, Farrow, and Burke[18] studied the effect of air and impure helium on the creep and rupture behavior of Type 316ss at 800°C. The helium environments were maintained at two impurity levels: "nominally pure", with a maximum total impurity level of ~1000 ppm (largely H_2, CO, H_2O, and N_2), and "nominally impure", with a nominal composition of 1000 ppm H_2, 1000 ppm CO, and 100 ppm H_2O. The rupture times were found to be shorter and creep rates higher in both helium environments than in air. A rough averaging of the widely scattered data points yields a factor of four lower creep rate in air than in the helium environments, and a factor of three increase in rupture time in air over the helium environments. Metallographic examination of failed specimens revealed a pronounced difference in oxidation between the specimens tested in air and those tested in helium. Specimens tested in air showed thick, relatively uniform scales, while those tested in helium showed non-uniform oxide layers, grain boundary oxide penetration, and generally selective attack. The authors suggest that the lower creep strength in the contaminated helium is due to preferential oxidation of Cr, Al, and Ti at the grain boundaries in the low-oxidizing-potential helium, resulting in a lowering of the grain boundary surface energy and mechanical opening of the grain boundaries.

Cook, Barford, and Willoughby[19] cite some preliminary results for Type 316ss creep tested at 750°C in air, vacuum (10^{-5} Torr), and impure helium (He + 500 ppm CO, 500 ppm H_2, and 50 ppm H_2O at 10 psig). The creep rate in the impure helium was substantially higher (about a factor of two) than the

creep rates in the air and vacuum environments. Again, the higher rate is ascribed to a selective oxidation of the alloy in the impure helium, with sub-surface penetration of the reactive environment and depletion of alloying elements near grain boundaries. These findings are consistent with those of Wood, et.al.[18]

Board[21], Huddle[22], and Darras[23] have all noted the apparent superiority of Nb-stabilized steels, such as Type 347, to Ti-stabilized steels, such as Type 321, in contaminated helium environments. These conclusions are consistent with the findings of Weinberg and Scoffin,[17] who reported an example of poor performance of Type 321 steel. Board[21] further concludes that "it would seem prudent at this stage to restrict the choice of materials for the steam cycle HTR [High Temperature Reactor] to alloys which do not depend on titanium and aluminum for strengthening." Such a restriction would, of course, rule out the use of gamma-prime hardened alloys, such as Incoloy 800 and Nimonic PE-16.

It must be recognized that stainless steels are being used extensively in high-temperature gas-cooled fission reactors. The alloys are generally performing well. Dragon Project and AVR (Arbeitsgemeinschaft Versuchsreaktor AVR GmbH., Dusseldorf) experience indicate essentially no compatibility problems with structural materials in normal (contaminated) helium service.[24,25]

Sulfur and carbonaceous materials must be rigorously excluded from the primary coolant. Board[20] points out that sulfur in ppm quantities can attack nickel-bearing alloys by forming the NiS/S eutectic, which melts at 508°C. The eutectic may then oxidize, freeing the sulfur. Carbonaceous materials, such as methane, lubricating oils or greases, diffusion pump oil, etc., can react rapidly with stainless steel surfaces at high temperature,

causing gross carburization and embrittlement. While this type of attack may be considered beyond that expected from lightly contaminated helium, there is a possibility that it could occur, e.g., in the event of an oil leak or some other unexpected ingress of carbon-bearing material. Such fault conditions must be anticipated and appropriately guarded against.

REFERENCES

1. D. Caplan, M. Cohen, "High Temperature Oxidation of Chromium-Nickel Steels", Corrosion, Vol. 15, No. 3, March, 1959, pp. 141t-146t.

2. H. J. Yearian, E. C. Randell, T. A. Longo, "The Structure of Oxide Scales on Chromium Steels", Corrosion, Vol. 12, No. 10, October, 1956, pp. 515t-525t.

3. J. T. Bittel, L. H. Sjodahl, J. F. White, "Oxidation of 304L Stainless Steel by Steam and by Air", Corrosion, Vol. 25, No. 1, January, 1969, pp. 7-14.

4. W. G. Hagel, "Factors Controlling the High-Temperature Oxidation of Chromium", ASM Transactions, Vol. 56, 1963, pp. 583-599.

5. Reference 2, p. 64. Work of Rickett, et.al., Heindlehofer et.al., and McCullough et.al. cited.

6. F. Eberle, F. G. Ely, J. A. Dillon, "Experimental Superheater for Steam at 2000 psi and 1250°F-Progress Report after 12,000 hr of Operation", Trans. ASME, Vol. 76, 1954, pp. 665-677.

7. L. A. Charlot, R. E. Westerman, "High Temperature Corrosion and Evaporation of Haynes 25 and Hastelloy X-280", Corrosion, Vol. 23, February, 1967, pp. 50-56.

8. S. T. Wlodek, "The Oxidation of Hastelloy Alloy X", Trans. AIME, Vol. 230, 1964, pp. 177-185.

9. S. Dushman, J. M. Lafferty, "Scientific Foundations of Vacuum Technique," Second Edition, John Wiley and Sons, Inc., New York, p. 14.

10. L. Wittenberg, unpublished work.

11. L. H. Kirschler, R. C. Andrews, "A Limited Comparison of the Mechanical Strength of Austenitic Steel in 1200°F Sodium, Air, and Helium", Trans. ASME, J. of Basic Engineering, Paper No. 69-Met-F, 1969. See also ANL 7520, Pt. 1.

12. I. LeMay, K. J. Truss, P. S. Sethi, "Effect of Some Gaseous Environments on the Creep of a Stainless Steel," ASME Paper 69-Met-3, 1969.

13. H. E. McCoy, "The Influence of Various Gaseous Environments in the Creep-Rupture Properties of Nuclear Materials Selected for High-Temperature Service", Proceedings of the Conference on Corrosion of Reactor Materials, Vol. 1; Vienna, International Atomic Energy Agency, pp. 263-296, 1962.

14. P. Rodriguez, High Temperature Creep Behavior of Type 304 Stainless Steel in Argon-Oxygen Environments of Different Oxygen Partial Pressures, ORNL-TM-1124, May 5, 1965.

15. H. H. Smith, P. Shahinian, M. Achter, "Fatigue Crack Growth Rates in Type 316 Stainless Steel at Elevated Temperature as a Function of Oxygen Pressure," Trans. AIME, Vol. 245, pp. 947-953, 1969.

16. H. H. Smith, P. Shahinian, "Effect of an Oxygen Atmosphere in Cyclic Hardening in Type 316 Stainless Steel," Metallurgical Transactions, Vol. 1, pp. 2007-2009, 1970.

17. A. F. Weinberg, J. M. Scoffin, Exposure of Reactor Structural Materials to Impure Helium at Elevated Temperatures, GA 2998, March, 1962.

18. D. S. Wood, M. Farrow, W. T. Burke, "A Preliminary Study of the Effect of Helium Environment on the Creep and Rupture Behavior of Type 316 Stainless Steel and Incoloy 800", Effects of Environment on Material Properties in Nuclear Systems, BNES Conference on Corrosion, pp. 213-228, 1971.

19. R. H. Cook, J. Barford, G. Willoughly, Ibid., p. 234.

20. J. Board, "Metallurgical Aspects of the Fast Breeder Reactor and the High-Temperature Gas-Cooled Reactor", Paper No. 4, Power Conference, Lausanne, Conf-720578-1, 1972.

22. R. A. U. Huddle, "The Influence of HTR Helium on the Behavior of Metals in High Temperature Reactors", Effects of Environment on Material Properties in Nuclear Systems, BNES Conference on Corrosion, pp. 203-212, 1971.

23. R. Darras, Ibid., p. 230.

24. R. Nieder, G. Ivens, "The Effect of Coolant Gas Impurities and Fast Neutron Dose on the Materials of the Primary Circuit of the AVR," Ibid.

25. High Temperature Reactor Project Dragon, 8th Annual Report 1966-67, O.E.C.D., European Nuclear Energy Agency, 1967, pp. 39-49.